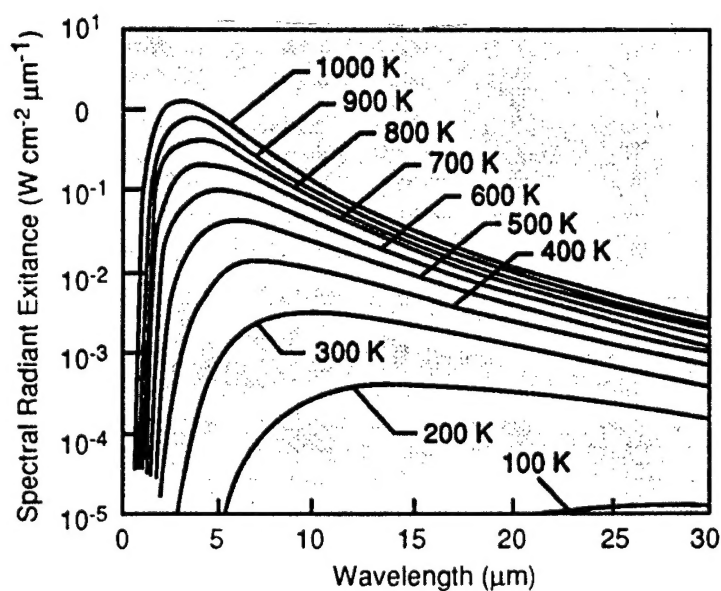


The Infrared & Electro-Optical Systems Handbook

VOLUME 1

Sources of Radiation

George J. Zissis, Editor



DISTRIBUTION STATEMENT A:
Approved for Public Release -
Distribution Unlimited

Sources of Radiation

V O L U M E

1

The Infrared and Electro-Optical
Systems Handbook

199906661
470 40906661

The Infrared and Electro-Optical Systems Handbook

Joseph S. Accetta, David L. Shumaker, *Executive Editors*

- **VOLUME 1. Sources of Radiation,** George J. Zissis, *Editor*
 - Chapter 1. Radiation Theory, William L. Wolfe
 - Chapter 2. Artificial Sources, Anthony J. LaRocca
 - Chapter 3. Natural Sources, David Kryskowski, Gwynn H. Suits
 - Chapter 4. Radiometry, George J. Zissis

- **VOLUME 2. Atmospheric Propagation of Radiation,** Fred G. Smith, *Editor*
 - Chapter 1. Atmospheric Transmission, Michael E. Thomas, Donald D. Duncan
 - Chapter 2. Propagation through Atmospheric Optical Turbulence, Robert R. Beland
 - Chapter 3. Aerodynamic Effects, Keith G. Gilbert, L. John Otten III, William C. Rose
 - Chapter 4. Nonlinear Propagation: Thermal Blooming, Frederick G. Gebhardt

- **VOLUME 3. Electro-Optical Components,** William D. Rogatto, *Editor*
 - Chapter 1. Optical Materials, William L. Wolfe
 - Chapter 2. Optical Design, Warren J. Smith
 - Chapter 3. Optomechanical Scanning Applications, Techniques, and Devices, Jean Montagu, Herman DeWeerd
 - Chapter 4. Detectors, Devon G. Crowe, Paul R. Norton, Thomas Limperis, Joseph Mudar
 - Chapter 5. Readout Electronics for Infrared Sensors, John L. Vampola
 - Chapter 6. Thermal and Mechanical Design of Cryogenic Cooling Systems, P. Thomas Blotter, J. Clair Batty
 - Chapter 7. Image Display Technology and Problems with Emphasis on Airborne Systems, Lucien M. Biberman, Brian H. Tsou
 - Chapter 8. Photographic Film, H. Lou Gibson
 - Chapter 9. Reticles, Richard Legault
 - Chapter 10. Lasers, Hugo Weichel

- **VOLUME 4. Electro-Optical Systems Design, Analysis, and Testing,** Michael C. Dudzik, *Editor*
 - Chapter 1. Fundamentals of Electro-Optical Imaging Systems Analysis, J. M. Lloyd
 - Chapter 2. Electro-Optical Imaging System Performance Prediction, James D. Howe

-
- Chapter 3. Optomechanical System Design, Daniel Vukobratovich
 - Chapter 4. Infrared Imaging System Testing, Gerald C. Holst
 - Chapter 5. Tracking and Control Systems, Robert E. Nasburg
 - Chapter 6. Signature Prediction and Modeling, John A. Conant,
Malcolm A. LeCompte

■ **VOLUME 5. Passive Electro-Optical Systems,**

Stephen B. Campana, *Editor*

- Chapter 1. Infrared Line Scanning Systems, William L. McCracken
- Chapter 2. Forward-Looking Infrared Systems, George S. Hopper
- Chapter 3. Staring-Sensor Systems, Michael J. Cantella
- Chapter 4. Infrared Search and Track Systems, Joseph S. Accetta

■ **VOLUME 6. Active Electro-Optical Systems,** Clifton S. Fox, *Editor*

- Chapter 1. Laser Radar, Gary W. Kamerman
- Chapter 2. Laser Rangefinders, Robert W. Byren
- Chapter 3. Millimeter-Wave Radar, Elmer L. Johansen
- Chapter 4. Fiber Optic Systems, Norris E. Lewis, Michael B. Miller

■ **VOLUME 7. Countermeasure Systems,** David Pollock, *Editor*

- Chapter 1. Warning Systems, Donald W. Wilmot, William R. Owens, Robert J. Shelton
- Chapter 2. Camouflage, Suppression, and Screening Systems, David E. Schmieder, Grayson W. Walker
- Chapter 3. Active Infrared Countermeasures, Charles J. Tranchita, Kazimieras Jakstas, Robert G. Palazzo, Joseph C. O'Connell
- Chapter 4. Expendable Decoys, Neal Brune
- Chapter 5. Optical and Sensor Protection, Michael C. Dudzik
- Chapter 6. Obscuration Countermeasures, Donald W. Hoock, Jr., Robert A. Sutherland

■ **VOLUME 8. Emerging Systems and Technologies,**

Stanley R. Robinson, *Editor*

- Chapter 1. Unconventional Imaging Systems, Carl C. Aleksoff, J. Christopher Dainty, James R. Fienup, Robert Q. Fugate, Jean-Marie Mariotti, Peter Nisenson, Francois Roddier
- Chapter 2. Adaptive Optics, Robert K. Tyson, Peter B. Ulrich
- Chapter 3. Sensor and Data Fusion, Alan N. Steinberg
- Chapter 4. Automatic Target Recognition Systems, James W. Sherman, David N. Spector, C. W. "Ron" Swonger, Lloyd G. Clark, Edmund G. Zelnio, Terry L. Jones, Martin J. Lahart
- Chapter 5. Directed Energy Systems, Gary Golnik
- Chapter 6. Holography, Emmett N. Leith
- Chapter 7. System Design Considerations for a Visually-Coupled System, Brian H. Tsou

Copublished by



Infrared Information Analysis Center
Environmental Research Institute of Michigan
Ann Arbor, Michigan USA

and



SPIE OPTICAL ENGINEERING PRESS
Bellingham, Washington USA

Sponsored by

Defense Technical Information Center, DTIC-DF
Cameron Station, Alexandria, Virginia 22304-6145

Sources of Radiation

George J. Zissis, *Editor*
Environmental Research Institute of Michigan

V O L U M E

1

The Infrared and Electro-Optical Systems Handbook

Joseph S. Accetta, David L. Shumaker, *Executive Editors*
Environmental Research Institute of Michigan

Library of Congress Cataloging-in-Publication Data

The Infrared and electro-optical systems handbook / Joseph S. Accetta,
David L. Shumaker, executive editors.

p. cm.

Spine title: IR/EO systems handbook.

Cover title: The Infrared & electro-optical systems handbook.

Completely rev. ed. of: Infrared handbook. 1978

Includes bibliographical references and indexes.

Contents: v. 1. Sources of radiation / George J. Zissis, editor —

v. 2. Atmospheric propagation of radiation / Fred G. Smith, editor —

v. 3. Electro-optical components / William D. Rogatto, editor —

v. 4. Electro-optical systems design, analysis, and testing /

Michael C. Dudzik, editor — v. 5. Passive electro-optical systems /

Stephen B. Campana, editor — v. 6. Active electro-optical systems /

Clifton S. Fox, editor — v. 7. Countermeasure systems / David Pollock, editor —

v. 8. Emerging systems and technologies / Stanley R. Robinson, editor.

ISBN 0-8194-1072-1

1. Infrared technology—Handbooks, manuals, etc.

2. Electrooptical devices—Handbooks, manuals, etc. I. Accetta, J.

S. II. Shumaker, David L. III. Infrared handbook. IV. Title:

IR/EO systems handbook. V. Title: Infrared & electro-optical

systems handbook.

TA1570.I5 1993

621.36'2—dc20

92-38055

CIP

Copublished by

Infrared Information Analysis Center

Environmental Research Institute of Michigan

P.O. Box 134001

Ann Arbor, Michigan 48113-4001

and

SPIE Optical Engineering Press

P.O. Box 10

Bellingham, Washington 98227-0010

Copyright © 1993 The Society of Photo-Optical Instrumentation Engineers

All rights reserved. No part of this publication may be reproduced or distributed in any form or by any means without written permission of one of the publishers. However, the U.S. Government retains an irrevocable, royalty-free license to reproduce, for U.S. Government purposes, any portion of this publication not otherwise subject to third-party copyright protection.

PRINTED IN THE UNITED STATES OF AMERICA

Preface

The Infrared and Electro-Optical Systems Handbook is a joint product of the Infrared Information Analysis Center (IRIA) and the International Society for Optical Engineering (SPIE). Sponsored by the Defense Technical Information Center (DTIC), this work is an outgrowth of its predecessor, *The Infrared Handbook*, published in 1978. The circulation of nearly 20,000 copies is adequate testimony to its wide acceptance in the electro-optics and infrared communities. *The Infrared Handbook* was itself preceded by *The Handbook of Military Infrared Technology*. Since its original inception, new topics and technologies have emerged for which little or no reference material exists. This work is intended to update and complement the current *Infrared Handbook* by revision, addition of new materials, and reformatting to increase its utility. Of necessity, some material from the current book was reproduced as is, having been adjudged as being current and adequate. The 45 chapters represent most subject areas of current activity in the military, aerospace, and civilian communities and contain material that has rarely appeared so extensively in the open literature.

Because the contents are in part derivatives of advanced military technology, it seemed reasonable to categorize those chapters dealing with systems in analogy to the specialty groups comprising the annual Infrared Information Symposia (IRIS), a Department of Defense (DoD) sponsored forum administered by the Infrared Information Analysis Center of the Environmental Research Institute of Michigan (ERIM); thus, the presence of chapters on active, passive, and countermeasure systems.

There appears to be no general agreement on what format constitutes a "handbook." The term has been applied to a number of reference works with markedly different presentation styles ranging from data compendiums to tutorials. In the process of organizing this book, we were obliged to embrace a style of our choosing that best seemed to satisfy the objectives of the book: to provide derivational material data, descriptions, equations, procedures, and examples that will enable an investigator with a basic engineering and science education, but not necessarily an extensive background in the specific technology, to solve the types of problems he or she will encounter in design and analysis of electro-optical systems. Usability was the prime consideration. In addition, we wanted each chapter to be largely self-contained to avoid time-consuming and tedious referrals to other chapters. Although best addressed by example, the essence of our handbook style embodies four essential ingredients: a brief but well-referenced tutorial, a practical formulary, pertinent data, and, finally, example problems illustrating the use of the formulary and data.

The final product represents varying degrees of success in achieving this structure, with some chapters being quite successful in meeting our objectives and others following a somewhat different organization. Suffice it to say that the practical exigencies of organizing and producing a compendium of this magnitude necessitated some compromises and latitude. Its ultimate success will be judged by the community that it serves. Although largely oriented toward system applications, a good measure of this book concentrates on topics endemic and fundamental to systems performance. It is organized into eight volumes:

Volume 1, edited by George Zissis of ERIM, treats sources of radiation, including both artificial and natural sources, the latter of which in most military applications is generally regarded as background radiation.

Volume 2, edited by Fred Smith of OptiMetrics, Inc., treats the propagation of radiation. It features significant amounts of new material and data on absorption, scattering, and turbulence, including nonlinear propagation relevant to high-energy laser systems and propagation through aerodynamically induced flow relevant to systems mounted on high-performance aircraft.

Volume 3, edited by William Rogatto of Santa Barbara Research Center, treats traditional system components and devices and includes recent material on focal plane array read-out electronics.

Volume 4, edited by Michael Dudzik of ERIM, treats system design, analysis, and testing, including adjunct technology and methods such as trackers, mechanical design considerations, and signature modeling.

Volume 5, edited by Stephen Campana of the Naval Air Warfare Center, treats contemporary infrared passive systems such as FLIRs,IRSTs, IR line scanners, and staring array configurations.

Volume 6, edited by Clifton Fox of the Night Vision and Electronic Sensors Directorate, treats active systems and includes mostly new material on laser radar, laser rangefinders, millimeter-wave systems, and fiber optic systems.

Volume 7, edited by David Pollock, consultant, treats a number of countermeasure topics rarely appearing in the open literature.

Volume 8, edited by Stanley Robinson of ERIM, treats emerging technologies such as unconventional imaging, synthetic arrays, sensor and data fusion, adaptive optics, and automatic target recognition.

Acknowledgments

It is extremely difficult to give credit to all the people and organizations that contributed to this project in diverse ways. A significant amount of material in this book was generated by the sheer dedication and professionalism of many esteemed members of the IR and EO community who unselfishly contributed extensive amounts of precious personal time to this effort and to whom the modest honorarium extended was scarcely an inducement. Their contributions speak elegantly of their skills.

Directly involved were some 85 authors and editors from numerous organizations, as well as scores of technical reviewers, copyeditors, graphic artists, and photographers whose skill contributed immeasurably to the final product.

We acknowledge the extensive material and moral support given to this project by various members of the managements of all the sponsoring and supporting organizations. In many cases, organizations donated staff time and internal resources to the preparation of this book. Specifically, we would like to acknowledge J. MacCallum of DoD, W. Brown and J. Walker of ERIM, and J. Yaver of SPIE, who had the foresight and confidence to invest significant resources in the preparation of this book. We also extend our appreciation to P. Klinefelter, B. McCabe, and F. Frank of DTIC for their administrative support during the course of this program.

Supporting ERIM staff included Ivan Clemons, Jenni Cook, Tim Kellman, Lisa Lyons, Judy Steeh, Barbara Wood, and the members of their respective organizations that contributed to this project.

We acknowledge Lorretta Palagi and the publications staff at SPIE for a professional approach to the truly monumental task of transforming the manuscripts into presentable copy and the patience required to interact effectively with the authors.

We would like to pay special tribute to Nancy Hall of the IRIA Center at ERIM who administrated this at times chaotic project with considerable interpersonal skill, marshaling the numerous manuscripts and coordinating the myriad details characteristic of a work of this magnitude.

We properly dedicate this book to the people who created it and trust it will stand as a monument to their skills, experience, and dedication. It is, in the final analysis, a product of the community it is intended to serve.

Joseph S. Accetta
David L. Shumaker
Ann Arbor, Michigan

January 1993

Notices and Disclaimer

This handbook was prepared by the Infrared Information Analysis Center (IRIA) in cooperation with the International Society for Optical Engineering (SPIE). The IRIA Center, Environmental Research Institute of Michigan, is a Defense Technical Information Center-sponsored activity under contract DLA-800-C-393 and administrated by the Defense Electronics Supply Center, Defense Logistics Agency.

This work relates to the aforementioned ERIM contract and is in part sponsored by the Department of Defense; however, the contents do not necessarily reflect the position or the policy of the Department of Defense or the United States government and no official endorsement should be inferred.

The use of product names does not in any way constitute an endorsement of the product by the authors, editors, Department of Defense or any of its agencies, the Environmental Research Institute of Michigan, or the International Society for Optical Engineering.

The information in this handbook is judged to be from the best available sources; however, the authors, editors, Department of Defense or any of its agencies, the Environmental Research Institute of Michigan, or the International Society for Optical Engineering do not assume any liability for the validity of the information contained herein or for any consequence of its use.

Contents

	Introduction	xiii
CHAPTER 1	Radiation Theory, William L. Wolfe	
	1.1 Introduction	3
	1.2 Blackbody (Planckian) Functions	8
	1.3 Properties of Radiators	21
	1.4 Radiation Geometry	27
	1.5 Radiometric Temperatures	30
	1.6 Radiation Processes	32
CHAPTER 2	Artificial Sources, Anthony J. LaRocca	
	2.1 Introduction	51
	2.2 Standard Laboratory Sources	52
	2.3 Commercial Laboratory Sources	64
	2.4 Field Sources (Man-Made Targets)	108
	2.5 IR Simulation and Modeling Overview	128
CHAPTER 3	Natural Sources, David Kryskowski, Gwynn H. Suits	
	3.1 Introduction	139
	3.2 Radiative Transfer Modeling	140
	3.3 The Sun	151
	3.4 The Moon	157
	3.5 The Celestial Background	160
	3.6 The Sky	194
	3.7 The Earth	210
	3.8 Properties of Natural Materials	230
	3.9 Statistical Measures of Infrared Backgrounds	285
CHAPTER 4	Radiometry, George J. Zissis	
	4.1 Introduction	317
	4.2 Radiometers	318
	4.3 Spectroradiometers	334
	4.4 Interferometers	347
	4.5 Other Spectroscopic Instruments and Techniques	360
	Index	365

Introduction

This volume contains four chapters derived from Chapters 1, 2, 3, and 20 of the original *Infrared Handbook*. Volume 1 is intended to provide a foundation for the treatment of sources of radiation for use in later volumes on systems and applications.

Chapter 1, as well as Chapters 2 and 4, were written in 1991 with a final review in 1992. They were especially updated to reflect the influence of the powerful new calculatory and computational capabilities now available.

Chapter 1 presents and discusses general calculational procedures with blackbody radiators, but the treatment has been extended to include a review of the basics of line and band spectral radiators.

Radiometric data are discussed in Chapter 3 on natural sources, which was written well into 1992 by Kryskowski and Suits. They introduce a newly developed emphasis on models and modeling methods.

In 1992 dramatic demonstrations of the new space-based radiometric instruments were obtained. This development in precision radiometry is briefly reviewed and referenced in Chapter 4.

The editor is grateful to the authors and to the many reviewers for their efforts to attain this goal.

January 1993

George J. Zissis
Ann Arbor, Michigan

CHAPTER 1

Radiation Theory

William L. Wolfe

*Optical Sciences Center/University of Arizona
Tucson, Arizona*

CONTENTS

1.1	Introduction	3
1.1.1	Radiometric Symbols and Nomenclature	3
1.1.2	Use of Subscripts	6
1.1.3	Fluometry	6
1.1.4	Nicodemus System	7
1.1.5	Chinese Restaurant System	7
1.1.6	Photometric Terms	7
1.2	Blackbody (Planckian) Functions	8
1.2.1	Spectral Radiant Exitance and Radiance	8
1.2.2	Conversion to Photons	9
1.2.3	Spectral Scale Conversions	9
1.2.4	Conversions to Other Geometries	10
1.2.5	Universal Curves and Equations	10
1.2.6	Contrasts	11
1.2.7	Maxima	11
1.2.8	Total Integrals	12
1.2.9	Computer Programs	13
1.3	Properties of Radiators	21
1.3.1	Nomenclature	21
1.3.2	Emission, Emittance (Emissance?), and Emissivity	23
1.3.3	Absorption, Absorptance, and Absorptivity	23
1.3.4	Reflection, Reflectance, and Reflectivity	26
1.3.5	Transmission	26
1.3.6	Kirchhoff's Law	26
1.3.7	Interrelationships	27
1.4	Radiation Geometry	27
1.4.1	Transfer Equation	27
1.4.2	Isotropic Radiators	28

2 IR/EO HANDBOOK

1.4.3	Anisotropic Radiators	28
1.4.4	Isotropic Disks	29
1.4.5	Configuration Factors	29
1.4.6	General Geometric Transfer	30
1.5	Radiometric Temperatures	30
1.5.1	Radiation Temperature	30
1.5.2	Radiance Temperature	30
1.5.3	Distribution Temperature	31
1.5.4	Color Temperature	32
1.6	Radiation Processes	32
1.6.1	Atomic Spectra	32
1.6.2	Molecular Spectra of Gases	34
1.6.3	Spectra of Solids	36
1.6.4	Spectral Line Shapes	36
	References	48

1.1 INTRODUCTION

This chapter deals with blackbody radiation in its various forms because it is the fundamental radiative process for all equilibrium radiators. In addition to discussing the various forms, we discuss some of the radiometric properties of materials, radiometric temperatures, and some of the *many* radiative processes that exist in gases, liquids, and solids, but this treatment here is surely not complete or exhaustive.

First a description of nomenclature and symbols is given. The reader is again cautioned that this is not all-inclusive, and some systems use the same words for different meanings than are given here and different words for the same meanings. The Queen of Hearts lives in spirit, and people make words mean exactly what they want them to mean, no more, no less.

Blackbodies are fundamental thermodynamic radiators. Thus, their descriptions in Sec. 1.2 are relatively complete. Expressions are given for calculating the various types of blackbody quantities, wavelength distributions, total integrals, maxima, contrasts, power, and photons. The change with temperature is described for both BASIC and spreadsheet programs for band-limited calculations.

Real materials transmit, reflect, emit, absorb, and scatter in their own special ways. Real radiator properties and the methods of describing the different spectral and geometric distributions are presented in Sec. 1.3. Section 1.4 describes radiative transfer for different geometries.

Temperature is a very common concept, and various radiometric temperatures are used in the field. Hence, it is measured and described radiometrically in several different ways. Some of these ways are described in Sec. 1.5, as well as information about how these radiometric temperatures vary from true thermodynamic temperatures.

The radiative processes of atomic and molecular gases and solids that are of the most importance to the infrared spectrum are presented in Sec. 1.6. Many books have been written on the classical and quantum theories of just some of these processes and this section is merely a brief review.

The references at the end of the chapter are meant to be representative. An effort has been made to provide references to a variety of sources, which will surely entice the interested reader.

1.1.1 Radiometric Symbols and Nomenclature

Many nomenclature schemes are used for characterizing radiometric symbols. The reader should be aware that the system described here is not unique. Other scientific disciplines have chosen other words and other symbols for similar and even identical concepts. Two recommendations are made here. The first is that in reading, the reader write down the units of each of the concepts described by the author to make sure the radiometric concepts and quantities are well defined and consistent. The second recommendation is that the reader, as an author, carefully define appropriate terms at the outset of every article he or she writes.

Table 1.1 gives the symbols, nomenclature, and units for radiometric quantities. One of the most basic of the radiometric quantities is radiant energy. This is usually denoted by the symbol Q or U . Then the (volume) density of

Table 1.1 Symbols, Nomenclature, and Units

Symbol	Description	Units
B	Rotational constant	cm^{-1}
C	Constant	—
c	Speed of light in vacuum	m s^{-1}
c_1	First radiation constant	W cm^2
c_2	Second radiation constant	cm K
E	Incidence [irradiance]	W m^{-2}
h	Planck's constant	J s
I	Radiance intensity	W sr^{-1}
I_0	Moment of inertia	g cm^2
i	Running index, 1, 2, 3, ...	—
K, L, M, N	Atomic shell designations	—
k	Boltzmann constant	J K^{-1}
k	Force constant	J m^{-2}
k	Radian wave number	m^{-1}
L	Radiance [sterance]	$\text{W m}^{-2} \text{sr}^{-1}$
l	Orbital quantum number	—
M	Radiant exitance [emittance]	W m^{-2}
m	Integers 1, 2, 3, ...	—
m	Magnetic quantum number	—
m	Reduced mass	g
n	Principal quantum number	—
P	Pressure	P
P, Φ	Flux	$\text{J s}^{-1}, \text{W}$
$P()$	Legendre polynomial	—
Q	Quantity	Various
q	Volume density of Q	Various, m^{-3}
R	Distance	m
R	General radiometric variable	Various
R_H	Rydberg constant for hydrogen	cm^{-1}
$R()$	Radial wave function	—
r	Axial distance	m
S	Line strength	—
T	Temperature	K
U	Energy	J
u	Energy density	J m^{-3}
x	Dimensionless frequency = $c_2/\lambda T$	—
y	General spectral variable	Various
α	Absorptivity	—
$\alpha()$	Absorption coefficient	cm^{-1}
$\Delta\lambda, \Delta\nu$	Bandwidth	$\mu\text{m}, \text{cm}^{-1}$
ϵ	Emissivity	—
ζ	Variable of integration	—
$\Theta()$	Azimuthal wave function	—
θ	Angle	r, deg
λ	Wavelength	μm
ν	Frequency	Hz
ν	Wave number	cm^{-1}
π	3.14159...	—
ρ	Reflectivity	—
σ	Stephan-Boltzmann constant	$\text{W m}^{-2} \text{K}^{-4}$
τ	Transmissivity	—
$\Phi()$	Angular wave function	—
ϕ	Angle	r, deg
Ω	Solid angle	sr
Ω'	Projected solid angle	sr
<i>Superscripts:</i>		
BB	Blackbody	
<i>Subscripts:</i>		
b	Bidirectional	
h	Hemispheric	
q	Photonic	
s	Specular	
u	Energetic	
v	Visible	
λ	Wavelength	
∞	Indicating a property with infinite number of passes	

radiant energy is denoted by q or u . The flux is the time rate of change of the energy, the power, and it is given the symbol P or Φ . Many prefer the former for its ease in typing and its representation of power, while others prefer Φ as a better representation of flux (Flux?). The latter is the recommendation of the international standardization body.¹ Flux density is usually used to indicate the flux per unit area, the areal density. There seems to be no recommended symbol for the general quantity of flux density, only the incident or exitent values. These are called radiant incidence or irradiance and radiant exitance or radiant emittance. In the rest of this chapter irradiance and exitance will be used, followed by the others in brackets. The flux per unit solid angle is called the intensity; the flux per unit projected area and per unit solid angle is called radiance or sterance. The two alternate words will be handled the same way: radiance [sterance].

These represent a sufficient set of symbols for the description of radiative transfer, but it has been suggested that a special name be used for the flux per unit area and solid angle that is both reflected and emitted from a surface. The term is *radiosity*. Most workers use radiance to indicate this concept, and specify emitted and reflected radiance when necessary for clarity. In a medium that emits or scatters, the radiance changes with path length, and this is characterized by specifying the path radiance, which has units of radiance per unit path length, or watts per square centimeter per steradian per centimeter, for instance. This quantity is called alternately *path radiance* and *sterisent*.

Table 1.2 lists the various commonly used radiometric terms with their definitions and preferred symbols, based on the recommendations of the CIE

Table 1.2 Radiometric Terms

Name	Symbol	Definition	Expression	Units	Alternates
Quantity	Q, U	Radiant energy		Joule [J]	
Flux	Φ, P	Time rate of quantity	$\frac{\partial Q}{\partial t}$	Watt [W]	
Flux density		Flux per unit normal area	$\frac{\partial \Phi}{\partial A}$	W m^{-2}	
Exitance	M [W]	Exitent flux density	$\frac{\partial \Phi}{\partial A}$	W m^{-2}	Areance Radiant emittance
Incidence	E [H]	Incident flux density	$\frac{\partial \Phi}{\partial A}$	W m^{-2}	Areance Irradiance
Intensity	I [J]	Flux per solid angle	$\frac{\partial \Phi}{\partial \Omega}$	W sr^{-2}	Pointance
Sterance	L [N]	Flux density per solid angle	$\frac{\partial^2 \Phi}{\cos \theta \partial A \partial \Omega}$	$\text{W m}^{-2} \text{sr}^{-1}$	Radiance
Sterisent		Sterance per unit pathlength	$\frac{\partial^3 P}{\cos \theta \partial A \partial \Omega \partial l}$	$\text{W m}^{-3} \text{sr}^{-1}$	Path radiance
Fluence exposure		Incidence times time	$\frac{\partial Q}{\partial A}$	J m^{-2}	
Radiosity		Emitted and reflected radiance	$\frac{\partial^2 P}{\cos \theta \partial A \partial \Omega}$	$\text{W m}^{-2} \text{sr}^{-1}$	Radiance Sterance

and the promulgations in the United States by the American National Standards Institute.² Also given in brackets are the former symbols, still used in much of the literature, and the alternates suggested by Jones³ and by Nicodemus.⁴

1.1.2 Use of Subscripts

Each of the radiometric terms has a certain spectral characteristic. The radiance may be on a wavelength-by-wavelength basis, in which case it is called the spectral radiance. It may be for the entire spectrum, in which case it is called total radiance, or it may be for a specific spectral band, in which case it is called weighted or band radiance, and may be visible radiance (luminance) if that is the weighting. If the radiometric quantities are spectral and the context is not clear, then a subscript indicating wavelength or frequency should be appended. If it is for a specific waveband, then that waveband should be appended. Usually, if it is for photon (quantum) flux quantities, a subscript q should be affixed to indicate this. If it is for a luminous quantity, then a subscript v should be affixed. Often, if the context is clear, the subscript is omitted. Usually, in the infrared the subscript is omitted if energy is the basic quantity, and a q is used as a subscript if the quantity is photons. It is sometimes important to note that the subscript λ (or any other spectral variable) indicates a differentiation, a distribution of the quantity. For example,

$$L_{\lambda} = \frac{\partial L}{\partial \lambda} . \quad (1.1)$$

However, any weighted quantity, like visible or erythemic, is represented as

$$L_v = \int_0^{\infty} W(\lambda) L_{\lambda}(\lambda) d\lambda , \quad (1.2)$$

where W is the spectral weighting function.

1.1.3 Fluometry

In 1963 Jones³ introduced the concept of *fluometry* and generalized the concepts of energy and power transfer. He pointed out that the various geometrical quantities occur independently of whether the basic quantities are energy, photons, the variation in these quantities, electrons, or others. Therefore, he described flux as, whatever its quantity, the time rate of change of that quantity. The flux density is the areal density of the flux. He then coined two words: *exitance* for the emitted flux density and *incidence* for the received flux density. The flux per unit solid angle he called radiant intensity, and the flux per unit area and per unit solid angle, formerly called radiance, he called sterance for the generalized quantity. The path radiance was dubbed the steriscent. This is a little esoteric but very useful. The adjectives now take care of everything. One has, for example, radiant sterance, visible sterance, electron sterance, photon sterance, and so on. The same system can be used for exitance, incidence, and steriscent.

1.1.4 Nicodemus System

As an application and extension of Jones's fluometric system, Nicodemus suggested several modifications.⁴ He suggested that intensity be replaced by pointance and flux density be replaced by areance. Although these modifications have been used, no widespread acceptance has occurred.

1.1.5 Chinese Restaurant System

To represent as clearly as possible the full description of radiometric terms, Geist and Zalewski⁵ suggested a system whereby many modifiers are used. They suggested the use of four terms for every quantity, thus four columns of a table. One describes the spectral nature of the quantity, another the origin, a third the geometry, and the fourth the type of flux or the quantity. This is akin to selecting a variety of different entrees in a Chinese restaurant and, thus, the name. Table 1.3 shows a list of some of the terms. For example, one would choose (initially) one word from each of the columns, such as scattered, spectral, energetic radiance.

Table 1.3 The Chinese Restaurant Nomenclature

Source	Spectrum	Quantity	Geometry
Incident	Spectral	Energetic	Radiance
Scattered	Photopic	Entropic	Incidence
Emitted	Weighted	Photon	Flux density

1.1.6 Photometric Terms

Terms used in photometry have an old and venerable lineage, but they are also overly complicated and somewhat esoteric. To simplify the spoken and written language, many terms have been invented as shorthand for longer ones, and early workers have been honored by having certain quantities named after them. The basic photometric quantity is the lumen or light watt. It is now defined⁶ as 680 lumens per watt times the integral of the spectral flux weighted by the spectral response of the eye, called the *luminous efficacy*. It may be written

$$L_v = \int_0^\infty L_\lambda(\lambda) K(\lambda) d\lambda, \quad (1.3)$$

where $K(\lambda)$ is the response of the eye:

$$K(\lambda) = \frac{\Phi_{\lambda,v}(\lambda)}{\Phi_{\lambda,e}(\lambda)} = V(\lambda) K_{\max}, \quad (1.4)$$

where K_{\max} is maximum; $V(\lambda)$ is the normalized function; and the function extends from 380 to 780 nm, and is zero elsewhere. The value of K_{\max} , as stated previously, is 680 lumens per watt. This definition replaces the earlier one based on the output of a blackbody at the temperature of freezing platinum.⁷

Table 1.4 Basic Photometric Terms

Generic Quantity	Symbol	Photometric Name	Unit Name	Abbreviation
Quantity	Q_v	Luminous energy	Talbot	
Flux	P_v, Φ_v		Lumen	lm
Exitance	M_v	Luminous exitance	Lumen m ⁻² Lumen cm ⁻²	lux, lx phot, ph
Incidence	E_v	Illuminance	Lumen m ⁻² Lumen cm ⁻²	lux, lx phot, ph
Intensity	I_v	Luminous intensity	Lumen sr ⁻¹	candela, cd
Sterance	L_v	Luminance	Lumen sr ⁻¹ cm ⁻²	nit
Fluence		Luminous fluence	Talbot	
Exposure		Exposure	Talbot m ⁻²	

The basic energetic-type quantity, the luminous energy, is the lumen second, also called the talbot. Luminous energy density is given in lumens per cubic meter or cubic centimeter. The number of lumens per square meter is called a *lux*, while a lumen per square centimeter is a *phot*, and a lumen per square foot is a *foot-candle*. This is because a unit of luminous intensity is a candela, and the illuminance one foot from a source of one candela (one candle) is one candela per square foot. Table 1.4 gives a summary of the basic units in photometry. Note that a stilb is 10,000 nits, or one lumen per steradian per square centimeter. An apostilb is just π times a stilb, accounting for the relationship between the luminance and illuminance of an isotropic radiator. A lambert is $1/\pi$ times a stilb for similar reasons.

1.2 BLACKBODY (PLANCKIAN) FUNCTIONS

The blackbody or Planck equation was one of the milestones of physics.⁸ It is also an extremely important part of many infrared calculations. It can be represented in different ways. This section provides a number of the various forms and the constants and coefficients that go with them. Several BASIC programs for generating various spectral radiometric curves are listed in Sec. 1.2.9.

1.2.1 Spectral Radiant Exitance and Radiance

The usual form of the equation is in terms of the radiant exitance as a function of wavelength:

$$M_\lambda = \frac{c_1}{\lambda^5(e^x - 1)}, \quad (1.5)$$

where

$$x = c_2/\lambda T. \quad (1.6)$$

Here c_1 is the first radiation constant and c_2 is the second radiation constant. They are given by⁹ (values of the physical constants are from the same reference):

$$c_1 = 2\pi c^2 h = 3.741844 \times 10^4 \text{ [W cm}^{-2} \mu\text{m}^{-1}] , \quad (1.7)$$

$$c_2 = hc/k = 1.438769 \text{ [cm K]} , \quad (1.8)$$

where c is the speed of light *in vacuo*, h is Planck's constant, k is Boltzmann's constant, and T is the temperature in kelvins. The radiance of a blackbody is numerically $1/\pi$ times the radiant exitance. Thus, one can write

$$L_\lambda = \frac{2c^2 h}{\lambda^5 (e^x - 1)} . \quad (1.9)$$

1.2.2 Conversion to Photons

These same equations can be written in terms of photons. In this case, for monochromatic light, the equation in terms of photons is the equation in terms of energy divided by the energy of a photon, which is hc/λ :

$$L_{q\lambda} = \frac{2c}{\lambda^4 (e^x - 1)} , \quad (1.10)$$

$$M_{q\lambda} = \frac{2\pi c}{\lambda^4 (e^x - 1)} . \quad (1.11)$$

1.2.3 Spectral Scale Conversions

Sometimes it is useful or necessary to write the equation in terms of spectral variables other than wavelength. The conversion is carried out by the following relationship, where R is any radiometric variable and x and y are any two spectral variables:

$$R_y dy = R_x dx , \quad (1.12)$$

$$R_y = R_x \left(\frac{dx}{dy} \right) . \quad (1.13)$$

An example will illustrate. To convert from spectral radiant exitance in wavelength to wave number $\bar{\nu}$, we perform the following calculation:

$$M_{\bar{\nu}} = M_\lambda \left| \frac{d\lambda}{d\bar{\nu}} \right| , \quad (1.14)$$

$$\lambda = 1/\bar{\nu} , \quad (1.15)$$

$$\left| \frac{d\lambda}{d\tilde{\nu}} \right| = \frac{1}{\tilde{\nu}^2} = \lambda^2, \quad (1.16)$$

$$M_{\tilde{\nu}} = \frac{c_1 \lambda^2}{\lambda^5 (e^x - 1)} = \frac{c_1 \tilde{\nu}^3}{(e^x - 1)}. \quad (1.17)$$

1.2.4 Conversions to Other Geometries

The several forms of the blackbody relationship are radiant exitance, radiance, and energy density. To convert from radiance to radiant exitance for an isotropic radiator, such as a blackbody, multiply the radiance by π [sr]. To convert from energy density to radiant exitance *in vacuo*, multiply the energy density by $c/4$. The same relations hold true for photon and visible quantities. These are geometric relationships, fluometries. They also hold true, of course, no matter what the spectral scale. Thus, the general relationships can be written

$$M = \pi L, \quad (1.18)$$

$$M = cu/4. \quad (1.19)$$

1.2.5 Universal Curves and Equations

Each of the different spectral distributions has a different equation. Each different temperature has a different curve. It is often useful to bring things to a common ground, to obtain, as much as possible, a universal curve or equation. For blackbody functions, there is no such thing, but some normalization can be carried out for some convenience in applications. The spectral curves can all be plotted in terms of either x or λT , the common variable. This can be seen by carrying out the spectral variable conversion from λ to x , as follows:

$$\begin{aligned} M_x &= M_\lambda \left| \frac{\partial \lambda}{\partial x} \right| \\ &= c_1 \left(\frac{T}{c_2} \right)^4 \frac{x^3}{(e^x - 1)}. \end{aligned} \quad (1.20)$$

A plot of the function in terms of x is a single curve. The actual value must be obtained by multiplying by c_1 and the fourth power of T/c_2 . The peak value occurs at about $x = 2.82$ (as shown in Table 1.5), and the value of the integral at that point is 1.4214. Thus, the curve can be normalized to these values. This is one form of a "universal" curve. With such a curve, or table of values, we can calculate x based on given values for λ and T . Then we read the ratio of the value to the maximum and multiply by the maximum and the required constants to find the desired value. A program (see Sec. 1.2.9) is easier, but this is more portable. A similar situation exists for photons, but the maximum occurs at $x = 1.59$ and has a value of 0.6476. The constant is c_1 times T/c_2 to

the third power. Two more similar functions for the cumulative energy flux and photon flux exist. This makes four "universal" functions.

Four more universal functions exist. They are plots of the analogs of the four above, but for the contrast functions.

1.2.6 Contrasts

The contrast may be defined as the change in the spectral radiance (or other radiometric variable) as a function of temperature. It is the temperature derivative of the function. By taking the derivative directly, it may be shown that

$$\frac{\partial R_y}{\partial T} = \frac{xe^x}{T(e^x - 1)} R_y \approx x \frac{dT}{T}, \quad (1.21)$$

where R is any spectral radiometric function, radiance, radiant emittance, etc., and y is any spectral variable. The approximation holds for large enough values of x . These functions indicate the change in any spectral radiometric function with temperature; they are useful in the evaluation of systems that sense temperature differences. A closely related term is the relative contrast, which may be defined as

$$\frac{dR_\lambda}{R_\lambda} = \frac{xe^x}{e^x - 1} \frac{dT}{T}. \quad (1.22)$$

Once again, R is any radiometric function, e.g., M, L, E, I , with respect to any spectral variable, not necessarily λ . This relationship points out that the relative change of a radiometric variable is not linearly related to the relative change in temperature. Rather it is a function of the temperature and the part of the spectrum, inherent in the variable x .

1.2.7 Maxima

The maxima of the Planck functions in the spectral domain may be found by differentiating with respect to the spectral variable, setting the result to zero, and solving the equation. The well-known result for the wavelength distribution is known as the Wien displacement law, and is written

$$\lambda_{\max} T = 2897.885 \quad [\mu\text{m K}]. \quad (1.23)$$

This is obtained from the solution described above by successive approximations to the solution given by

$$\frac{xe^x}{e^x - 1} = 5. \quad (1.24)$$

The result is that x is 4.96511423. Therefore the Wien displacement law may be written more accurately as

$$\lambda_{\max} T = c_2/4.96511423 = 2897.756 \quad [\mu\text{m K}]. \quad (1.25)$$

Table 1.5 Maxima for Different Planck Functions

Function	Spectral Variable	m	x_{\max}	R_{\max}
Photons	Frequency	2	1.593624260	0.6476
Power	Frequency	3	2.821439372	1.4214
Photons	Wavelength	4	3.920690395	4.7796
Power	Wavelength	5	4.96511423	21.2036
Power contrast	Wavelength	6	5.96940917	115.9359

The maxima are different for different functions. It may be shown that the maximum is given by the following relationship, where m represents the power of the spectral variable in the equation for radiance or radiant emittance:

$$\frac{xe^x}{e^x - 1} = |m| . \quad (1.26)$$

A similar treatment can be developed to obtain the expression for the maximum of the contrast functions, the temperature derivatives:

$$\frac{xe^x}{e^x - 1} = \left| \frac{x + m + 1}{2} \right| . \quad (1.27)$$

The values of the maxima for the different spectral distributions are displayed in Table 1.5. The entry for R_{\max} is related to the maximum of the function.

1.2.8 Total Integrals

It is usually more useful to know the value of the total power emitted from a body, rather than its spectral extent. The well-known Stephan-Boltzmann law gives the total radiant exitance as

$$M = \sigma T^4 , \quad (1.28)$$

where σ is the Stephan-Boltzmann constant. It has been evaluated¹⁰ and is given by

$$\sigma = \frac{\pi^5 k^4}{45c^2 h^3} = 5.66961 \times 10^{-8} \text{ [W m}^{-2} \text{ K}^4] . \quad (1.29)$$

This expression permits the evaluation of sigma to any desired accuracy (at least to that of the fundamental constants). A similar expression can be obtained for the total output of photons:

$$M_q = \frac{2.4041(2\pi k^3 T^3)}{c^2 h^3} = 1.5202 \times 10^{11} \text{ [s}^{-1} \text{ m}^{-2}] . \quad (1.30)$$

1.2.9 Computer Programs

This section provides a listing of the programs that can be used for generating the various spectral radiometric curves, the universal curves, and the integral expressions. Figure 1.1 is a plot of the expression $xe^x/(e^x - 1)$ as a function of x and therefore shows the normalized temperature contrast for different parts of the spectrum. This is the first BASIC program given at the end of this chapter. Figure 1.2 is a plot of the spectral radiant exitance [emittance] as a function of wavelength. It is generated by the second of the BASIC programs listed at the end of this chapter. They are written in QuickBasic for a VGA monitor. For other monitors the SCREEN instruction and limits on the VIEW instruction may have to be changed and some of the instructions rewritten, but it is fairly general. The program can be used for generating either a plot with the PSET instruction or a table by REMARKING the PSET instruction and unREMARKING the PRINT instruction. The spectral interval may be changed by changing the STEP value in the lambda FOR loop. The constants may be changed as the user desires. All the LOCATE instructions will have to be changed if the user desires a different set of temperatures for the program. Figure 1.3 is a plot of spectral radiant exitance [emittance] as a function of wave number. The only part of the program that is different is the settings of the WINDOW values and the FOR loop that calculated the values. The values of this spectral radiant exitance [emittance] are much smaller than those for the wavelength because the spectral interval is much smaller. Figure 1.4 is a logarithmic plot of the spectral radiant emittance [exitance] as a function of

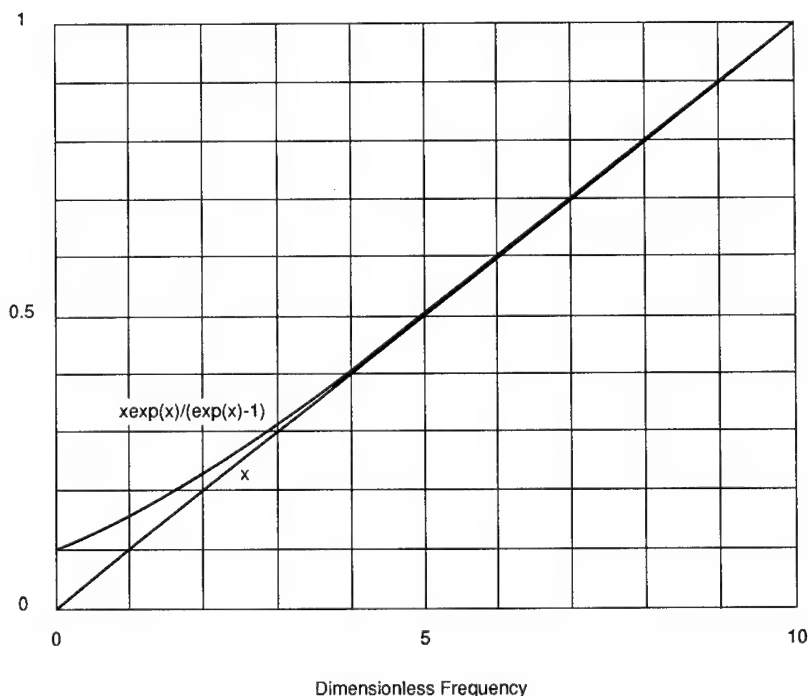


Fig. 1.1 The expression $x\exp(x)/[\exp(x) - 1]$ versus x .

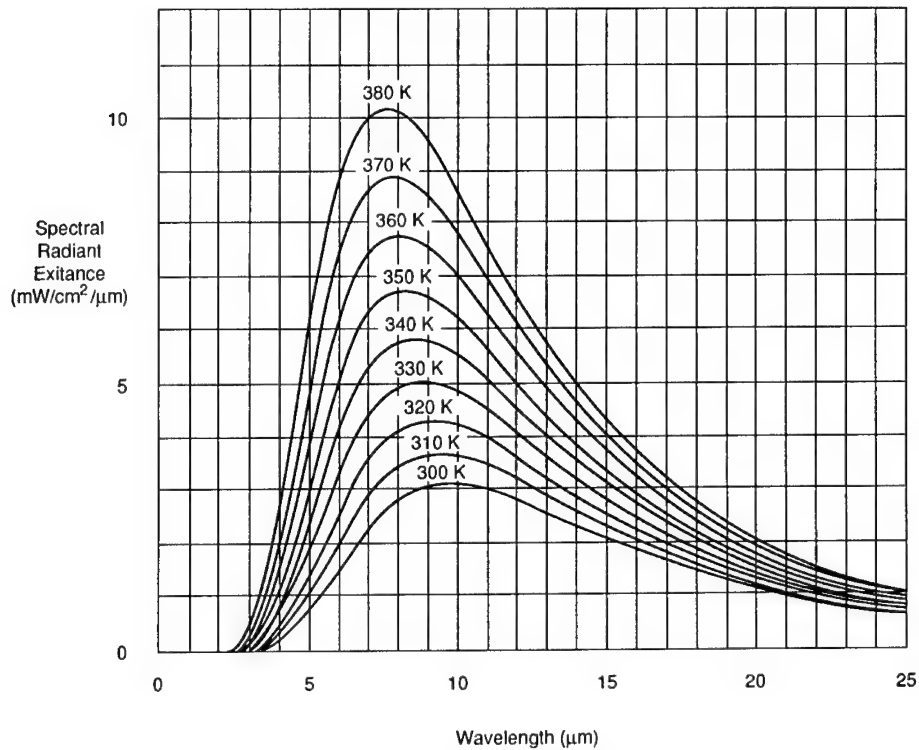


Fig. 1.2 Spectral radiant exitance versus wavelength.

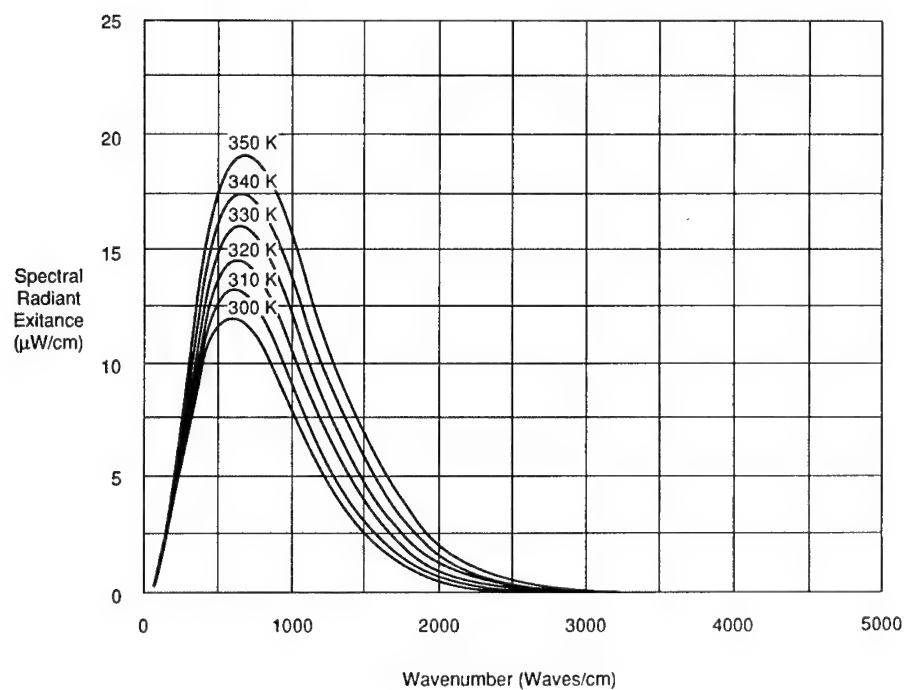


Fig. 1.3 Spectral radiant exitance versus wave number.

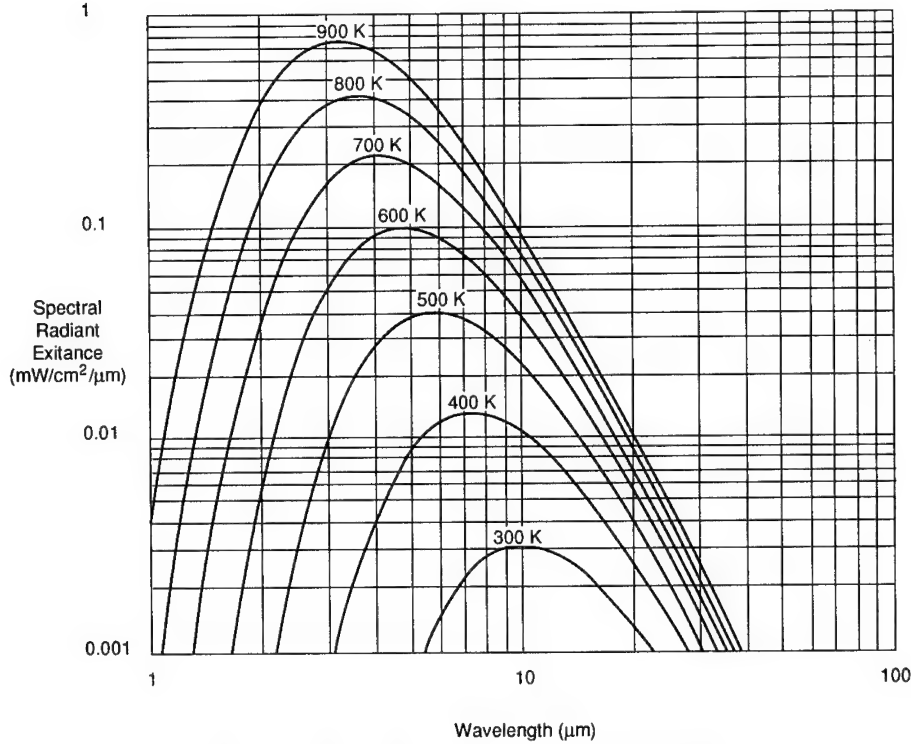


Fig. 1.4 Spectral radiant exitance versus wavelength.

the wavelength. It illustrates the fact that the curves are all the same shape in this scale. They merely slide along the line that represents the Wien displacement law, which in this scale is a straight line. Figure 1.5 is a similar curve for the spectral radiant exitance [emittance] on a wave number basis.

The next two curves are so-called universal ones. Figure 1.6 is a plot of the spectral radiant exitance [emittance] as a function of x , and normalized to its maximum value of 1.4214 at its (dimensionless) frequency of 2.8214, as given in Table 1.5. To obtain a value for a particular wavelength or wave number and temperature, calculate x ; find the fractional value from this curve or table at that x ; then multiply by 1.4214 and the appropriate version of the constant, such as $c_1(T/c_2)^4$ for the wavelength distribution. Figure 1.7 is a similar curve for the photon distribution. Figures 1.8 and 1.9 are the cumulative curves for the energy and photon distributions, respectively. They have both been generated using the series calculation for the integral. This approximation arises as follows. The Planck function can be written in terms of the dimensionless frequency x as follows:

$$M_x = c_1 \left(\frac{T}{c_2} \right)^4 \frac{x^3}{e^x - 1} . \quad (1.31)$$

The integral may then be written as

$$M_{0-x} = \frac{c_1}{c_2^4} T^4 \int_0^x \frac{x^3}{e^x - 1} dx . \quad (1.32)$$

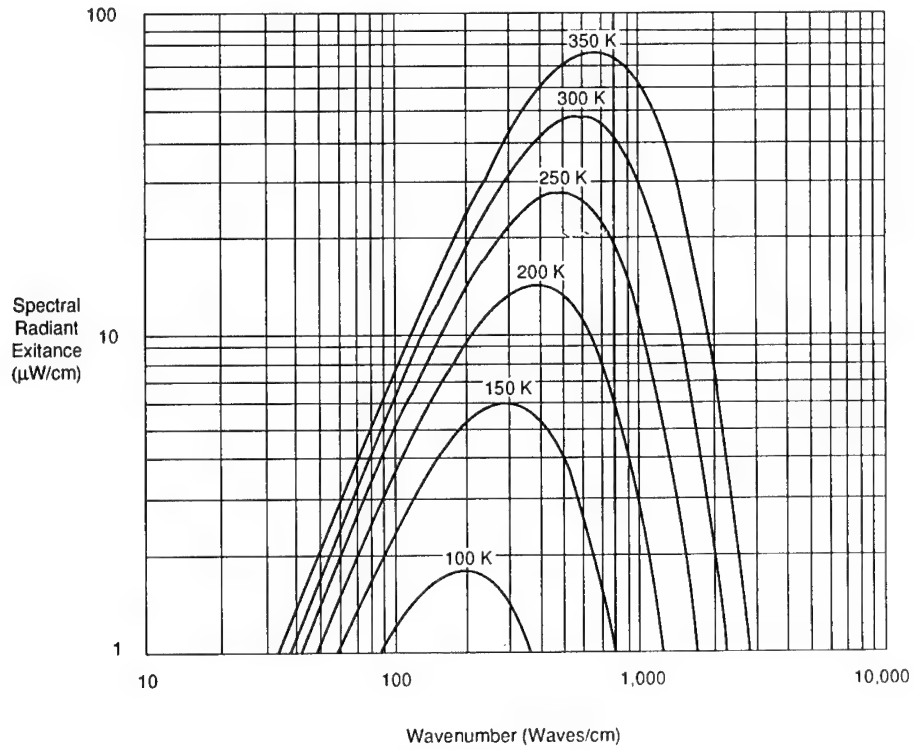


Fig. 1.5 Spectral radiant exitance versus wave number.

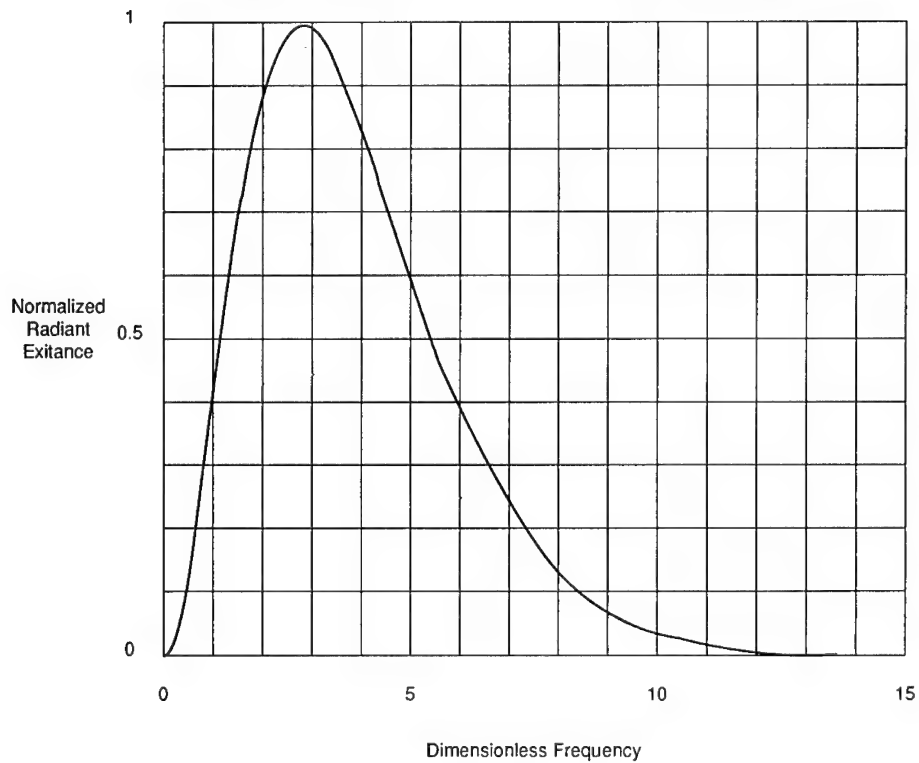


Fig. 1.6 Normalized spectral radiant exitance versus dimensionless frequency.

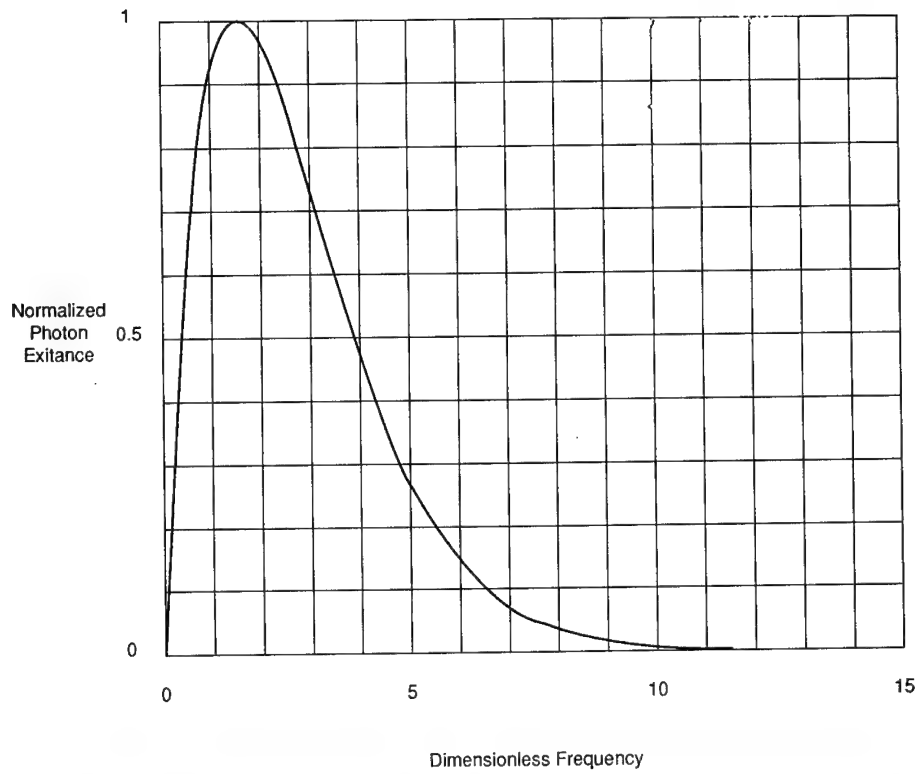


Fig. 1.7 Normalized spectral photon exitance versus dimensionless frequency.

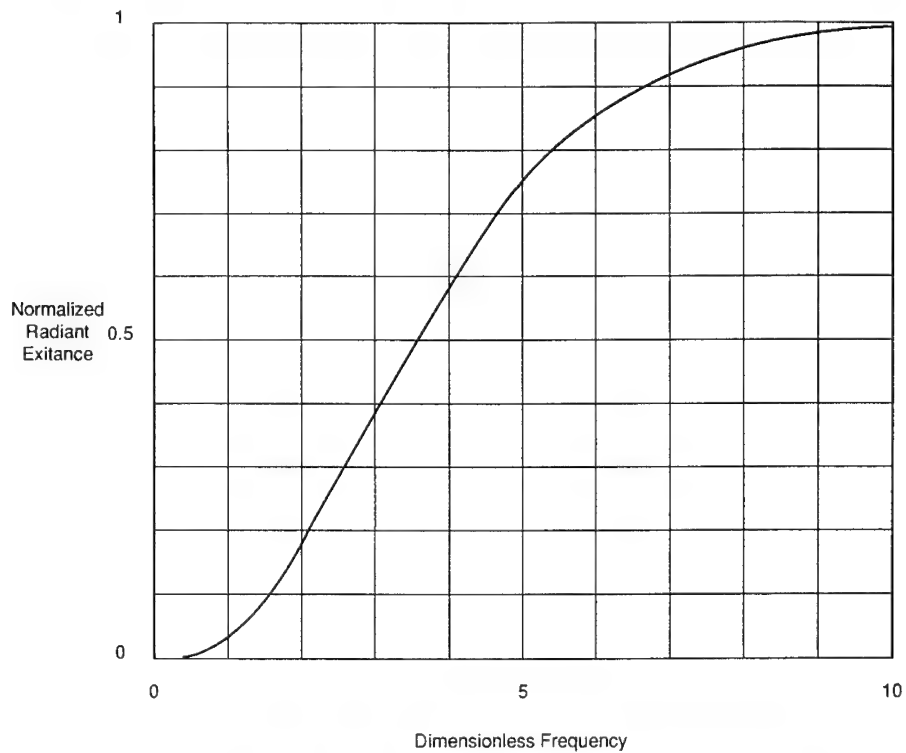


Fig. 1.8 Normalized radiant exitance versus dimensionless frequency.

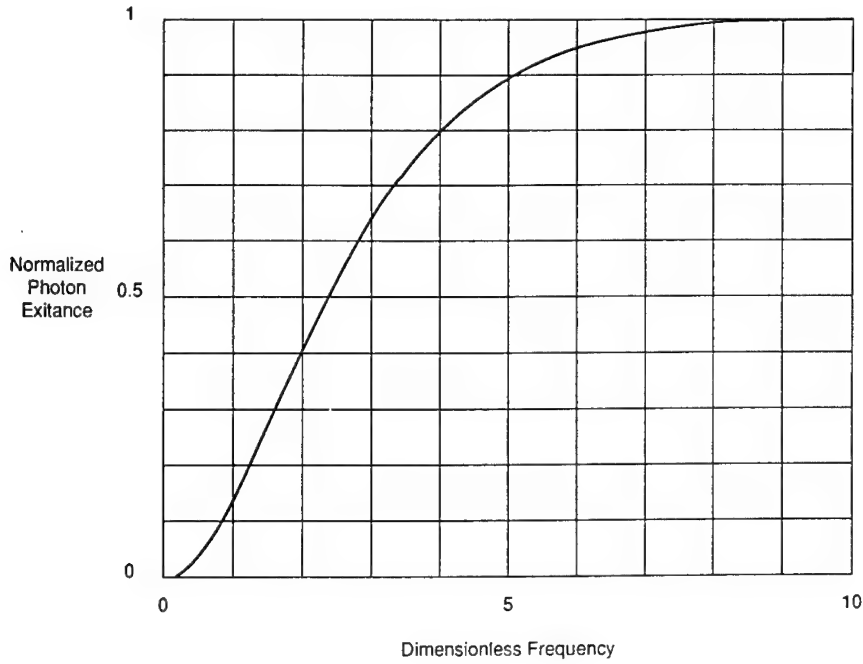


Fig. 1.9 Normalized photon exitance versus dimensionless frequency.

The integrand may be represented as an infinite geometric series:

$$\frac{x^3}{e^x - 1} = x^3 \sum_{m=0}^{\infty} e^{-mx} . \quad (1.33)$$

Then the integral may be integrated successively by parts to yield the result:

$$\int_0^{x_1} \frac{x^3}{e^x - 1} dx = \sum_{m=1}^{\infty} [(mx)^3 + 3(mx)^2 + 6(mx) + 6] e^{-mx} m^{-4} . \quad (1.34)$$

The integral in any spectral band can then be found by integrating from 0 to x_1 and from 0 to x_2 and subtracting. Other forms are found the same way. Any integral applies for any spectral function, but they are different for energy, photons, energy contrast, and photon contrast. They are

$$M_{q0-x} = 2\pi c \frac{T^3}{c_2^3} \sum_{m=0}^{\infty} [(mx)^2 + 2mx + 2] e^{-mx} m^{-3} , \quad (1.35)$$

$$\begin{aligned} \frac{\partial M_{0-x}}{\partial T} &= \frac{c_1 T^3}{c_2^4} \sum_{m=0}^{\infty} [(mx)^4 + 4(mx)^3 + 12(mx)^2 \\ &\quad + 24mx + 24] e^{-mx} m^{-4} , \end{aligned} \quad (1.36)$$

$$\frac{\partial M_{q0-x}}{\partial T} = \frac{2\pi c T^2}{c_2^3} \sum_{m=0}^x [(mx)^3 + 3(mx)^2 + 6mx + 6] e^{-mx} m^{-3} . \quad (1.37)$$

Other methods have been used to obtain these functions,¹¹ but these have been found to be accurate when the convergence criterion requires that the next term be less than 10^{-8} of the sum of the series to that point. When the values of x are extremely high or low, rounding errors in the computation can affect the accuracy. The range of x from 1 to 15 seems to be entirely satisfactory. Figures 1.10 through 1.13 are for the spectral and cumulative power and photon contrasts.

These equations may also be evaluated on spreadsheets. Spreadsheet programs do not like to iterate and usually describe such a situation with the diagnostic "Unable to resolve circular references." Thus, the simple way to handle the same algorithm, using the series approach, is to lay out the terms and look to see if convergence has occurred. An example that calculates radiance is given in Tables 1.6 and 1.7. The first shows the values; the second shows the formulas. In Table 1.6, cells A1 through A25 indicate what is being calculated or input. Row 2 indicates the required atomic constants, which must be inserted in the cells just below them, in row 3. The B5 value is the required temperature and B6 and B7 show the short and long wavelengths. The entry in B8 is the calculated value of x for the short wavelength, the dimensionless frequency. Row 9 displays the set of iterative constants m ; row 10 displays the calculated values of mx ; and row 11 displays the m 'th term of the series. Row 12 is the running series sum, a higher order sum in each successive cell across the row. Row 13 is the ratio test. Notice that for this example, the series converges satisfactorily at the fourth term, although eight are calculated. Rows 15 through 20 are exactly the same as 8 through 13 but represent the upper

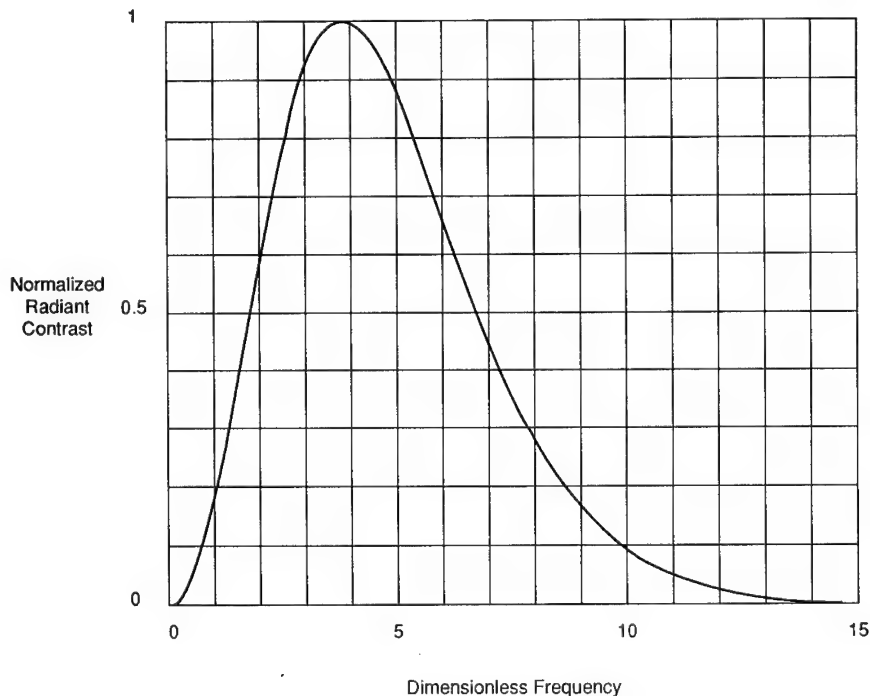


Fig. 1.10 Normalized spectral radiant contrast versus dimensionless frequency.

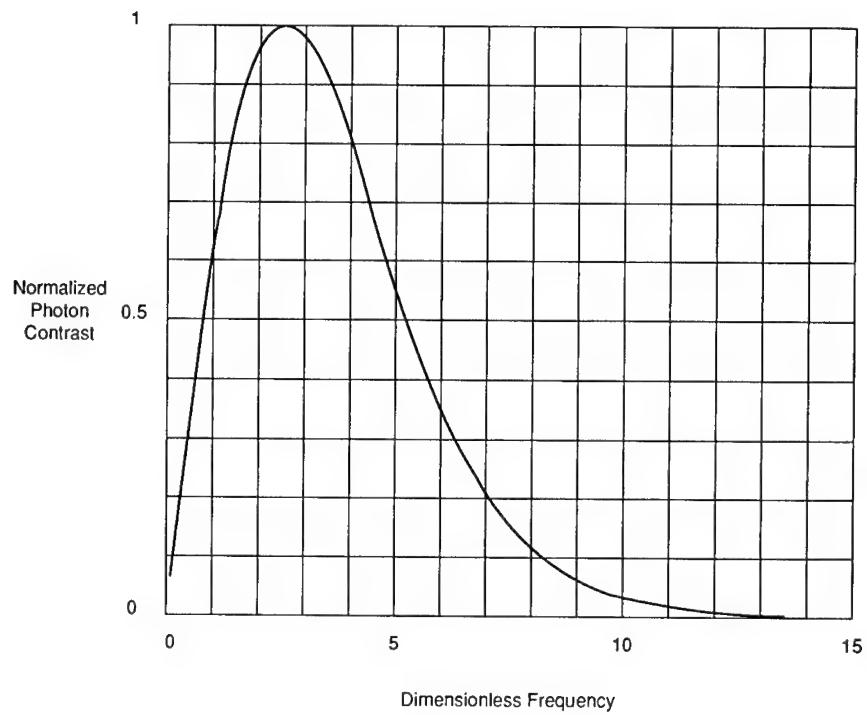


Fig. 1.11 Normalized spectral photon contrast versus dimensionless frequency.

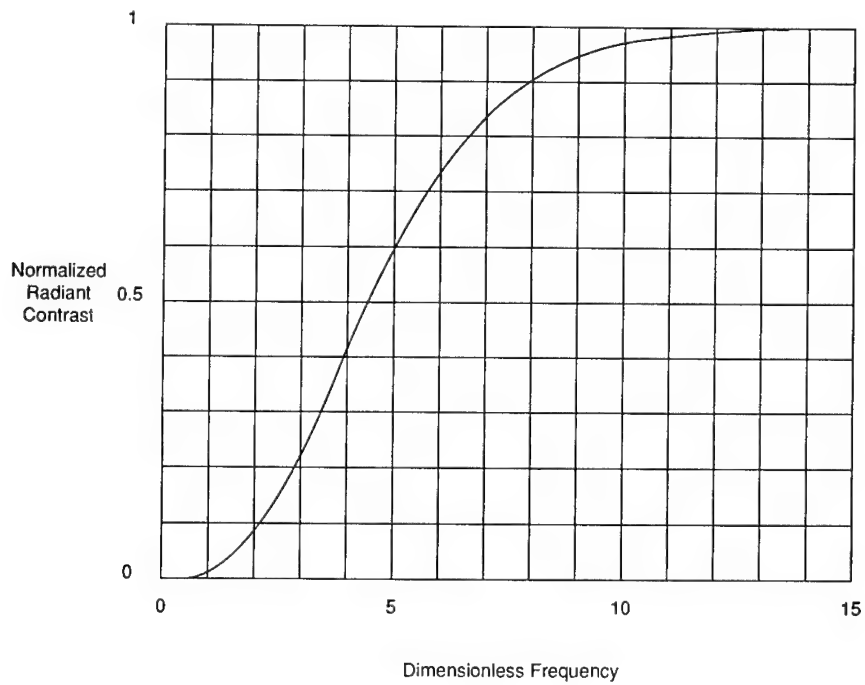


Fig. 1.12 Normalized radiant contrast versus dimensionless frequency.

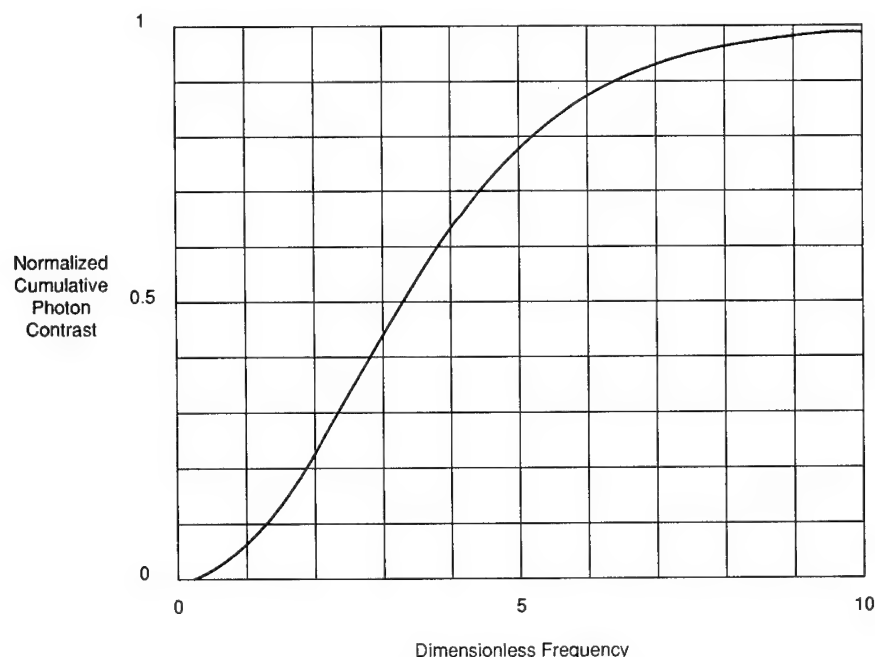


Fig. 1.13 Normalized photon contrast versus dimensionless frequency.

wavelength. B22 calculates the constant for radiance; B23 calculates the fourth power of the temperature divided by the second radiation constant; B24 is the difference of the two sums; and B25 is the product of the last three terms, the integral between the limits—the answer!

1.3 PROPERTIES OF RADIATORS

Equilibrium radiators are all limited by the blackbody relationships. Emissivity describes the efficiency with which they radiate. Absorptivity describes the efficiency with which they absorb. Reflectivity refers to the efficiency with which they reflect, and transmissivity to their transmission efficiency.

1.3.1 Nomenclature

One school of thought¹² prescribes that the words used to describe the various radiometric properties of materials should have very specific meanings, especially their endings. Thus, any word that ends in *ion* describes a process: transmission, absorption, emission, and reflection. Any word that ends in *ance* represents the property of a specific sample. Any word that ends in *ivity* represents a property of the generic material. Certain difficulties are inherent with this scheme. One is that emittance is used by some to mean a flux density; in this scheme, however, it also means a radiation efficiency. The use of *exitance* for the process or *emissance* for the property solves that problem, but it does not resolve the issue of the perfectly representative sample. The reflectivity of a material, for instance, must have been measured on a sample that has

Table 1.6 Planck Integration

	A	B	C	D	E	F	G	H	I
1									
2	Constants	c	pi	c2[cm]	c2 [um]	h	c1		
3		2.9975E+10	3.14259	1.4388	14388	6.626E-34	3.7419E-12		
4									
5	Temperature	300							
6	Lambda1	8							
7	Lambda2	12							
8	x	5.995							
9	m	1	2	3	4	5	6	7	8
10	mx	5.995	11.99	17.985	23.98	29.975	35.97	41.965	47.96
11	m th term	0.00070443	6.7051E-07	1.0198E-09	1.8245E-12	3.5433E-15	7.2308E-18	1.5253E-20	3.2945E-23
12	sum		7.05E-04	7.05E-04	7.05E-04	7.05E-04	7.05E-04	7.05E-04	7.05E-04
13	ratio		0.00095093	1.4464E-06	2.5875E-09	5.0252E-12	1.0255E-14	2.1632E-17	4.6724E-20
14									
15	x	3.99666667							
16	m	1	2	3	4	5	6	7	8
17	mx	3.99666667	7.99333333	11.99	15.9866667	19.9833333	23.98	27.9766667	31.9733333
18	m th term	0.01020871	6.2569E-05	6.7051E-07	8.6505E-09	1.2228E-10	1.8245E-12	2.8212E-14	4.4742E-16
19	sum		1.03E-02	1.03E-02	1.03E-02	1.03E-02	1.03E-02	1.03E-02	1.03E-02
20	ratio		0.00609161	6.5275E-05	8.4214E-07	1.1904E-08	1.7762E-10	2.7465E-12	4.3557E-14
21									
22	c1/pi	1.1907E-12							
23	(T/c2)-4	1890093560							
24	Sum	0.00956686							
25	Answer	2.153E-05							

been sufficiently well polished that it does not affect the measurement. It is impossible to accomplish this for all samples if the measurements are of sufficient accuracy. For these reasons, not everyone abides by the teachings of this school.¹³

1.3.2 Emission, Emittance (Emissance?), and Emissivity

The emission of a sample will at best be that of a blackbody, the perfect emitter. The ratio of the emission of a sample to that of a blackbody at the same temperature and in the same spectral interval is defined as its emissivity. There are several varieties of emissivity: spectral, total, weighted, directional, and hemispherical. Spectral, weighted, and total emissivity describe the spectral distributions, while directional and hemispherical describe the geometrical distributions. A hemispherical emissivity is the ratio of two radiant exitances [emittances], while a directional emissivity is the ratio of two radiances [sterances]. The latter is a measure of the efficiency of the body in a given direction. The former is the efficiency of radiation into the entire overlying hemisphere. Spectral emissivity is defined as either of the geometries on a wavelength-by-wavelength basis. Weighted emissivity is defined over a spectral region, and total emissivity refers to the entire spectrum. The spectral, directional emissivity is defined as

$$\varepsilon_{sd}(\lambda, \theta, \phi) = \frac{L_{\lambda}(\lambda, \theta, \phi)}{L_{\lambda}^{BB}(\lambda, \theta, \phi)} \quad (1.38)$$

The spectral, hemispherical emissivity is defined as

$$\varepsilon_{sh}(\lambda) = \frac{M_{\lambda}(\lambda)}{M_{\lambda}^{BB}(\lambda)} \quad (1.39)$$

For total quantities, the numerators become the infinite integrals and the denominators the expressions for total radiation:

$$\varepsilon_{td} = \frac{\pi \int_0^{\infty} L_{\lambda}(\lambda) d\lambda}{\sigma T^4} \quad (1.40)$$

$$\varepsilon_{th} = \frac{\int_0^{\infty} M_{\lambda}(\lambda) d\lambda}{\sigma T^4} \quad (1.41)$$

1.3.3 Absorption, Absorptance, and Absorptivity

The same definitions and descriptions apply to absorption because, by Kirchhoff's law, emission and absorption are equal when the same conditions apply for both. In the equations above, simply replace α for ε and E for M .

Table 1.7 Planck Integration

	A	B	C	D
1				
2	Constants	c	pi	c2 [cm]
3		2997500000	3.14259	1.4388
4				
5	Temperature	300		
6	Lambda1	8		
7	Lambda2	12		
8	x	= \$E3/\$B6/\$B5		
9	m	1	2	3
10	mx	= B9*\$B8	= C9*\$B8	= D9*\$B8
11	m th term	= (B10^3 + 3*B10*B10 + 6*	= (C10^3 + 3*C10*C10 + 6*	= (D10^3 + 3*D10*D10 + 6*
12	sum		= B11 + C11	= C12 + D11
13	ratio		= C11/C12	= D11/D12
14				
15	x	= \$E3/\$B5/\$B7		
16	m	1	2	3
17	mx	= \$B15*B16	= \$B15*C16	= \$B15*D16
18	m th term	= (B17^3 + 3*B17*B17 + 6*	= (C17^3 + 3*C17*C17 + 6*	= (D17^3 + 3*D17*D17 + 6*
19	sum		= B18 + C18	= C19 + D18
20	ratio		= C18/C19	= D18/D19
21				
22	c1/pi	= \$G3/C3		
23	(T/c2)^4	= (\$B5/\$D3)^4		
24	Sum	= I19 - I12		
25	Answer	= B22*B23*B24		

Table 1.7 (continued)

	E	F	G	H	I
1					
2	c2 [um]	h	c1		
3	14388	6.626E-34	= 2*C3*B3*B3*F3		
4					
5					
6					
7					
8					
9	4	5	6	7	8
10	= E9*\$B8	= F9*\$B8	= G9*\$B8	= H9*\$B8	= I9*\$B8
11	= (E10*3+3*E10*E10+6*	= (F10*3+3*F10*F10+6*	= (G10*3+3*G10*G10+6*	= (H10*3+3*H10*H10+6*	= (I10*3+3*I10*I10+6*
12	= D12+E11	= E12+F11	= F12+G11	= G12+H11	= H12+I11
13	= E11/E12	= F11/F12	= G11/G12	= H11/H12	= I11/I12
14					
15					
16	4	5	6	7	8
17	= \$B15*E16	= \$B15*F16	= \$B15*G16	= \$B15*H16	= \$B15*I16
18	= (E17*3+3*E17*E17+6*	= (F17*3+3*F17*F17+6*	= (G17*3+3*G17*G17+6*	= (H17*3+3*H17*H17+6*	= (I17*3+3*I17*I17+6*
19	= D19+E18	= E19+F18	= F19+G18	= G19+H18	= H19+I18
20	= E18/E19	= F18/F19	= G18/G19	= H18/H19	= I18/I19
21					
22					
23					
24					
25					

1.3.4 Reflection, Reflectance, and Reflectivity¹⁴

Reflection is a bidirectional process. One must describe both the incident and the exitent geometries. The spectral descriptions of spectral, weighted, and total reflectivity are the same as for absorption. Specular reflectivity is defined as the ratio of flux or flux density in the reflected beam to the same quantity in the incident beam. The light, of course, moves in the direction dictated by Snell's laws. Diffuse reflectivity relates to scattered light. The ratio of the light collected in the entire overlying hemisphere to an incident beam is called directional-hemispheric; hemispherical-directional is the reverse, and they are equal by virtue of Helmholtz's reciprocity theorem.¹⁵ Bihemispherical reflectivity relates to both incident and reflected light covering the entire hemisphere. The bidirectional reflectance distribution function (BRDF) is defined as the reflected radiance divided by the incident irradiance.¹⁶ It is a function of both angles of incidence and of reflection and has the units of reciprocal steradians, although it is dimensionless. The specular spectral reflectivity may be written

$$\rho_{ss} = \frac{M_{\lambda}^{\text{refl}}}{E_{\lambda}^{\text{inc}}} \quad (1.42)$$

The total specular reflectivity is

$$\rho_{ts} = \frac{\int_0^{\infty} M_{\lambda}^{\text{refl}}(\lambda) d\lambda}{\int_0^{\infty} E_{\lambda}^{\text{inc}}(\lambda) d\lambda} \quad (1.43)$$

The bidirectional reflectivity (occasionally denoted as f_r) is

$$\rho_b = \frac{L^{\text{refl}}(\theta_r, \phi_r)}{E^{\text{inc}}(\theta_i, \phi_i)} \quad (1.44)$$

It may be thought of as the reflectivity per solid angle, and has the units of reciprocal steradians. It can have any of the spectral representations described above.

1.3.5 Transmission

The definitions of the various kinds of transmission follow those of reflections exactly.

1.3.6 Kirchhoff's Law

In 1860 Kirchhoff¹⁷ pointed out that for equilibrium conditions the absorptivity of a sample is exactly equal to its emissivity. This applies to total and spectral quantities, to each polarization component, and for each direction.

1.3.7 Interrelationships

For a plane parallel plate, taking into account all the interreflections, the transmission for unpolarized light is given by¹⁸

$$\tau_{\infty} = \frac{(1 - \rho)^2 \tau}{1 - \rho^2 \tau^2}, \quad (1.45)$$

where τ_{∞} is the transmission of the plate taking into account all the reflections, τ is the single-pass internal transmission of the sample, and ρ is the single-surface, Fresnel reflectivity of the sample. The reflectivity under these conditions can also be found to be

$$\rho_{\infty} = \rho - \frac{(1 - \rho)^2 \tau^2 \rho}{1 - \rho^2 \tau^2}. \quad (1.46)$$

The effective emissivity for this set of conditions is found to be

$$\varepsilon_{\infty} = \frac{(1 - \rho)(1 - \tau)}{1 - \rho\tau}. \quad (1.47)$$

The conservation of power requires that the sum of the absorbed, reflected, and transmitted power be equal to the incident power, so that one can write

$$\alpha + \rho + \tau = 1. \quad (1.48)$$

This is certainly true for total power and hemispherical quantities. Under equilibrium conditions it is true for spectral quantities. If there is scattering, it is not true for directional quantities, nor can one relate a hemispherical reflection to a directional emission. It is not true for each component of polarization either.

1.4 RADIATION GEOMETRY

The fundamentals of radiative transfer for simple geometries are given in the following subsections.

1.4.1 Transfer Equation

The fundamental equation of radiative transfer may be written as follows for a vacuum:

$$d\Phi = \frac{L dA_1 \cos\theta_1 dA_2 \cos\theta_2}{R^2}. \quad (1.49)$$

The differential element of power $d\Phi$ is transferred from the differential area dA_1 to dA_2 according to the product of the radiance and the projected areas and the reciprocal of the square of the distance R between them. The radiance may be any of the different varieties discussed in Sec. 1.1—energy, photon,

visible, weighted, spectral, etc. The equation may be written other ways. It may be written in terms of either differential area and the corresponding solid angle:

$$\begin{aligned} d\Phi &= L dA_1 \cos\theta_1 d\Omega_2 \\ &= L d\Omega_1 dA_2 \cos\theta_2 . \end{aligned} \quad (1.50)$$

It may be written in terms of either area and the projected solid angle:

$$\begin{aligned} d\Phi &= dA_1 d\Omega'_2 \\ &= L d\Omega'_1 dA_2 . \end{aligned} \quad (1.51)$$

In each case the projected solid angle is the area divided by the square of the distance and multiplied by *both* cosines. The quantity that multiplies the radiance is called the throughput or the etendue.

In a vacuum the radiance has been shown¹⁹ to be constant, no matter how the solid angles and areas are changed. If the radiance is constant, then by conservation of energy, the throughput must also be constant. It is an invariant of the system, and is closely related to the Lagrange and Helmholtz invariants²⁰ of optical systems. When media of different refractive indices are involved, the basic radiance is invariant.²¹ It is equal to the radiance divided by the square of the refractive index. The throughput must then be defined as the square of the refractive index times the area–solid angle product. The equation in this form still applies to a nonabsorbing, nonscattering, nonemitting medium.

1.4.2 Isotropic Radiators

The equation may be applied to an isotropic radiator, which has a radiance that is independent of angle. This is often called a Lambertian radiator. By direct integration, we find that for a circularly symmetric system the flux density in a cone of half-angle θ is given by

$$M = L\pi \sin^2\theta . \quad (1.52)$$

The radiant exitance [emittance] into the entire overlying hemisphere is given by

$$M = \pi L . \quad (1.53)$$

1.4.3 Anisotropic Radiators

There are no truly isotropic radiators. Their degree of directionality can be nicely approximated by a cosine series with appropriately determined coefficients; that is, the radiance may be written as

$$L(\theta) = \sum L_i \cos^i\theta . \quad (1.54)$$

It is the sum of each radiance amplitude L_i with a distribution that may be described by the i 'th power of the cosine, $\cos^i\theta$. For $i = 0$, the first term

represents the isotropic surface. The succeeding terms represent more directional radiators. The relations between radiance and radiant exitance [emittance] then are given by the following two equations, one for a specified cone half-angle ω and the other for the hemisphere:

$$\begin{aligned} M &= 2\pi \sum \frac{L_i}{i+2} (1 - \cos^{i+2}\theta) \\ &= 2\pi \sum \frac{L_i}{i+2} . \end{aligned} \quad (1.55)$$

1.4.4 Isotropic Disks

The relation between the radiance and the flux density for a differential element and an isotropic disk is the same as for the differential element and a hemisphere. The solid angle is determined by the perimeter of the intercepted area and not the internal shape—convex, concave, or undulating. The relationship may be put in a way that provides additional insight. The isotropic disk of radius r is placed an axial distance R away from the differential element. Then

$$M = \pi L \sin^2\theta = \pi L \frac{r^2}{R^2 + r^2} = \frac{\pi r^2 L}{R^2} \frac{1}{1 + (r/R)^2} . \quad (1.56)$$

The term πr^2 represents the area of the disk, L the radiance, and the denominator the inverse square law. This first part of the equation is classical inverse square radiometric transfer. The next term is a correction term that takes into account the finite size of the disk. It may be expanded and rewritten as intensity to give the following series representation:

$$M = \frac{I}{R^2} [1 - (r/R)^2 + (r/R)^4 - + \dots] . \quad (1.57)$$

1.4.5 Configuration Factors

A large number of so-called geometric configuration factors,²² angle factors, or interaction factors have been developed for heat transfer applications. They deal with various geometries for isotropic radiators. These can sometimes be used as beginning points for more complicated designs. The basic equation of transfer can be written in terms of the radiance exitance [emittance] for an isotropic source as

$$\Phi = M \frac{dA_1 \cos\theta_1 dA_2 \cos\theta_2}{\pi R^2} . \quad (1.58)$$

The geometric configuration factor (GCF) is the entire fraction that multiplies M . In this definition, it is $1/\pi$ times the throughput. Unfortunately, these extensive tables^{23,24} only apply to isotropic transfer.

1.4.6 General Geometric Transfer

The general case must be treated by computer programs, generally with some form of finite element treatment. The chief difficulty with such programs is the definition of the boundaries.

1.5 RADIOMETRIC TEMPERATURES

Since temperature is a well-known concept, several "effective" temperatures have been defined. They are generally the temperature a particular body would be if it were a blackbody and radiated the equivalent amount of some radiometric quantity. These temperatures are radiation temperature, brightness (radiance) temperature, distribution temperature, and color temperature.

1.5.1 Radiation Temperature

The radiation temperature²⁵ of a body is the temperature of a blackbody that emits the same amount of total radiation. It would seem that a better monicker would be total temperature. If M is the total radiation of the body in question, then the radiation temperature T_r is given in terms of the thermodynamic temperature by

$$T_r = \left(\frac{M}{\sigma} \right)^{1/4}. \quad (1.59)$$

For a graybody, this may be written as

$$T_r = \epsilon^{1/4} T. \quad (1.60)$$

For a colored body, the expression is

$$T_r = \left[\sigma^{-1} \int_0^{\infty} \epsilon c_1 \lambda^{-5} (e^x - 1)^{-1} d\lambda \right]^{1/4}. \quad (1.61)$$

The relative error for a graybody is given by

$$\text{RE} = 1 - \frac{T_r}{T} = 1 - \epsilon^{1/4}. \quad (1.62)$$

The detailed evaluation requires knowledge of the constant value of the gray-body emissivity.

1.5.2 Radiance Temperature

Radiance temperature²⁶ has traditionally been called *brightness temperature* when the applications are in the visible part of the spectrum. It is defined as the value of temperature from a blackbody that has the same output as the real body at a specific wavelength. *Monochromatic temperature* would seem to be a better name. For many cases in the visible region a particular wavelength,

about 600 nm, is assumed. In the more general case, both the value and the wavelength must be known and cited. Based on the Planck equation, the "brightness" temperature is given implicitly by

$$\frac{c_1}{\lambda^5 [\exp(c_2/\lambda T_b) - 1]} = \frac{\epsilon(\lambda)c_1}{\lambda^5 [\exp(c_2/\lambda T) - 1]} \quad (1.63)$$

Because the constants and the wavelengths are identical for the blackbody and the real body,

$$\exp(c_2/\lambda T_b) - 1 = \epsilon^{-1} [\exp(c_2/\lambda T) - 1] \quad (1.64)$$

This can be solved explicitly for T_b , but not much is added to the understanding. It is

$$T_b = \frac{\lambda}{c_2} \ln \{1 + \epsilon^{-1} [\exp(c_2/\lambda T) - 1]\} \quad (1.65)$$

In the region for which the exponential is much greater than one, the expression simplifies to

$$T_b = c_2 (\lambda \ln \epsilon + c_2)^{-1} \quad (1.66)$$

1.5.3 Distribution Temperature

Distribution temperature²⁷ is defined as the temperature of a blackbody that best matches the spectral distribution of the real body. A subcategory is the ratio temperature, which requires only that the match be made at two spectral points, for example, wavelengths. For this ratio temperature, the equality of the radiant exitances [emittances] dictates

$$\epsilon_1 \lambda_1^{-5} [\exp(c_2/\lambda_1 T) - 1]^{-1} = \epsilon_2 \lambda_2^{-5} [\exp(c_2/\lambda_2 T) - 1]^{-1} \quad (1.67)$$

For the Wien approximation, the expression reduces to

$$T_d = \frac{c_2 \lambda_1 \lambda_2}{(\lambda_1 - \lambda_2)} \ln \left[\frac{M_1 \epsilon_1 \left(\frac{\lambda_1}{\lambda_2}\right)^5}{M_2 \epsilon_2} \right] \quad (1.68)$$

This may also be written with the reduced wavelength as

$$T_d = \frac{c_2 \Lambda}{\ln \left[\frac{M_1 \epsilon_1 \left(\frac{\lambda_1}{\lambda_2}\right)^5}{M_2 \epsilon_2} \right]} \quad (1.69)$$

where

$$\frac{1}{\Lambda} = \frac{1}{\lambda_1} + \frac{1}{\lambda_2} \quad (1.70)$$

1.5.4 Color Temperature

The color temperature²⁸ of a body is the temperature of a blackbody that has the same set of color coordinates on the chromaticity diagram as the body itself. Since this is never used in the infrared, no further mention is made of it here.

1.6 RADIATION PROCESSES

All materials radiate, and materials in thermal equilibrium radiate at most as a blackbody. The levels and spectral regions in which they radiate are dictated by the detailed properties of the materials. Gases generally have rather narrow spectral lines that can make up spectral bands, while solids and liquids have broader regions of absorption and emission. Most atomic processes generate spectral lines in the visible and the ultraviolet, while molecular vibrations and rotations are often in the infrared. Of course, the continuum radiations are blackbody-type functions, the spectra of which are dictated by temperature. Spectra from gases arise from the transitions between different atomic levels and from the vibrations and rotations of the molecules that make up the gas.

1.6.1 Atomic Spectra²⁹

The Bohr model of the atom describes a nucleus surrounded by orbits of electrons in various degrees of detail. The Sommerfeld model is a solution of the wave equation in spherical coordinates, and the solutions are quantized. Each orbit is related to a particular energy state. Each energy state is also related to a specific set of quantum numbers. Some are radial, representing approximately the main orbits; others are azimuthal and angular. Transitions of electrons from one of these states to another are associated with a fixed (quantized) amount of energy that is either absorbed or emitted. A detailed description of the energy levels of the atom (the energy level diagram) is essential for the prediction of the transitions. It is intuitively useful to realize that there is a correspondence principle that closely relates the quantum states to more easily visualized changes in the physical state of the atom. In the Bohr model, the total quantum number n determines the size of the orbit, and the azimuthal quantum number k determines its shape; the magnetic quantum number determines their orientation in space. In the Sommerfeld model, k is replaced by $l + 1$.

Spectra of Atoms with One Valence Electron. The simplest situation to consider in atomic spectra is the atom that has only one valence electron. It can then be considered as a positively charged nucleus, with its nuclear mass, and a negatively charged electron, with its small mass. The solution of the Schrödinger wave equation for such a one-valence electron is given by

$$\psi = \Phi_m(\phi)\Theta_{l,m}(\theta)R_{n,l}(r) \quad (1.71)$$

The three functions are each functions of only one variable, an angular, an azimuthal, and a radial variable. The subscripts represent the quantum numbers of the eigenstates. The first equation is

$$\frac{d^2\Phi}{d\phi^2} = -m^2\Phi . \quad (1.72)$$

Its solutions are

$$\Phi_m(\phi) = \frac{1}{\sqrt{2\pi}} \exp(im\phi) . \quad (1.73)$$

The factor is for normalization so the probability that the electron will be some place in ϕ space is 1. The magnetic quantum number m can take on values of 0, +1, -1, +2, -2, The azimuthal equation is

$$\frac{1}{\Theta \sin\theta} \frac{d}{d\theta} \left(\sin\theta \frac{d\Theta}{d\theta} \right) - \frac{m^2}{\sin^2\theta} = \text{constant} . \quad (1.74)$$

The normalized solution is

$$\Theta_{l,m}(\theta) = \left[\frac{2l+1}{2} \frac{(l-m)!}{(l+m)!} \right]^{1/2} P_l^m(\cos\theta) , \quad (1.75)$$

where the P 's are associated Legendre polynomials. The radial solution is found to be

$$R_{n,l} = \left\{ \frac{4(n-l-1)! Z^3}{[(n+l)!]^3 n^4 a_1^3} \right\}^{1/2} \frac{2Zr}{na_1} \exp\left(-\frac{2Zr}{na_1}\right) L_{n-l-1}^{2l+1}\left(\frac{2Zr}{na_1}\right) , \quad (1.76)$$

where the L 's are Legendre polynomials, a_1 is the Bohr atomic radius, Z is the atomic number, and the quantum numbers were defined earlier. Together, the solutions give the probabilities that the electron lies in various (two-dimensional) angular positions around the nucleus. To this must be added the possibility of spin of the electron, and the quantum number s for this is either $\frac{1}{2}$ or $-\frac{1}{2}$.

In summary, the quantum numbers can have the following values:

$$n = 1, 2, 3, \dots, n-1 , \quad (1.77a)$$

$$l = 0, 1, 2, 3, \dots , \quad (1.77b)$$

$$s = \pm \frac{1}{2} , \quad (1.77c)$$

$$m = 0, \pm 1, \pm 2, \pm 3, \dots, \pm l . \quad (1.77d)$$

The shells of the atom have been labeled K, L, M, N, \dots ; they correspond to the total quantum number $n = 1, 2, 3, 4, \dots$. The states in any shell are further divided according to the azimuthal quantum number l . Electrons for which $l = 0, 1, 2, 3$ are called s, p, d, f electrons. In the simple hydrogen spectrum, the Lyman ($n_1 = 1$), Balmer ($n_1 = 2$), and Paschen ($n_1 = 3$) series are given by

$$\nu = R_H \left(\frac{1}{n_1^2} - \frac{1}{n_2^2} \right) . \quad (1.78)$$

These transitions can be seen to be a series of unequally spaced lines crowding into a band head for very large values of n_2 .

The spectrum for hydrogen can be found by inserting values for the Rydberg constant for hydrogen and for the quantum number l :

$$\nu = \frac{2\pi^2 m e^4}{c h^3} \left(\frac{1}{n_1^2} - \frac{1}{n_2^2} \right) = 109,737 . \quad (1.79)$$

The result is a line at high frequencies and short wavelength, about $0.12 \mu\text{m}$ in the ultraviolet. This is equivalent to the binding energy of the electron in hydrogen.

Helium has two electrons, both in the same orbit. The elements in the second period, Li, Be, B, C, N, O, F, and N, build up electrons in the second shell. Therefore, they may have transitions from $n = 1$ to $n = 2$.

The spectra of the alkali halides may be estimated by taking the Rydberg constant for hydrogen and considering a transition from the second shell to the first. Then

$$\nu = 109,737(1 - 1/4) = 82,303 \rightarrow 0.12 \mu\text{m} . \quad (1.80)$$

These spectra will all be in the ultraviolet region as well.

The spectra of the elements of the third period, Na, Mg, Al, Si, P, S, Cl, and Ar will also be in the visible or the ultraviolet. Electrons that have been excited to higher states can still be calculated this way, and will have larger energy differences, concomitant higher frequencies, and shorter wavelengths. All of these calculations are for changes only in the total quantum number n . The spinning electron provides a small energy difference, and yields doublets of these lines. One has a spin of $+1/2$ and the other a spin of $-1/2$, as indicated above in the summary. In any electron transition, the quantum number l can only change by $+1$ or -1 , and the spin quantum number by 0 or 1 . These doublet separations vary from about 5 to $10,000 \text{ cm}^{-1}$. Fine structure is associated with even the hydrogen atom, and is linked closely to relativistic corrections for the mass of the moving electron, but it is not important to infrared radiation.

Other effects include additional splitting of the lines due to the application of an electric or magnetic field.

1.6.2 Molecular Spectra of Gases

The spectra of gases are characterized by longer wavelengths (lower frequencies) than those of atoms and consist primarily of two types: those that arise from rotations and those that arise from vibrations of the ionic dipoles.

Diatomic Molecules. The diatomic molecules³⁰ of most importance in the infrared are CO, HF, and NO. The rotational frequency, obtained by the solution of the Schrödinger equation that uses their rotational energy, is

$$\nu_{\text{rot}} = [K(K + 1)]^{1/2} \frac{h}{4\pi^2 I_{\omega}} = 2B(J + 1) , \quad (1.81)$$

where J can take on any integer values starting with 0, and I_{ω} is the moment of inertia of the atomic system μr^2 , where r is the interatomic distance and μ is the reduced mass given by

$$\frac{1}{\mu} = \frac{1}{m_1} + \frac{1}{m_2} . \quad (1.82)$$

The approximate frequency of a rotational line of a molecule of CO can be obtained by realizing that the interatomic distance is 1.13×10^{-8} cm. The atomic weights are approximately 12 and 16, so that the reduced molecular weight is 7 and the actual molecular weight (obtained by dividing by Avogadro's number, 6.023×10^{23}) is 1.99×10^{-23} g. Thus, the moment of inertia is 1.46×10^{-39} g cm². The frequency of rotation then is 3515 cm^{-1} .

The vibrational spectra can be obtained by means of a simple Hooke's law model of restoring force. Then the frequency of vibration is found to be

$$\nu = \sqrt{\frac{k}{\mu}} \text{ [Hz]} , \quad (1.83)$$

where k is the binding force and μ is the reduced mass.

Triatomic Molecules. Carbon dioxide and water are the most important of the triatomic molecules in the infrared. They have both vibrational and rotational excitations, but the modes of motion are more complex than those of the diatomic molecules. They include simple stretching and rotations about various axes.

Spectral Summary. The characteristic vibrational modes of most of the molecules of importance in infrared radiation problems are summarized³¹ in Table 1.8. The characteristic modes are given in wave numbers (cm^{-1}) and may easily be converted to wavelengths or to frequencies (Hz). The wavelength in micrometers is 10,000 divided by the wave number in reciprocal centimeters. The frequency in hertz is the speed of light times the wave number in reciprocal centimeters, where the speed of light must be given in centimeters per second.

Table 1.8 Spectral Lines of Important Gases

Species	ν_1 (cm^{-1})	ν_2 (cm^{-1})	ν_3 (cm^{-1})	ν_4 (cm^{-1})
CO	2143			
CO ₂		667	2349	
N ₂ O	1285	589	2224	
H ₂ O	3657	1595	3776	
O ₃	1110	705	1043	
NO	1904			
NO ₂	1306	755	1621	
CH ₄	2917	1534	3019	1904

Table 1.9 Characteristic Spectra of Solids

Type	Occurrence	Characteristic	Bandwidth Q	Region
Crystal vibrations	Ionic crystals	Reststrahlen	2–30	15–300
Crystal vibrations on electronic transitions	Anions with rare earths or transition metals	Increased repetition of pattern	10^4 – 10^5	UV and visible
Free-electron oscillations	Metals	High reflectivity	Continuum	Everywhere
Plasmas	Metals	Light spot	Bands	
Unfilled shell transitions	$4f$, $5f$, $3d$, $4d$, $5d$	Sharp fluorescence lines	10^4 – 10^5	UV and visible
Excitons	Alkali halides		10^4	$h\nu > E_g$
Color centers	Defects in ionic crystals	Absorption, coloring	5	UV and visible
Band-to-band transitions	Intrinsic semiconductors	Photoconduction	10–100	$h\nu > E_g$
Impurity transitions	Extrinsic semiconductors	Photoconduction	Continuum	Everywhere
Free carriers	Semiconductors	Weak absorption	Continuum	Everywhere

1.6.3 Spectra of Solids

The spectra of solids can be very complex. The band theory of solids predicts that there are allowable energy states that are filled with electrons up to the valence band. The conduction band, lying above it, can be empty or partially filled. One form of radiation occurs from the deceleration or oscillation of free carriers in the conduction band. Another occurs for the transition of carriers from the conduction band to the valence band. Another is a result of a fall to an impurity state.

Solids also have the characteristic vibration bands of gases (but not rotations). Excitations may be considered as excited electron-hole pairs, and radiation occurs upon deexcitation. Color centers occur after the impingement of high-energy radiation. They may be characterized by crystal imperfections, where, for instance, a hole is bound to a cation or a cation is missing from its normal site. They come in other guises as well. Some of these mechanisms are combined. They are summarized³² in Table 1.9.

1.6.4 Spectral Line Shapes

No spectral line is truly monochromatic. This may be thought of as the result of a transition taking place in a finite amount of time. This finiteness of time requires that the spectrum must also be finite. It can also be considered in terms of the Heisenberg uncertainty principle, which is related to the finite width of the function and its spectrum. The shape and width of a line are determined by the length of the transition, the Doppler effect, and the temperature and pressure of the gas. The latter two widen the ideal Lorentzian shape.

Lorentz Line. A line shape based strictly on the time it takes for a transition is called a natural line, and its width is called a natural linewidth. The expression for the absorption coefficient of such a line is

$$\alpha_L(\nu) = \frac{S}{\pi} \frac{\delta\nu_L}{(\nu - \nu_0)^2 + \delta\nu_L^2} . \quad (1.84)$$

This function is also called a Lorentzian function, and the line a Lorentz line. The full width at half-maximum (FWHM) is given by $\delta\nu_L$.

This line is broadened by an increase in temperature or pressure; the expression for the increase in the half-width, with the same shape, is

$$\delta\lambda = \delta\lambda_0 \frac{P}{P_0} \sqrt{\frac{T}{T_0}} . \quad (1.85)$$

Doppler Line. Lines are broadened in part by the Doppler effect, because the photons in the source move in more than one direction and consequently have slightly different Doppler shifts. The expression for a Doppler line is

$$\alpha_D(\nu) = \frac{S}{\delta\nu_D} \sqrt{\frac{\ln 2}{\pi}} \exp \left[-\frac{\ln 2}{\pi} \frac{(\nu - \nu_0)^2}{(\delta\nu_D)^2} \right] . \quad (1.86)$$

The Doppler width (FWHM) is given by

$$\delta\nu_D = \frac{\nu_0}{c} \sqrt{2 \ln 2 \frac{kT}{m}} . \quad (1.87)$$

The Doppler line shape usually exists when the half-width due to pressure and temperature broadening is much smaller than the half-width of the natural linewidth.

Mixed or Voigt Line. When the Doppler effect and the pressure broadening are of approximately equal importance in the line shape, they convolve in such a way that a mixed line results. The expression for its absorption coefficient is

$$\alpha(\nu) = \frac{\alpha_0}{\pi} \int_{-\infty}^{\infty} \frac{e^{-\zeta^2}}{u^2 + \left[\frac{\nu - \nu_0}{\delta\nu_L} \sqrt{\ln 2} - \zeta \right]^2} d\zeta , \quad (1.88)$$

where ζ is an arbitrary variable of integration, and u is given by

$$u = \frac{\delta\nu_D}{\delta\nu_L} \sqrt{\ln 2} . \quad (1.89)$$

In the treatment above, the resolving power or bandwidth has been switched back and forth from $d\nu$ to $d\lambda$ with abandon, but that is what happens. The reader may recall that

$$\frac{d\nu}{\nu} = \frac{d\lambda}{\lambda} . \quad (1.90)$$

BASIC Programs for Blackbody Functions

```

'x exp(x)/exp(x)-1 vs x
CLS
SCREEN 9
VIEW (100, 40)-(600, 275)
xmin = 0: xmax = 25
ymin = 0: ymax = 25
WINDOW (xmin, ymin)-(xmax, ymax)

'insert captions
LOCATE 23, 15: PRINT "Figure 1. f= x exp(x)/exp(x)-1 vs x"
LOCATE 22, 35: PRINT "x"
LOCATE 10, 1: PRINT "x or f"
LOCATE 20, 10: PRINT 0
LOCATE 13, 10: PRINT 5
LOCATE 6, 9: PRINT 10
LOCATE 21, 12: PRINT 0
LOCATE 21, 24: PRINT 5
LOCATE 21, 36: PRINT 10
LOCATE 21, 49: PRINT 15
LOCATE 21, 62: PRINT 20
LOCATE 21, 74: PRINT 25

'draw the grid lines
FOR x = xmin TO xmax STEP 5
  LINE (x, ymin)-(x, ymax), 8
NEXT x
FOR y = ymin TO 1.1 * ymax STEP 5
  LINE (xmin, y)-(xmax, y), 8
NEXT y

'calculate f and x vs x
FOR x = .001 TO 25 STEP .01
  f = x * EXP(x) / (EXP(x) - 1)
  PSET (x, x)
  PSET (f, x)
NEXT x

END

```

```

'Radiant exitance vs wavelength
CLS
SCREEN 9
VIEW (100, 40)-(600, 275)
xmin = 0: xmax = 25
ymin = 0: ymax = .012
WINDOW (xmin, ymin)-(xmax, ymax)

'set up constants
c = 2.9975E+10
h = 6.626E-34
pi = 3.14159
c2 = 14399
c1 = 2 * pi * c * c * h * 1E+16

'insert captions and tick values
LOCATE 23, 15: PRINT "Figure 2. Spectral radiant exitance vs wavelength"
LOCATE 22, 35: PRINT "Wavelength [um]"
LOCATE 8, 1: PRINT "Spectral"
LOCATE 9, 1: PRINT "Radiant"
LOCATE 10, 1: PRINT "Exitance"
LOCATE 11, 1: PRINT "[mW/cm2/um]"
LOCATE 20, 10: PRINT 0
LOCATE 13, 10: PRINT 5
LOCATE 6, 9: PRINT 10
LOCATE 21, 12: PRINT 0
LOCATE 21, 24: PRINT 5
LOCATE 21, 36: PRINT 10
LOCATE 21, 49: PRINT 15
LOCATE 21, 62: PRINT 20
LOCATE 21, 74: PRINT 25

```

```

'draw the grid lines
FOR x = xmin TO xmax STEP 1          'vertical lines
  LINE (x, ymin)-(x, ymax), 8        'the 8 gives gray grid lines
NEXT x
FOR y = ymin TO 1.1 * ymax STEP .001 'horizontal lines
  LINE (xmin, y)-(xmax, y), 8        '1.1x to get top line
NEXT y

'calculate the curve for different values of T and lambda
FOR T = 300 TO 380 STEP 10
  FOR lambda = 1 TO 25 STEP .01
    x = c2 / lambda / T                'the expression for x
    M = c1 / lambda ^ 5 / (EXP(x) - 1) 'Planck's equation
    'PRINT lambda, M                  'option for printing
    PSET (lambda, M), 12              'plotting the values;
                                      'the 12 gives a red line
  NEXT lambda
NEXT T

'Calculate the Wien displacement law
FOR T = 100 TO 400 STEP .1
  lambdax = 2898.8 / T
  x = c2 / lambdax / T                'the expression for x
  M = c1 / lambdax ^ 5 / (EXP(x) - 1) 'Planck's equation
  'PRINT lambda, M                  'option for printing
  PSET (lambdax, M), 14              'plotting the values
NEXT T

'Radiant exitance vs wavenumber
CLS
SCREEN 9                             'set the screen for EGA
VIEW (100, 60)-(600, 275)           'set an screen area
xmin = 0: xmax = 5000               'set extreme ordinate values
ymin = 0: ymax = .0001              'set extreme abscissa values
WINDOW (xmin, ymin)-(xmax, ymax)    'set appropriate calculational values

'set up constants
c = 2.9975E+10
h = 6.626E-34
pi = 3.14159
c2 = 14399
c1 = 2 * pi * c * c * h              'c1 in units of W/cm2
                                      'per reciprocal cm

'locate titles and axis values appropriately
LOCATE 23, 15: PRINT "Figure 3. Spectral radiant exitance vs wavenumber"
LOCATE 22, 35: PRINT "Wavenumber [waves/cm]"
LOCATE 8, 1: PRINT "Spectral"
LOCATE 9, 1: PRINT "Radiant"
LOCATE 10, 1: PRINT "Exitance"
LOCATE 11, 1: PRINT "[uW/cm]"
LOCATE 20, 10: PRINT 0
LOCATE 17, 10: PRINT 5
LOCATE 14, 9: PRINT 10
LOCATE 11, 9: PRINT 15
LOCATE 8, 9: PRINT 20
LOCATE 5, 9: PRINT 25
LOCATE 21, 12: PRINT 0
LOCATE 21, 23: PRINT 1000
LOCATE 21, 35: PRINT 2000
LOCATE 21, 48: PRINT 3000
LOCATE 21, 61: PRINT 4000
LOCATE 21, 73: PRINT 5000

'draw the grid lines
FOR x = xmin TO xmax STEP 500        'vertical lines
  LINE (x, ymin)-(x, ymax), 8        'the 8 gives gray lines
NEXT x
FOR y = ymin TO 1.1 * ymax STEP .00001 'horizontal lines
  LINE (xmin, y)-(xmax, y), 8
NEXT y

'calculate the curve for different values of T and nu
FOR T = 300 TO 350 STEP 10
  FOR nu = 40 TO 5000 STEP 10
    x = c2 * nu / 10000 / T          'the expression for x
    M = c1 * nu ^ 3 / (EXP(x) - 1)   'Planck's equation
    'PRINT nu, M                    'option for printing
    PSET (nu, M), 12                'plotting the values
  NEXT nu
NEXT T

```

40 IR/EO HANDBOOK

```

'Calculate the Wien displacement law
constant = 2.82143977# / 1.4399      'Wien constant for nu
FOR T = 400 TO 100 STEP -1
  FOR nu = 0 TO 5000 STEP 1000
    numax = constant * T
    x = 1.4399 * numax / T            'the expression for x in nu
    M = c1 * numax ^ 3 / (EXP(x) - 1) 'Planck's equation
    'PRINT numax, M                  'option for printing
    PSET (numax, M), 14              'plotting the values
  NEXT nu
NEXT T
END

'Log of spectral radiant exitance vs log of wavelength
CLS                                  'clear the screen
SCREEN 9                             'set the screen for EGA
VIEW (100, 40)-(600, 275)           'set an appropriate screen area
xmin = 0: xmax = 2                  'set extreme ordinate values
ymin = -3: ymax = 0                 'set extreme abscissa values
WINDOW (xmin, ymin)-(xmax, ymax)    'set appropriate calculational values

'set up constants
c = 2.9975E+10
h = 6.626E-34
pi = 3.14159
c2 = 14399
c1 = 2 * pi * c * c * h * 1E+16     'c1 in units of W/cm2/um

'locate titles and axis values appropriately
LOCATE 23, 15: PRINT "Figure 4. Spectral radiant exitance vs Wavelength"
LOCATE 22, 35: PRINT "Wavelength [um]"
LOCATE 10, 1: PRINT "Spectral"
LOCATE 11, 1: PRINT "Radiant"
LOCATE 12, 1: PRINT "Exitance"
LOCATE 13, 1: PRINT "[mW/cm2/um]"
LOCATE 20, 8: PRINT .001
LOCATE 15, 9: PRINT .01
LOCATE 9, 10: PRINT .1
LOCATE 4, 10: PRINT 1
LOCATE 21, 11: PRINT 1
LOCATE 21, 43: PRINT 10
LOCATE 21, 74: PRINT 100

'draw the grid lines
FOR n = .001 TO .01 STEP .001
  y = .4343 * LOG(n)
  LINE (xmin, y)-(xmax, y), 8
NEXT n
FOR n = .01 TO .1 STEP .01
  y = .4343 * LOG(n)
  LINE (xmin, y)-(xmax, y), 8
NEXT n
FOR n = .1 TO 1 STEP .1
  y = .4343 * LOG(n)
  LINE (xmin, y)-(xmax, y), 8
NEXT n
FOR n = 1 TO 10 STEP 1
  x = .4343 * LOG(n)
  LINE (x, ymin)-(x, ymax), 8
NEXT n
FOR n = 10 TO 100 STEP 10
  x = .4343 * LOG(n)
  LINE (x, ymin)-(x, ymax), 8
NEXT n
LINE (xmin, ymin)-(xmax, ymin)
LINE (xmin, ymin)-(xmin, ymax)
LINE (xmax, ymin)-(xmax, ymax)
LINE (xmin, ymax)-(xmax, ymax)

'calculate the curve for different values of T and lambda
FOR T = 200 TO 900 STEP 100
  FOR lambda = 1 TO 40 STEP .01
    x = c2 / lambda / T 'the expression for x

```

```

M = c1 / lambda ^ 5 / (EXP(x) - 1)      'Planck's equation
'PRINT .4343 * LOG(lambda), .4343 * LOG(M) 'option for printing
PSET (.4343 * LOG(lambda), .4343 * LOG(M)), 12 'plotting the values
NEXT lambda
NEXT T

'Calculation of the Wien displacement law
FOR T = 1000 TO 200 STEP -1
  lambdax = 2898.8 / T
  x = c2 / lambdax / T 'the expression for x
  M = c1 / lambdax ^ 5 / (EXP(x) - 1)      'Planck's equation
  'PRINT lambda, M 'option for printing
  PSET (.4343 * LOG(lambdax), .4343 * LOG(M)), 14 'plotting the values
NEXT T
END

'Log radiant exitance vs wavenumber
CLS
SCREEN 9                                'set the screen for EGA
VIEW (100, 60)-(600, 275)              'set an appropriate screen area
xmin = 1: xmax = 4                      'set extreme ordinate values
ymin = -6: ymax = -4                    'set extreme abscissa values
WINDOW (xmin, ymin)-(xmax, ymax)        'set appropriate calculational values

'set up constants
c = 2.9975E+10
h = 6.626E-34
pi = 3.14159
c2 = 14399
c1 = 2 * pi * c * c * h

'locate titles and axis values appropriately
LOCATE 23, 15: PRINT "Figure 5. Spectral radiant exitance vs wavenumber"
LOCATE 22, 35: PRINT "Wavenumber [waves/cm]"
LOCATE 8, 1: PRINT "Spectral"
LOCATE 9, 1: PRINT "Radiant"
LOCATE 10, 1: PRINT "Exitance"
LOCATE 11, 1: PRINT "[uW/cm]"
LOCATE 20, 11: PRINT 1
LOCATE 13, 10: PRINT 10
LOCATE 5, 9: PRINT 100
LOCATE 21, 12: PRINT 10
LOCATE 21, 32: PRINT 100
LOCATE 21, 52: PRINT 1000
LOCATE 21, 72: PRINT 10000

'draw the grid lines
FOR n = .00001 TO .0001 STEP .00001
  y = .4343 * LOG(n)
  LINE (xmin, y)-(xmax, y), 8
NEXT n
FOR n = .000001 TO .00001 STEP .000001
  y = .4343 * LOG(n)
  LINE (xmin, y)-(xmax, y), 8
NEXT n
FOR n = .1 TO 1 STEP .1
  y = .4343 * LOG(n)
  LINE (xmin, y)-(xmax, y), 8
NEXT n
FOR n = 10 TO 100 STEP 10
  x = .4343 * LOG(n)
  LINE (x, ymin)-(x, ymax), 8
NEXT n
FOR n = 100 TO 1000 STEP 100
  x = .4343 * LOG(n)
  LINE (x, ymin)-(x, ymax), 8
NEXT n
FOR n = 1000 TO 10000 STEP 1000
  x = .4343 * LOG(n)
  LINE (x, ymin)-(x, ymax), 8
NEXT n
LINE (xmin, ymin)-(xmax, ymin)
LINE (xmin, ymin)-(xmin, ymax)
LINE (xmax, ymin)-(xmax, ymax)
LINE (xmin, ymax)-(xmax, ymax)

```

```

'calculate the curve for different values of T and nu
FOR T = 100 TO 350 STEP 50
  FOR nu = 10 TO 5000 STEP 1
    x = c2 * nu / 10000 / T          'the expression for x
    M = c1 * nu ^ 3 / (EXP(x) - 1)   'Planck's equation
    'PRINT .4343 * LOG(nu), .4343 * LOG(M) 'printing option
    PSET (.4343 * LOG(nu), .4343 * LOG(M)), 12 'plotting the values
  NEXT nu
NEXT T

'Calculate the Wien displacement law
constant = 2.82143977# / 1.4399      'Wien constant for nu
FOR T = 400 TO 50 STEP -1
  FOR nu = 0 TO 5000 STEP 1000
    numax = constant * T
    x = 1.4399 * numax / T          'the expression for x in nu
    M = c1 * numax ^ 3 / (EXP(x) - 1) 'Planck's equation
    'PRINT .4343*LOG(numax), .4343*LOG(M) 'option for printing
    PSET (.4343 * LOG(numax), .4343 * LOG(M)), 14 'plotting the
  NEXT nu
NEXT T
END

'Universal curve for spectral power
CLS
CLS
SCREEN 9                                'set the screen for EGA
VIEW (100, 40)-(600, 275)             ' set an appropriate screen area
xmin = 0: xmax = 15                   'set extreme ordinate values
ymin = 0: ymax = 1                    'set extreme abscissa values
WINDOW (xmin, ymin)-(xmax, ymax)      'set appropriate calculational values

'set up constants
c = 2.9975E+10
h = 6.626E-34
pi = 3.14159
c2 = 14399
c1 = 2 * pi * c * c * h

'insert the captions
LOCATE 23, 15: PRINT "Figure 6. Normalized radiant exitance vs dimensionless f
LOCATE 22, 35: PRINT "Dimensionless frequency"
LOCATE 7, 1: PRINT "Normalized"
LOCATE 8, 1: PRINT "Radiant"
LOCATE 9, 1: PRINT "Exitance"
LOCATE 20, 10: PRINT 0
LOCATE 12, 9: PRINT .5
LOCATE 4, 10: PRINT 1
LOCATE 21, 12: PRINT 0
LOCATE 21, 33: PRINT 5
LOCATE 21, 54: PRINT 10
LOCATE 21, 74: PRINT 15

'setup the gridlines
FOR x = xmin TO xmax STEP 1           'vertical lines
  LINE (x, ymin)-(x, ymax), 8        'the 8 gives a gray grid structure
NEXT x
FOR y = ymin TO 1.1 * ymax STEP .1   'horizontal lines
  LINE (xmin, y)-(xmax, y), 8
NEXT y

'calculate the curve for different values of x
FOR x = .00001 TO 15 STEP .01        'blows up for 0; this is OK
  M = x ^ 3 / (EXP(x) - 1)            'Planck's equation in x with no constants
  'PRINT x, M                        'option for printing
  PSET (x, M / 1.4214), 12           'plotting the values
NEXT x

END

'Universal curve for photons
CLS
SCREEN 9                                'set the screen for EGA
VIEW (100, 40)-(600, 275)             'set an appropriate portion of the screen
xmin = 0: xmax = 15                   'set extreme ordinate values
ymin = 0: ymax = 1                    'set extreme abscissa values
WINDOW (xmin, ymin)-(xmax, ymax)      'set appropriate calculational values

```

```

'set up constants
c = 2.9975E+10
h = 6.626E-34
pi = 3.14159
c2 = 14399
c1 = 2 * pi * c * c * h

'insert the captions
LOCATE 23, 15: PRINT "Figure 7. Normalized photon exitance vs dimensionless fre
LOCATE 22, 35: PRINT "Dimensionless frequency"
LOCATE 7, 1: PRINT "Normalized"
LOCATE 8, 1: PRINT "Photon"
LOCATE 9, 1: PRINT "Exitance"
LOCATE 20, 10: PRINT 0
LOCATE 12, 9: PRINT .5
LOCATE 4, 10: PRINT 1
LOCATE 21, 13: PRINT 0
LOCATE 21, 33: PRINT 5
LOCATE 21, 53: PRINT 10
LOCATE 21, 74: PRINT 15

'draw the grid lines
FOR x = xmin TO xmax STEP 1      'vertical lines
    LINE (x, ymin)-(x, ymax), 8  'the 8 gives gray lines
NEXT x
FOR y = ymin TO 1.1 * ymax STEP .1 'horizontal lines
    LINE (xmin, y)-(xmax, y), 8
NEXT y

'calculate the curve for different values of x
FOR x = .00001 TO 15 STEP .01    'blows up for 0; this is OK
    M = x ^ 2 / (EXP(x) - 1)      'Planck's equation in x without constants
    ' PRINT x, M                  'option for printing
    PSET (x, M / .64761), 12      'plotting the values
NEXT x
END

'Cumulative curve for power
CLS
SCREEN 9                          'set the screen for EGA
VIEW (100, 40)-(600, 275)        'set an appropriate screen area
xmin = 0: xmax = 10              'set extreme ordinate values
ymin = 0: ymax = 1               'set extreme abscissa values
WINDOW (xmin, ymin)-(xmax, ymax) 'set appropriate calculational values

'insert the captions
LOCATE 23, 15: PRINT "Figure 8. Normalized cumulative radiant exitance vs dimen
LOCATE 22, 35: PRINT "Dimensionless frequency"
LOCATE 7, 1: PRINT "Normalized"
LOCATE 8, 1: PRINT "Radiant"
LOCATE 9, 1: PRINT "Exitance"
LOCATE 20, 10: PRINT 0
LOCATE 12, 9: PRINT .5
LOCATE 4, 10: PRINT 1
LOCATE 21, 12: PRINT 0
LOCATE 21, 43: PRINT 5
LOCATE 21, 74: PRINT 10

'print the grid lines
FOR x = xmin TO xmax STEP 1      'vertical lines
    LINE (x, ymin)-(x, ymax), 8  'the 8 gives gray lines
NEXT x
FOR y = ymin TO 1.1 * ymax STEP .1 'horizontal lines
    LINE (xmin, y)-(xmax, y), 8
NEXT y

'set up constants
c = 2.9975E+10
h = 6.626E-34
pi = 3.14159
c2 = 14399
c1 = 2 * pi * c * c * h

```

```

'calculate the curve for different values of x
FOR x = 0 TO 10 STEP .02
    sum = 0: m = 0
repeat:
    m = m + 1
    u = m * x
    term = (u ^ 3 + 3 * u ^ 2 + 6 * u + 6) * EXP(-u) / m ^ 4
    sum = sum + term: 'PRINT m, term, sum
    IF term / sum > 1E-09 THEN GOTO repeat
    constant = pi ^ 4 / 15
    integral = (constant - sum) / constant
    'PRINT x, integral
    PSET (x, integral), 12
NEXT x
END

```

'does not blow up for x=0
'initialize values
'for iteration
'increment index
'set convenient variable
'the sum from text
'add terms print to see converge
'test for convergence
'account for constants
'account for x=0 term
'option for printing

```

'Cumulative curve for photons
CLS
SCREEN 9
VIEW (100, 50)-(600, 270)
xmin = 0: xmax = 10
ymin = 0: ymax = 1
WINDOW (xmin, ymin)-(xmax, ymax)

'put in the captions
LOCATE 23, 15: PRINT "Figure 9. Normalized photon exitance vs dimensionless fr"
LOCATE 22, 35: PRINT "Dimensionless frequency"
LOCATE 7, 1: PRINT "Normalized"
LOCATE 8, 1: PRINT "Photon"
LOCATE 9, 1: PRINT "Exitance"
LOCATE 20, 10: PRINT 0
LOCATE 12, 9: PRINT .5
LOCATE 4, 10: PRINT 1
LOCATE 21, 12: PRINT 0
LOCATE 21, 43: PRINT 5
LOCATE 21, 74: PRINT 10

'set up constants
c = 2.9975E+10
h = 6.626E-34
pi = 3.14159
c2 = 14399
c1 = 2 * pi * c * c * h

'print the grid lines
FOR x = xmin TO xmax STEP 1
    LINE (x, ymin)-(x, ymax), 8
NEXT x
FOR y = ymin TO 1.1 * ymax STEP .1
    LINE (xmin, y)-(xmax, y), 8
NEXT y
FOR x = 0 TO 10 STEP .02

'calculate the integral from 0 to x by the summation technique
    sum = 0: m = 0
repeat:
    m = m + 1: u = m * x
    term = (u ^ 2 + 2 * u + 2) * EXP(-u) / m ^ 3
    sum = sum + term: 'PRINT m, term, sum
    IF term / sum > 1E-09 THEN GOTO repeat
    constant = 2.404095
    integral = (constant - sum) / constant
    'PRINT x, integral
    PSET (x, integral), 12
NEXT x
END

```

'set the screen for EGA
'set an appropriate portion of the screen
'set extreme ordinate values
'set extreme abscissa values
'set appropriate calculational values

'the 8 gives a gray grid structure

'get next term
'term calculation
'add terms
'convergence test
'using total integral value
'takes into account x=0 value
'option for printing it
'plotting the values

```

'Universal curve for spectral photon contrast
CLS
SCREEN 9 'set the screen for EGA
VIEW (100, 40)-(600, 275) 'set an appropriate portion of the screen
xmin = 0: xmax = 15 'set extreme ordinate values
ymin = 0: ymax = 1 'set extreme abscissa values
WINDOW (xmin, ymin)-(xmax, ymax) 'set appropriate calculational values

'set up constants
c = 2.9975E+10
h = 6.626E-34
pi = 3.14159
c2 = 14399
c1 = 2 * pi * c * c * h

'insert the captions
LOCATE 23, 15: PRINT "Figure 10. Normalized radiant contrast vs dimensionless
LOCATE 22, 35: PRINT "Dimensionless frequency"
LOCATE 7, 1: PRINT "Normalized"
LOCATE 8, 1: PRINT "Radiant"
LOCATE 9, 1: PRINT "Contrast"
LOCATE 20, 10: PRINT 0
LOCATE 12, 9: PRINT .5
LOCATE 4, 10: PRINT 1
LOCATE 21, 12: PRINT 0
LOCATE 21, 33: PRINT 5
LOCATE 21, 53: PRINT 10
LOCATE 21, 73: PRINT 15

'print the grid lines
FOR x = xmin TO xmax STEP 1
  LINE (x, ymin)-(x, ymax), 8 ' the 8 gives a gray grid structure
NEXT x
FOR y = ymin TO 1.1 * ymax STEP .1
  LINE (xmin, y)-(xmax, y), 8
NEXT y

'calculate the curve for different values of x
FOR x = .1 TO 15 STEP .01
  M = x ^ 2 / (EXP(x) - 1) 'Planck's equation in x without constants
  dMdt = x * EXP(x) / (EXP(x) - 1) * M
  'PRINT x, M, dMdt 'option for printing it out if so remark the n
  PSET (x, dMdt / 1.523432), 12 'plotting the values
NEXT x
END

```

```

'Cumulative curve for energy contrast
CLS
SCREEN 9 'set the screen for EGA
VIEW (100, 50)-(600, 270) 'set an appropriate screen area
xmin = 0: xmax = 15 'set extreme ordinate values
ymin = 0: ymax = 1 'set extreme abscissa values
WINDOW (xmin, ymin)-(xmax, ymax) 'set appropriate calculational values

'set up constants
c = 2.9975E+10
h = 6.626E-34
pi = 3.14159
c2 = 14399
c1 = 2 * pi * c * c * h

'put in the captions
LOCATE 23, 15: PRINT "Figure 11. Normalized cumulative power contrast vs dimens
LOCATE 22, 35: PRINT "Dimensionless frequency"

```



```

LOCATE 7, 1: PRINT "Normalized"
LOCATE 8, 1: PRINT "Energy"
LOCATE 9, 1: PRINT "Contrasts"
LOCATE 20, 10: PRINT 0
LOCATE 12, 9: PRINT .5
LOCATE 4, 10: PRINT 1
LOCATE 21, 12: PRINT 0
LOCATE 21, 33: PRINT 5
LOCATE 21, 54: PRINT 10
LOCATE 21, 74: PRINT 15

'print the grid lines
FOR x = xmin TO xmax STEP 1
    LINE (x, ymin)-(x, ymax), 8 ' the 8 gives a gray grid structure
NEXT x
FOR y = ymin TO 1.1 * ymax STEP .1
    LINE (xmin, y)-(xmax, y), 8
NEXT y

'calculate the integral from 0 to x by the summation technique
FOR x = 0 TO 15 STEP .04
    sum = 0: m = 0
    repeat:
        m = m + 1: u = m * x
        term = (u ^ 4 + 4 * u ^ 3 + 12 * u ^ 2 + 24 * u + 24) * EXP(-u) / m ^ 4
        sum = sum + term: ' PRINT m, term, sum
        IF term / sum > 1E-09 THEN GOTO repeat
        constant = 7.2123
        integral = (constant - sum) / constant
        ' PRINT x, integral
        PSET (x, integral), 12
    NEXT x
END

'Cumulative curve for energy contrast
CLS
SCREEN 9
VIEW (100, 50)-(600, 270)
xmin = 0: xmax = 15
ymin = 0: ymax = 1
WINDOW (xmin, ymin)-(xmax, ymax)

'set up constants
c = 2.9975E+10
h = 6.626E-34
pi = 3.14159
c2 = 14399
c1 = 2 * pi * c * c * h

'put in the captions
LOCATE 23, 15: PRINT "Figure 12. Normalized cumulative radiant contrast vs dime"
LOCATE 22, 35: PRINT "Dimensionless frequency"
LOCATE 7, 1: PRINT "Normalized"
LOCATE 8, 1: PRINT "Radiant"
LOCATE 9, 1: PRINT "Contrast"
LOCATE 20, 10: PRINT 0
LOCATE 12, 9: PRINT .5
LOCATE 4, 10: PRINT 1
LOCATE 21, 12: PRINT 0
LOCATE 21, 33: PRINT 5
LOCATE 21, 54: PRINT 10
LOCATE 21, 74: PRINT 15

'print the grid lines
FOR x = xmin TO xmax STEP 1
    LINE (x, ymin)-(x, ymax), 8 ' the 8 gives a gray grid structure
NEXT x
FOR y = ymin TO 1.1 * ymax STEP .1
    LINE (xmin, y)-(xmax, y), 8
NEXT y

```

```

'calculate the integral from 0 to x by the summation technique
FOR x = 0 TO 15 STEP .02
  sum = 0: m = 0
  repeat:
    m = m + 1: u = m * x
    term = (u ^ 4 + 4 * u ^ 3 + 12 * u ^ 2 + 24 * u + 24) * EXP(-u) / m ^ 4
    sum = sum + term: PRINT m, term, sum
    IF term / sum > 1E-09 THEN GOTO repeat
  constant = 25.975
  integral = (constant - sum) / constant
  PRINT x, integral
  PSET (x, integral), 12
NEXT x
END

```

```

'Cumulative curve for photon contrast
CLS
SCREEN 9
VIEW (100, 50)-(600, 270)
xmin = 0: xmax = 10
ymin = 0: ymax = 1
WINDOW (xmin, ymin)-(xmax, ymax)

'set up constants
c = 2.9975E+10
h = 6.626E-34
pi = 3.14159
c2 = 14399
c1 = 2 * pi * c * c * h

'insert the captions
LOCATE 23, 15: PRINT "Figure 13. Normalized cumulative photon contrast vs dimen"
LOCATE 22, 35: PRINT "Dimensionless frequency"
LOCATE 6, 1: PRINT "Normalized"
LOCATE 7, 1: PRINT "Cumulative"
LOCATE 8, 1: PRINT "Photon"
LOCATE 9, 1: PRINT "Contrast"
LOCATE 20, 10: PRINT 0
LOCATE 12, 9: PRINT .5
LOCATE 4, 10: PRINT 1
LOCATE 21, 12: PRINT 0
LOCATE 21, 43: PRINT 5
LOCATE 21, 74: PRINT 10

'print the grid lines
FOR x = xmin TO xmax STEP 1
  LINE (x, ymin)-(x, ymax), 8 ' the 8 gives a gray grid structure
NEXT x
FOR y = ymin TO 1.1 * ymax STEP .1
  LINE (xmin, y)-(xmax, y), 8
NEXT y

```

```

'calculate the integral from 0 to x by the summation technique
FOR x = 0 TO 10 STEP .02
  sum = 0: m = 0
  repeat:
    m = m + 1: u = m * x
    term = (u ^ 3 + 3 * u ^ 2 + 6 * u + 6) * EXP(-u) / m ^ 3
    sum = sum + term: PRINT m, term, sum
    IF term / sum > 1E-09 THEN GOTO repeat
  constant = 7.2123
  integral = (constant - sum) / constant
  PRINT x, integral
  PSET (x, integral), 12
NEXT x
END

```

References

1. "The International System of Units (SI)," Special Publication 330, The National Bureau of Standards (now The National Institute of Standards and Technology), U.S. Department of Commerce (1972).
2. ANSI Standard Z7.1-1967(RP-16), American National Standards Institute (1967).
3. R. C. Jones, "Terminology in photometry and radiometry," *Journal of the Optical Society of America* **53**, 1314 (1963).
4. F. E. Nicodemus in a discussion column of I. Spiro, *Optical Engineering* **13**, G165 and G173 (1974).
5. J. Geist and E. Zalewski, "Chinese restaurant nomenclature for radiometry," *Applied Optics* **12**, 435 (1973).
6. K. D. Mielenz, "International comparison of photometric base units," *Journal of Research of the NBS* **92**, 335 (1987).
7. *CIE Proceedings* **6**, 67 (1924); see also J. W. T. Walsh, *Photometry*, Dover (1965).
8. M. Planck, *Theory of Heat*, Macmillan, New York (1957).
9. E. R. Cohen and B. N. Taylor, "The 1986 adjustment of the fundamental physical constants," *Codata Bulletin* **63**, Pergamon Press, Elmsford, NY (1986).
10. M. A. Bramson, *Infrared, A Handbook for Applications*, Plenum Press, New York (1966).
11. R. B. Johnson and E. E. Branstetter, "Integration of Planck's equation by the Laguerre-Gauss quadrature method," *Journal of the Optical Society of America* **64**, 1445 (1974).
12. J. C. Richmond, "Rationale for emittance and reflectivity," *Applied Optics* **21**, 1 (1982).
13. W. L. Wolfe, "Proclivity for emissivity," *Applied Optics* **21**, 1 (1982).
14. F. E. Nicodemus, J. C. Richmond, J. J. Jsia, I. W. Ginsberg, and T. Limperis, "Geometrical considerations and nomenclature in reflectance," National Bureau of Standards, U.S. Department of Commerce (1977).
15. M. Born and E. Wolfe, *Electromagnetic Theory of Optics*, Pergamon Press, New York (1959).
16. F. E. Nicodemus, "Directional reflectance and emissivity of an opaque surface," *Applied Optics* **4**, 767 (1965).
17. G. Kirchhoff, "On the relation between the radiating and absorbing powers of different bodies for light and heat," *Philosophical Magazine and Journal of Science* **20** (Fourth Series), 130 (1860).
18. H. O. McMahon, "Thermal radiation from partially transparent bodies," *Journal of the Optical Society of America* **40**, 376 (1950).
19. F. E. Nicodemus, "Radiance," *American Journal of Physics* **31**, 368 (1963).
20. W. J. Smith, *Modern Optical Engineering*, 2nd ed., McGraw-Hill, New York (1990); see also J. Rainwater, "Generalization of the Abbe sine law in geometric optics," *American Journal of Physics* **32**, 626-631 (1964).
21. S. Liebes, Jr., "On the ray invariance of B/n^2 ," *American Journal of Physics* **37**, 932 (1969); see also A. Arkangy, "Liouville's theorem and the intensity of beams," *American Journal of Physics* **25**, 519 (1957).
22. H. C. Hottel and A. F. Sarophim, *Radiative Transfer*, McGraw-Hill, New York (1967).
23. P. Moon, *The Scientific Basis of Illuminating Engineering*, McGraw-Hill, New York (1936).
24. D. C. Hamilton and W. R. Morgan, National Advisory Committee on Aeronautics Technical Note 2836 (1952).
25. R. W. Boyd, *Radiometry and the Detection of Radiation*, John Wiley & Sons, New York (1983).
26. W. L. Wolfe, "Photometry and radiometry," in *Physical Optics and Light Measurements*, D. Malacara, Ed., Academic Press, New York (1980).
27. W. L. Wolfe, "Radiometry," in *Applied Optics and Optical Engineering*, R. R. Shannon, J. C. Wyant, Eds., Academic Press, New York (1980).
28. Committee on Colorimetry, *The Science of Color*, Thomas Y. Crowell (1963).
29. H. E. White, *Introduction to Atomic Spectra*, McGraw-Hill, New York (1934).
30. Herzberg, G., *Spectra of Diatomic Molecules*, Van Nostrand, New York (1950).
31. Adapted from E. J. McCartney, *Absorption and Emission by Atmospheric Gases*, John Wiley & Sons, New York (1983).
32. Adapted from M. Garbuny, *Optical Physics*, Academic Press, New York (1965).

CHAPTER 2

Artificial Sources

Anthony J. LaRocca

*Environmental Research Institute of Michigan
Ann Arbor, Michigan*

CONTENTS

2.1	Introduction	51
2.2	Standard Laboratory Sources	52
2.2.1	Blackbody Cavity Theory	52
2.2.2	Primary Standard of Light	57
2.2.3	Baseline Standard of Radiation	58
2.2.4	Working Standards of Radiation	59
2.3	Commercial Laboratory Sources	64
2.3.1	Blackbodies	64
2.3.2	Incandescent Nongaseous Sources	65
2.3.3	Carbon Arc	77
2.3.4	Enclosed Arc and Discharge Sources (High Pressure)	80
2.3.5	Enclosed Arc and Discharge Sources (Low Pressure)	90
2.3.6	Concentrated Arc Lamps	93
2.3.7	Glow Modulator Tubes	100
2.3.8	Hydrogen and Deuterium Arcs	103
2.3.9	Other Commercial Sources	108
2.4	Field Sources (Man-Made Targets)	108
2.4.1	Surface and Subsurface Vehicles	108
2.4.2	Aircraft	110
2.4.3	Muzzle Flash	117
2.4.4	Further Samples of Target Radiation	120
2.5	IR Simulation and Modeling Overview	128
2.5.1	Rationale	128
2.5.2	Overview of the Simulation Process	130
2.5.3	IR Image Simulation Outline Using SIRIM as an Example	130
	References	134

2.1 INTRODUCTION

This chapter deals with two sources of artificial radiation: laboratory and field sources. Normally, laboratory sources are used in some standard capacity and field sources are used as targets. Both varieties appear to be limitless.

The sources in this chapter were chosen arbitrarily, often depending upon manufacturer response to requests for information. The purpose of this chapter is to consolidate much of this information to assist the optical systems designer in making reasonable choices. Table 2.1 lists the symbols, nomenclature, and units used in this chapter.

Regarding the selection of a source, Worthing¹ suggests that the following questions be asked:

1. Does it supply energy at such a rate or in such an amount as to make measurements possible?
2. Does it yield an irradiation that is generally constant or that may be varied with time as desired?
3. Is it reproducible?
4. Does it yield irradiations of the desired magnitudes over areas of the desired extent?

Table 2.1 Symbols, Nomenclature, and Units*

<i>Symbols</i>	<i>Nomenclature</i>	<i>Units</i>
a	Ratio: l/r	—
B	Subscript used for blackbody radiation	—
c_2	Blackbody radiation constant	cm K
I	Radiant intensity	W sr ⁻¹
k	Emissivity corrective factor	—
L	Radiance	W cm ⁻² sr ⁻¹
l	Length (or depth) of cavity	cm
M	Radiant exitance	W cm ⁻²
m	Mach number	—
R	Cavity radius	cm
r	Aperture radius	cm
r_a^{bc}	Partial reflectivity of DeVos	sr ⁻¹
S	Interior surface area	cm ²
s	Aperture area	cm ²
T	Temperature	K, °C
x	Variable length	cm
y	Ratio: x/r	—
ϵ	Emissivity	—
θ	Angle of ray from surface normal	rad
λ	Wavelength	μm, Å
σ	Boltzmann constant	W cm ⁻² K ⁻⁴
Φ	Power, flux	W

*Most of the units, symbols and nomenclature in this chapter are shown in the tables and graphs corresponding to particular sources.

5. Has it the desired spectral distribution?
6. Has it the necessary operating life?
7. Has it sufficient ruggedness for the proposed problem?
8. Is it sufficiently easy to obtain and replace, or is its purchase price or its construction cost reasonable?

2.2 STANDARD LABORATORY SOURCES

2.2.1 Blackbody Cavity Theory

Radiation levels can be standardized by the use of a source that will emit a quantity of radiation that is both reproducible and predictable. Cavity configurations can be produced to yield radiation theoretically sufficiently close to Planckian such that it is necessary only to determine the amount of imprecision. Several theories have been expounded over the years to calculate the quality of a blackbody simulator.^a Two of the older, most straightforward, and demonstrable theories are those of Gouffé and DeVos.

The Method of Gouffé. For the total emissivity of the cavity forming a blackbody (disregarding temperature variations) Gouffé² gives

$$\varepsilon_0 = \varepsilon_0(1 + k) , \quad (2.1)$$

where

$$\varepsilon_0 = \frac{\varepsilon}{\varepsilon \left(1 - \frac{s}{S} \right) + \left(\frac{s}{S} \right)} \quad (2.2)$$

and

$k = (1 - \varepsilon)[(s/S) - (s/S_0)]$, and is always nearly zero—it can be either positive or negative

ε = emissivity of materials forming the blackbody surface

s = area of aperture

S = area of interior surface

S_0 = surface of a sphere of the same depth as the cavity in the direction normal to the aperture.

Figure 2.1 is a graph for determining the emissivities of cavities with simple geometric shapes. In the lower section, the value of the ratio s/S is given as a function of the ratio l/r . (Note the scale change at the value for $l/r = 5$.) The value of ε_0 is found by reading up from this value of the intrinsic emissivity of the cavity material. The emissivity of the cavity is found by multiplying ε_0 by the factor $(1 + k)$.

When the aperture diameter is smaller than the interior diameter of the cylindrical cavity or the base diameter of a conical cavity, the values of s/S determined from the graph must be multiplied by $(r/R)^2$, which is the ratio of the squares of the aperture and cavity radii (Fig. 2.1).

^aGenerically used to describe those sources designed to produce radiation that is nearly Planckian.

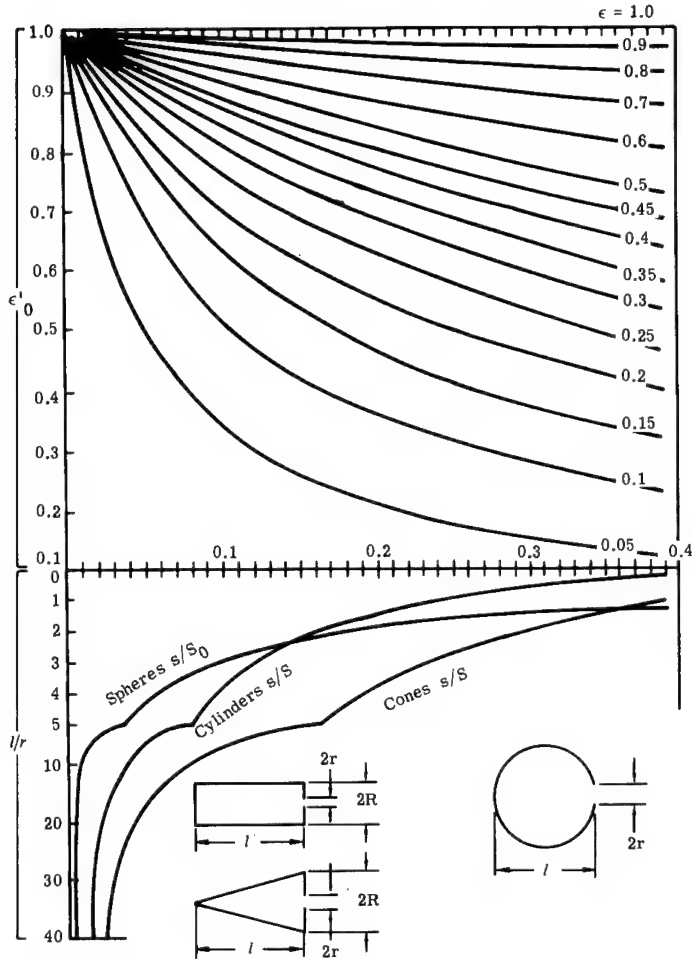


Fig. 2.1 Emissivities of conical, spherical, and cylindrical cavities.

The Method of DeVos. DeVos³ considers a cavity of arbitrary shape, with opaque walls, in a nonattenuating medium, initially at a uniform steady temperature with one small opening. He adds other openings and temperature variations along the cavity walls and indicates several practical approximations necessary for the calculation of numerical values (Fig. 2.2).

The power emitted from the opening $d0$ is

$$\text{em}\Phi_w^0 = \epsilon_w^0(\lambda, T) L_{\lambda, B}(\lambda, T) dw \cos\theta_w^0 d\Omega_w^0, \quad (2.3)$$

where

$\epsilon_w^0(\lambda, T)$ = the spectral emissivity of dw in the direction of $d0$ (indicated by subscripts and superscripts throughout) for temperature T at wavelength λ

$L_{\lambda, B}(\lambda, T)$ = the spectral radiance of a blackbody for temperature T and wavelength λ given by either the Planck equation or, approximately, by the Wien law

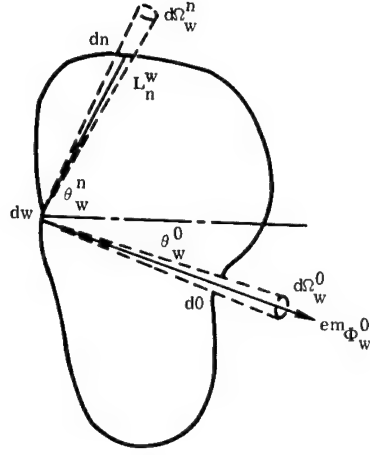


Fig. 2.2 Definition of terms for the DeVos method.

- $L_{\lambda,B}$ = (constant) $e^{-c_2/\lambda T}$
 dw = area of the emitting infinitesimal element
 Θ_w^0 = the angle of the direction from dw to $d0$ with respect to the normal to dw
 $d\Omega_w^0$ = the solid angle subtended by $d0$, the hole, as seen from dw .

The power from dw through $d0$, which is a result of the reflection of the power received at dw from some arbitrary elemental wall area, dn , is

$$\text{refl}\Phi_w^{n0} = L_{\lambda,n}^w(\lambda, T) d\Omega_w^n dw \cos\Theta_w^n r_w^{n0}(\lambda, T) d\Omega_w^0, \quad (2.4)$$

where

- Φ_w^{n0} = the power from dn to $d0$ via dw
 $L_{\lambda,n}^w(\lambda, T)$ = the spectral radiance from dn to dw for a temperature T and at a wavelength λ
 $d\Omega_w^n$ = the solid angle subtended by dn as seen from dw
 Θ_w^n = the angle to the normal to dw made by the direction from dw to dn
 $r_w^{n0}(\lambda, T)$ = the partial reflectivity of dw for radiation from dn at Θ_w^n reflected from dw toward $d0$ at Θ_w^0 at a wavelength λ for a temperature T .

Partial reflectivity^b can be defined as follows:

$$r_w^{n0} = \frac{L_w^{n0} \cos\Theta_w^0}{L_n^w \cos\Theta_w^n d\Omega_w^n} \quad (2.5)$$

or

$$r_w^{n0} = \frac{L_w^{n0}}{E_w^n} \cos\Theta_w^0. \quad (2.6)$$

^bThis terminology is slightly different from terminology used in other literature. The method of DeVos is retained here.

Integration over the walls excluding $d0$ gives the power from dw due to the reflection from dw of the radiation from all parts of the cavity wall except $d0$:

$$\text{refl}\Phi_w^0 = dw d\Omega_w^0 \int_{\text{alldn}} L_{\lambda,n}^w(\lambda, T) \cos\Theta_w^n r_w^{n0}(\lambda, T) d\Omega_w^n . \quad (2.7)$$

The reciprocity relation is

$$r^{ab} \cos\Theta^a = r^{ba} \cos\Theta^b . \quad (2.8)$$

By using the reciprocity relation, the following is obtained:

$$\text{refl}\Phi_w^0 = dw d\Omega_w^0 \cos\Theta_w^0 \int_{\text{alldn}} L_{\lambda,n}^w(\lambda, T) r_w^{0n}(\lambda, T) d\Omega_w^n . \quad (2.9)$$

To a first approximation, the following relationship is true:

$$L_{\lambda,n}^w(\lambda, T) = L_{\lambda,B}(\lambda, T) . \quad (2.10)$$

The hole can thus be considered to have an emissivity given by

$$\varepsilon_0 = 1 - r_w^{00} d\Omega_w^{h0} \quad (2.11)$$

to a first approximation neglecting temperature variations. If additional holes exist, then the reflected contributions of these elements must also be excluded. This leads to:

$$\varepsilon_0 = 1 - \sum_h r_w^{0h} d\Omega_w^h \quad (2.12)$$

for the emissivity of $d0$ in the direction from dw , when several holes exist numbered from $h=0$ to some finite integer.

For the second-order approximation, neglecting temperature variations, DeVos considers the use of a value for $L_{\lambda,n}^w$ which is not $L_{\lambda,B}$, but which is calculated by considering the effects of the holes on this spectral radiance (from each element dn).

The second-order approximation for the appropriate quantity is

$$\begin{aligned} \text{total}\Phi_w^0 &= L_{\lambda,B}(\lambda, T) dw \cos\Theta_w^0 d\Omega_w^0 \\ &\times \left(1 - \sum_h r_w^{0h} d\Omega_w^h - \sum_h \int r_n^{wh} d\Omega_n^h r_w^{0n} d\Omega_w^n \right) , \end{aligned} \quad (2.13)$$

where the integration is over the entire surface excluding the holes.

DeVos applied this theory to the V wedge, cylindrical (closed at one end), spherical, and tubular shapes. He did not treat the cone, a combination of cones, or a cone-cylinder.

For a cylinder of radius r and length l (Fig. 2.1), the value of ε_0 to a first-order approximation is

$$\varepsilon_0 \approx \left(1 - r_w^{00} \frac{\pi r^2}{l^2}\right) \approx \left(1 - r_w^{00} \frac{\pi}{a^2}\right), \quad (2.14)$$

where $a = l/r$.

For the second-order approximation (neglecting temperature gradients), one needs $d\Omega_w^n$ and $d\Omega_w^0$. If dn is an annulus of the cylinder with a length dx , then:

$$d\Omega_w^n = d\Omega_w^x = \frac{2\pi r^2 dx}{[(l-x)^2 + r^2]^{3/2}} \quad (2.15)$$

and

$$d\Omega_x^0 = \frac{\pi r^2}{x^2 + r^2}. \quad (2.16)$$

If $x/r = y$, then:

$$\varepsilon_0 = 1 - r_w^{00} \frac{\pi}{a^2} - 2\pi^2 \int_0^a \frac{r_w^{0y} r_y^{w0}}{(y^2 + 1)[(y - a)^2 + 1]^{3/2}} dy. \quad (2.17)$$

DeVos evaluated this expression by numerical integration. His values, corrected by Edwards⁴ for a small numerical error, are given in 2.2. For a similar calculation for a sphere, DeVos obtained the (corrected) results in Table 2.3.

Table 2.2 DeVos's Emissivities for a Cylindrical Blackbody* (from Ref. 4)

a	(d)	(s1)	(s2)	(s3)
6	0.970	0.954	0.865	0.668
10	0.990	0.985	0.953	0.864
15	0.995	0.994	0.980	0.947
20	0.997	0.997	0.989	0.972
30	0.999	0.999	0.996	0.988

*Emissivity values for a cylindrical blackbody with second-order corrections for various values of a ($= l/r$ = depth of cylinder/radius of hole) and surfaces of different smoothness. These are DeVos's values corrected for a numerical error.

Table 2.3 DeVos's Emissivities for a Spherical Blackbody* (from Ref. 4)

a	(d)	(s1)	(s2)	(s3)
10	0.992	0.989	0.963	0.894
20	0.998	0.993	0.991	0.976

*Emissivity values for a spherical blackbody with second-order corrections for various values of a ($= l/r$ = diameter of sphere/radius of hole) and surfaces of different smoothness. These are DeVos's values corrected for a numerical error.

DeVos made an attempt to examine the effect of temperature gradients in a cavity. This factor is the most important in determining the quality of a blackbody since it is not very difficult to achieve emissivities as near to unity as desired. Manufacturers of blackbody simulators strive to achieve uniform heating of the cavity because it is only under this condition that the radiation is Planckian. The ultimate determination of a radiator that is to be used as the standard is the quality of the radiation that it emits.

Leupin⁵ conducted a comparison of IR radiators. Incidentally, a division has historically existed between the standards of photometry and those used to establish thermal radiation and the thermodynamic temperature scale. Thus, in photometry the standard has changed from the use of candles, the Carcel lamp, the Harcourt pentane lamp, and the Hefner lamp⁶ to more modern radiators.

2.2.2 Primary Standard of Light

The primary standard now established is the candela, cd, corresponding to $1.0000 \text{ lm sr}^{-1}$. The construction of the primary standard of light is shown in Fig. 2.3. The radiator itself consists of a small cylinder of pure fused thoria, about 45 mm long, with an internal diameter of about 2.5 mm and a wall thickness of 0.2 to 0.3 mm. This cylinder, the bottom of which is packed with powdered fused thoria to a depth of 10 to 15 mm, is supported vertically in a fused-thoria crucible with an ~20-mm internal diameter nearly filled with pure platinum, as shown in Fig. 2.3. The crucible has a lid with a small hole in the center, about 1.5 mm in diameter. This hole, which is the source of light,

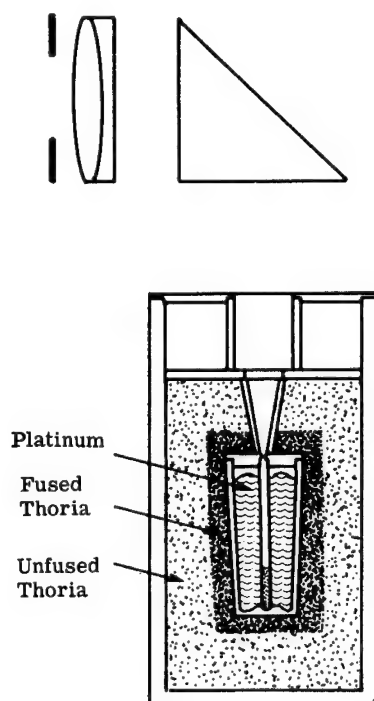


Fig. 2.3 The primary standard of light.⁶

is surrounded above by a funnel-shaped sheath forming part of the crucible lid. The crucible is embedded in powdered fused thoria in a larger refractory container and is heated by enclosing it in a high-frequency induction furnace. The power required to melt the platinum is about 7 kW at a frequency of the order of 1 MHz. With this arrangement, it is possible to regulate the temperature so closely that the period required for the solidification of the platinum may exceed 20 min. The purity of the platinum is controlled by taking samples before and after use and determining the ratio of the electric resistance at 100 and 0°C. A minimum value of 1.390 for this ratio is required to ensure that the temperature of solidification is sensibly the same as that of pure platinum. This corresponds to an impurity of less than 3 parts in 100,000. The luminance (radiance) of the hole is given the value of 60 cd cm^{-2} .

Note that this will soon be only of historical interest because the standard of light in this country will be based on a standard detector. A discussion of related issues was to appear in 1992 in the journal *Applied Optics*.

2.2.3 Baseline Standard of Radiation

Although there is no internationally accepted standard of radiation, the National Institute of Standards and Technology (NIST) uses as its substitute standard the goldpoint blackbody⁷ (see Fig. 2.4), which fixes one point on the international temperature scale, now reported to be $1337.33 \pm 0.34 \text{ K}$. Starting from this point, NIST is able to transfer fixed radiation values to working standards of radiation through an accurately constructed variable-temperature radiator⁸ as shown in Fig. 2.5.

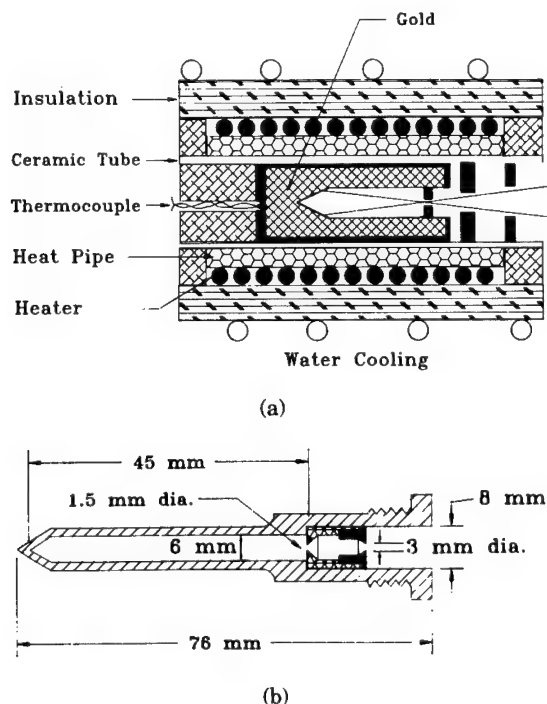


Fig. 2.4 (a) Cross section of heat-pipe blackbody furnace and (b) blackbody inner cavity dimensions.

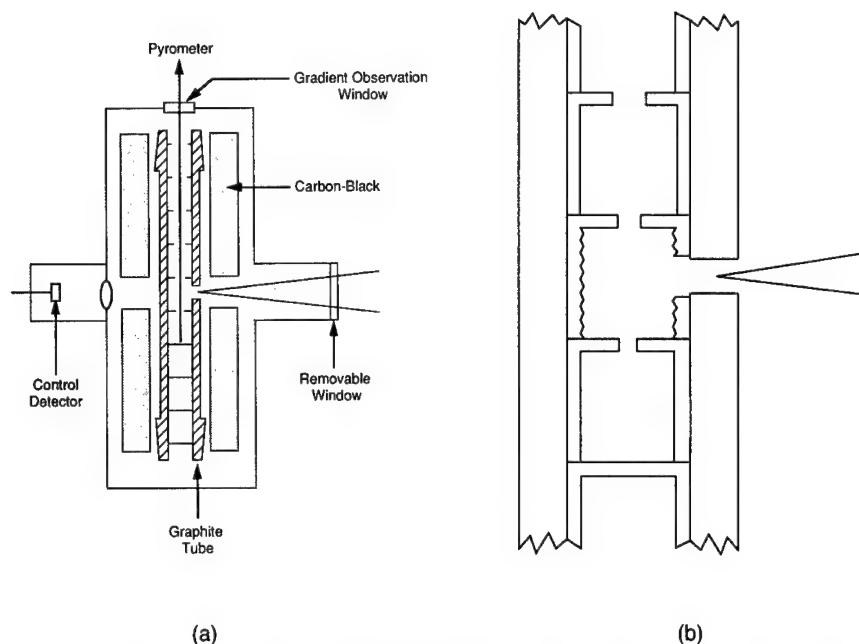


Fig. 2.5 (a) Variable temperature blackbody schematic and (b) central section of variable temperature blackbody.

The goldpoint blackbody is shown mainly for information. It is quite feasible to build a replica of the variable-temperature radiator, especially in a laboratory equipped to do fundamental radiation measurements.

2.2.4 Working Standards of Radiation

For the calibration of instruments in the ordinary laboratory, the user is likely to use a source that is traceable to NIST and generally supplied by NIST or one of the recognized vendors of calibrated sources. The sources are primarily in the form of a heated filament, or gaseous arc, enclosed in an envelope of glass or quartz (or fused silica), or in glass with a quartz or sapphire window.

Any source whose radiation deviates from that described by Planck's law is nonblackbody. Even the sources previously described are not strictly blackbodies, but can come as close as the user desires within the constraints of bulk and price. Any other source has an emissivity less than unity and can, and usually does, have a highly variable spectral emissivity. The lamps issued by NIST (and listed later in this chapter), for example, fit into this category; but they differ in one large respect. They are transfer standards, which have been carefully determined to emit specified radiation within certain specific spectral regions.

The following discussion of these types of sources is reproduced (in some cases with slight modifications), with permission, from NIST Special Publication 250.⁹ For specific details of calibration, and for the exact source designations, the user should contact the U.S. Department of Commerce, National Institute of Standards and Technology, Office of Physical Measurement Services, Room B362, Physics Building, Gaithersburg, MD 20899.

Photometric Standards. The following is a list of lamps available for photometric standards purposes:

- *Luminous intensity standard:* 100-W frosted tungsten lamp, 90 cd
- *Luminous intensity standard:* 100-W frosted tungsten lamp, color temperature, 2700 K
- *Luminous intensity standard:* 100-W frosted tungsten lamp, color temperature, 2856 K
- *Luminous intensity standard:* 500-W frosted tungsten lamp, 700 cd
- *Luminous intensity standard:* 1000-W frosted tungsten lamp, 1400 cd
- *Luminous intensity standard:* 1000-W frosted tungsten lamp, color temperature, 2856 K
- *Luminous flux standard:* 25-W vacuum lamp, about 270 lm
- *Luminous flux standard:* 60-W gas-filled lamp, about 870 lm
- *Luminous flux standard:* 100-W gas-filled lamp, about 1600 lm
- *Luminous flux standard:* 200-W gas-filled lamp, about 3300 lm
- *Luminous flux standard:* 500-W gas-filled lamp, about 10,000 lm
- *Luminous flux standard:* miniature lamps, seven sizes ranging from 6 to 400 lm
- *Airway beacon lamps for color temperature:* 500-W, one point in range, 2000 to 3000 K

Calibration services provide access to the photometric scales realized and maintained at NIST. Lamp standards of luminous intensity, luminous flux, and color temperature, as described in the following subsections, are calibrated on a routine basis.

Luminous Intensity Standards. Luminous intensity standard lamps supplied by NIST [100-W (90- to 140-cd), 500-W (approximately 700 cd), and 1000-W (approximately 1400 cd) tungsten filament lamps with C-13B filaments in inside-frosted bulbs with medium bipost bases] are calibrated at either a set current or a specified color temperature in the range from 2700 to 3000 K. Approximate 3σ uncertainties are 1% relative to the SI unit of luminous intensity and 0.8% relative to NIST standards.

Luminous Flux Standards. Vacuum tungsten lamps of 25 W and 60-, 100-, 200-, and 500-W gas-filled tungsten lamps that are submitted by customers are calibrated. Lamps must be base-up burning and rated at 120 V. Approximate 3σ uncertainties are 1.4% relative to SI units and 1.2% relative to NIST standards. Luminous flux standards for miniature lamps producing 6 to 400 lm are calibrated with uncertainties of about 2%.

Airway Beacon Lamps. Color temperature standard lamps supplied by NIST (airway beacon 500-W medium bipost lamps) are calibrated for color temperature in the range from 2000 to 3000 K with 3σ uncertainties ranging from 10 to 15 deg.

Infrared Radiometric Standards. The following is a list of lamps available for IR radiometric standards purposes:

- Spectral radiance ribbon filament lamps, 225 to 2400 nm
- Spectral radiance ribbon filament lamps, 225 to 800 nm
- Spectral radiance ribbon filament lamps, 650 to 2400 nm

- Spectral irradiance quartz-halogen lamps, 250 to 1600 nm
- Spectral irradiance quartz-halogen lamps, 250 to 2400 nm
- Spectral irradiance deuterium lamps, 200 to 350 nm

Spectral Radiance Ribbon Filament Lamps. These spectral radiance standards are supplied by NIST. Tungsten ribbon filament lamps (30A/T24/13) are provided as lamp standards of spectral radiance. The lamps are calibrated at 34 wavelengths from 225 to 2400 nm, with a target area 0.6 mm wide by 0.8 mm high. Radiance temperature ranges from 2650 K at 225 nm, and 2475 K at 650 nm, to 1610 K at 2400 nm, with corresponding uncertainties of 2, 0.6, and 0.4%. For spectral radiance lamps, errors are stated as the quadrature sum of individual uncertainties at the three standard deviation level.

Figure 2.6 summarizes the measurement uncertainty for NIST spectral radiance calibrations.

Spectral Irradiance Lamps. These spectral irradiance standards are supplied by NIST. Lamp standards of spectral irradiance are provided in two forms. Tungsten filament, 1000-W quartz-halogen-type FEL lamps are calibrated at 31 wavelengths in the range from 250 to 2400 nm. At the working distance of 50 cm, the lamps produce $0.2 \text{ W cm}^{-2} \text{ cm}^{-1}$ at 250 nm, $220 \text{ W cm}^{-2} \text{ cm}^{-1}$ at 900 nm, $115 \text{ W cm}^{-2} \text{ cm}^{-1}$ at 1600 nm, and $40 \text{ W cm}^{-2} \text{ cm}^{-1}$ at 2400 nm, with corresponding uncertainties of 2.2, 1.3, 1.9, and 6.5%. For spectral irradiance lamps, errors are stated as the quadrature sum of individual uncertainties at the three standard deviation level. Deuterium lamp standards of spectral irradiance are also provided and are calibrated at 16 wavelengths from 200 to 350 nm. At the working distance of 50 cm, the spectral irradiance produced by the lamp ranges from about $0.5 \text{ W cm}^{-2} \text{ cm}^{-1}$ at 200 nm and $0.3 \text{ W cm}^{-2} \text{ cm}^{-1}$ at 250 nm to $0.07 \text{ W cm}^{-2} \text{ cm}^{-1}$ at 350 nm. The deuterium lamps are intended primarily for the spectral region from 200 to 250 nm. The approximate uncertainty relative to SI units is 7.5% at 200 nm and 5% at 250 nm. The approximate uncertainty in relative spectral distribution is 3%. It is

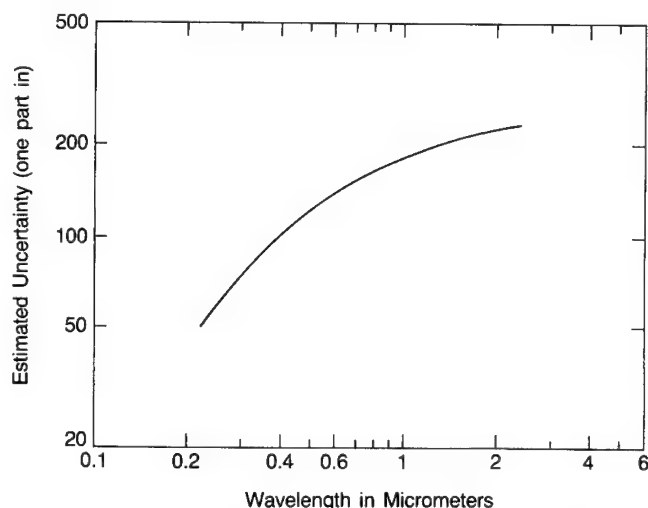


Fig. 2.6 Uncertainties for NIST spectral radiance calibrations.

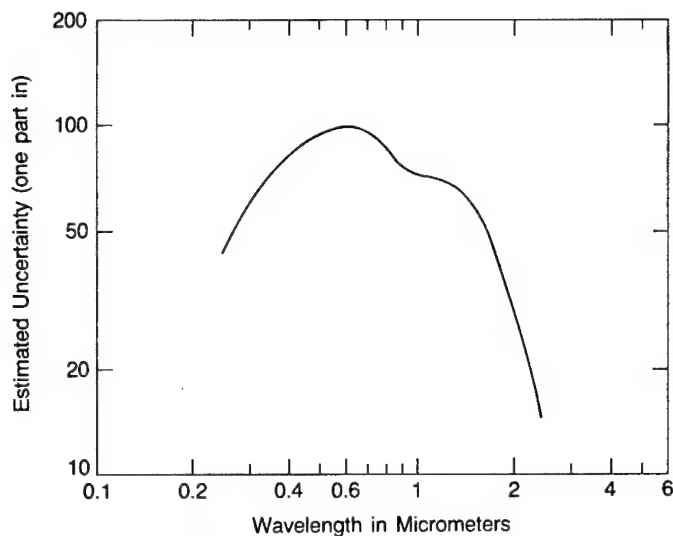


Fig. 2.7 Uncertainties for NIST spectral irradiance calibrations of FEL-type lamps.

strongly recommended that the deuterium standards be compared to an FEL tungsten standard over the range 250 to 300 nm each time the deuterium lamp is lighted to take advantage of the accuracy of the relative spectral distribution.

Figure 2.7 summarizes the measurement uncertainty for NIST spectral irradiance calibrations of FEL-type lamps.

Radiometric Sources in the Far-Ultraviolet Range. The following radiometric sources are available:

- *Spectral irradiance standard:* argon mini-arc, 140 to 330 nm
- *Spectral radiance standard:* argon mini-arc, 115 to 330 nm
- *Spectral irradiance standard:* deuterium arc lamp, 165 to 200 nm

Source Calibrations in the Ultraviolet Range. NIST maintains a collection of secondary sources such as argon maxi-arcs, argon mini-arcs, and deuterium arc lamps in the near and vacuum ultraviolet radiometric standards program to provide calibrations for user-supplied sources. The calibrations of these sources are traceable to a hydrogen arc whose radiance is calculable and which NIST maintains as a primary standard. The collection also includes tungsten strip lamps and tungsten halogen lamps whose calibrations are based on a blackbody rather than a hydrogen arc. Customer-supplied sources are calibrated in both radiance and irradiance by comparing them with NIST secondary standards.

Argon arcs are used to calibrate other sources in the wavelength range from 115 to 330 nm for radiance and 140 to 330 nm for irradiance. The lower wavelength limit is determined in radiance by the cutoff of the magnesium fluoride windows used in the arcs, and in irradiance by the decrease in signal produced by the addition of a diffuser. Deuterium arc lamps are used in the range from 165 to 200 nm, with the low-wavelength cutoff due to the onset of blended molecular lines.

The high-wavelength limit is the starting point of the range for the radiometric standards group. The tungsten lamps are used at 250 nm and above because their signals are too weak at shorter wavelengths. Note that the wavelength range of the NIST arcs partially overlaps the range of tungsten lamps, thus providing an independent check on calibrations.

An argon mini-arc lamp supplied by the customer is calibrated for spectral irradiance at 10-nm intervals in the wavelength region of 140 to 330 nm. Absolute values are obtained by comparison of the radiative output with laboratory standards of both spectral irradiance and spectral radiance. The spectral irradiance measurement is made at a distance of 50 cm from the field stop. Uncertainties are estimated to be less than $\pm 10\%$ in the wavelength region of 140 to 200 nm and within $\pm 5\%$ in the wavelength region of 200 to 330 nm. A measurement of the spectral transmission of the lamp window is included so that the calibration is independent of possible window deterioration or damage. The uncertainties are taken to be two standard deviations.

The spectral radiance of argon mini-arc radiation sources is determined to within an uncertainty of less than 7% over the wavelength range of 140 to 330 nm and 20% over the wavelength range of 115 to 140 nm. The calibrated area of the 4-mm-diam radiation source is the central 0.3-mm-diam region. Typical values of the spectral radiance are as follows: at 250 nm, $L(\lambda) = 30 \text{ mW cm}^{-2} \text{ nm}^{-1} \text{ sr}^{-1}$; and at 150 nm, $L(\lambda) = 3 \text{ mW cm}^{-2} \text{ nm}^{-1} \text{ sr}^{-1}$. The transmission of the demountable lamp window and that of an additional MgF_2 window are determined individually so that the user may check periodically for possible long-term variations.

The deuterium arc lamp is calibrated at 10 wavelengths from 165 to 200 nm, at a distance of 50 cm, at a spectral irradiance of about $0.5 \text{ W cm}^{-2} \text{ cm}^{-1}$ at 165 nm, $0.3 \text{ W cm}^{-2} \text{ cm}^{-1}$ at 170 nm, and $0.5 \text{ W cm}^{-2} \text{ cm}^{-1}$ at 200 nm. The approximate uncertainty relative to SI units is estimated to be less than 10%. The lamp is normally supplied by NIST and requires 300 mA at about 100 V.

Laser Power and Energy. Table 2.4 lists laser sources. These sources used at NIST are naturally only samples of the numerous lasers obtainable on the open market. But they represent a range of wavelengths obtainable in this

Table 2.4 Laser Sources

Source	Wavelength Range (μm)	Power Range (W)	Uncertainty (%)
Argon ion	0.488	1E-6 to 1E0	± 0.5 to 1.0
	0.5145	1E-6 to 1E0	± 0.5 to 1.0
Helium-neon	0.6328	1E-6 to 2E-3	± 0.5 to 1.0
Diode laser (GaAlAs)	0.830	1E-4 to 2E-2	± 0.5 to 1.0
Nd:YAG (cw)	1.064	1E-3 to 1E0	± 0.5 to 1.0
Nd:YAG (Q-switched)	1.064	<110 mJ/pulse	± 1.1 to 1.9
Nd:YAG (cw)	1.32	1E-4 to 1E-1	± 0.5 to 1.0
Helium-neon	1.53	1E-4 to 1E-3	± 0.5 to 1.0
Carbon dioxide	10.6	1E0 to 3E2	± 1.6 to 2.5
Carbon dioxide	10.6	4E-2 to 4E1	± 2.5 to 3.5

arena of sources, while at the same time being representable by NIST for traceability. To attempt to include the hundreds of types of lasers—and the thousands of varieties—would be superfluous for several reasons, but particularly because they change often. A summary chart is given in Ref. 10 that is very useful in helping the buyer choose among the different varieties. That chart is reproduced here in Table 2.5 with permission. The lasers listed in this chart represent most of what the ordinary laser user will want to know about these sources. A much more comprehensive source of this information can be found in Ref. 11.

2.3 COMMERCIAL LABORATORY SOURCES

2.3.1 Blackbodies

Virtually any cavity can be used to produce radiation of high quality, but practicality limits the shapes to a few. Popular shapes are cones and cylinders, with the former being more popular. Spheres, combinations of shapes, and even flat-plate radiators are used occasionally. Blackbodies can be bought rather inexpensively, but a fairly direct correlation exists between cost and quality (i.e., the higher the cost the better the quality).

Few manufacturers specialize in blackbody construction. Some, whose products are specifically described here, have been specializing in blackbody construction for many years. Other companies of this type may be found, for example, in the latest *Photonics Directory of Optical Industries*.¹²

A large selection of standard (or blackbody) radiators is offered by Electro-Optical Industries (EOI) of Santa Barbara, California.^c Most blackbodies can be characterized as one of the following: primary, secondary, or working standard. The output of the primary must, of course, be checked with those standards retained at NIST. Figure 2.8 pictures an EOI blackbody and its controller. Figure 2.9 pictures a similar blackbody and its controller from Mikron. All of the companies sell separate apertures (some of which are water cooled) for controlling the radiation output of the radiators. Another piece of auxiliary equipment that can be purchased is a multispeed chopper. It is impossible to cite all of the companies that sell these kinds of sources; therefore, the reader is referred to one of the buyer's guides already referenced for a relatively complete list. It is prudent to shop around for the source that suits one's own purpose.

Figure 2.10 demonstrates a less conventional working standard manufactured by EOI. Its grooves-and-honeycomb structure is designed to improve the absorptance of such a large and open structure. A coating with a good absorbing paint increases its absorptance further.

^cMany of the sources in the text are portrayed using certain specific company products merely for the sake of demonstration. This does not necessarily imply an endorsement of these products by the author. The reader is encouraged in all cases to consult Ref. 12 or a similar directory for competitive products.

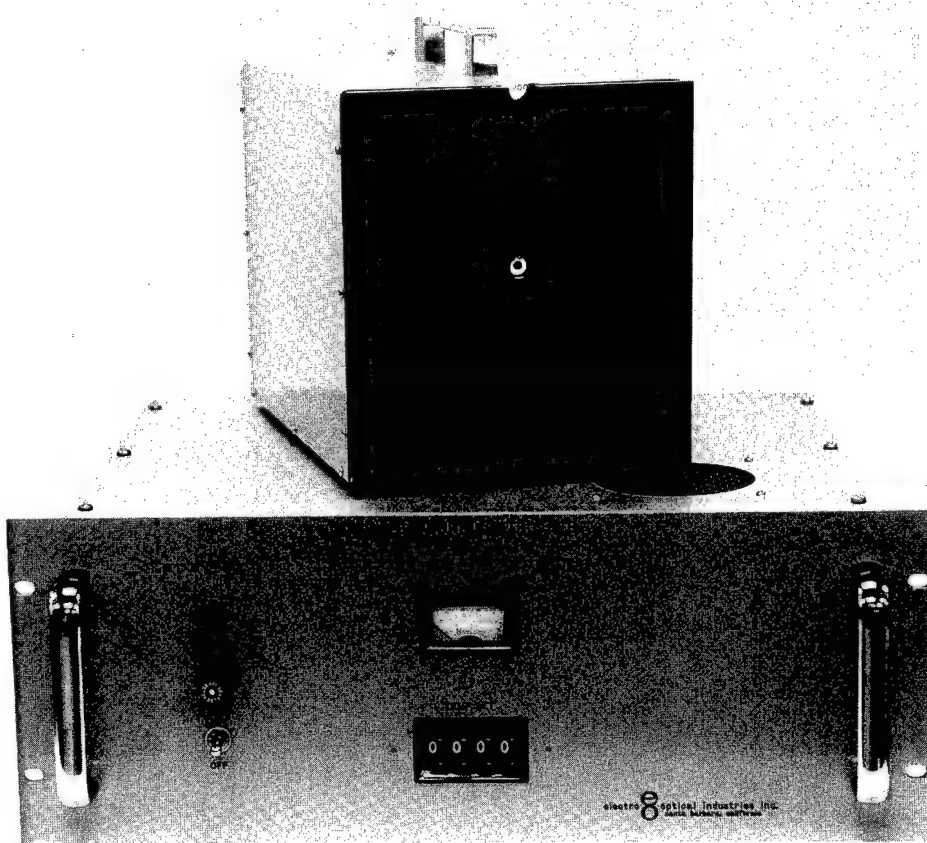


Fig. 2.8 EOI blackbody.

2.3.2 Incandescent Nongaseous Sources

This section deals with incandescent nongaseous sources exclusive of high-temperature blackbodies.

Nernst Glower. The Nernst glower is usually constructed in the form of a cylindrical rod or tube from refractory materials (usually zirconia, yttria, beria, and thoria) in various sizes. Platinum leads at the ends of the tube conduct power to the glower from the source. Since the resistivity of the material at room temperature is quite high, the working voltage is insufficient to get the glower started. Once started, its negative temperature coefficient-of-resistance tends to increase current, which would cause its destruction, so that a ballast is required in the circuit. Starting is effected by applying external heat, either with a flame or an adjacent electrically heated wire, until the glower begins to radiate.

Data from a typical glower are as follows:

1. power requirements: 117 V, 50 to 60 A, 200 W
2. color temperature range: 1500 to 1950 K
3. dimensions: 0.05 in. in diameter by 0.3 in.

Table 2.5 Laser Applications Matrix—A Guide to Commercial Lasers (from Ref. 10)

Hundreds, even thousands, of types of lasers have been operated under laboratory conditions over the last 26 years. But most are too inefficient to become commercial products; only about 30 types of lasers are regularly manufactured. The operating characteristics of these lasers differ widely from type to type; a key parameter for an excimer laser, for example, may not even exist for a solidstate laser. These tables depict a concise summary of the main operating characteristics of the major types of commercial lasers.

The most detailed descriptions cover the most widely used and manufactured types of lasers. Briefer descriptions are given for less common lasers, often devices for which there exist only one or two manufacturers. To keep the task manageable, characteristics relevant to only a few types of lasers or dependent on accessories (such as external optics) have generally been omitted.

This table is intended only to give an idea of the performance that can be expected from certain lasers. The ranges reflect those which are covered by all commercial devices; we know of no specific model that can cover the full ranges of all the operating parameters listed for a given laser.

Several families of laser types share important common features. These include:

- **Excimer lasers**, in which different gases are used in the same hardware (usually) to produce different emission wavelengths. The misnomer "excimer," which should be "exciplex," refers to the light-emitting species, a diatomic molecule consisting of a rare gas atom and a halogen atom. This diatomic molecule exists only in its excited state, a feature that enhances laser operation by eliminating lower-level bottlenecks.
- **Dye lasers**, which rely on a family of related active media, organic dyes carried in a liquid solvent. The energy needed to

Type of Laser	Wavelength	Power	Nature of Output	Price	Medium and Structure	Energy Requirements
Excimer: Argon Fluoride	193 nm	Up to 50 W avg.	5-25 ns pulses, to 500 mJ at 1-1000 Hz	\$30,000 to \$200,000	Gas mixture containing argon and fluorine	110 or 220 V to drive pulsed high-voltage discharge
Krypton Fluoride	248 nm	Up to 100 W avg.	2-50 ns pulses, to 1 J at 1-500 Hz	\$30,000 to \$200,000	Gas mixture containing krypton and fluorine	110 or 220 V to drive pulsed high-voltage discharge
Xenon Chloride	308 nm	Up to 150 W avg.	1-80 ns pulses, to 1.5 J at 1-500 Hz	\$30,000 to \$200,000	Gas mixture containing xenon and chlorine	110 or 220 V to drive pulsed high-voltage discharge
Xenon Fluoride	351 nm	Up to 30 W avg.	1-30 ns pulses, to 500 mJ at 1-500 Hz	\$30,000 to \$200,000	Gas mixture containing xenon and fluorine	110 or 220 V to drive pulsed high-voltage discharge
Dye Laser pumped by: Nitrogen, Excimer, Nd:YAG	Tunable from 300-1000 nm	0.05-15 W avg.	3-50 ns pulses at 0-10 kHz	\$4,000 to \$100,000	Dye in liquid solvent	110 or 220 V, plus pumping pulses from other laser
Flashlamp	Tunable from 340-940 nm	0.25 to 50 W avg.	0.2 to 4 μ s pulses, 0.05 to 50 J at 0.03 to 50 Hz	\$6,000 to \$50,000	Dye in liquid solvent	110 or 220 V to drive pulsed power supply for flashlamp
Ion Laser	Tunable from 400-1000 nm	To 2 W	Cw or picosecond pulses from mode-locked systems	\$8,000 to \$50,000	Dye in liquid solvent	110 or 220 V, 1 W or more (optical) from Ar or Kr pump laser
Nitrogen	337 nm	1-330 mW avg.	0.3-10 ns pulses at 1-1000 Hz (0.001-10 mJ)	\$1,500 to \$30,000	Flowing nitrogen gas in channel or sealed tube	110 V for pulsed high-voltage discharge or 12-V battery pack
Ion: Argon	Several lines 351-528 nm (main lines at 488 and 514.5 nm)	2 mW to 20 W	Cw (can be mode-locked)	\$3,000 to \$50,000	Argon gas in sealed tube	110, 220, or 440 V to drive high-voltage dc supply
Krypton	Several lines 350-800 nm (main line at 647.1 nm)	5 mW to 6 W (10-20% of argon output in same tube)	Cw (can be mode-locked)	\$10,000 to \$50,000	Krypton gas in sealed tube	110, 220, or 440 V to drive high-voltage dc supply
Argon-Krypton	Several lines 450-670 nm	0.5-6 W	Cw	\$12,000 to \$30,000	Argon-krypton gas mixture in sealed tube	220 or 440 V to drive high-voltage dc supply
Helium-Cadmium	442 or 325 nm	2-50 mW at 442 nm; 1.5-10 mW at 325 nm	Cw	\$3,000 to \$10,000	Ionized cadmium vapor mixed with helium in sealed tube	110 V to operate heater and high-voltage dc supply
Helium-Neon	543, 594, 604, 633, 1152, 1523, and 3391 nm	0.1-50 mW at 633 nm; to 15 mW at 1152 or 3391 nm; \approx 1 mW on other lines	Cw	\$140 to \$16,000	Helium-neon mixture in sealed tube	110 or 220 V at 20-400 W for high-voltage dc supply
Ruby	694 nm	Pulses of 0.03-100 J, durations from 10 ns to 10 ms	Pulse rates 0.01-4 Hz	\$15,000 to \$70,000	Synthetic ruby crystal with chromium impurity	110, 220, or 440 V for flashlamp power supply

Table 2.5 (continued)

drive the laser reaction comes from another laser or, in some cases, from flashlamps. Many organic dyes will lase under proper excitation; several dyes are needed to span the full wavelength tuning ranges listed. The emission characteristics of dye lasers pumped by different pumping sources vary widely and are generally similar to the characteristics of the pump source.

- **Ion lasers**, in which the light-emitting species is ionized argon, krypton, or a mixture of the two. Very similar hardware is used to build argon, krypton, and mixed-gas lasers. A related ion laser, the xenon laser, is listed under "Other Commercial Lasers" because of its limited market penetration, which is partly due to its pulsed output—in contrast to the continuous-wave output of argon and krypton lasers.

- **Semiconductor diode lasers**, where light is emitted at a p-n junction in a semiconductor. Wavelength depends on the composition of the semiconductor; operating characteristics depend on doping and structure of the device, among other parameters.

- **Solidstate lasers**, in which light from a flashlamp, arc lamp, or (most recently) a phase-coupled diode laser array excites laser emission from atoms in a crystalline or glass host. Design of different types is very similar and is sometimes essentially identical except for the rod and any special optical elements used.

- **Chemical lasers**, in which the same hardware is used to obtain laser action from ordinary hydrogen fluoride or from its isotopic variant, deuterium fluoride. HF and DF emit at different wavelengths.

- **Carbon-dioxide lasers**, which all rely on the same active medium, a gas mixture of CO₂ and nitrogen and helium buffer gases. But five different configurations, each with distinct operating characteristics, are available in the marketplace.

Efficiency	Weight	Cooling	Lifetime	Beam Diameter	Beam Divergence	Special Notes	Typical Applications
Up to 1%	50-500 kg	Air or water	10 ⁴ to 5 × 10 ⁶ shots per gas fill	2 × 4 to 25 × 30 mm	2 to 6 mrad in rectangular beam	Requires regular replenishment of dangerous gases	R&D, spectroscopy, photochemistry, medicine
Up to 2%	50-500 kg	Air or water	10 ⁴ to 10 ⁷ shots per gas fill	Similar to ArF	Similar to ArF	Similar to ArF	R&D, spectroscopy, photochemistry, medicine
Up to 2.5%	50-1000 kg	Air or water	10 ⁵ to 2 × 10 ⁷ shots per gas fill	Similar to ArF	Similar to ArF	Similar to ArF	R&D, spectroscopy, photochemistry, dye pumping, medicine
Up to 2%	50-500 kg	Air or water	10 ⁴ to 10 ⁷ shots per gas fill	Similar to ArF	Similar to ArF	Similar to ArF	R&D, spectroscopy, photochemistry, dye pumping, medicine
5-25% conversion of pump light	3.2-100 kg	Air, dye-solvent flow	Dye-limited (hours to a month or two)	2-10 mm	0.3-6 mrad	Pump laser usually separate, change dyes to span tuning range	R&D, spectroscopy, fluorescence studies, medicine
0.2-1% overall	30-110 kg	Water, dye-solvent flow	10 ⁴ to 10 ⁶ shots per flashlamp	5-20 mm	0.5-5 mrad	Linear or coaxial flash lamps used	R&D, spectroscopy, fluorescence studies, medicine
10-20% conversion of pump light	50-200 kg	Water, dye-solvent flow	Dye-limited (hours to a week or so)	0.6-1.0 mm	1-2 mrad	Requires external pump laser; ring or linear cavity	R&D, spectroscopy, fluorescence studies, medicine
Up to 0.1%	2.3-60 kg	Air	Thousands of hours; clean after 10 ⁶ shots	2 × 3 to 6 × 30 mm	0.3 to 3 × 7 mrad	Nearly superradiant; some require nitrogen supply	Dye pumping, nonlinear spectroscopy, Raman scattering
0.01-0.1%	10-300 kg	Water or forced air	1,000 hours to 5 years	0.6-2.0 mm	0.4-1.0 mrad	Single- or multiline output in visible or ultraviolet	Recording, spectroscopy, dye pumping, reprographics, medicine
0.001-0.05%	10-300 kg	Water or forced air	10 ³ to 10 ⁴ hours	0.6-2.0 mm	0.4-1.5 mrad	Single- or multiline output in visible or ultraviolet	Multicolor light shows and displays dye pumping
0.005-0.02%	60-100 kg	Water	10 ³ hours plus	2 mm	2 mrad	Generally built for multiline visible emission	Multicolor light shows and displays
0.01-0.1%	10-20 kg	Air	4,000 hours visible; 2,000 hours ultraviolet	0.3-1.2 mm	0.4-1.9 mrad	Tubes built either for visible or ultraviolet output	Recording, reprographics, spectroscopy, micro-lithography, medicine
0.01-0.1%	1.5-100 kg	Air	5 × 10 ³ to 10 ⁵ hours	0.3-3.0 mm	0.6-6.0 mrad	Most tubes single-line emission; a few are line-tunable in visible	Construction, recording, holography, reprographics, measurement
0.1-0.5%	30-700 kg	Water	About 10 ⁶ shots per flashlamp	1.5-25 mm	0.2-10 mrad	Pulse lengths can be controlled; double pulsing for holography	R&D, holography, materials working

(continued)

Table 2.5 (continued)

Type of Laser	Wavelength	Power	Nature of Output	Price	Medium and Structure	Energy Requirements
Semiconductor Diode: GaAlAs	750-905 nm (composition-dependent)	1-40 mW, average or cw	Cw or pulsed	\$20 to \$6,000	p-n junction in semi- conducting GaAs or GaAlAs	10-500 mA at about 2 V
Phase-coupled GaAlAs Arrays	790-850 nm (composition-dependent)	100 mW to 1 W cw, 1 W to 10 W peak power in pulse mode	Cw or pulsed with durations 1 ns to 200 μ s	\$150 to \$5,000	Multiple quantum well semiconductor junc- tion in GaAlAs	0.3-3 A cw, 1.6-50 A pulsed
InGaAsP	1100-1600 nm (composition-dependent)	1-10 mW	Cw or pulsed	\$1,000 to \$7,000	p-n junction in quaternary semiconductor	20-200 mA at 1.5 V
Neodymium-doped YAG (pulsed)	1.064 μ m (1.32 μ m is lower-powered alternative)	To 600 W average	Pulses, 0.01 to rates to 50 kHz	\$8,000 to \$125,000	Synthetic crystal of yttrium aluminum garnet, doped with neodymium	110 to 440 V to drive flashlamp power supply
Diode-pumped Neodymium-doped YAG	1.064 μ m (1.32 μ m is lower-powered alternative)	0.5-10 mW	Cw or pulsed, can be modelocked or Q-switched	\$3,000 to \$15,000	YAG crystal doped with neodymium, selectively driven by diode laser	110 or 220 V for diode power supply, lower voltage possible
Neodymium-doped YAG (CW)	1.064 μ m (1.32 μ m is lower-powered alternative)	0.04 to 600 W	Cw	\$3,000 to \$95,000	YAG crystal doped with neodymium	110 or 220 V for flashlamp power supply
Neodymium-doped Glass	1.06 μ m	Pulses of 0.1-100 J	Pulsed at 0.1-2 Hz	\$10,000 to \$125,000	Glass doped with neodymium	220 V to drive flashlamp power supply
F-center	1.43-1.58 μ m and 2.3-3.5 μ m	1-100 mW	Cw or modelocked pulses of a few picoseconds	\$35,000 to \$50,000	F-centers (impurities) in alkali halide crystals	110 or 220 V, 1-2 W (optical) from ion or Nd YAG pump laser
Hydrogen Fluoride (chemical)	2.6-3 μ m (many discrete lines)	0.01-150 W cw or 2-600 mJ pulses	Cw or 50-200 ns pulses at 0.5-20 Hz	\$10,000 to \$90,000	Low-pressure gas containing chemically produced hydrogen fluoride	110 or 220 V to drive pulsed or cw high- voltage discharge
Deuterium Fluoride (chemical)	3.6-4 μ m (many discrete lines)	0.01-100 W cw or 2-600 mJ pulses	Cw or 50-200 ns pulses at 0.5-20 Hz	\$10,000 to \$90,000	Low-pressure gas containing chemically produced deuterium fluoride	110 or 220 V to drive pulsed or cw high- voltage discharge
Carbon Dioxide: Axial Gas Flow	9-11 μ m or 10.6 μ m	20 W to 5 kW	Cw or long pulses	\$15,000 to \$300,000	Flowing gas mixture containing CO ₂ and other gases	110, 220, or 440 V
Transverse Gas Flow	9-11 μ m or 10.6 μ m	500 W to 15 kW	Cw or long pulses	\$80,000 to \$500,000	Flowing gas mixture containing CO ₂ and other gases	110, 220, or 440 V
Sealed-tube	9-11 μ m or 10.6 μ m	3-100 W	Generally cw	\$5,000 to \$35,000	Gas mixture containing CO ₂ in sealed tube	110 V
Pulsed, TEA	9-11 μ m or 10.6 μ m	0.03-150 J pulses	50 ns to 100 μ s pulses at 0.1-1000 Hz	\$5,000 to \$125,000	Gas mixture containing CO ₂ at near- atmospheric pressure	110 or 220 V to drive pulsed high-voltage discharge
Waveguide	9-11 μ m or 10.6 μ m	0.1-50 W	Cw or pulsed	\$3,000 to \$25,000	Gas mixture containing CO ₂ in a waveguide tube	110 V to drive power supply

Other Commercial Lasers

Type	Wavelength	Comments
Fluorine	157 nm	F ₂ in excimer laser, used in R&D
Krypton Chloride	222 nm	Similar to other excimer lasers
Copper Vapor	510 and 578 nm	Requires heating to vaporize copper, used for dye pump and forensics
Xenon	540 nm	Pulsed output, used for electronic production applications
Gold Vapor	628 nm	Similar to copper vapor, used mostly in medical R&D
Ti: Sapphire	700-980 nm	Continuously tunable argon-pumped solidstate laser
Alexandrite	730-780 nm	Continuously tunable flashlamp-pumped solidstate laser
GSGG	745-835 nm	Nd and/or Cr doped crystal of gallium scandium gadolinium garnet
Perkovskite	780-850 nm	Cr doped crystal of potassium zinc fluoride, used in R&D

Table 2.5 (continued)

Efficiency	Weight	Cooling	Lifetime	Beam Diameter	Beam Divergence	Special Notes	Typical Applications
1-20%	1 gm or less (package-dependent)	Air, heat sink	10^4 to 10^7 hours	Not meaningful	About $10 \times 35^\circ$	Modulated directly by drive current, sold without power supply	Printing, recording, reading, optical communications
20-40%	1-5 gm	Air, heat sink	10^4 to 7×10^4 hours	Not meaningful	$5 \times 10^\circ$ to $10 \times 35^\circ$	10-1000 stripes in array, phase coupled, addressed in parallel	Optical pumping, illumination, rangefinding, fiber sensors
1-20%	1 gm or less (package-dependent)	Air, heat sink	to 10^5 hours	Not meaningful	$10 \times 30^\circ$ to $20 \times 40^\circ$	Modulated directly by drive current, sold without power supply	Fiberoptic communications
0.1-2.0% overall	30-700 kg	Water	About 10^5 shots per flashlamp	1-10 mm	0.3-20 mrad	Can Q-switch or modelock, divergence rises with output power	R&D, materials working, rangefinding, medicine, dye pump
5-8% overall	negligible (package-dependent)	Air	10^4 hours plus (depends on diode laser)	1-2 mm typ.	0.5-2.0 mrad typ.	Highly efficient, compact, singlemode output stable to 10 kHz	Fiber communications (1.32 μm), R&D, holography, laser radar
0.1-3.0% overall	30-700 kg	Water	Arc lamps last about 200 hours	0.7-8 mm	2-25 mrad	Can Q-switch or modelock	R&D, materials working, medicine, inspection
1-5%	100-500 kg	Water	About 10^5 shots per flashlamp	3-25 mm (some rectangular)	3-10 mrad	Can Q-switch or modelock	R&D, materials working
To 10% conversion of pump light	15 kg	Liquid nitrogen	Thousands of hours	1.35 mm	1.6 mrad	Pump laser requirements dependent on wavelength region	R&D, spectroscopy, nonlinear fiber studies
0.1-1.0%	150-2000 kg	Flowing gas or water	Needs maintenance every 50-100 hours	2-40 mm	1-15 mrad	Operates on one or many lines, needs vacuum pump, exhaust is toxic	Atmospheric research, other R&D
0.1-1.0%	150-2000 kg	Flowing gas or water	Needs maintenance every 50-100 hours	2-40 mm	1-15 mrad	Similar to HF, exhaust is toxic	R&D
5-15%	100 kg to several tons	Air, water/glycol	Thousands of hours	3-25 mm	1-3 mrad	Needs gas supply and vacuum system, gas can be recirculated	Materials working, surgery (low power)
5-15%	100 kg to several tons	Air, water/glycol	Thousands of hours	10-50 mm	1-3 mrad	Needs gas supply and vacuum system, gas can be recirculated	Materials working
5-15%	to 50 kg	Water or air	10^4 hours	3-4 mm	1-2 mrad	Can fill with isotopic gases to select specific wavelengths	R&D, surgery, low-power materials working
1-10%	35-1000 kg	Water or air	10^5 or more shots	5-100 mm	0.5-10 mrad	Single- or multiline output, discharge transverse to beam	R&D, materials working, photochemistry, laser radar, remote sensing
About 5%	5-20 kg	Air	to 10^4 hours	1-10 mm	4-10 mrad	Single- or multiline output, gas flow typically rapid	Materials working, surgery, laser radar, other R&D

Other Commercial Lasers (cont.)

Type	Wavelength	Comments
Erbium:YLF	850 or 1730 nm	Erbium-doped yttrium lithium fluoride, similar to Nd:YAG
Iodine	1.3 μm	High power R&D tool
Erbium: Glass	1.54 μm	Erbium-doped glass, used in "eyesafe" rangefinders
Holmium	2.06 μm	Ho:YLF; similar to Nd:YAG; some interest in rangefinding
Erbium:YAG	2.94 μm	Pulsed erbium-doped YAG, for medical applications
Lead-salt Semiconductor Diode	3-30 μm	Tens of mW; requires cryogenics; several diodes needed for full range
Carbon Monoxide	5-7 μm (many discrete lines)	Cw or pulsed, single- or multiline operation
Far Infrared	30-1000 μm	Organic vapors pumped by CO_2 laser, used in R&D

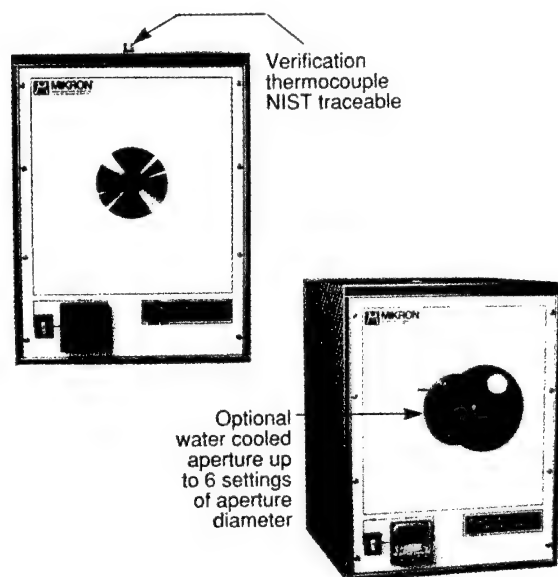


Fig. 2.9 Mikron blackbody.

The spectral characteristics of a Nernst glower in terms of the ratio of its output to that of a 900°C blackbody are shown in Fig. 2.11.

The life of the Nernst glower diminishes as the operating temperature is increased. Beyond a certain point, depending on the particular glower, no great advantage is gained by increasing the current through the element. The glower is fragile, with low tensile strength, but can be maintained intact with rigid support. The life of the glower depends on the operating temperature, care in handling, and the like. Lifetimes of 200 to 1000 h are claimed by various manufacturers.

Since the Nernst glower is made in the form of a long thin cylinder, it is particularly useful for illuminating spectrometer slits. Its useful spectral range is from the visible region to almost 30 μm , although its usefulness compared with other sources diminishes beyond about 15 μm . As a rough estimate, the radiance of a glower is nearly that of a graybody at the operating temperature with an emissivity in excess of 75%, especially below about 15 μm . The relatively low cost of the glower makes it a desirable source of moderate radiant power for optical uses in the laboratory. The makers of spectroscopic equipment constitute the usual source of supply of glowers (or of information about suppliers).

Globar. The globar is a rod of bonded silicon carbide and is usually capped with metallic caps, which serve as electrodes for the conduction of current through the globar from the power source. The passage of current causes the globar to heat, yielding radiation at a temperature greater than 1000°C. A flow of water through the housing that contains the rod is needed to cool the electrodes (usually silver). This complexity makes the globar less convenient to use than the Nernst glower and necessarily more expensive. This source can be obtained already mounted, from a number of manufacturers of spectroscopic equipment. Feedback in the controlled power source makes it possible to obtain high radiation output.

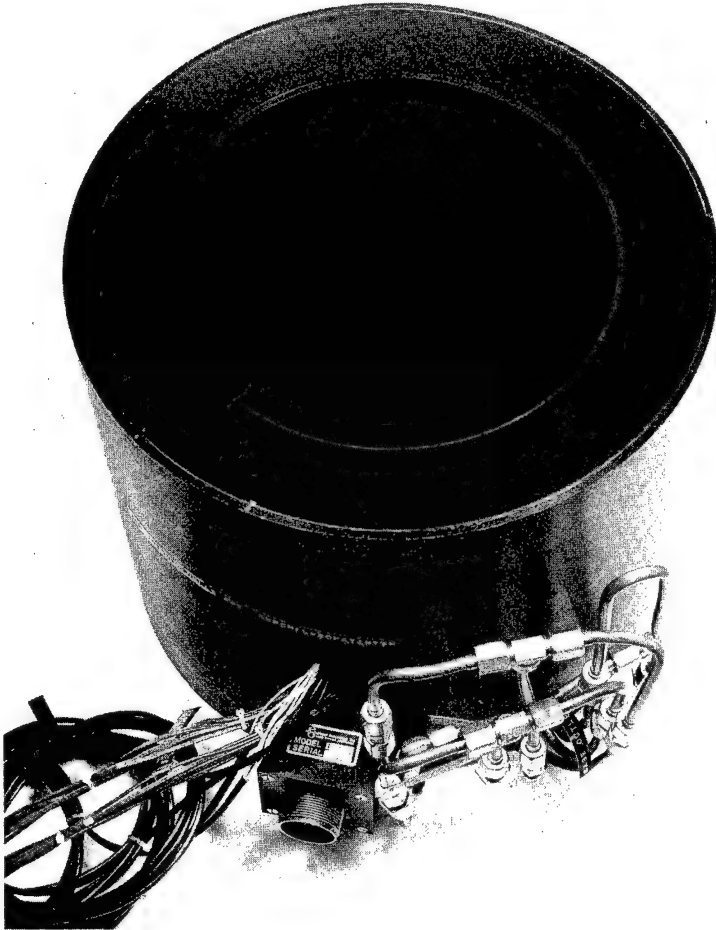


Fig. 2.10 EOI working standard.

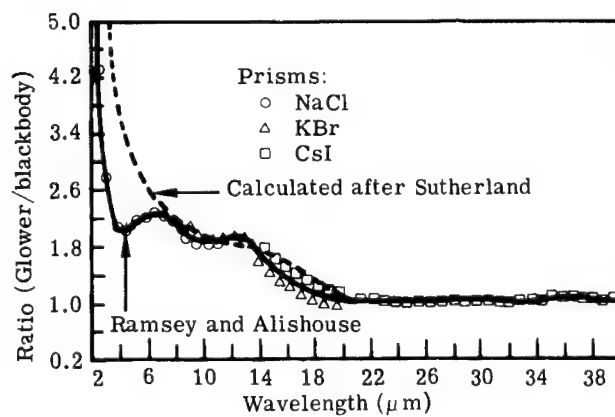


Fig. 2.11 The ratio of a Nernst glower to a 900°C blackbody versus wavelength.¹³

Ramsey and Alishouse¹³ provide information on a particular sample globar as follows:

1. power consumption: 200 W, 6 A
2. color temperature: 1470 K.

They also provide the spectral characteristics of the globar in terms of the ratio of its output to that of a 900°C blackbody. This ratio is plotted as a function of wavelength in Fig. 2.12. Figure 2.13 is a representation of the spectral emissivity of a globar as a function of wavelength. The emissivity values are only representative and can be expected to change considerably with use.

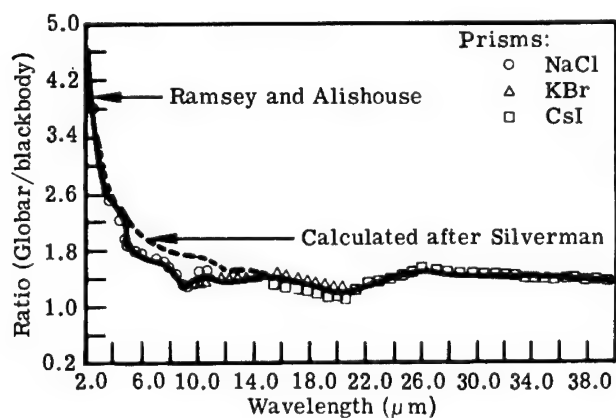


Fig. 2.12 The ratio of a globar to a 900°C blackbody versus wavelength.¹³

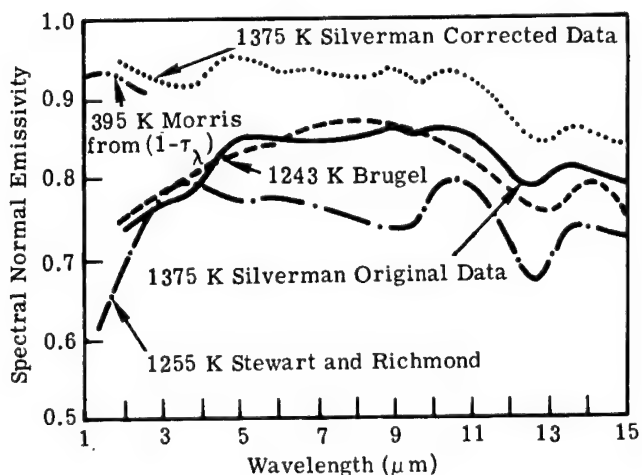


Fig. 2.13 The spectral emissivity of a globar.¹⁴

Gas Mantle. The Welsbach mantle is typified by the type found in high-intensity gasoline lamps used where electricity is not available. The mantle is composed of thorium oxide with some additive to increase its efficiency in the visible region. Its near-infrared emissivity is quite small, except for regions exemplified by gaseous emission, but increases considerably beyond $10\ \mu\text{m}$.

Ramsey and Alishouse¹³ provide information on a propane-heated sample from an experiment in which a comparison of several sources is made:

1. color temperature: 1670 K
2. dimensions: 25.4 by 38.1 mm.

The spectral characteristics of the mantle in terms of the ratio of its output to that of a 900°C blackbody are shown in Fig. 2.14.

Pfund¹⁵ modified the gas mantle so that it became more of a laboratory experimental source than an ordinary radiator. By playing a gas flame on an electrically heated mantle, he was able to increase its radiation over that from the gas mantle itself. Figure 2.15 shows a comparison of the gas mantle and the electrically heated gas mantle with a Nernst glower. Strong¹⁶ points out that playing a flame against the mantle at an angle produces an elongated area of intense radiation useful for illuminating the slits of a spectrometer.

Comparison of Nernst Glower, Globar, and Gas Mantle. Figure 2.16 compares these three types of sources, omitting a consideration of differences in the instrumentation used in making measurements of the radiation from the sources.

Availability, convenience, and cost usually influence a choice of sources. At the very long wavelength regions in the infrared, the gas mantle and the globar have a slight edge over the Nernst glower because the Nernst glower (a convenient, small, and inexpensive source) does not have the power of the gas mantle and globar.

Tungsten-Filament Lamps. A comprehensive discussion of tungsten-filament lamps is given by Carlson and Clark.¹⁷ Figures 2.17, 2.18, and 2.19 show the configurations of lamp housings and filaments. The types and variations of lamps are too numerous to be meaningfully included in this volume. The reader

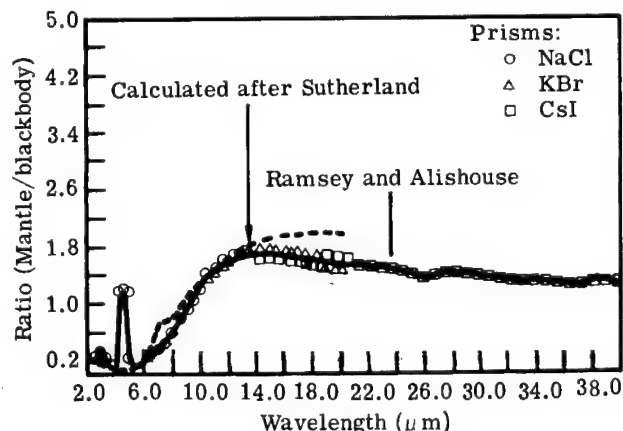


Fig. 2.14 The ratio of the gas mantle to a 900°C blackbody versus wavelength.¹³

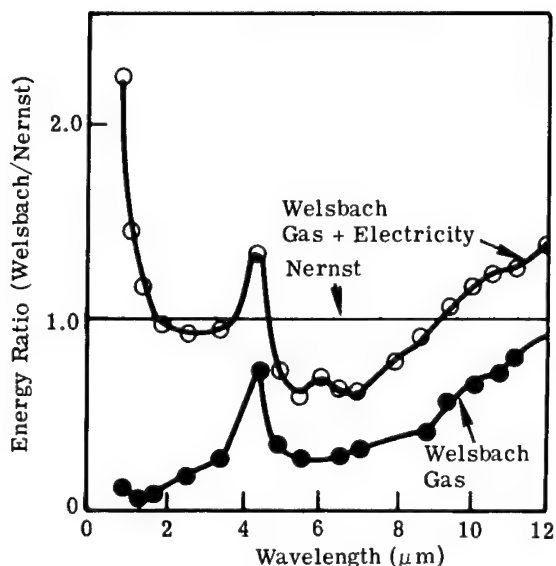


Fig. 2.15 Emission relative to that of a Nernst glower (2240 K) of the gas-heated mantle (lower curve) and that of the mantle heated by gas plus electricity (upper curve).¹⁵

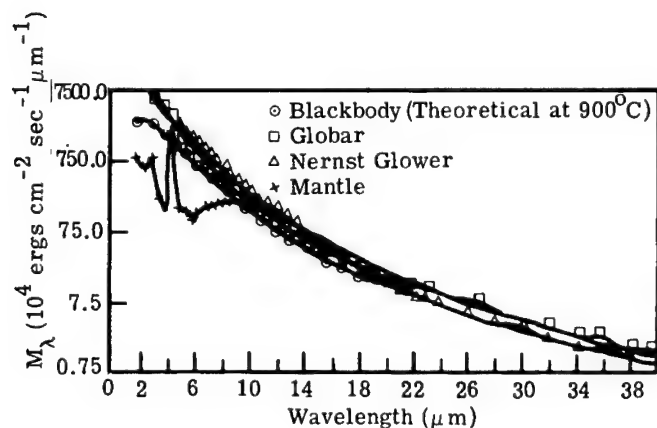


Fig. 2.16 The spectral radiant emittances of a globar, Nernst glower, 900°C blackbody, and gas mantle versus wavelength.¹³

is referred to one of the buyer's guides for a comprehensive delineation of manufacturers from whom literature can be obtained.

Tungsten lamps have been designed for a variety of applications; few lamps are directed toward scientific research, but some bear directly or indirectly on scientific pursuits insofar as they can provide steady sources of numerous types of radiation. One set of sources cited here, particularly for what the manufacturer calls their "scientific usefulness," is described in Ref. 18. Their filament structures are similar to those already described, but their designs reduce extraneous radiation and ensure the quality and stability of the desired ra-

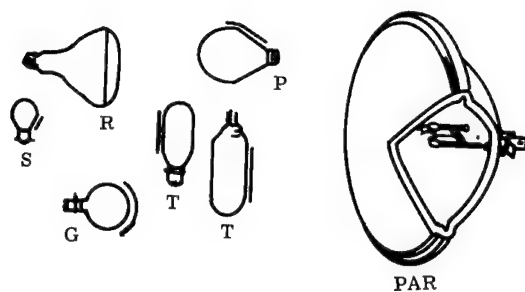


Fig. 2.17 Bulk shapes most frequently used for lamps in optical devices. Letter designations are for particular shapes.¹⁷

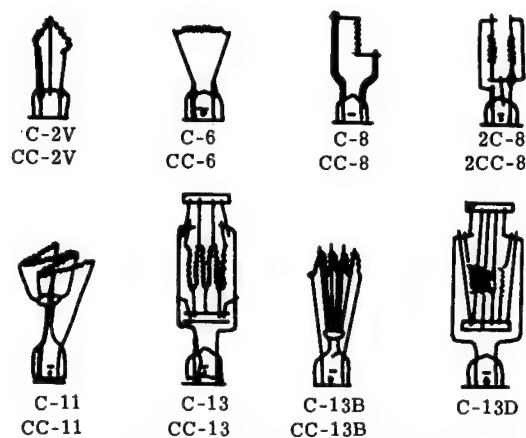


Fig. 2.18 Most commonly used filament forms. Letters designate the type of filament.¹⁷

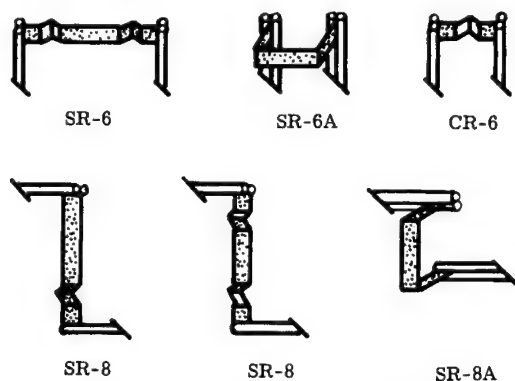
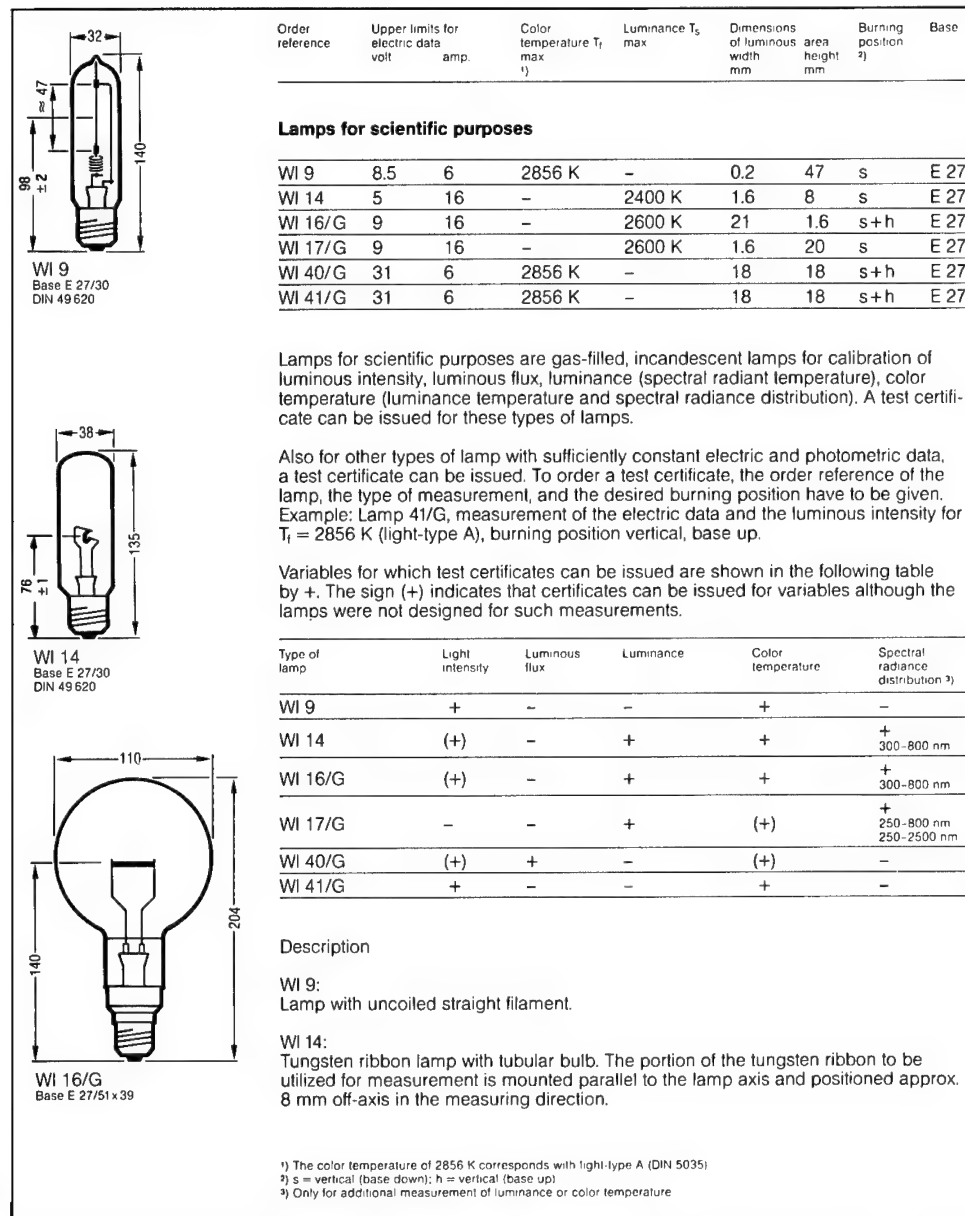


Fig. 2.19 Ribbon-type tungsten filaments. Type designations are by number.¹⁷

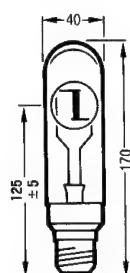
diation. The lamps can be obtained with a certification of their calibration values.

The physical descriptions of some of these sources are given in Fig. 2.20. Applications (according to the manufacturer, Osram) are photometry, pyrometry, optical radiometry, sensitometry, spectroscopy, spectrometry, polarim-

Fig. 2.20 Lamps for scientific purposes.¹⁸

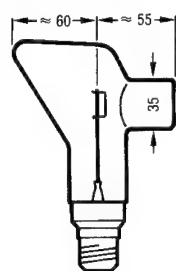
etry, saccharimetry, spectrophotometry, colorimetry, microscopy, microphotography, microprojection, and stroboscopy.

Quartz envelope lamps are particularly useful as standards because they are longer lasting (due to action of iodine in the quartz-iodine series), can be heated to higher temperatures, are sturdier, and can transmit radiation to longer wavelengths in the infrared than glass-envelope lamps. Studer and Van Beers¹⁹ have shown the spectral deviation to be expected of lamps containing no iodine. The deviation, when known, is readily acceptable in lieu of the degradation in the lamp caused by the absence of iodine. The particular tung-



WI 16/G:

Tungsten ribbon lamp with spherical bulb. Horizontal tungsten ribbon with a small notch to indicate the measuring point. The ribbon is positioned approx. 3 mm off axis.



WI 17/G:

Tungsten ribbon lamp with horn-shaped bulb. The bulb has a tubular extension with a sealed-on quartz glass window (homogenized ultrasil). Vertical tungsten ribbon with a small notch to indicate the measuring point.

WI 40/G:

Standard lamp for total radiation, luminous flux and color temperatures with conic bulb. The bulb shape prevents reflections in the direction of the plane normal of the luminous area, which is formed by the meandrous-shaped filament.

WI 41/G:

Standard lamp for light intensity and color temperature with conic bulb. Differs from the WI 40/G lamp by a black, opaque coating which covers one side of the bulb. A window is left open in the coating opposite the filament, through which over an angle of approx. $\pm 3^\circ$ a constant light intensity is emitted. The black coating prevents stray light being reflected in the measuring direction.

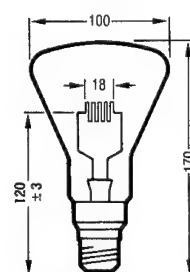
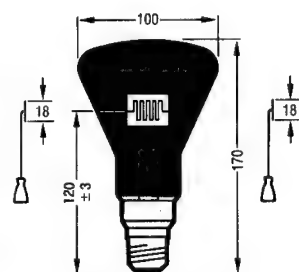
WI 17/G
Base E 27/51 x 39WI 40/G
Base E 27/51 x 39WI 41/G
Base E 27/51 x 39

Fig. 2.20 (continued)

sten-quartz-iodine lamps used in accordance with the NIST were described earlier in this chapter. Others can be obtained in a variety of sizes and wattages from General Electric, Sylvania, and a variety of other lamp manufacturers, and secondary sources.

2.3.3 Carbon Arc

The carbon arc has been passed down from early lighting applications in three forms: low-intensity arc; flame; and high-intensity arc. The low- and high-intensity arcs are usually operated on direct current; the flame type adapts to

either direct or alternating current. In all cases, a ballast must be used. "In the alternating current arc, the combined radiation from the two terminals is less than that from the positive crater of the direct-current arc of the same wattage."¹ Spatial variation in the amount of light energy across the crater of dc arcs for different currents is shown in Fig. 2.21.

The carbon arc is a good example of an open arc, widely used because of its very high radiation and color temperatures (from approximately 3800 to 6500 K or higher). The rate at which the material is consumed and expended during burning (5 to 30 cm/h) depends on the intensity of the arc. The arc is discharged

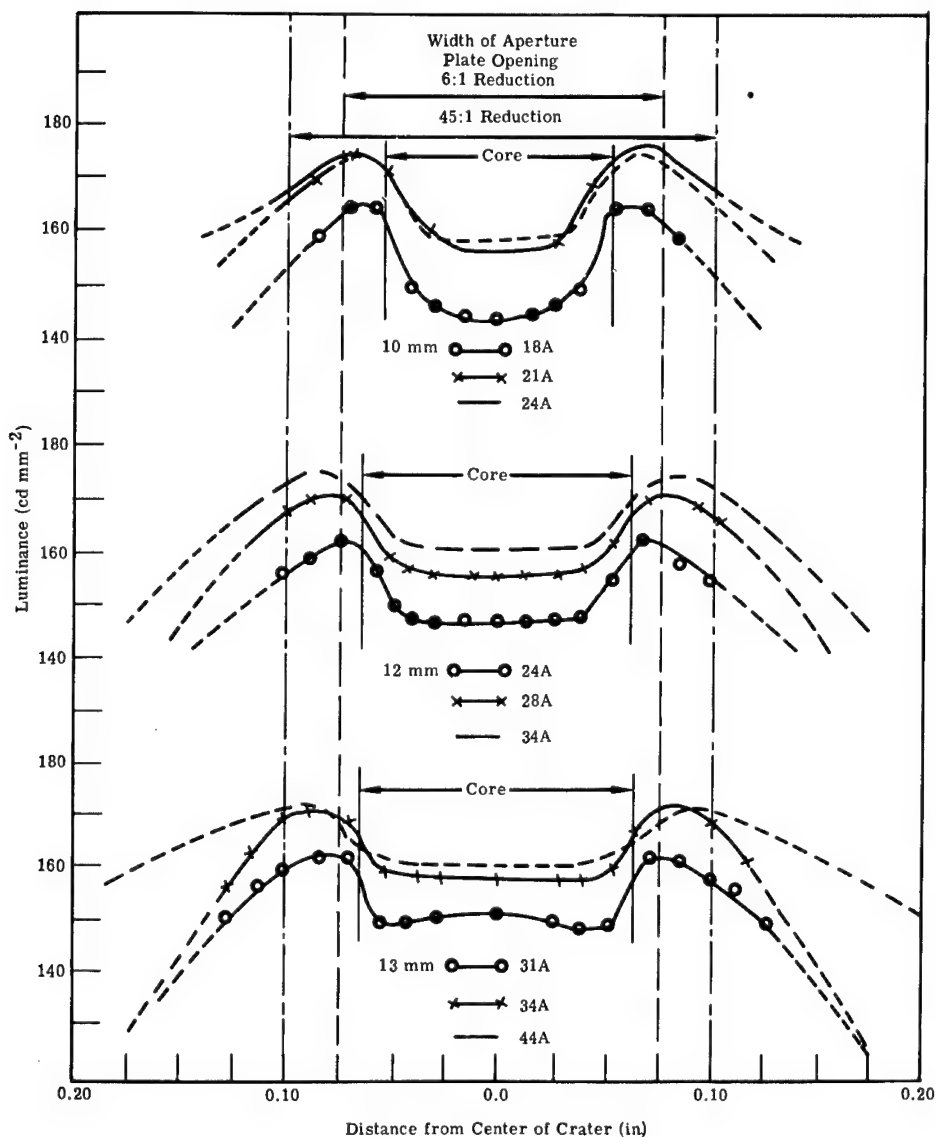


Fig. 2.21 Variations in brightness across the craters of 10-, 12-, and 13-mm positive carbons of dc plain arcs operated at different currents in the regions of recommended operation.¹

between two electrodes that are moved to compensate for the rate of consumption of the material. The anode forms a crater of decomposing material, which provides a center of very high luminosity. Some electrodes are hollowed out and filled with a softer carbon material, which helps keep the arc fixed in the anode and prevents it from wandering on the anode surface.

In some cored electrodes, the center is filled with whatever material is needed to produce the desired spectral characteristics in the arc. In such devices,²⁰ the flame between the electrodes becomes the important center of luminosity, and color temperatures reach values as high as 8000 K. An example of this so-called flaming arc is shown in Fig. 2.22(a). Figures 2.22(b) and 2.22(c) show the low-intensity dc carbon arc and the high-intensity dc carbon arc with rotating positive electrodes. Tables 2.6 and 2.7 give characteristics of flame and dc high-intensity carbon arcs.

A spectrum of low-intensity arc (Fig. 2.23) shows the similarity between the radiation from it and a 3800 K blackbody, except for the band structure at 0.25 and 0.39 μm . In Koller²⁰ an assortment of spectra is given for cored carbons containing different materials. Those for a core of soft carbon and for a polymetallic core are shown in Figs. 2.24 and 2.25. Because radiation emitted from the carbon arc is very intense, this arc supplants, for many applications, sources that radiate at lower temperatures. Among the disadvantages of the carbon arc are its inconvenience relative to the use of other sources (e.g., lamps) and its relative instability. However, Null and Lozier²¹ have studied the properties of the low-intensity carbon arc extensively and have found that under the proper operating conditions the carbon arc can be made quite stable; in

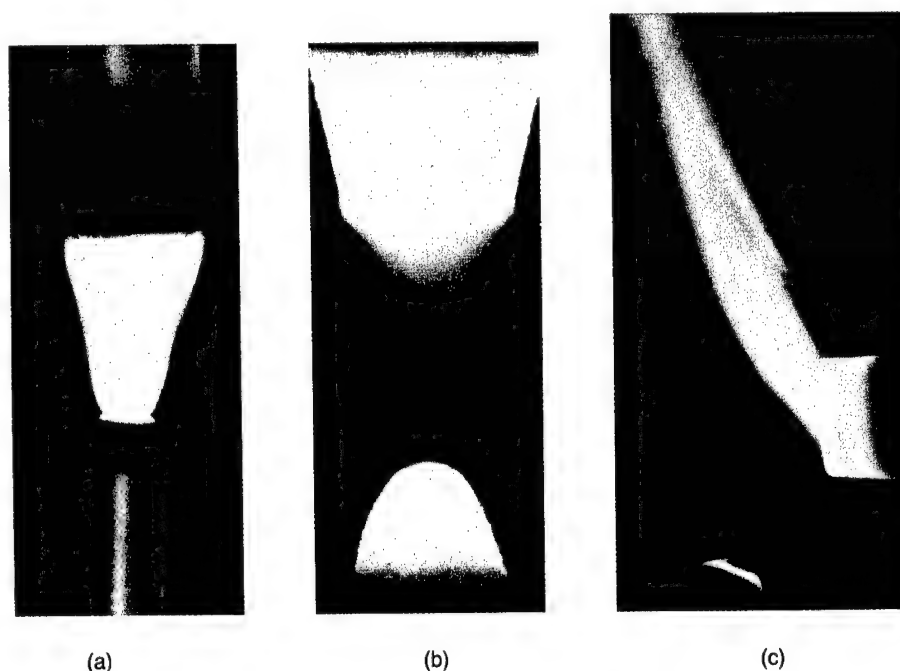


Fig. 2.22 Various types of carbon arcs²⁰: (a) flame type, (b) low-intensity dc arc, and (c) high-intensity dc arc with rotating positive carbon.

Table 2.6 Flame-Type Carbon Arcs (from Ref. 23)

	Application Number ^a			
	1	3	3	4
Type of carbon	C	E	Sunshine	Sunshine
Flame materials	Polymetallic	Strontium	Rare earth	Rare earth
Burning position ^b	Vertical	Vertical	Vertical	Vertical
Upper carbon ^d				
Diameter	22 mm	22 mm	22 mm	22 mm
Length (in.)	12	12	12	12
Lower carbon ^d				
Diameter	13 mm	13 mm	13 mm	13 mm
Length (in.)	12	12	12	12
Arc current (A)	60	60	60	80
Arc voltage (ac) ^h	50	50	50	50
Arc power (kW)	3	3	3	4
Candlepower ⁱ	2100	6300	9100	10000
Lumens	23000	69000	100000	110000
Lumens per arc watt	7.6	23	33.3	27.5
Color temperature (K)			12800 ^j	24000 ^j
Spectral intensity ($\mu\text{W cm}^{-2}$)				
1 m from arc axis:				
Below 270 nm	540.0	180.0	102	140
270-320 nm	540.0	150.0	186	244
320-400 nm	1800.0	1200.0	2046	2816
400-450 nm	300.0	1100.0	1704	2306
450-700 nm	600.0	4050.0	3210	3520
700-1125 nm	1580.0	2480.0	3032	3500
Above 1125 nm	9480.0	10290.0	9820	11420
Total	14930	19460	20100	24000
Spectral radiation (percent of input power):				
Below 270 nm	1.8	0.6	0.34	0.35
270-320 nm	1.8	0.5	0.62	0.61
320-400 nm	6.0	4.0	6.82	7.04
400-450 nm	1.3	3.7	5.68	5.90
450-700 nm	2.0	13.5	10.7	8.80
700-1125 nm	5.27	8.27	10.1	8.75
Above 1125 nm	31.6	34.3	32.7	28.55
Total	49.77	64.87	67.00	60.00

^aTypical applications: 1 to 5 and 8, photochemical, therapeutic, accelerated exposure testing, or accelerated plant growth; 6, 7, and 9 blue-printing diazo printing, photo copying, and graphic arts; 10, motion-picture and television studio lighting.

^bPhotographic white-flame carbons.

^cHigh intensity copper-coated sunshine carbons.

^dBoth carbons are same in horizontal, coaxial arcs.

fact, in their treatise they recommend its use as a standard of radiation at high temperatures.

2.3.4 Enclosed Arc and Discharge Sources (High Pressure)

Koller²⁰ states that the carbon arc is generally desired if a high intensity is required from a single unit but that it is less efficient than the mercury arc.

Table 2.6 (continued)

5	6	7 ^b	8 ^{c,d}	9 ^{d,e}	10 ^f
W Polymetallic Vertical	Enclosed arc None Vertical	Photo Rare earth Vertical	Sunshine Rare earth Horizontal	Photo Rare earth Horizontal	Studio Rare earth Vertical
22 mm	1/2 in.	1/2 in.	6 mm	9 mm	8 mm
12	3-16	12	6.5	8	12
13 mm	1/2 in.	1/2 in.	6 mm	9 mm	7 mm
12	3-16	12	6.5	8	9
80	16	38	40	95	40
50	138	50	24	30	37 dc
4	2.2	1.9	1	2.85	1.5
8400	1170	6700	4830	14200	11000
92000	13000	74000	53000	156000	110000
23	5.9	39.8	53	54.8	73.5
		7420 ^j	6590	8150	4700
1020		95	11		12
1860		76	49	100	48
3120	1700	684	415	1590	464
1480	177	722	405	844	726
2600	442	2223	1602	3671	3965
3220	1681	1264	1368	5632	2123
14500	6600	5189	3290	8763	4593
27800	10600	10253	7140	20600	11930
2.55		0.5	0.11		0.08
4.65		0.4	0.49	0.35	0.32
7.80	7.7	3.6	4.15	5.59	3.09
3.70	0.8	3.8	4.05	2.96	4.84
6.50	2.0	11.7	16.02	12.86	26.43
8.05	7.6	6.7	13.68	10.75	14.15
36.25	29.9	27.3	32.90	30.60	30.62
69.50	48.0	54.0	71.40	72.20	79.53

^eHigh-intensity photo carbons.^fMotion-picture-studio carbons.^gAll combinations shown are operated coaxially.^hAll operated on alternating current except item

10.

ⁱHorizontal candlepower, transverse to arc axis.^jDeviates enough from blackbody colors to make color temperature of doubtful meaning.

Other disadvantages are the short life of the carbon with respect to mercury and resulting combustion products, which may be undesirable. Worthing¹ describes a number of the older, enclosed, metallic arc sources, many of which can be built in the laboratory for laboratory use. Today, however, it is rarely necessary to build one's own source unless it is highly specialized.

Table 2.7 dc Carbon Arcs (from Ref. 23)

	Low Intensity	Nonrotating High Intensity	Rotating High Intensity							
			Application Number ^a							
	1	2	3	4	5	6	7	8	9	10
Type of carbon:	Microscope	Projector	Projector	Projector	Projector	Projector	Projector	Searchlight	Studio	
Positive carbon:										
Diameter (mm)	5	7	8	10	11	13.6	13.6	16	16	16
Length (in.)	8	12-14	12-14	20	20	22	22	22	22	22-30
Negative carbon:										
Diameter	6 mm	6 mm	7 mm	11/32 in.	3/8 in.	0.5 in.	0.5 in.	11 mm	17/32 in.	7/16 in.
Length (in.)	4.5	9	9	9	9	9	9	12	9	12-48
Arc current (A)	5	50	70	105	120	160	180	150	225	400
Arc volts (dc)	59	40	42	59	57	66	74	78	70	80
Arc power (W)	295	2000	2940	6200	6840	10600	13300	11700	15800	32000
Burning rate (in. h ⁻¹)										
Positive carbon	4.5	11.6	13.6	21.5	16.5	17	21.5	8.9	20.2	55
Negative carbon	2.1	4.3	4.3	2.9	2.4	2.2	2.5	3.9	2.2	3.5
Approximate crater diameter (in.)	0.12	0.23	0.28	0.36	0.39	0.5	0.5	0.55	0.59	0.59
Maximum luminance of crater (cd cm ⁻²)	15000	55000	83000	90000	85000	96000	95000	65000	68000	45000
Forward crater candlepower	975	10500	22000	36000	44000	63000	78000	68000	99000	185000
Crater lumens ^b	3100	36800	77000	126000	154000	221000	273000	250000	347000	660000
Total lumens ^c	3100	55000	115000	189000	231000	368000	410000	374000	521000	999000
Total lumens per arc watt	10.4	29.7	39.1	30.5	33.8	34.7	30.8	32	33	30.9
Color temperature (K) ^d	3600	5950	5500-6500	5500-6500	5500-6500	5500-6500	5500-6500	5400	4100	5800-6100

^aTypical applications: 1, microscope illumination and projection; 2 to 7, motion-picture projection; 8, searchlight projection; 9, motion-picture-set lighting and motion-picture and television background projection.

^bIncludes light radiated in forward hemisphere.

^cIncludes light from crater and arc flame in forward hemisphere.

^dCrater radiation only.

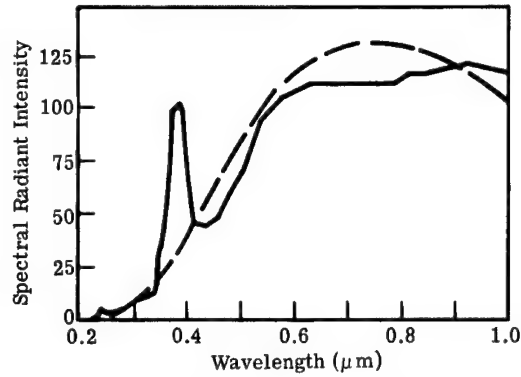


Fig. 2.23 Spectral distribution of radiant flux from a 30-A, 55-V dc low-intensity arc with 12-mm positive carbon (solid line) and a 3800 K blackbody radiator (broken line).¹⁷

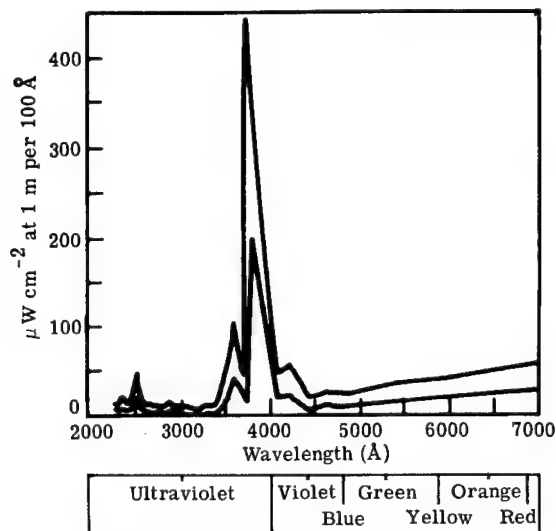


Fig. 2.24 Spectral energy distribution of carbon arc with core of soft carbon. Upper curve: 60-A ac 50-V across the arc; lower curve: 30-A ac 50-V across the arc.²⁰

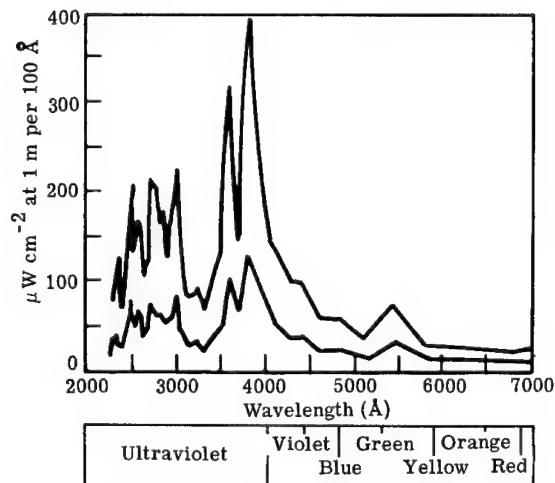


Fig. 2.25 Spectral energy distribution of carbon arc with polymetallic-cored carbons. Upper curve: 60-A ac 50-V across the arc; lower curve: 30-A ac 50-V across the arc.²⁰

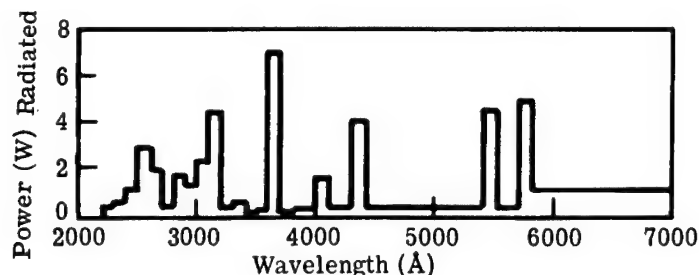


Fig. 2.26 Intensity distribution of UA-2 intermediate-pressure lamp.²⁰

A large number of these types of sources are compiled in Ref. 22. Some are repeated here in case Ref. 22 is not readily accessible to the reader. However, the reader should be aware that many changes might have occurred in the characteristics of these sources and in the supplier whose product is preferred. Consulting current product literature is usually a good procedure. In some cases a certain type of source described previously may not currently exist.

Uviarc.^d This lamp is an efficient radiator of ultraviolet radiation. The energy distribution of one type is given in Fig. 2.26. Since the pressure of this mercury-vapor lamp is intermediate between the usual high- and the low-pressure lamps, little background (or continuum) radiation is present.

In the truly high-pressure lamp, considerable continuum radiation results from greater molecular interaction. Figure 2.27 shows the dependence on pressure of the amount of continuum in mercury lamps of differing pressure. Bulb shapes and sizes are shown in Fig. 2.28.

Mercury Arcs. A widely used type of high-pressure, mercury-arc lamp and the components necessary for its successful operation are shown in Fig. 2.29. The coiled tungsten cathode is coated with a rare-earth material (e.g., thorium). The auxiliary electrode is used to help in starting. A high resistance limits the starting current. Once the arc is started, the operating current is limited by ballast supplied by the high reactance of the power transformer. Spectral data for clear 400-W mercury lamps of this type are given in Fig. 2.30.

Multivapor Arcs. In these lamps, argon and mercury provide the starting action. Then sodium iodide, thallium iodide, and indium iodide vaporize and dissociate to yield the bulk of the lamp radiation. The physical appearance is like that of mercury lamps of the same general nature. Ballasts are similar to their counterparts for the mercury lamp. Up-to-date information on these sources should be obtained from the General Electric Corporation Lamp Division, Cleveland, Ohio. Spectral features of these sources are given in Fig. 2.31.

^dRegistered trademark of General Electric.

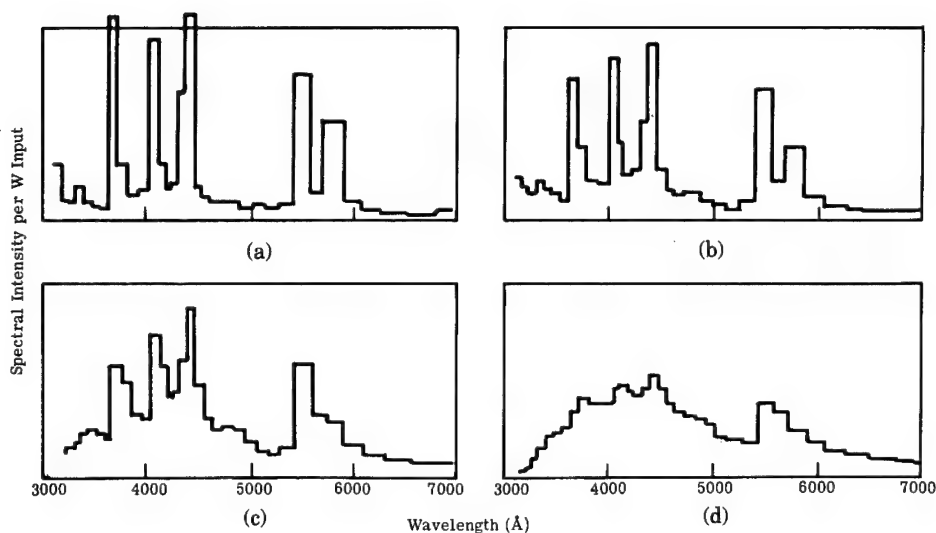


Fig. 2.27 Emission spectrum of high-pressure mercury-arc lamps showing continuum background²⁴: (a) 31 atm, (b) 75 atm, (c) 165 atm, and (d) 285 atm.

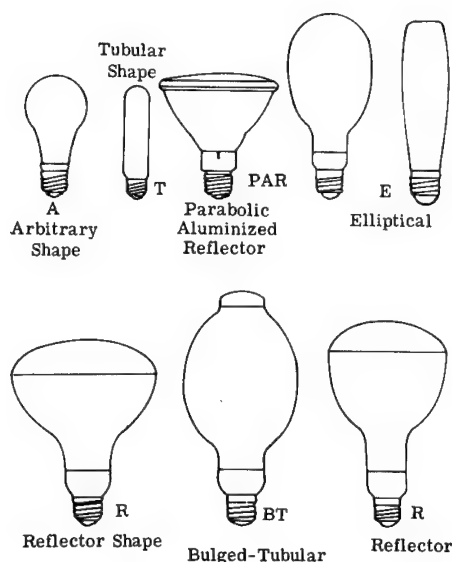


Fig. 2.28 Bulb shapes and sizes (not to scale).²⁵

Lucalox® Lamps. The chief characteristics of this lamp are high-pressure sodium discharge and a high-temperature-withstanding ceramic, Lucalox (translucent aluminum oxide), to yield performance typified in the spectral output of the 400-W Lucalox lamp shown in Fig. 2.32. Ballasts for this lamp are described in Ref. 25.

[®]Registered trademark of General Electric.

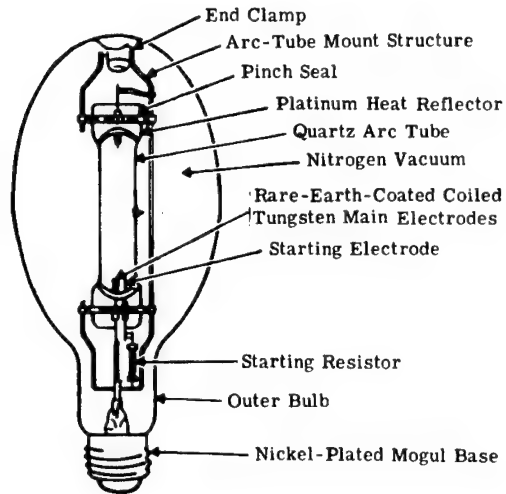


Fig. 2.29 High-pressure mercury lamp showing various components.²⁵

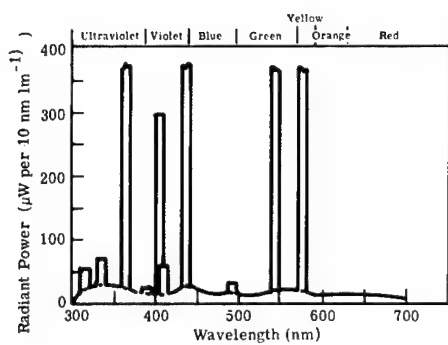


Fig. 2.30 Spectral energy distribution for clear mercury-arc lamp.²⁵

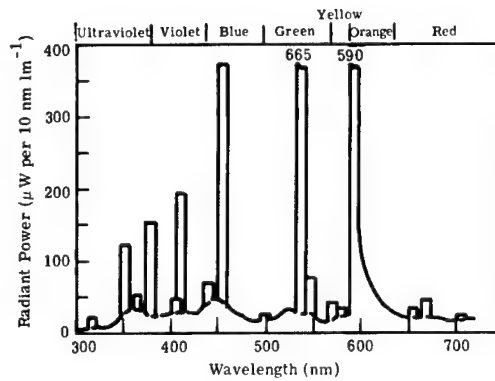


Fig. 2.31 Spectral energy distribution of multivapor-arc lamp.²⁵

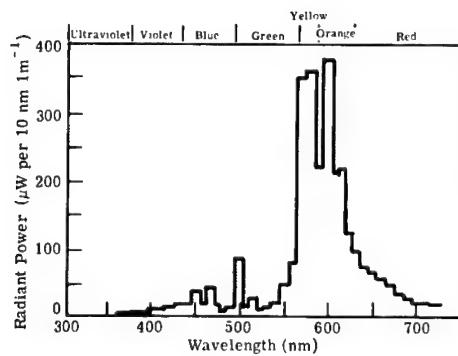


Fig. 2.32 Spectral output of 400-W Lucalox lamp.²⁵

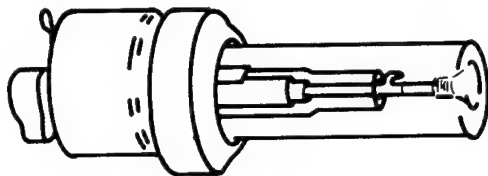


Fig. 2.33 Water-cooled high-pressure (110 atm) mercury-arc lamp showing lamp in water jacket.²⁰

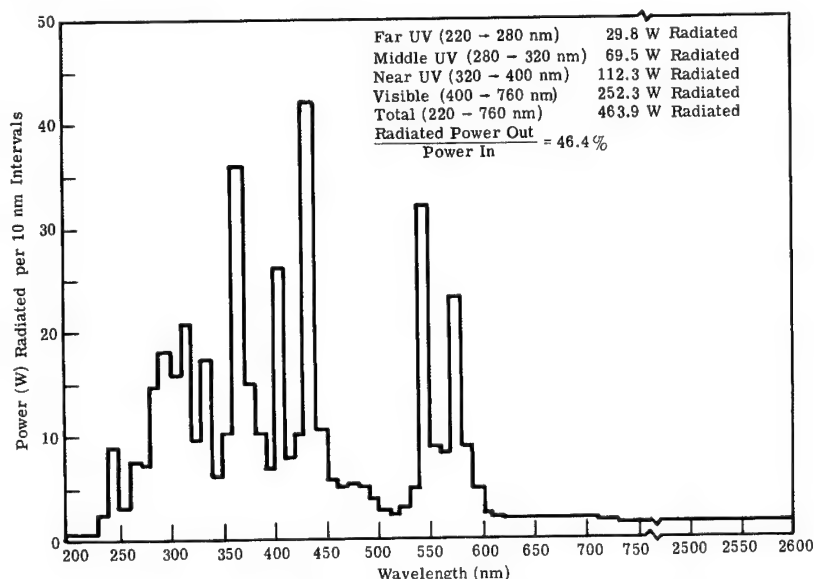


Fig. 2.34 Spectral energy distribution of type BH6-1 mercury capillary lamp.²⁶

Capillary Mercury-Arc Lamps. As the pressure of the arc increases, cooling is required to avoid catastrophic effects on the tube. The AH6 tube (Fig. 2.33) is constructed with a quartz bulb wall and a quartz outer jacket to allow 2800 K radiation to pass, or a Pyrex[®] outer jacket to eliminate ultraviolet. Pure water is forced through at a rapid rate, while the tube is maintained at a potential of 840 V. The spectral characteristics of certain tubes²⁶ are shown in Fig. 2.34.

Compact-Source Arcs. Some common characteristics of currently available compact-source arc lamps^{17,27} are as follows:

1. A clear quartz bulb of roughly spherical shape with extensions at opposite ends constituting the electrode terminals. In some cases, the quartz bulb is then sealed within a larger glass bulb, which is filled with an inert gas.
2. A pair of electrodes with relatively close spacing (from less than 1 mm to about 1 cm); hence the sometimes-used term "short-arc lamps."
3. A filling of gas or vapor through which the arc discharge takes place.
4. Extreme electrical loading of the arc gap, which results in very high luminance, internal pressures of many atmospheres, and bulb tem-

[®]Registered trademark of Corning Glass Works.

peratures as high as 900°C. Precautions are necessary to protect people and equipment in case the lamps should fail violently.

5. The need for a momentary high-voltage ignition pulse and a ballast or other auxiliary equipment to limit current during operation.
6. Clean, attention-free operation for long periods of time. These lamps are designated by the chief radiating gases enclosed as mercury, mercury-xenon, and xenon lamps.

Figure 2.35 shows a compact-source construction for a 1000-W lamp. Since starting may be a problem, some lamps (Fig. 2.36) are constructed with a third (i.e., a starting) electrode, to which a momentary high voltage is applied for starting (and especially restarting) while hot. The usual ballast is required for compact-source arcs. For stability, these arcs, particularly mercury and mercury-xenon, should be operated near rated power on a well-regulated power supply.²⁷

The spatial distribution of luminance from these lamps is reported in the literature already cited, and typical contours are shown in Fig. 2.37. Polar distributions are similar to those shown in Fig. 2.38. Spectral distributions are given in Figs. 2.39, 2.40, and 2.41 for a 1000-W ac mercury lamp, a 5-kW dc xenon lamp, and a 1000-W dc mercury-xenon lamp. Lamps are available at considerably less wattage.

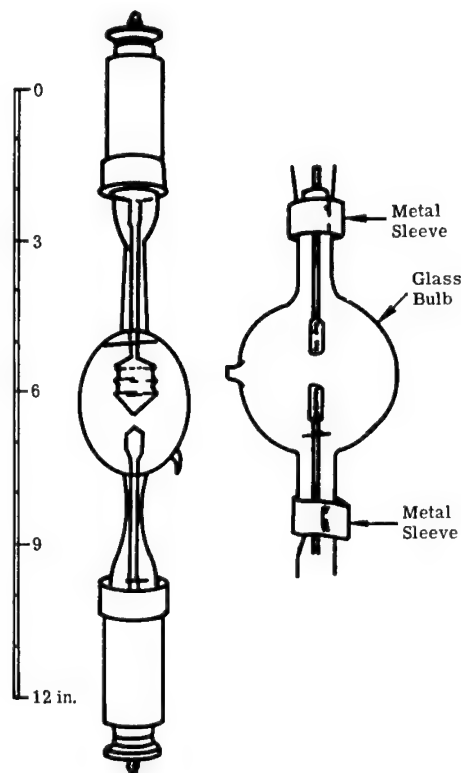
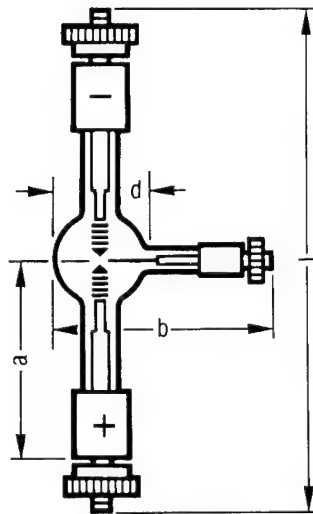


Fig. 2.35 Construction of different lamps showing differences in relative sizes of electrodes for dc (left) and ac (right) operation.¹⁷



Lamp (Order Reference)		HBO 200 W ¹	
Type of current		DC	AC
Lamp supply voltage	V	> 105	220
Operating voltage of lamp	$V \frac{L_1}{L_2}$	65...47	$\frac{61 \pm 4}{53 \pm 4}$
Operating current at operating voltage range	$A \frac{L_1}{L_2}$	3.1...4.2	$\frac{3.6}{4.2}$
Rated power of lamp	W	200	
Luminous flux	lm	9500	
Luminous efficacy	lm/W	47.5	
Light intensity	cd	1000	
Average luminance	cd/cm ²	40000	
Arc (width w x height h ⁴)	mm	0.6 x 2.2	
Average lamp life	h	200	
Diameter d	mm	18	
Length l max.	mm	108	
Distance a	mm	41 ± 2	
Width b	mm	45	
Burning position with stamped base down		s45	

Fig. 2.36 Construction of a lamp with a third, starting electrode.¹⁸

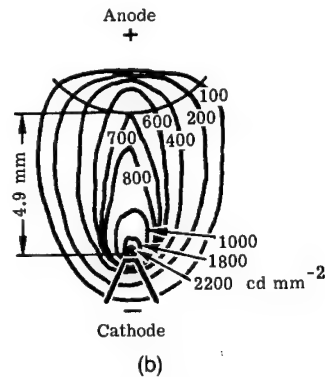
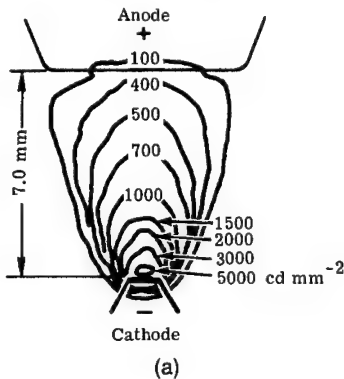


Fig. 2.37 Spatial luminance distribution of compact-arc lamps¹⁷: (a) 5-kW dc xenon lamp and (b) 5-kW dc mercury-xenon lamp.

Cann²⁷ reports on some interesting special lamps tested by Jet Propulsion Laboratories for the purpose of obtaining a good spectral match to the solar distribution. The types of lamps tested were Xe, Xe-Zn, Xe-Cd, Hg-Xe-Zn, Hg-Xe-Cd, Kr, Kr-Zn, Kr-Cd, Hg-Kr-Zn, Hg-Kr-Cd, Ar, Ne, and Hg-Xe with variable mercury vapor pressure. For details, the reader should consult the literature.

A special design of a short-arc lamp manufactured by Varian²⁸ is shown in Fig. 2.42. Aside from its compactness and parabolic selector, it has a sapphire window, which allows a greater amount of IR energy to be emitted. It is operated either dc or pulsed, but the user should obtain complete specifications because the reflector can become contaminated, with a resultant decrease in output.

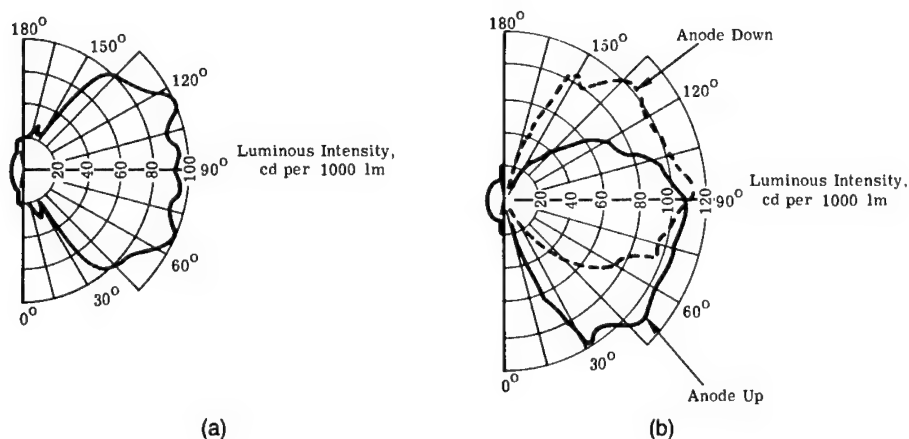


Fig. 2.38 Polar distribution of radiation in planes that include arc axis: (a) 7.5-kW ac mercury lamp and (b) 2.5-kW dc mercury-xenon lamp. The asymmetry in (b) is due to unequal size of electrodes.¹⁷

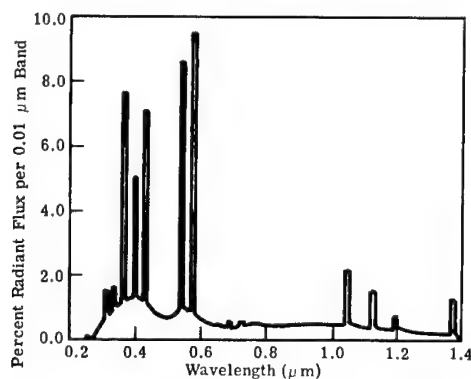


Fig. 2.39 Spectral distribution of radiant intensity from a 1000-W ac mercury lamp perpendicular to the lamp axis.¹⁷

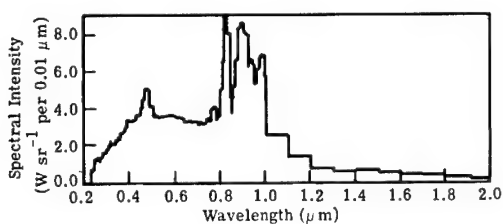


Fig. 2.40 Spectral distribution of radiant intensity from a 5-kW dc xenon lamp perpendicular to the lamp axis with electrode and bulb radiation excluded.¹⁷

2.3.5 Enclosed Arc and Discharge Sources (Low Pressure)

With pressure reduction in a tube filled with mercury vapor, the 2537-Å line becomes predominant so that low-pressure mercury tubes are usually selected for their ability to emit ultraviolet radiation.²⁰

Germicidal Lamps. These are hot-cathode lamps that operate at relatively low voltages. They differ from the ordinary fluorescent lamps used in lighting

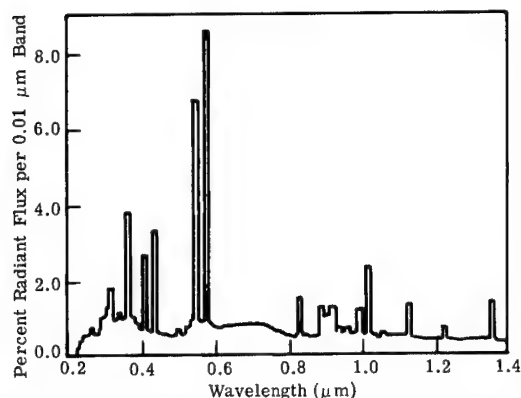


Fig. 2.41 Spectral distribution of radiant flux from a 1000-W mercury-xenon lamp.¹⁷

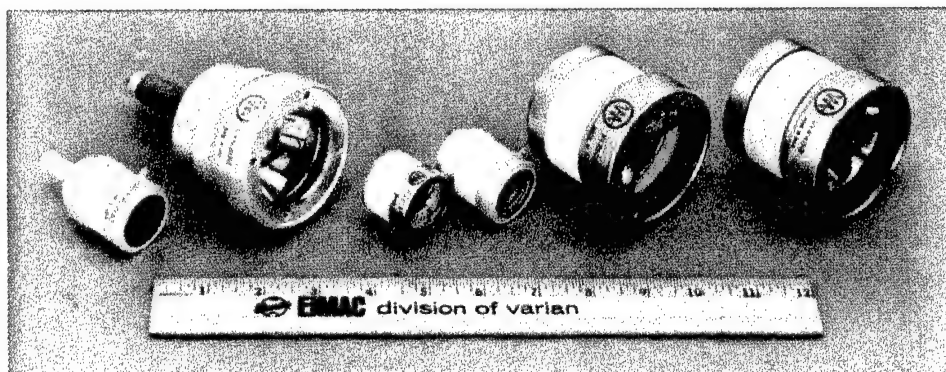


Fig. 2.42 High-pressure, short-arc xenon illuminators with sapphire windows. Low starting voltage, 150 through 800 W; VIX150, VIX300, VIX500, VIX800.²⁸

in that they are designed to transmit ultraviolet, whereas the wall of the fluorescent lamp is coated with a material that absorbs ultraviolet and reemits visible light. The germicidal lamp is constructed of 1-mm-thick glass, which transmits about 65% of the 2537-Å radiation and virtually cuts off shorter wavelength ultraviolet radiation.

Sterilamp[®] Types. These cold cathode lamps start and operate at higher voltages than the hot-cathode type and can be obtained in relatively small sizes as shown in Fig. 2.43. The operating characteristics of Sterilamps should be obtained from the manufacturer.

Black-Light Fluorescent Lamps. This fluorescent lamp is coated with a phosphor efficient in the absorption of 2537-Å radiation, emitting ultraviolet radiation in a broad band around 3650 Å. The phosphor is a cerium-activated calcium phosphate, and the glass bulb is impervious to shorter wavelength ultraviolet radiation. Characteristics of one type are given in Table 2.8.

Hollow-Cathode Lamps. A device described early in this century and used for many years by spectroscopists is the hollow-cathode tube. The one used by

[®]Registered trademark of Westinghouse Electric.

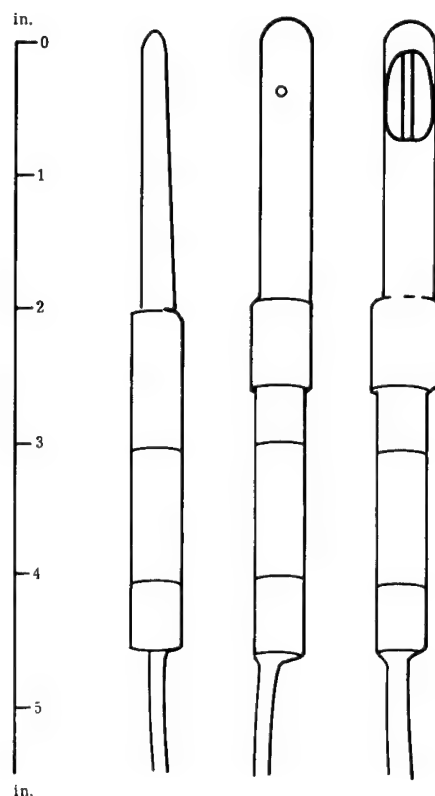


Fig. 2.43 Pen-Ray low-pressure lamp.²⁰ (Pen-Ray® is a registered trademark of Ultraviolet Products, Inc.)

Paschen¹ consisted of a hollow metal cylinder and contained a small quantity of inert gas, yielding an intense cathode glow characteristic of the cathode constituents. Materials that vaporize easily can be incorporated into the tube so that their spectral characteristics dominate.¹

A number of companies sell hollow-cathode lamps that do not differ significantly from those constructed in early laboratories. The external appearance of these modern tubes shows the marks of mass production and emphasis on convenience. They come with a large number of vaporizable elements, singly or in multiples, and with Pyrex® or quartz windows. A partial list of the characteristics of the lamps available from two manufacturers is given in Table 2.9. Their physical appearance is shown in Fig. 2.44(a). A schematic of the different elements obtainable in various lamps is shown in Fig. 2.44(b).²⁹

Electrodeless Discharge Lamps. The electrodeless lamp³⁰⁻³² gained popularity when Meggers used it in his attempt to produce a highly precise standard of radiation. Simplicity of design makes laboratory construction of this type of lamp easy. Some of the simplest lamps consist of a tube, containing the radiation-producing element, and a microwave generator for producing the electric field (within the tube), which in turn excites the elemental spectra. Lamps of this type can be purchased with specially designed microwave cavities for greater efficiency in coupling. Those made of fused quartz can transmit from ultraviolet to near infrared. The electrodeless lamp is better able than

Table 2.8 Spectral Energy Distribution for Black-Light (360 BL) Lamps (from Ref. 20)

(W)	Length (in.)	3200-3800 Å		Total Ultra- violet below 3800 Å		Total Visible (W)	3800- 7600 Å % ^a	Erythmal Flux
		(W)	% ^a	(W)	% ^a			
6	9	0.55	9.1	0.56	9.4	0.1	1.7	250
15	18	2.10	14.0	2.20	14.6	0.4	2.7	950
30	36	4.60	15.3	4.70	15.8	0.9	3.0	2100
40	48	6.70	16.8	6.90	17.3	1.5	3.8	3000

^aPercentage of input power.

the arc lamp to produce stable radiation of sharp spectral lines; this makes it useful in spectroscopy and interferometry. The Hg 198 lamp makes a suitable secondary standard of radiation.

Spectral Lamps. Some manufacturers produce groups of arc sources, which are similar in construction and filled with different elements and rare gases, and which yield discontinuous or monochromatic radiation throughout most of the ultraviolet and visible spectrum. They are called spectral lamps.³¹ The envelopes of these lamps are constructed of glass or quartz, depending on the part of the spectrum desired. Thus, discrete radiation can be obtained from around 2300 Å into the near infrared. Figure 2.45 represents the various atomic lines observable from Osram spectral lamps.¹⁸ Figure 2.46 gives a physical description of various spectral lamps obtainable from Philips.³³ Table 2.10 lists the characteristics of the various types of lamps obtainable from Philips.

Pluecker Spectrum Tubes. Pluecker spectrum tubes³⁴ are inexpensive tubes made of glass (Fig. 2.47) with an overall length of 25 cm and capillary portion 8.5 to 10 cm long. They operate from an ordinary supply with a special transformer that supports the tubes in a vertical position and maintains the voltage and current values adequate to operate the discharge and regulate the spectral intensity. Table 2.11 lists the various gases in available tubes.

2.3.6 Concentrated Arc Lamps

Zirconium Arc. The cathodes of zirconium arc lamps²⁵ are made of a hollow refractory metal containing zirconium oxide. The anode, a disk of metal with an aperture, resides directly above the cathode with the normal to the aperture coincident with the longitudinal axis of the cathode. Argon gas fills the tube. The arc discharge causes the zirconium to heat (to about 3000 K) and produce an intense, very small source of light. These lamps have been demonstrated in older catalogs from the Cenco Company in a number of wattages (from 2 to 300). The end of the bulb through which the radiation passes comes with ordinary curvature or flat (for a slight increase in price). Examples are shown in Fig. 2.48.

Tungsten-Arc (Photomicrographic) Lamp. The essential elements of this discharge-type lamp²⁵ (Fig. 2.49) are a ring electrode and a pellet electrode,

Table 2.9 Single-Element and Multiple-Element Hollow-Cathode Lamps (from Ref. 29). (Tubes listed in this table are issued by Fisher Scientific and produced by Westinghouse Electric.)

Element	Window ^a	Gas Filt ^b	Size ^c	Analytical Line (Å)	Catalog Number ^d	Element	Window ^a	Gas Filt ^b	Size ^c	Analytical Line (Å)	Catalog Number ^d
Single-Element 22000 Series											
Aluminum	Q	A	B	3092	WL22804	Copper	P	N	A	3247	JA-45-458
	P	N	A	3092	JA-45-452		Q	A	B	3247	WL22606
	Q	A	A	3092	WL22870		Q	N	A	3247	WL22879
Antimony	Q	N	B	3092	WL22929	Dysprosium	Q	N	A	3247	JA-45-490
	Q	N	A	3092	WL22954		Q	N	B	3247	WL23042
	Q	A	B	2311	WL22840		Q	N	A	4212	JA-45-595
Arsenic	Q	A	A	2311	WL22872	Erbium	Q	N	A	4008	WL22880
	Q	A	A	2311	JA-45-461		Q	N	B	4008	JA-45-571
	Q	N	B	2311	WL22956	Europium	Q	N	A	4008	WL22881
Barium	Q	N	A	1937	JA-45-315		Q	N	A	4594	JA-45-572
	Q	N	B	1937	WL22873		P	N	A	4079	WL22882
	Q	N	A	1937	JA-45-315	Gadolinium	Q	N	B	4079	WL22975
Beryllium	Q	A	B	1937	JA-45-480		Q	N	A	4079	JA-45-573
	P	N	A	5536	JA-45-480		Q	N	A	4079	WL22986
Bismuth	Q	N	B	2349	WL23407	Gallium	Q	N	B	4172	JA-45-470
	Q	A	B	3068	WL22841		Q	N	A	4172	WL22884
	Q	A	A	3068	WL22874	Germanium	Q	A	B	2651	JA-45-575
Boron	Q	A	B	3068	JA-45-469		Q	N	B	2651	JA-45-313
	Q	N	B	3068	WL22957		Q	A	B	2676	WL22839
	Q	N	A	2497	JA-45-568	Gold	Q	A	A	2676	WL22883
Cadmium	Q	A	B	2497	WL22917		Q	N	B	2676	JA-45-467
	Q	A	A	3261	WL22816		Q	N	A	2676	WL22960
	Q	A	B	3261	WL22875	Hafnium	Q	N	B	3072	JA-45-303
Calcium	Q	N	A	3261	JA-45-462		Q	N	A	4104	WL22885
	Q	N	B	3261	WL22958		Q	N	B	4104	JA-45-576
Cerium	Q	N	A	4227	JA-45-440	Indium	Q	A	B	3040	WL22867
	P	N	A	—	JA-45-569		Q	A	A	3040	WL22915
	Q	N	B	—	WL22978		Q	A	A	3040	JA-45-471
Cesium	Q	N	A	4556	WL22817	Iridium	Q	A	A	2850	JA-45-577
	P	A	A	4556	JA-45-441		P	A	A	3270	WL22602
	P	N	A	3579	WL22812	Iron	Q	A	A	3720	WL22611
Chromium	Q	A	B	3579	WL22821		Q	N	B	3720	JA-45-455
	Q	A	A	3579	WL22877		Q	N	A	3720	WL22820
	Q	N	B	3579	JA-45-454	Iron, high-purity	Q	A	A	3720	WL22886
Cobalt	Q	N	A	3579	WL22959		Q	N	A	3720	WL22887
	Q	N	A	3454	WL22813		Q	N	B	3720	WL22837
	P	A	A	3454	WL22814	Lanthanum	Q	N	A	3720	WL22888
	Q	A	B	3454	WL22878		Q	A	B	5501	WL22846
	Q	A	A	3454	JA-45-456		Q	A	A	5501	WL22889
	Q	N	A	3454	WL22953		Q	N	B	5501	JA-45-495

Table 2.9 (continued)

Element	Window ^a	Gas Fill ^b	Size ^c	Analytical Line (Å)	Catalog Number ^d	Element	Window ^a	Gas Fill ^b	Size ^c	Analytical Line (Å)	Catalog Number ^d
Lead	Q	A	B	2833	WL22838	Palladium	Q	A	B	3404	WL22857
	Q	A	A	2833	WL22890		Q	A	A	3404	WL22911
	Q	N	A	2833	JA-45-468		Q	N	B	3404	JA-45-475
Lithium 6	Q	N	B	2833	WL22952	Phosphorus	Q	N	A	3404	WL22970
	P	N	A	6708	JA-45-579		Q	N	B	2136	JA-45-449
	P	N	A	6708	WL22925	Platinum	Q	N	A	2136	WL22990
Lithium 7	P	N	A	6708	JA-45-580		Q	A	B	2659	WL22851
	P	N	A	6708	WL22926		Q	A	A	2659	WL22896
Lithium, natural	P	A	A	6708	WL22825	Potassium	Q	N	B	2659	JA-45-466
	P	N	A	6708	JA-45-444	Praseodymium	P	N	A	4044	JA-45-484
	P	A	B	6708	WL23115		Q	N	B	4951	JA-45-585
Lutetium	Q	N	B	3282	JA-45-581	Rhenium	Q	N	A	4951	WL22982
	Q	N	A	3282	WL23010		Q	N	B	3460	JA-45-489
Magnesium	Q	N	B	2852	WL22609	Rhodium	Q	N	A	3435	WL22967
	Q	A	B	2852	WL22891		Q	A	B	3435	WL22850
	Q	A	A	2852	WL22951		Q	A	A	3435	WL22897
	Q	N	A	2852	JA-45-451	Rubidium	Q	N	B	3435	JA-45-476
Manganese	Q	A	B	2795	WL22608		P	N	A	7800	JA-45-443
	P	A	A	2795	WL22815	Ruthenium	Q	N	B	7800	WL23046
	Q	N	B	2795	JA-45-472		Q	N	B	3499	JA-45-586
	Q	N	A	2795	WL22961	Samarium	Q	N	B	4760	JA-45-587
	Q	N	A	2795	WL22876		Q	N	A	4760	WL22899
Mercury	Q	A	A	2537	JA-45-493	Scandium	Q	N	B	3912	JA-45-309
	Q	A	B	2537	WL22892	Selenium	Q	A	B	1960	WL22843
	Q	A	A	3133	WL22805		Q	A	A	1960	WL22898
Molybdenum	Q	A	B	3133	WL22893		Q	N	B	1960	JA-45-477
	Q	A	A	3133	JA-45-460	Silicon	Q	N	A	1960	WL22963
	Q	N	B	3133	WL22962		Q	A	B	2516	WL22832
	Q	N	A	3133	JA-45-582		Q	A	A	2516	WL22900
Neodymium	Q	N	B	4925	WL22980		Q	N	B	2516	JA-45-479
	Q	N	A	4925	WL22605	Silver	Q	N	A	2516	WL22964
Nickel	P	A	A	3415	WL22605		Q	N	B	3281	JA-45-483
	Q	A	B	3415	WL22663		Q	A	B	3281	WL22901
	Q	N	B	3415	JA-45-457	Sodium	P	A	A	5890	WL22864
	Q	A	A	3415	WL22894		P	A	A	5890	JA-45-485
	Q	A	A	3415	WL22895	Strontium	P	N	A	5890	JA-45-481
Niobium	Q	N	B	4059	JA-45-486	Sulphur	P	N	A	4607	JA-45-588
	Q	N	A	4059	WL22912		Q	N	B	-	
Osmium	Q	A	B	2909	JA-45-584						

^aP = Pyrex, Q = quartz; ^bN = neon, A = argon; ^cA = 1½ in. diameter, B = 1 in. diameter, C = 2 in. diameter; ^dWL = Westinghouse, JA = Jarrell-Ash.

(continued)

Table 2.9 (continued)

Element	Window ^a	Gas Fill ^b	Size ^c	Analytical Line (Å)	Catalog Number ^d	Element	Window ^a	Gas Fill ^b	Size ^c	Analytical Line (Å)	Catalog Number ^d
Tantalum	Q	A	B	2714	JA-45-488	Zirconium	Q	A	B	3601	JA-45-482
	Q	A	A	2714	WL22913		Q	A	A	3601	WL22914
Tellurium	Q	N	A	2714	WL22971		Q	N	B	3601	WL22998
	Q	A	B	2143	WL22842	Single-Element 36000 Series					
	Q	A	A	2143	WL22902	Aluminum	P	N	C	3092	JA-45-36009
	Q	N	A	2143	JA-45-473	Antimony	Q	N	C	2311	JA-45-36010
	Q	N	A	2143	WL22965	Arsenic	Q	N	C	1937	JA-45-36011
	Q	N	B	4326	JA-45-589	Barium	P	N	C	5536	JA-45-36012
	Q	N	A	4326	WL22903	Beryllium	Q	N	C	2349	JA-45-36013
	Q	N	B	3776	WL23408	Bismuth	Q	N	C	3068	JA-45-36014
	Q	N	A	3245	WL23028	Boron	Q	A	C	2497	JA-45-36015
	Q	N	B	3245	JA-45-590	Cadmium	Q	N	C	3261	JA-45-36016
	Q	N	B	4105	JA-45-591	Calcium	P	N	C	4227	JA-45-36017
	Q	N	A	4105	WL23008	Cerium	Q	N	C	-	JA-45-36019
	Q	A	B	2863	WL22822	Cesium	Q	N	C	4556	JA-45-36020
	Q	A	A	2863	WL22904	Chromium	P	N	C	3579	JA-45-36021
	Q	N	B	2863	JA-45-463	Cobalt	Q	N	C	3454	JA-45-36022
	Q	N	A	2863	WL22966	Copper	P	N	C	3247	JA-45-36024
	Q	N	B	3643	JA-45-592	Dysprosium	P	N	C	4212	JA-45-36025
	Q	N	A	3643	WL22992	Erbium	P	N	C	4008	JA-45-36026
	Q	N	B	4009	JA-45-465	Europium	P	N	C	4594	JA-45-36027
	Q	A	B	4009	WL22849	Gadolinium	P	N	C	4079	JA-45-36028
	Q	N	A	4009	WL22905	Gallium	Q	N	C	4172	JA-45-36029
	Q	A	A	4009	WL22906	Germanium	Q	N	C	2651	JA-45-36030
	Q	N	B	5027	JA-45-447	Gold	Q	N	C	2676	JA-45-36031
	Q	N	A	5027	WL22907	Hafnium	Q	N	C	3072	JA-45-36032
	Q	A	B	3184	WL22856	Holmium	P	N	C	4104	JA-45-36033
	Q	A	A	3184	WL22910	Iridium	Q	N	C	3040	JA-45-36034
	Q	N	B	3184	JA-45-453	Indium	Q	N	C	2850	JA-45-36036
	Q	N	A	3184	WL22974	Iridium	Q	N	C	3720	JA-45-36037
	Q	A	B	3988	JA-45-593	Iron	Q	N	C	5501	JA-45-36038
	Q	A	A	3988	WL22984	Lanthanum	P	N	C	2833	JA-45-36039
	P	N	A	4102	WL22976	Lead	Q	N	C	6708	JA-45-36090
	Q	N	B	4102	JA-45-594	Lithium 6	P	N	C	6708	JA-45-36091
	Q	N	A	4102	WL22988	Lithium 7	P	N	C	6708	JA-45-36091
	Q	N	B	2139	WL22607	Lithium, natural	P	N	C	3282	JA-45-36040
	Q	N	A	2139	JA-45-459	Luettium	P	N	C	3282	JA-45-36041
	Q	A	A	2139	WL22908	Magnesium	Q	N	C	2852	JA-45-36042
	Q	N	A	2139	WL22909	Manganese	Q	N	C	2795	JA-45-36043

Table 2.9 (continued)

Element	Window ^a	Gas Filp ^b	Size ^c	Analytical Line (Å)	Catalog Number ^d	Element	Window ^a	Gas Filp ^b	Size ^c	Analytical Line (Å)	Catalog Number ^d
Mercury	Q	A	C	2537	JA-45-36044	Aluminum, calcium	Q	N	B	—	WL23246
Molybdenum	Q	N	C	3133	JA-45-36045	Aluminum, calcium, magnesium	Q	A	B	—	WL23604
Neodymium	P	N	C	4925	JA-45-36046	Aluminum, calcium, magnesium	Q	A	A	—	WL22871
Nickel	Q	N	C	3413	JA-45-36047	Aluminum, calcium, magnesium	Q	N	B	—	JA-45-450
Niobium	P	N	C	4059	JA-45-36053	Aluminum, calcium, magnesium	Q	N	A	—	WL22955
Osmium	Q	A	C	2909	JA-45-36048	Aluminum, calcium, magnesium	Q	N	B	—	JA-45-310
Palladium	Q	N	C	3404	JA-45-36049	Aluminum, calcium, magnesium	Q	N	B	—	JA-45-436
Phosphorus	Q	N	C	2136	JA-45-36050	Aluminum, calcium, magnesium	Q	N	A	—	WL23036
Platinum	Q	N	C	2659	JA-45-36051	Aluminum, calcium, magnesium	Q	N	A	—	WL23403
Potassium	P	N	C	4044	JA-45-36052	Aluminum, calcium, magnesium	Q	N	B	—	WL23147
Praseodymium	P	N	C	4951	JA-45-36053	Aluminum, calcium, magnesium	Q	N	B	—	JA-45-434
Rhenium	P	N	C	3460	JA-45-36056	Aluminum, calcium, magnesium	Q	N	B	—	JA-45-598
Rhodium	P	N	C	3435	JA-45-36057	Aluminum, calcium, magnesium	Q	N	A	—	JA-45-437
Rubidium	P	N	C	7800	JA-45-36058	Aluminum, calcium, magnesium	Q	N	B	—	JA-45-478
Ruthenium	P	A	C	3499	JA-45-36059	Aluminum, calcium, magnesium	Q	N	B	—	JA-45-597
Samarium	P	N	C	4760	JA-45-36060	Aluminum, calcium, magnesium	Q	N	B	—	JA-45-308
Scandium	P	N	C	3912	JA-45-36061	Aluminum, calcium, magnesium	Q	N	B	—	WL23605
Selenium	Q	N	C	1960	JA-45-36062	Aluminum, calcium, magnesium	Q	N	B	—	JA-45-311
Silicon	Q	N	C	2516	JA-45-36063	Aluminum, calcium, magnesium	Q	N	B	—	WL23158
Silver	P	A	C	3281	JA-45-36064	Aluminum, calcium, magnesium	Q	N	B	—	JA-45-304
Sodium	P	N	C	5890	JA-45-36065	Aluminum, calcium, magnesium	Q	N	B	—	JA-45-442
Strontium	P	N	C	4607	JA-45-36066	Aluminum, calcium, magnesium	Q	N	B	—	WL23174
Sulphur	Q	N	C	—	JA-45-36067	Aluminum, calcium, magnesium	Q	N	B	—	JA-45-306
Tantalum	Q	A	C	2714	JA-45-36068	Aluminum, calcium, magnesium	Q	N	B	—	—
Tellurium	Q	N	C	2143	JA-45-36069	Aluminum, calcium, magnesium	Q	N	B	—	—
Terbium	P	N	C	4326	JA-45-36070	Aluminum, calcium, magnesium	Q	N	B	—	—
Thallium	Q	N	C	3776	JA-45-36071	Aluminum, calcium, magnesium	Q	N	B	—	—
Thorium	Q	N	C	3245	JA-45-36072	Aluminum, calcium, magnesium	Q	N	B	—	—
Thulium	P	N	C	4105	JA-45-36073	Aluminum, calcium, magnesium	Q	N	B	—	—
Tin	Q	N	C	2863	JA-45-36074	Aluminum, calcium, magnesium	Q	N	B	—	—
Titanium	Q	N	C	3643	JA-45-36075	Aluminum, calcium, magnesium	Q	N	B	—	—
Tungsten	P	N	C	4009	JA-45-36076	Aluminum, calcium, magnesium	Q	N	B	—	—
Uranium	Q	N	C	5027	JA-45-36077	Aluminum, calcium, magnesium	Q	N	B	—	—
Vanadium	P	N	C	3184	JA-45-36078	Aluminum, calcium, magnesium	Q	N	B	—	—
Ytterbium	P	N	C	3988	JA-45-36079	Aluminum, calcium, magnesium	Q	N	B	—	—
Yttrium	P	N	C	4102	JA-45-36080	Aluminum, calcium, magnesium	Q	N	B	—	—
Zinc	Q	N	C	2139	JA-45-36081	Aluminum, calcium, magnesium	Q	N	B	—	—
Zirconium	P	A	C	3601	JA-45-36082	Aluminum, calcium, magnesium	Q	N	B	—	—

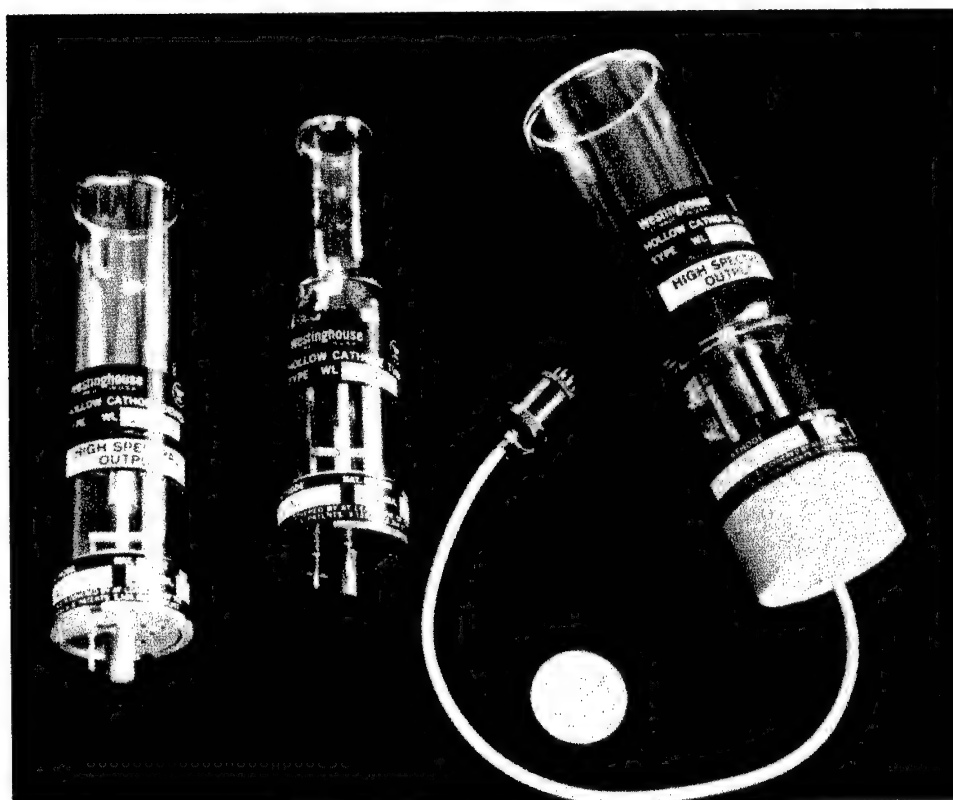
^aP = Pyrex, Q = quartz; ^bN = neon, A = argon; ^cA = 1½ in. diameter, B = 1 in. diameter, C = 2 in. diameter; ^dWL = Westinghouse, JA = Jarrell-Ash.

(continued)

Table 2.9 (continued)

Element	Window ^a	Gas Fill ^b	Size ^c	Analytical Line (Å)	Catalog Number ^d	Element	Window ^a	Gas Fill ^b	Size ^c	Analytical Line (Å)	Catalog Number ^d
Chromium, manganese, cobalt, copper, manganese, nickel	Q	N	B	—	WL23499	Antimony, arsenic, bismuth	Q	N	C	—	JA-45-36203
Chromium, cobalt, copper, iron, manganese, nickel	Q	N	B	—	WL23601	Barium, calcium, strontium, magnesium	Q	N	C	—	JA-45-36228
Cobalt, copper	Q	N	B	—	JA-45-599	Cadmium, silver, zinc, lead	Q	N	C	—	JA-45-36205
Cobalt, copper, gold, nickel	Q	N	B	—	JA-45-305	Cadmium, copper, zinc, lead	Q	N	C	—	JA-45-36227
Cobalt, copper, zinc, molybdenum	Q	N	B	—	WL23595	Calcium, magnesium	Q	N	C	—	JA-45-36092
Cobalt, iron	Q	N	B	—	JA-45-596	Calcium, magnesium, zinc	Q	N	C	—	JA-45-36097
Cobalt, nickel	Q	N	B	—	WL23291	Calcium, zinc	Q	N	C	—	JA-45-36093
Copper, gallium	Q	N	B	—	WL23426	Chromium, iron, manganese, nickel	Q	N	C	—	JA-45-36201
Copper, iron	Q	N	B	—	JA-45-431	Chromium, cobalt, copper, manganese, nickel	Q	N	C	—	JA-45-36094
Copper, iron, manganese	Q	N	B	—	JA-45-312	Chromium, cobalt, copper, manganese, nickel	Q	N	C	—	JA-45-36103
Copper, iron, molybdenum	Q	N	B	—	JA-45-435	Chromium, copper, nickel, silver	Q	N	C	—	JA-45-36096
Copper, iron, gold, nickel	Q	N	B	—	JA-45-301	Chromium, copper, iron, nickel, silver	Q	N	C	—	JA-45-36108
Copper, iron, manganese, zinc	Q	N	B	—	JA-45-307	Cobalt, copper, iron, manganese, molybdenum	Q	N	C	—	JA-45-36102
Copper, manganese	Q	N	B	—	JA-45-492	Copper, zinc, lead, tin	Q	N	C	—	JA-45-36202
Copper, nickel	Q	N	B	—	JA-45-491	Copper, iron	Q	N	C	—	JA-45-36200
Copper, nickel, zinc	Q	N	B	—	WL23441A	Copper, iron, nickel	Q	N	C	—	JA-45-36101
Copper, zinc, molybdenum	Q	N	B	—	WL23405	Copper, iron, lead, nickel, zinc	Q	N	C	—	JA-45-36204
Copper, zinc, lead, silver	Q	N	B	—	JA-45-496	Copper, iron, manganese, zinc	Q	N	C	—	JA-45-36105
Copper, zinc, lead, tin	Q	N	B	—	JA-45-448	Sodium, potassium	P	A	C	—	JA-45-36095
Gold, nickel	Q	N	B	—	JA-45-438						
Gold, silver	Q	N	B	—	JA-45-433						
Indium, silver	Q	N	B	—	WL23269						
Lead, silver, zinc	Q	N	B	—	WL23171						
Manganese, zinc	Q	N	B	—	WL23455						
Sodium, potassium	P	A	A	—	JA-45-439						
Sodium, potassium, zinc, lead, tin	P	A	A	—	WL23230						
	Q	N	B	—	WL23404						
Multiple-Element 36000 Series											
Aluminum, calcium, magnesium	Q	N	C	—	JA-45-36099						
Aluminum, calcium, magnesium, lithium	Q	N	C	—	JA-45-36250						

^aP = Pyrex, Q = quartz; ^bN = neon, A = argon; ^cA = 1½ in. diameter, B = 1 in. diameter, C = 2 in. diameter; ^dWL = Westinghouse, JA = Jarrell-Ash.



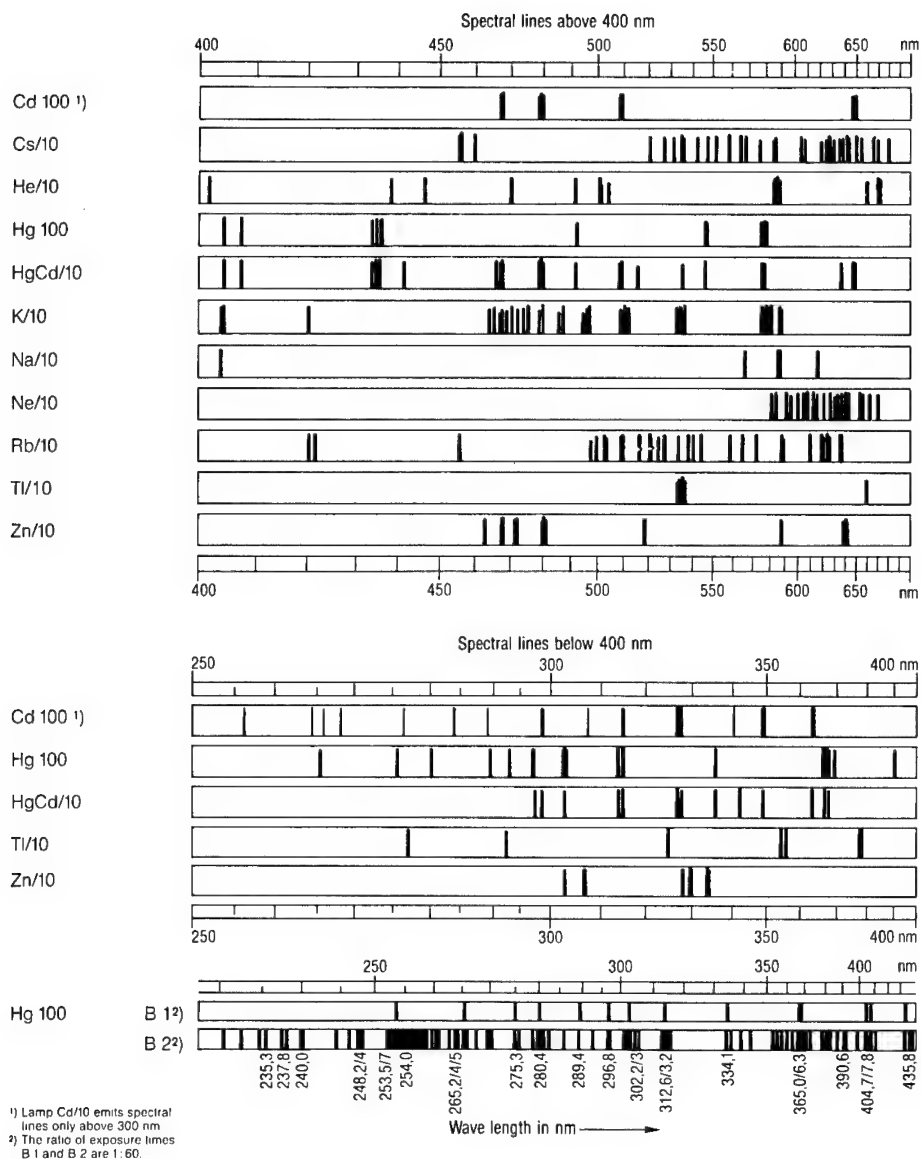
(a)

		Transition Elements															
Li	Be	Group 8										B					
Na	Mg											Al	Si	P	S		
K	Ca	Sc	Ti	V	Cr	Mn	Fe	Co	Ni	Cu	Zn	Ga	Ge	As	Se		
Rb	Sr	Y	Zr	Nb	Mo		Ru	Rh	Pd	Ag	Cd	In	Sn	Sb	Te		
Cs	Ba	La	Hf	Ta	W	Re	Os	Ir	Pt	Au	Hg	Tl	Pb	Bi			
Lanthanides	Ce	Pr	Nd		Sm	Eu	Gd	Tb	Dy	Ho	Er	Tm	Yb	Lu			
Actinides	Th		U														

(b)

Fig. 2.44 (a) Hollow-cathode spectral tubes described in Table 2.9 and (b) periodic table showing the prevalence of elements obtainable in hollow-cathode tubes.

both made of tungsten. The arc forms between these electrodes, causing the pellet to heat incandescently. The ring also incandesces but to a lesser extent. Thus, the hot pellet (approximately 3100 K) provides an intense source of small-area radiation. A plot of the spectral variation of this radiation is given in Fig. 2.50. As with all tungsten sources, evaporation causes a steady erosion of the pellet surface with the introduction of gradients, which is not serious if the pellet is used as a point source.

Fig. 2.45 Spectral lamps.¹⁸

General Electric, manufacturer of the 30A/PS22 photomicrographic lamp, which uses a 30-Å operating current, states that this lamp requires a special heavy-duty socket obtainable through certain manufacturers. Contact GE for more information.

2.3.7 Glow Modulator Tubes

According to technical data supplied by Sylvania, glow modulator tubes³⁵ are cold-cathode light sources uniquely adaptable to high-frequency modulation.

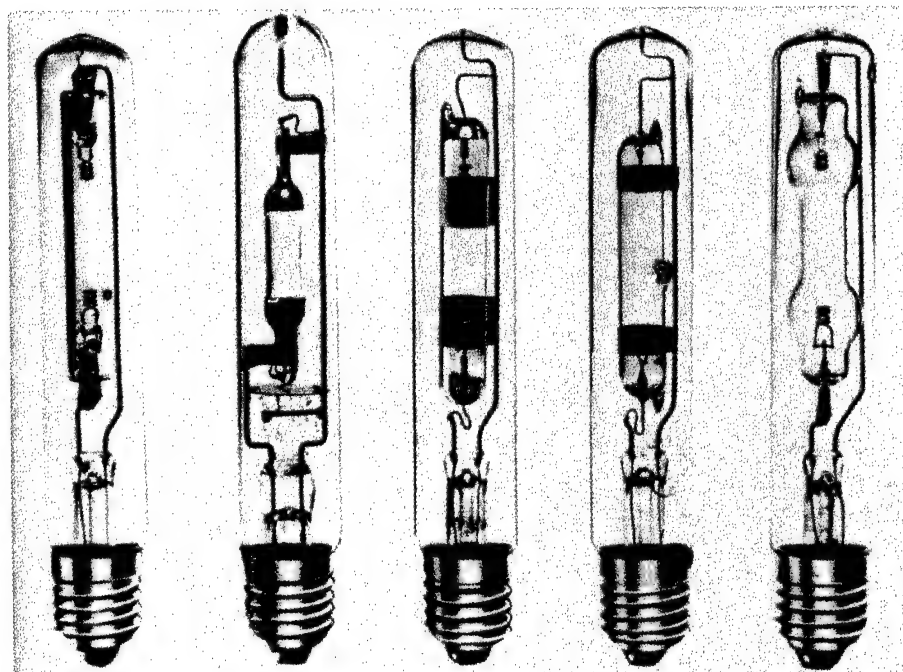
Fig. 2.46 Examples of Philips spectral lamps.³³

Table 2.10 Specifications of Philips Spectral Lamps (from Ref. 33)

Catalog Number	Symbols	Type	Material		Operating Current (A)	Wattage	Arc Length (mm)
			Burner	Envelope			
26-2709	Hg	Mercury (low-pressure)	Quartz	Glass	0.9	15	40
26-2717	Hg	Mercury (high-pressure)	Quartz	Glass	0.9	90	30
26-2725	Cd	Cadmium	Quartz	Glass	0.9	25	30
26-2733	Zn	Zinc	Quartz	Glass	0.9	25	30
26-2741	Hg, Cd, Zn	Mercury, cadmium, and zinc	Quartz	Glass	0.9	90	30
26-2758	He	Helium	Glass	Glass	0.9	45	32
26-2766	Ne	Neon	Glass	Glass	0.9	25	40
26-2774	A	Argon	Glass	Glass	0.9	15	40
26-2782	Kr	Krypton	Glass	Glass	0.9	15	40
26-2790	Xe	Xenon	Glass	Glass	0.9	10	40
26-2808	Na	Sodium	Glass	Glass	0.9	15	40
26-2816	Rb	Rubidium	Glass	Glass	0.9	15	40
26-2824	Cs	Caesium	Glass	Glass	0.9	10	40
26-2832	K	Potassium	Glass	Glass	0.9	10	40
26-2857	Hg	Mercury (low-pressure)	Quartz	Quartz	0.9	15	40
26-2865	Hg	Mercury (high-pressure)	Quartz	Quartz	0.9	90	30
26-2873	Cd	Cadmium	Quartz	Quartz	0.9	25	30
26-2881	Zn	Zinc	Quartz	Quartz	0.9	25	30
26-2899	Hg, Cd, Zn	Mercury, cadmium, and zinc	Quartz	Quartz	0.9	90	30
26-2907	In	Indium ^a	Quartz	Quartz	0.9	25	25
26-2915	Tl	Thallium	Quartz	Quartz	0.9	20	30
26-2923	Ga	Gallium	Quartz	Quartz	0.9	20	30

^aRequires a Tesla coil to cause it to strike initially



Fig. 2.47 Physical construction of Pluecker spectrum tubes.³⁴

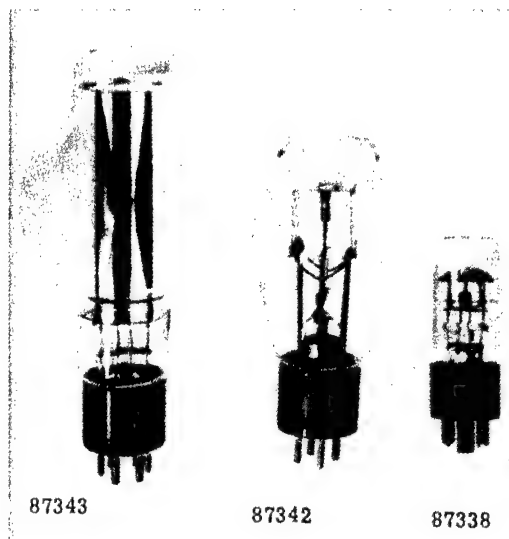


Fig. 2.48 Physical construction of some zirconium arc lamps.³⁸ Two 2-W lamps are available, but not shown here.²⁵

Table 2.11 Gas Fills in Pluecker Tubes^a
(from Ref. 34)

<i>Cenco Number</i>	<i>Type</i>
87210	Argon Gas
87215	Helium Gas
87220	Neon Gas
87225	Carbonic Acid Gas
87230	Chlorine Gas
87235	Hydrogen Gas
87240	Nitrogen Gas
87242	Air
87245	Oxygen Gas
87255	Iodine Vapor
87256	Krypton Gas
87258	Xenon
87260	Mercury Vapor
87265	Water Vapor

^aConsists of glass tube with overall length of 25 cm with capillary portion about 8.5 to 10 cm long. Glass-to-metal seal wires are welded in metal caps with loops for wire connection firmly sealed to the ends. Power supply no. 87208 is recommended as a source of excitation.

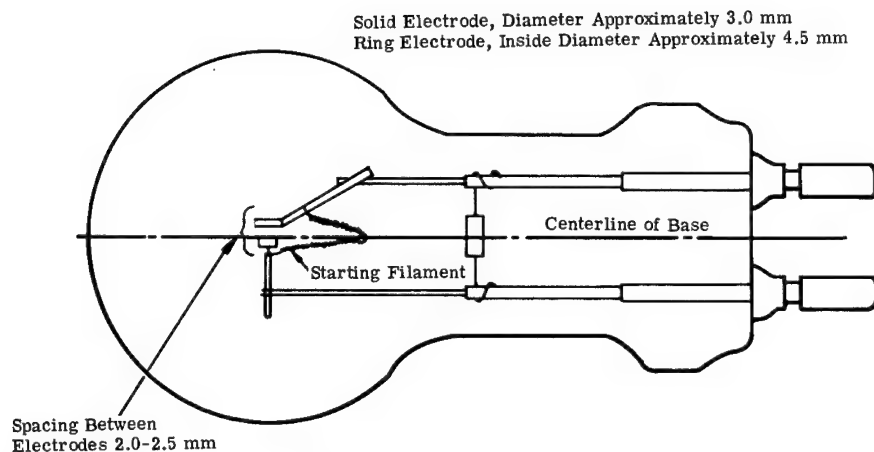


Fig. 2.49 Construction of tungsten-arc lamp. The lamp must be operated base-up on a well-ventilated housing and using a special high-current socket that does not distort the position of the posts.²⁵

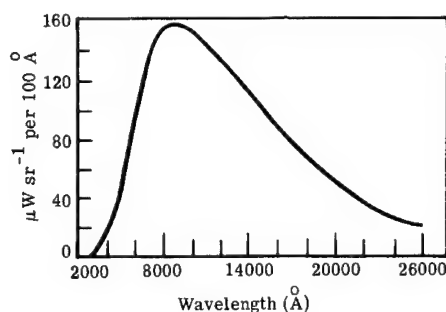


Fig. 2.50 Spectral distribution of a 30 PS 22 photomicrographic lamp.²⁵

(These tubes are now manufactured by The English Electric Valve Company, Elmsford, New York.) Pictures of two types are shown in Fig. 2.51. The cathode is a small hollow cylinder, and the high ionization density in the region of the cathode provides an intense source of radiation. Figure 2.52 is a graph of the light output as a function of tube current. Figure 2.53 is a graph depicting the response of the tube to a modulating input. The spectral outputs of a variety of tubes are shown in Fig. 2.54. Table 2.12 gives some of the glow modulator specifications.

2.3.8 Hydrogen and Deuterium Arcs

For applications requiring a strong continuum in the ultraviolet region, the hydrogen arc at a few millimeters of pressure provides a useful source. It can be operated with a cold or hot cathode. One hot-cathode type is shown in Fig. 2.55. Koller²⁰ plots a distribution for this lamp down to about 200 Å.

Deuterium lamps (Fig. 2.56) provide a continuum in the ultraviolet with increased intensity over the hydrogen arc. Both lamps have quartz envelopes.

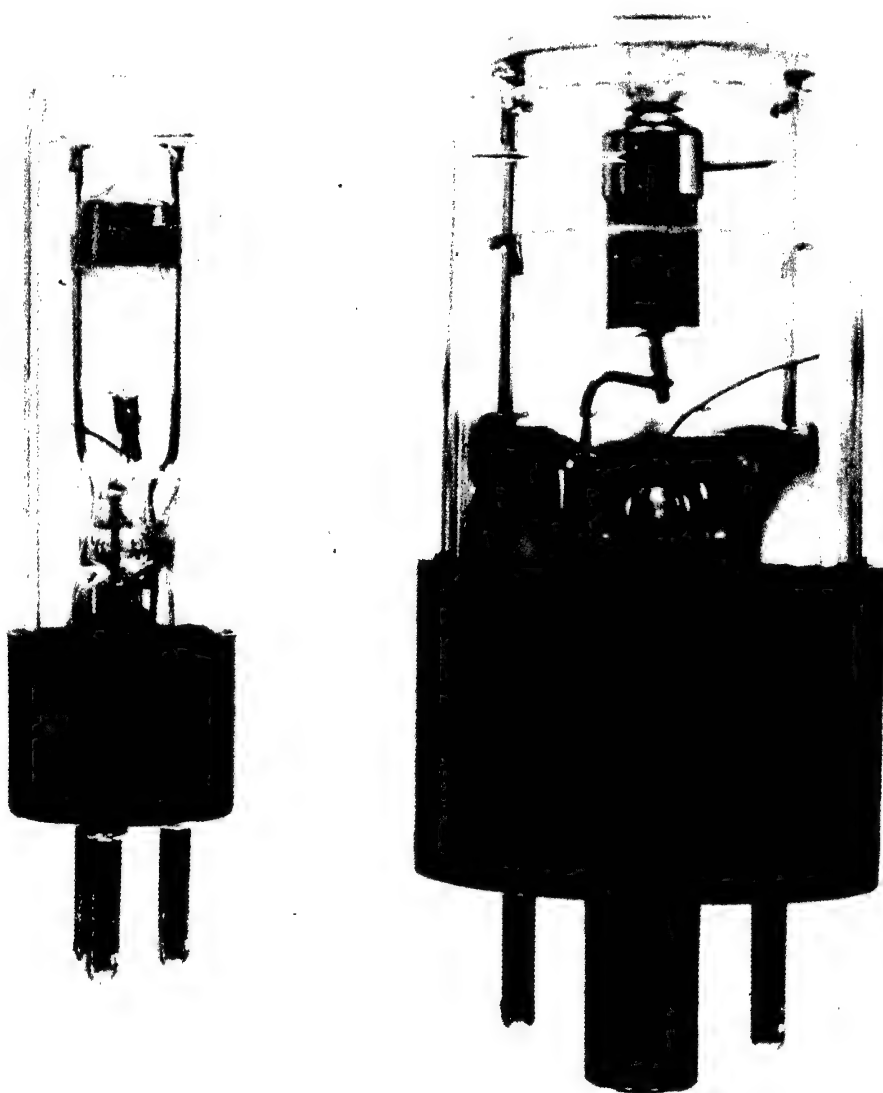


Fig. 2.51 Construction of two glow modulator tubes.³⁵

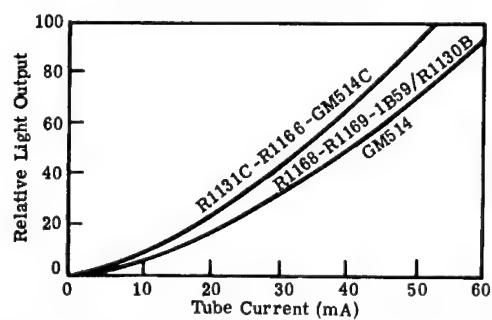


Fig. 2.52 Variations of the light output from a glow modulator tube as a function of tube current.³⁵

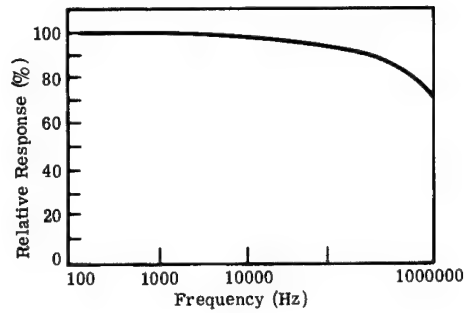


Fig. 2.53 Response of the glow modulator tube to a modulating input.³⁵

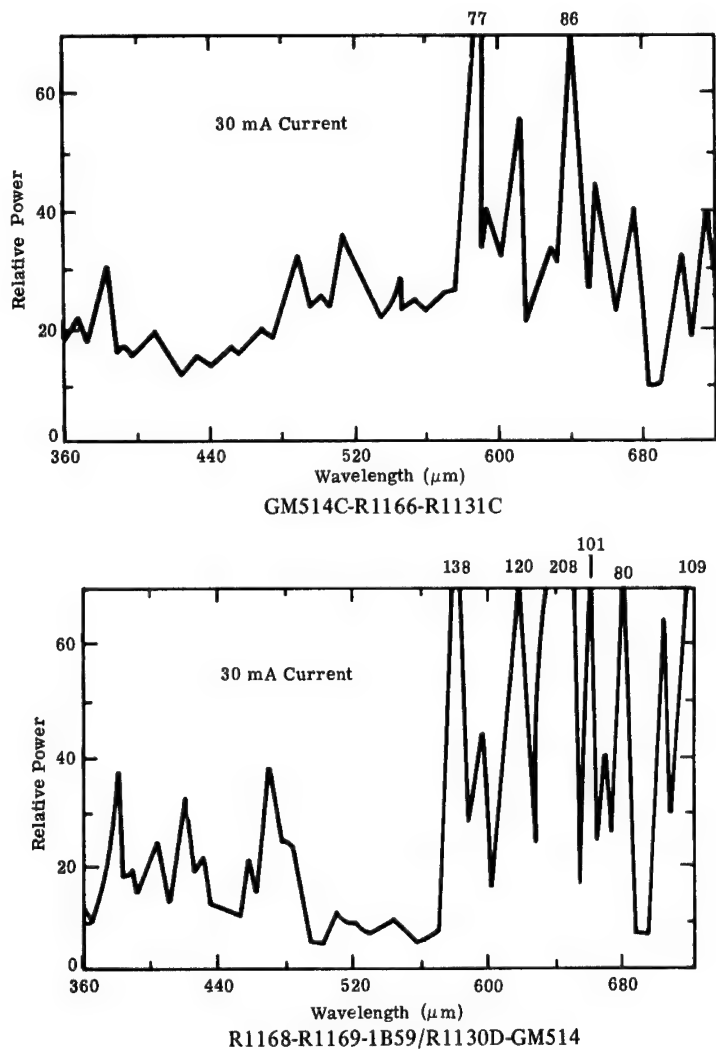


Fig. 2.54 Spectral variation of the output of glow modulator tubes.³⁵

Table 2.12 Glow Modulator Specifications (from Ref. 35)

No. ^a	Maximum Operating Voltage	Current (mA)		Minimum Starting Voltage (V)	Crater Diameter (in.)	Approximate Light Center Length (in.)	Light Output (cd)	Brightness (cd in. ⁻²)	Rated Life (h)	Base Type	Bulb Type	Maximum Overall Length (in.)	Maximum Diameter (in.)	Color of Discharge
		Average	Peak											
GM-514	160	5-25	55	240	0.056	1-3/4	0.1 at 25 mA	41 at 25 mA	100 at 15 mA	3-pin miniature ^b	T-4½	2-5/8	41/64	Blue-red
GM-514C	160	5-15	35	240	0.093	1-3/4	0.1 at 15 mA	15 at 15 mA	25 at 10 mA	3-pin miniature ^b	T-4½	2-5/8	41/64	White
1B59/ R-1130B	150	5-35	75	225	0.056	2	0.13 at 30 mA	43 at 30 mA	250 at 20 mA	Intermediate shell oct. ^c	T-9	3-1/16	1-9/32	Blue-red
R-1131C	150	3-25	55	225	0.093	2	0.2 at 25 mA	29 at 25 mA	150 at 15 mA	Intermediate shell oct. ^c	T-9	3-1/16	1-9/32	White
R-1166	150	3-25	55	225	0.093	2	0.2 at 25 mA	29 at 25 mA	150 at 15 mA	Intermediate shell oct. ^c	T-9	3-1/16	1-9/32	White
R-1168	150	5-15	30	225	0.015	2	0.023 at 15 mA	132 at 15 mA	150 at 15 mA	Intermediate shell oct. ^c	T-9	3-1/16	1-9/32	Blue-red
R-1169	150	5-25	45	225	0.025	2	0.036 at 15 mA	72 at 15 mA	250 at 15 mA	Intermediate shell oct. ^c	T-9	3-1/16	1-9/32	Blue-red

^aType R-1166 is opaque-coated with the exception of a circle 3/8 inch in diameter at end of lamp. All other types have clear-finish bulb.^bPins 1 and 3 are anode; pin 2 cathode.^cPin 7 anode; pin 3 cathode.

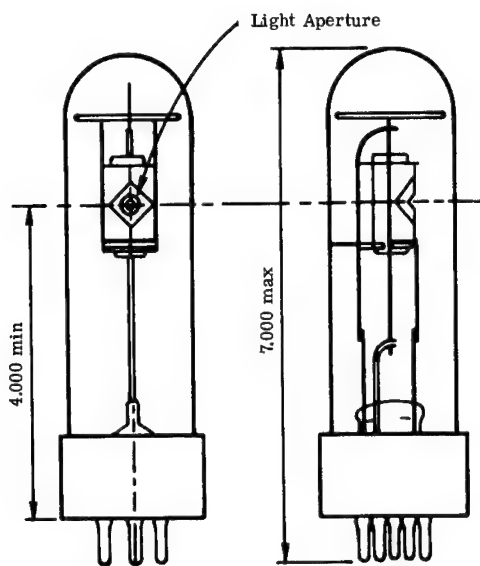


Fig. 2.55 Hydrogen-arc lamp.³⁵

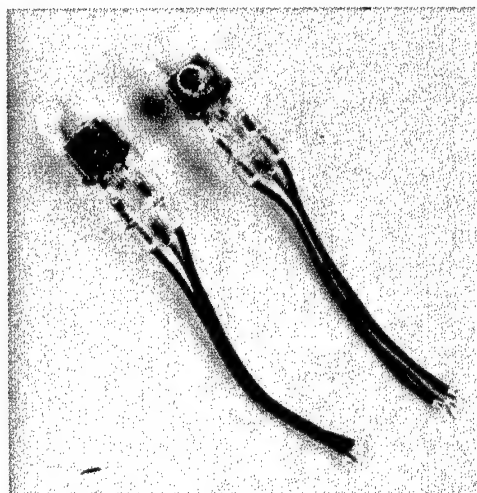


Fig. 2.56 Two types of deuterium-arc lamps.³³

The one on the left is designed for operation down to 2000 Å; the one on the right is provided with a Suprasil^h window to increase the ultraviolet range down to 1650 Å. NIST is offering a deuterium lamp standard of spectral irradiance between 200 and 350 nm. The lamp output at 50 cm from its medium bipost base is about 0.7 W cm^{-3} at 200 nm and drops off smoothly to 0.3 W cm^{-3} at 250 nm and 0.07 W cm^{-3} at 350 nm. A working standard of the deuterium lamp can be obtained also, for example, from Optronic Laboratories, Orlando, Florida.

^hRegistered trademark of Heraeus-Amersil.

2.3.9 Other Commercial Sources

Activated-Phosphor Sources. Of particular importance and convenience in the use of photometers are sources composed of a phosphor activated by radioactive substances. Readily available, and not subject to licensing with small quantities of radioactive material, are the ^{14}C -activated phosphor light sources. These are relatively stable sources of low intensity, losing about 0.02% per year due to the half-life of ^{14}C and the destruction of phosphor centers.

Light-Emitting Diodes (LEDs). These sources fit most readily into the category of display devices. However, for some special purposes they are often useful since they are small, simple to integrate into a system, and can be made highly directional. They emit very narrowband radiation, usually in the visible, but some are designed to operate in the infrared. The performance characteristics of different types of LEDs are shown in Table 2.5.

Other High-Energy Sources. Radiation at very high powers can be produced. Sources are synchrotrons, plasmotrons, arcs, sparks, exploding wires, shock tubes, and atomic and molecular beams, to name but a few. Among these, one can purchase in convenient, usable form, precisely controlled spark-sources for yielding many joules of energy in a time interval of the order of microseconds. The number of vendors will be few, but check the directories.

Other Special Sources. An enormous number of special-purpose sources are obtainable from manufacturers and scientific instrument suppliers. One source that remains to be mentioned is the so-called miniature, subminiature, and microminiature lamps. These are small, even tiny, incandescent bulbs of glass or quartz, containing tungsten filaments. They work very well in certain applications where small, intense radiators of visible and near-infrared radiation are needed. Information about vendors of these sources can be found in the trade magazines.

2.4 FIELD SOURCES (MAN-MADE TARGETS)

2.4.1 Surface and Subsurface Vehicles

This group includes surface land vehicles (i.e., trucks, tanks, personnel carriers, automobiles, motorcycles, trains, hovercraft, and others) and ships (i.e., aircraft carriers, missile ships, cargo vessels, hydrofoil craft, small wooden and metal boats, and submarines). Specific radiation characteristics are seldom, if ever, reported in the open literature. For the sake of visualization, however, a thermal image of an army shop van is given³⁶ in Fig. 2.57. Whereas specific radiative patterns may be of use in certain instances, many of the target data are calculated by the use of predictive models. Figures 2.58 and 2.59 show moderately resolved faceted models (i.e., they are made of many facets placed so as to approximate the actual shape of whatever target is to be calculated).ⁱ The faces or facets are composed of radiating material with appropriate emissivities, emitting at temperatures that have been derived from the conditions

ⁱSee the Sec. 2.5 description of the SIRIM model for a more complete and detailed description of faceted models.

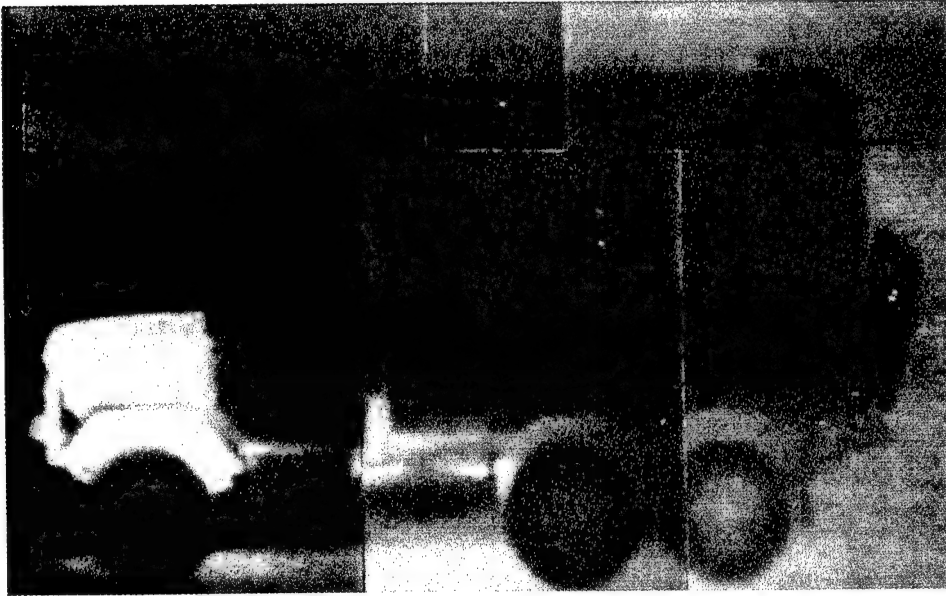


Fig. 2.57 Thermal image of an army 6×6 shop van.³⁶

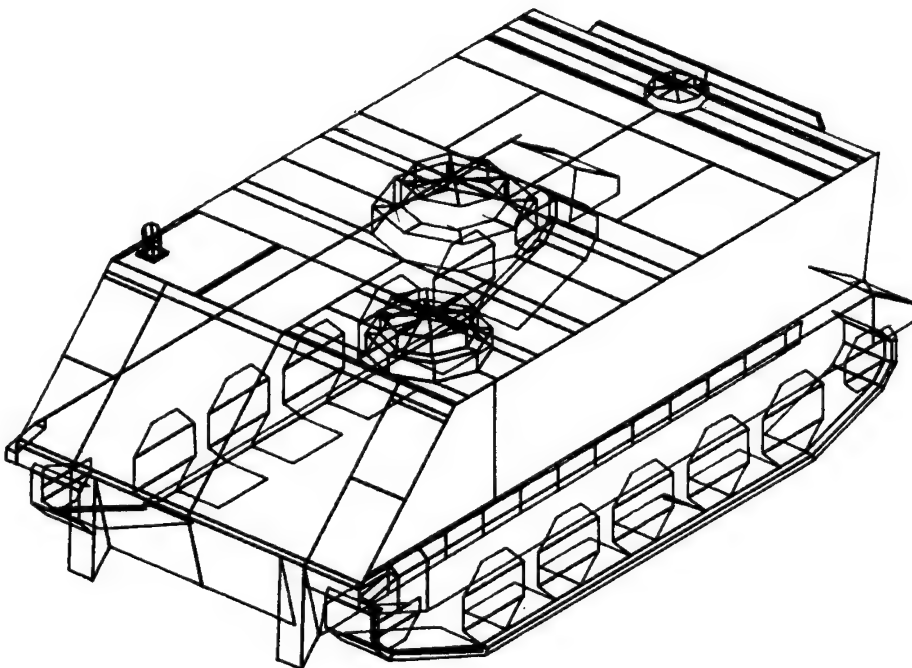


Fig. 2.58 Faceted model of an armored personnel carrier.

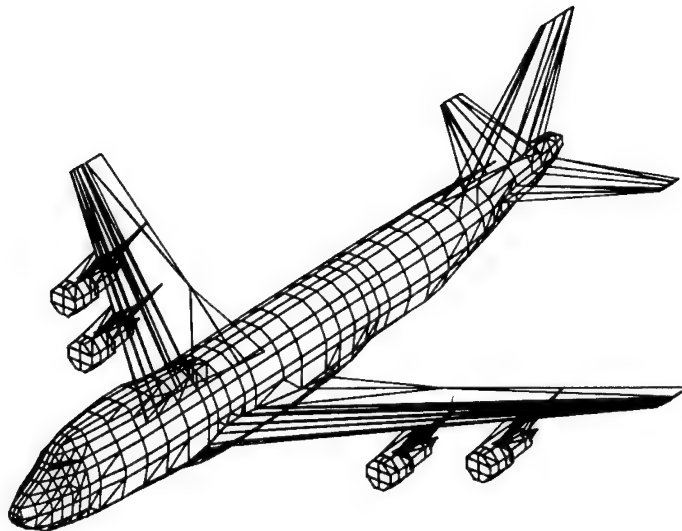


Fig. 2.59 Faceted model of a jet aircraft.

under which the vehicle has been operating. Because these conditions vary considerably, it is often not feasible to report specific radiative properties except in special cases suited to special purposes. The faceted models in Figs. 2.58 and 2.59, taken from Ref. 22, are rather crude compared to those currently achieved as represented in Fig. 2.60.³⁷

Painted surfaces usually have emissivities in the infrared of about 0.9. This can change in reality because of weathering and general deterioration. Dust and dirt can accumulate to add their effects. Furthermore, different parts of the vehicle are at different temperatures, exhaust parts being the hottest. The uncertainty, however, of the exact amount of radiation coming from the exhaust is increased by the use of suppression devices on military vehicles and the presence of hot exhaust gases. Therefore, models are used to predict the radiative output as a function of whatever parameters are desired.

Total (i.e., spectrally integrated) normal emissivities of selected materials are shown in Tables 2.13 and 2.14. Data are shown in Fig. 2.61 on the diffuse spectral reflectances of various target materials in the near IR and visible regions.³⁸

2.4.2 Aircraft

Many of the general statements about surface vehicles apply to aircraft as well. However, aircraft have rather special signatures resulting from the fact that they exhaust hot gases in large quantities. A good example of the spectral quality of aircraft radiation as observed from the tail aspect is shown in Fig. 2.62. Compare this spectrum with that obtained from a high-temperature industrial smokestack, as shown in Fig. 2.63. The scales are of relative values. Note in Fig. 2.64 that the radiation viewed away from the tail of the aircraft, part of which is obscured by the body of the aircraft, has the typical structure of gaseous radiation. Figure 2.65, for example, shows the evolution of fine structure with increasing resolution. In fact, if the fine structure could be seen

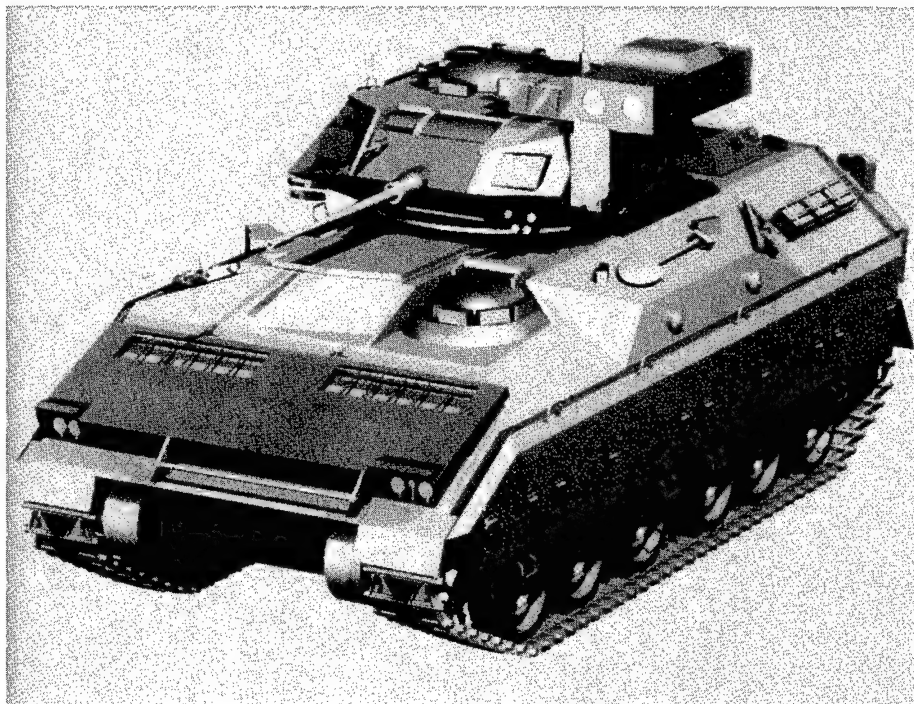


Fig. 2.60 Exterior view of the Bradley armored fighting vehicle.³⁷

with infinite resolution, the individual lines would be apparent that represent transitions between various energy states of the molecules composing the exhaust.

For hydrocarbon fuels, the exhaust consists mainly of H_2O vapor and CO_2 . Because of these, a lot of radiation occurs in certain spectral regions, especially around 2.7 and 4.3 μm , at which the emissivities of these gases are quite high. However, the atmosphere, composed also of H_2O vapor and CO_2 , tends to absorb quite readily at these wavelengths. Since the gases are hotter than the atmosphere, some molecular lines radiate outside of the region of strong atmospheric absorption and propagate with much less attenuation than in the atmospheric bands. This effect is pronounced in the 4.3- μm region of CO_2 absorption. As the observation angle changes to the tail, the continuum radiation emitted from the tail pipe is clearly seen. The radiation from the hot gases is, of course, still present. For a more thorough dissertation on the calculation of the radiance from the plume of a jet engine, the reader is referred to other chapters in this handbook.

In a more straightforward, less sophisticated approach, the following calculations are for the radiation emitted from a Boeing 707 jet transport.³⁹ The features of a turbojet engine are shown in Fig. 2.66 with temperatures and pressures given in the lower portion of the figure. The higher temperature in afterburning gives rise to more radiation than obtained otherwise. But the calculation would be further complicated by the fact that large amounts of hot gases would be emitted with an accompanying increase in molecular band radiation.

The turbofan exhaust of a 707 jet transport is cooler than that of the turbojet. The characteristics of each are given in Table 2.15. The total radiance from

Table 2.13 Emissivity (Total Normal) of Various Common Materials (from Ref. 39)

<i>Material</i>	<i>Temperature (°C)</i>	<i>Emissivity</i>
METALS AND THEIR OXIDES		
Aluminum: polished sheet	100	0.05
sheet as received	100	0.09
anodized sheet, chromic acid process	100	0.55
vacuum deposited	20	0.04
Brass: highly polished	100	0.03
rubbed with 80-grit emery	20	0.20
oxidized	100	0.61
Copper: polished	100	0.05
heavily oxidized	20	0.78
Gold: highly polished	100	0.02
Iron: cast, polished	40	0.21
cast, oxidized	100	0.64
sheet, heavily rusted	20	0.69
Magnesium: polished	20	0.07
Nickel: electroplated, polished	20	0.05
electroplated, no polish	20	0.11
oxidized	200	0.37
Silver: polished	100	0.03
Stainless steel: type 18-8, buffed	20	0.16
type 18-8, oxidized at 800°C	60	0.85
Steel: polished	100	0.07
oxidized	200	0.79
Tin: commercial tin-plated sheet iron	100	0.07
OTHER MATERIALS		
Brick: red common	20	0.93
Carbon: candle soot	20	0.95
graphite, filed surface	20	0.98
Concrete	20	0.92
Glass: polished plate	20	0.94
Lacquer: white	100	0.92
matte black	100	0.97
Oil, lubricating (thin film on nickel base):		
nickel base alone	20	0.05
film thickness of 0.001, 0.002, 0.005 in.	20	0.27, 0.46, 0.72
thick coating	20	0.82
Paint, oil: average of 16 colors	100	0.94
Paper: white bond	20	0.93
Plaster: rough coat	20	0.91
Sand	20	0.90
Skin, human	32	0.98
Soil: dry	20	0.92
saturated with water	20	0.95
Water: distilled	20	0.96
ice, smooth	-10	0.96
frost crystals	-10	0.98
snow	-10	0.85
Wood: planed oak	20	0.90

Table 2.14 Solar Absorptance α and Low-Temperature (300 K) Emissivity ϵ for Spacecraft Materials (from Ref. 39)

<i>Material</i>	α	ϵ	α/ϵ
Aluminum:			
polished and degreased	0.387	0.027	14.35
foil, dull side, crinkled and smoothed	0.223	0.030	7.43
foil, shiny side	0.192	0.036	5.33
sandblasted	0.420	0.210	2.00
oxide, flame sprayed, 0.001 inch thick	0.422	0.765	0.55
anodized	0.150	0.770	0.19
Fiberglass:	0.850	0.750	1.13
Gold: plated on stainless steel and polished	0.301	0.028	10.77
Magnesium: polished	0.300	0.070	4.30
Paints:			
Aquadag, 4 coats on copper aluminum	0.782	0.490	1.60
aluminum	0.540	0.450	1.20
Microbond, 4 coats on magnesium	0.936	0.844	1.11
TiO ₂ , gray	0.870	0.870	1.00
TiO ₂ , white	0.190	0.940	0.20
Rokide A	0.150	0.770	0.20
Stainless steel: type 18-8, sandblasted	0.780	0.440	1.77

the tailpipe of the aircraft can be calculated from a knowledge of the emissivities and the temperatures of the emitting surfaces. Gouffé's results, given at the beginning of this chapter, make it reasonable to assume a cavity emissivity of better than 0.9. Using this value and a uniform temperature equal to the exhaust gas temperature for maximum cruise (from Table 2.15), the radiant intensity (W sr^{-1}) normal to the exit plane of a single engine is calculated from:

$$\begin{aligned}
 I &= \frac{\epsilon \sigma T^4 A}{\pi} \\
 &= \frac{0.9 \times 5.67 \times 10^{-12} \times (485 + 273)^4 \times 3660}{\pi} \\
 &= 1963 \text{ W sr}^{-1} .
 \end{aligned} \tag{2.18}$$

Total radiation from the aircraft (when all engines are in the field of view of the instrument) is four times that from one engine, or 7852 W sr^{-1} . As a radiation slide rule shows, the spectrum for this temperature peaks at about $3.8 \mu\text{m}$, and the region between 3.2 and $4.8 \mu\text{m}$ passes radiation between the H₂O absorption bands between 2.7 and $6.3 \mu\text{m}$. The radiation from an engine in this spectral region is thus 580 W sr^{-1} , as obtained by using a simple hand-calculator program. Total engine radiation in this region is 2320 W sr^{-1} . Similar values for the turbofan airplane are 6085 W sr^{-1} total radiation and 1500 W sr^{-1} in the 3.2 - to $4.8\text{-}\mu\text{m}$ region.

Using a relatively crude spectrum for the gaseous emission and an approximation to the gas temperature, Hudson calculates the radiance of the hot gases in the 4.3 - to $4.55\text{-}\mu\text{m}$ region and estimates the tail pipe radiation to be greater than gaseous radiation.³⁹ Similar calculations can be made for the

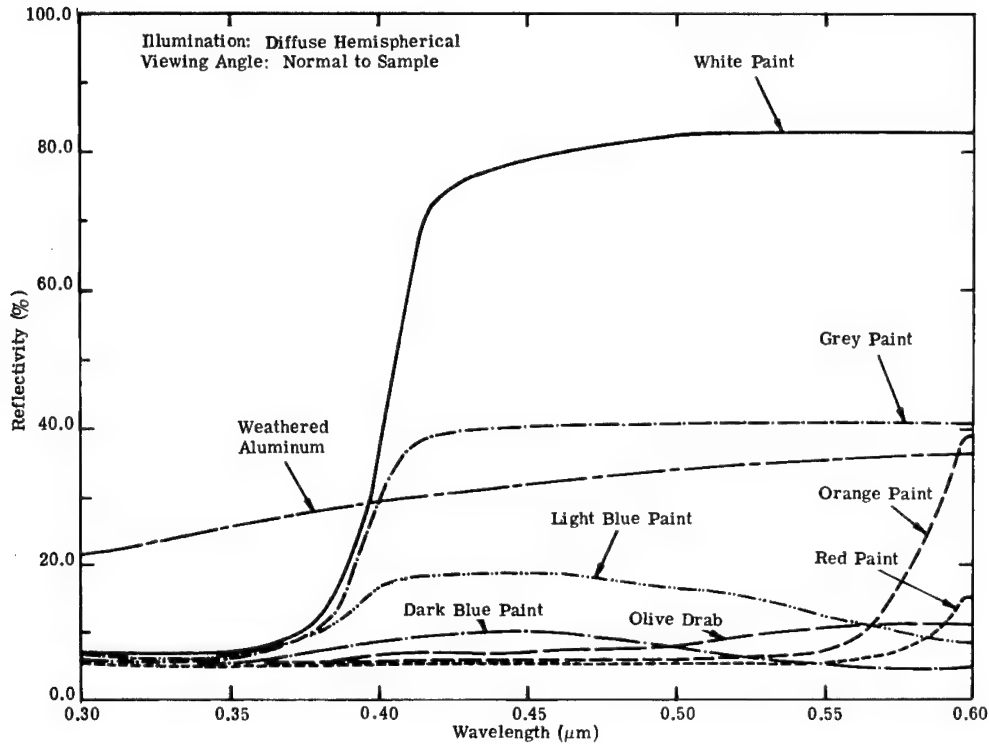


Fig. 2.61 Diffuse spectral reflectance of various materials in the near-UV/VIS.³⁸

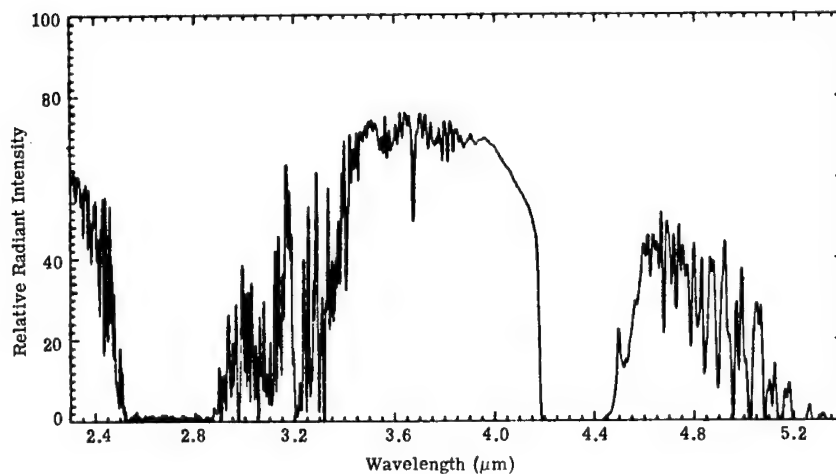


Fig. 2.62 Relative spectrum of jet aircraft as seen from tail aspect at a range of 1.5 miles.³⁶

aircraft using afterburners, for which exhaust conditions are shown in Fig. 2.67. Compare also Fig. 2.68. The radiation is considerably more intense. More accurate determinations can be made by using more precise spectral data from actual aircraft as shown²² in Figs. 2.62 through 2.65. The conditions, of course, are not the same as for the 707 and adjustments, therefore, must be made. Furthermore, it becomes necessary, for greater accuracy, to take into account

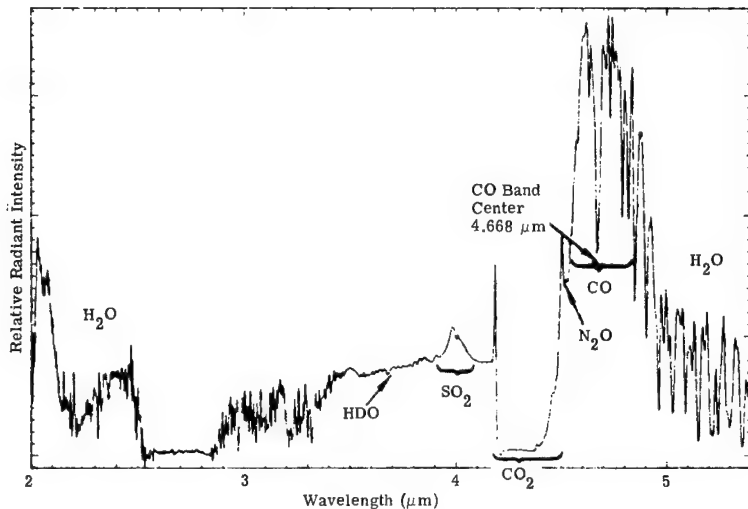


Fig. 2.63 Emission from a high-temperature industrial smokestack.³⁶

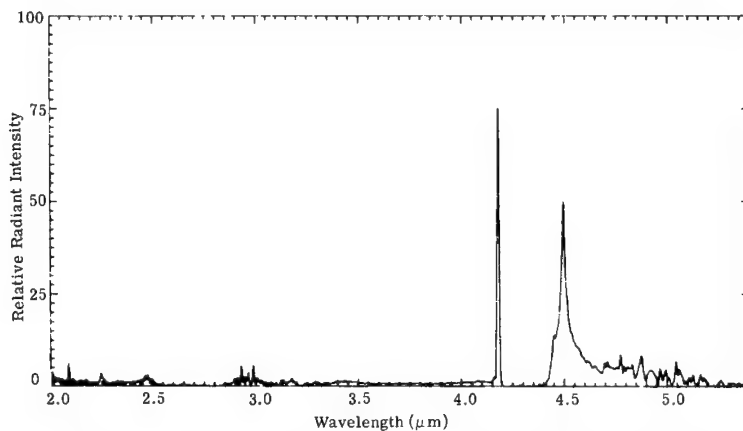


Fig. 2.64 Relative spectrum of target exhaust plume emission.³⁶

the actual aircraft structure as shown in Figs. 2.67 and 2.68, for which it is pertinent to use one of the mathematical models cited earlier.

As the speed of an aircraft increases, the temperature of the skin reaches high enough temperatures to produce radiation, which becomes readily observed at large distances, often competitive with other sources from the aircraft. Figure 2.69 represents centigrade temperatures as a function of Mach number M for laminar flow over a surface above 37,000 ft of altitude. The equation of this curve is:

$$T [K] = 216.7(1 + 0.164M^2), \quad (2.19)$$

which is compared to some data obtained as shown in the legend to the figure. Hudson explains that the low values for the X-15 can be explained by the short flight time and by the high emissivity of the blackened surface, reducing the likelihood of equilibrium.

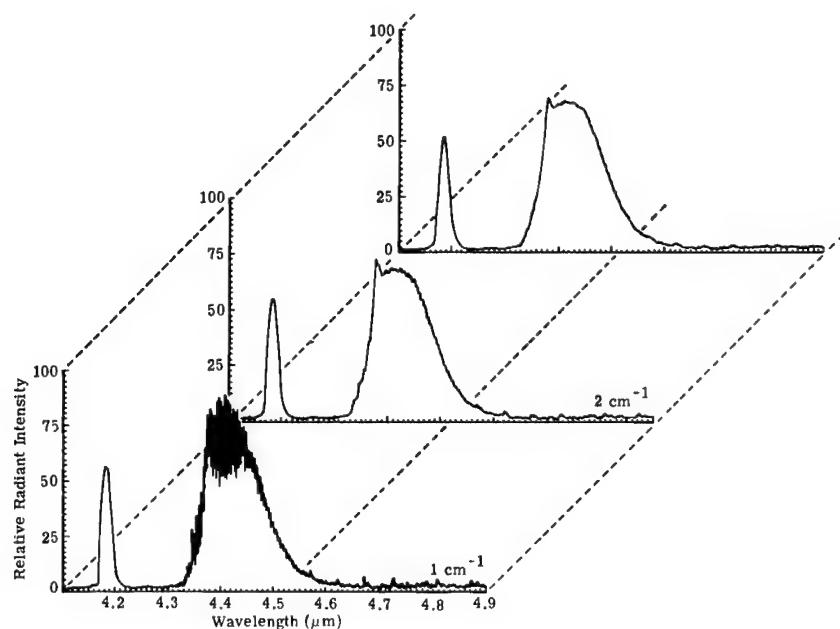


Fig. 2.65 Aircraft exhaust plume as seen through 200 ft of atmosphere and measured with three different spectral resolutions.³⁶

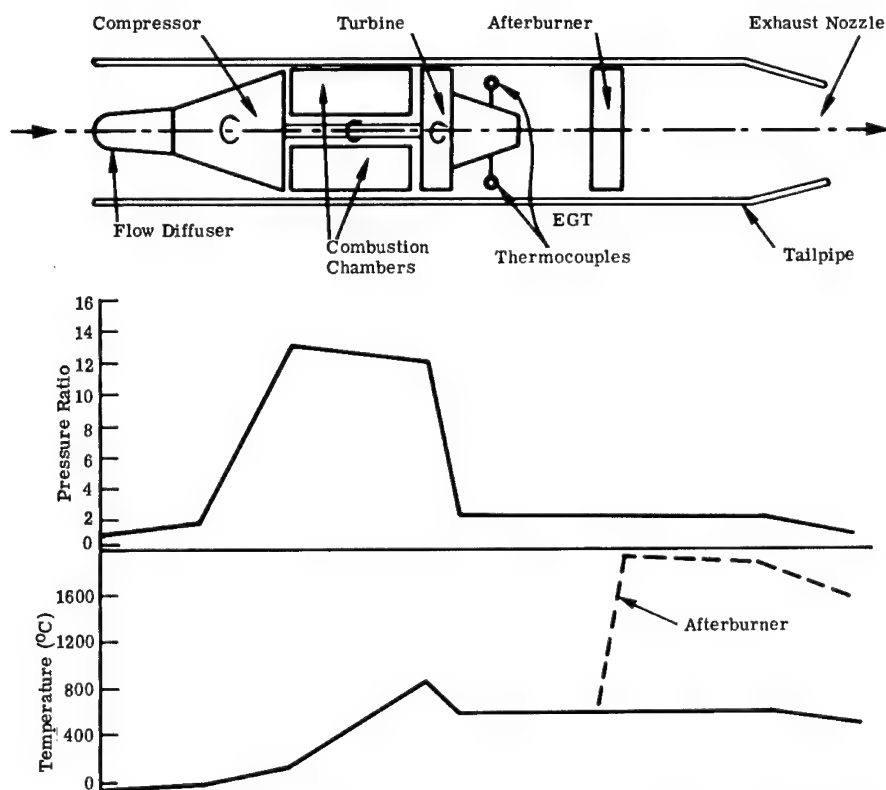
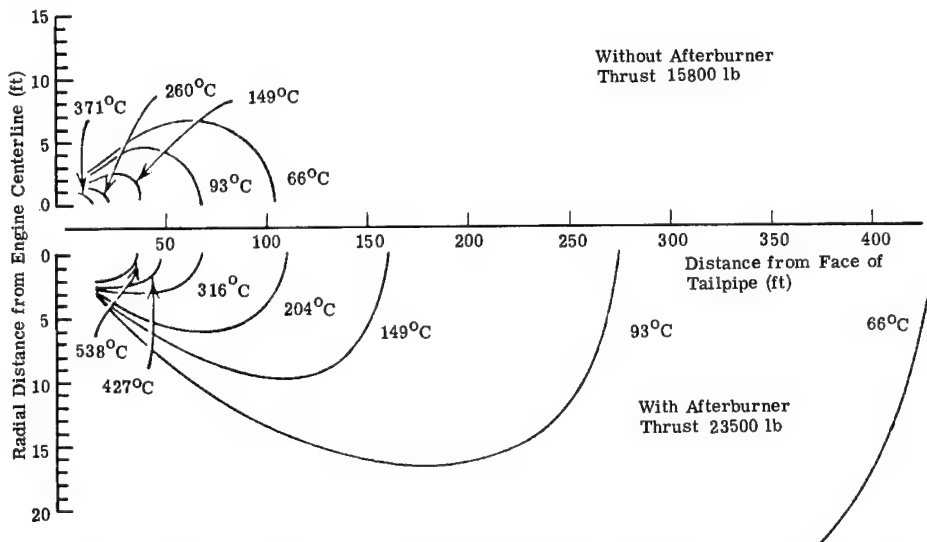


Fig. 2.66 The turbojet engine.³⁹

Table 2.15 Characteristics of the Boeing 707 Intercontinental Jet Transport
(from Ref. 39)

<i>Model</i>	707-320	707-320B
Engines	4-P&WA JT4A-9	4-P&WA JT3D-3
Type of engine	Turbojet	Turbofan
Maximum rated thrust (lb per engine)	16800	18000
Area of engine exhaust nozzle (cm ²)	3660	3502
Exhaust gas temperatures:		
Maximum allowable takeoff (°C)	635	555
Maximum continuous thrust (°C)	515	490
Maximum cruise thrust (°C)	485	445
Fuel flow (per engine):		
Sea level, Mach 0.4 (lb h ⁻¹)	10814	9068
35 000 ft. Mach 0.8 (lb h ⁻¹)	4819	3962
Spacing between engines		
Inner engines (ft)	66	66
Outer engines (ft)	104	104
Maximum speed (mph)	585	592

**Fig. 2.67** Exhaust temperature contours for the Pratt and Whitney JT4a turbojet engines at maximum sea level thrust with and without afterburner.³⁹

2.4.3 Muzzle Flash

The hot gases ejected from the muzzle of a gun contain, among other things, a large amount of combustible constituents, such as CO and H₂, along with CO₂, N₂, and H₂O at a sufficiently high temperature to cause the accompanying particulate matter to radiate visible radiation. In addition, considerable IR radiation is emitted from these same hot gases, which accumulate near the muzzle exit. The radiation from this volume is called *primary flash*. A gaseous

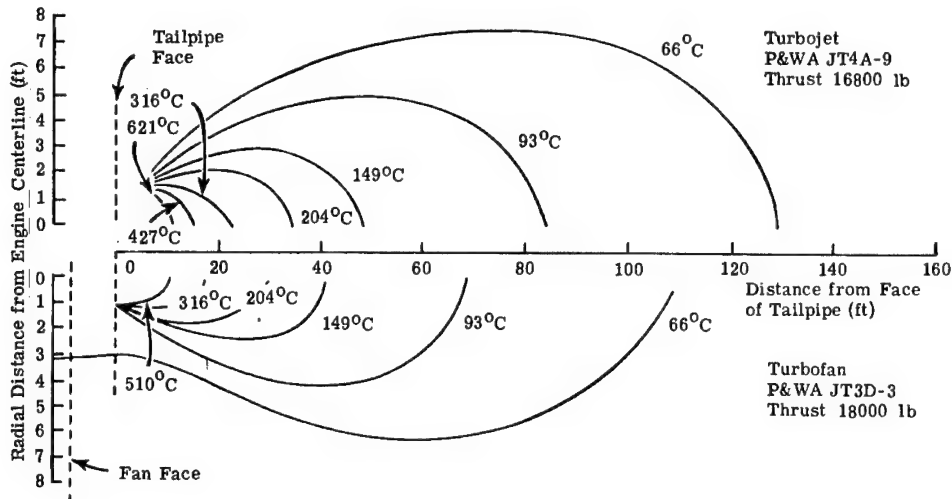


Fig. 2.68 Exhaust temperature contours for the turbojet and turbofan engines used on the Boeing 707.³⁹

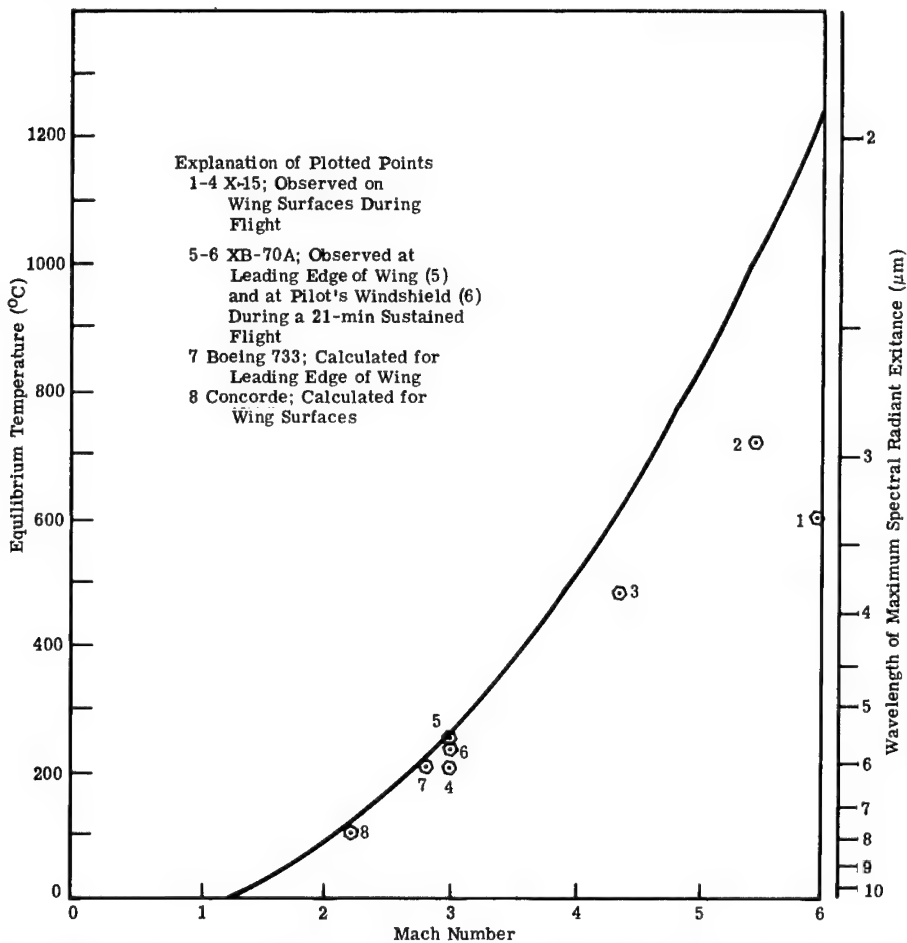


Fig. 2.69 Equilibrium surface temperature caused by aerodynamic heating (for altitudes above 37,000 ft and laminar flow).³⁹

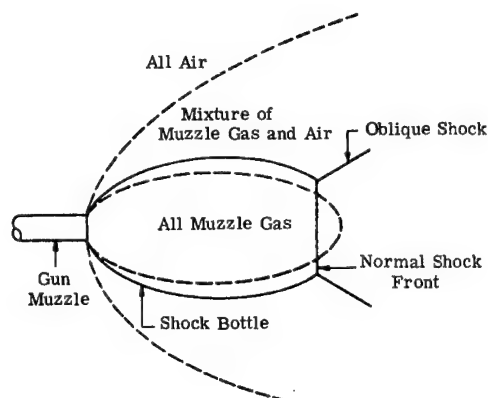


Fig. 2.70 Flow pattern at a gun muzzle (dashed lines indicate composition boundaries).⁴⁰
(By permission of Headquarters, U.S. Army Material Development and Readiness Command.)

flow pattern, shown schematically in Fig. 2.70, is set up in front of the gun. As the gases flow through the normal shock, they are heated and radiate in what is called the *intermediate flash*. On mixing with the atmosphere, the hot gases ignite and burn with a large luminous flame, giving rise to what is known as *secondary flash*.

To suppress the secondary flash, which emits large quantities of radiation, the gun is often fitted with a device attached to the muzzle that thwarts the formation of a shock wave. In other cases, suppressants are added chemically to the propellant to prevent ignition of the muzzle combustible gases. Reference 40 describes muzzle flash in all its aspects for a range of weapon types and sizes. A well-controlled experiment on a special .50-caliber test gun (with a 20-mm chamber) was made by the Franklin Institute to obtain spectra in the UV, visible, and IR regions. Results showed that a rather weak UV spectrum of secondary radiation developed, yielding a continuum on which was superimposed strong lines of atomic potassium (4044 to 4047 Å), medium-strength lines of atomic copper (3248 to 3274 Å), strong bands of CuCl (4300 to 4900 Å), relatively strong bands of CuH (4005 and 4280 Å), weak OH bands (2811 and 3064 Å), and very weak NH bands (3360 and 3370 Å).

In the visible region of the spectrum, the intermediate (suppressed) flash consists of a continuum with a superposition of radiation of Na (5890 Å) and CuOH (6230 Å). Incandescent solids contribute to the continuum. Copper compounds are also present, although when the copper-jacketed projectiles are replaced by steel projectiles with steel rotating bands, the radiation from the copper compounds disappears.

Infrared radiation is copious in muzzle flash and IR radiation from large-caliber weapons has been measured. The relative spectral intensity of the secondary flash from a 155-mm artillery weapon at different observation distances is reported in Ref. 40. The barrel of the gun was 40 calibers long and the projectile was a dummy HE (M101) weighing 95 lb. The muzzle velocity was 2100 ft s^{-1} . A relative spectrum for a 200-ft observation distance is shown in Fig. 2.71.

Time records of the relative radiant intensity from a 280-mm gun are given in Fig. 2.72. These are given, however, only as specially chosen, representative

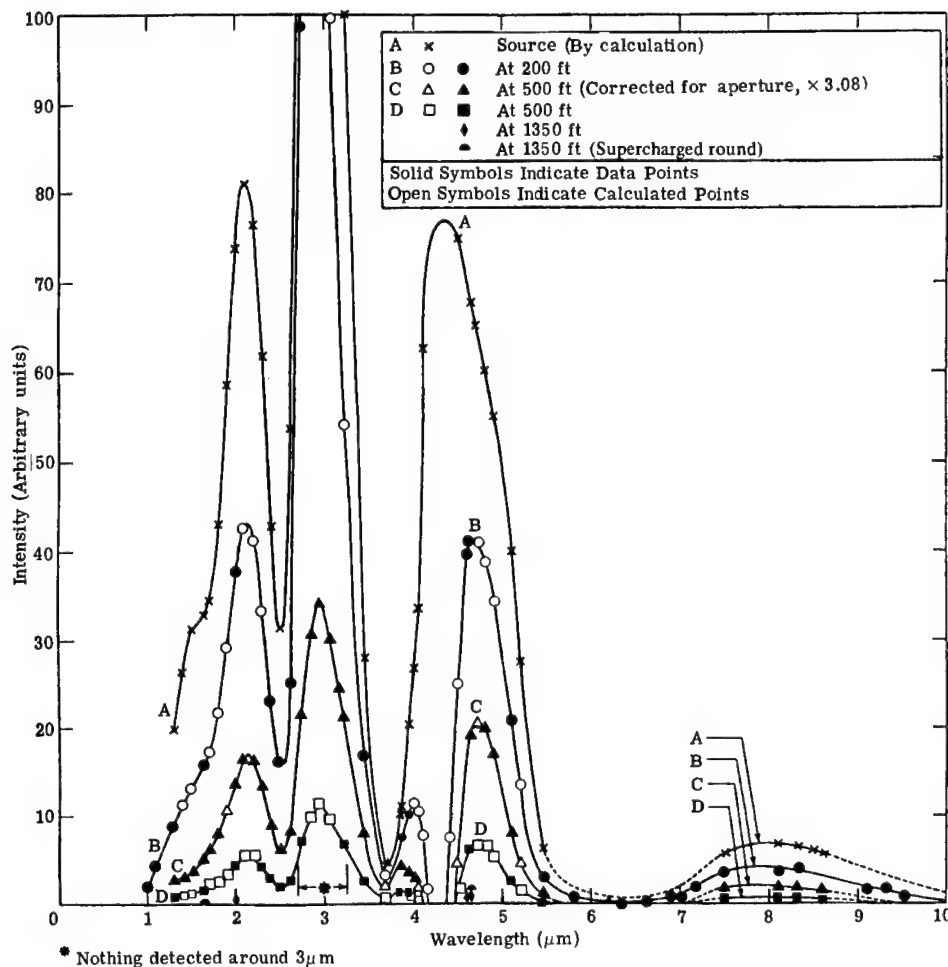


Fig. 2.71 Variation of spectral distribution of radiation from secondary flash with distance from the gun. The weapon is a 155-mm M2 artillery gun.⁴⁰ (By permission of Headquarters, U.S. Army Material Development and Readiness Command.)

examples. In observing other records, given, for example, in Ref. 40, huge variations in the time histories are evident, depending on a large number of factors including gun size, propellant type and charge, firing history of the gun, etc. These factors often determine whether or not secondary flash will occur, causing multiple peaks in the time record.

2.4.4 Further Samples of Target Radiation¹

A reasonably large collection of data exists for various targets, unfortunately the data are not easily obtainable or reproducible in the open literature. One prolific source of data is the division of General Dynamics now known as the Air Defense Systems Division (formerly the Valley Systems Division). An

¹The author wishes to acknowledge the kindness and help of Dennis Blay of General Dynamics in providing him with this material. Slight modifications have been made in the material sent by Mr. Blay to make it fit our format.

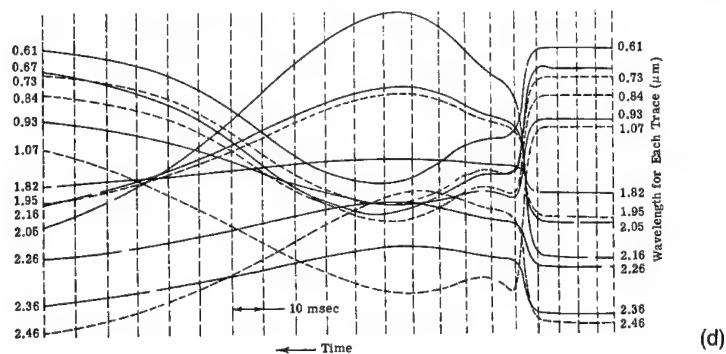
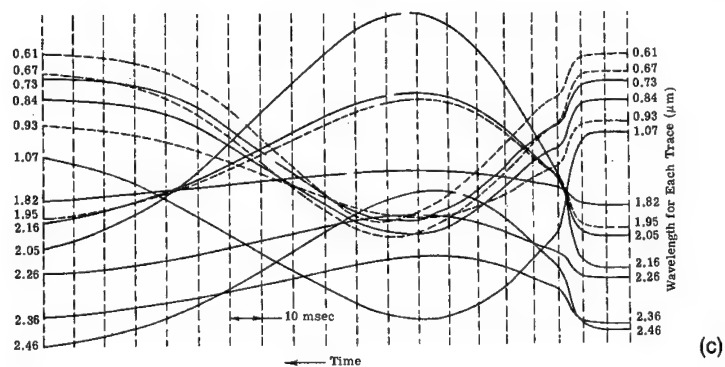
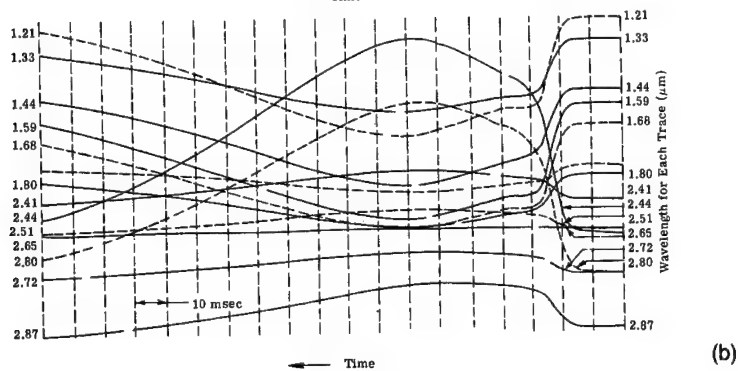
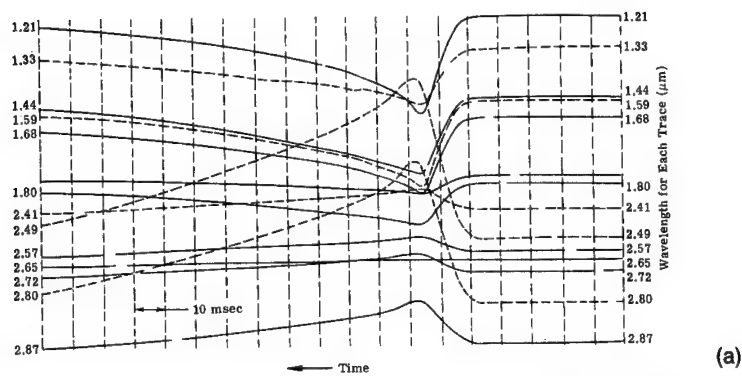


Fig. 2.72 Spectrograms of flash from 280-mm gun. Both solid and dotted curves are used for clarity. Positive deflection is downward for traces having wavelengths between 1.21 and 1.80 μm : (a) round 39, record 1689; (b) round 95, record 1759; (c) round 40, record 1690, and (d) round 92, record 1756. (By permission of Headquarters, U.S. Army Material Development and Readiness Command.)

example of their data format for measurement and general reporting of data of this type is given in Fig. 2.73 showing a visual photograph of the target and a thermal image. Also shown are the spectra of the target in background, and of background alone, from which can be obtained the spectrum of the target-background contrast.

The display of target data in Figs. 2.73 through 2.84 is made purposely qualitative to avoid any issues of sensitivity. Furthermore, these can only be strictly representative of the particular results for the situations defining a given measurement program. It is impossible, therefore, to classify generally a given target in terms of any particular measurement, given the numerous factors that cause the results of different measurements to differ, sometimes

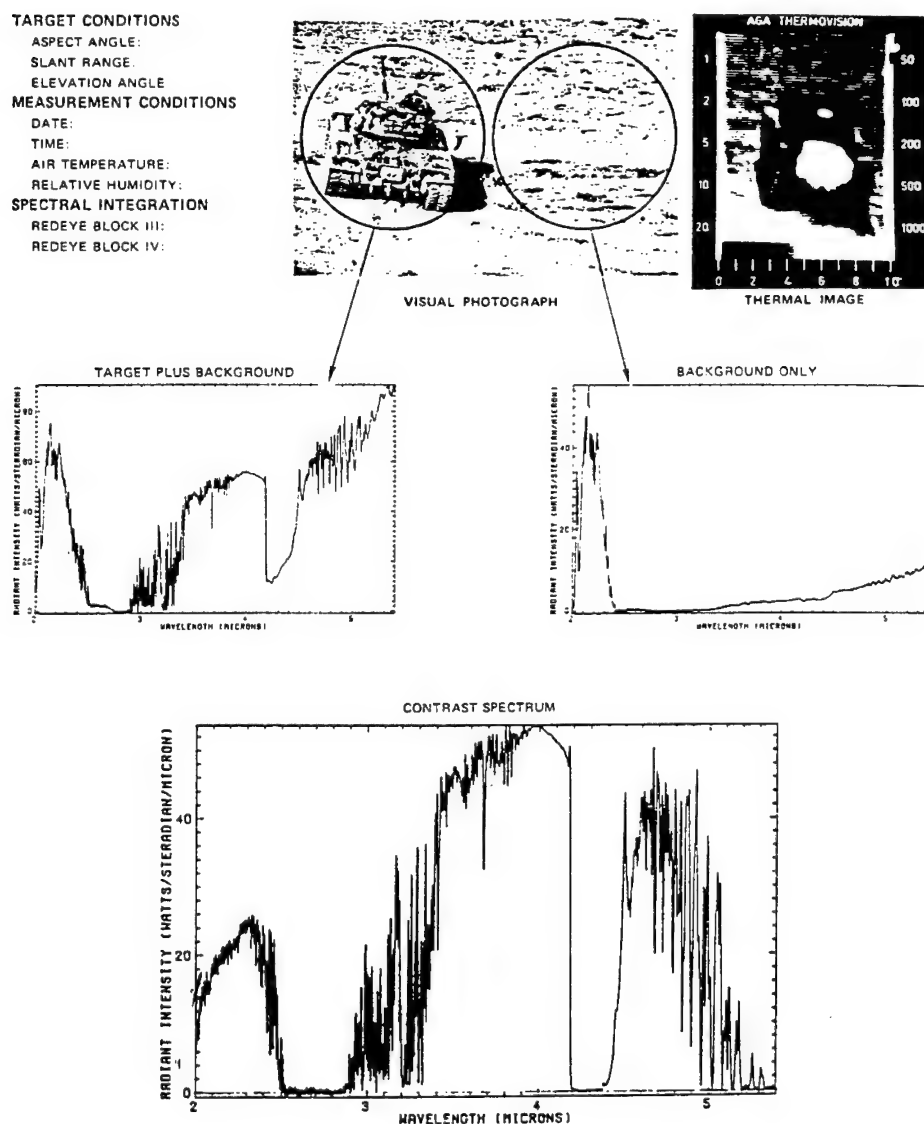


Fig. 2.73 Data format example, basic signature data.

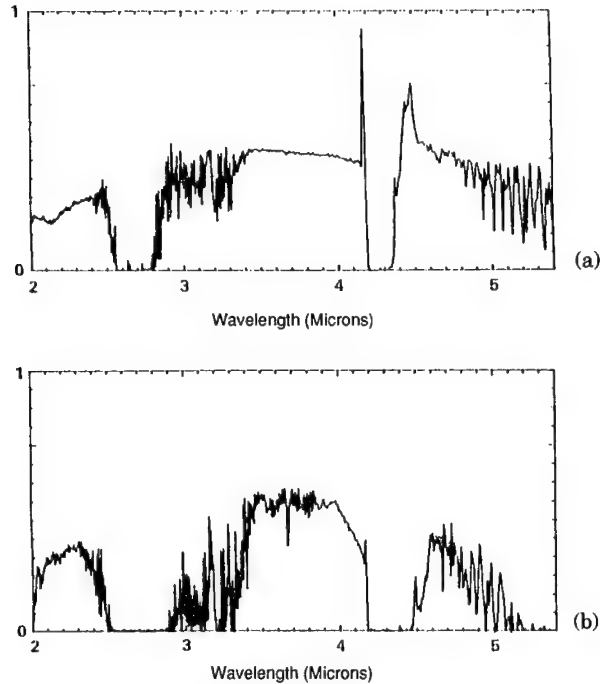


Fig. 2.74 Effects of atmospheric attenuation on turbojet aircraft signatures (150-deg aspect, military power): (a) 300 m and (b) 5000 m.

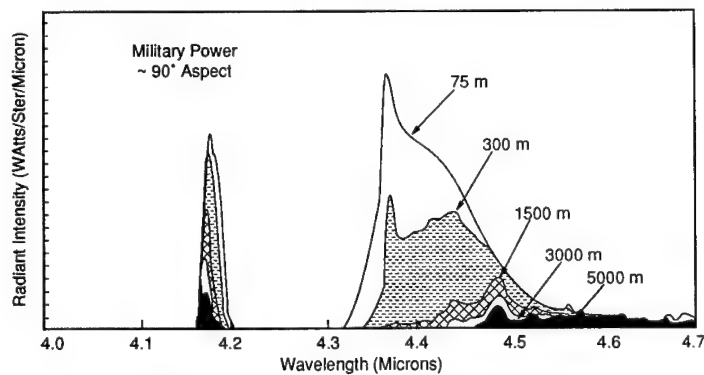


Fig. 2.75 Atmospheric attenuation effects.

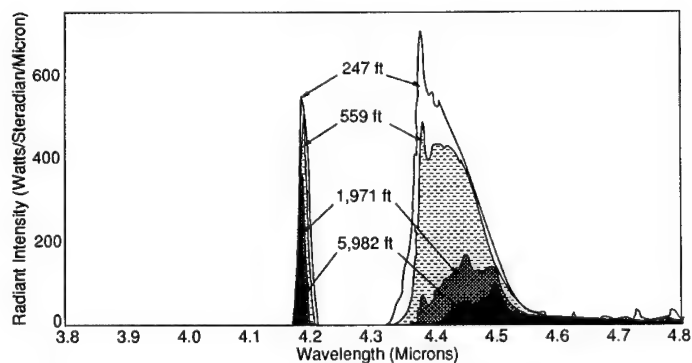


Fig. 2.76 Spectral emission of a jet exhaust plume as transmitted through four atmospheric path lengths (temperature: 71°F, humidity: 18%, H₂O concentration: 0.35 cm/km, altitude: 2160 ft, date: 3-29-71).

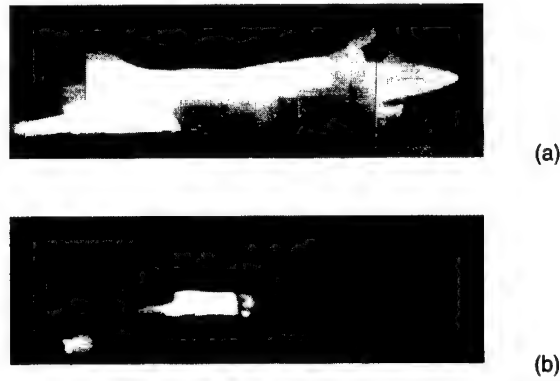


Fig. 2.77 LWIR thermal images of an A-4A aircraft at 100% throttle setting with thermovision atten. of (a) 5 and (b) 10.

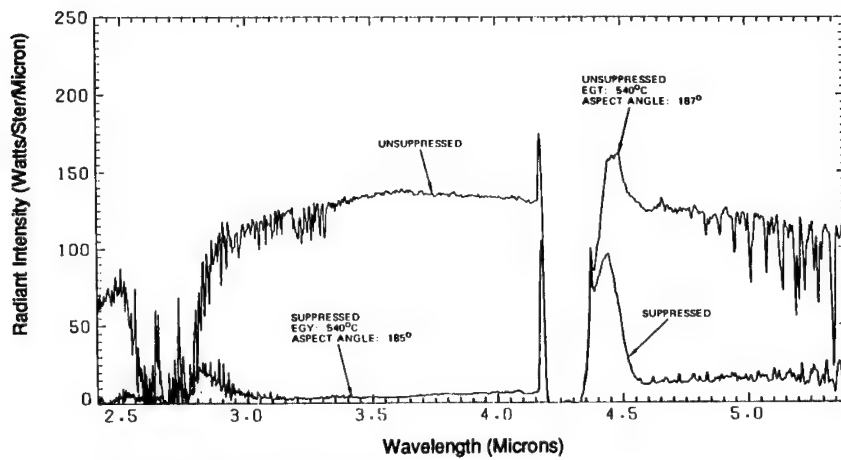


Fig. 2.78 Comparison of suppressed and unsuppressed helicopter.

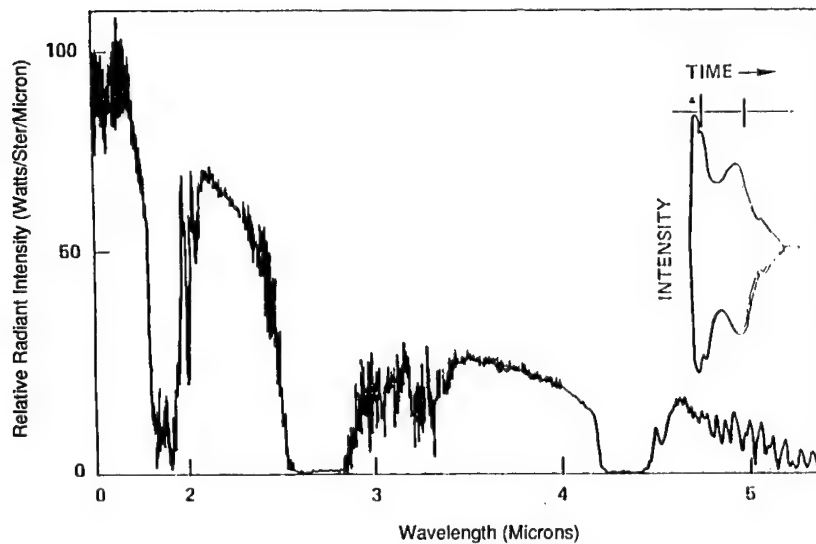


Fig. 2.79 Typical flare spectral radiant intensity.

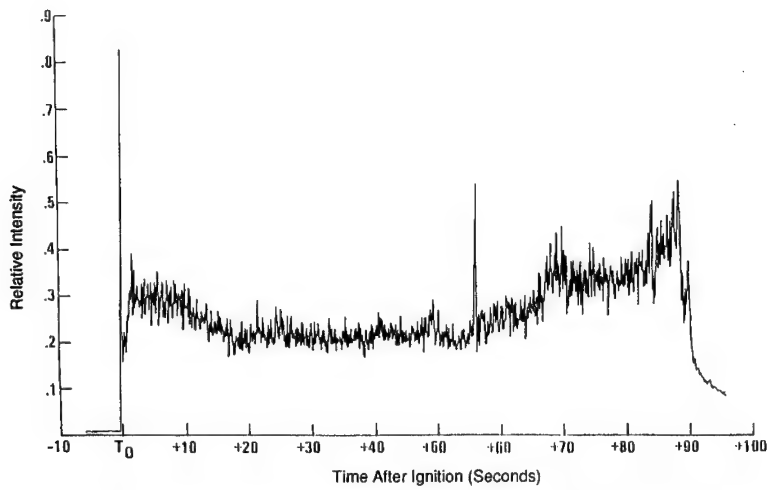


Fig. 2.80 Temporal characteristics of the M49-A1 flare, 3.5- to 5.0- μ m band.

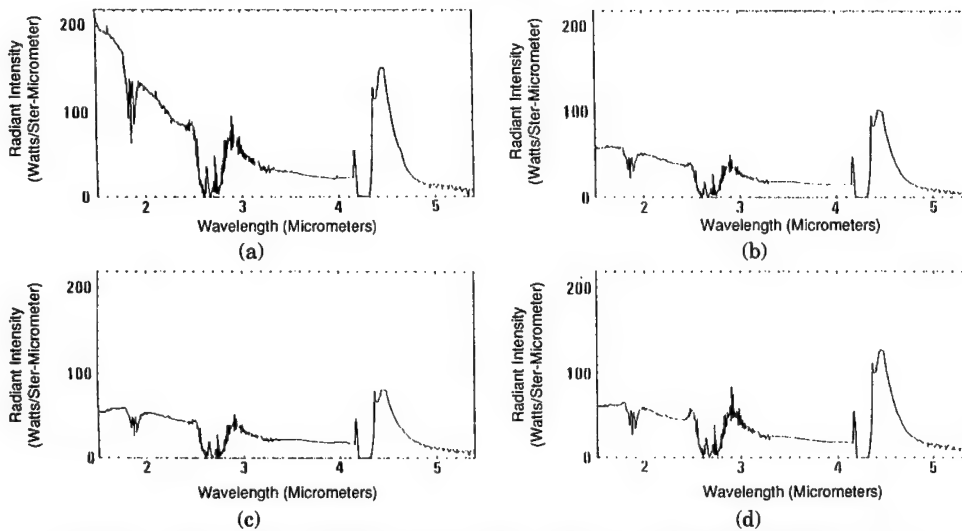


Fig. 2.81 M49-A1 static measurements (range=200 ft) in seconds after ignition: (a) 2.8 s, (b) 21.8 s, (c) 43.8 s, and (d) 62.8 s.

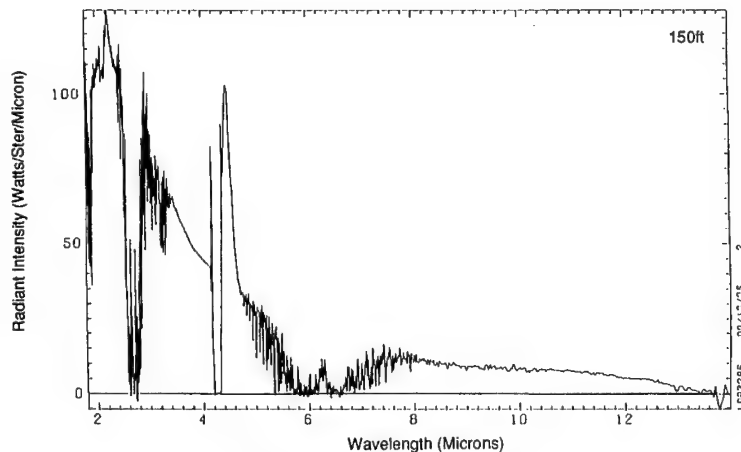


Fig. 2.82 PFS-201 napalm fire.

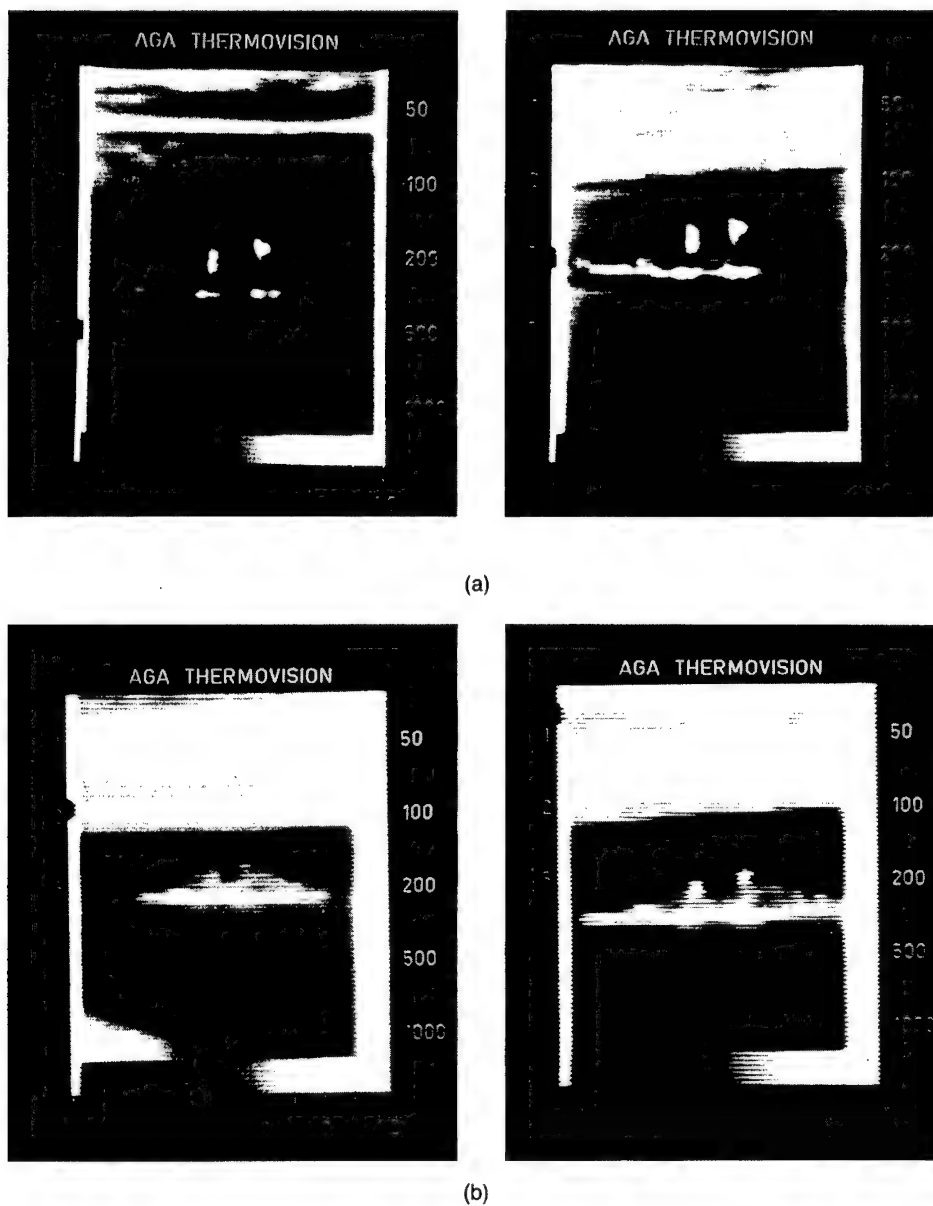


Fig. 2.83 Thermal images of naval vessels: (a) short-wavelength IR (SWIR) and (b) long-wavelength IR (LWIR).

considerably, from one another. However, one can obtain an idea of what features to look for in differentiating between targets and backgrounds—and, of course, between different kinds of targets—from both a spectral and a spatial point of view. Given sufficient understanding of the processes that contribute to target emission, one can also guesstimate temporal differences within a given target class.

The description of each event is given in the caption of each figure. No attempt is made to qualify or quantify the results. The terms “relative” and

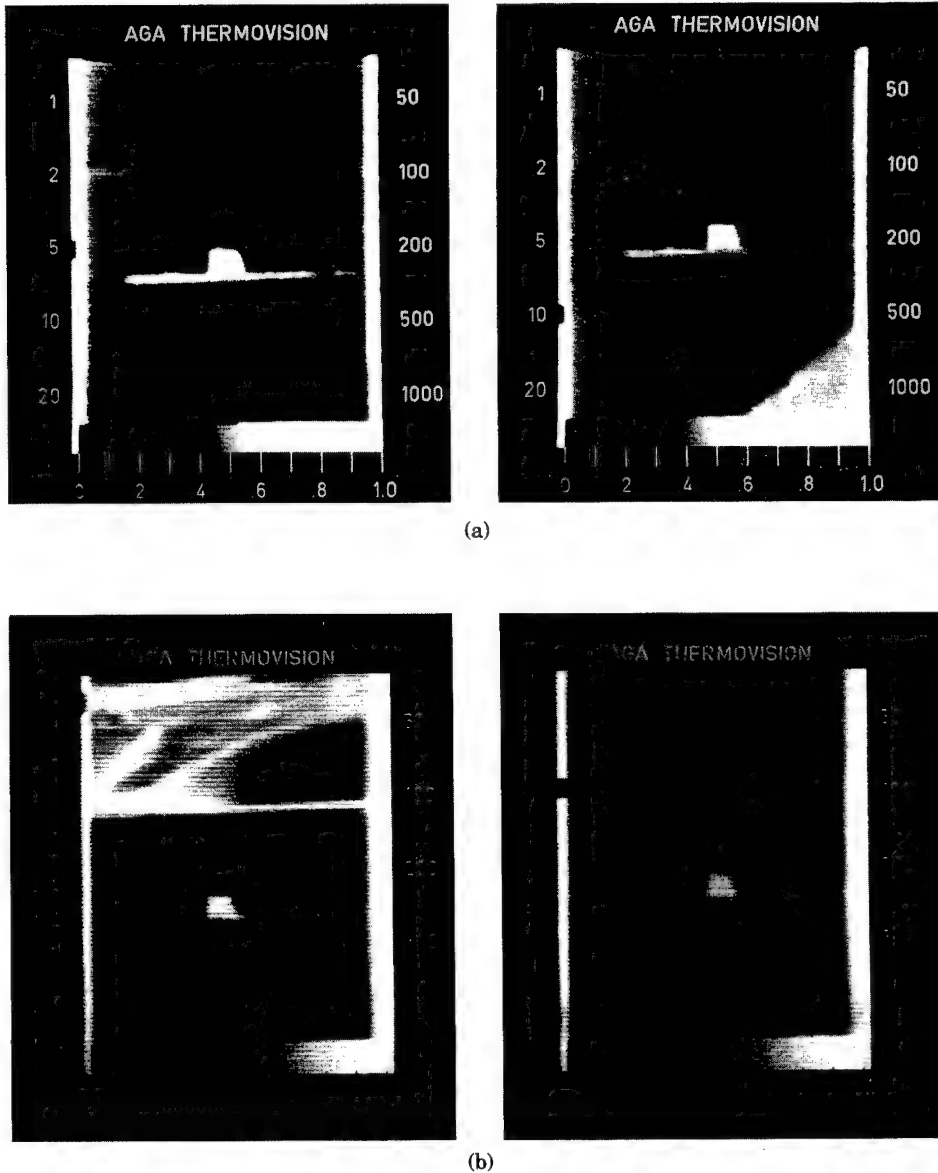


Fig. 2.84 Thermal images of naval vessels: (a) short-wavelength IR (SWIR) and (b) long-wavelength IR (LWIR).

"typical" are used purposely in some cases to maintain circumstances as general as possible. The reader is left to his or her own resources. It should be noted, however, that most of these data result from the subtraction of the data in a field of view, which contains both the target and background surrounding the target, and one which contains only the background. The result is a target-background contrast and not an absolute target intensity. Also, of course, atmospheric effects are always present.

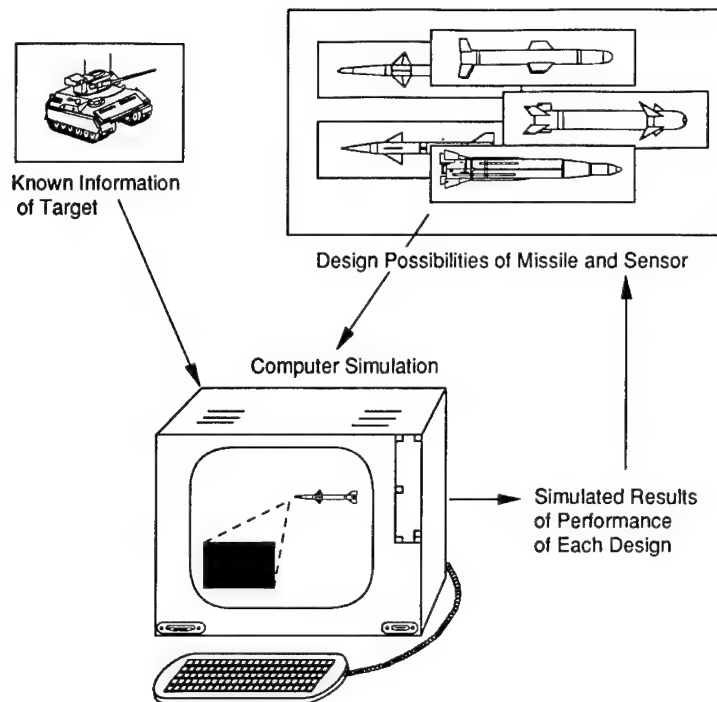


Fig. 2.85 A description of simulation used to aid in the design of a weapons sensor.

2.5 IR SIMULATION AND MODELING OVERVIEW^k

With the growing power of computers and the constant or increasing expense of field data collections, simulation of threat signatures is becoming more important as well as more feasible.

2.5.1 Rationale

Field experiments are expensive and provide limited information against the numerous possible scenarios in which a system must operate. The relatively cheaper cost of simulation can be used to provide a more thorough statistical picture of expected system performance, although confidence might be diminished somewhat in the absence of a real test. Figure 2.85 illustrates the process of using simulation in the conceptual design phase of a development program. Figure 2.86 illustrates the use of simulation in the design of a threat surrogate. Field tests become important, not only as trials of system performance in their own right, but also as validations of the IR simulation. Figure 2.87 illustrates how simulation and field trials can be used in a program of system validation.

^kThe author wishes to acknowledge the very useful contribution of Bruce Morey and Jayne Lyons of ERIM to this chapter for their writing of the section on computer modeling. The ERIM model is called SIRIM, and it has enjoyed great success in their hands.

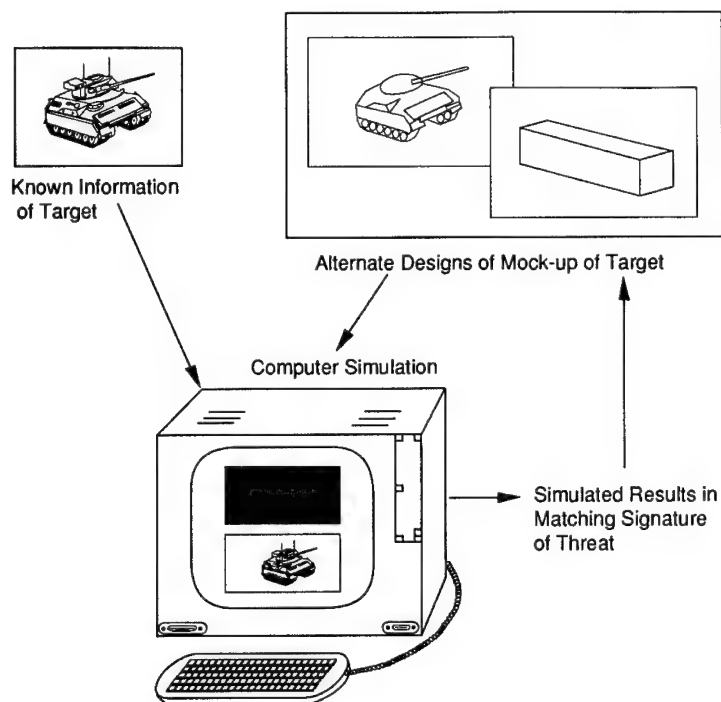


Fig. 2.86 Diagram showing use of computer simulation in designing construction of a threat surrogate.

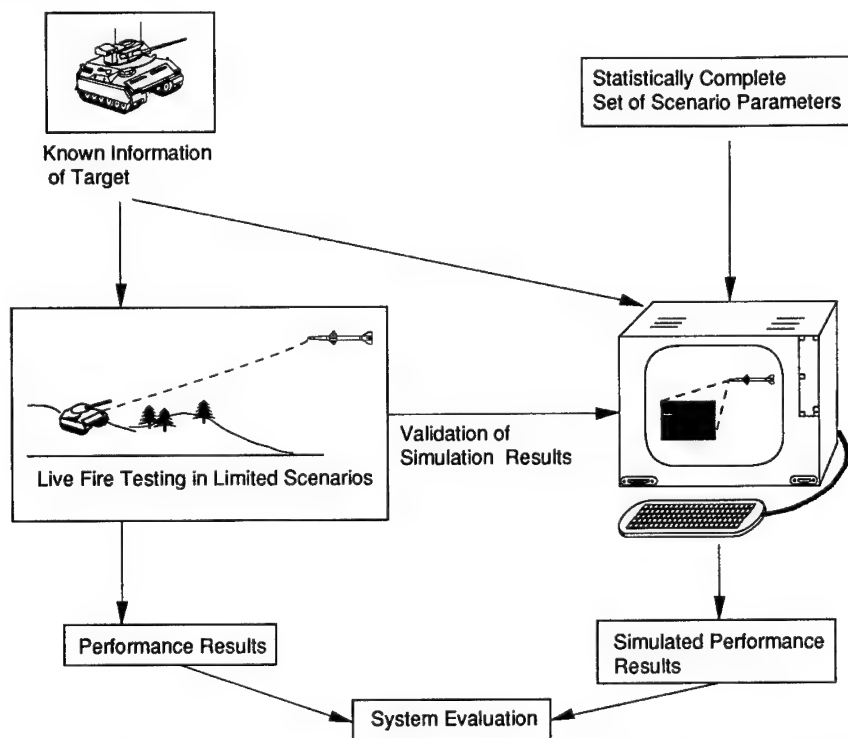


Fig. 2.87 Mutually supporting roles of simulation and field trials in a program of system evaluation and development.

2.5.2 Overview of the Simulation Process

Some of the factors that are important to consider in an IR simulation based on predicting temperatures are:

- geometry of the target/background (including internal structure)
- material properties of the target/background
- weather and environmental conditions
- operating condition of the target (engine on or off, running or stationary, etc.)
- relative health of living background material
- sensor characteristics.

Although all of these factors may seem overwhelming, they can be constructed into a process that makes proper modeling manageable. Conceptually, there are four steps required to calculate an image. They are (for a target):

1. Derive a mathematical description of the geometry of the target, based on available information.
2. Convert the geometry description into a prediction of the temperatures, given a specific scenario. Other information needed at this step includes material properties (steel, rubber, etc.), operating characteristics (size and efficiency of engine, friction of tracks, etc.), and prevailing weather conditions.
3. Convert geometry and temperatures into an IR radiance map. Source of possible reflection, as well as wavelength band, must be considered.
4. Include the effects of atmospheric and sensor degradation. Such degradation blurs the image, reduces contrast, and introduces noise that would be present in a real sensor.

Figure 2.88 shows the four conceptual steps needed to calculate a simulated IR image of a target. The process for backgrounds is similar in concept, although different in the details of implementation.

2.5.3 IR Image Simulation Outline Using SIRIM as an Example

Literally dozens of modeling techniques have been described in the literature (see, for example, Refs. 41 through 46), in varying degrees of sophistication, that perform the function of simulating targets, backgrounds, and sensors. The model outlined here is the one most familiar to the authors of this section and is, therefore, the one that will be discussed. A flow diagram is shown in Fig. 2.89. A pictorial description of the algorithm is shown in Fig. 2.90.

1. *Model object mathematically:* Use constructed solids geometry (other methods of object representation exist, such as facets).
2. *Convert geometry model to thermal model:* If necessary (faceted approaches do not require this step):
 - a. Identify special time-dependent boundary conditions (i.e., engine compartment, exhaust, track frictional heating).
 - b. Identify regions that are composed of thin sheets of metal for use with thin-shelled conduction model.

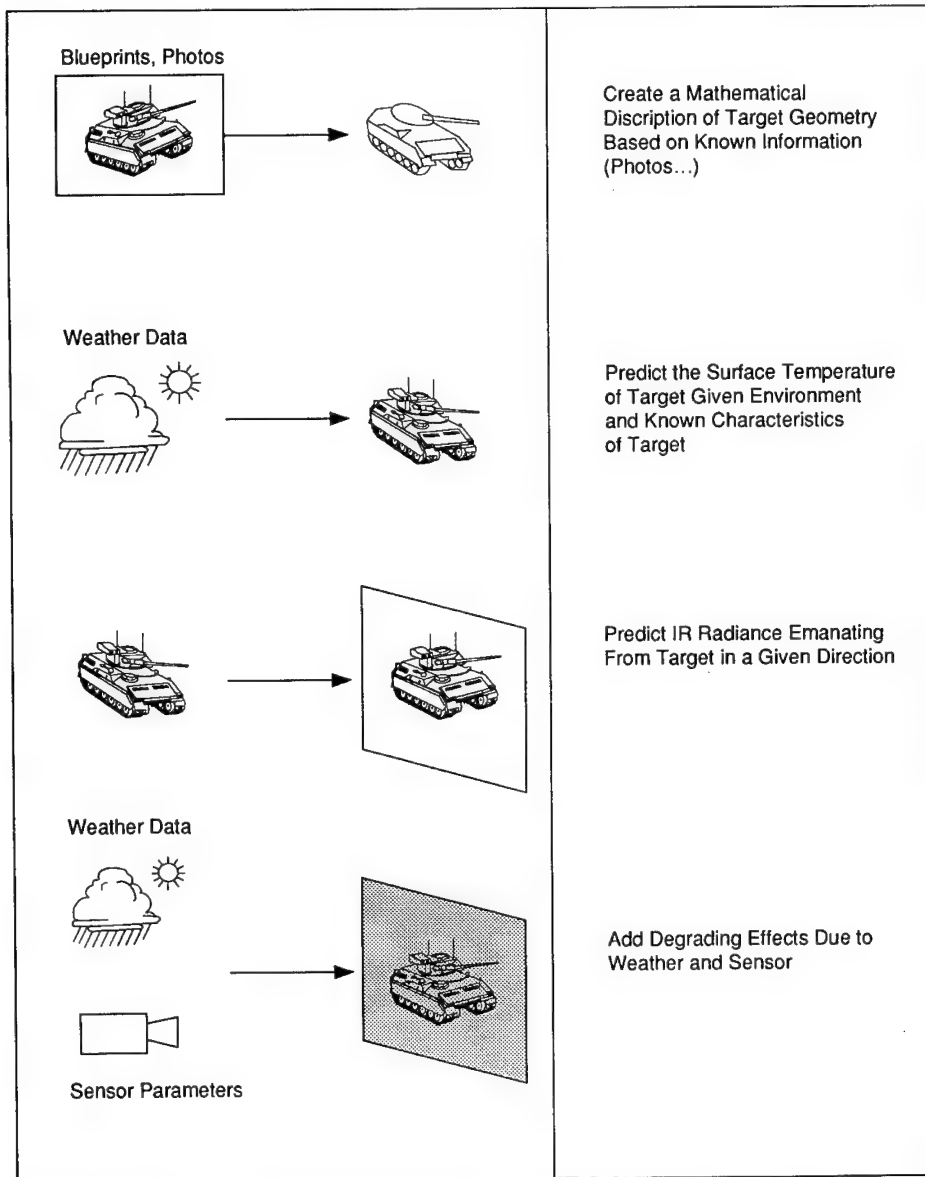


Fig. 2.88 Conceptual steps in IR image simulation.

- c. Create a finite volume mesh—using the voxel¹ approach—attaching the geometry region number, thin-shell identifier, and associated boundary condition to each voxel.

3. *Compute the temperature history of each voxel:*

- a. Identify sun intensity and position relative to the target as a function of time (voxsun).
- b. Determine which voxels have line of sight to the sun and at each time increment. Store the information for use in temperature calculations.
- c. Identify the weather inputs (air temperature, wind speed, insolation) as a function of time.
- d. Identify the surface (broadband emissivity and solar absorptivity) and bulk (density, specific heat, conductivity) material properties for the object.
- e. Initialize the temperature of the voxels.
- f. Compute heat input due to radiation and convection. Treat these inputs as boundary conditions to the surface voxels.
- g. If the voxel is thin shelled, compute the new temperature using 0-D approximation; otherwise, compute a new temperature for each voxel using 3-D conduction equation and the Gauss-Seidel iteration method—an explicit time-stepping scheme.
- h. Save surface temperatures at desired time increments.

4. *Calculate the radiance at the target:*

- a. Identify incident angle-dependent emissivity properties for the object materials.
- b. Identify background radiance information.
- c. Compute blackbody radiance by integrating Planck's equation over the desired wavelength band. Multiply the blackbody radiance by the polarized emissivities to obtain the emitted radiation at the target.
- d. Compute background irradiance from information supplied by the background radiance file.
- e. Calculate total Stoke's vector leaving the surface of the object using the Mueller matrices for the emitted and reflected energy. From the total Stoke's vector, calculate the total radiant intensity; two linearly polarized output images result. A fourth image containing the polarization content is calculated from the ratio of the square of the two polarization images added together and the total intensity image.

¹A voxel is the three-dimensional analog of the two-dimensional pixel.

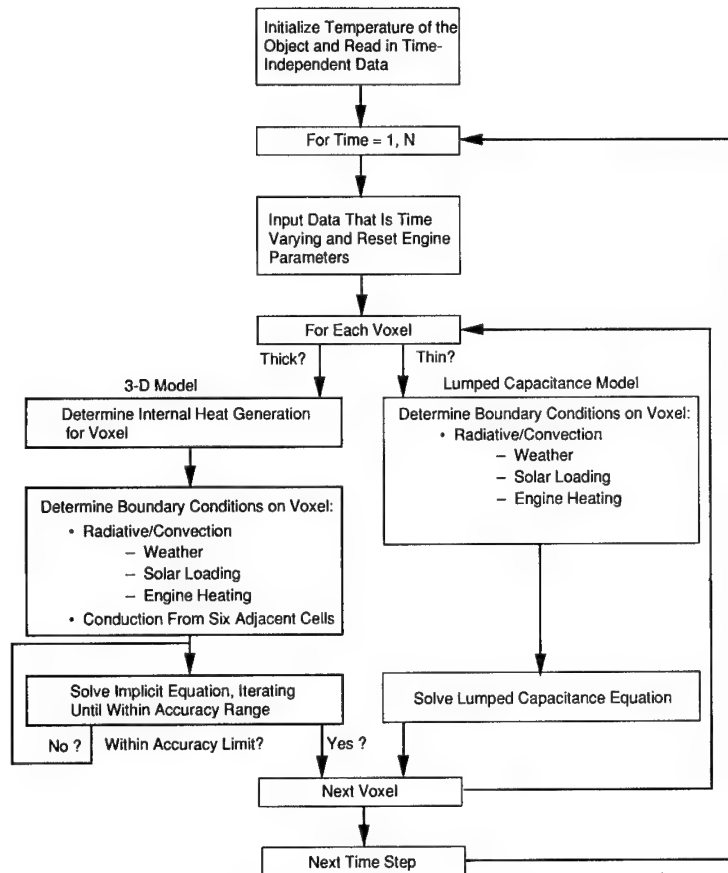


Fig. 2.89 SIRIM flow diagram.

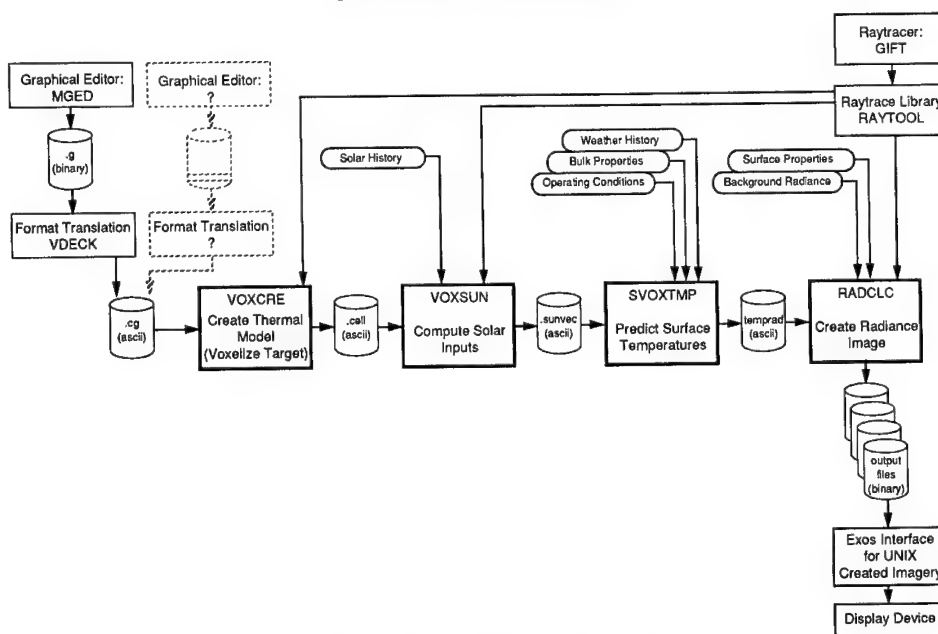


Fig. 2.90 Current SIRIM functional flow.

References

1. A. G. Worthing, "Sources of radiant energy," Chap. 2 in *Measurement of Radiant Energy*, W. E. Forsythe, Ed., McGraw-Hill, New York (1937).
2. Andre Gouffé, "Corrections d'ouverture des corps-noir artificiels compte tenu des diffusions multiples internes," *Revue d'Optique* **24**, 1 (1945).
3. J. C. DeVos, "Evaluation of the quality of a blackbody," *Physica* **20**, 669 (1954).
4. David F. Edwards, "The emissivity of a conical blackbody," 2144-105-T, The University of Michigan Engineering Research Institute, Ann Arbor, MI (1956).
5. A. Leupin et al., "Investigation, comparison, and improvement of technical infrared radiators," *Infrared Physics* **30**(3), 199-258 (1990).
6. J. W. T. Walsh, *Photometry*, 3rd ed., Dover, New York (1965).
7. K. D. Mielenz et al., "Spectroradiometric determination of the freezing temperature of gold," *Journal of Research of the National Institute of Standards and Technology* **95**(1), 49-67 (Jan.-Feb. 1990).
8. *Spectral Radiance Calibrations*, NBS Special Publication 250-1 (Jan. 1987).
9. *NIST Calibration Services Users Guide 1989*, NIST Special Publication 250.
10. Lasers and Optronics 1990 Buying Guide. Please note that, although reference is made only to the few sources from which information was derived (as in this and the succeeding reference), there are many other so-called "trade" journals that should be consulted. The best way to be aware of many of them is to access one of the on-line information services.
11. *CRC Handbook of Laser Science and Technology, Supplement 1: Lasers*, CRC Press, Boca Raton, FL (1991).
12. Photonics Directory of Optical Industries.
13. W. Y. Ramsey and J. C. Alishouse, "A comparison of infrared sources," *Infrared Physics* **8**, 143 (1968).
14. J. C. Morris, "Comments on the measurement of emittance of the Globar radiation source," *Journal of the Optical Society of America* **51**, 798 (July 1961).
15. A. H. Pfund, "The electric Welsbach lamp," *Journal of the Optical Society of America* **26**, 439 (Dec. 1936).
16. J. Strong, *Procedures in Experimental Physics*, p. 346, Prentice-Hall, New York (1938).
17. F. E. Carlson and C. N. Clark, "Light sources for optical devices," in *Applied Optics and Optical Engineering*, R. Kingslake, Ed., Vol. 1, p. 80, Academic Press, New York (1965).
18. Osram GMBH, "Lamps for scientific purposes," München, West Germany (1966). See also the later Osram brochure, "Light for cine projection, technology, and science" (circa 1987).
19. F. J. Studer and R. F. Van Beers, "Modification of spectrum of tungsten filament quartz-iodine lamps due to iodine vapor," *Journal of the Optical Society of America* **54**(7), 945 (July 1964).
20. L. R. Koller, *Ultraviolet Radiation*, 2nd ed., John Wiley & Sons, New York (1965).
21. M. R. Null and W. W. Lozier, "Carbon arc as a radiation standard," *Journal of the Optical Society of America* **52**(10), 1156-1162 (Oct. 1962).
22. A. J. LaRocca, "Artificial sources," Chap. 2 in *The Infrared Handbook*, W. L. Wolfe, G. J. Zissis, Eds., Environmental Research Institute of Michigan, Ann Arbor, MI (Revised 1985).
23. J. E. Kaufman, Ed., *IES Lighting Handbook*, 5th ed., Illuminating Engineering Society, New York (1972).
24. E. B. Noel, "Radiation from high pressure mercury arcs," *Illuminating Engineering* **36**, 243 (1941).
25. Bulletin TP-109R, General Electric, Cleveland, OH (1975).
26. Catalog No. 108-6-72-3M, Illumination Industries, Sunnyvale, CA (1972).
27. M. W. P. Cann, "Light sources for remote sensing systems," NASA-CR-854, National Aeronautics and Space Administration (Aug. 1967).
28. Varian Associates, Palo Alto, CA (1969).
29. "Special catalog to spectrophotometer users," Fisher Scientific, Pittsburgh, PA (1972).
30. E. F. Worden, R. G. Gutmacher, and J. F. Conway, "Use of electrodeless discharge lamps in the analysis of atomic spectra," *Applied Optics* **2**(7), 707-713 (July 1963).
31. W. F. Meggers and F. O. Westfall, "Lamps and wavelengths of mercury 198," *NBS Journal of Research* **44**, 447-455 (1950).

32. W. F. Meggers, "Present experimental status of rare earth spectra," *Journal of the Optical Society of America* **50**, 405 (1960).
33. "Ealing catalog, Optical Components Section, 1976-1977," Ealing Corporation, South Natick, MA; see also "Optical services supplement, No. 1, 1969-1970," p. 26; see also "Ealing Electro-optics product guide" (circa 1990).
34. "Cenco scientific educational catalog, Physics-Light Section," p. 602, Central Scientific, Chicago, IL (1975).
35. "Special purpose lamps," TR-29R, GTE Sylvania, Lighting Products Group, Danvers, MA (May 1966).
36. "Optical radiation: measurement and analysis capability," General Dynamics, Applied Research Laboratories, Electro Dynamics Division, Pomona, CA (1975).
37. P. Deitz et al., "Synthesized CAD methods for combat vehicle survivability analysis," in *Combat Vehicle Survivability Proceedings*, March 26-29, 1990, Vol. II, pp. 203-231, U.S. Army Tank Automotive Command, Warren, MI. The distribution of this unclassified paper is limited.
38. Dennis Blay, General Dynamics (now the Air Defense Systems Division), Pomona, CA, private communication (1977).
39. R. D. Hudson, *Infrared System Engineering*, Chap. 2, John Wiley & Sons, New York (1969).
40. S. P. Carfagno, "Spectral characteristics of muzzle flash," in *Engineering Design Handbook*, AMCP-706-255, Headquarters, U.S. Army Materiel Command, Alexandria, VA (June 1967). Available through NTIS, AD-818 532/PDM.
41. J. Jones and T. Gonda, "A thermal model preprocessor for graphics and material database generation," *Proceedings of the SPIE* **1098**, 42-54 (1989).
42. S. P. Sullivan and W. R. Reynolds, "Validation of the physically reasonable infrared signature model (PRISM)," *Proceedings of the SPIE* **890**, 104-110 (1988).
43. W. R. Owens, "Data-base methodology for infrared signature projection," *Proceedings of the SPIE* **636**, 96-99 (1986).
44. A. D. Sheffer and F. L. Thompson, "Simulation of laser radar imagery," *Proceedings of the SPIE* **636**, 92-95 (1986).
45. A. M. Millman, "An application of computer graphics to combat vehicle design," in *25th Midwest Symposium on Circuits and Systems*, pp. 211-216.
46. J. Hinderer, "Model for generating synthetic three-dimensional (3D) images of small vehicles," *Proceedings of the SPIE* **302**, 8-13 (1981).

CHAPTER 3

Natural Sources

David Kryskowski

Gwynn H. Suits

Environmental Research Institute of Michigan

Ann Arbor, Michigan

CONTENTS

3.1	Introduction	139
3.1.1	Idealized Sources	139
3.1.2	Alternate Source Specifiers	139
3.2	Radiative Transfer Modeling	140
3.2.1	Plane Mixtures Model	140
3.2.2	Plane Stacking Reflectance Model	141
3.2.3	The Concepts of Surface and Bulk Reflectance	142
3.2.4	The Wet-Dry Plane Stacking Model	144
3.2.5	Vegetative Canopy Models	145
3.2.6	Thermal Modeling	145
3.3	The Sun	151
3.3.1	Exoatmospheric Solar Radiation	151
3.3.2	Terrestrial Solar Radiation	151
3.4	The Moon	157
3.5	The Celestial Background	160
3.5.1	Coordinates on the Celestial Sphere	160
3.5.2	Cosmic Microwave Background	165
3.5.3	Celestial Background in the Visible Range	165
3.5.4	Celestial Background in the Spectral Range from 2.0 to 100.0 μm	175
3.6	The Sky	194
3.6.1	Scattered Solar Radiation	194
3.6.2	Thermal Radiation	199
3.6.3	Particulate Statistics	199
3.6.4	Aurora	200
3.6.5	Night Airglow	204
3.6.6	Meteoroid Radiation	210

3.7	The Earth	210
3.7.1	High-Altitude and Space Views	210
3.7.2	Albedo	213
3.7.3	Emission from the Surface	214
3.7.4	Cloud Meteorology	219
3.8	Properties of Natural Materials	230
3.8.1	Soils, Rocks, and Minerals	230
3.8.2	Construction Materials	233
3.8.3	Water	245
3.8.4	Snow and Ice	267
3.8.5	Biological Materials	277
3.9	Statistical Measures of Infrared Backgrounds	285
3.9.1	Probabilistic Description	285
3.9.2	Correlation Function Representation	287
3.9.3	Power Spectra Representation	297
3.9.4	Nonisotropic Correlation Functions	298
3.9.5	Statistics of Various Terrain Backgrounds	299
	References	309

3.1 INTRODUCTION

Natural sources constitute a large and diverse class of radiators including terrestrial, atmospheric, and extraterrestrial materials. Some materials that occur often in terrestrial environments are human artifacts—such as road materials, paints, oil slicks, and construction materials. These common environmental materials are included as “natural” sources. Natural sources are not only emitters of radiation but are also sources of reflected radiation.

3.1.1 Idealized Sources

Idealized sources are often used to approximate natural sources. An *isotropic point source* is a source with an intensity that is the same in all directions and the physical dimensions are immaterial in the conditions under consideration. The sun is usually considered to be an isotropic point source when it is the environmental illuminant, but must be considered a large sphere if it is to be imaged with optics. The *Lambertian source* is a plane source with radiance that is the same in all directions. This source is also called the *ideal diffuse source*. The radiance is related to the exitance by the simple relation $L_\lambda = M_\lambda/\pi$. New fallen snow is very nearly Lambertian. The *ideal specular* or *mirror surface* reflects radiation in such directions as to appear to originate from an image of the source located behind the specular surface. The radiance of the image source is related to the object source by the simple relation $L_\lambda(\text{image}) = \rho(\lambda)L_\lambda(\text{object})$, where the reflectance $\rho(\lambda)$ is derived from Fresnel's law. A ripple-free surface of standing water is the most common example of a specular surface. Natural sources are usually diffuse but only approximate a Lambertian source at illumination and viewing angles well above grazing. Natural sources are usually assumed to be Lambertian for ballpark calculations.

3.1.2 Alternate Source Specifiers

The emission from natural sources may be expressed in terms other than radiant intensity (for distant point sources) or radiance for extended sources. Some commonly used alternatives are apparent temperature, color or distribution temperature, and magnitude.

Apparent Temperature. The *apparent temperature* of an extended source is the temperature of a blackbody surface that will yield the same signal as the natural source when the blackbody is placed at the receiver aperture. The source temperature may differ from the apparent temperature if the emissivity is less than one, if there is attenuation between the source and the receiver, if the source temperature is not uniform, or if some radiation is reflected from another source. The common term used in radio astronomy for apparent temperature is *brightness temperature*.

Distribution or Color Temperature. The *distribution* or *color temperature* is the blackbody temperature for which the spectral exitance $M_\lambda(\lambda, T)$ is spectrally a best fit, except for magnitude, to the spectral irradiance $E_\lambda(\lambda)$ at the receiver aperture in some spectral range of interest. If the color temperature of a source is known and the spectral irradiance at any one wavelength is measured, then the remaining source spectrum may be estimated using Planck's formula.

Magnitude. The *magnitude* of an astronomical object is a relative measure of source intensity based on the irradiance produced by the source at the earth. A source of visual magnitude +1 is defined as a source that produces an illuminance of $0.832 \times 10^{-10} \text{ lm/cm}^2$ outside the earth's atmosphere. In keeping with historical tradition, the magnitude scale was adjusted in an attempt to match old visual observations where fainter stars were ranked in cardinal order with the first magnitude as bright, the second magnitude as less bright, and the sixth magnitude being assigned to stars at the threshold of night vision. The scale of magnitudes is proportional to the logarithm of the illuminance. Additional details are given in the sections on celestial backgrounds.

3.2 RADIATIVE TRANSFER MODELING

Natural sources of radiation are almost always composites of a number of constituents of common materials in a variety of spatial arrangements. Consequently, no handbook can contain data covering all of the properties of these composites. The alternative is to use the known laws of radiative transfer to calculate the radiative properties of composites of interest by using the properties of their constituents. The constituents are geometrically arranged in some idealized fashion in order to resemble the composite. Such an arrangement is called a *model*. The following simple models may be used to extend the limited amount of data available to estimate the radiative properties of composites using known radiative properties of the constituents.

3.2.1 Plane Mixtures Model

The *plane mixtures model* is very simple and is the most commonly used model. When a distant radiometer images a plane section of terrain delimited by the radiometer entrance window or instantaneous field of view (IFOV), this area is sometimes called a *pixel* (picture element). If the plane section contains only one type of known constituent, it is called a *pure pixel*; otherwise, it is called a *mixed pixel*. In a mixed pixel, the radiometer will respond to an average radiance equal to the area-weighted average of the radiances of each constituent within that pixel. Thus, a knowledge of the constituent radiances and their corresponding fractional coverage areas in the pixel will be sufficient to specify the pixel radiance.

By means of the plane mixtures model, one can predict that the signal received by a scanning radiometer will be the area weighted average of the signals that would have been received from each pixel constituent separately.

An example of a plane mixtures model is a composite of two types of plane sources, type A and type B, covering a plane surface without overlap (Fig. 3.1). The spectral radiance of the composite plane section C is the area-weighted average of the spectral radiance of A and B. Thus,

$$L_{\lambda}(C) = fL_{\lambda}(A) + (1 - f)L_{\lambda}(B) , \quad (3.1)$$

where f is the fraction of the section covered by type A sources. The extension to any number of types of sources is straightforward. If the spectral radiance of the sources is due to reflectance under uniform illumination, then the re-

flectance of the composite will be the area-weighted average of the reflectances of the constituents.

Some inaccuracy in the plane mixtures model may occur when the pixel under observation is surrounded by adjacent pixels having a high value of radiance. Atmospheric particulates may allow some adjacent pixel radiation to scatter into the line of sight of the radiometer and be counted as radiation from the pixel under observation.

It may be possible in some applications to find a spectral band where the radiance of most natural background material is low and the material of interest (the target) has a high value of radiance. Even though the pixel size of the scanning radiometer may be quite large, the radiance difference between a pure background pixel and a mixed pixel containing only a small area of target can still be detected. Two common examples are the detection of small smoldering camp fires against natural terrain using the 3- to 5- μm band and the detection of narrow roads surrounded by vegetation using the 0.6- to 0.7- μm band.

3.2.2 Plane Stacking Reflectance Model

The *plane stacking reflectance model* is applicable when two plane sections of constituent materials *A* and *B* are stacked with *A* on top of *B*. One may estimate the reflectance of composite stack *C* if the transmittance and reflectance of the constituents are known. The contact of *A* with *B* is assumed to be nonwetting, i.e., not an optical contact; and the particular mode of propagation, specular or diffuse, through the stack is assumed to be immaterial. A typical stack might be a leaf, *A*, lying on a concrete sidewalk, *B*.

The reflectance of stack *C* is calculated using the following simultaneous equations as illustrated in Fig. 3.2:

$$M(\text{ref}) = E(\text{on}) \rho(A, t) + E(\text{up}) \tau(A) , \quad (3.2)$$

$$E(\text{down}) = E(\text{on}) \tau(A) + E(\text{up}) \rho(A, b) , \quad (3.3)$$

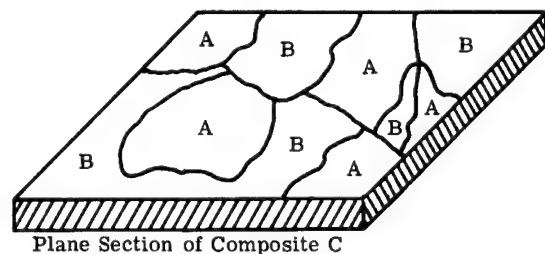


Fig. 3.1 Plane mixture of type *A* and *B* materials comprising a composite plane section.

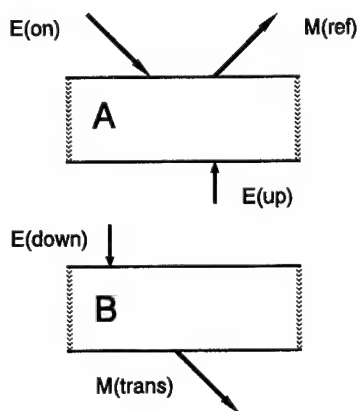


Fig. 3.2 Plane stacking model geometry. Incident radiation is on panel *A*.

$$E(\text{up}) = E(\text{down}) \rho(B, t) , \quad (3.4)$$

$$M(\text{trans}) = E(\text{down}) \tau(B) , \quad (3.5)$$

where

- $M(\text{ref})$ = reflected exitance from the top of the stack
- $E(\text{down})$ = downward-welling irradiance between constituents
- $E(\text{up})$ = upward-welling irradiance between constituents
- $M(\text{trans})$ = transmitted exitance from the stack
- $\rho(A, t)$ = reflectance of the top of A material
- $\rho(A, b)$ = reflectance of the bottom of A material
- $\rho(B, t)$ = reflectance of the top of B material
- $\tau(A)$ = transmittance of A material
- $\tau(B)$ = transmittance of B material.

The reflectance of stack C is $\rho(C) = M(\text{ref})/E(\text{on})$ and the transmittance is $\tau(C) = M(\text{trans})/E(\text{on})$. Thus,

$$\rho(C) = \rho(A, t) - \frac{\tau(A)^2 \rho(B, t)}{1 - \rho(A, b) \rho(B, t)} , \quad (3.6)$$

$$\tau(C) = \frac{\tau(A) \tau(B)}{1 - \rho(A, b) \rho(B, t)} . \quad (3.7)$$

A top and a bottom reflectance must be specified for each material since some materials, a leaf, for example, will often have a different reflectance on the dorsal side than on the ventral side. In addition, the model can be iterated. One may wish to model a stack of three materials. A stack of two is modeled first to estimate the composite values, and then this composite is considered the new B constituent of another pair with the third on top as the new A material.

Applications of the Plane Stacking Model. Occasions may arise when the diffuse transmittance and reflectance of a material is needed where the material cannot be prepared in a thin plane section—e.g., a thin layer of dry sand, dust, or new fallen snow. The material could, however, be placed on a thin, transparent piece of plastic whose reflectance and transmittance has been measured. After measuring the combined reflectance and transmittance, the values that belong to the unknown material can be calculated.

If the unknown material can be placed on two different substrates, one with high and one with low known reflectance, the combined reflectances of these two arrangements will allow one to calculate both the reflectance and transmittance of the unknown material by solving two simultaneous equations.

3.2.3 The Concepts of Surface and Bulk Reflectance

The reflectance of electromagnetic radiation by many natural materials is usually a very complicated process. One can analyze the reflection from a smooth plane interface between two homogeneous media using Maxwell's

equations and derive a rigorous formulation; however, this formulation simplifies only for two ideal materials—the perfect conductor and the perfect lossless dielectric—where total specular reflection is predicted for the conductor and specular reflection and refractive transmission are predicted for the dielectric.

Natural dielectric materials, even though approximately plane in small areas, are rarely specular, homogeneous, and lossless. A rigorous analysis would probably not be useful even if it were successful. A useful alternative is to consider the incident radiation to be divided into two parts at a surface—a part that is reflected at the surface without penetration and a part that is refracted at the surface and transmits into the body of the material.

The reflected part is assumed to be uninfluenced by the absorption of the material below the surface, but reflects only in accordance with the change in the index of refraction between the two media. The transmitted part may undergo spectrally selective absorption in the transmitted path. The fraction of incident flux reflected at the surface is called *surface reflectance*. The spectral features of surface reflectance will be limited only to those regions where the index of refraction changes noticeably with wavelength. The inhomogeneity below the surface will cause transmitted flux to scatter randomly with a portion returning through the surface. The fraction of flux exiting the surface after transmission into the material is called *bulk (or volume) reflectance*. The spectral features of bulk reflectance are those of the spectral transmittance through the underlying medium, which allows one to identify the material.

A rough surface will cause the surface reflected radiation to scatter in all directions, but more flux will scatter in the specular direction of the plane of the surface. Some amount of polarization effect will be observed on reflection in the neighborhood of the specular direction in accordance with Fresnel's law, whereas bulk reflected radiation will tend to be scattered uniformly in all directions and lose the polarization features of the incident radiation. Some Fresnel law polarization may reappear when the radiation exits the surface.

The surface reflectance will be independent of the scattering conditions below the surface, whereas the bulk reflectance may change markedly. If the separation of subsurface scattering centers is much less than the inverse of the absorption coefficient of the material, then the subsurface scattering reduces the mean free path of the radiation through the material so that it exits back through the surface without much absorption. Additionally, the bulk reflectance will increase and the spectral features will be less pronounced. On the other hand, if subsurface scattering is slight and allows a very long mean free path, very little radiation will be left to exit the surface; bulk reflectance will approach zero.

The reflectance of a natural material is the sum of these two effects. Consider a highway as you drive into the sun. The surface reflectance glare from the road dominates the visual color compared to the view of the same road as seen through the rearview mirror where bulk reflectance dominates. The glare from the road is much reduced by wearing polarizing sunglasses showing that the surface reflectance tends to be polarized horizontally as would be expected from Fresnel's law. The spectral reflectances of common materials listed in this chapter are the sums of the bulk and surface reflectances. One can expect that the interesting spectral features are due only to the bulk reflectance part.

When the incident radiation frequencies approach the resonant absorption frequencies of a uniform mineral, the index of refraction of the mineral also changes markedly while the absorption coefficient increases to a maximum. The bulk reflectance approaches zero and the surface reflectance passes through a maximum. These regions of surface reflectance maxima (and, consequently, emissivity minima) are called *reststrahlen bands*. Many reststrahlen bands due to minerals in rocks, sands, and soils can be observed in the 8- to 14- μm atmospheric window.

3.2.4 The Wet-Dry Plane Stacking Model

The *wet-dry plane stacking model* applies to a common condition occurring in nature in which a rough diffuse reflecting material is covered by a thin sheet of a smooth dielectric such as water. The contact is without airspace. The surface reflectance of the stack is the specular reflectance of the smooth dielectric and can be calculated using Fresnel's law. The bulk reflectance will be less than that of the dry substrate material alone due primarily to the multiple internal reflections between the dielectric surface and the substrate.

Radiation that penetrates the surface continues into the dielectric at an angle determined by Snell's law, is transmitted to the substrate, and is diffusely reflected. Some fraction of the reflected radiation that falls within the cone less than the critical angle is transmitted back to the surface, and it exits after some surface reflection. The fraction of diffusely reflected radiation falling outside the cone of critical angle is also transmitted back to the surface, but suffers total internal reflection and returns to the substrate to be reflected again. The reduction in bulk reflectance is due mainly to the multiple transits through the dielectric and losses due to absorptance of the substrate on each round trip.

An approximate bulk reflectance can be derived for the wet-dry plane stacking model using reasoning similar to that used for the plane stacking model, but accounting for the internal reflectance of the dielectric surface:

$$\rho(\text{wet}) = \frac{(1 - \rho')\tau^2(1 - \rho)\rho(\text{dry})}{N^2 - \rho(\text{dry})\tau^2(N^2 - 1 + \rho')} \quad (3.8)$$

where

- $\rho(\text{wet})$ = wet stack bulk reflectance
- ρ' = hemispherical average dielectric reflectance
- τ = transmittance through dielectric to substrate
- N = index of refraction of dielectric
- ρ = Fresnel reflectance for dielectric
- $\rho(\text{dry})$ = reflectance of dry substrate.

Soil moisture tends to adhere to soil particulates making a thin, smooth dielectric film. Although this film is by no means planar, one may expect that internal total reflection may still cause substantial reductions in the reflectance of dry soils when wetted. (The soil spectra shown in Fig. 3.104 indicate the change of soil reflectances when wet. In a number of cases the change is close to that predicted by the wet-dry model.)

3.2.5 Vegetative Canopy Models

A number of models of vegetative canopy reflectance have been developed in order to understand how the physical features of the canopy affect the reflectance. A convenient summary of these models and a guide to the literature is given by Vygodskaya and Gorshokova in Ref. 1. In general, these models are more complex than the simple plane mixtures and plane stacking models discussed previously. Both spectral properties and structural features of such canopies are needed as parameters for these models.

Many vegetative canopies tend to exhibit a layered structure with particular botanical features occupying the top, middle, and lower layers. Soil forms the lower boundary. The materials at the top tend to provide the dominant influence on bidirectional reflectance because the line of sight from the sun to the top layer and from the top layer to the observer is more certain. Vertically standing opaque parts such as stems cast shadows on other components and the soil. Such shadows are not resolved at large distances. The reflectance of a canopy as viewed remotely will be the sum of directly illuminated components, shadowed components, and components indirectly illuminated by multiple scattering within the canopy. Aesop's fable states that the grass is greener on the other side of the fence as an illustration of the apparent attractiveness of things that are out of reach. However, a spectroradiometer will prove that it really is greener due to the slant angle of view where the bare soil is not in the line of sight.

3.2.6 Thermal Modeling

The thermal emission of a natural source depends on the absolute temperature of the material and its spectral emissivity. To calculate the spectral exitance from a surface, these two parameters must be known. If the emissivity is independent of direction of view, then

$$M_{\lambda} = \epsilon(\lambda) M_{\lambda}(\text{BB}, \lambda, T) , \quad (3.9)$$

where

- $\epsilon(\lambda)$ = spectral emissivity of the surface
- $M_{\lambda}(\text{BB}, \lambda, T)$ = blackbody spectral exitance (Planck's formula)
- T = absolute temperature of emitting material.

If the emissivity varies with direction of view, then the directional variation of emissivity must also be known:

$$L_{\lambda} = \frac{1}{\pi} \epsilon(\lambda, \theta, \phi) M_{\lambda}(\text{BB}, \lambda, T) , \quad (3.10)$$

where L_{λ} is the spectral radiance of emission, and $\epsilon(\lambda, \theta, \phi)$ is the spectral directional emissivity.

The temperature of emission need not be the surface contact temperature. By reciprocity, thermal emission from a material is the reverse process of absorption. Consequently, the temperature that characterizes the emission is the temperature at a depth equal to the inverse of the absorption coefficient. If a temperature gradient exists between the outer surface and the interior,

the temperature of emission will not be the same as the contact temperature at the surface.

One can expect that terrestrial solids and liquids will have very large spectral absorption coefficients in the region $3 < \lambda < 100 \mu\text{m}$, thus the depth of emission is from a very thin layer a fraction of a millimeter thick and, under terrestrial environments, the temperature difference between contact temperature and emission temperature should be negligible.

The same reciprocity relation allows one to calculate the emissivity of opaque materials from the directional-hemispherical reflectance of the material. The emissivity in the reverse direction of the incident beam is equal to one minus the directional-hemispherical reflectance for that beam. Spectrometers using a diffusion chamber usually yield the appropriate reflectance for the particular direction of incidence built into the spectrometer. However, field measurements that compare the radiance of the illuminated unknown with the radiance of a known Lambertian reference panel may yield a reflectance that depends on the direction of view. Such a reflectance will approximate the directional-hemispherical reflectance if the unknown is also close to a Lambertian reflector.

In the case of specular dielectric surfaces in spectral ranges where bulk reflectance falls to zero, the emissivity may be calculated using Fresnel's reflectance.

A material surface may not be laterally isothermal. The contact temperature of some common materials, such as concrete under daylight conditions, will exhibit spot to spot variations in contact temperature by as much as 5°C . In such cases, the effective temperature of emission may be taken to be the area-weighted mean temperature. As long as the change in emission within the band of operation is approximately linear with such temperature variations, the mean temperature will be sufficient to estimate the thermal emission.

In general, the sum of two blackbody spectral exitances at two different temperatures is not a blackbody spectrum. The blackbody spectrum at the mean temperature is merely a good fit. Emission spectra from the lunar surface may be the sum of emissions at widely different temperatures of sloping surfaces toward and away from the sun. Even if the spectral emissivity were the same from spot to spot, the spectral exitance from a pixel containing such sloping surfaces might not be accurately estimated using Eq. (3.9) at the mean surface temperature.

Estimation of Surface Temperature Using Heat Exchange Relations. The surface temperature varies considerably with environmental conditions from time to time during the day. To complete the thermal model for emission, the temperature must be estimated using heat exchange relations. The estimation of surface temperatures from heat exchange relations is an important task in mechanical engineering designs of apparatus and in agriculture for calculations of microclimates. The literature on heat exchange is enormous and extends in time back to the days of Fourier. The following discussion of heat exchange is offered as a simplified alternative for the purpose of obtaining rough estimates of surface temperatures for natural sources in order to estimate sensor responses and to aid in thermal image interpretation.

A number of important assumptions are required in this simplified version of environmental heat exchange. The material is a homogeneous slab oriented horizontally. The radiative heat exchange occurs only in a very thin layer at

the material-air interface (hereafter called the surface) such that the surface maintains a steady-state temperature under current environmental conditions. The surface is Lambertian with a known average absorptance for daylight of 0.4 to 3 μm and a known average absorptance for thermal radiation longer than 3 μm .

The steady-state condition requires that the heat flux income to the surface must equal the heat flux outgoing from the surface at all times. The surface temperature changes in order to maintain this steady state.

The radiative income is derived from the absorption of three components: the direct sunlight, which contributes the major amount during daytime; diffuse skylight, which is a minor contributor; and thermal downward-welling atmospheric radiation, which contributes significantly both day and night.

The daylight components may be taken from the data shown in Fig. 3.10 for lack of more specific information. A curve fit to these data for direct sunlight is

$$E(\text{direct}) = \left(\frac{1089.5}{m_a} \right) \exp(-0.2819m_a) \quad [\text{W m}^{-2}] , \quad (3.11)$$

where m_a is the number of air masses (approximately secant of the polar sun angle).

The diffuse skylight contributes an additional 40 to 60 W/m^2 . The thermal component may be estimated using the Idso-Jackson² or Brunt empirical formulas. The Idso-Jackson estimation is close to that of Brunt in the range from 0 to 30°C for a relative humidity of 0.8.

The Idso-Jackson formula for a horizontal surface is

$$E(\text{atmos}) = M(\text{BB}, T_a) \{1 - 0.261 \times \exp[-7.77 \times 10^{-4} (273 - T_a)^2]\} \quad [\text{W m}^{-2}] , \quad (3.12)$$

where $M(\text{BB}, T_a)$ is the total blackbody exitance, and T_a is the meteorological air temperature in kelvins. The corresponding two-parameter relation by Brunt requires the partial pressure P of water vapor in millibars and the air temperature T_a .

The downward-welling irradiance on a horizontal plane is then

$$E(\text{atmos}) = M(\text{BB}, T_a) (0.605 + 0.048\sqrt{P}) \quad [\text{W m}^{-2}] . \quad (3.13)$$

The partial pressure P may be determined from the relative humidity and the air temperature using vapor pressure tables. A least-squares fit to table values for the range from 0 to 30°C is

$$P = 1.333R_h \{[(C_3T_c + C_2) T_c + C_1] T_c + C_0\} \quad [\text{mbar}] , \quad (3.14)$$

where

- R_h = relative humidity
- T_c = air temperature, °C
- C_0 = 4.5678
- C_1 = 0.35545

$$C_2 = 0.00705$$

$$C_3 = 3.7911 \times 10^{-4}.$$

The heat flux income is the absorbed portion of the incident radiation. The income is determined entirely from environmental conditions and is independent of surface temperature:

$$\text{income} = \alpha(s)E(\text{daylight}) + \alpha(l)E(\text{atmos}) , \quad (3.15)$$

where $\alpha(s)$ is the mean absorptance for daylight, 0.3 to 3 μm , and $\alpha(l)$ is the mean absorptance for long-wave, 3 μm and longer.

The outgo has four components:

$$\text{outgo} = M(\text{surface}) + J(\text{air}) + J(\text{cond}) + J(\text{evap}) , \quad (3.16)$$

where

$$M(\text{surface}) = [1 - \alpha(l)]M(\text{BB}, T)$$

$$J(\text{air}) = H_c(T - T_a), \text{ convective heat flux density to air}$$

$$J(\text{cond}) = H_k(T - T_o), \text{ conductive heat flux density to interior}$$

$$J(\text{evap}) = \text{evaporative heat flux density due to moisture}$$

$$T = \text{surface temperature, K}$$

$$H_c = \text{convective heat transfer coefficient, W m}^{-2} \text{ K}^{-1}$$

$$H_k = \text{conductive heat transfer coefficient, W m}^{-2} \text{ K}^{-1}$$

$$T_o = \text{temperature in bulk material below the surface, K.}$$

The surface exitance is always a positive outgo while the other three can be negative depending on the relative temperatures and whether the change of state of moisture is evaporation or condensation. All of these outgo components vary with the surface temperature, which is the desired unknown parameter. The steady-state temperature for a particular environmental condition may be found by iteration using a starting estimated surface temperature equal to T_a in the relation requiring the balance between income and outgo.

In some special cases, such as dry wood planks, dry dust layers, desert sand, and layers of dry straw or other thin layers where thermal conduction to the interior and evaporation is negligible, the outgo contains only two terms, $M(\text{surface})$ and $J(\text{air})$. The steady-state surface temperature should follow the current environmental conditions with no more than a few minutes delay.

The convective heat transfer coefficient must be calculated to complete the computation of $J(\text{air})$. Convective heat transfer is a complex phenomenon, but for rough estimates the following relation seems to be sufficient:

$$H_c = 1.7|T - T_a|^{1/3} + \frac{6V_a^{0.8}}{L_c^{0.2}} \quad [\text{W m}^{-2} \text{ K}^{-1}] , \quad (3.17)$$

where V_a is the local wind speed in meters per second, and L_c is the characteristic lateral dimension of surface in meters. The first term represents the effect of free convection. For surface to air temperature differences of 10 K and dimensions of 10 m, H_c reduces to

$$H_c = 4 + 3.8V_a^{0.8} \quad [\text{W m}^{-2} \text{ K}^{-1}] . \quad (3.18)$$

Only a light breeze of a few meters per second will cause the forced convection term to dominate.

When the surface is only the top thin layer of a much thicker material, then the conductive heat transfer term must be added to the outgo. Both the conductive heat transfer coefficient and the internal temperature T_o must be calculated.

The heat flux density from the surface to the interior, $J(\text{cond})$, is stored in the interior and changes the interior temperature T_o using the relation

$$J(\text{cond}) = 2C_p h D \frac{dT_o}{dt} \quad (3.19)$$

or

$$H_k(T - T_o) = 2C_p h D \frac{dT_o}{dt}, \quad (3.20)$$

where

- C_p = specific heat in bulk material, $\text{J kg}^{-1} \text{K}^{-1}$
- D = density of material, kg m^{-3}
- dT_o = change in interior temperature, K
- $H_k = k/h$, $\text{W m}^{-2} \text{K}^{-1}$
- k = thermal conductivity of bulk material, $\text{W m}^{-1} \text{K}^{-1}$
- h = effective thermal depth of heat storage, m
- dt = short time interval allowed for temperature change, s.

The specific heat, density, and thermal conductivity for many materials may be found in various handbooks of physical properties. The effective thermal depth h at which heat is stored depends on the rate at which the environmental income changes. For the diurnal cycle from night to day, the effective depth of heat penetration is taken to be twice the depth at which heat is stored:

$$2h = \left(\frac{2k}{2\pi C_p D} \right)^{1/2}. \quad (3.21)$$

For very thick materials, the diurnal depth of heat penetration is surprisingly small, as shown in Table 3.1. For materials that are thinner than this depth, the depth of penetration is assumed to be the physical thickness, and the effective depth of heat storage then is one-half of the physical thickness.

The surface temperature calculation requires an initial internal temperature T_o , which could be estimated to be the mean diurnal temperature for the current season. The first calculation for surface temperature may be in error because of the coarseness of estimate for T_o . However, as subsequent surface temperatures are calculated at intervals of dt , the internal temperature will approach and track a more realistic temperature. Consequently, the computed surface temperature will also more closely approximate the expected surface temperature. Therefore, if one wishes to estimate a surface temperature at some fixed time of day, a series of calculations must be started many hours before the desired time using the environmental conditions preceding that time.

Table 3.1 Thermal Properties of Common Materials (from Refs. 3 and 4)

<i>Material</i>	$k/c_h D$ ($\text{m}^2 \text{sec}^{-1}$)	k ($\text{W m}^{-1} \text{ }^\circ\text{C}$)	<i>Diurnal Depth, d</i> (m)
Stone concrete	4.8×10^{-7}	0.92	0.115
Granite	12.7×10^{-7}	1.9	0.187
Pine wood (cross grain)	0.7×10^{-7}	0.1	0.043
Lime stone	8.1×10^{-7}	0.7	0.149
Ice	11.2×10^{-7}	2.2	0.176
Damp soil	5.0×10^{-7}	2.6	0.116
Dry soil	3.1×10^{-7}	0.35	0.093
Building brick	4.4×10^{-7}	0.63	0.11
Cast iron	121.0×10^{-7}	57.0	1.73
Aluminum	860.0×10^{-7}	203.0	4.48

The interchange of heat energy between the surface and the bulk material below the surface where heat energy is stored results in a time delay in surface temperature changes. This time delay is responsible for what is called *thermal inertia*. The maximum surface temperature occurs at some time after maximum income. The surface temperature of concrete slabs may reach a maximum diurnal temperature as much as 3 h after solar noon.

Thermal modeling involving moisture evaporation or condensation is still more complex. In the case of bodies of water, such as ponds, lakes, rivers, and seas, the short-wave daylight is absorbed deep within the bulk while long-wavelength radiation is absorbed within a tenth of a millimeter of the surface where convective and evaporative heat exchange occurs. Typically, such bodies of water exhibit very slight diurnal temperature variations because of their enormous capacity to store heat. The evaporative cooling may reduce the surface temperature by as much as 0.5°C below the bulk water temperature.

Soil moisture is usually distributed in depth below the surface. The surface dries, first leaving an increasing moisture content with depth. The evaporation from the surface becomes a minor component in the heat exchange. However, the soil moisture below the surface increases both the heat capacity and the conductive heat exchange coefficient of the subsurface soil so that moist soil will exhibit a greater thermal inertia than when dry.

The most common and important effect of evaporative heat exchange occurs in the transpiration of growing temperate zone plants. Soil moisture in the root zone is transported out of the stomates of the leaves of healthy plants during daylight hours. The surface leaf temperature is significantly reduced below that which would be expected if evaporative heat exchange were missing.

Special Cases of Heat Transfer. Certain special cases of heat transfer are of interest that involve buried heat sources which influence the surface temperature. Buried heating pipes will often increase the surface temperature of the ground sufficiently to produce a temperature increase along the line of the pipe. Such a linear feature can be easily observed when the covering terrain

is otherwise fairly uniform. The very slow diffusion of heat from the pipe to the surface may require many days to affect the surface heat balance at the surface after the pipe is initially heated.

A second buried heat source of interest is volcanic magma at the melting point of rock. However, the depth of magma may be more than 100 m so that heat flow to the surface will take many centuries to influence the surface temperature. The occurrence of hot spots on the surface over volcanic regions is usually due to convective heating by hot gases escaping through cracks that connect the magma level to the surface.

A third interesting case occurs in subarctic regions in winter when terrain is covered by a uniform blanket of snow. The soil temperature below the snow cover is normally higher than that of the snow surface due to heat stored during the summer. The radiant income is the same everywhere; the convective heat loss is the same for the snow, and the evaporative loss of heat by the snow, although small, should be the same. Therefore, an observed difference in radiative heat loss will be due to a difference in subsurface convective heat exchange. The temperature of snow lying over a frozen pond will be very slightly higher than snow lying over soils due to the higher temperature of the pond water. Compressed snow due to tracked vehicles will have a higher temperature than uncompacted snow due to the increase in the conductive heat transfer coefficient.

3.3 THE SUN

The sun is a G class star with a mean radius of about 695,000 km. The surface temperature is approximately 5900 K by best-fit blackbody curve, or about 5770 K for the temperature of a blackbody source that is the size and distance of the sun and that would produce an exoatmospheric total irradiance of 1353 W m^{-2} at the earth.

The surface is largely a heated plasma, which should radiate very nearly as a blackbody. However, the cooler atomic gases of the solar atmosphere and the large temperature gradient below the surface, coupled with the nonisothermal character of transient surface features, lead to deviations from blackbody radiation.

3.3.1 Exoatmospheric Solar Radiation

Table 3.2 lists a proposed, standard solar spectral irradiance ($m_a = 0$) at the mean distance of the earth from the sun, where the mean distance is $149.68 \times 10^6 \text{ km}$ or 149.68 Gm. Figure 3.3 shows the spectral irradiance of exoatmospheric solar radiation, the comparable blackbody spectrum for a temperature of 5900 K, and the approximate solar spectral irradiance at sea level through one atmospheric air mass ($m_a = 1$).

3.3.2 Terrestrial Solar Radiation

The spectral irradiance of the sun at sea level is modified by the transmittance and scattering of the atmosphere. The direct sunlight will decrease with increasing path length through the atmosphere. The path length is expressed

Table 3.2 Solar Spectral Irradiance ($m_a = 0$)—Proposed Standard Curve (from Ref. 5)

λ — Wavelength in micrometers
 $E_\lambda (\lambda)$ — Solar spectral irradiance averaged over small bandwidth centered at λ , in $\text{W m}^{-2} \mu\text{m}^{-1}$
 $D(0-\lambda)$ — Percentage of the solar constant associated with wavelengths shorter than λ
 Solar Constant — 1353 W m^{-2}

λ	$E_\lambda (\lambda)$	$D(0-\lambda)$	λ	$E_\lambda (\lambda)$	$D(0-\lambda)$	λ	$E_\lambda (\lambda)$	$D(0-\lambda)$
0.120	0.100	0.00044	0.375	1157.0	6.582	0.575	1719.0	32.541
0.140	0.030	0.00053	0.380	1120.0	7.003	0.580	1715.0	33.176
0.150	0.07	0.00057	0.385	1098.0	7.413	0.585	1712.0	33.809
0.160	0.23	0.00068	0.390	1098.0	7.819	0.590	1700.0	34.439
0.170	0.63	0.00100	0.395	1189.0	8.241	0.595	1682.0	35.064
0.180	1.25	0.00169	0.400	1429.0	8.725	0.600	1666.0	35.683
0.190	2.71	0.00316	0.405	1644.0	9.293	0.605	1647.0	36.295
0.200	10.7	0.00811	0.410	1751.0	9.920	0.610	1635.0	36.902
0.210	22.9	0.02053	0.415	1774.0	10.571	0.620	1602.0	38.098
0.220	57.5	0.05024	0.420	1747.0	11.222	0.630	1570.0	39.270
0.225	64.9	0.0728	0.425	1693.0	11.858	0.640	1544.0	40.421
0.230	66.7	0.0971	0.430	1639.0	12.473	0.650	1511.0	41.550
0.235	59.3	0.1204	0.435	1663.0	13.083	0.660	1486.0	42.657
0.240	63.0	0.1430	0.440	1810.0	13.725	0.670	1456.0	43.744
0.245	72.3	0.1680	0.445	1922.0	14.415	0.680	1427.0	44.810
0.250	70.4	0.1944	0.450	2006.0	15.140	0.690	1402.0	45.855
0.255	104.0	0.2266	0.455	2057.0	15.891	0.700	1369.0	46.879
0.260	130.0	0.2698	0.460	2066.0	16.653	0.710	1344.0	47.882
0.265	185.0	0.3280	0.465	2048.0	17.413	0.720	1314.0	48.864
0.270	232.0	0.4051	0.470	2033.0	18.167	0.730	1290.0	49.826
0.275	204.0	0.4857	0.475	2044.0	18.921	0.740	1260.0	50.769
0.280	222.0	0.5644	0.480	2074.0	19.681	0.750	1235.0	51.691
0.285	315.0	0.6636	0.485	1976.0	20.430	0.760	1211.0	52.595
0.290	482.0	0.8109	0.490	1950.0	21.155	0.770	1185.0	53.480
0.295	584.0	1.0078	0.495	1960.0	21.878	0.780	1159.0	54.346
0.300	514.0	1.2107	0.500	1942.0	22.599	0.790	1134.0	55.194
0.305	603.0	1.4171	0.505	1920.0	23.312	0.800	1109.0	56.023
0.310	689.0	1.6558	0.510	1882.0	24.015	0.810	1085.0	56.834
0.315	764.0	1.9243	0.515	1833.0	24.701	0.820	1060.0	57.627
0.320	830.0	2.2188	0.520	1833.0	25.379	0.830	1036.0	58.401
0.325	975.0	2.552	0.525	1852.0	26.059	0.840	1013.0	59.158
0.330	1059.0	2.928	0.530	1842.0	26.742	0.850	990.0	59.899
0.335	1081.0	3.323	0.535	1818.0	27.418	0.860	968.0	60.622
0.340	1074.0	3.721	0.540	1783.0	28.084	0.870	947.0	61.330
0.345	1069.0	4.117	0.545	1754.0	28.737	0.880	926.0	62.022
0.350	1093.0	4.517	0.550	1725.0	29.380	0.890	908.0	62.700
0.355	1083.0	4.919	0.555	1720.0	30.017	0.900	891.0	63.365
0.360	1068.0	5.316	0.560	1695.0	30.648	0.910	880.0	64.019
0.365	1132.0	5.723	0.565	1705.0	31.276	0.920	869.0	64.665
0.370	1181.0	6.150	0.570	1712.0	31.907	0.930	858.0	65.304

Table 3.2 (continued)

λ - Wavelength in micrometers
 $E_\lambda(\lambda)$ - Solar spectral irradiance averaged over small bandwidth centered at λ , $\text{W m}^{-1} \mu\text{m}^{-1}$
 $D(0-\lambda)$ - Percentage of the solar constant associated with wavelengths shorter than λ
 Solar Constant - 1353 W m^{-2}

λ	$E_\lambda(\lambda)$	$D(0-\lambda)$	λ	$E_\lambda(\lambda)$	$D(0-\lambda)$	λ	$E_\lambda(\lambda)$	$D(0-\lambda)$
0.940	847.0	65.934	2.40	62.0	95.8580	9.0	.367	99.91673
0.950	837.0	66.556	2.50	55.0	96.2903	10.0	.241	99.93920
0.960	820.0	67.168	2.60	48.0	96.6710	11.0	.165	99.95420
0.970	803.0	67.768	2.70	43.0	97.0073	12.0	.117	99.96462
0.980	785.0	68.355	2.80	39.0	97.3103	13.0	.0851	99.97209
0.990	767.0	68.928	2.90	35.0	97.5838	14.0	.0634	99.97758
1.000	748.0	69.488	3.00	31.0	97.8277	15.0	.0481	99.98170
1.050	668.0	72.105	3.10	26.0	98.0383	16.0	.0371	99.98485
1.100	593.0	74.435	3.20	22.6	98.2179	17.0	.0291	99.98730
1.150	535.0	76.519	3.30	19.2	98.3724	18.0	.0231	99.98923
1.200	485.0	78.404	3.40	16.6	98.5047	19.0	.0186	99.99077
1.250	438.0	80.109	3.50	14.6	98.6200	20.0	.0152	99.99202
1.300	397.0	81.652	3.60	13.5	98.7238	25.0	.00617	99.99596
1.350	358.0	83.047	3.70	12.3	98.8192	30.0	.00297	99.99765
1.400	337.0	84.331	3.80	11.1	98.9056	35.0	.00160	99.99850
1.450	312.0	85.530	3.90	10.3	98.9847	40.0	.000942	99.99897
1.500	288.0	86.639	4.00	9.5	99.0579	50.0	.000391	99.99946
1.550	267.0	87.665	4.10	8.70	99.1252	60.0	.000190	99.99967
1.600	245.0	88.611	4.20	7.80	99.1861	80.0	6.16E-5	99.99986
1.650	223.0	89.475	4.30	7.10	99.2412	100.0	2.57E-5	99.99992
1.70	202.0	90.261	4.40	6.50	99.29150	120	1.26E-5	99.99995
1.75	180.0	90.967	4.50	5.92	99.33740	150	5.23E-6	99.99997
1.80	159.0	91.593	4.60	5.35	99.37905	200	1.69E-6	99.99999
1.85	142.0	92.149	4.70	4.86	99.41678	250	0.70E-6	99.99999
1.90	126.0	92.644	4.80	4.47	99.45127	300	0.34E-6	99.99999
1.95	114.0	93.088	4.90	4.11	99.48299	400	0.11E-6	99.99999
2.00	103.0	93.489	5.00	3.79	99.51219	1000	0.00E-6	100.0000
2.10	90.0	94.202	6.00	1.82	99.71950	-	-	-
2.20	79.0	94.826	7.00	.990	99.82335	-	-	-
2.30	69.0	95.373	8.00	.585	99.88155	-	-	-

in atmospheric masses m_a , through which the sunlight must penetrate. Figure 3.4 shows the relationship between air mass m_a of penetration and the solar zenith angle. For small zenith angles, the air mass is equal to the secant of the solar zenith angle.

Figures 3.5 through 3.8 show the spectral irradiance of direct sunlight normal to the rays at sea level for air masses 1, 2, 3, and 4 respectively. These spectra were calculated using LOWTRAN 7 for the 1976 U.S. standard at-

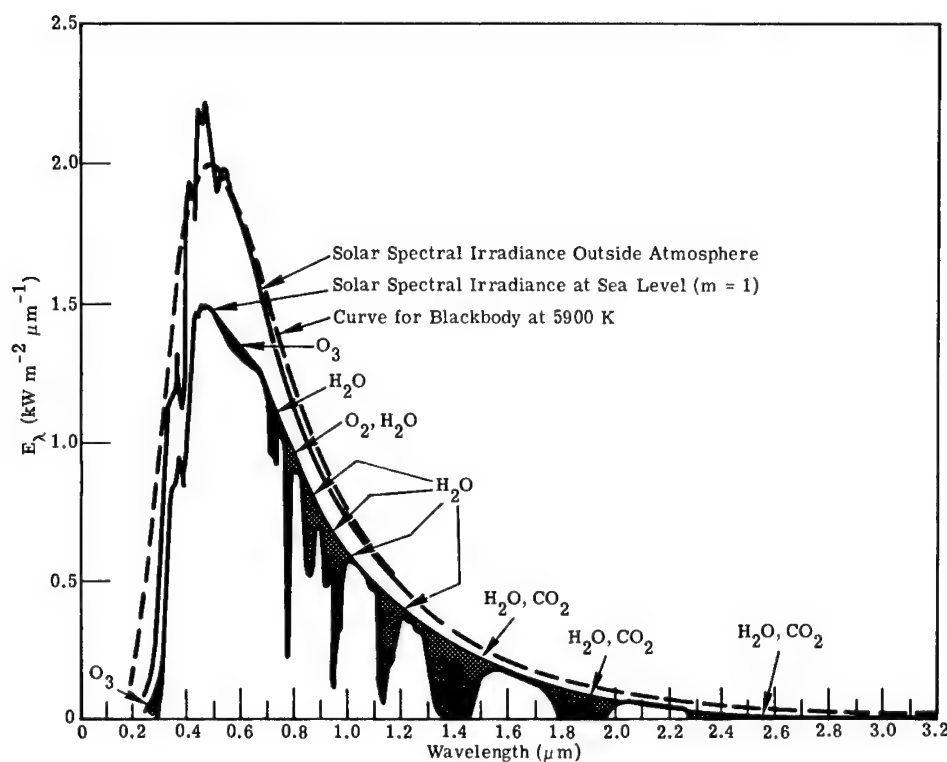


Fig. 3.3 Spectral distribution curves related to the sun. The shaded areas indicate absorption at sea level due to the atmospheric constituents shown.

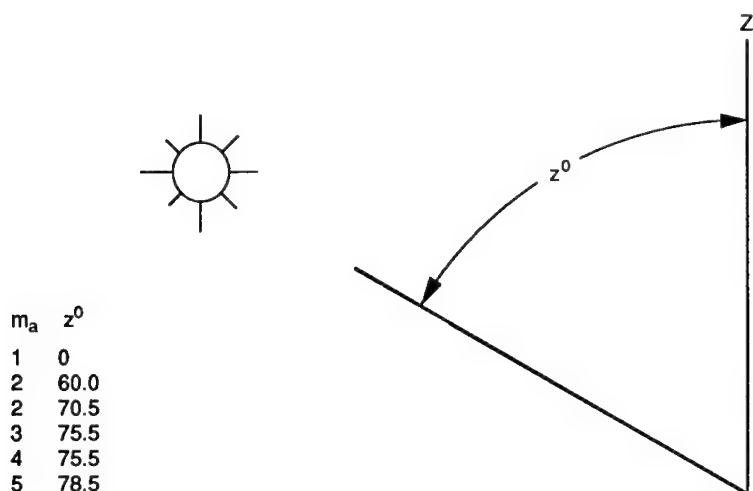


Fig. 3.4 The relationship between air mass m_a and the solar zenith angle.

mosphere. The largest changes in the solar spectrum are in the ultraviolet and visible ranges. These data are tabulated in Tables 3.3 through 3.6 so that calculations can be made of the spectral radiances of terrestrial materials for estimating sensor signals under favorable conditions.

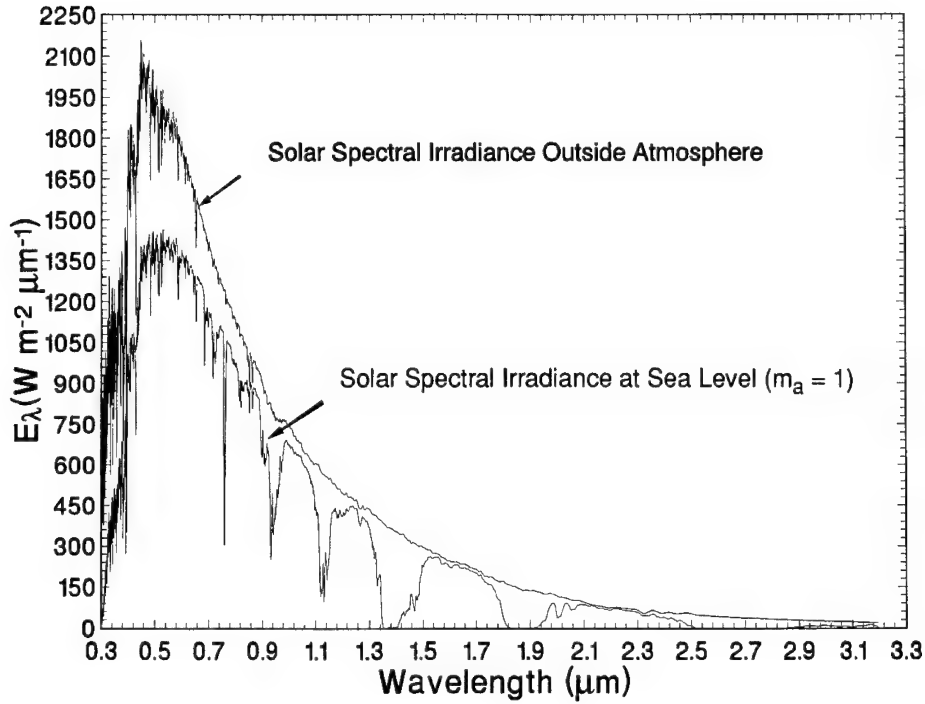


Fig. 3.5 Spectral irradiance of direct sunlight normal to the rays for $m_a = 1$ as calculated by LOWTRAN.

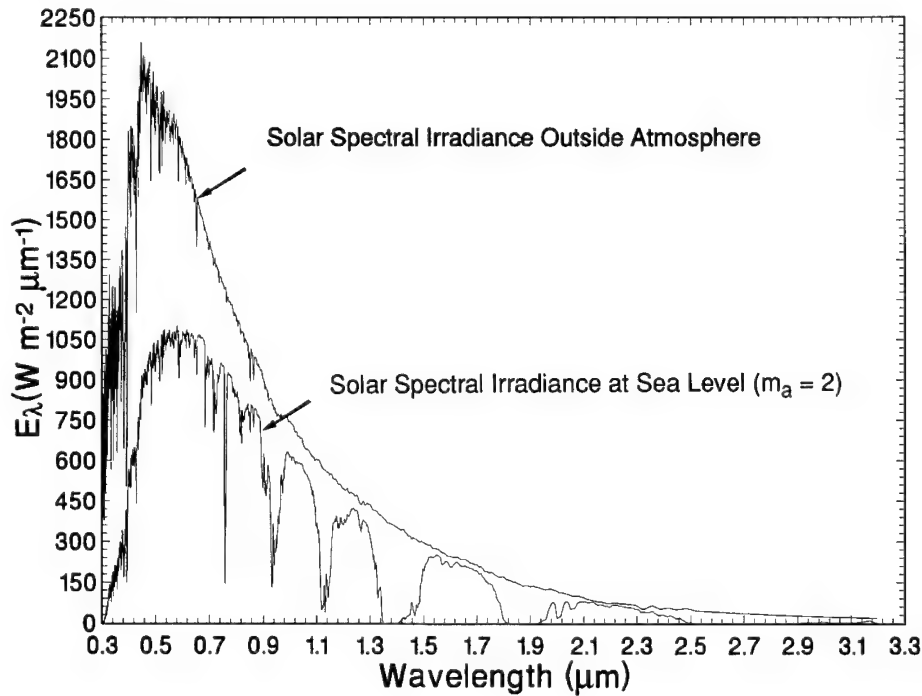


Fig. 3.6 Spectral irradiance of direct sunlight normal to the rays for $m_a = 2$ as calculated by LOWTRAN.

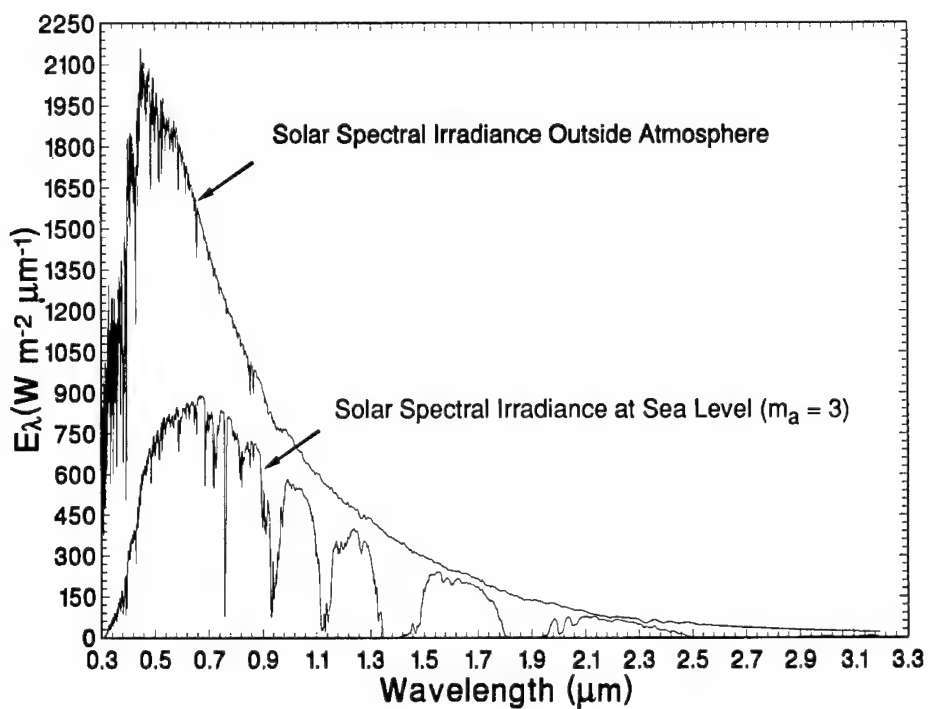


Fig. 3.7 Spectral irradiance of direct sunlight normal to the rays for $m_a = 3$ as calculated by LOWTRAN.

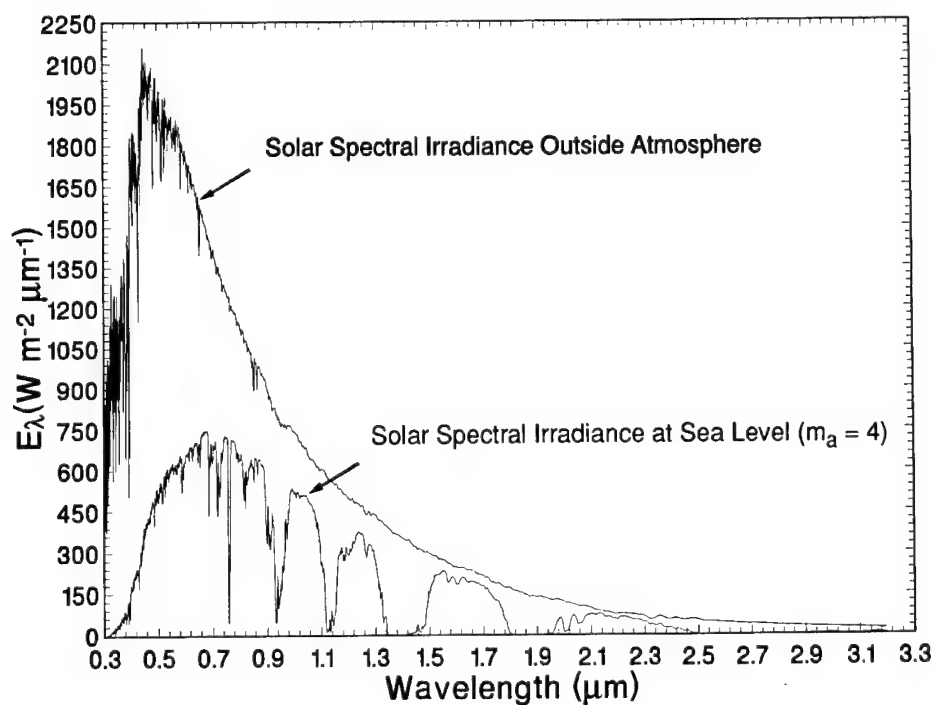


Fig. 3.8 Spectral irradiance of direct sunlight normal to the rays for $m_a = 4$ as calculated by LOWTRAN.

Table 3.3 Solar Spectral Irradiance at Sea Level ($m_a = 1$)

λ (μm)	$E_\lambda(\lambda)$ ($\text{W m}^{-2} \mu\text{m}^{-1}$)	λ (μm)	$E_\lambda(\lambda)$ ($\text{W m}^{-2} \mu\text{m}^{-1}$)	λ (μm)	$E_\lambda(\lambda)$ ($\text{W m}^{-2} \mu\text{m}^{-1}$)	λ (μm)	$E_\lambda(\lambda)$ ($\text{W m}^{-2} \mu\text{m}^{-1}$)
.302	9.66	.640	1310.	1.140	270.	1.640	222.
.303	21.8	.650	1280.	1.150	232.	1.650	219.
.304	25.6	.660	1290.	1.160	385.	1.660	221.
.305	32.6	.670	1270.	1.170	432.	1.670	217.
.306	33.8	.680	1250.	1.180	424.	1.680	210.
.307	49.9	.690	1120.	1.190	425.	1.690	207.
.308	70.3	.700	1130.	1.200	411.	1.700	203.
.309	57.3	.710	1140.	1.210	416.	1.710	194.
.310	92.9	.720	939.	1.220	435.	1.720	193.
.311	108.	.730	1000.	1.230	445.	1.730	176.
.312	113.	.740	1070.	1.240	449.	1.740	166.
.313	111.	.750	1100.	1.250	440.	1.750	160.
.314	83.1	.760	317.	1.260	411.	1.760	158.
.315	140.	.770	1050.	1.270	377.	1.770	139.
.316	145.	.780	1040.	1.280	405.	1.780	112.
.317	195.	.790	990.	1.290	390.	1.790	102.
.318	164.	.800	971.	1.300	371.	1.800	47.7
.319	165.	.810	953.	1.310	325.	1.810	19.3
.320	239.	.820	888.	1.320	261.	1.820	3.91
.330	306.	.830	891.	1.330	177.	1.830	.277
.340	393.	.840	906.	1.340	199.	1.840	.008
.350	497.	.850	873.	1.350	22.9	1.850	.017
.360	438.	.860	891.	1.360	.082	1.860	.060
.370	517.	.870	884.	1.370	.048	1.870	.008
.380	640.	.880	859.	1.380	.241	1.880	.178
.390	769.	.890	843.	1.390	2.90	1.890	.487
.400	914.	.900	637.	1.400	2.18	1.900	.083
.410	868.	.910	615.	1.410	13.6	1.910	.157
.420	1050.	.920	681.	1.420	37.2	1.920	1.26
.430	713.	.930	495.	1.430	60.4	1.930	3.58
.440	1090.	.940	499.	1.440	60.2	1.940	12.3
.450	1390.	.950	404.	1.450	66.0	1.950	25.7
.460	1360.	.960	487.	1.460	119.	1.960	28.2
.470	1290.	.970	629.	1.470	64.9	1.970	66.5
.480	1410.	.980	641.	1.480	104.	1.980	85.3
.490	1410.	.990	691.	1.490	176.	1.990	89.7
.500	1340.	1.000	679.	1.500	232.	2.000	53.9
.510	1410.	1.010	661.	1.510	242.	2.010	40.8
.520	1350.	1.020	648.	1.520	254.	2.020	57.1
.530	1440.	1.030	641.	1.530	262.	2.030	86.0
.540	1330.	1.040	636.	1.540	256.	2.040	89.6
.550	1410.	1.050	623.	1.550	261.	2.050	76.9
.560	1390.	1.060	598.	1.560	258.	2.060	67.5
.570	1340.	1.070	585.	1.570	238.	2.070	69.8
.580	1410.	1.080	552.	1.580	235.	2.080	82.4
.590	1330.	1.090	526.	1.590	237.	2.090	85.9
.600	1350.	1.100	435.	1.600	225.	2.100	85.1
.610	1340.	1.110	424.	1.610	221.	2.110	84.3
.620	1370.	1.120	145.	1.620	230.	2.120	80.6
.630	1310.	1.130	185.	1.630	232.	2.130	81.4

Figure 3.9 shows the spectral variation to be expected on terrain at higher elevations when the penetration to sea level is 1.5 air masses. Figure 3.10 shows the global and direct solar irradiance on a horizontal surface for various slant paths.

3.4 THE MOON

The illuminance of moonlight on a horizontal surface through a clear atmosphere on the surface of the earth is given as a function of lunar elevation angle and phase angle in Ref. 7. These data are taken from Bond and Henderson.⁸

Table 3.4 Solar Spectral Irradiance at Sea Level ($m_a = 2$)

λ (μm)	$E_\lambda(\lambda)$ ($\text{W m}^{-2} \mu\text{m}^{-1}$)	λ (μm)	$E_\lambda(\lambda)$ ($\text{W m}^{-2} \mu\text{m}^{-1}$)	λ (μm)	$E_\lambda(\lambda)$ ($\text{W m}^{-2} \mu\text{m}^{-1}$)	λ (μm)	$E_\lambda(\lambda)$ ($\text{W m}^{-2} \mu\text{m}^{-1}$)
.302	.187	.640	1060.	1.140	176.	1.640	212.
.303	.627	.650	1040.	1.150	142.	1.650	209.
.304	.902	.660	1060.	1.160	312.	1.660	211.
.305	1.63	.670	1060.	1.170	377.	1.670	207.
.306	1.91	.680	1050.	1.180	372.	1.680	201.
.307	3.74	.690	900.	1.190	376.	1.690	198.
.308	6.12	.700	929.	1.200	363.	1.700	193.
.309	5.81	.710	958.	1.210	372.	1.710	184.
.310	10.7	.720	726.	1.220	398.	1.720	183.
.311	13.5	.730	807.	1.230	415.	1.730	165.
.312	16.7	.740	918.	1.240	422.	1.740	153.
.313	17.1	.750	952.	1.250	414.	1.750	146.
.314	14.8	.760	154.	1.260	382.	1.760	143.
.315	25.4	.770	915.	1.270	341.	1.770	121.
.316	29.6	.780	917.	1.280	376.	1.780	88.4
.317	41.3	.790	856.	1.290	358.	1.790	76.2
.318	38.0	.800	842.	1.300	333.	1.800	23.2
.319	37.8	.810	831.	1.310	278.	1.810	5.36
.320	59.1	.820	759.	1.320	203.	1.820	.394
.330	99.1	.830	764.	1.330	114.	1.830	.005
.340	148	.840	796.	1.340	133.	1.840	.000
.350	206	.850	774.	1.350	4.18	1.850	.000
.360	195	.860	797.	1.360	.001	1.860	.000
.370	246	.870	793.	1.370	.000	1.870	.000
.380	323.	.880	771.	1.380	.003	1.880	.003
.390	408	.890	756.	1.390	.122	1.890	.014
.400	506	.900	508.	1.400	.091	1.900	.001
.410	500	.910	494.	1.410	1.95	1.910	.003
.420	626	.920	585.	1.420	11.0	1.920	.070
.430	440	.930	362.	1.430	23.5	1.930	.413
.440	695	.940	368.	1.440	23.9	1.940	3.31
.450	907	.950	275.	1.450	28.6	1.950	10.8
.460	905	.960	371.	1.460	70.6	1.960	13.0
.470	875	.970	546.	1.470	28.6	1.970	47.2
.480	980	.980	563.	1.480	59.2	1.980	69.4
.490	996	.990	629.	1.490	132.	1.990	75.9
.500	959	1.000	622.	1.500	201.	2.000	35.5
.510	1020	1.010	602.	1.510	216.	2.010	23.8
.520	988	1.020	595.	1.520	234.	2.020	39.7
.530	1060.	1.030	593.	1.530	245.	2.030	74.8
.540	991.	1.040	590.	1.540	243.	2.040	80.5
.550	1060.	1.050	579.	1.550	249.	2.050	64.8
.560	1050.	1.060	556.	1.560	248.	2.060	54.2
.570	1020.	1.070	540.	1.570	222.	2.070	57.3
.580	1080.	1.080	502.	1.580	220.	2.080	73.6
.590	1000.	1.090	471.	1.590	227.	2.090	79.1
.600	1040	1.100	358.	1.600	211.	2.100	79.2
.610	1050	1.110	343.	1.610	207.	2.110	79.6
.620	1090	1.120	67.4	1.620	220.	2.120	76.0
.630	1040.	1.130	97.2	1.630	223.	2.130	78.3

The lunar spectral albedo as well as calculated tables of spectral irradiance of moonlight plus air glow as a function of air mass of optical path and fraction of full moon are given in Biberman and Nudelman.⁹ Tables of measured monochromatic, U, B, and V magnitudes of the moon in various phases are given in Lane and Irvine.¹⁰

The reflectance of sunlight from the lunar surface is not Lambertian. The lunar phase function is less than the phase function of a Lambertian sphere by about a factor of 2 at quarter (90°) phase, indicating a tendency to retroreflect.

Table 3.5 Solar Spectral Irradiance at Sea Level ($m_a = 3$)

λ (μm)	$E_\lambda(\lambda)$ ($\text{W m}^{-2} \mu\text{m}^{-1}$)	λ (μm)	$E_\lambda(\lambda)$ ($\text{W m}^{-2} \mu\text{m}^{-1}$)	λ (μm)	$E_\lambda(\lambda)$ ($\text{W m}^{-2} \mu\text{m}^{-1}$)	λ (μm)	$E_\lambda(\lambda)$ ($\text{W m}^{-2} \mu\text{m}^{-1}$)
.302	.004	.640	859.	1.140	121.	1.640	203.
.303	.020	.650	845.	1.150	94.0	1.650	199.
.304	.035	.660	875.	1.160	259.	1.660	202.
.305	.089	.670	882.	1.170	335.	1.670	199.
.306	.117	.680	885.	1.180	332.	1.680	193.
.307	.302	.690	736.	1.190	337.	1.690	189.
.308	.569	.700	772.	1.200	325.	1.700	185.
.309	.624	.710	808.	1.210	337.	1.710	175.
.310	1.30	.720	574.	1.220	366.	1.720	174.
.311	1.78	.730	659.	1.230	387.	1.730	156.
.312	2.59	.740	789.	1.240	398.	1.740	142.
.313	2.75	.750	828.	1.250	390.	1.750	135.
.314	2.75	.760	84.8	1.260	356.	1.760	131.
.315	4.79	.770	800.	1.270	311.	1.770	107.
.316	6.22	.780	806.	1.280	351.	1.780	72.6
.317	9.04	.790	743.	1.290	331.	1.790	59.3
.318	9.03	.800	733.	1.300	303.	1.800	12.5
.319	8.94	.810	728.	1.310	243.	1.810	1.75
.320	15.0	.820	655.	1.320	164.	1.820	.052
.330	32.7	.830	661.	1.330	79.9	1.830	.000
.340	56.1	.840	702.	1.340	94.3	1.840	.000
.350	86.1	.850	689.	1.350	.949	1.850	.000
.360	98.3	.860	715.	1.360	.000	1.860	.000
.370	119.	.870	713.	1.370	.000	1.870	.000
.380	164.	.880	693.	1.380	.000	1.880	.000
.390	218.	.890	680.	1.390	.007	1.890	.001
.400	283.	.900	416.	1.400	.005	1.900	.000
.410	291.	.910	407.	1.410	.358	1.910	.000
.420	376.	.920	509.	1.420	3.91	1.920	.005
.430	273.	.930	276.	1.430	10.6	1.930	.063
.440	443.	.940	281.	1.440	11.0	1.940	1.08
.450	594.	.950	198.	1.450	14.2	1.950	5.22
.460	606.	.960	293.	1.460	45.5	1.960	6.94
.470	599.	.970	478.	1.470	14.6	1.970	35.6
.480	682.	.980	499.	1.480	37.0	1.980	58.4
.490	706.	.990	574.	1.490	104.	1.990	66.1
.500	689.	1.000	571.	1.500	178.	2.000	25.3
.510	743.	1.010	551.	1.510	196.	2.010	15.3
.520	727.	1.020	548.	1.520	218.	2.020	29.6
.530	791.	1.030	548.	1.530	231.	2.030	66.6
.540	743.	1.040	547.	1.540	231.	2.040	73.6
.550	802.	1.050	538.	1.550	239.	2.050	56.2
.560	799.	1.060	517.	1.560	238.	2.060	45.3
.570	771.	1.070	500.	1.570	208.	2.070	48.7
.580	827.	1.080	459.	1.580	207.	2.080	66.9
.590	762.	1.090	426.	1.590	218.	2.090	73.7
.600	808.	1.100	303.	1.600	199.	2.100	74.4
.610	827.	1.110	284.	1.610	195.	2.110	75.6
.620	864.	1.120	35.2	1.620	210.	2.120	72.2
.630	829.	1.130	56.1	1.630	215.	2.130	75.5

The thermal emission from the lunar surface is also non-Lambertian. Calculations given in Sexl et al.¹¹ indicate that the emission expected from a model of the lunar surface consisting of craters with a diameter-to-depth ratio of 3 to 1 covering 50% of the surface area fits the experimental data of Saari and Shorthill. The radiance is greatest normal to the surface.

The spectral irradiance of the full moon normal to the rays at sea level is shown in Fig. 3.11 for $m_a = 1$ and in Fig. 3.12 for $m_a = 2$. These spectra were calculated by LOWTRAN 7 using the same conditions used for sunlight. The

Table 3.6 Solar Spectral Irradiance at Sea Level ($m_a = 4$)

λ (μm)	$E_\lambda(\lambda)$ ($\text{W m}^{-2} \mu\text{m}^{-1}$)	λ (μm)	$E_\lambda(\lambda)$ ($\text{W m}^{-2} \mu\text{m}^{-1}$)	λ (μm)	$E_\lambda(\lambda)$ ($\text{W m}^{-2} \mu\text{m}^{-1}$)	λ (μm)	$E_\lambda(\lambda)$ ($\text{W m}^{-2} \mu\text{m}^{-1}$)
.302	.000	.640	698	1.140	86.1	1.640	194
.303	.001	.650	690	1.150	64.5	1.650	190
.304	.002	.660	723	1.160	219	1.660	193
.305	.005	.670	737	1.170	300	1.670	191
.306	.008	.680	746	1.180	297	1.680	185
.307	.026	.690	605	1.190	304	1.690	182
.308	.057	.700	644	1.200	293	1.700	177
.309	.071	.710	683	1.210	306	1.710	167
.310	.168	.720	458	1.220	337	1.720	166
.311	.247	.730	542	1.230	363	1.730	148
.312	.419	.740	680	1.240	375	1.740	133
.313	.463	.750	720	1.250	368	1.750	125
.314	.529	.760	50.0	1.260	332	1.760	121
.315	.936	.770	700	1.270	286	1.770	95.4
.316	1.35	.780	710	1.280	328	1.780	60.8
.317	2.04	.790	648	1.290	307	1.790	47.2
.318	2.20	.800	641	1.300	276	1.800	7.14
.319	2.17	.810	639	1.310	214	1.810	.623
.320	3.90	.820	567	1.320	135	1.820	.008
.330	11.0	.830	575	1.330	58.0	1.830	.000
.340	21.6	.840	621	1.340	68.8	1.840	.000
.350	36.5	.850	614	1.350	.241	1.850	.000
.360	40.2	.860	641	1.360	.000	1.860	.000
.370	57.5	.870	641	1.370	.000	1.870	.000
.380	84.2	.880	624	1.380	.000	1.880	.000
.390	118	.890	611	1.390	.000	1.890	.000
.400	159	.900	345	1.400	.000	1.900	.000
.410	170	.910	340	1.410	.075	1.910	.000
.420	228	.920	445	1.420	1.53	1.920	.000
.430	170	.930	215	1.430	5.20	1.930	.011
.440	284	.940	219	1.440	5.47	1.940	.388
.450	391	.950	146	1.450	7.62	1.950	2.71
.460	407	.960	236	1.460	30.5	1.960	3.97
.470	411	.970	422	1.470	7.96	1.970	27.6
.480	476	.980	445	1.480	24.3	1.980	50.1
.490	502	.990	525	1.490	83.3	1.990	58.4
.500	496	1.000	525	1.500	159	2.000	18.8
.510	542	1.010	504	1.510	179	2.010	10.4
.520	537	1.020	506	1.520	203	2.020	22.8
.530	589	1.030	507	1.530	219	2.030	60.1
.540	559	1.040	508	1.540	220	2.040	67.8
.550	609	1.050	500	1.550	229	2.050	49.5
.560	609	1.060	481	1.560	228	2.060	38.6
.570	588	1.070	463	1.570	196	2.070	42.2
.580	638	1.080	421	1.580	196	2.080	61.4
.590	583	1.090	386	1.590	209	2.090	69.1
.600	630	1.100	260	1.600	188	2.100	70.3
.610	653	1.110	240	1.610	184	2.110	72.1
.620	690	1.120	19.6	1.620	202	2.120	68.9
.630	665	1.130	34.0	1.630	207	2.130	73.0

spectral reflectances of selected lunar rock and soil samples are shown^{12,13} in Figs. 3.13 and 3.14.

3.5 THE CELESTIAL BACKGROUND

3.5.1 Coordinates on the Celestial Sphere

Celestial coordinates^{14,15} are defined by referring to the following points and great circles on the celestial sphere:

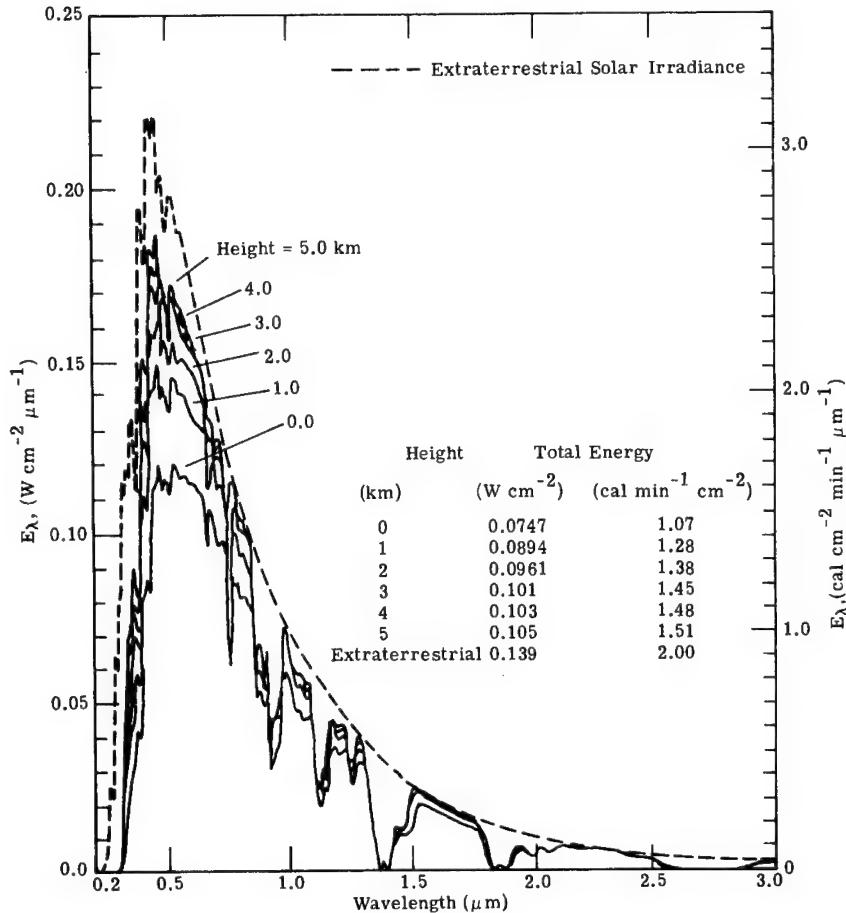


Fig. 3.9 Variation with altitude of spectral irradiance versus wavelength normal to the sun's rays for an air mass of 1.5 (Ref. 6).

- *North and south celestial poles:* The respective points of intersection of the celestial sphere with the northward and southward prolongations of the earth's axis of rotation.
- *Zenith and nadir:* The respective points of intersection of the celestial sphere with the upward and downward prolongations of the observer's plumb line.
- *Celestial equator:* The great circle defined by the intersection of the celestial sphere and the projection of the plane of the earth's equator.
- *Ecliptic:* The apparent great-circle path of the sun on the celestial sphere during the course of a year. The plane of the ecliptic is inclined at an angle of about $23^{\circ}27'$ to the plane of the celestial equator.
- *Vernal equinox:* That point of intersection of the ecliptic and the celestial equator that occurs when the sun is going from south to north. The vernal equinox has the symbol γ and is sometimes called the first point of Aries.

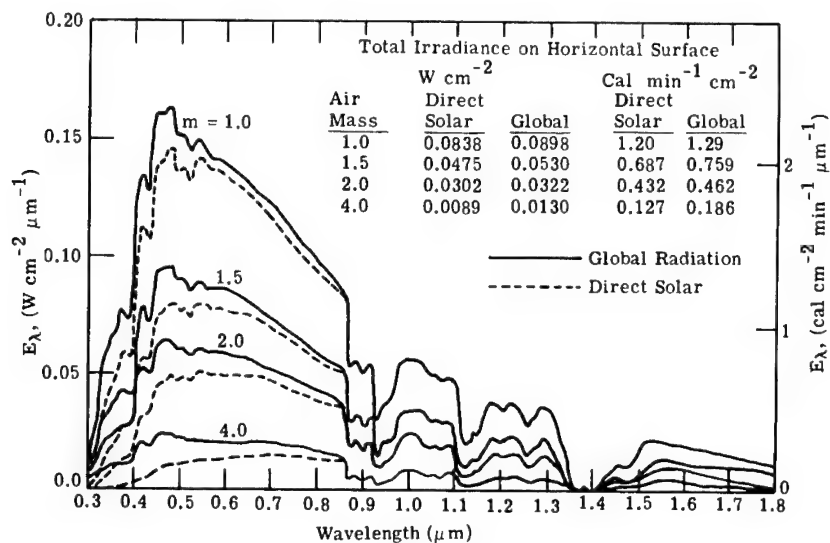


Fig. 3.10 Spectral distribution as a function of wavelength of the global and direct solar radiation incident at sea level on a horizontal surface for various slant paths corresponding to air mass 1.0, 1.5, 2.0, and 4.0 (Ref. 6).

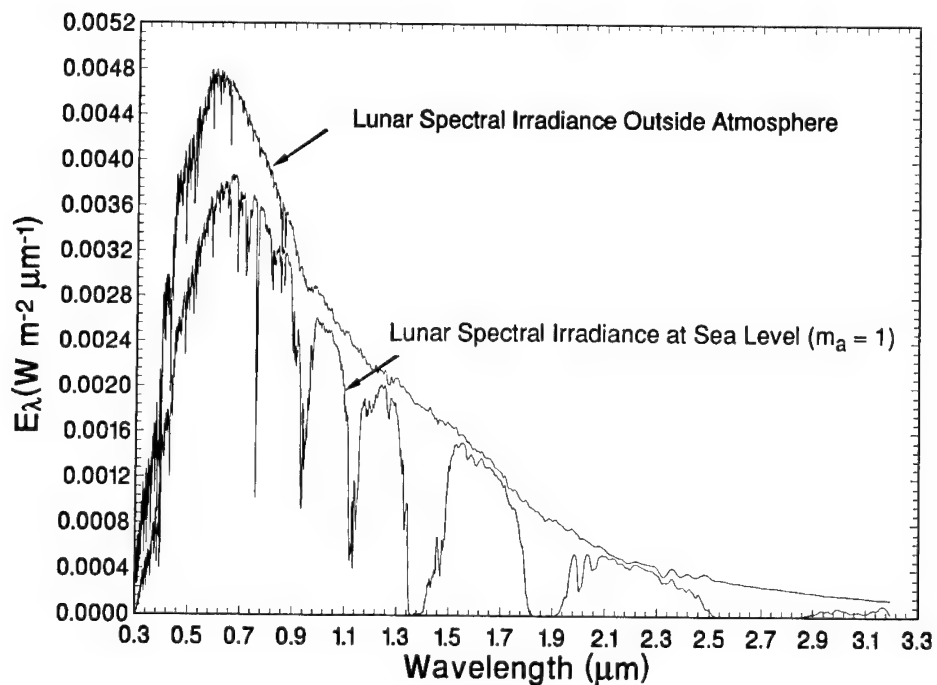


Fig. 3.11 Spectral irradiance normal to the rays of the full moon at sea level for air mass $m_a = 1$ as calculated by LOWTRAN.

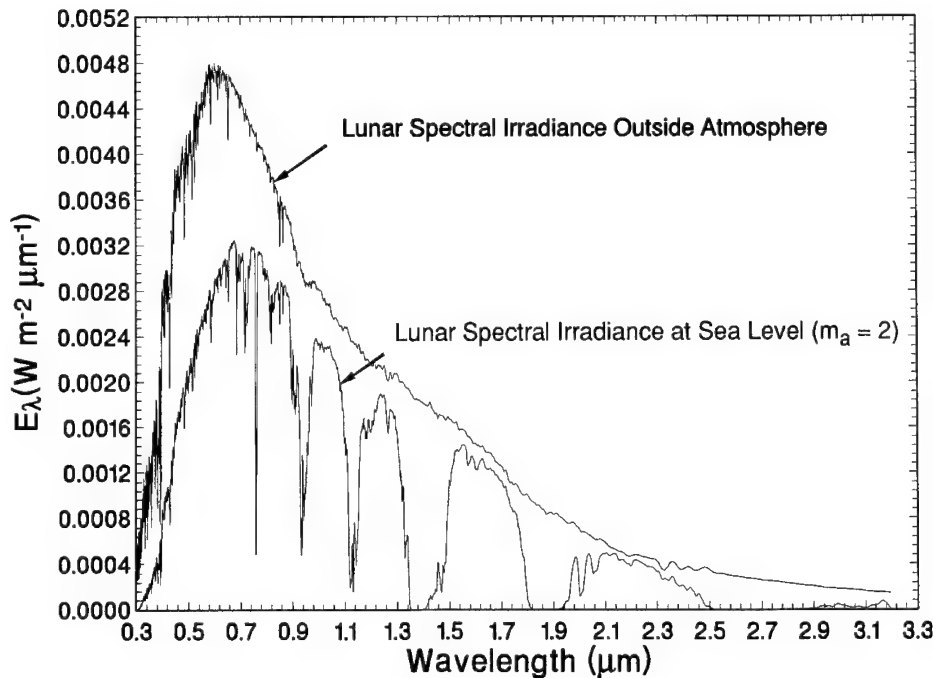


Fig. 3.12 Spectral irradiance normal to the rays of the full moon at sea level for air mass $m_a = 2$ as calculated by LOWTRAN.

- *Horizon*: The great circle defined by the intersection of the celestial and that plane which is perpendicular to the observer's plumb line at the position of the observer.
- *Meridian*: The great circle that is perpendicular to the horizon and passes through the zenith and the north celestial pole.
- *North point*: The northward point of intersection of the meridian and the horizon.
- *Vertical circle*: Any great circle that passes through the zenith and nadir and is therefore perpendicular to the horizon.
- *Hour circle*: Any great circle that passes through the north and south celestial poles and is therefore perpendicular to the celestial equator.
- *Circle of celestial latitude*: Any great circle that passes through the poles of the ecliptic and is therefore perpendicular to the ecliptic.
- *Galactic equator*: The great circle defined by the intersection of the celestial sphere and the projection of the plane of our galaxy. The plane of the galactic equator is inclined at an angle of $62^\circ 36'$ to the plane of the celestial equator.
- *North galactic pole*: The point of intersection of the celestial sphere with the northward prolongation of the rotation axis of the galaxy. The equatorial coordinates of this point are $\alpha = 12^{\text{h}}49^{\text{m}}$ and $\delta = 27^\circ 24'$ for the equinox 1950.0.
- *Galactic center*: The center of our galaxy has the equatorial coordinates $\alpha = 17^{\text{h}}42^{\text{m}}24^{\text{s}}$ and $\delta = -28^\circ 55'$ for the equinox 1950.0.

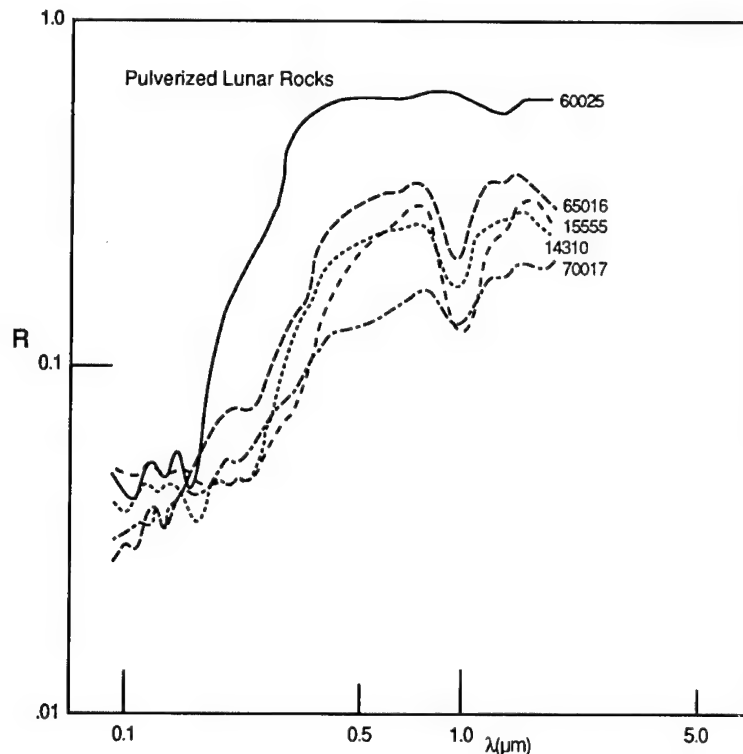


Fig. 3.13 Reflectance spectra versus wavelength of several lunar crystalline rocks (pulverized to finer than $74\ \mu\text{m}$). The samples are 60025 (anorthosite), 65016 (anorthositic gabbro), 15555 (low-Ti basalt), 14310 (KREEP basalt), and 70017 (high-Ti basalt).¹²

- *Circle of galactic latitude:* Great circle that passes through the galactic poles and is therefore perpendicular to the galactic equator.
- *The ecliptic coordinate system:* The ecliptic plane is the plane of symmetry for objects in the solar system. The ecliptic longitude λ is measured from the vernal equinox eastward along the ecliptic. The ecliptic latitude β is the angular distance from the ecliptic along a vertical great circle. Elongation angle ϵ is the angle along a great circle between the sun and the point in question.
- *The equatorial coordinate system:* The declination δ of the celestial object is the angle in degrees from the celestial equator to the object as measured along the hour circle that passes through the object. The declination is positive or negative, respectively, when measured north or south of the celestial equator. The right ascension α is the angle in degrees (or hours) measured from the vernal equinox along the celestial equator toward the east to the foot of the hour circle that passes through the object. The hour angle h is the angular distance in degrees (or hours) measured along the celestial equator from the foot of the meridian toward the west to the foot of the hour circle that passes through the object.
- *The galactic coordinate system:* The galactic latitude b of the celestial object is the angle in degrees from the galactic equator to the object as measured along the circle of galactic latitude that passes through the

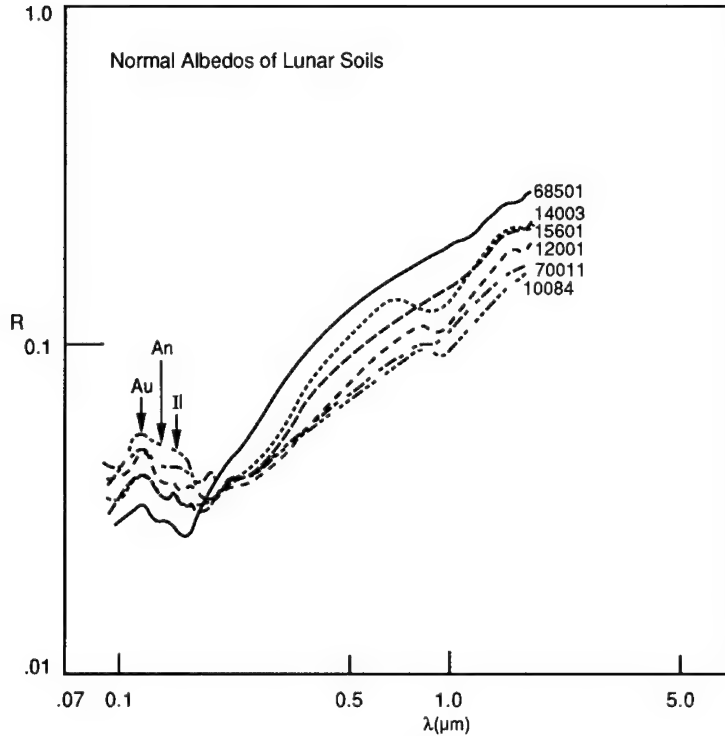


Fig. 3.14 Reflectance spectra versus wavelength of six Apollo lunar fines.¹³

object. The galactic latitude is positive or negative, respectively, when measured north or south of the galactic equator. The galactic longitude l is the angle in degrees measured eastward along the galactic equator from the galactic center to the foot of the circle of galactic latitude that passes through the object.

3.5.2 Cosmic Microwave Background¹⁶

Measurements from the Cosmic Background Explorer (COBE) satellite (launched in November 1989) indicate that the cosmic background temperature is 2.735 ± 0.06 K with no point deviating from its predicted value by more than 1%. Preliminary measurements completed over about 75% of the sky indicate no anisotropies at all to an accuracy of one part in 10^4 .

3.5.3 Celestial Background in the Visible Range

Stellar Magnitudes¹⁷. The brightness of celestial bodies is usually measured in magnitudes. The scale is defined so that the exoatmospheric irradiance $E(m_2)$ of any celestial body with apparent magnitude m_2 is related to the exoatmospheric irradiance $E(m_1)$ with apparent magnitude m_1 by

$$E(m_2) = E(m_1)10^{0.4(m_1 - m_2)} \quad (3.22)$$

In actual practice, the energy received from an object is measured over a finite band of wavelengths, and apparent magnitudes are designated by a subscript

that denotes the center wavelength used. The subscripts U, pg, B, V, and R denote, respectively, the ultraviolet, photographic, blue, yellow or visual, and red bands, and have center wavelengths given by¹⁵

$$\begin{aligned} m_U &= U = 3650 \text{ \AA} \\ m_{pg} &= 4400 \text{ \AA} \\ m_B &= B = 4350 \text{ \AA} \\ m_V &= V = 5500 \text{ \AA} \\ m_R &= 7000 \text{ \AA} . \end{aligned}$$

The effective wavelengths, effective bandwidths, and flux for a zero magnitude star within the respective band pass is given^{15,18} in Table 3.7.

A body that has a visual magnitude of $m_V = +1$ and $m_V = 0$ gives an exoatmospheric illuminance normal to the rays of $8.32 \times 10^{-11} \text{ lm cm}^{-2}$ and $2.65 \times 10^{-10} \text{ lm cm}^{-2}$, respectively.

The absolute magnitude M is defined as the apparent magnitude a star would have at a distance of 10 parsecs ($\text{pc} = 202,625 \text{ AU} = 3.09 \times 10^{18} \text{ cm}$). With R as the interstellar distance in kiloparsecs (kpc) and $A(R)$ the interstellar extinction in magnitudes to the star, the absolute and apparent magnitudes are related by

$$M = m - 10 - 5 \log_{10} R - A(R) . \quad (3.23)$$

Table 3.7 Definition of Zero Magnitude Spectral Flux Density as a Function of Wavelength (from Ref. 15)

Band	$\lambda_C (\mu\text{m})$	$\Delta\lambda_C (\mu\text{m})$	Flux ($m_\lambda=0$) $\text{W cm}^{-2}\mu\text{m}^{-1}$
U	0.365	0.068	4.27×10^{-12}
B	0.44	0.098	6.61×10^{-12}
V	0.55	0.089	3.72×10^{-12}
R	0.70	0.72	1.74×10^{-12}
I	0.88	0.24	8.32×10^{-13}
J	1.25	0.38	3.31×10^{-13}
H	1.65	0.30	1.28×10^{-13}
K	2.22	0.48	4.14×10^{-14}
L	3.6	0.70	6.38×10^{-15}
M	5.0	1.73	1.82×10^{-15}
N	10.6	4.33	8.7×10^{-17}
Q	21	5.8	6.5×10^{-18}

The interstellar extinction is given by¹⁹

$$A(R) = A_D \int_0^R \times \exp \left[-\frac{(R_0^2 + r^2 - 2rR_0 \cos l)^{1/2} - R_0}{h_a} - \frac{r \sin|b|}{\beta_a} \right] dr, \quad (3.24)$$

where

- β_a = vertical scale height = 0.1 kpc
- h_a = in plane scale height = 4.0 kpc
- $A_D = 0.07[2.2 \mu\text{m}/\lambda (\mu\text{m})]^2 \text{ mag kpc}^{-1}$
- R = distance to point from sun, kpc
- R_0 = distance of the sun from the galactic center = 8.5 kpc
- b = galactic latitude
- l = galactic longitude.

For the sun $M_U = 5.51$, $M_B = 5.41$, $M_V = 4.79$, $m_U = -26.06$, $m_B = -26.16$, and $m_V = -26.78$.

Common Radiometric Units in Astronomy. A common measure of radiance is the S_{10} unit defined as the number of equivalent tenth-magnitude stars per square degree; hence, $1 S_{10} = 1.23 \times 10^{-12} \text{ W cm}^{-2} \text{ sr}^{-1} \mu\text{m}^{-1}$ at $0.55 \mu\text{m}$. A Rayleigh is defined as a total volume emission rate of $1 \times 10^6 \text{ photons s}^{-1} \text{ cm}^{-2}$. Therefore, 1 Rayleigh corresponds to a surface brightness of $1/4\pi \times 10^6 \text{ photons s}^{-1} \text{ cm}^{-2} \text{ sr}^{-1}$. Thus, $1 S_{10} = 1.899 \times 10^6 \text{ photons s}^{-1} \text{ cm}^{-2} \text{ sr}^{-1}$ at $0.55 \mu\text{m}$.

Stellar Spectral Classes. The main stellar spectral classes^{14,20} are designated by the letters Q, P, W, O, B, A, F, G, K, M, S, R, and N. Each class is divided into 10 groups designated by a digit 0 to 9 placed after the capital letter for each class. When the spectra do not seem to form a continuous sequence, lowercase letters are used in place of numbers. Peculiarities in the spectra are designated by the prefix c, g, or d accordingly, as the emission lines are narrow, the stars are giants or dwarfs. The suffix letters n, s, e, ev, v, k, and pec denote, respectively, wide and diffuse (nebulous) lines, sharp lines, emission lines, variable spectrum, H and K lines of Ca^+ , and peculiar lines that tend to remove it from the class given. The main series from B to M contains 99% of apparently bright stars, while classifications P, W, O, Q, R, N, and S are comparatively rare. The criteria for the "Henry Draper" (HD) classification are given¹⁴ in Table 3.8.

Number of Stars. Table 3.9 shows²¹ the estimated number of stars brighter than a given magnitude for both photographic and visual magnitudes. From magnitude 0 to 18.5, the figures are based on direct observation; the values from magnitude 18.5 to 21 are extrapolated.

The photographic results are based on material such as photographs, star charts, and catalogs. The data for visual magnitudes are derived from the photographic results by allowing for the color of the stars. Very few stars are bluer than class A-O, for which the visual and photographic magnitudes are

Table 3.8 The "Henry Draper" (HD) Classification of Types O–M (from Ref. 14)

Type	Main Characteristics	Subtypes	HD Criteria	Typical Stars
O	Hottest Stars, Continuum Strong in UV	Oa Ob Oc Od Oe Oe5	O II λ 4650 Dominates He II λ 4686 Dominates } Emission Lines Narrower } Absorption Lines Dominate; Only He II, O II in Emission Si IV λ 4089 at Maximum O II λ 4649, He II λ 4686 Strong	BD + 35°4013 BD + 35°4001 BD + 36°3987 ξ Pup, λ Cep 29 CMa τ CMa
B	Neutral Helium Dominates	B0 B1 B2 B3 B5 B8 B9	C III λ 4650 at Maximum He I λ 4472 > O II λ 4649 He I Lines Are Maximum He II Lines Are Disappearing Si λ 4128 > He λ 4121 λ 4472 = Mg λ 4481 He I λ 4026 Just Visible	ε Ori β CMa, β Cen δ Ori, α Lup π^4 Ori, α Pav 19 Tau, ϕ Vel β Per, δ Gru λ Aql, λ Cen
A	Hydrogen Lines Decreasing From Maximum at A0	A0 A2 A3 A5	Balmer Lines at Maximum Ca II K=0.4 H δ K=0.8 H δ K>H δ	α CMi S CMa, ι Cen α PsA, τ^3 Eri β Tri, α Pic
F	Metallic Lines Becoming Noticeable	F0 F2 F5 F8	K=H+H δ G Band Becoming Noticeable G Band Becoming Continuous Balmer Lines Slightly Stronger Than in Sun	δ Gem, α Car π Sgr α CMi, ρ Pup β Vir, α For
G	Solar-Type Spectra	G0 G5	Ca λ 4227=H δ Fe λ 4325>Hy on Small-Scale Plates	α Aur, β Hya κ Gem, α Ret
K	Metallic Lines Dominate	K0 K2 K5	H and K at Maximum Strength Continuum Becoming Weak in Blue G Band No Longer Continuous	α Bov, α Phe β Cnc, ν Lib α Tau
M	TiO Bands	Ma Mb Mc Md	TiO Bands Noticeable Bands Conspicuous Spectrum Fluted by the Strong Bands Mira Variables, Hy, H δ in Emission	α Ori, α Hya ρ Per, γ Cru W Cyg, RX Aqr X Cyg, σ Cet

equal; but many stars are redder and have color indices of +1 magnitude or more. A list of stars brighter visually than the tenth magnitude, for example, will contain many red stars that are photographically of eleventh magnitude or fainter, and a great many that are photographically fainter than the tenth magnitude. On the other hand, a list of stars to the tenth photographic magnitude will contain a few blue stars that are visually below the tenth magnitude, but not many. The difference in the numbers in the two columns is thus explained. As seen by the table, this effect increases for the fainter stars, which are generally redder than the brighter ones. Table 3.10 shows²¹ the

Table 3.9 Estimated Total Number of Stars Brighter Than a Given Magnitude (from Ref. 21)

<i>Magnitude</i>	<i>Number of Stars</i>	
	<i>Photographic</i>	<i>Visual</i>
-1	—	1
0	—	2
1	—	12
2	—	40
3	—	140
4	360	530
5	1,030	1,620
6	2,940	4,850
7	8,200	14,300
8	22,800	41,000
9	62,000	117,000
10	166,000	324,000
11	431,000	870,000
12	1,100,000	2,270,000
13	2,720,000	5,700,000
14	6,500,000	13,800,000
15	15,000,000	32,000,000
16	33,000,000	71,000,000
17	70,000,000	150,000,000
18	143,000,000	296,000,000
19	275,000,000	560,000,000
20	505,000,000	1,000,000,000
21	890,000,000	—

percentage of stars in the six principal spectral classes for various ranges of magnitudes.

Galactic Concentration of Stars. Table 3.11 shows²¹ the number of stars per square degree brighter than a given photographic magnitude for different galactic latitudes. An approximation of the number of stars of a certain spectral class and magnitude range can be obtained by applying the data of Table 3.10 to Table 3.9, since Table 3.9 gives the estimated number of stars brighter than a given magnitude for each magnitude. For example, by interpolation of Table 3.9, one can estimate the number of stars brighter than magnitudes 7.25 and 8.25. The number of stars in the magnitude range 7.25 to 8.25 can be determined by subtraction. The percentage of stars of the six principal spectral classes for this range of magnitudes, as shown in Table 3.10, can be used to obtain the approximate number of stars in these spectral classes for this range of magnitudes.

Table 3.12 shows the average number of stars per 100 square degrees, near the galactic equator and in regions remote from it, for the six principal spectral classes.

Table 3.10 Percentage of Stars of Various Spectral Classes (from Ref. 21)

<i>Visual Magnitude</i>	<i>B-0 to B-5</i>	<i>B-8 to A-3</i>	<i>A-5 to F-2</i>	<i>F-5 to G-0</i>	<i>G-5 to K-2</i>	<i>K-5 to M-8</i>
<2.24	28	28	7	10	15	12
2.25 to 3.24	25	19	10	12	22	12
3.25 to 4.24	16	22	7	12	35	8
4.25 to 5.24	9	27	12	12	30	10
5.25 to 6.24	5	38	13	10	28	6
6.26 to 7.25	5	30	11	14	32	7
7.26 to 8.25	2	26	11	16	37	7
8.5 to 9.4	2	18	13	20	36	12
9.5 to 10.4	1	16	12	24	38	9
For all Magnitudes	2	29	9	21	33	6
<i>Photographic Magnitude</i>	<i>B-0 to B-5</i>	<i>B-6 to A-4</i>	<i>A-5 to F-4</i>	<i>F-5 to G-4</i>	<i>G-5 to K-4</i>	<i>K-5 to M-8</i>
8.5 to 9.5	2	31	16	24	24	3
9.5 to 10.5	1	24	16	31	26	3
10.5 to 11.5	1	17	13	40	27	3
11.5 to 12.5	0	10	13	47	26	3
12.5 to 13.5	0	3	10	58	26	2

Table 3.13 gives more detailed information on the distribution of stars by spectral class and magnitude. There are differences in the data of Tables 3.12 and 3.13 because somewhat different areas of the sky were considered in preparing the tables. For example, in arriving at an average galactic distribution, Table 3.12 considers the latitude from 40 to 90°, whereas Table 3.13 considers the latitude from 60 to 90°. The most important difference is that Table 3.13 has been prepared by selecting narrower ranges of stellar magnitude.

Galactic distribution is not presented for stars of magnitudes less than 5 because the total number of these stars is not large enough to make the concept of the number of stars per square degree meaningful.

Table 3.14, an index of apparent galactic concentration, has been prepared from Table 3.13 by taking the ratios of numbers of stars in low latitudes to numbers of stars in high latitudes. For a given spectral class, more stars are concentrated in the lower galactic latitudes as the galactic concentration index number becomes higher.

Spectral Distribution of Stellar Radiation. Figure 3.15 shows²¹ the relative spectral distribution of stellar radiation as a function of star class and surface temperature. The terrestrial exoatmospheric spectral irradiance $E_{\lambda}(\lambda)$ of a celestial body may be calculated if its visual magnitude m_v and its distribution temperature T_c (sometimes called color temperature) are known. In this case, distribution temperature is the blackbody temperature for which $M_{\lambda}(\lambda, T_c)$ is

Table 3.11 Number of Stars Per Square Degree Brighter Than Photographic Magnitude as a Function of Galactic Latitudes
(from Ref. 21)

Photographic Magnitude	+90°	+40°	+20°	+10°	0°	-10°	-20°	-40°	-90°
5.0	0.014	0.0175	0.023	0.031	0.059	0.045	0.032	0.0178	0.012
6.0	0.039	0.053	0.071	0.089	0.166	0.126	0.087	0.051	0.042
7.0	0.015	0.151	0.20	0.257	0.436	0.323	0.224	0.144	0.123
8.0	0.275	0.42	0.59	0.741	1.230	0.851	0.617	0.398	0.316
9.0	0.724	1.12	1.62	2.14	3.55	2.34	1.69	1.10	0.832
10.0	1.78	2.95	4.50	5.89	10.5	6.61	4.68	2.95	2.09
11.0	4.3	7.4	12.0	16.2	30.9	18.2	12.8	7.76	5.25
12.0	10.2	18.2	32.0	43.6	89.1	50.1	34.7	19.50	13.2
13.0	24.0	43.0	79.0	112.0	245.0	138.0	89.1	47.8	30.2
14.0	50.0	93.0	190.0	282.0	661.0	371.0	218.0	107.0	60.3
15.0	95.0	200.0	457.0	708.0	1660.0	977.0	525.0	218.0	104.0
16.0	182.0	407.0	1047.0	1778.0	3981.0	2455.0	1175.0	436.0	182.0
17.0	338.0	794.0	2291.0	4365.0	9120.0	5754.0	2512.0	832.0	302.0
18.0	616.0	1413.0	4677.0	9330.0	20890.0	2590.0	4786.0	1514.0	501.0
19.0	770.0	2180.0	6860.0	—	—	—	—	—	—
20.0	—	—	—	—	—	—	—	—	—
21.0	1670.0	5000.0	21200.0	—	—	—	—	—	—

Table 3.12 Galactic Concentration of Stars of the Principal Spectral Classes in 100 Square Degrees Near Galactic Equator (from Ref. 21)

<i>Stellar Magnitudes</i>	<i>Galactic Latitudes</i>	<i>B</i>	<i>A</i>	<i>F</i>	<i>G</i>	<i>K</i>	<i>M</i>	<i>Total</i>
Above 7 ^m .0	40° - 90°	0.2	6.6	3.0	3.4	10.2	1.5	24.9
	0°	10.8	21.1	5.1	5.1	15.1	3.9	61.1
7 ^m .0 to 8 ^m .25	40° - 90°	0.1	6.6	9.5	16.4	32.8	6.1	71.5
	0°	18.9	75.8	13.6	20.9	53.9	13.6	196.7

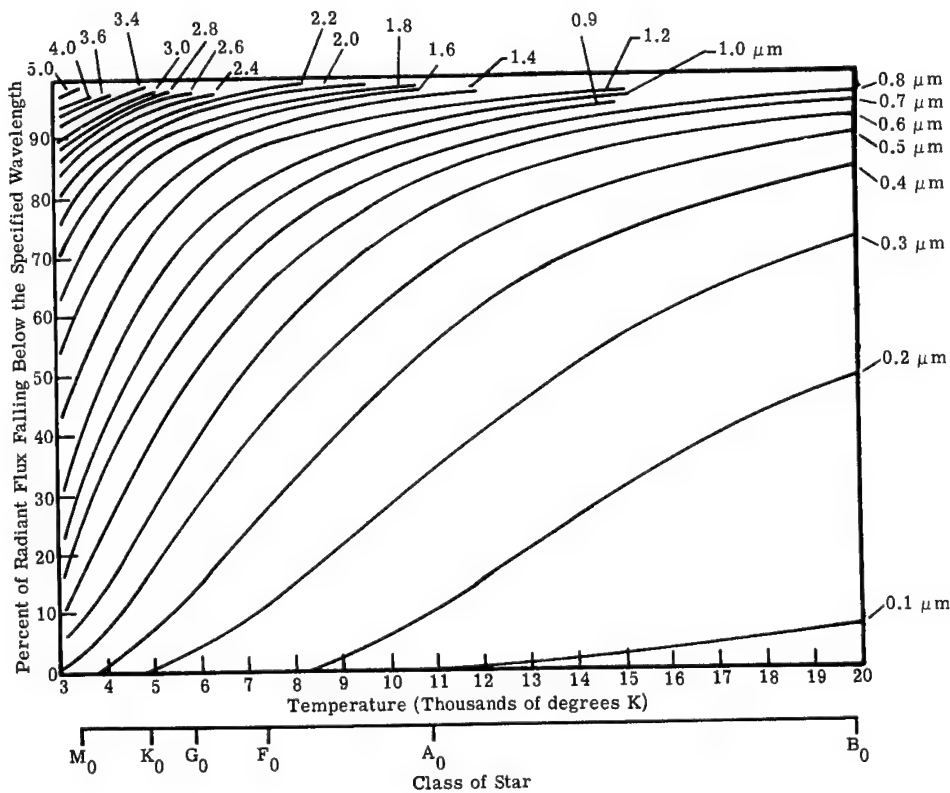
Table 3.13 Galactic Concentration of Stars of Various Spectral Classes (from Ref. 21)

<i>Spectrum Visual Magnitude</i>	<i>Galactic Latitude 0° to 5°</i>					
	<i>B</i>	<i>A</i>	<i>F</i>	<i>G</i>	<i>K</i>	<i>M</i>
<6.0	4.5	6.0	1.7	2.1	3.5	1.3
6.0 to 7.0	6.3	15.0	3.4	3.0	12.0	2.6
7.0 to 8.25	19.0	76.0	14.0	21.0	54.0	14.0
8.5 to 9.4	46.0	190.0	85.0	96.0	200.0	57.0
9.5 to 10.4	82.0	610.0	240.0	310.0	490.0	150.0
<i>Photographic Magnitude</i>						
9.5 to 10.5	38.0	510.0	150.0	220.0	180.0	19.0
10.5 to 11.5	87.0	970.0	430.0	720.0	460.0	42.0
11.5 to 12.5	100.0	1390.0	1200.0	1960.0	940.0	140.0
<i>Visual Magnitude</i>	<i>Galactic Latitude 60° to 90°</i>					
	<i>B</i>	<i>A</i>	<i>F</i>	<i>G</i>	<i>K</i>	<i>M</i>
<6.0	0.2	2.6	0.8	1.0	2.9	0.7
6.0 to 7.0	0.0	3.8	1.8	2.4	7.5	0.7
7.0 to 8.25	0.0	7.4	9.2	16.0	32.0	6.3
8.5 to 9.4	0.0	8.0	20.0	83.0	75.0	0.0
9.5 to 10.4	0.0	8.0	20.0	170.0	210.0	16.0
<i>Photographic Magnitude</i>						
9.5 to 10.5	0.0	9.0	32.0	120.0	75.0	9.0
10.5 to 11.5	0.0	10.0	27.0	290.0	160.0	12.0
11.5 to 12.5	0.9	14.0	34.0	680.0	270.0	26.0

Table 3.14 Index of Apparent Galactic Concentration* (from Ref. 21)

<i>Visual Magnitude</i>	<i>B</i>	<i>A</i>	<i>F</i>	<i>G</i>	<i>K</i>	<i>M</i>
<6.0	22.0	2.8	2.3	2.1	1.2	1.9
6.0 to 7.0	—	4.0	1.9	1.2	1.5	3.7
7.0 to 8.25	—	10.0	1.5	1.3	1.7	2.2
8.5 to 9.4	—	24.0	4.2	1.2	2.7	—
9.5 to 10.4	—	76.0	12.0	1.8	2.3	0.9
<i>Photographic Magnitude</i>						
9.5 to 10.5	—	56.0	4.8	1.8	2.4	2.1
10.5 to 11.5	—	97.0	16.0	2.5	2.9	3.5
11.5 to 12.5	—	99.0	35.0	2.9	3.5	5.5

*The irregularities here are attributable in part to inadequate sampling.

**Fig. 3.15** Relative spectral distribution of stellar radiation as a function of star classes.²¹

spectrally best fit to $E_\lambda(\lambda)$ in the spectral range of interest where $M_\lambda(\lambda, T_c)$ is given by Planck's radiation law. The defining relation between exoatmospheric illuminance and visual magnitude is

$$m_v = -2.5 \log_{10} \left[\frac{E_v(m_v)}{E_v(m_v = 0)} \right], \quad (3.25)$$

where $E_v(m_v = 0)$ for zero magnitude is $2.65 \times 10^{-6} \text{ lm m}^{-2}$.

The luminous exitance $M_v(T_c)$ and total radiant exitance $M(T_c)$ are found by using Planck's radiation law and the color temperature:

$$M_v(T_c) = 680 \int_0^\infty M_\lambda(\lambda, T_c) V(\lambda) d\lambda, \quad (3.26)$$

where $V(\lambda)$ is the spectral luminous efficiency^{7,20} and

$$M(T_c) = \int_0^\infty M_\lambda(\lambda, T_c) d\lambda. \quad (3.27)$$

Assuming no spectrally selective absorption in the path between the celestial body and earth, one may relate luminous and radiant quantities by

$$\frac{E_v}{E} = \frac{M_v(T_c)}{M(T_c)} \quad (3.28)$$

and also relate spectral quantities to the total by

$$\frac{E_\lambda(\lambda)}{E} = \frac{M_\lambda(\lambda, T_c)}{M(T_c)} \quad (3.29)$$

because only the geometric factors of size and distance are involved. Therefore,

$$E_\lambda(\lambda) = M_\lambda(\lambda, T_c) \frac{E_v(m_v)}{M_v(T_c)}, \quad (3.30)$$

where $M_\lambda(\lambda, T_c)$ is the spectral exitance given by Planck's radiation law; $E_v(m_v)$ is derived from Eq. (3.25); and $M_v(T_c)$ is derived from Eq. (3.26).

The relationship between peak spectral irradiance, color temperature, and visual magnitude from Larmore¹⁷ is shown in Fig. 3.16. The relations used pertain to irradiance received above the atmosphere. Values for absorption by the atmosphere in the various spectral regions can be readily applied to the chart values.

Table 3.15 shows the visual magnitude and color temperature for the brightest celestial bodies and also for the important red stars. The list contains all the stars in Schlesinger's *Catalog of Bright Stars* that give an irradiance of at

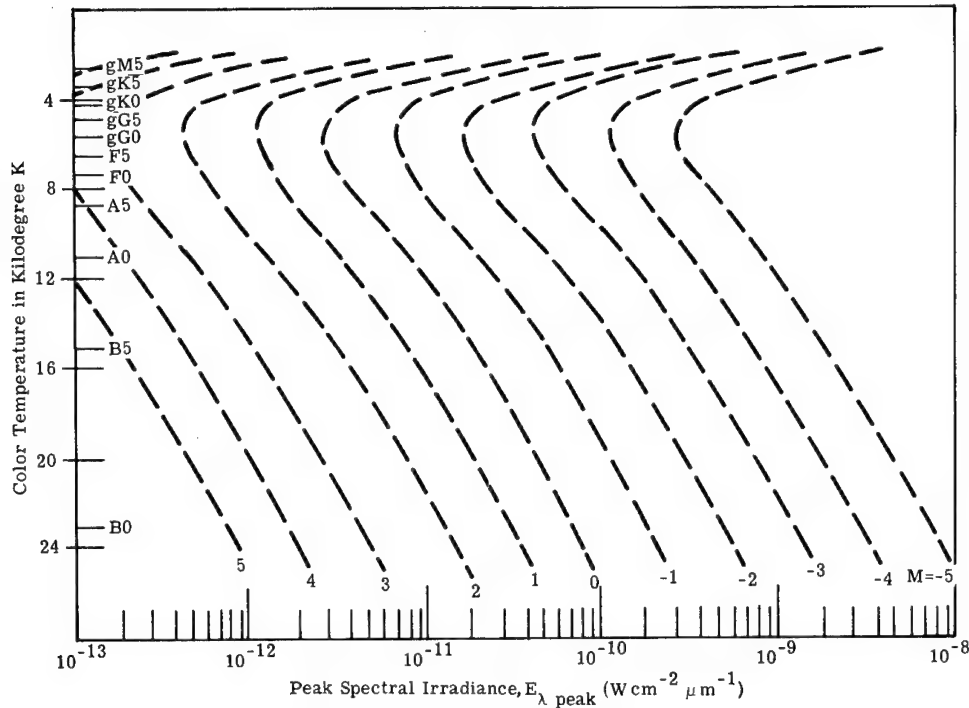


Fig. 3.16 Peak spectral irradiance from values of visual magnitude and effective temperature or spectral class.

least $10^{-12} \text{ W cm}^{-2}$ in either the PbS region, 1 to 3 μm , or the bolometer region, 0.3 to 13.5 μm . (See also the revised edition of *Catalog of Bright Stars* by Hoffleit.) Using Fig. 3.16 and Planck's law, one may obtain the spectral irradiance curves for any star or planet. In determining the spectral irradiance of the moon and planets, one may assume an effective temperature of 5900 K for reflected sunlight. Thermal emission must be added.

One may have to use the visual magnitudes of bright stars to compute their infrared irradiance. Computations using visual magnitudes will not adequately predict the irradiance from massive cool stars whose infrared magnitude might far exceed their visual magnitude.²² For additional information, see Refs. 18, 20, and 23 through 41.

3.5.4 Celestial Background in the Spectral Range from 2.0 to 100.0 μm

Infrared emission from solid material (dust, ice, metal condensates, etc.) distributed throughout our galaxy becomes increasingly important at wavelengths longer than about 4 μm . While it is true that the infrared flux from most main sequence stars (A through M dwarfs) is fairly well represented by the spectrum of a blackbody at the star's distribution temperature, many giant and supergiant stars show large amounts of infrared flux in excess of that predicted on the basis of the star's distribution temperature. Furthermore, the spectrum is nonthermal in shape, showing emission peaks characteristic of particulate materials (such as carbon and silicates) in a cloud or shell surrounding the star. Stars of the early spectral type showing emission lines in

Table 3.15 Visual Magnitudes and Color Temperature of Planets and the Brightest Visual and Red Stars (from Ref. 17)

<i>Name</i>	<i>Visual Magnitude, m_V</i>	<i>Color Temperature, T (K)</i>
1. Moon (full)	-12.2	5,900
<i>Planets</i>		
2. Venus (at brightest)	- 4.28	5,900
3. Mars (at brightest)	- 2.25	5,900
4. Jupiter (at brightest)	- 2.25	5,900
5. Mercury (at brightest)	- 1.8	5,900
6. Saturn (at brightest)	- 0.93	5,900
<i>Stars</i>		
1. Sirius	- 1.60	11,200
2. Canopus	- 0.82	6,200
3. Rigel Kent (double)	0.01	4,700
4. Vega	0.14	11,200
5. Capella	0.21	4,700
6. Arcturus	0.24	3,750
7. Rigel	0.34	13,000
8. Procyon	0.48	5,450
9. Achernar	0.60	15,000
10. β Centauri	0.86	23,000
11. Altair	0.89	7,500
12. Betelguex (variable)	0.92	2,810
13. Aldebaran	1.06	3,130
14. Pollux	1.21	3,750
15. Antares	1.22	2,900
16. α Crucis	1.61	2,810
17. Mira (variable)	1.70	2,390
18. β Gruis	2.24	2,810
19. R. Hydrae (variable)	3.60	2,250

the visible and ultraviolet (e.g., B stars) are often found to have strong infrared excesses due to free-free transitions of electrons and molecules in their extended atmospheres.

At wavelengths longer than 10 μm , emission nebulae, such as regions of ionized hydrogen gas, compact nebulae, and planetary nebulae, become strong sources of infrared radiation. The spectral envelopes of these sources are characteristic of the emission from dust mixed with a highly excited gas and often show emission lines such as that of Ne^+ at 12.8 μm . Between 7 and 30 μm , H II regions are the brightest discrete objects in the galaxy. Dust mixed with and surrounding gas ionized by the embedded hot star(s) absorbs the visible and ultraviolet stellar radiation and reemits the energy in the infrared.

The celestial background in the infrared is also discussed by Price and Murdock in Chapter 25 of Ref. 15.

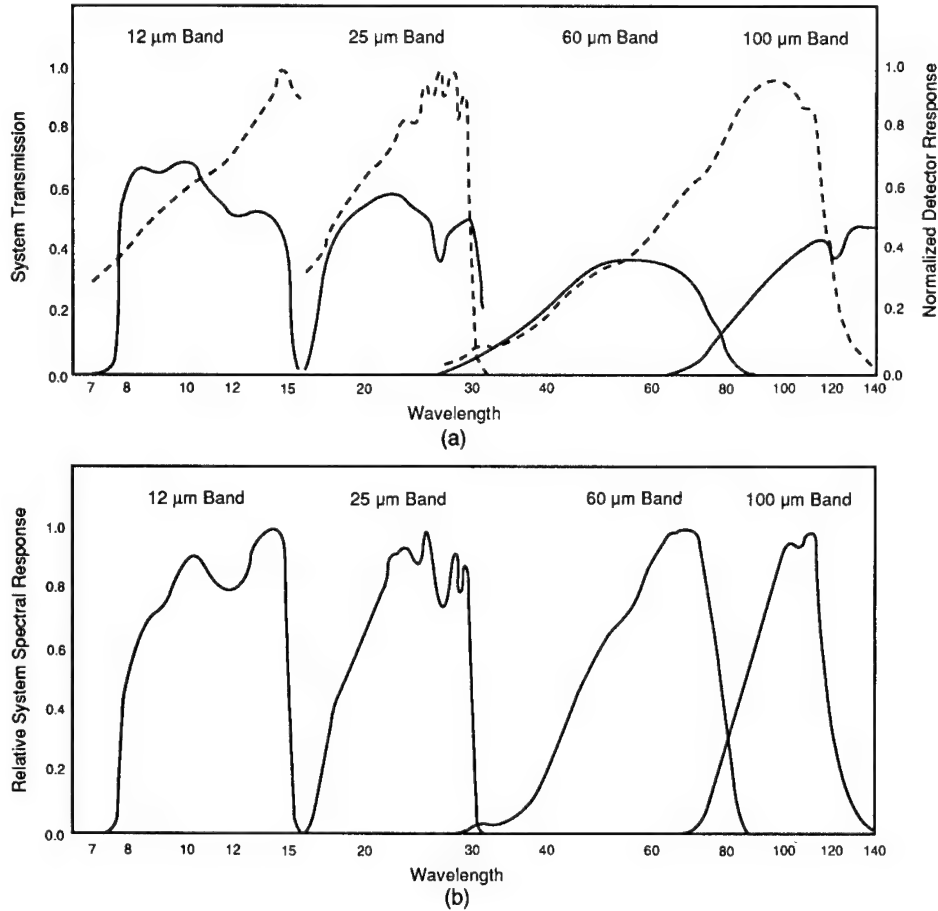


Fig. 3.17 (a) Response versus wavelength of optical components. Solid lines show the transmission of filters and lenses. Dashed lines show relative detector response to constant energy input. (b) Relative system spectral response.³⁰

Infrared Astronomical Satellite (IRAS). The primary mission of the Infrared Astronomical Satellite (IRAS)³⁰ was to conduct a sensitive and unbiased survey of the sky in four wavelength bands at 12, 25, 60, and 100 μm (Fig. 3.17). The IRAS survey was conducted over a 10-month period starting early February 1983 and covered about 95% of the sky at least twice. Figure 3.18 is a representation, in equatorial coordinates, of the sky area covered in the IRAS survey. The survey was conducted with the telescope field held to within 30° of the radial vector of the satellite in its sun synchronous orbit. Thus, the *ecliptic coordinate system* was the fundamental reference frame with the majority of scans at elongations between 70 and 101°. A small number of scans late in the survey included solar elongations between 60 and 120°. The survey is complete over most of the sky to the flux level of 0.4 Jy at 12 and 25 μm, 0.5 Jy at 60 μm, and 2.5 Jy at 100 μm.^a The angular resolution of the instru-

^aThe IRAS Point Source Catalog uses as its unit of flux density the Jansky (Jy). Janskys may be converted to spectral irradiance by the relation $E_\lambda = 3.0 \times 10^{-16} \lambda^{-2} \text{ Jy}$ where λ is the wavelength in microns, and E_λ is in $\text{W cm}^{-2} \mu\text{m}^{-1}$. At 12 and 25 μm, $1.5 \text{ Jy} = 3.125 \times 10^{-18}$ and $7.2 \times 10^{-19} \text{ W cm}^{-2} \mu\text{m}^{-1}$, respectively.

Equatorial Right Ascension and Declination

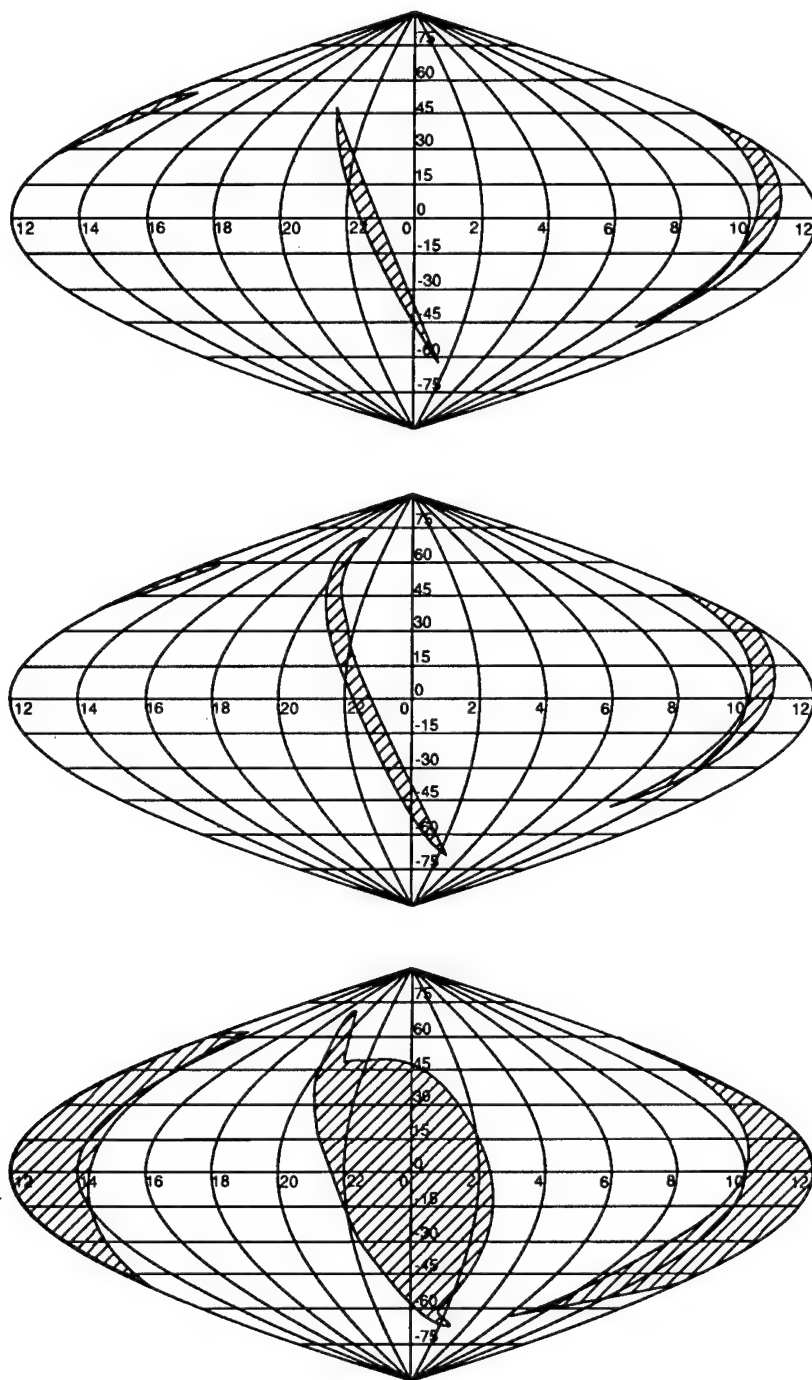


Fig. 3.18 Sky coverage of the IRAS survey. Three plots of the entire sky are shown with an equal area projection in equatorial coordinates.³⁰

ment varied between 0.23×1.3 mr at $12 \mu\text{m}$ to 0.9×1.5 mrad at $100 \mu\text{m}$. Near the galactic plane, where the source density is much higher, the IRAS sensor was "confusion limited" in the 12- and $25\text{-}\mu\text{m}$ bands at source densities exceeding 45 sources per square degree and only the brightest, highly confirmed sources are included in the IRAS Point Source Catalog. The survey was confusion noise limited within about 10° of the galactic plane and in several areas of the sky such as the Ophiuchus and Orion-Taurus regions (high stellar density areas). The interstellar dust (infrared cirrus) and galaxies dominate the celestial background at the longer wavelengths. Estimates are that almost half of the $100\text{-}\mu\text{m}$ listings in the IRAS Point Source Catalog are actually due to knots in the cirrus. Although concentrated near the galactic plane, the cirrus can be found almost all the way up to the galactic poles. About 25,000 galaxies were detected by IRAS, only half of which were previously cataloged. In general, the galaxies, mostly late-type spirals, are readily detected at $60 \mu\text{m}$ and are the dominant type of object at this wavelength away from the galactic plane.

Density of Galactic Infrared Point Sources. Walker and Sears³¹ have developed an empirical model for the galactic point source distribution from the observed sources listed in the IRAS Point Source Catalog. The model has been developed based on counts of point sources observed at 12 and $25 \mu\text{m}$. The major assumptions of the model follow: (1) The number of sources per square degree brighter than a fixed irradiance is a smoothly varying function of galactic latitude and longitude. This implies that density enhancements due to spiral structure or local features can be averaged. (2) The mean relative spectral energy distribution of the sources can be represented by the shape of a 3750 K Planckian radiator plus an infrared excess with spectral index varying smoothly with galactic latitude. (3) The galaxy is north-south symmetrical in source density at about 0° galactic latitude, and is east-west symmetrical at about 0° galactic longitude.

The model can be used with reasonable confidence in the region from about 2.0 to $40.0 \mu\text{m}$. The model is most uncertain in the galactic longitude range $0^\circ \leq l \leq 90^\circ$ and $270^\circ \leq l \leq 360^\circ$ for galactic latitudes $\pm 3^\circ$ of the galactic equator due to the uncertainties caused by source confusion in the IRAS data. Uncertainties grow for all positions in the galaxy as the threshold is decreased below that at which the data were derived, $\approx 2.5 \times 10^{-18} \text{ W cm}^{-2} \mu\text{m}^{-1}$ at $12 \mu\text{m}$.

Defining $N_\lambda[s(b)]$ as the number of sources per square degree brighter than the irradiance at wavelength λ in micrometers as a function of spectral index $s(b)$, an empirical relation derived from the IRAS Point Source Catalog is

$$\log N_\lambda[s(b)] = \log[A(b,l)] + B(b,l) \log\{E_{12}[\lambda, s(b)]\}, \quad (3.31)$$

where

$$\begin{aligned} E_{12}[\lambda, s(b)] &= \text{equivalent spectral irradiance at } 12 \mu\text{m producing} \\ &\quad N_\lambda[s(b)] \text{ sources per square degree, Jy} \\ b &= \text{galactic latitude, } 0^\circ \leq b \leq 90^\circ \\ l &= \text{galactic longitude in degrees } 0^\circ \leq l \leq 180^\circ \end{aligned}$$

and

$$\log[A(b,l)] = 0.000488l - 0.78 + \frac{0.000061l^2 - 0.02082l + 3.0214}{\left[1 + \left(\frac{b}{12}\right)^{1.4}\right]}, \quad (3.32)$$

$$B(b,l) = (-0.00978l + 0.88) \left[1.0 - \exp\left(-\frac{b}{8.0 - 0.05l}\right)\right] + (0.00978l - 1.8) \quad (3.33)$$

for $0^\circ \leq l \leq 90^\circ$.

For $l > 90^\circ$, $B = -0.92$. It is the role of the spectral index to extend the model to other wavelengths. To do so, the spectral energy distribution of the mean ensemble of sources must be known. A model that is in qualitative agreement with existing observations of late-type stars is obtained through the ratio of the irradiance at 25 μm to the irradiance at 12 μm that produced the same number N sources per square degree:

$$s = \frac{\log\left(\frac{E_{12}}{E_{25}}\right)}{\log\left(\frac{12}{25}\right)}. \quad (3.34)$$

The spectral index $s(b)$ is defined as the ratio of the 12- μm spectral irradiance to the 25- μm spectral irradiance that produced the same source count N (N sources brighter than $E_{25} = 1.5$ Jy at 25 μm). The spectral index as a function of galactic latitude is given by

$$s(b) = -0.22 - 1.38 \left[1.0 - \exp\left(-\frac{b}{15}\right)\right]. \quad (3.35)$$

The infrared spectrum is modeled as a composite of a stellar photosphere plus an infrared excess due to a low-temperature shell of dust surrounding the star. Both are assumed to radiate as blackbodies. If E_λ is the flux received from the source at wavelength λ , then the flux at 12 μm is given by

$$E_{12}[\lambda, s(b)] = E_\lambda \frac{M_\lambda(\text{BB}, 12, T_{\text{star}}) + pM_\lambda(\text{BB}, 12, T_{\text{shell}})}{M_\lambda(\text{BB}, \lambda, T_{\text{star}}) + pM_\lambda(\text{BB}, \lambda, T_{\text{shell}})}. \quad (3.36)$$

Here $M_\lambda(\text{BB}, \lambda, T)$ is the blackbody spectral exitance ($T_{\text{star}} = 3750$ K and $T_{\text{shell}} = 300$ K) and p is the ratio of the solid angle subtended by the shell to that subtended by the star and is given by

$$p = \frac{M_\lambda(\text{BB}, 12, T_{\text{star}}) - rM_\lambda(\text{BB}, 25, T_{\text{star}})}{rM_\lambda(\text{BB}, 25, T_{\text{shell}}) - M_\lambda(\text{BB}, 12, T_{\text{shell}})} \quad (3.37)$$

and $r = E_{12}/E_{25}$ determined by Eqs. (3.34) and (3.35). This model was used to generate Tables 3.16 to 3.23 with spectral irradiance in units of $\text{W cm}^{-2} \mu\text{m}^{-1}$.

Density of Extragalactic Infrared Sources. Extragalactic sources³² are significant contributors to the background at the fainter levels and longer wavelengths. Visual star counts have been extrapolated into the infrared by dividing the galactic background into four categories: Seyfert galaxies type 1 and 2, emission line, and normal spirals. The number of extragalactic sources per square degree brighter than apparent magnitude m is given by (λ in micrometers)

$$N_G(\text{Seyfert 1}) = 4 \times 10^{-6} \left(\frac{\lambda}{10} \right)^{3.8} 10^{0.6(m-A_G)}, \quad (3.38)$$

$$N_G(\text{Seyfert 2}) = 3.4 \times 10^{-6} \left(\frac{\lambda}{10} \right)^5 10^{0.6(m-A_G)}, \quad (3.39)$$

$$N_G(\text{normal} + \text{emission line}) = 8.3 \times 10^{-6} \left(\frac{\lambda}{10} \right)^{5.4} 10^{0.6(m-A_G)}, \quad (3.40)$$

where A_G is the interstellar extinction obtained by integrating Eq. (3.24) and is

$$A_G = \frac{0.07 \left(\frac{2.2}{\lambda} \right)^2}{\sin|b| + 0.01 (2 - \cos l)}, \quad (3.41)$$

where b is the galactic latitude and l is galactic longitude.

Diffuse Background Radiance Caused by Extragalactic Sources. For a homogeneous, isotropic, expanding universe,^{14,34} an observer only detects radiation from distances out to cH_0^{-1} , where H_0 is Hubble's constant. The background radiance L_G , caused by the integrated light from all extragalactic sources, is given by

$$L_G = \frac{n_G c}{4\pi H_0} \sum_{i=1}^m \Omega_i \Phi_{\lambda_i}, \quad (3.42)$$

where

$$\begin{aligned} L_G &= \text{extragalactic background radiance, } \text{W cm}^{-2} \text{ sr}^{-1} \\ n_G &= \text{number density of galaxies, cm}^{-3} \\ H_0 &= \text{Hubble constant}^b \end{aligned}$$

^bThe Hubble constant is $100 h \text{ km s}^{-1} \text{ Mpc}^{-1}$ (as of 1990) where $0.4 \leq h \leq 1.0$ and continually changes with new measurements.

Table 3.16 Number of Sources Per Square Degree with Greater Spectral Irradiance Specified at Left at 2 μm for a Given Latitude and Longitude in $\text{W cm}^{-2} \mu\text{m}^{-1}$ (from Ref. 31)

Spectral Irradiance	Galactic Latitude									Galactic Longitude
	0.0	2.0	5.0	10.0	20.0	30.0	45.0	60.0	90.0	
1.0E-14	2.4E-01 2.2E-01 3.5E-01 1.6E-01	3.6E-01 2.5E-01 2.3E-01 1.1E-01	3.0E-01 1.9E-01 1.3E-01 7.0E-02	2.0E-01 1.2E-01 7.8E-02 5.2E-02	1.1E-01 7.4E-02 5.2E-02 4.3E-02	6.1E-02 4.5E-02 3.6E-02 3.2E-02	3.5E-02 2.9E-02 2.6E-02 2.5E-02	2.6E-02 2.3E-02 2.1E-02 2.1E-02	1.8E-02 1.7E-02 1.7E-02 1.7E-02	0.0 45.0 90.0 180.0
1.0E-15	1.5E+01 5.0E+00 2.9E+00 1.3E+00	1.5E+01 4.2E+00 1.9E+00 9.1E-01	7.5E+00 2.4E+00 1.1E+00 5.8E-01	3.0E+00 1.2E+00 6.5E-01 4.3E-01	1.1E+00 6.3E-01 4.4E-01 3.6E-01	5.3E-01 3.7E-01 3.0E-01 2.7E-01	3.0E-01 2.4E-01 2.1E-01 2.1E-01	2.2E-01 1.9E-01 1.8E-01 1.8E-01	1.5E-01 1.4E-01 1.4E-01 1.4E-01	0.0 45.0 90.0 180.0
1.0E-16	9.6E+02 1.1E+02 2.4E+01 1.1E+01	5.9E+02 7.1E+01 1.6E+01 7.6E+00	1.8E+02 3.0E+01 8.8E+00 4.8E+00	4.5E+01 1.2E+01 5.4E+00 3.6E+00	1.1E+01 5.4E+00 3.6E+00 3.0E+00	4.6E+00 3.1E+00 2.5E+00 2.2E+00	2.5E+00 2.0E+00 1.8E+00 1.7E+00	1.8E+00 1.6E+00 1.5E+00 1.5E+00	1.2E+00 1.2E+00 1.1E+00 1.2E+00	0.0 45.0 90.0 180.0
1.0E-17	6.0E+04 2.6E+03 2.0E+02 9.0E+01	2.4E+04 1.2E+03 1.3E+02 6.3E+01	4.5E+03 3.8E+02 7.3E+01 4.0E+01	6.6E+02 1.2E+02 4.5E+01 3.0E+01	1.0E+02 4.7E+01 3.0E+01 2.5E+01	4.0E+01 2.6E+01 2.1E+01 1.9E+01	2.1E+01 1.7E+01 1.5E+01 1.4E+01	1.5E+01 1.3E+01 1.2E+01 1.2E+01	1.0E+01 9.7E+00 9.5E+00 1.0E+01	0.0 45.0 90.0 180.0
1.0E-18	3.8E+06 6.0E+04 1.7E+03 7.5E+02	9.5E+05 2.1E+04 1.1E+03 5.2E+02	1.1E+05 4.8E+03 6.1E+02 3.4E+02	9.9E+03 1.2E+03 3.7E+02 2.5E+02	1.0E+03 4.0E+02 2.5E+02 2.1E+02	3.5E+02 2.2E+02 1.7E+02 1.6E+02	1.7E+02 1.4E+02 1.2E+02 1.2E+02	1.2E+02 1.1E+02 1.0E+02 1.0E+02	8.5E+01 8.1E+01 7.9E+01 8.3E+01	0.0 45.0 90.0 180.0
1.0E-19	2.4E+08 1.4E+06 1.4E+04 6.2E+03	3.8E+07 3.5E+05 9.0E+03 4.4E+03	2.7E+06 6.2E+04 5.1E+03 2.8E+03	1.5E+05 1.2E+04 3.1E+03 2.1E+03	1.0E+04 3.4E+03 2.1E+03 1.7E+03	3.1E+03 1.8E+03 1.4E+03 1.3E+03	1.5E+03 1.2E+03 1.0E+03 1.0E+03	1.0E+03 9.1E+02 8.4E+02 8.6E+02	7.1E+02 6.7E+02 6.6E+02 6.9E+02	0.0 45.0 90.0 180.0
1.0E-20	1.5E+10 3.1E+07 1.1E+05 5.2E+04	1.5E+09 6.0E+06 7.5E+04 3.6E+04	6.7E+07 7.8E+05 4.2E+04 2.3E+04	2.2E+06 1.2E+05 2.6E+04 1.7E+04	9.9E+04 2.9E+04 1.7E+04 1.4E+04	2.7E+04 1.5E+04 1.2E+04 1.1E+04	1.2E+04 9.7E+03 8.5E+03 8.3E+03	8.6E+03 7.5E+03 7.0E+03 7.1E+03	5.9E+03 5.6E+03 5.5E+03 5.8E+03	0.0 45.0 90.0 180.0

Table 3.17 Number of Sources Per Square Degree with Greater Spectral Irradiance Specified at Left at 4 μm for a Given Latitude and Longitude in $\text{W cm}^{-2} \mu\text{m}^{-1}$ (from Ref. 31)

Spectral Irradiance	Galactic Latitude									Galactic Longitude
	0.0	2.0	5.0	10.0	20.0	30.0	45.0	60.0	90.0	
1.0E-14	4.8E-03	1.1E-02	1.5E-02	1.6E-02	1.3E-02	7.8E-03	4.7E-03	3.5E-03	2.4E-03	0.0
	1.1E-02	1.7E-02	1.7E-02	1.4E-02	9.6E-03	6.0E-03	3.9E-03	3.1E-03	2.3E-03	45.0
	4.7E-02	3.1E-02	1.7E-02	1.0E-02	7.0E-03	4.8E-03	3.5E-03	2.8E-03	2.2E-03	90.0
	2.1E-02	1.5E-02	9.4E-03	7.0E-03	5.8E-03	4.4E-03	3.4E-03	2.9E-03	2.3E-03	180.0
1.0E-15	3.0E-01	4.4E-01	3.6E-01	2.3E-01	1.2E-01	6.8E-02	4.0E-02	2.9E-02	2.0E-02	0.0
	2.6E-01	2.9E-01	2.1E-01	1.4E-01	8.2E-02	5.0E-02	3.3E-02	2.5E-02	1.9E-02	45.0
	3.9E-01	2.5E-01	1.4E-01	8.7E-02	5.9E-02	4.0E-02	2.9E-02	2.4E-02	1.8E-02	90.0
	1.8E-01	1.2E-01	7.8E-02	5.8E-02	4.8E-02	3.6E-02	2.8E-02	2.4E-02	1.9E-02	180.0
1.0E-16	1.9E+01	1.8E+01	8.9E+00	3.5E+00	1.2E+00	5.9E-01	3.3E-01	2.4E-01	1.7E-01	0.0
	5.9E+00	4.9E+00	2.7E+00	1.4E+00	7.1E-01	4.2E-01	2.7E-01	2.1E-01	1.6E-01	45.0
	3.2E+00	2.1E+00	1.2E+00	7.2E-01	4.9E-01	3.3E-01	2.4E-01	2.0E-01	1.5E-01	90.0
	1.5E+00	1.0E+00	6.5E-01	4.8E-01	4.0E-01	3.0E-01	2.3E-01	2.0E-01	1.6E-01	180.0
1.0E-17	1.2E+03	7.1E+02	2.2E+02	5.1E+01	1.2E+01	5.2E+00	2.8E+00	2.0E+00	1.4E+00	0.0
	1.4E+02	8.3E+01	3.4E+01	1.4E+01	6.1E+00	3.5E+00	2.3E+00	1.8E+00	1.3E+00	45.0
	2.7E+01	1.8E+01	9.8E+00	6.0E+00	4.1E+00	2.8E+00	2.0E+00	1.6E+00	1.3E+00	90.0
	1.2E+01	8.5E+00	5.4E+00	4.0E+00	3.3E+00	2.5E+00	1.9E+00	1.7E+00	1.3E+00	180.0
1.0E-18	7.6E+04	2.9E+04	5.4E+03	7.7E+02	1.2E+02	4.5E+01	2.3E+01	1.7E+01	1.1E+01	0.0
	3.1E+03	1.4E+03	4.4E+02	1.4E+02	5.2E+01	2.9E+01	1.9E+01	1.5E+01	1.1E+01	45.0
	2.2E+02	1.5E+02	8.2E+01	5.0E+01	3.4E+01	2.3E+01	1.7E+01	1.4E+01	1.1E+01	90.0
	1.0E+02	7.0E+01	4.5E+01	3.3E+01	2.8E+01	2.1E+01	1.6E+01	1.4E+01	1.1E+01	180.0
1.0E-19	4.8E+06	1.2E+06	1.3E+05	1.1E+04	1.2E+03	3.9E+02	2.0E+02	1.4E+02	9.5E+01	0.0
	7.1E+04	2.4E+04	5.5E+03	1.4E+03	4.5E+02	2.4E+02	1.6E+02	1.2E+02	9.0E+01	45.0
	1.9E+03	1.2E+03	6.8E+02	4.2E+02	2.8E+02	1.9E+02	1.4E+02	1.1E+02	8.8E+01	90.0
	8.4E+02	5.9E+02	3.8E+02	2.8E+02	2.3E+02	1.7E+02	1.3E+02	1.1E+02	9.3E+01	180.0
1.0E-20	3.0E+08	4.7E+07	3.2E+06	1.7E+05	1.1E+04	3.4E+03	1.6E+03	1.2E+03	7.9E+02	0.0
	1.6E+06	4.1E+05	7.1E+04	1.3E+04	3.8E+03	2.0E+03	1.3E+03	1.0E+03	7.5E+02	45.0
	1.5E+04	1.0E+04	5.7E+03	3.5E+03	2.3E+03	1.6E+03	1.1E+03	9.4E+02	7.4E+02	90.0

Table 3.18 Number of Sources per Square Degree with Greater Spectral Irradiance Specified at Left at 8 μm for a Given Latitude and Longitude in $\text{W cm}^{-2} \mu\text{m}^{-1}$ (from Ref. 31)

Spectral Irradiance	Galactic Latitude									Galactic Longitude
	0.0	2.0	5.0	10.0	20.0	30.0	45.0	60.0	90.0	
1.0E-14	1.5E-04	3.4E-04	5.9E-04	9.5E-04	1.1E-03	7.6E-04	4.8E-04	3.5E-04	2.4E-04	0.0
	8.2E-04	1.2E-03	1.3E-03	1.3E-03	9.7E-04	6.1E-04	4.0E-04	3.1E-04	2.3E-04	45.0
	8.0E-03	4.2E-03	2.1E-03	1.2E-03	7.4E-04	4.9E-04	3.5E-04	2.9E-04	2.3E-04	90.0
	3.6E-03	2.0E-03	1.1E-03	7.7E-04	6.1E-04	4.5E-04	3.4E-04	2.9E-04	2.4E-04	180.0
1.0E-15	9.4E-03	1.4E-02	1.5E-02	1.4E-02	1.1E-02	6.7E-03	4.0E-03	2.9E-03	2.0E-03	0.0
	1.9E-02	2.0E-02	1.7E-02	1.3E-02	8.4E-03	5.1E-03	3.3E-03	2.6E-03	1.9E-03	45.0
	6.6E-02	3.5E-02	1.7E-02	9.6E-03	6.1E-03	4.1E-03	2.9E-03	2.4E-03	1.9E-03	90.0
	3.0E-02	1.7E-02	9.4E-03	6.4E-03	5.1E-03	3.7E-03	2.9E-03	2.4E-03	2.0E-03	180.0
1.0E-16	5.9E-01	5.5E-01	3.6E-01	2.1E-01	1.1E-01	5.8E-02	3.4E-02	2.4E-02	1.7E-02	0.0
	4.3E-01	3.4E-01	2.1E-01	1.3E-01	7.2E-02	4.3E-02	2.8E-02	2.2E-02	1.6E-02	45.0
	5.5E-01	2.9E-01	1.4E-01	8.0E-02	5.1E-02	3.4E-02	2.4E-02	2.0E-02	1.6E-02	90.0
	2.5E-01	1.4E-01	7.8E-02	5.3E-02	4.2E-02	3.1E-02	2.4E-02	2.0E-02	1.6E-02	180.0
1.0E-17	3.7E+01	2.2E+01	8.8E+00	3.1E+00	1.1E+00	5.1E-01	2.8E-01	2.0E-01	1.4E-01	0.0
	9.8E+00	5.8E+00	2.7E+00	1.3E+00	6.2E-01	3.6E-01	2.3E-01	1.8E-01	1.3E-01	45.0
	4.6E+00	2.4E+00	1.2E+00	6.7E-01	4.2E-01	2.8E-01	2.0E-01	1.7E-01	1.3E-01	90.0
1.0E-18	2.4E+03	8.9E+02	2.2E+02	4.6E+01	1.0E+01	4.4E+00	2.4E+00	1.7E+00	1.2E+00	0.0
	2.3E+02	9.8E+01	3.4E+01	1.3E+01	5.3E+00	3.0E+00	1.9E+00	1.5E+00	1.1E+00	45.0
	3.8E+01	2.0E+01	9.8E+00	5.5E+00	3.5E+00	2.4E+00	1.7E+00	1.4E+00	1.1E+00	90.0
	1.7E+01	9.6E+00	5.4E+00	3.7E+00	2.9E+00	2.1E+00	1.6E+00	1.4E+00	1.1E+00	180.0
1.0E-19	1.5E+05	3.6E+04	5.3E+03	6.9E+02	1.0E+02	3.9E+01	2.0E+01	1.4E+01	9.7E+00	0.0
	5.2E+03	1.7E+03	4.4E+02	1.2E+02	4.5E+01	2.5E+01	1.6E+01	1.2E+01	9.2E+00	45.0
	3.2E+02	1.7E+02	8.2E+01	4.6E+01	2.9E+01	2.0E+01	1.4E+01	1.2E+01	9.0E+00	90.0
	1.4E+02	8.0E+01	4.5E+01	3.1E+01	2.4E+01	1.8E+01	1.4E+01	1.2E+01	9.4E+00	180.0
1.0E-20	9.4E+06	1.4E+06	1.3E+05	1.0E+04	1.0E+03	3.4E+02	1.7E+02	1.2E+02	8.1E+01	0.0
	1.2E+05	2.8E+04	5.5E+03	1.2E+03	3.9E+02	2.1E+02	1.3E+02	1.0E+02	7.6E+01	45.0
	2.6E+03	1.4E+03	6.8E+02	3.8E+02	2.4E+02	1.6E+02	1.2E+02	9.6E+01	7.5E+01	90.0
	1.2E+03	6.6E+02	3.7E+02	2.6E+02	2.0E+02	1.5E+02	1.1E+02	9.7E+01	7.8E+01	180.0

Table 3.19 Number of Sources Per Square Degree with Greater Spectral Irradiance Specified at Left at 12 μm for a Given Latitude and Longitude in $\text{W cm}^{-2} \mu\text{m}^{-1}$ (from Ref. 31)

Spectral Irradiance	Galactic Latitude									Galactic Longitude
	0.0	2.0	5.0	10.0	20.0	30.0	45.0	60.0	90.0	
1.0E-14	5.1E-05	9.0E-05	1.4E-04	2.3E-04	2.9E-04	2.0E-04	1.2E-04	9.1E-05	6.3E-05	0.0
	3.7E-04	4.2E-04	4.2E-04	3.8E-04	2.7E-04	1.6E-04	1.0E-04	8.0E-05	5.9E-05	45.0
	4.6E-03	2.0E-03	7.9E-04	3.8E-04	2.1E-04	1.3E-04	9.2E-05	7.5E-05	5.8E-05	90.0
	2.1E-03	9.4E-04	4.4E-04	2.5E-04	1.7E-04	1.2E-04	9.0E-05	7.6E-05	6.1E-05	180.0
1.0E-15	3.2E-03	3.6E-03	3.5E-03	3.4E-03	2.8E-03	1.7E-03	1.0E-03	7.6E-04	5.2E-04	0.0
	8.4E-03	7.2E-03	5.3E-03	3.8E-03	2.3E-03	1.4E-03	8.7E-04	6.7E-04	4.9E-04	45.0
	3.9E-02	1.6E-02	6.6E-03	3.1E-03	1.7E-03	1.1E-03	7.7E-04	6.2E-04	4.8E-04	90.0
	1.7E-02	7.8E-03	3.6E-03	2.1E-03	1.4E-03	1.0E-03	7.5E-04	6.3E-04	5.1E-04	180.0
1.0E-16	2.0E-01	1.5E-01	8.5E-02	5.0E-02	2.8E-02	1.5E-02	8.7E-03	6.3E-03	4.3E-03	0.0
	1.9E-01	1.2E-01	6.8E-02	3.8E-02	2.0E-02	1.1E-02	7.2E-03	5.6E-03	4.1E-03	45.0
	3.2E-01	1.4E-01	5.5E-02	2.6E-02	1.5E-02	9.2E-03	6.4E-03	5.2E-03	4.0E-03	90.0
	1.4E-01	6.5E-02	3.0E-02	1.7E-02	1.2E-02	8.4E-03	6.2E-03	5.3E-03	4.2E-03	180.0
1.0E-17	1.3E+01	5.9E+00	2.1E+00	7.5E-01	2.7E-01	1.3E-01	7.3E-02	5.3E-02	3.6E-02	0.0
	4.4E+00	2.1E+00	8.6E-01	3.8E-01	1.7E-01	9.6E-02	6.0E-02	4.6E-02	3.4E-02	45.0
	2.7E+00	1.1E+00	4.6E-01	2.2E-01	1.2E-01	7.7E-02	5.3E-02	4.3E-02	3.3E-02	90.0
	1.2E+00	5.4E-01	2.5E-01	1.4E-01	9.9E-02	7.0E-02	5.2E-02	4.4E-02	3.5E-02	180.0
1.0E-18	8.2E+02	2.4E+02	5.2E+01	1.1E+01	2.7E+00	1.2E+00	6.1E-01	4.4E-01	3.0E-01	0.0
	1.0E+02	3.6E+01	1.1E+01	3.7E+00	1.5E+00	8.0E-01	5.0E-01	3.9E-01	2.8E-01	45.0
	2.2E+01	9.4E+00	3.8E+00	1.8E+00	1.0E+00	6.4E-01	4.4E-01	3.6E-01	2.8E-01	90.0
	9.9E+00	4.5E+00	2.1E+00	1.2E+00	8.3E-01	5.8E-01	4.3E-01	3.6E-01	2.9E-01	180.0
1.0E-19	5.1E+04	9.6E+03	1.3E+03	1.7E+02	2.6E+01	1.0E+01	5.1E+00	3.6E+00	2.5E+00	0.0
	2.3E+03	6.0E+02	1.4E+02	3.7E+01	1.3E+01	6.7E+00	4.2E+00	3.2E+00	2.4E+00	40.0
	1.8E+02	7.8E+01	3.2E+01	1.5E+01	8.4E+00	5.3E+00	3.7E+00	3.0E+00	2.3E+00	90.0
	8.3E+01	3.7E+01	1.7E+01	1.0E+01	6.9E+00	4.8E+00	3.6E+00	3.0E+00	2.4E+00	180.0
1.0E-20	3.2E+06	3.9E+05	3.1E+04	2.5E+03	2.6E+02	8.8E+01	4.3E+01	3.0E+01	2.1E+01	0.0
	5.3E+04	1.0E+04	1.8E+03	3.7E+02	1.1E+02	5.6E+01	3.5E+01	2.7E+01	2.0E+01	45.0
	1.5E+03	6.5E+02	2.6E+02	1.3E+02	6.9E+01	4.4E+01	3.0E+01	2.5E+01	1.9E+01	90.0
	6.9E+02	3.1E+02	1.4E+02	8.3E+01	5.7E+01	4.0E+01	3.0E+01	2.5E+01	2.0E+01	180.0

Table 3.20 Number of Sources Per Square Degree with Greater Spectral Irradiance Specified at Left at 20 μm for a Given Latitude and Longitude in $\text{W cm}^2 \mu\text{m}^{-1}$ (from Ref. 31)

Spectral Irradiance	Galactic Latitude									Galactic Longitude
	0.0	2.0	5.0	10.0	20.0	30.0	45.0	60.0	90.0	
1.0E-14	2.8E-05	4.4E-05	6.2E-05	9.4E-05	1.1E-04	7.5E-05	4.5E-05	3.2E-05	2.2E-05	0.0
	2.3E-04	2.4E-04	2.2E-04	1.8E-04	1.1E-04	6.3E-05	3.8E-05	2.8E-05	2.1E-05	45.0
	3.4E-03	1.3E-03	4.6E-04	1.9E-04	8.8E-05	5.1E-05	3.3E-05	2.6E-05	2.0E-05	90.0
	1.5E-03	6.2E-04	2.6E-04	1.3E-04	7.2E-05	4.6E-05	3.3E-05	2.7E-05	2.1E-05	180.0
1.0E-15	1.8E-03	1.8E-03	1.5E-03	1.4E-03	1.1E-03	6.5E-04	3.8E-04	2.7E-04	1.8E-04	0.0
	5.3E-03	4.2E-03	2.8E-03	1.8E-03	9.6E-04	5.2E-04	3.1E-04	2.4E-04	1.7E-04	45.0
	2.8E-02	1.1E-02	3.9E-03	1.6E-03	7.3E-04	4.2E-04	2.8E-04	2.2E-04	1.7E-04	90.0
	1.3E-02	5.2E-03	2.1E-03	1.0E-03	6.0E-04	3.8E-04	2.7E-04	2.2E-04	1.8E-04	180.0
1.0E-16	1.1E-01	7.1E-02	3.8E-02	2.1E-02	1.1E-02	5.7E-03	3.1E-03	2.2E-03	1.5E-03	0.0
	1.2E-01	7.1E-02	3.5E-02	1.8E-02	8.3E-03	4.4E-03	2.6E-03	2.0E-03	1.4E-03	45.0
	2.3E-01	8.9E-02	3.2E-02	1.3E-02	6.1E-03	3.5E-03	2.3E-03	1.8E-03	1.4E-03	90.0
	1.1E-01	4.3E-02	1.8E-02	8.7E-03	5.0E-03	3.2E-03	2.2E-03	1.9E-03	1.5E-03	180.0
1.0E-17	7.0E+00	2.9E+00	9.3E-01	3.1E-01	1.1E-01	5.0E-02	2.6E-02	1.9E-02	1.3E-02	0.0
	2.8E+00	1.2E+00	4.5E-01	1.8E-01	7.1E-02	3.7E-02	2.2E-02	1.6E-02	1.2E-02	45.0
	1.9E+00	7.4E-01	2.7E-01	1.1E-01	5.0E-02	2.9E-02	1.9E-02	1.5E-02	1.2E-02	90.0
	8.7E-01	3.6E-01	1.5E-01	7.3E-02	4.1E-02	2.7E-02	1.9E-02	1.5E-02	1.2E-02	-180.0
1.0E-18	4.4E+02	1.2E+02	2.3E+01	4.6E+00	1.0E+00	4.3E-01	2.2E-01	1.5E-01	1.0E-01	0.0
	6.4E+01	2.0E+01	5.7E+00	1.8E+00	6.1E-01	3.1E-01	1.8E-01	1.4E-01	9.9E-02	45.0
	1.6E+01	6.2E+00	2.2E+00	9.1E-01	4.2E-01	2.4E-01	1.6E-01	1.3E-01	9.7E-02	90.0
	7.3E+00	3.0E+00	1.2E+00	6.0E-01	3.5E-01	2.2E-01	1.6E-01	1.3E-01	1.0E-01	180.0
1.0E-19	2.8E+04	4.6E+03	5.6E+02	6.8E+01	1.0E+01	3.8E+00	1.8E+00	1.3E+00	8.7E-01	0.0
	1.5E+03	3.5E+02	7.3E+01	1.8E+01	5.2E+00	2.6E+00	1.5E+00	1.1E+00	8.3E-01	45.0
	1.3E+02	5.1E+01	1.8E+01	7.5E+00	3.5E+00	2.0E+00	1.3E+00	1.1E+00	8.1E-01	90.0
	6.0E+01	2.5E+01	1.0E+01	5.0E+00	2.9E+00	1.8E+00	1.3E+00	1.1E+00	8.5E-01	180.0
1.0E-20	1.8E+06	1.9E+05	1.4E+04	1.0E+03	1.0E+02	3.3E+01	1.5E+01	1.1E+01	7.3E+00	0.0
	3.3E+04	5.9E+03	9.3E+02	1.7E+02	4.5E+01	2.1E+01	1.2E+01	9.4E+00	6.9E+00	45.0
	1.1E+03	4.3E+02	1.5E+02	6.3E+01	2.9E+01	1.7E+01	1.1E+01	8.8E+00	6.7E+00	90.0
	5.0E+02	2.1E+02	8.5E+01	4.2E+01	2.4E+01	1.5E+01	1.1E+01	8.9E+00	7.1E+00	180.0

Table 3.21 Number of Sources Per Square Degree with Greater Spectral Irradiance Specified at Left at 25 μm for a Given Latitude and Longitude in $\text{W cm}^{-2} \mu\text{m}^{-1}$ (from Ref. 31)

Spectral Irradiance	Galactic Latitude									Galactic Longitude
	0.0	2.0	5.0	10.0	20.0	30.0	45.0	60.0	90.0	
1.0E-14	2.7E-06	5.4E-06	9.8E-06	1.9E-05	2.7E-05	1.9E-05	1.1E-05	8.1E-06	5.5E-06	0.0
	4.0E-05	4.9E-05	5.0E-05	4.6E-05	3.0E-05	1.6E-05	9.6E-06	7.2E-06	5.2E-06	45.0
	1.0E-03	3.9E-04	1.4E-04	5.4E-05	2.4E-05	1.3E-05	8.5E-06	6.7E-06	5.1E-06	90.0
	4.6E-04	1.9E-04	7.5E-05	3.6E-05	1.9E-05	1.2E-05	8.3E-06	6.8E-06	5.4E-06	180.0
1.0E-15	1.7E-04	2.2E-04	2.4E-04	2.8E-04	2.7E-04	1.7E-04	9.5E-05	6.8E-05	4.6E-05	0.0
	9.2E-04	8.3E-04	6.4E-04	4.6E-04	2.5E-04	1.4E-04	8.0E-05	6.0E-05	4.4E-05	45.0
	8.6E-03	3.2E-03	1.1E-03	4.5E-04	2.0E-04	1.1E-04	7.0E-05	5.6E-05	4.3E-05	90.0
	3.9E-03	1.6E-03	6.2E-04	3.0E-04	1.6E-04	1.0E-04	6.9E-05	5.6E-05	4.5E-05	180.0
1.0E-16	1.1E-02	8.7E-03	5.9E-03	4.2E-03	2.6E-03	1.4E-03	8.0E-04	5.6E-04	3.8E-04	0.0
	2.1E-02	1.4E-02	8.1E-03	4.5E-03	2.2E-03	1.1E-03	6.6E-04	5.0E-04	3.6E-04	45.0
	7.2E-02	2.7E-02	9.4E-03	3.7E-03	1.6E-03	9.2E-04	5.9E-04	4.6E-04	3.5E-04	90.0
	3.2E-02	1.3E-02	5.2E-03	2.5E-03	1.3E-03	8.3E-04	5.7E-04	4.7E-04	3.7E-04	180.0
1.0E-17	6.9E-01	3.5E-01	1.5E-01	6.2E-02	2.6E-02	1.3E-02	6.7E-03	4.7E-03	3.2E-03	0.0
	4.8E-01	2.4E-01	1.0E-01	4.5E-02	1.9E-02	9.5E-03	5.5E-03	4.1E-03	3.0E-03	45.0
	5.9E-01	2.2E-01	7.8E-02	3.1E-02	1.4E-02	7.6E-03	4.9E-03	3.8E-03	2.9E-03	90.0
	2.7E-01	1.1E-01	4.3E-02	2.1E-02	1.1E-02	6.9E-03	4.8E-03	3.9E-03	3.1E-03	180.0
1.0E-18	4.3E+01	1.4E+01	3.6E+00	9.2E-01	2.5E-01	1.1E-01	5.6E-02	3.9E-02	2.6E-02	0.0
	1.1E+01	4.1E+00	1.3E+00	4.5E-01	1.6E-01	8.0E-02	4.6E-02	3.4E-02	2.5E-02	45.0
	4.9E+00	1.9E+00	6.5E-01	2.6E-01	1.1E-01	6.3E-02	4.1E-02	3.2E-02	2.4E-02	90.0
	2.2E+00	8.9E-01	3.6E-01	1.7E-01	9.3E-02	5.8E-02	4.0E-02	3.3E-02	2.6E-02	180.0
1.0E-19	2.7E+03	5.7E+02	8.8E+01	1.4E+01	2.5E+00	9.6E-01	4.7E-01	3.3E-01	2.2E-01	0.0
	2.5E+02	7.0E+01	1.7E+01	4.5E+00	1.4E+00	6.7E-01	3.8E-01	2.9E-01	2.1E-01	45.0
	4.1E+01	1.5E+01	5.4E+00	2.1E+00	9.4E-01	5.3E-01	3.4E-01	2.7E-01	2.0E-01	90.0
	1.8E+01	7.4E+00	3.0E+00	1.4E+00	7.7E-01	4.8E-01	3.3E-01	2.7E-01	2.1E-01	180.0
1.0E-20	1.7E+05	2.3E+04	2.2E+03	2.0E+02	2.4E+01	8.3E+00	3.9E+00	2.7E+00	1.8E+00	0.0
	5.8E+03	1.2E+03	2.1E+02	4.4E+01	1.2E+01	5.6E+00	3.2E+00	2.4E+00	1.7E+00	45.0
	3.4E+02	1.3E+02	4.5E+01	1.8E+01	7.8E+00	4.4E+00	2.8E+00	2.2E+00	1.7E+00	90.0
	1.5E+02	6.2E+01	2.5E+01	1.2E+01	6.4E+00	4.0E+00	2.7E+00	2.2E+00	1.8E+00	180.0

Table 3.22 Number of Sources Per Square Degree with Greater Spectral Irradiance Specified at Left at 30 μm for a Given Latitude and Longitude in $\text{W cm}^{-2} \mu\text{m}^{-1}$ (from Ref. 31)

Spectral Irradiance	Galactic Latitude									Galactic Longitude
	0.0	2.0	5.0	10.0	20.0	30.0	45.0	60.0	90.0	
1.0E-14	3.6E-06	6.8E-06	1.2E-05	2.2E-05	2.9E-05	2.0E-05	1.2E-05	8.4E-06	5.7E-06	0.0
	5.0E-05	5.9E-05	5.8E-05	5.2E-05	3.2E-05	1.7E-05	9.9E-06	7.4E-06	5.4E-06	45.0
	1.2E-03	4.5E-04	1.5E-04	5.9E-05	2.5E-05	1.4E-05	8.8E-06	6.9E-06	5.2E-06	90.0
	5.4E-04	2.1E-04	8.5E-05	4.0E-05	2.1E-05	1.3E-05	8.6E-06	7.0E-06	5.5E-06	180.0
1.0E-15	2.3E-04	2.7E-04	2.9E-04	3.2E-04	2.9E-04	1.7E-04	9.9E-05	7.0E-05	4.7E-05	0.0
	1.1E-03	1.0E-03	7.4E-04	5.1E-04	2.7E-04	1.4E-04	8.3E-05	6.2E-05	4.5E-05	45.0
	9.9E-03	3.7E-03	1.3E-03	4.9E-04	2.1E-04	1.2E-04	7.3E-05	5.7E-05	4.4E-05	90.0
	4.5E-03	1.8E-03	7.1E-04	3.3E-04	1.7E-04	1.1E-04	7.2E-05	5.8E-05	4.6E-05	180.0
1.0E-16	1.4E-02	1.1E-02	7.1E-03	4.8E-03	2.8E-03	1.5E-03	8.3E-04	5.8E-04	3.9E-04	0.0
	2.6E-02	1.7E-02	9.4E-03	5.1E-03	2.3E-03	1.2E-03	6.9E-04	5.1E-04	3.7E-04	45.0
	8.3E-02	3.1E-02	1.1E-02	4.1E-03	1.8E-03	9.7E-04	6.1E-04	4.8E-04	3.6E-04	90.0
	3.7E-02	1.5E-02	5.9E-03	2.7E-03	1.4E-03	8.8E-04	5.9E-04	4.8E-04	3.8E-04	180.0
1.0E-17	9.1E-01	4.5E-01	1.8E-01	7.1E-02	2.8E-02	1.3E-02	6.9E-03	4.8E-03	3.3E-03	0.0
	6.0E-01	2.9E-01	1.2E-01	5.1E-02	2.0E-02	1.0E-02	5.7E-03	4.3E-03	3.1E-03	45.0
	6.9E-01	2.6E-01	8.9E-02	3.4E-02	1.5E-02	8.0E-03	5.1E-03	4.0E-03	3.0E-03	90.0
	3.1E-01	1.2E-01	4.9E-02	2.3E-02	1.2E-02	7.3E-03	4.9E-03	4.0E-03	3.2E-03	180.0
1.0E-18	5.8E+01	1.8E+01	4.3E+00	1.1E+00	2.7E-01	1.2E-01	5.8E-02	4.0E-02	2.7E-02	0.0
	1.4E+01	4.9E+00	1.5E+00	5.0E-01	1.7E-01	8.4E-02	4.8E-02	3.5E-02	2.6E-02	45.0
	5.7E+00	2.1E+00	7.4E-01	2.8E-01	1.2E-01	6.7E-02	4.2E-02	3.3E-02	2.5E-02	90.0
	2.6E+00	1.0E+00	4.1E-01	1.9E-01	1.0E-01	6.1E-02	4.1E-02	3.3E-02	2.6E-02	180.0
1.0E-19	3.6E+03	7.2E+02	1.1E+02	1.6E+01	2.7E+00	1.0E+00	4.9E-01	3.4E-01	2.3E-01	0.0
	3.1E+02	8.4E+01	1.9E+01	5.0E+00	1.5E+00	7.0E-01	4.0E-01	3.0E-01	2.1E-01	45.0
	4.8E+01	1.8E+01	6.1E+00	2.4E+00	1.0E+00	5.6E-01	3.5E-01	2.7E-01	2.1E-01	90.0
	2.1E+01	8.5E+00	3.4E+00	1.6E+00	8.3E-01	5.1E-01	3.4E-01	2.8E-01	2.2E-01	180.0
1.0E-20	2.3E+05	2.9E+04	2.6E+03	2.3E+02	2.6E+01	8.8E+00	4.1E+00	2.8E+00	1.9E+00	0.0
	7.2E+03	1.4E+03	2.5E+02	5.0E+01	1.3E+01	5.9E+00	3.3E+00	2.5E+00	1.8E+00	45.0
	4.0E+02	1.5E+02	5.1E+01	2.0E+01	8.4E+00	4.6E+00	2.9E+00	2.3E+00	1.7E+00	90.0
	1.8E+02	7.1E+01	2.8E+01	1.3E+01	6.9E+00	4.2E+00	2.8E+00	2.3E+00	1.8E+00	180.0

Table 3.23 Number of Sources Per Square Degree with Greater Spectral Irradiance Specified at Left at 40 μm for a Given Latitude and Longitude in $\text{W cm}^{-2} \mu\text{m}^{-1}$ (from Ref. 31)

Spectral Irradiance	Galactic Latitude									Galactic Longitude
	0.0	2.0	5.0	10.0	20.0	30.0	45.0	60.0	90.0	
1.0E-14	7.0E-07	1.5E-06	3.2E-06	7.0E-06	1.1E-05	7.6E-06	4.5E-06	3.2E-06	2.1E-06	0.0
	1.4E-05	1.9E-05	2.1E-05	2.0E-05	1.2E-05	6.6E-06	3.8E-06	2.8E-06	2.0E-06	45.0
	5.1E-04	1.9E-04	6.5E-05	2.5E-05	1.0E-05	5.4E-06	3.3E-06	2.6E-06	2.0E-06	90.0
	2.3E-04	9.1E-05	3.6E-05	1.6E-05	8.3E-06	4.9E-06	3.3E-06	2.6E-06	2.1E-06	180.0
1.0E-15	4.4E-05	6.2E-05	7.9E-05	1.0E-04	1.1E-04	6.6E-05	3.7E-05	2.6E-05	1.8E-05	0.0
	3.3E-04	3.2E-04	2.6E-04	2.0E-04	1.1E-04	5.6E-05	3.1E-05	2.3E-05	1.7E-05	45.0
	4.3E-03	1.6E-03	5.4E-04	2.0E-04	8.4E-05	4.5E-05	2.8E-05	2.2E-05	1.6E-05	90.0
	1.9E-03	7.6E-04	3.0E-04	1.4E-04	6.9E-05	4.1E-05	2.7E-05	2.2E-05	1.7E-05	180.0
1.0E-16	2.8E-03	2.5E-03	1.9E-03	1.5E-03	1.0E-03	5.8E-04	3.1E-04	2.2E-04	1.5E-04	0.0
	7.5E-03	5.4E-03	3.3E-03	1.9E-03	9.2E-04	4.6E-04	2.6E-04	1.9E-04	1.4E-04	45.0
	3.6E-02	1.3E-02	4.5E-03	1.7E-03	7.0E-04	3.7E-04	2.3E-04	1.8E-04	1.4E-04	90.0
	1.6E-02	6.3E-03	2.5E-03	1.1E-03	5.7E-04	3.4E-04	2.3E-04	1.8E-04	1.4E-04	180.0
1.0E-17	1.8E-01	1.0E-01	4.8E-02	2.3E-02	1.0E-02	5.0E-03	2.6E-03	1.8E-03	1.2E-03	0.0
	1.7E-01	9.2E-02	4.2E-02	1.9E-02	7.9E-03	3.9E-03	2.2E-03	1.6E-03	1.2E-03	45.0
	3.0E-01	1.1E-01	3.7E-02	1.4E-02	5.8E-03	3.1E-03	1.9E-03	1.5E-03	1.1E-03	90.0
	1.3E-01	5.3E-02	2.1E-02	9.4E-03	4.8E-03	2.8E-03	1.9E-03	1.5E-03	1.2E-03	180.0
1.0E-18	1.1E+01	4.1E+00	1.2E+00	3.4E-01	1.0E-01	4.4E-02	2.2E-02	1.5E-02	1.0E-02	0.0
	3.9E+00	1.6E+00	5.4E-01	1.9E-01	6.8E-02	3.2E-02	1.8E-02	1.3E-02	9.7E-03	45.0
	2.5E+00	9.1E-01	3.1E-01	1.2E-01	4.8E-02	2.6E-02	1.6E-02	1.2E-02	9.4E-03	90.0
	1.1E+00	4.4E-01	1.7E-01	7.8E-02	4.0E-02	2.4E-02	1.6E-02	1.3E-02	9.9E-03	180.0
1.0E-19	7.0E+02	1.6E+02	2.9E+01	5.1E+00	9.9E-01	3.8E-01	1.8E-01	1.3E-01	8.5E-02	0.0
	9.0E+01	2.7E+01	6.9E+00	1.9E+00	5.8E-01	2.7E-01	1.5E-01	1.1E-01	8.0E-02	45.0
	2.0E+01	7.6E+00	2.6E+00	9.8E-01	4.0E-01	2.2E-01	1.3E-01	1.0E-01	7.9E-02	90.0
	9.2E+00	3.6E+00	1.4E+00	6.5E-01	3.3E-01	2.0E-01	1.3E-01	1.1E-01	8.3E-02	180.0
1.0E-20	4.4E+04	6.6E+03	7.1E+02	7.5E+01	9.7E+00	3.3E+00	1.5E+00	1.1E+00	7.1E-01	0.0
	2.1E+03	4.5E+02	8.7E+01	1.9E+01	5.0E+00	2.3E+00	1.3E+00	9.3E-01	6.7E-01	45.0
	1.7E+02	6.3E+01	2.1E+01	8.1E+00	3.3E+00	1.8E+00	1.1E+00	8.6E-01	6.5E-01	90.0
	7.6E+01	3.0E+01	1.2E+01	5.4E+00	2.7E+00	1.6E+00	1.1E+00	8.7E-01	6.9E-01	180.0

Table 3.24 Absolute Magnitude, Flux, and Volume Density of Optical Galaxies (from Ref. 34)

M_B (mag)	ϕ (Watts)	$n_G(\phi)$ (Mpc ⁻³)
< -21	10^{44}	$10^{-3.5}$
< -20	10^{44}	$10^{-2.5}$
< -19	10^{44}	$10^{-1.5}$
< -18	10^{43}	10^{-1}

c = velocity of light, cm s^{-1}

Ω_i = fraction of galaxies with radiant flux Φ_{λ_i}

Φ_{λ_i} = spectral radiant flux, $\text{W } \mu\text{m}^{-1}$.

Table 3.24 gives parameters for Eq. (3.42) for optical galaxies. Equations (3.38) through (3.41) should be used for longer wavelengths.

Density of Asteroids. Asteroids are solid bodies orbiting the sun between the orbits of Mars and Jupiter. Their surface temperatures are normally in the range of 180 to 280 K, with a weighted mean spectral temperature of about 255 K. In general, asteroids have albedos that run between 0.065 and 0.23 with near graybody behavior in the 5- to 30- μm range. The IRAS Asteroid and Comet Survey³⁵ yielded a data base of infrared flux densities for 1811 individual asteroids. Albedos and diameters for these have been derived via a standard thermal model, and useful low-resolution spectra were obtained for 47 numbered asteroids. A number of asteroids prior to IRAS have been observed in the infrared.³⁶ Statistical treatment of these and other data available on about 1800 asteroids³⁷ leads to the relation

$$N_{\lambda,a} = 4.6 \times 10^{-19} \frac{L_{\lambda}(\text{BB},225)}{L_{11}(\text{BB},225)} E_{\lambda}^{-1}(\text{lim}) \exp(-0.14\beta) \quad (3.43)$$

for the number of asteroids per square degree observed to a limiting irradiance $E_{\lambda}(\text{lim})$, in $\text{W cm}^{-2} \mu\text{m}^{-1}$ at the ecliptic latitude β degrees. The $N_{\lambda,a}$ is independent of ecliptic longitude and $L_{\lambda}(\text{BB},225)$ is the blackbody radiance at $T = 225$ K.

Extended Galactic Background. The extended LWIR galactic background³⁸ is dominated by the emission from dust. Galactic gas and dust are concentrated to the galactic plane with a thickness of about 200 pc inside the solar circle (the annulus at the radius of the sun from the galactic center) and increasing height with galactocentric distance beyond the sun. The distribution of this material is patchy, being concentrated in interstellar clumps, molecular clouds, and H II regions (neutral elements are designated with the roman numeral I, single ionization by II, etc.). Prodigious IR emitters are the H II regions created around newly formed O stars, early B stars, or stellar clusters. Most of the

visual and UV flux from the embedded star(s) is absorbed by the dust in and surrounding the H II region and then is thermally reemitted in the IR. The flux from a typical H II region generally peaks at about 70 μm , but a large LWIR component broadens the spectral energy distribution over that from a single temperature blackbody. The large size and high luminosity of these regions make them easily detectable throughout the galaxy. The closer regions are resolved at moderate resolution (<1 mrad) and can cover a large area of sky; for example, the Orion complex spans more than 100 square degrees in area.

An even more pervasive large-scale background is from interstellar dust or IR cirrus. This highly structured emission was first observed in the background images created from the IRAS 100- μm band data during the first all-sky survey. The background cirrus structure is characterized by its appearance at all galactic latitudes and longitudes, its anomalous spectral radiance, which has intensity peaks in both the 12- and 100- μm bands, and its fine-scaled structure showing significant intensity structure at spatial scales as fine as the IRAS resolution limit of about 300 μrad . Presence of a strong 12- μm structure component without corresponding intensities in the 25- and 60- μm bands indicates that whatever the source of radiation, its temperature distribution or spectral emission characteristics must be complex. The appearance of IR cirrus has been described as having long, spider-like filaments, clumps and long arching structures composed of small wisps, filaments, and clumps. Estimates are that roughly 9% of the sources in the IRAS Point Source Catalog (47% of the entries with 100- μm observations) are either condensation (knots) in the IR cirrus or wisps of cirrus oriented perpendicular to the scan direction and narrow enough to be detected as a point source by the 100- μm detectors.

Walker and Sears³¹ report that the pixel-to-pixel rms radiance fluctuation appears to vary from a few percent to almost 50%, with 10% or so being typical. The power spectral densities for the IR cirrus in seven fields containing bright IR cirrus near the north equatorial pole have been determined with the result that a power law distribution fit the spectra well for all areas but that the index was a strong function of wavelength. At 100 μm a power law index of -2.4 was representative for all fields, but a significantly shallower value, between -0.9 and -1.9 , was derived for the 12- μm emission.

Zodiacal Radiance. The zodiacal light³⁸ is associated with dust in the solar system. The visual manifestation is due to reflected sunlight and the infrared from thermal reemission of absorbed sunlight. It is visually most prominent as an ellipsoidal glow in the twilight of the springtime setting sun or before sunrise in the fall. Zodiacal emission is brightest near the sun and ecliptic plane, where the density of the zodiacal dust is greatest. Within 20 to 30° of the sun, the zodiacal background is bright enough to fill in the spectral windows in the earth's atmosphere. In addition to the gegenshein (enhanced backscattering of the dust particles at the antisolar point), small-scale structure has been observed in the visible region. These local variations are reported to be about 10% in amplitude with a 7 to 10° scale length.

The largest data base on the LWIR emission from the zodiacal dust cloud is that obtained by the Optical Physics Division of the Air Force Geophysical Laboratory (AFGL) on a series of probe-rocket-borne experiments from 1974

to 1983 and by the IRAS survey during 1983. Extensive coverage (22 to 85° and 137 to 180° elongation; from -60° ecliptic latitude to the north ecliptic pole) was obtained on the Zodiacal Infrared Project (ZIP), a two-flight experiment that sampled the zodiacal background in 15 spectral bands spanning the region from 2 to 30 μm . IRAS observed the zodiacal emission between 60 and 120° elongation continuously over a 10-month period in 1983. The survey aspect was restricted to within 30° of quadrature (the large majority of data lie in the region $75^\circ \leq e \leq 105^\circ$) where the in-plane brightness varied by a factor of only 4. Over most of the celestial sphere, the IR radiance of the zodiacal light is of the order of 10^{-11} to $10^{-9} \text{ W cm}^{-2} \text{ sr}^{-1} \mu\text{m}^{-1}$ concentrated primarily in the wavelength region of 7 to 30 μm .

Several models are available for predicting the infrared zodiacal emission. A simple model by Murdock and Price³⁹ adopts a mean particle size, albedo, and a fan-shaped density distribution with a $1/R$ in-plane variation. The $1/R$ density variation provides a reasonable fit to the observations at elongations less than 90°, the region interior to the earth's orbit. A more detailed model by Frazier^{40,41} assumes a $1/R$ density variation, a three-regime power law distribution of particle sizes, and albedos derived from the optical constants for the adopted chemical composition of the material and Mie theory. Good et al.⁴² produced a model using the IRAS sky survey measurements. They conclude that the cloud is inclined to the ecliptic by about 1.7° with its line of ascending nodes at 70° ecliptic longitude. They obtain good fits to the data at 12 and 25 μm for an exponential form of dust distribution using dust grains of emissivity 1 and an equilibrium temperature of 280 K at 1 AU. Tigg and Pearce⁴³ observed that the power law and exponential variation were a poor fit to the observed IRAS infrared data. They derive a different form of the dust distribution valid in the range of $0.87 \text{ AU} \leq R \leq 30 \text{ AU}$. They assume a mean particle size of 10 μm and emissivity of 1.

Frazier's model equates the incident solar flux absorbed by the particle to the flux emitted by the particle into $4\pi \text{ sr}$ to obtain the temperature of the particle as a function of the distance of the particle to the sun R and particle radius s :

$$\left(\frac{R_\odot}{R}\right)^2 \int_0^\infty Q(\lambda, s) F_\odot(\lambda) d\lambda = 4 \int_0^\infty Q(\lambda, s) L_\lambda(\text{BB}, T) d\lambda, \quad (3.44)$$

where

- R_\odot = radius of the sun
- R = distance, sun to particle
- $F_\odot(\lambda)$ = the spectral solar radiance
- $Q(\lambda, s)$ = particle absorption efficiency (absorption cross section divided by the geometric cross section)
- $L_\lambda(\text{BB}, T)$ = blackbody radiance, $\text{W cm}^{-2} \text{ sr}^{-1} \mu\text{m}^{-1}$
- s = particle radius.

The integral on the left side of Eq. (3.44) extends over the solar spectrum, which is primarily in the visible, and the integral on the right side extends primarily over the particle's thermal spectrum. Equation (3.44) can be solved

easily for the distance of the particle from the sun R , as a function of T and s , i.e., $R(T,s)$. The function $R(T,s)$ can be retabulated to obtain $T(R,s)$, which is the desired temperature function.

The emission of a single particle of radius s at vector position \mathbf{r} into a unit solid angle in the direction of earth is multiplied by the distribution function $n(\mathbf{r},s)$, the number of particles/cm³ at location \mathbf{r} with the radius between s and $s + ds$. This is then integrated over the distribution of particle radii and along the line of sight to obtain the observed radiance:

$$L_\lambda(\epsilon, \eta) = \int_0^\infty dl \int_0^\infty ds n(\mathbf{r}, s) \pi s^2 Q(\lambda, s) L_\lambda[BB, T(R, s)] , \quad (3.45)$$

where $L_\lambda(\epsilon, \eta)$ is the spectral radiance of the particle in $\text{W cm}^{-2} \text{sr}^{-1} \mu\text{m}^{-1}$, ϵ, η is the earth-centered ecliptic elongation and elevation, and l is the distance from earth to the particle. The particle density function is assumed to be separable and of the form

$$n(\mathbf{r}, s) = N_0 n(R) n(\beta) n(s) , \quad (3.46)$$

where β is the ecliptic latitude. The assumption of separability is valid everywhere except close to the sun (within 3°) where the particles begin to sublimate. The distribution of particles outside the plane of the ecliptic is well represented by the function

$$n(\beta) = \exp(-2.6|\sin^{1.3}\beta|) . \quad (3.47)$$

The factor $n(R)$ is assumed to be of the form

$$n(R) = \left(\frac{R_\oplus}{R} \right)^v , \quad (3.48)$$

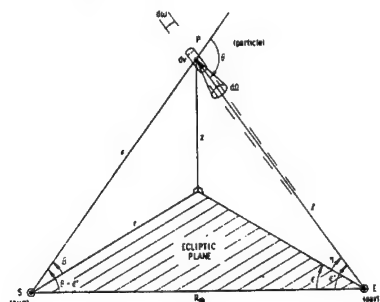
where $v = 1$. The factor $n(s)$ is given by

$$n(s) = s^{-k} . \quad (3.49)$$

Parameters for this model are listed in Table 3.25. Regions A, B, and C listed in Table 3.25 correspond to various particle radius ranges. See Refs. 42 and 43 for different forms of the particle density function based on IRAS observations.

Table 3.25 Model Parameters for Zodiacal Radiance with R_\oplus as Distance of Earth to Sun (from Ref. 40)

	$s(\mu\text{m})$	$N_0(\text{cm}^{-3})$	$n(R)$	$n(s)$
A	0.008–0.16	0.95×10^{-12}	R_\oplus/R	$s^{-2.7}$
B	0.16–28.8	1.12×10^{-14}	R_\oplus/R	$s^{-2.0}$
C	28.8–339	1.91×10^{-17}	R_\oplus/R	$s^{-4.33}$



In practice, the integral over s in Eq.(3.45) is limited numerically between the upper and lower size limits s_0 and s_1 , respectively (see Table 3.25). Further, it is better for computational purposes to transform the variable l to the "scattering angle" θ (see pictorial in Table 3.25). This transformation is given by

$$\begin{aligned} l &= R_{\oplus}(\cos \epsilon' - \sin \epsilon' \cot \theta) \\ dl &= R_{\oplus} \left(\frac{\sin \epsilon'}{\sin^2 \theta} \right) d\theta \\ l = 0 &\rightarrow \theta = \epsilon' \\ l = \infty &\rightarrow \theta = \pi . \end{aligned} \quad (3.50)$$

Using Eqs. (3.47) through (3.50), Eq. (3.45) can be written

$$\begin{aligned} L_{\lambda}(\epsilon, \eta) &= \pi R_{\oplus} \sin \epsilon' \int_{\epsilon'}^{\pi} \frac{d\theta}{\sin^2 \theta} \left(\frac{R_{\oplus}}{R} \right)^v \\ &\quad \times n(\beta) N_0 \int_{s_0}^{s_1} ds s^{2-k} Q(\lambda, s) L_{\lambda}(\text{BB}, T) . \end{aligned} \quad (3.51)$$

To solve this equation for $L_{\lambda}(\epsilon, \eta)$, additional equations expressing the trigonometric relations are needed:

$$\begin{aligned} \cos \epsilon' &= \cos \epsilon \cos \eta, \quad (0 \leq \epsilon' \leq \pi) , \\ \sin \beta &= \sin \eta \sin \theta (\cot \epsilon' - \cot \theta), \quad (0 \leq \beta \leq \pi/2) , \\ R &= R_{\oplus} \frac{\sin \epsilon'}{\sin \theta} . \end{aligned} \quad (3.52)$$

3.6 THE SKY

3.6.1 Scattered Solar Radiation

There is a moderate amount of literature on the spatial and temporal fluctuations of the sky background.⁴⁴⁻⁵⁰

Clear Sky. Sky background radiation in the infrared is caused by scattering of the sun's radiation and by emission from atmospheric constituents. Figure 3.19 illustrates the separation of the spectrum into two regions: the solar scattering region short of 3 μm and the thermal emission region beyond 4 μm . Solar scattering is represented by reflection from a bright sunlit cloud and, alternatively, by a curve for clear-air scattering. The thermal region is represented by a 300 K blackbody. Figure 3.20 shows blackbody curves for temperatures ranging from 0 to 40°C. This simple model is modified by a number of factors: In the solar region there are absorption bands of water vapor at

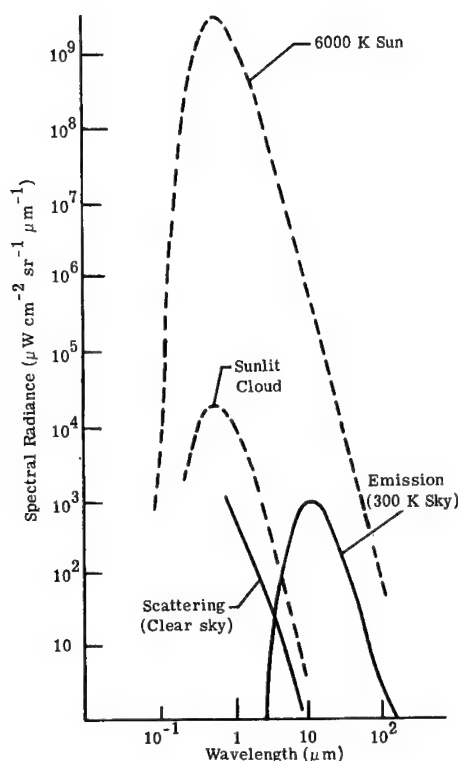


Fig. 3.19 Contributions from scattering and atmospheric emission to background radiation.⁵¹

0.94, 1.1, 1.4, 1.9, and 2.7 μm , and of carbon dioxide at 2.7 μm . The effect of these bands is shown in Fig. 3.21.

In the thermal region, curves for those bands with strong absorption (and thus strong emission) will approach the blackbody curve appropriate to the temperature of the atmosphere. Less strongly emitting regions may contribute only a small fraction of the radiation of a blackbody at the temperature of the atmosphere. The bottom curve in Fig. 3.22 is a good example. This zenith measurement, taken from a high, dry location, shows low emission except in the strong band of CO_2 at 15 μm and of H_2O at 6.3 μm . There is also a weak emission peak, due to ozone, at 9.6 μm . The low-level continuum is due to the wings of the strong bands of H_2O and CO_2 . The effect of increased humidity and air mass can be seen by comparing the bottom curves of Figs. 3.22 and 3.23. Figure 3.23 shows measurements taken at a humid sea-level location.

The effect of increasing air mass alone can be seen in both Figs. 3.22 and 3.23 by comparing curves taken from the same altitude at various elevation angles. The emission shows a systematic decrease with increasing elevation angle. The direction of look also has an effect in the solar scattering region, as seen in Fig. 3.21, where, for a clear sky, the sun's position is fixed and the spectral radiance is plotted for several observer angles.

The position of the sun has a strong effect on the scattered radiation in the solar region, as shown in Fig. 3.24. Here, the observer looks at the zenith. The elevation angle of the sun is varied, but has little effect on the radiation in

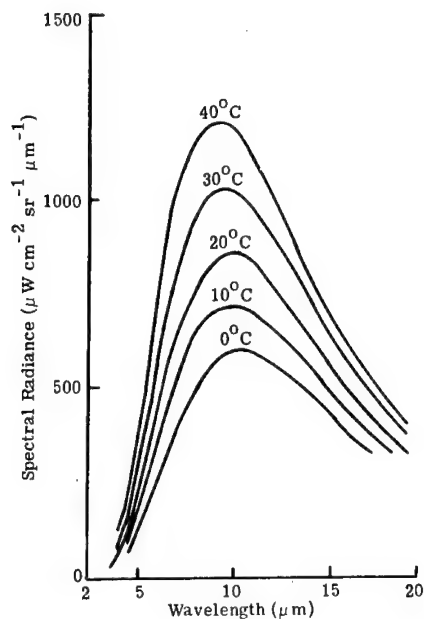


Fig. 3.20 Spectral radiance of a blackbody with a temperature range of 0 to 40°C. (Ref. 51).

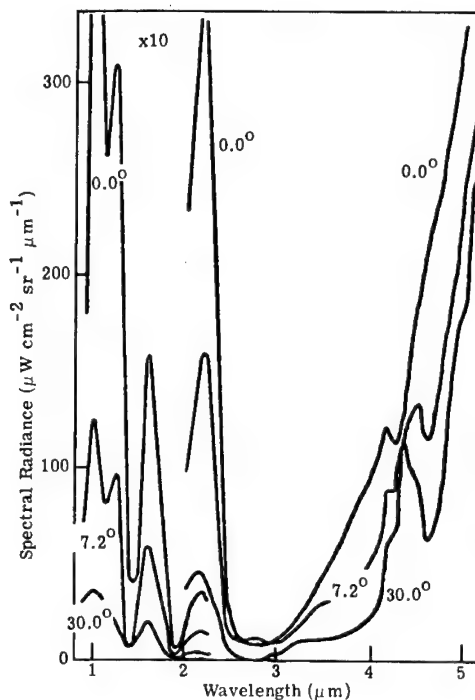


Fig. 3.21 The spectral radiance of a clear daytime sky.⁵¹

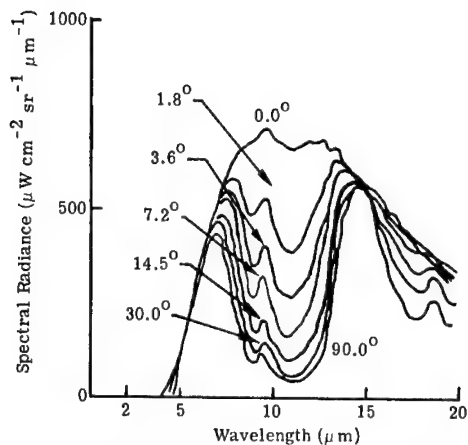


Fig. 3.22 The spectral radiance of a clear nighttime sky. It is for several angles of elevation above the horizon (Elk Park Station, Colorado).⁵¹

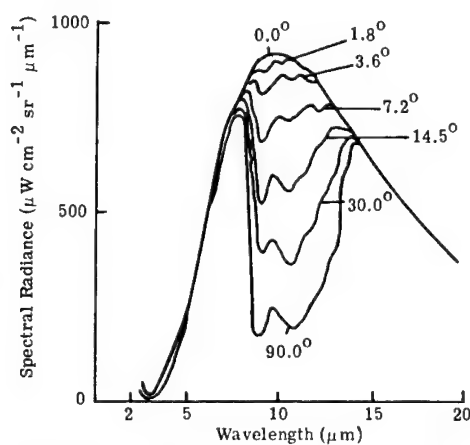


Fig. 3.23 The spectral radiance of a clear nighttime sky. It is for several angles of elevation above the horizon (Cocoa Beach, Florida).⁵¹

the thermal region. The temperature of the atmosphere, on the other hand, has a strong effect on the radiation in the thermal region but little effect in the solar region. The presence of clouds will affect both near-infrared solar scattering and thermal region emission.

Near-infrared radiation exhibits strong forward scattering in clouds. Thus the relative positions of sun, observer, and cloud cover become especially im-

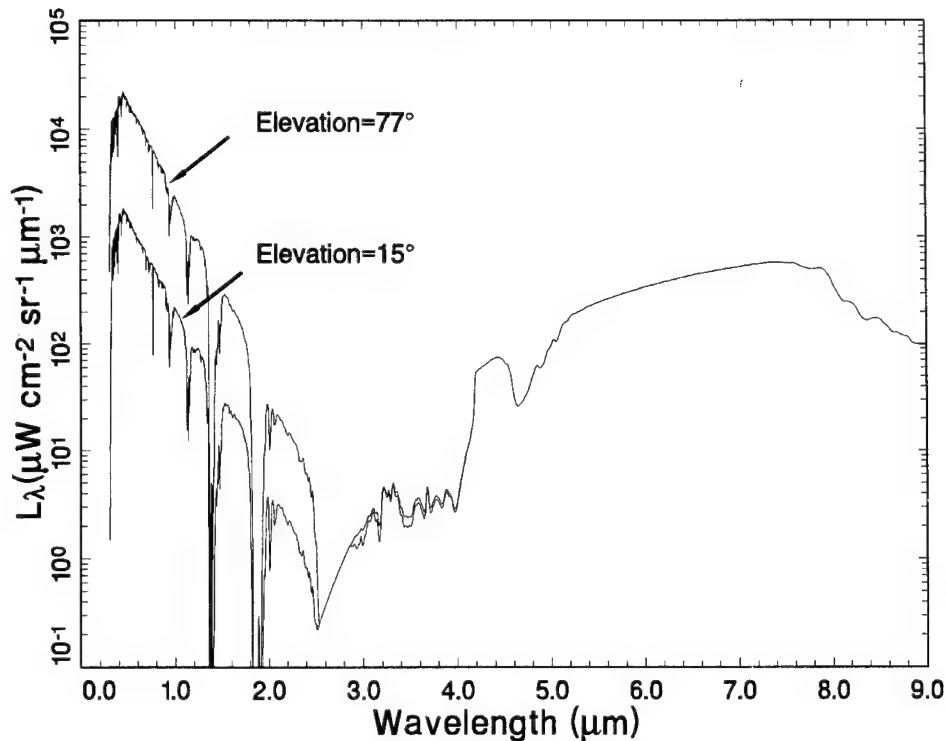


Fig. 3.24 The spectral radiance of a clear sky as a function of sun elevation calculated by LOWTRAN 7.

portant. For a heavy, overcast sky, multiple scattering reduces the strong forward-scattering effect.

Thick clouds are good blackbodies. Emission from clouds is in the 8- to 13- μm region and is, of course, dependent on the cloud temperature. Because of the emission and absorption bands of the atmosphere at 6.3 and 15.0 μm , a cloud may not be visible in these regions and the radiation here is determined by the temperature of the atmosphere. A striking example is given in Fig. 3.25. Here, the atmospheric temperature at ground level is $+10^\circ\text{C}$ and the radiation in the emission bands at 6.3 and 15.0 μm approaches a value appropriate to that temperature. The underside of the cloud has a temperature of -10°C , and the radiation in the 8- to 13- μm window approaches that of a blackbody at -10°C .

Figure 3.26 shows the variation of sky radiance as a function of elevation angle. Figure 3.27 shows the variation with respect to variations of ambient air temperature, and Fig. 3.28 shows seasonal variations.

Data on the infrared spectral radiance of the night horizon and sky are reported in Ref. 54. The data, accumulated by sounding rockets, show that the 4.3- μm night sky is measurably bright at altitudes up to 50 km. Definite horizon limb brightening was observed at this wavelength of strong carbon dioxide emission-absorption. A peak limb spectral radiance of $3.2 \times 10^{-5} \text{ W cm}^{-2} \text{ sr}^{-1} \mu\text{m}^{-1}$ at 4.3 μm was measured.

Data on zenith sky spectra are reported in Ref. 55 for various sky conditions. Ground temperature and ground level water vapor concentration were recorded as well.

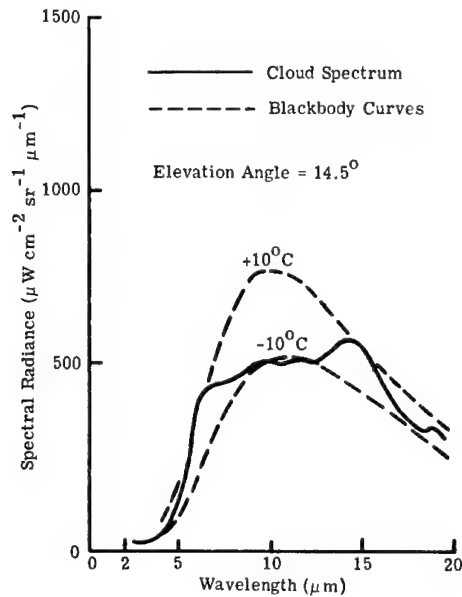


Fig. 3.25 The spectral radiance of the underside of a dark cumulus cloud.⁵²

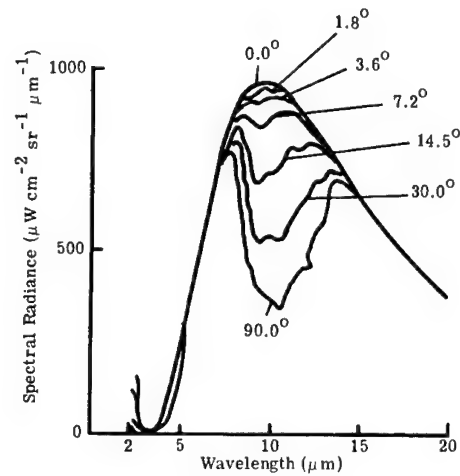


Fig. 3.26 The spectral radiance of sky covered with cirrus clouds at several angles of elevation.⁵¹

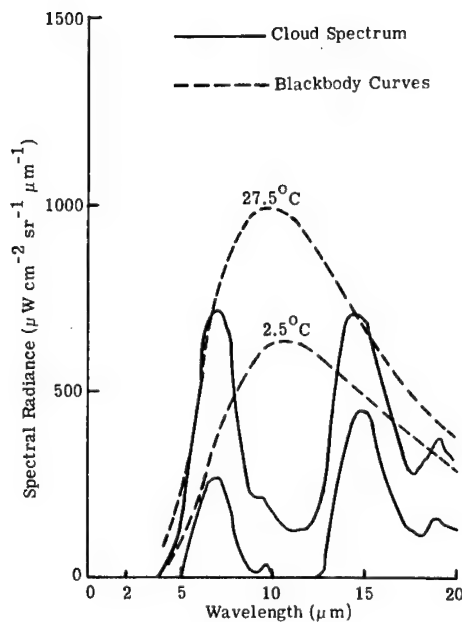


Fig. 3.27 Zenith sky spectral radiance showing the large variation with ambient air temperature.⁵¹

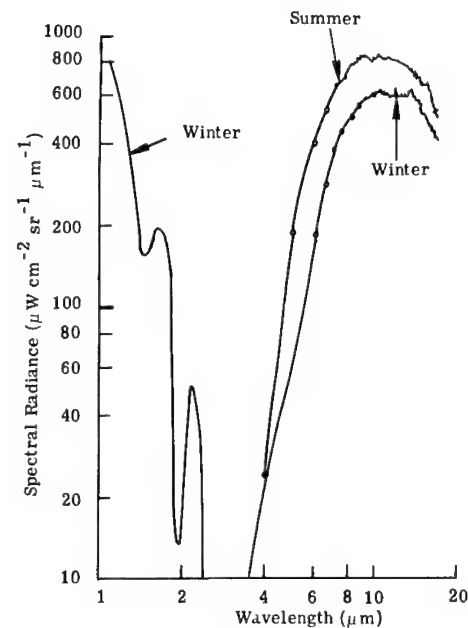


Fig. 3.28 Spectral radiance of overcast skies in winter and summer.⁵³

Overcast Sky. An approximate relation for the overcast sky luminance as viewed from ground level is reported as

$$L_v(\theta) = L_v(\text{horizon})(1 + A \cos\theta) , \quad (3.53)$$

where θ is the angle from zenith. The value of A is 2.0 according to Moon and Spencer. However, Hood and also Kasten and Moller have found A to be about 1.0 for arctic skies and skies over snow.⁵⁶

3.6.2 Thermal Radiation

The total thermal irradiance of a clear sky at sea level, $E(\text{sky})$, may be estimated from the Idso-Jackson² empirical relation using ground-level meteorological absolute air temperature T_a :

$$E(\text{sky}) = \sigma T_a^4 \{1 - 0.261 \exp[-7.77 \times 10^{-4}(273 - T_a)^2]\} . \quad (3.54)$$

This relation is primarily for heat transfer applications. Most of the irradiance is due to emission in the absorption bands on either side of the 8- to 14- μm atmospheric window.

3.6.3 Particulate Statistics

Stratospheric Aerosols. A uniform distribution of the stratospheric aerosol^{52,57-62} content tends to decrease infrared gradients. Apparently the stratosphere will contribute to background noise because of the tendency of particles to form clouds, which become arranged in periodic structures. Intensities will be high at small scattering angles, and atmospheric attenuation is negligible at these high altitudes. Table 3.26 presents a summary of information on the particle content of the stratosphere.

Table 3.26 Particle Content of the Stratosphere (from Ref. 57)

Altitude (km)	Concentrations (no. per cm^3)	Radii (μm)	Remarks	Typical Band Spacings (km)
10-30	10^{-1} to 1	>0.08 or ~ 0.10	Stable dust layer, 17 to 22 km — sulfur	—
10-30	10^{-2} to 10^{-1}	~ 0.15	Stable dust layer, 17 to 22 km — sulfur	—
10-30	$\sim <10^3$	~ 0.8 (horizontal orientation)	Temporary layers of volcanic pumice	1
17-31	$\sim <1$	~ 1.5	Nacreous clouds consisting of ice crystals	40
30-80	1	~ 0.1 (assumed)	Theoretical by measurements of con- ductivity	—
74-92	10^{-2}	~ 0.1	Noctilucent cloud (dust layer or ice crystal)	10 and 60
80	10^{-4} to 10^{-1}	0.1 (assumed)	Theoretical interplanetary dust sources, 10^{-23} to $10^{-20} \text{ g cm}^{-3}$	—

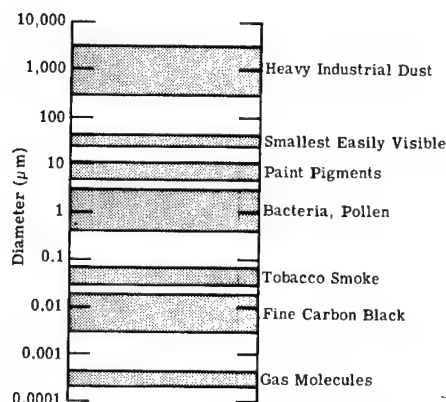


Fig. 3.29 Examples of particle sizes.⁵⁷

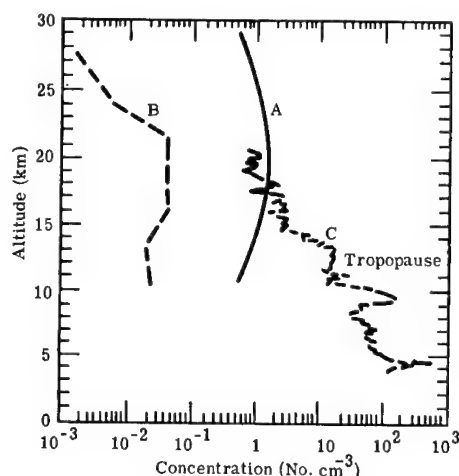


Fig. 3.30 Vertical profiles of particle concentrations. Curve A = radii greater than 0.08 μm ; curve B = radii greater than 0.1 to 0.3 μm ; curve C = Aitken nuclei, 0.01 μm radii.⁵⁷

Stratospheric particulate matter may be divided into two classes: dust particles and condensed water. Catastrophic volcanic eruptions and forest fires have deposited vast quantities of dust in the upper atmosphere. These can indirectly increase the upward intensity of reflected sunlight by acting as nucleating agents for ice.

The earth is surrounded by belts of dust, smoke, and ice particles. Encounters with the dust by the earth's gravitational field cause an accretion of 10 to 50 lb of matter per square mile per year, based on an estimate of 24,000,000 visible meteors per day.⁶³ Some of these particles are concentrated into two extreme outer shells: the lighter smoke between altitudes of 2000 to 4000 miles, and dust from 600 to 1000 miles. In general, the total particle concentrations just above the tropopause are between 10 and 100 cm^{-3} , but decrease to 1 cm^{-3} or less above about 20 km.

The manner in which a particle scatters light depends on the ratio of its radius to the wavelength of light. For ratios up to about 0.08, Rayleigh's laws hold; between 0.08 and 3, Mie theory is used; and at larger values, the laws of geometrical optics are satisfactory. Figure 3.29 gives examples of particle sizes, and Fig. 3.30 shows the concentration of different particle sizes at various altitudes.

3.6.4 Aurora^{57,64}

Auroral Spectral. Major aurora emission lines occur at 0.92, 1.04, and 1.11 μm . The measured brightness is about $6 \times 10^{-8} \text{ W cm}^{-2} \text{ sr}^{-1} \text{ line}^{-1}$ (Ref. 65). It is difficult to investigate the aurora and airglow beyond 2.0 μm because of absorption and thermal emission processes in the atmosphere. Reference 66 gives some predicted values for the 2.0- to 3.5- μm region. General reviews and one case of an application are covered in Refs. 67 through 70.

The green color of a bright aurora is attributed to a 557.7-nm atomic oxygen line. The red color is attributed to an atomic oxygen doublet at 630.0 and

636.4 nm; the bluish purple color is attributed to molecular nitrogen. Combinations of these excitations may result in the visual perception of white and yellow. The photon radiance of an aurora ranges from 10^3 to 10^6 Ry. (Ry is the unit symbol used here for a Rayleigh where 1 Ry corresponds to a photon radiance of $1/4\pi \times 10^6$ photons $\text{s}^{-1} \text{cm}^{-2} \text{sr}^{-1}$.)

Figure 3.31 shows the auroral spectrum between 0.9 and 1.2 μm . This curve was obtained by averaging a number of individual spectra. Figure 3.32 shows auroral spectra between 1.4 and 1.65 μm . The dotted curve is the airglow spectrum fitted to the auroral spectrum in a region where the auroral emission appears feeble. Spectra a, b, and c were made in consecutive scans, with a total time of 3 min. The relative intensities of features on a single scan are not significant since the aurora fluctuates in brightness during the scanning period.

High-altitude, rocket-borne spectrometers were used to obtain⁷² aurora spectra in 1973. Figures 3.33 and 3.34 show the spectral radiance in the short-wavelength infrared range (SWIR) from 1.6 to 5.6 μm and in the long-wavelength infrared (LWIR) from 7.0 to 23.0 μm . Figure 3.35 shows a profile of spectral radiance at 4.3 μm as a function of altitude. The unit MRy is a megarayleigh.

Auroral Zones. Auroral zones⁶⁴ are divided into three areas: the north and south auroral regions extending from geomagnetic latitudes 60° to the poles, the subauroral belts between 45 and 60° , and the minauroral belt between 45°N and 45°S . The auroral regions include the auroral zones (the regions of maximum occurrence) and the auroral caps (the polar regions within the auroral zones).

Although aurora occur primarily in the auroral regions, large displays may occur in quite low latitudes. However, in tropical and even low-temperature latitudes they are extremely rare.

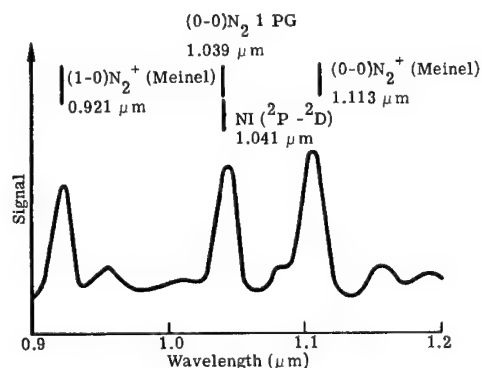


Fig. 3.31 Auroral spectrum between 0.9 to 1.2 μm . It was obtained with a lead sulfide spectrometer; projected slit width 100 \AA (Ref. 65).

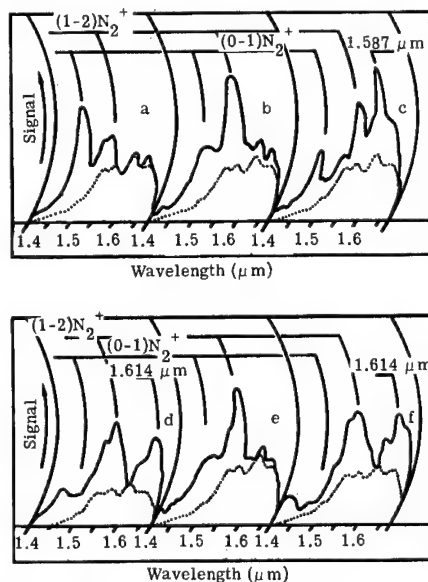
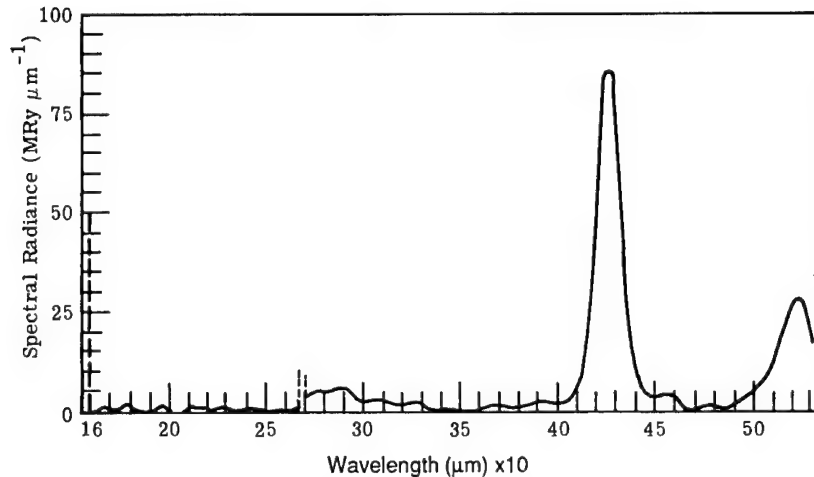
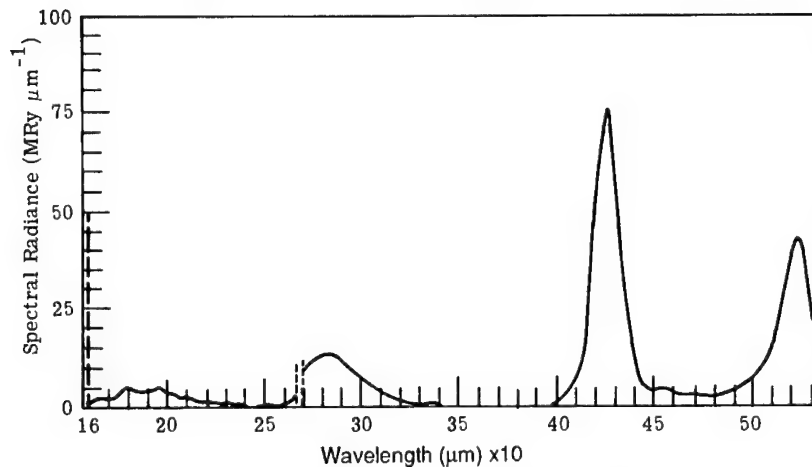


Fig. 3.32 Auroral spectra between 1.4 to 1.65 μm . It was obtained with a lead sulfide spectrometer; projected slit width 200 \AA (Ref. 71).



(a) Paiute Tomahawk 10.205-2 97 km.



(b) Paiute Tomahawk 10.205-2 86 km.

Fig. 3.33 Sample spectral scans from a SWIR spectrometer aboard a Paiute-Tomahawk rocket launched from Poker Flat, Alaska, 24 March 73. Although uncorrected for actual rocket aspect, the data approximate the zenith radiance.⁷²

The frequency of auroral occurrences is at a maximum of 20 to 25° from the geomagnetic poles. Figure 3.36 shows the geographic distribution of the frequency of aurora in the northern hemisphere. The isochasms refer to the number of nights during the year in which an aurora might be seen at some time during the night, in any part of the sky, if clouds and other factors affecting visual detection of aurora do not interfere. Figure 3.37 shows the zone of maximum auroral frequency in the southern hemisphere.

Periodic Variations. The number of aurora observed from a particular point over the course of a year may vary widely and is strongly correlated with solar activity. Minimum auroral activity corresponds with minimum solar activity. Maximum auroral activity usually occurs about two years after sunspot maximum.

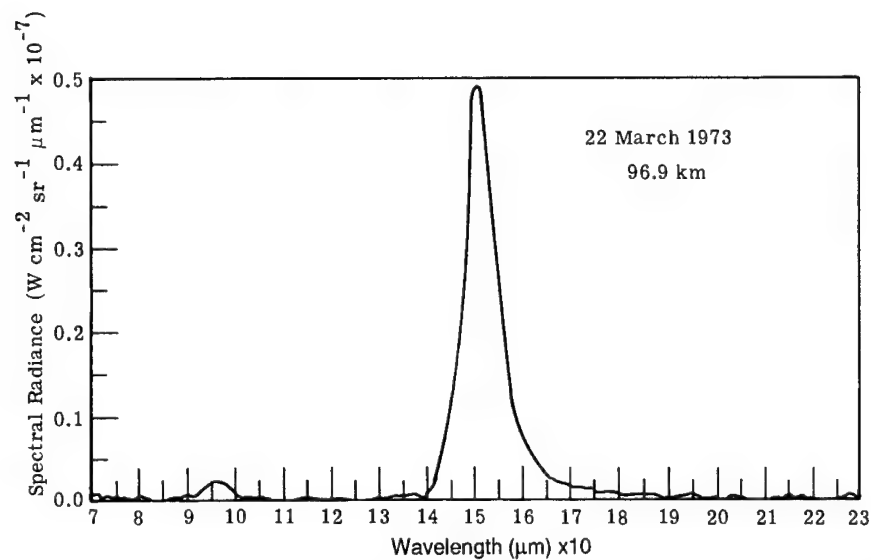


Fig. 3.34 Sample spectrum scan (vertical) from a LWIR spectrometer aboard a Black Brant rocket flown from Poker Flat, Alaska, 22 March 73. The rocket altitude is 96.9 km on rocket descent.⁷²

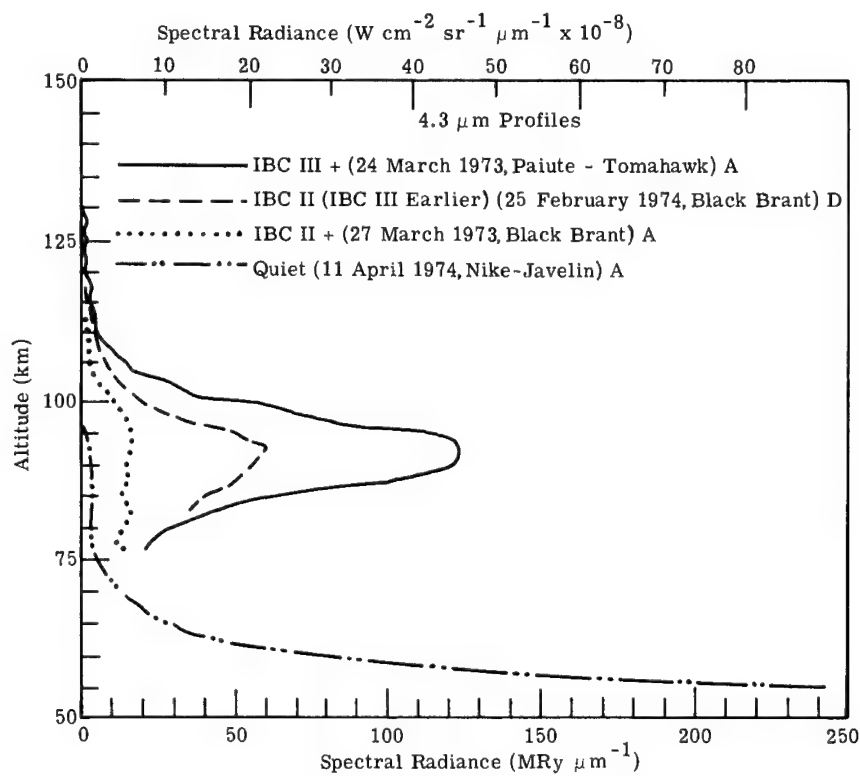


Fig. 3.35 Zenith peak spectral radiance at 4.3 μm measured with SWIR spectrometers flown on four different rockets under various auroral conditions.⁷²

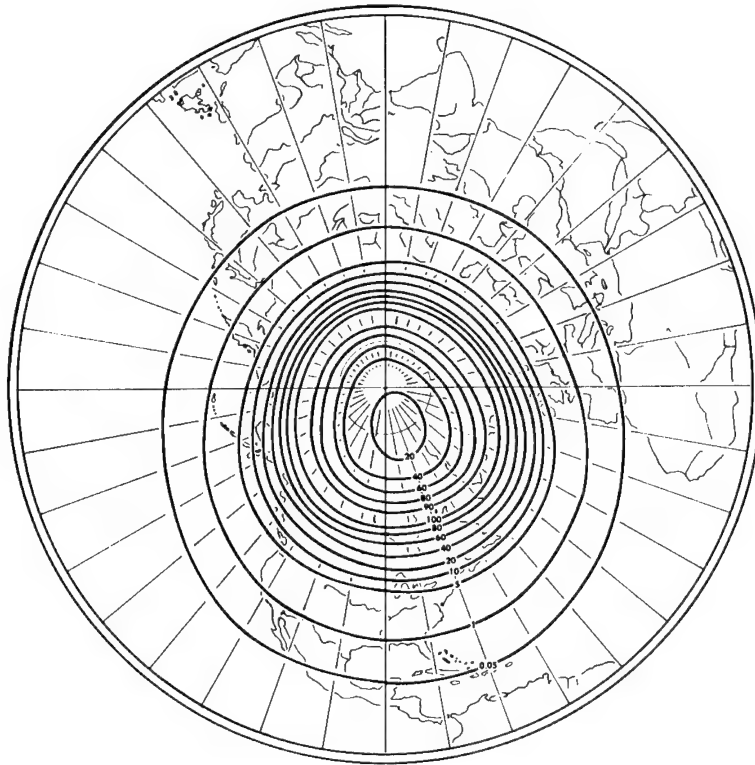


Fig. 3.36 Geographic distribution of the frequency of aurora in the northern hemisphere.⁷³

Height and Vertical Extent. On auroral arcs and bands, the most convenient height to measure is the apparent lower border, which is fairly sharp. An example of a set of such measurements in and near the auroral zone is shown in Fig. 3.38. The total number of measurements shows a concentration between 95 and 110 km, with a double peak. The lower limits of individual rays appear 10 or 15 km higher than the lower edges of most arcs, bands, and draperies. Sunlit auroral rays appear systematically higher than displays in the dark atmosphere. Figure 3.39 shows the heights of rays over southern Norway. A few sunlit rays extend higher than 1000 km.

An extensive discussion of aurora and auroral processes is given in Chapter 13 of the *Handbook of Geophysics and the Space Environment*.¹⁵

3.6.5 Night Airglow

Airglow may be defined as the nonthermal radiation emitted by the earth's atmosphere. The exceptions are auroral emission and radiation of a cataclysmic origin, such as lightning and meteor trails.⁶⁴ Night airglow spectral radiance is of an order of magnitude of microwatts per square centimeter-steradian-micrometer with banded spectral features characteristic of molecular emission.

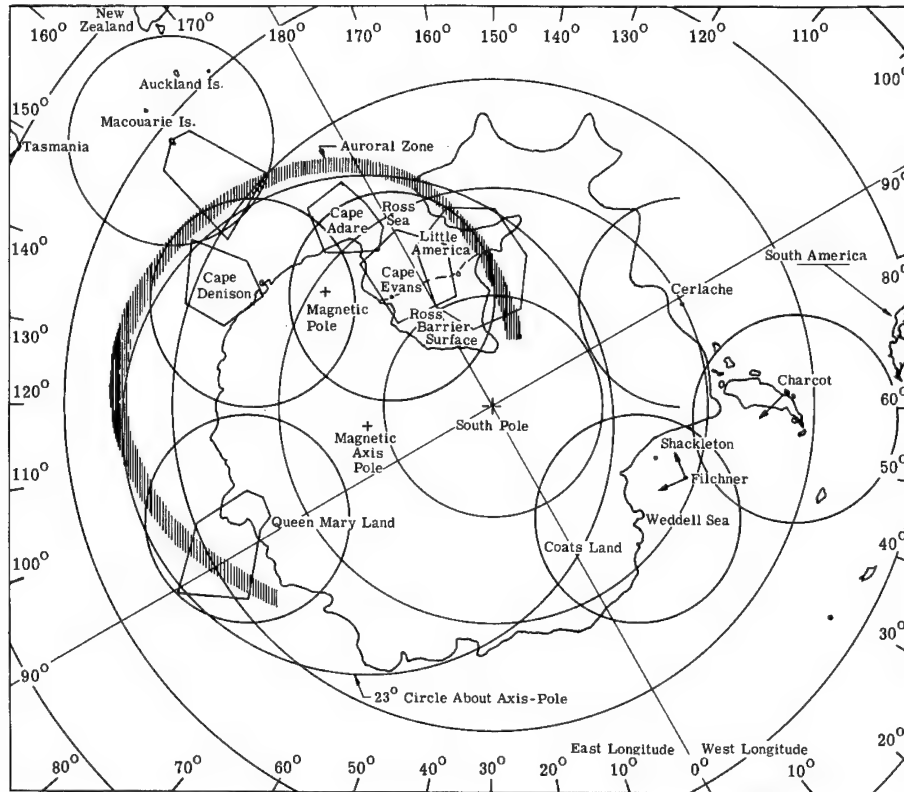


Fig. 3.37 Zone of maximum auroral frequency in the southern hemisphere.⁷⁴

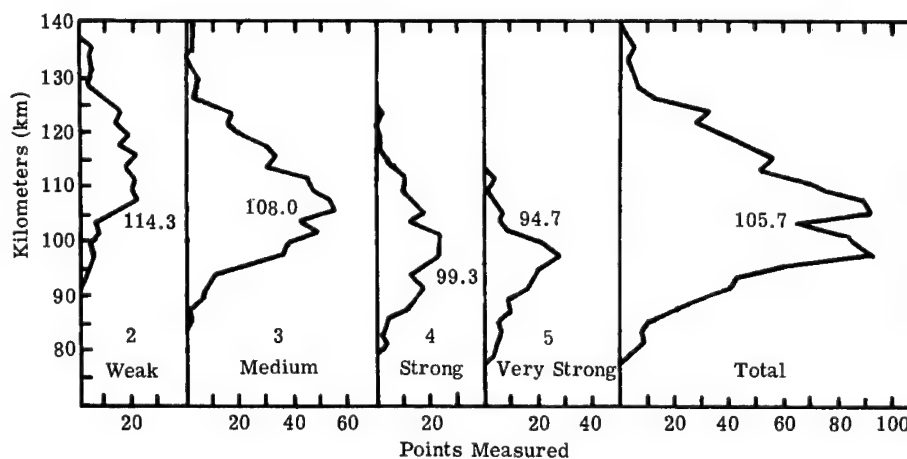
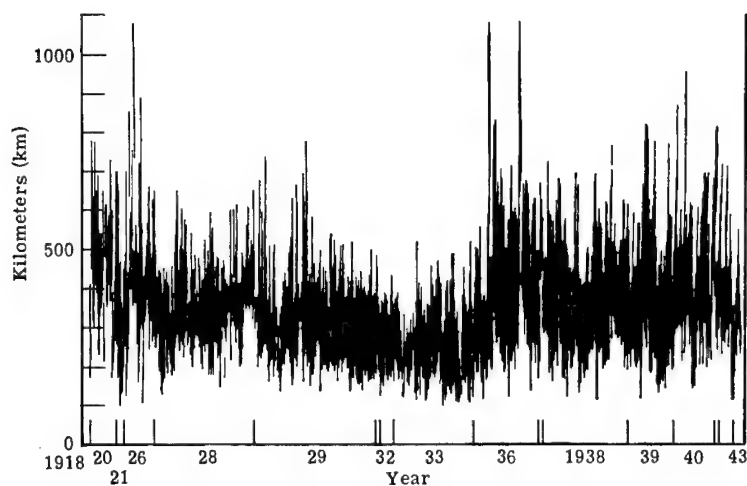
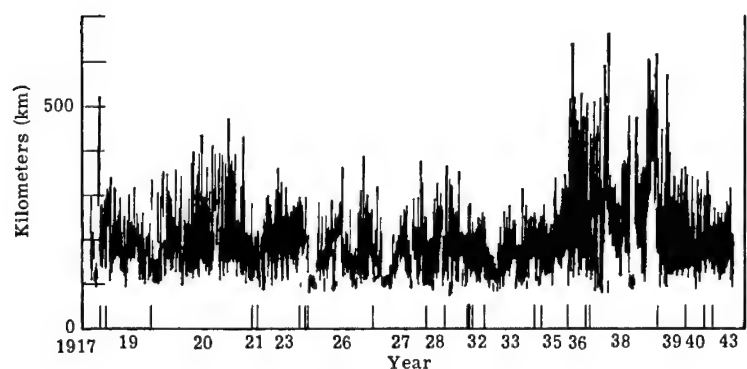


Fig. 3.38 Frequency distribution of heights of lower borders of auroral arcs.⁷⁵

Night airglow emissions in the infrared are caused by transitions between vibrational states of the OH^- radical. The exact mechanism of excitation is still unclear, but the effect is to release energy from solar radiation stored during the daytime. Airglow occurs at all latitudes.



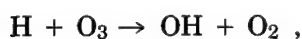
(a) Sunlight.



(b) Earth's shadow.

Fig. 3.39 Length and position in the atmosphere of the vertical projections of auroral rays (1917 to 1943).⁷⁶

There is evidence⁷⁷ that some of the excitation is



Thus, it appears that the distribution of night airglow is related to that of ozone. The measured heights of the airglow range from 70.0 to 90.0 km, which correspond to the location of ozone. The nightglow increases with angle θ away from the zenith approximately as $\sec\theta$. Measurements usually are reported normalized to the zenith.

Variations in airglow radiance during the night seem⁷⁸ to be caused by the motion of large patches (airglow cells) with dimensions of about 2500 km, moving with velocities of about 70 m s^{-1} .

Figure 3.40 shows⁷⁹ the relative airglow radiance. Airglow emissions caused by OH— appear as small maxima in the vicinity of 1.6 and $2.15 \mu\text{m}$. Although

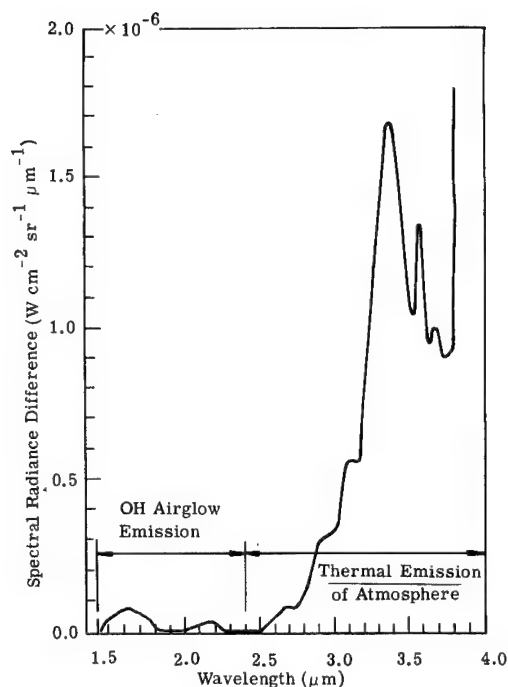


Fig. 3.40 Airglow intensity.⁷⁹

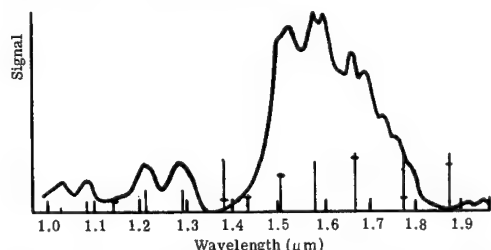


Fig. 3.41 Nightglow spectrum. It is obtained with a scanning spectrometer (projecting slit width of 200 Å). The origins and expected intensities of OH bands are shown by vertical lines; the horizontal strokes indicate the reduction due to water vapor.⁸⁰

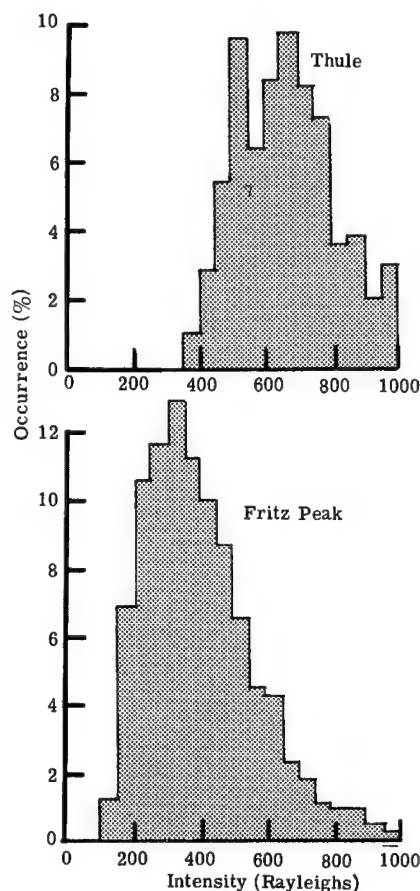


Fig. 3.42 Frequency distribution of airglow.⁷⁵

further emission bands are predicted in the range from 2.8 to 4.5 μm , they are thoroughly masked by the thermal emission of the atmosphere. Figure 3.41 shows the nightglow spectrum in the 1- to 2- μm region.

If one looks straight down from a satellite, the atmospheric spectrum should be very similar to that shown in Figs. 3.40 and 3.41. Table 3.27 compares⁶⁴ the approximate rates of emission for various airglow and auroral lines. The references should be consulted for further details. Note that for the airglow all results are given for the zenith itself rather than for the angles at which observations are usually made. Figure 3.42 shows the frequency distribution of airglow and weak auroral radiance near the geomagnetic pole (Thule, Greenland) and at a subauroral station (Fritz Peak, Colorado).

Table 3.27 Comparison of Aurora and Airglow Photon Emission Rates (from Ref. 64)

<i>Source</i>	<i>Emission</i>	<i>Airglow Brightness</i>
Aurora, IBC* I	[OI] ₃₂ 5577 Å	1 kRy
	II	10 kRy
	III	100 kRy
	IV	1000 kRy
Night airglow** (in the zenith)	[OI] ₃₂ 5577 Å	250 Ry
	[OI] ₂₁ 6300 Å	50-100 Ry
	Na 5893 Å	—
	summer	<30 Ry
	winter	200 Ry
	H α 6563 Å	5-20 Ry
	Ly α 1215 Å	2.5 kRy
	O ₂ Atmospheric (0-1) 8645 Å	1.5 kRy
	O ₂ Herzberg (observable range)	430 Ry
	OH (4-2) 1.58 μ m	175 kRy
	OH (estimated total)	4500 kRy
Twilight airglow† (referred to the zenith)	N ₂ ⁺ 3914 Å	1 kRy
	(quiet magnetic conditions)	—
	Na I 5893 Å	—
	summer	1 kRy
	winter	5 kRy
	[OI] ₂₁ 6300 Å	1 kRy
	Ca II 3933 Å	150 Ry
	Li I 6708 Å	200 Ry
	[NI] ₂₁ 5199 Å	10 Ry
	O ₂ IR Atmospheric (0-1) 1.58 μ m	20 kRy
Day airglow†† (referred to the zenith)	Na 5893 Å	—
	summer	2 kRy
	winter	15 kRy
	[OI] ₂₁ 6300 Å	50 kRy
	OI 8446 Å	0.5 kRy
	OI 11,290 Å	0.5 kRy
	N ₂ ⁺ 3914 Å	<70 kRy
		> 1 kRy

*Recommended as definitions of the International Brightness Coefficients (IBC) (Refs. 81 and 82).

**Average values.

†Approximate values of the maximum emission rates that are observed during twilight. These values are often governed by the time after sunset when observation first become possible.

††Values predicted from theory (Refs. 83 through 86).

Some evidence suggests a general increasing radiance of airglow emissions toward higher latitudes and a bright belt at middle latitudes. Chandra et al.⁸⁸ have made satellite observations of the 6300-Å emissions of oxygen. They show the global distribution from -40 to 40° of latitude around the globe for October 1967 passes during post-sunset conditions.

Figure 3.43 shows a spectrum of night airglow observed from high altitude. Sharma et al.⁹⁰ have developed a computer model, SHARC, to calculate the

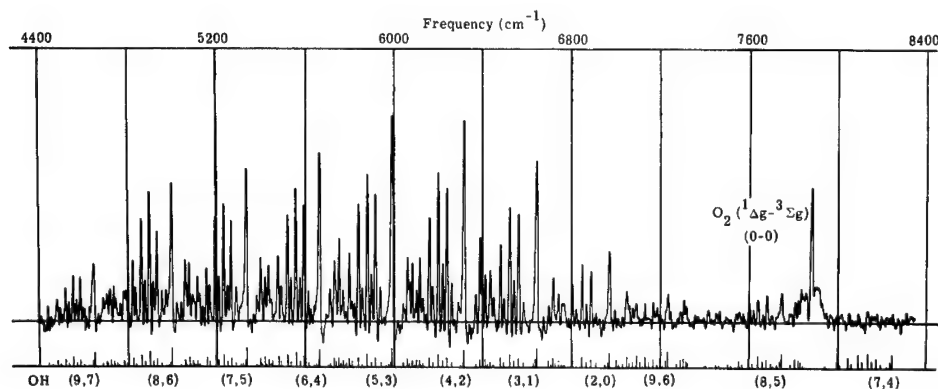


Fig. 3.43 Spectrum of night airglow observed from an altitude of about 80,000 ft. The total recording time of the 12 interferograms from which this spectrum is calculated equals 141 minutes.⁸⁷

night airglow from CO_2 , NO , O_3 , H_2O , CO , and OH in the spectral range of 2 to 20 μm . The model makes use of various standard atmospheres. Some example calculated spectra are shown in Figs. 3.44 and 3.45. The line of sight is through the limb of the earth where the tangent altitudes are the heights of the line of sight at closest approach to the surface of the earth.

Infrared airglow is described in more detail in Chapter 13 of the *Handbook of Geophysics and the Space Environment*.¹⁵

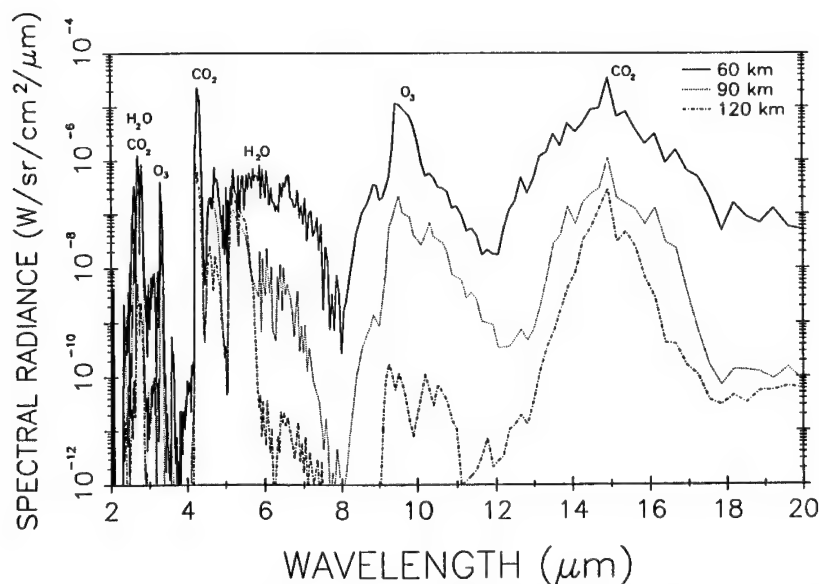


Fig. 3.44 SHARC calculation under daytime conditions for three limb viewing paths at tangent altitudes of 60, 90, and 120 km altitude.⁹⁰

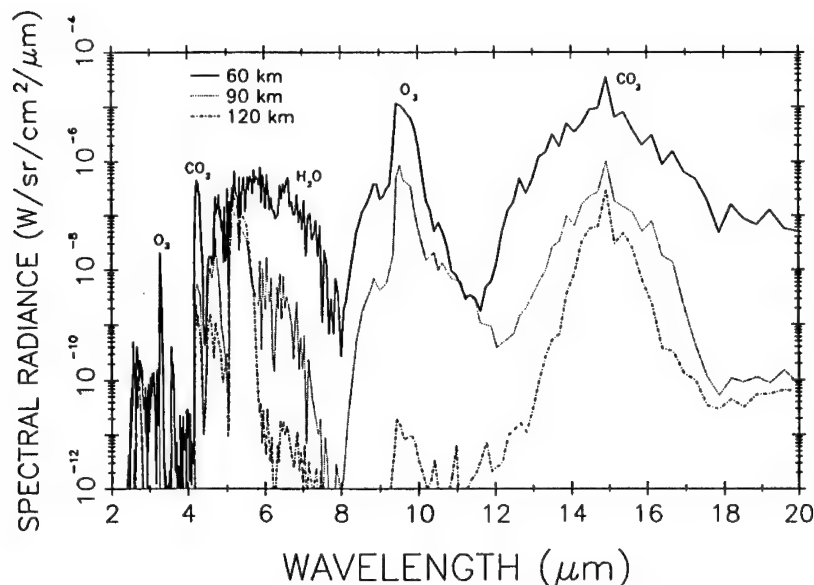


Fig. 3.45 SHARC calculation under nighttime conditions for three limb viewing paths at tangent altitudes of 60, 90, and 120 km altitude.⁹⁰

3.6.6 Meteoroid Radiation⁹¹

Elements contributing to meteor spectra are N, Ca, Cr, Fe, H, Mg, Mn, Na, Ni, Si, Sr, O, and N. The absolute visual magnitude M_v of a meteor for an observer on the ground is the magnitude it would have at 100 km through one air mass. The symbol M_v in this section should not be confused with luminous exitance. Apparent visual magnitude m_v requires a correction for τ/R^2 :

$$M_v = 6.8 - 2.5 \log_{10} \left[\frac{\int V(\lambda) \Phi_\lambda d\lambda}{1 \text{ lm}} \right], \quad (3.55)$$

where $V(\lambda)$ is the visual efficiency. The maximum luminous intensity is reached in the range of 78 to 95 km.

3.7 THE EARTH

3.7.1 High-Altitude and Space Views

Geometric Relationships. Figures 3.46 and 3.47 present some important relationships bearing on satellite viewing of the earth. In Fig. 3.47, point P (as an example) represents a vehicle 400 nmi high at an elevation of 35° . The slant range is 655 nmi, and the great circle arc (angle between vectors located at the center of the earth and pointing, respectively, to the satellite and to the ground point viewed) is 7° .

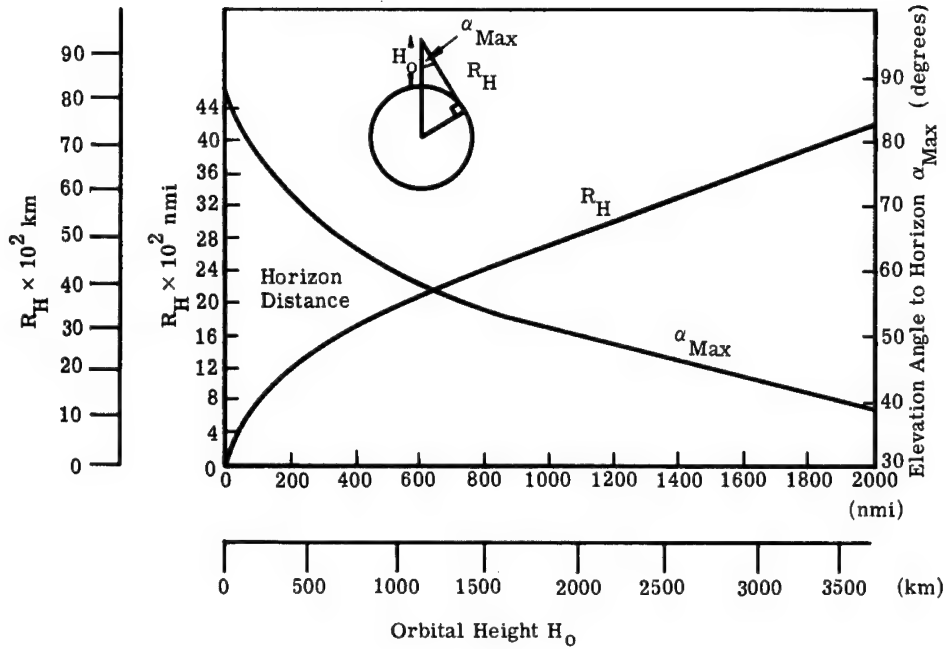


Fig. 3.46 Ranges and view angles.²⁵

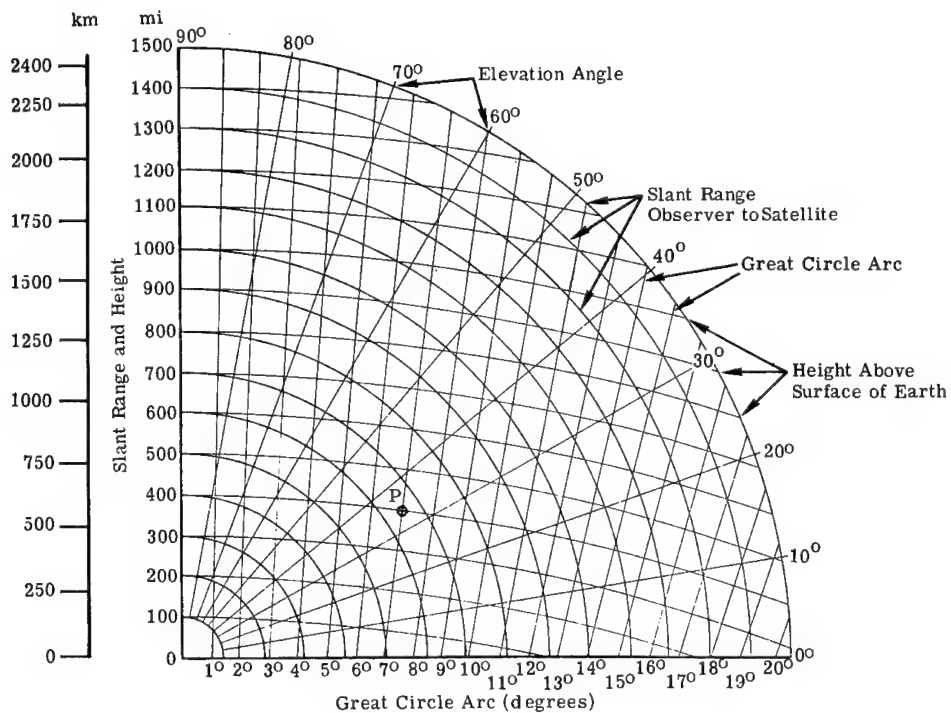


Fig. 3.47 Satellite coordinate conversion.²⁷

Path Lengths. The length L of a line (see Fig. 3.48) between any two points at different altitudes is found according to the following general equations:

$$\begin{aligned}(R_E + C_0)^2 &= (R_E + A_B)^2 + 2L(R_E + A_B) \cos \delta \\ &= (R_E + A_B)^2 + 2L(R_E + A_B) \sin \gamma_e ,\end{aligned}\tag{3.56}$$

$$L^2 = (R_E + C_0)^2 - (R_E + A_B)^2 - 2L(R_E + A_B) \sin \gamma_e ,$$

$$L = [(R_E + C_0)^2 - (R_E + A_B)^2 \cos^2 \gamma_e]^{1/2} - (R_E + A_B) \sin \gamma_e ,$$

where

R_E = radius of sphere

A_B = altitude of the background point

C_0 = altitude of the observer

γ_e = elevation angle of the background point position (from local horizontal)

α = elevation angle from nadir at observer's point.

The angle α is computed by the following relationship:

$$\alpha = \cos^{-1} \left[\frac{(R_E + C_0)^2 + L^2 - (R_E + A_B)^2}{2(R_E + C_0)L} \right] .\tag{3.57}$$

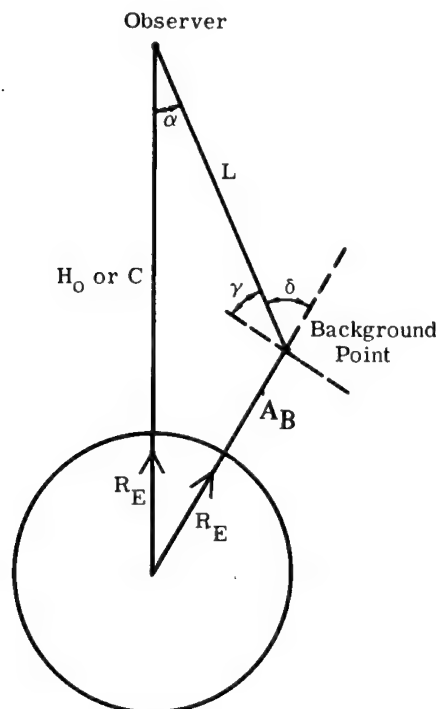


Fig. 3.48 Path length diagram.

Figure 3.49 illustrates the scattering angle β , the sun's elevation angle γ_e , the satellite scanner's elevation angle α , and the scanner's azimuth angle ϕ from the direction of the sun. The scattering angle is:

$$\beta = \cos^{-1}(\cos\gamma \sin\alpha \cos\phi - \sin\gamma \cos\alpha) . \quad (3.58)$$

Figure 3.50 illustrates these angles for a spherical earth. Equation (3.58) becomes

$$\beta = \cos^{-1}\{\cos[90^\circ - (\xi - \Delta)] \sin\alpha \cos\phi - \sin[90^\circ - (\xi - \Delta)]\} , \quad (3.59)$$

where ξ is the elevation angle (latitude) of the observed point from the earth's equatorial plane and Δ is the latitude of the sun's prime ray.

Figure 3.51 shows⁵⁷ the range of the sun's declination angle. (Both ξ and Δ are taken to be positive for a northern latitude.)

3.7.2 Albedo

Spectra in the Scattering Region. The daytime spectra of objects at ambient temperatures show minima around 3 to 4 μm . In the more transparent regions of the spectrum, between 3 and 5 μm in the daytime, the sky radiates less a few degrees above the horizon than the ground a few degrees below the horizon. In the scattering region of the spectrum, the sky and the ground often show radiances of comparable magnitude. Usually the ground radiance is somewhat higher than that of the sky and it is frequently at a minimum near the horizon.

Figures 3.52 and 3.53 are elevation scans of the spectral radiance near the horizon at different wavelengths. The scans cover alternating patches of shaded and sunlit ground, trees, and mountains (the northern slope of Pike's Peak in Colorado), as well as the clear sky up to 15 to 20° near the horizon.

Average spectral reflectances of common terrains are shown in Fig. 3.54. Figures 3.55, 3.56, and 3.57 provide information on spectral reflectance, luminance, and variations in reflectance, respectively. Figures 3.58 through 3.61 show the upwelling, reflected, spectral radiance for an exoatmospheric observer as calculated with Turner's atmospheric scattering model.⁹⁸

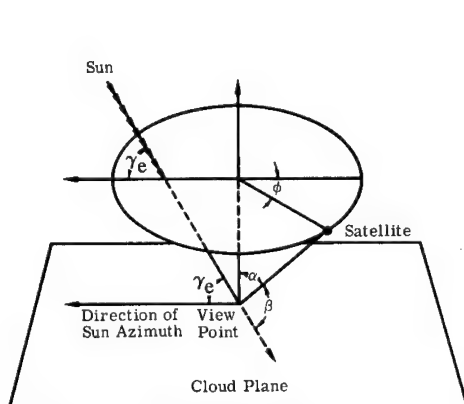


Fig. 3.49 Scattering angle geometry.⁵⁷

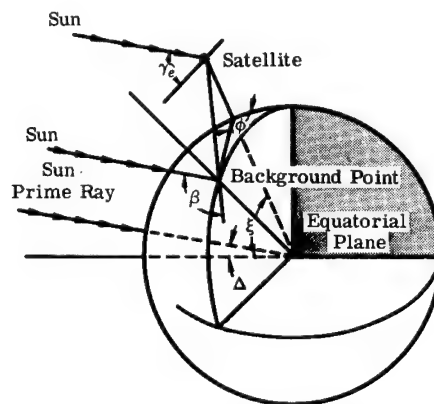
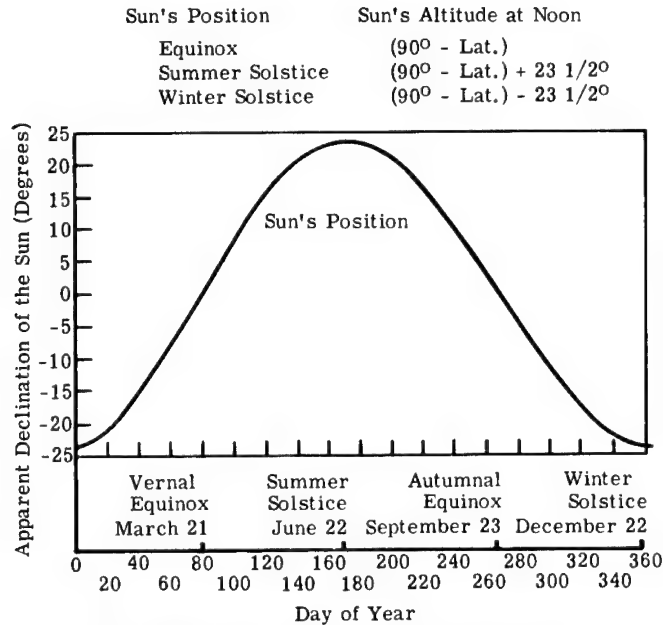
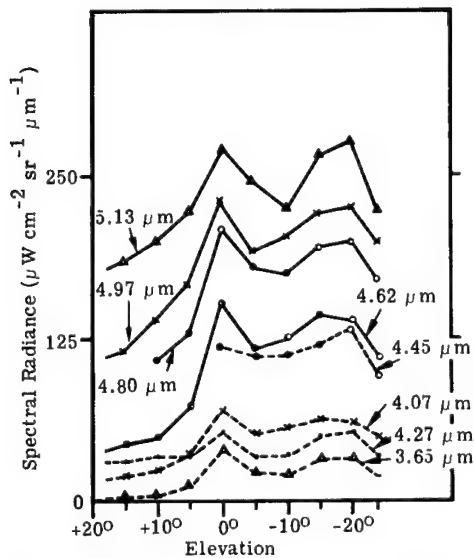
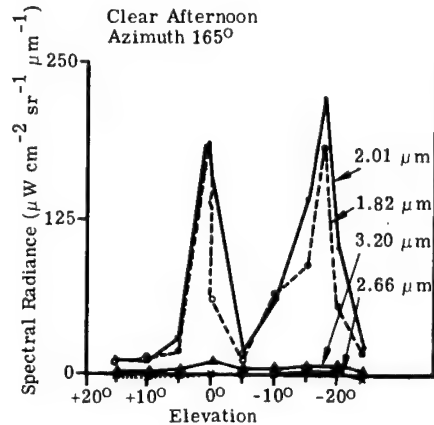


Fig. 3.50 Solar scattering angle.⁵⁷

Fig. 3.51 Solar declination to the equator.⁵⁷Fig. 3.52 Elevation scans across mountainous terrain at fixed wavelengths in the interval of 1.8 to 3.2 μm (Ref. 92).Fig. 3.53 Elevation scans across terrain at the same time as in Fig. 3.52 at fixed wavelengths in the interval of 3.5 to 5.2 μm (Ref. 92).

3.7.3 Emission from the Surface⁹²

Measured Spectra in the Emission Region. Figure 3.62 shows the comparative spectral radiances of a patch of ground at an airfield observed on a clear night and during the following morning with the sun shining on it. For comparison, Fig. 3.63 shows the radiance of the night sky just above the horizon and that of the ground at the same angle below the horizon.

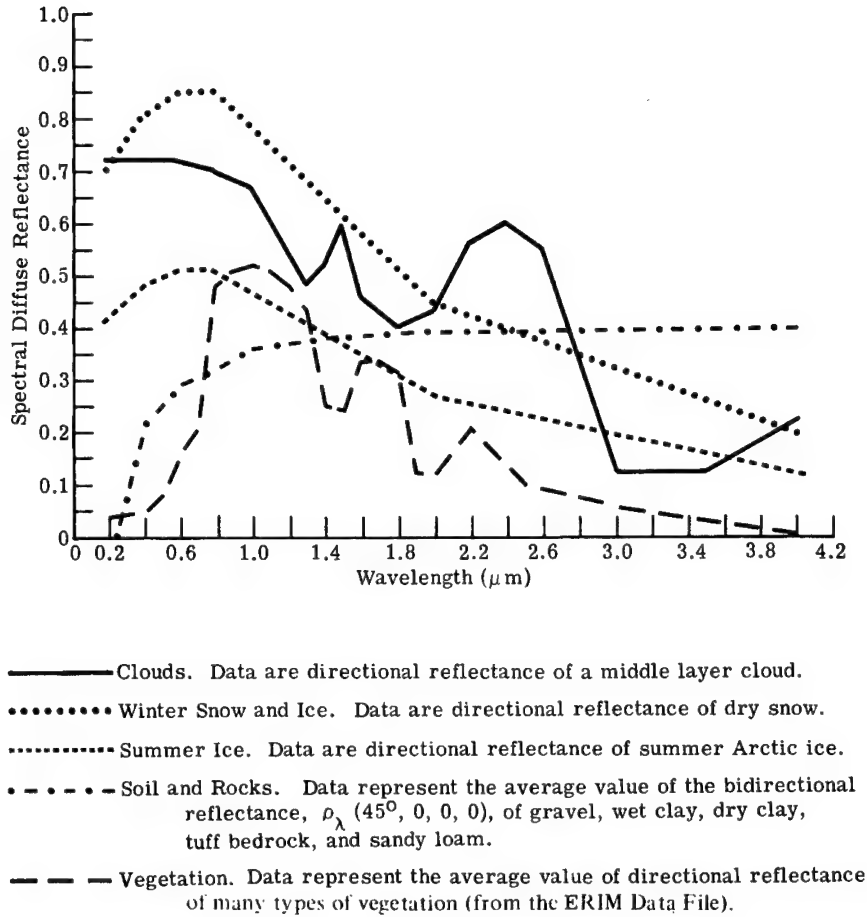


Fig. 3.54 Spectral diffuse reflectance of earth-atmosphere constituents.⁹³⁻⁹⁷

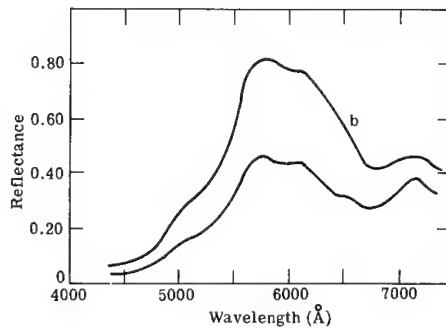


Fig. 3.55 Spectral reflectance, measured at 90,000-ft (27.5-km) altitude above summertime cultivated farmland at 50° solar zenith angle. Curve b shows the effect of the intrusion of 0.6 cumular cloud structure.⁹³

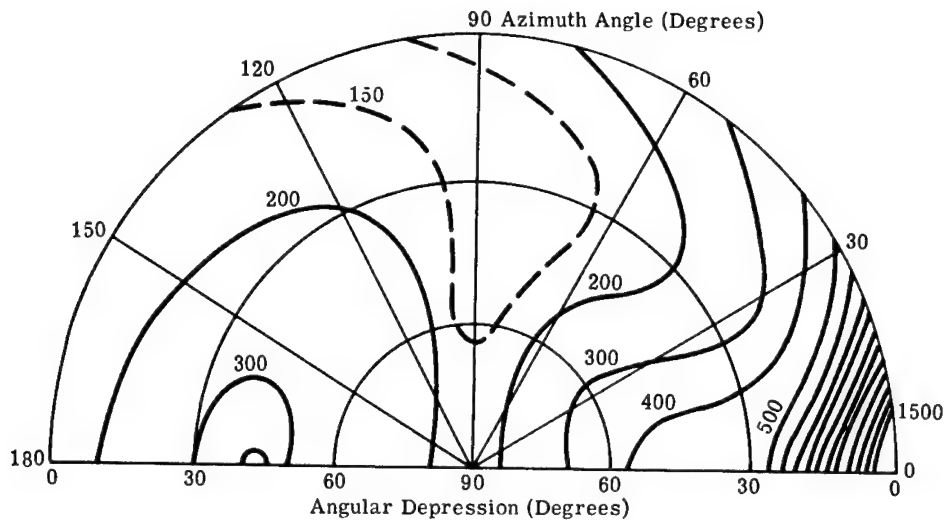


Fig. 3.56 Luminance (cd ft^{-2}) over the downward hemisphere. It is measured with balloon-borne equipment over a mountain area in early autumn at an altitude of 98,000 ft (29.8 km) in a relatively turbid atmosphere. (For results in cd m^{-2} , multiply cd ft^{-2} by 10.764.)⁹¹

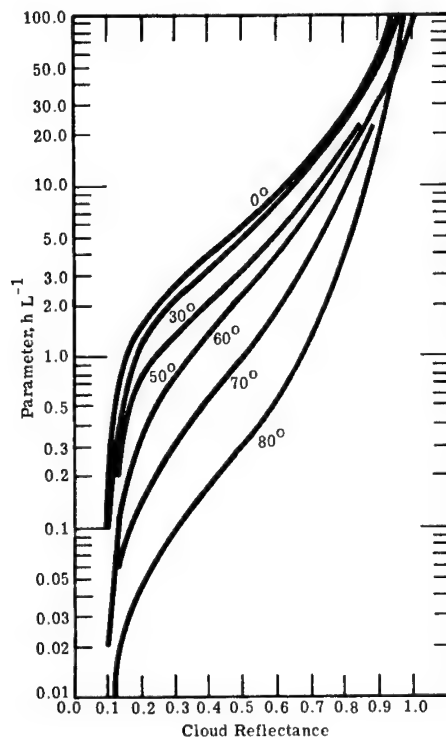


Fig. 3.57 The variation in reflectance as a function of cloud thickness parameter hL^{-1} for different solar zenith angles. The cloud thickness is h and the mean free path of a light ray is L (Ref. 91).

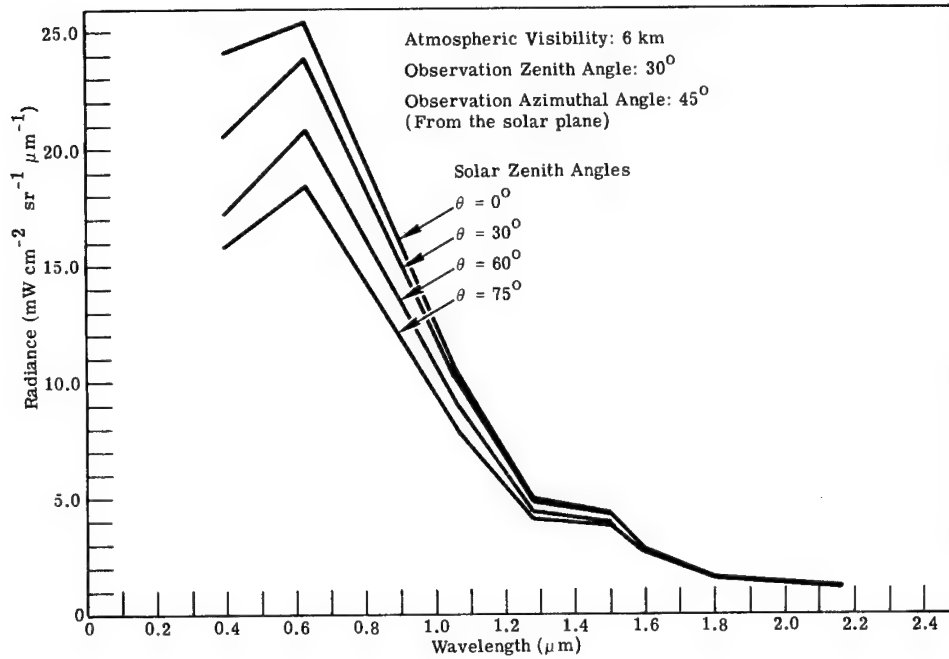


Fig. 3.58 Upwelling spectral radiance observed at the top of a plane parallel atmosphere with the earth's surface obscured by a low-altitude cloud deck.⁹⁸

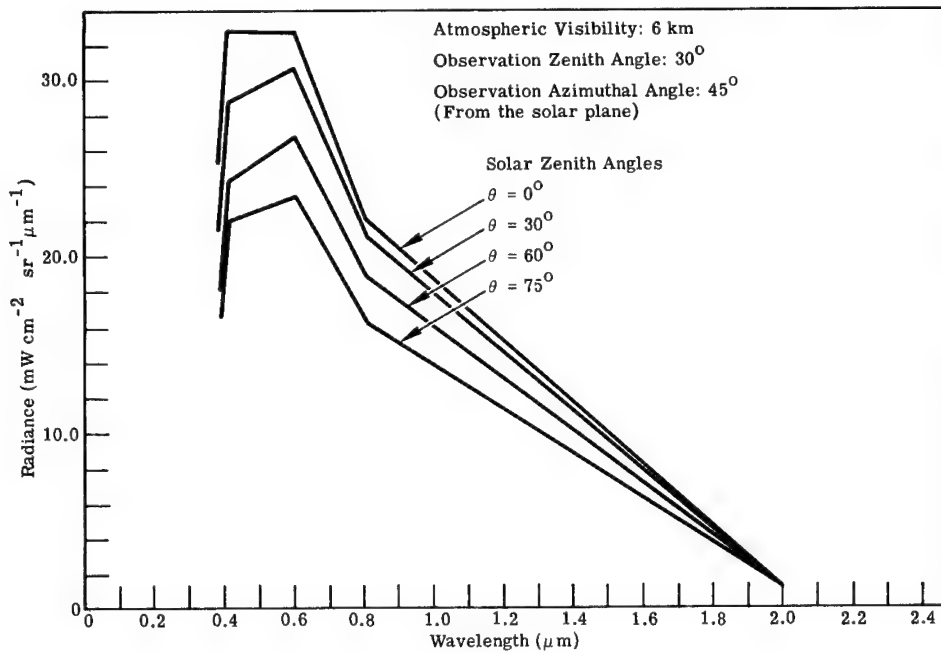


Fig. 3.59 Upwelling spectral radiance observed at the top of a plane parallel atmosphere with the earth's surface composed of winter snow and ice.⁹⁸

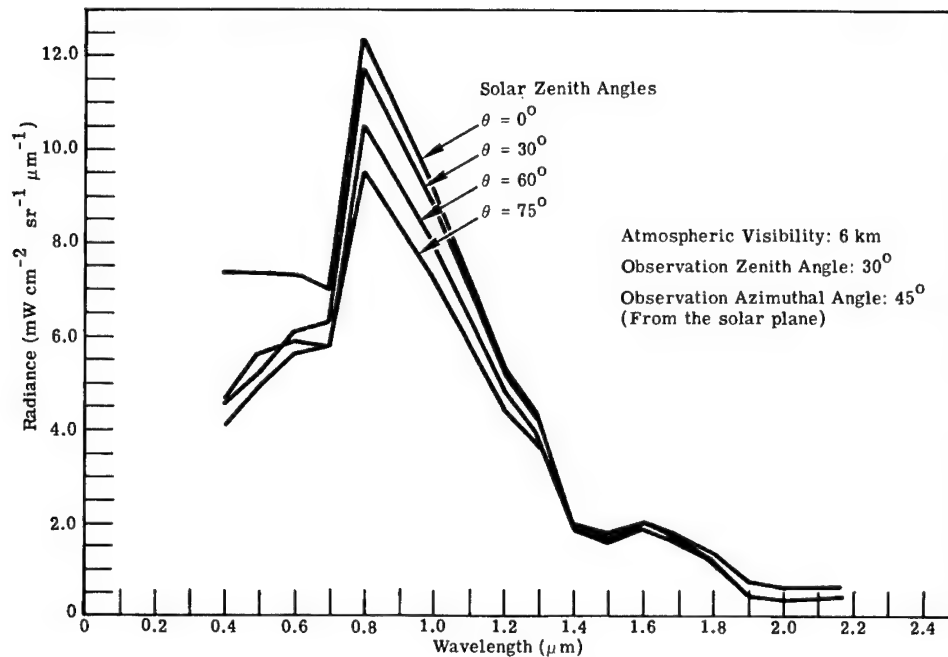


Fig. 3.60 Upwelling spectral radiance observed at the top of a plane parallel atmosphere with the earth's surface composed of vegetation.⁹⁸

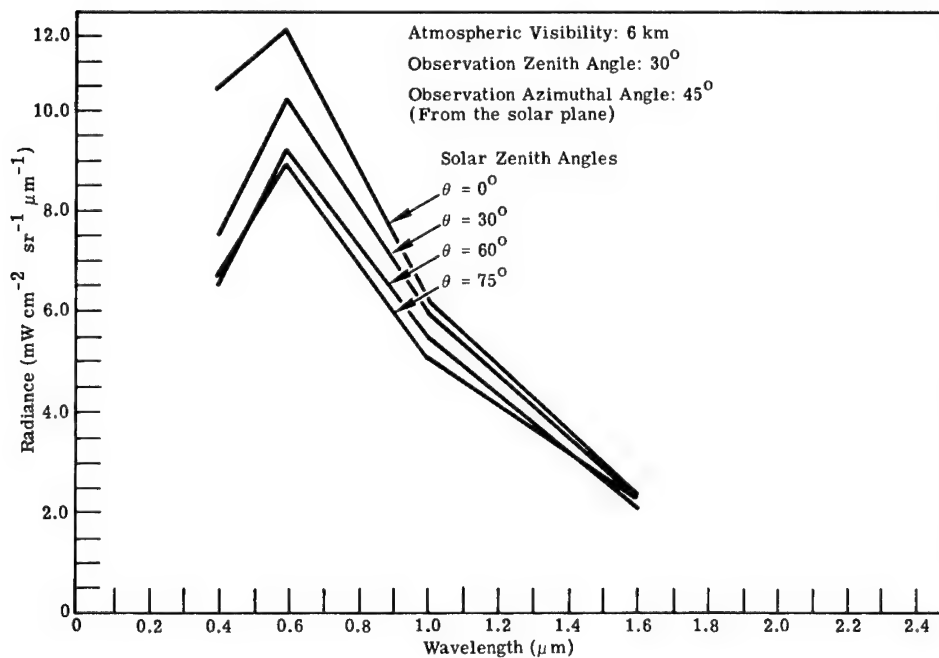


Fig. 3.61 Upwelling spectra radiance observed at the top of a plane parallel atmosphere with the earth's surface composed of soil and rocks.⁹⁸

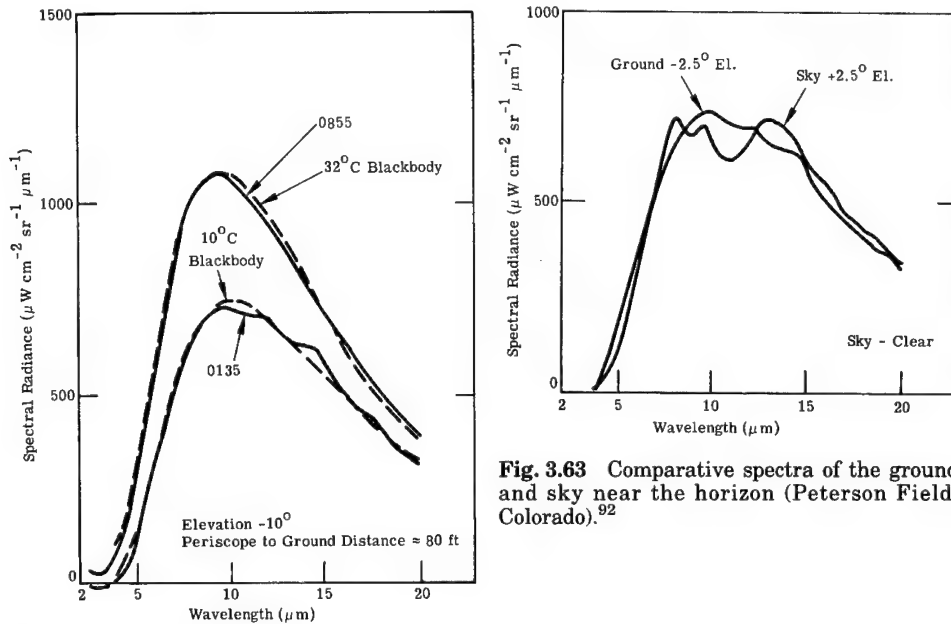


Fig. 3.63 Comparative spectra of the ground and sky near the horizon (Peterson Field, Colorado).⁹²

Fig. 3.62 Day and night radiances of grass-covered field (Peterson Field, Colorado).⁹²

The spectra of distant terrain do not always conform to the blackbody characteristics observed in the radiance of nearby terrain. This can be seen in Fig. 3.64, where the upper curve represents the radiance of a city on a plain as viewed from the summit of a mountain at a distance of about 15 miles.

Figure 3.65 shows the diurnal variation in the 10- μm radiance of selected backgrounds on the plains as measured from the summit of Pike's Peak in Colorado. The line-of-sight distances are: forest, 30 miles; grassy plains, 21 miles; airfield, 19 miles; city, 15 miles.

Figure 3.66 shows the spectral radiance of dry sand. The 9- μm dips in the reflectance of the sand for curves A and C correspond with a wavelength of relative poor emissivity. The reason is that the crystals of common silica sand exhibit reststrahlen at 9 μm . With overcast sky (curve B), the added sky radiance reflected at this wavelength just compensates for the loss of emissivity.

The effect of moisture on the radiance of sand is shown in Fig. 3.67.

Calculated Spectra in the Emission Region. Figure 3.68 shows the cross-section view of the geometry used in calculating thermal spectra from the surface by modeling. Figure 3.69 illustrates the meaning of the terms *limb darkening* and *limb brightening*. Figures 3.70 to 3.77 show calculated spectral radiances to be expected by an exoatmospheric observer over various portions of North America for different seasons of the year. The prominent absorption band between 9 and 10 μm is due to ozone.

3.7.4 Cloud Meteorology

Clouds are classified into 10 main groups called genera. These are cirrus, cirrocumulus, cirrostratus, altocumulus, altostratus, nimbostratus, stratocumulus, stratus, cumulus, and cumulonimbus.

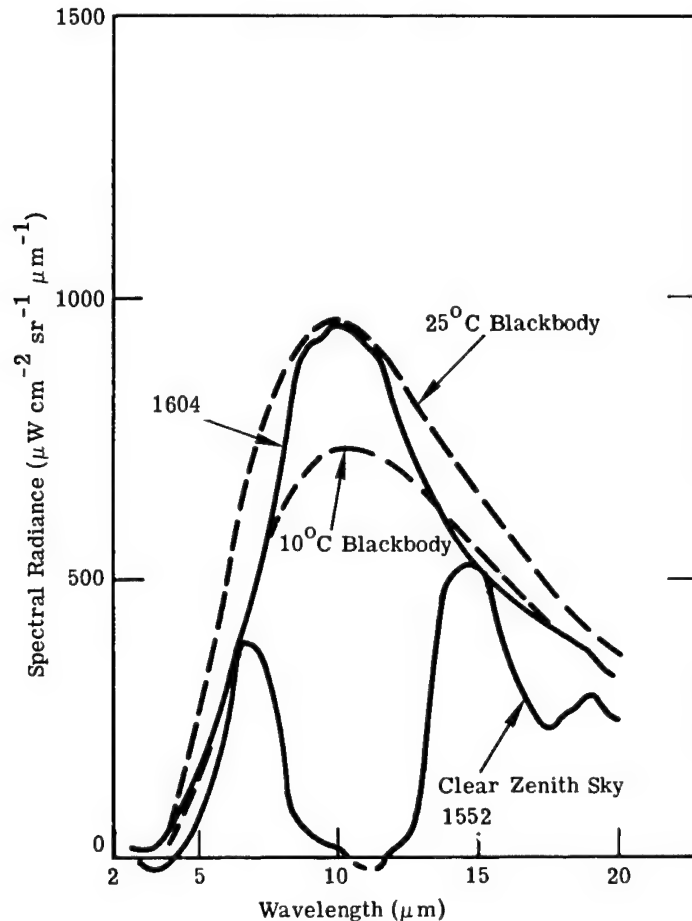


Fig. 3.64 Radiance of an urban area and of clear zenith sky (Colorado Springs from Pikes Peak).⁹²

The part of the atmosphere in which clouds are usually present is divided into three regions. Each region is defined by the range of levels at which clouds of certain genera occur most frequently:

1. high-level clouds—cirrus, cirrocumulus, and cirrostratus
2. middle-level clouds—altocumulus
3. low-level clouds—stratocumulus and stratus.

The regions overlap and their limits vary with latitude. Their approximate ranges are shown in Table 3.28. Figures 3.78 to 3.83 show the mean cloudiness in percentage of sky cover throughout the world for various months of the year.

Cirrus Clouds. The tropopause represents the upper limit of the cloud atmosphere. The highest clouds appearing within the troposphere are composed of large ice crystals of about 100 μm . Frequently these particles become oriented in the same direction, giving rise to unusual visible (and possibly infrared) effects such as halos and arcs.

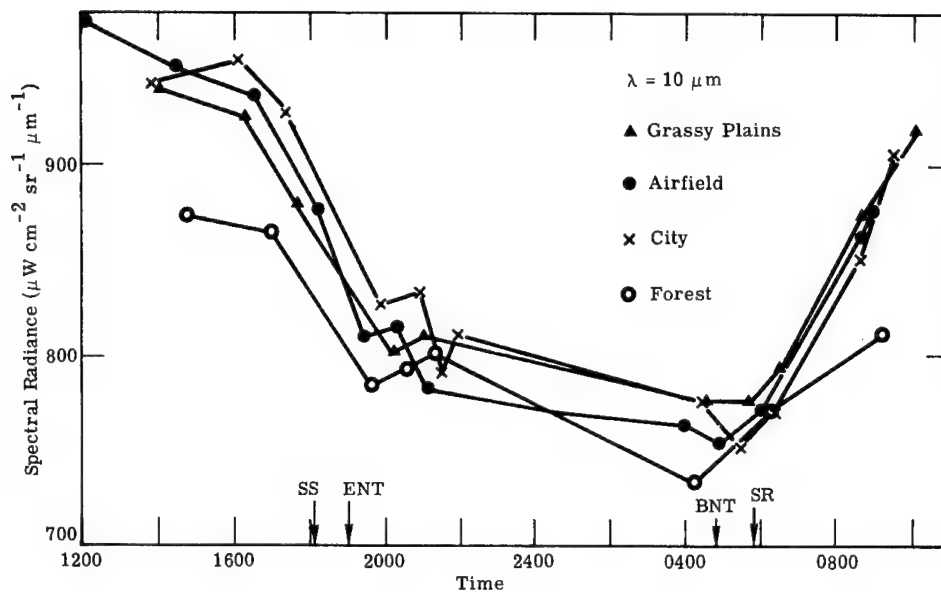


Fig. 3.65 Diurnal variation in the 10- μm radiance of selected backgrounds. SS = sunset; SR = sunrise; ENT = end of nautical twilight; BNT = beginning of nautical twilight.⁹²

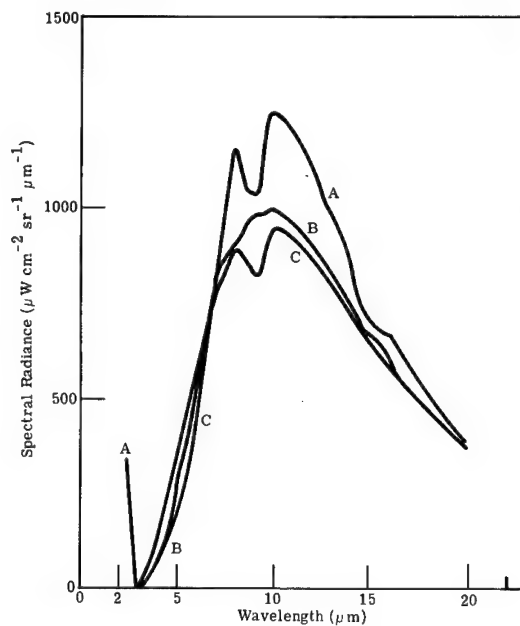


Fig. 3.66 Spectral radiance of dry sand (Cocoa Beach, Florida). A = sunlit sand; B = sand under a cloudy night sky; C = sand on a clear night.⁹²

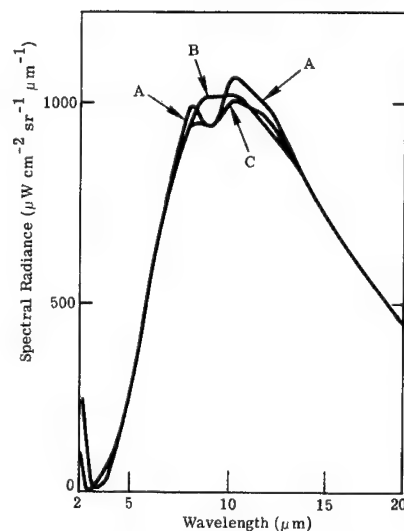


Fig. 3.67 Spectral radiance of moist sand (Cocoa Beach, Florida). A = dry sand; B = extremely wet sand; C = moist sand.⁹²

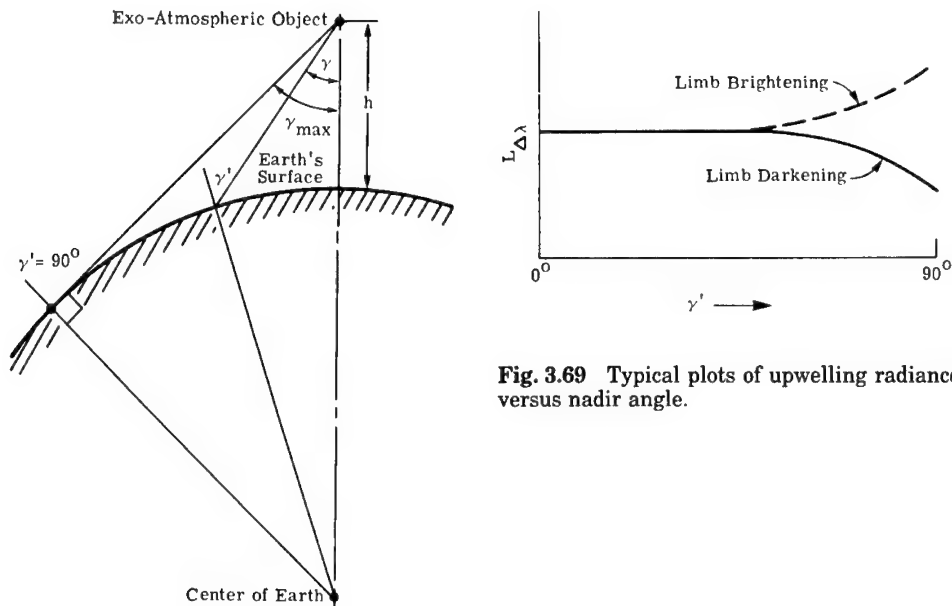


Fig. 3.69 Typical plots of upwelling radiance versus nadir angle.

Fig. 3.68 Cross-section view of the geometry pertaining to the calculation of the thermal radiance field at an exoatmospheric object.

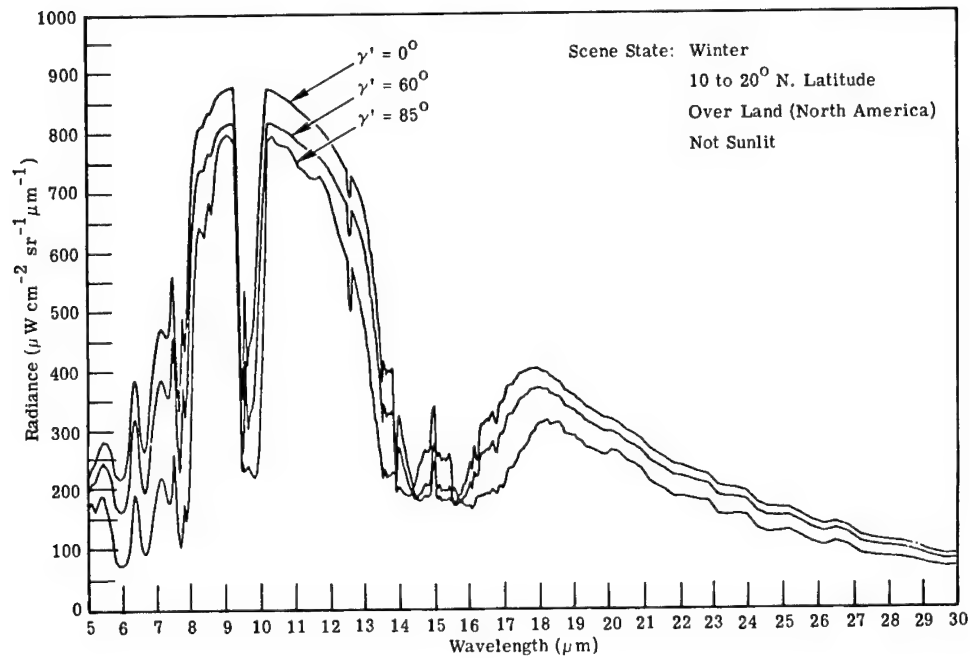


Fig. 3.70 The expected value of spectral radiance for three γ' angles.⁹³

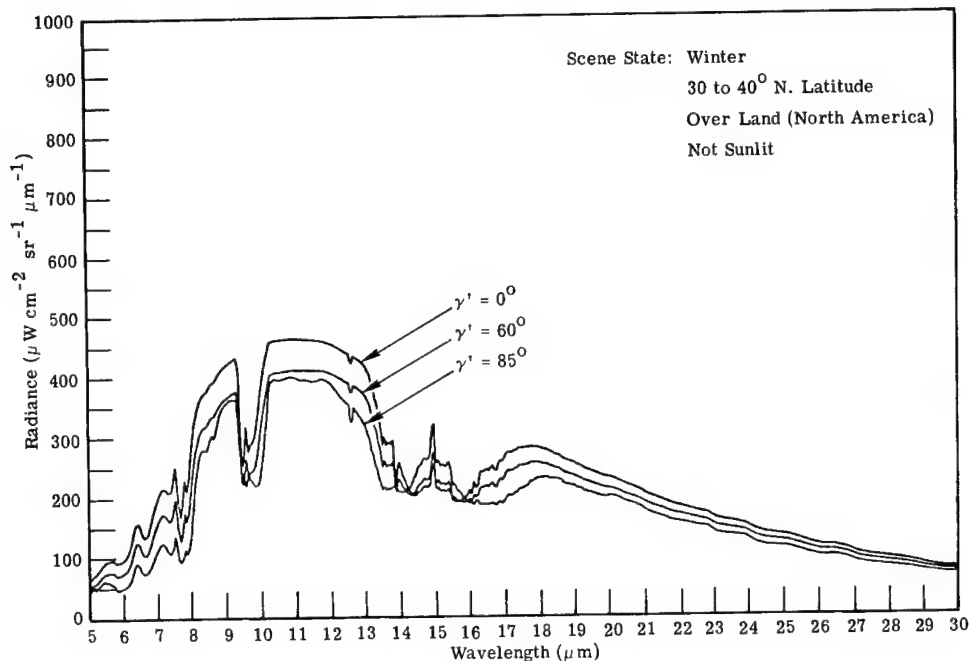


Fig. 3.71 The expected value of spectral radiance for three γ' angles.⁹³

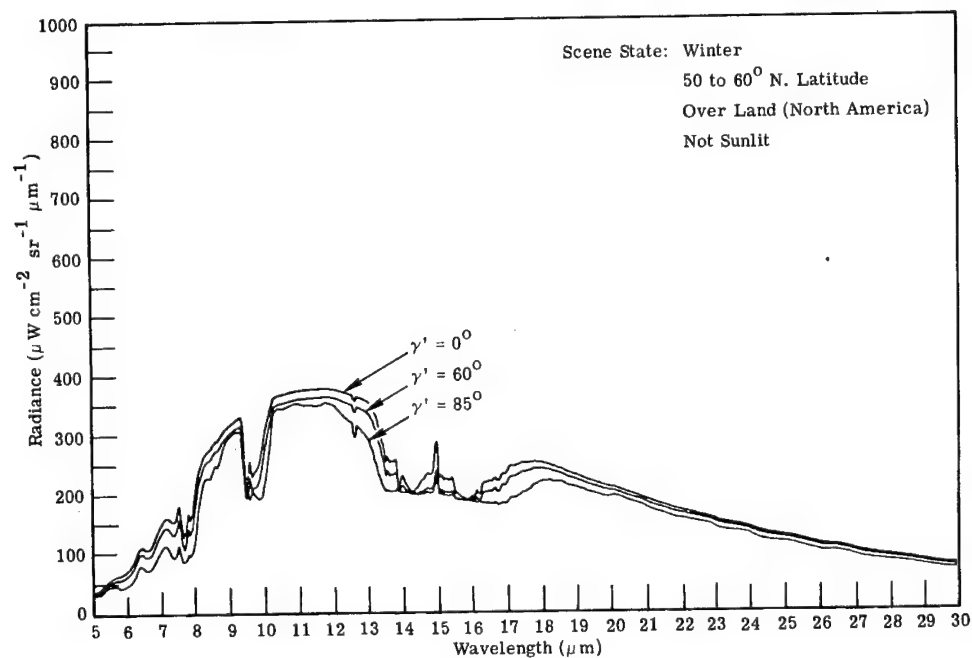


Fig. 3.72 The expected value of spectral radiance for three γ' angles.⁹³

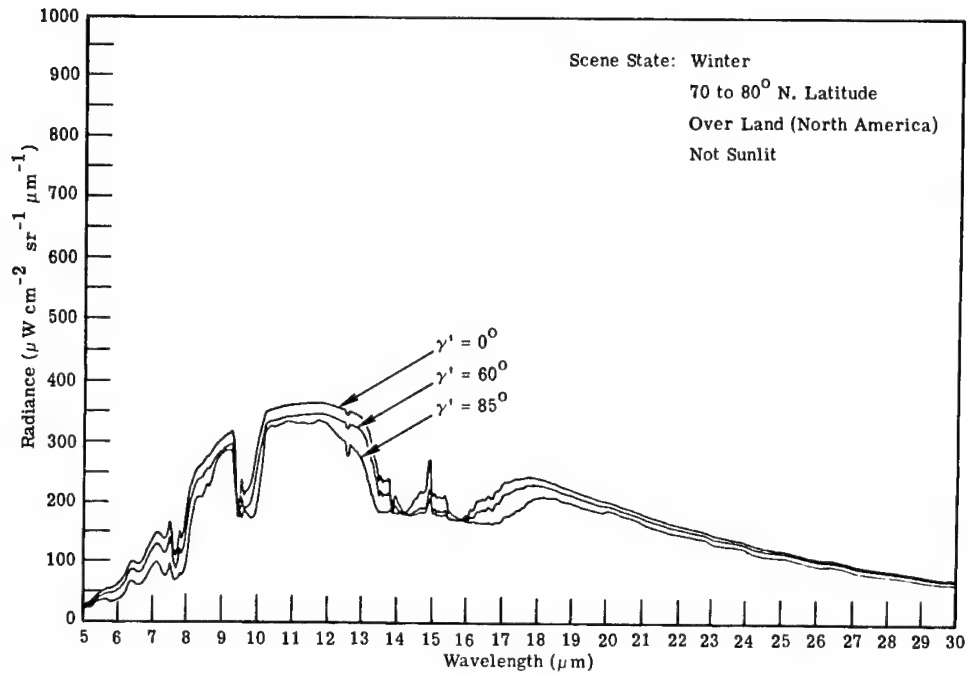


Fig. 3.73 The expected value of spectral radiance for three γ' angles.⁹³

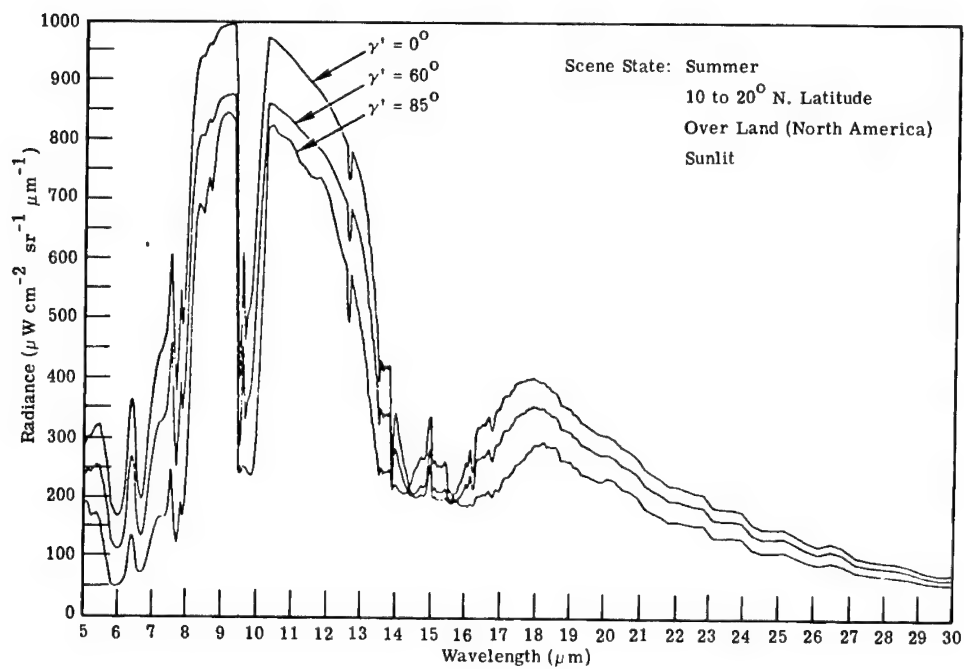


Fig. 3.74 The expected value of spectral radiance for three γ' angles.⁹³

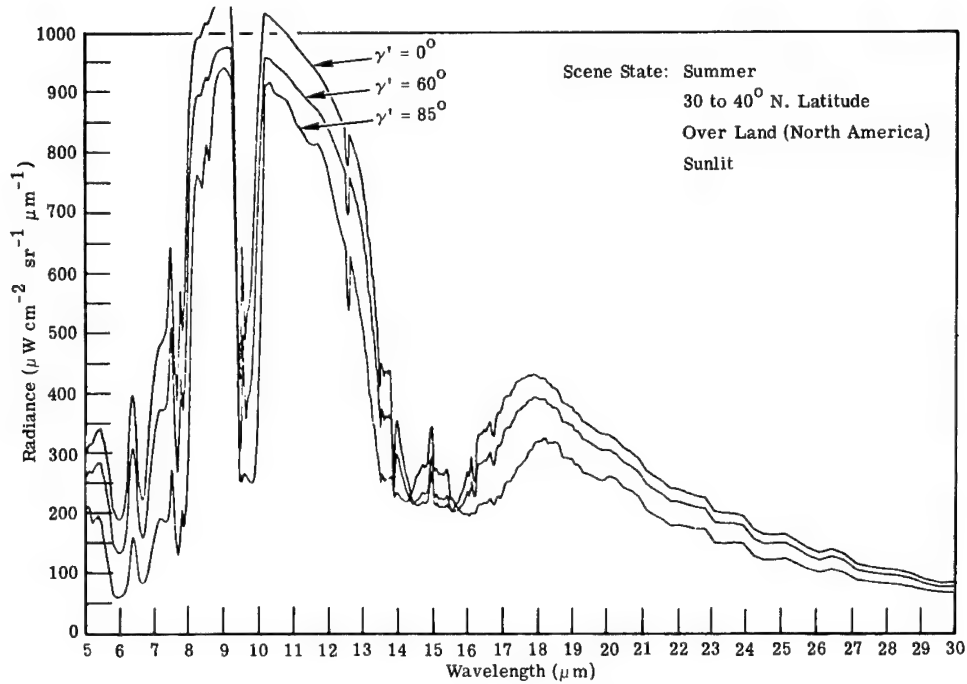


Fig. 3.75 The expected value of spectral radiance for three γ' angles.⁹³

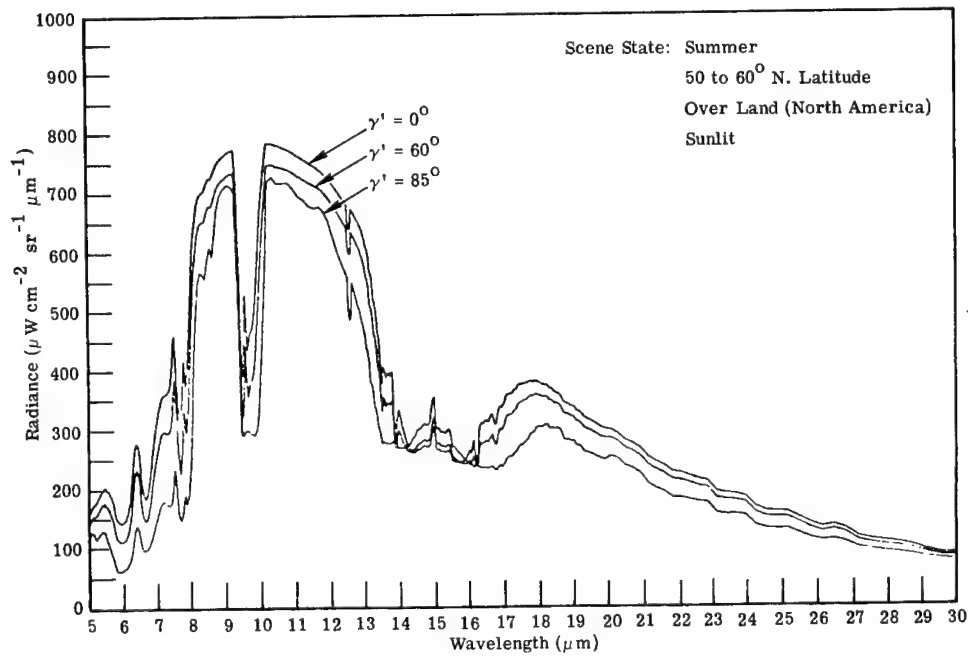


Fig. 3.76 The expected value of spectral radiance for three γ' angles.⁹³

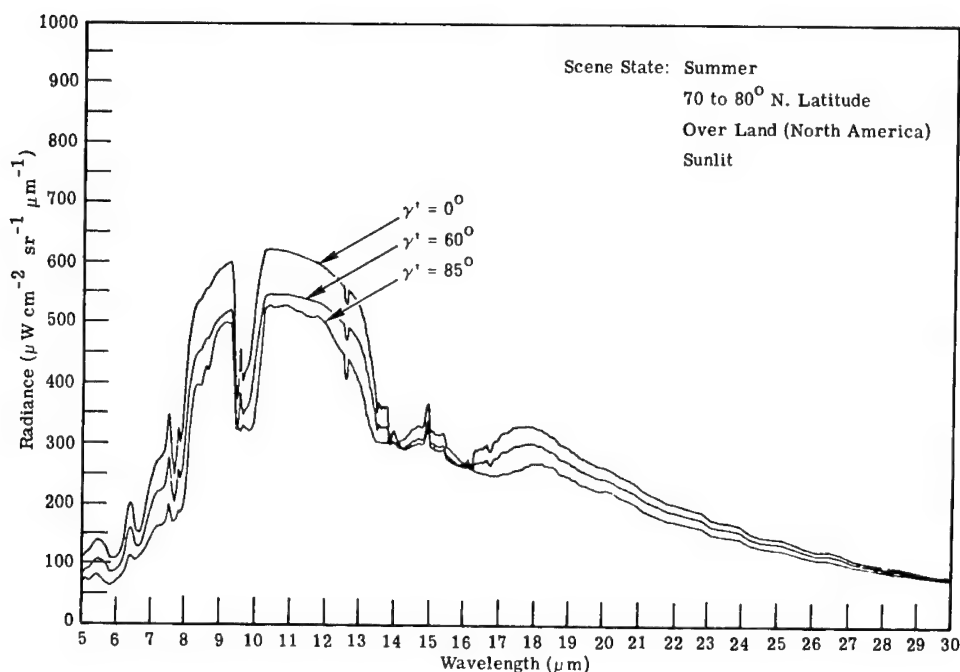


Fig. 3.77 The expected value of spectral radiance for three γ' angles.⁹³

Tropopause and cloud top statistics are not available for the central Eurasian land mass. Cirrus height observations have not been reported anywhere north of 55° latitude. Inferences can be made about the annual tropopause distribution over Eurasia, and from this a cirrus top height model can be constructed. The correlation between the two parameters is based on American statistics. Between 50 and 70°N it is expected that 90% of the annual clouds will be below 32,000 ft, and 99% will be below 36,000 ft.

Figure 3.84 shows cloud top and tropopause heights based on a collation of cirrus and tropopause data averaged on a yearly basis for the entire United States. Figures 3.85 and 3.86 represent the distribution of tropopause and cloud heights between 50 and 90° latitude.

Table 3.28 Definition of Cloud State Altitudes (from Ref. 57)

Cloud Level	Polar Regions	Temperate Regions	Tropical Regions
High	3-8 km (10,000-25,000 ft)	5-13 km (16,500-45,000 ft)	6-18 km (20,000-60,000 ft)
Middle	2-4 km (6500-13,000 ft)	2-7 km (6500-23,000 ft)	2-8 km (6500-25,000 ft)
Low	Earth's surface to 2 km (6500 ft)	Earth's surface to 2 km (6500 ft)	Earth's surface to 2 km (6500 ft)

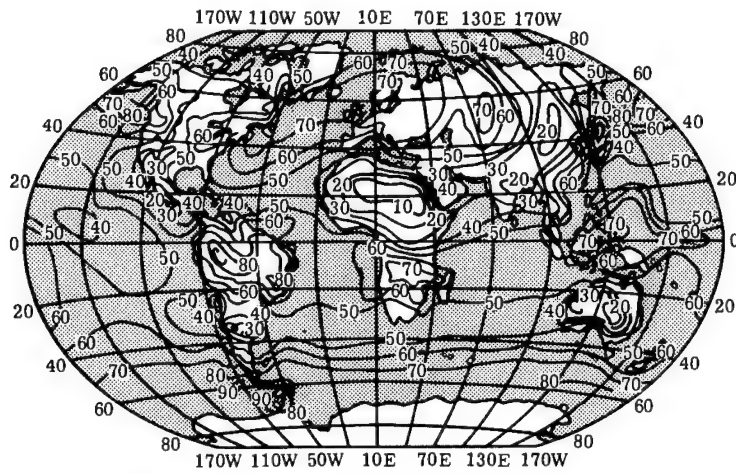


Fig. 3.78 Mean cloudiness in percentage of sky cover for the month of January.⁶³

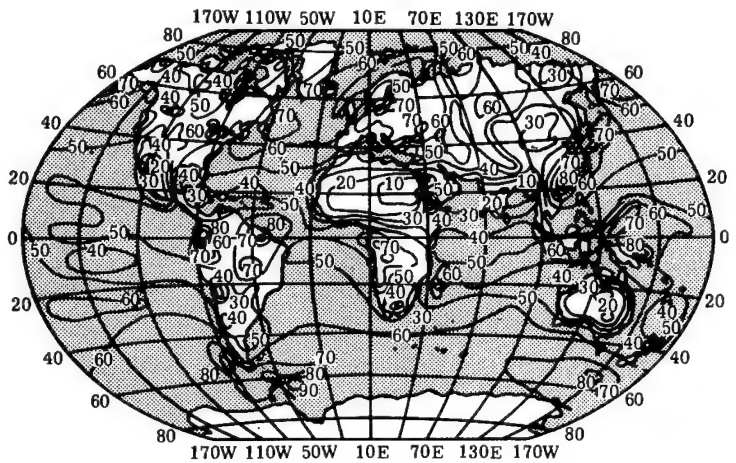


Fig. 3.79 Mean cloudiness in percentage of sky cover for the month of March.⁶³

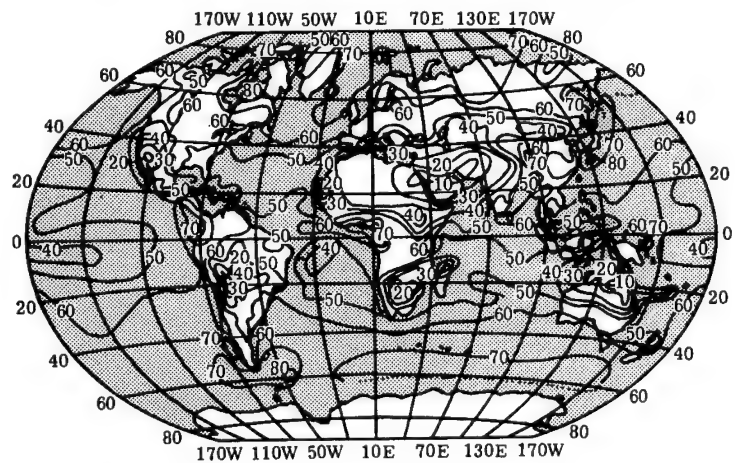


Fig. 3.80 Mean cloudiness in percentage of sky cover for the month of May.⁶³

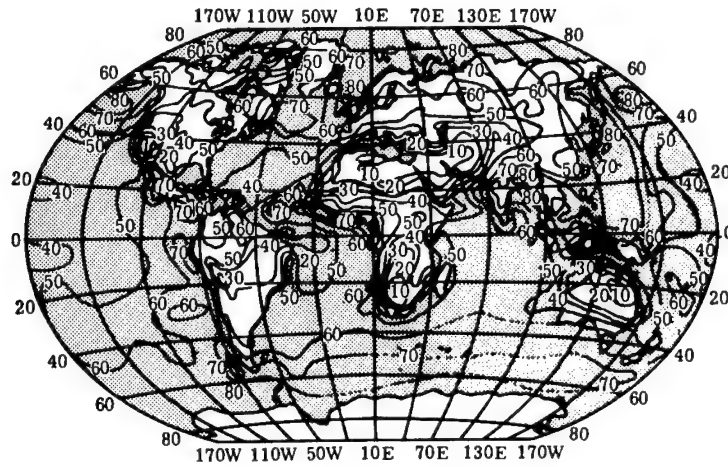


Fig. 3.81 Mean cloudiness in percentage of sky cover for the month of July.⁶³

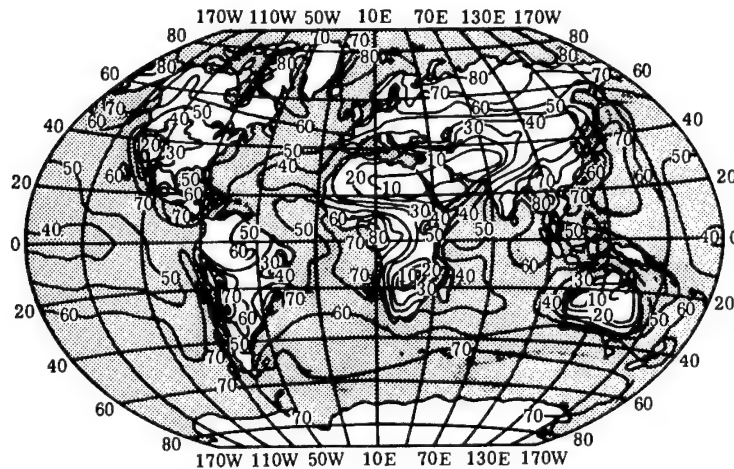


Fig. 3.82 Mean cloudiness in percentage of sky cover for the month of September.⁶³

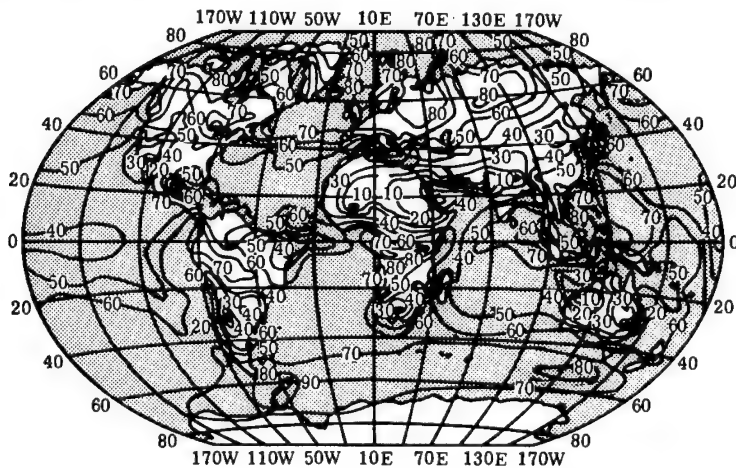


Fig. 3.83 Mean cloudiness in percentage of sky cover for the month of November.⁶³

Based on deductions from Asian climatology, a crude time-frequency occurrence chart for cirriform clouds has been estimated and is shown in Fig. 3.87. Averaging the entire year between 50 and 70°N, one may expect cirrus clouds 35% of the time. This means that cirrus clouds will be encountered 1% of the time above 34,000 ft, and 10% of the time above 30,000 ft.

Stratospheric Clouds.⁵⁷ Two types of clouds appear in the upper stratosphere: nacreous clouds, at an average height of 24 km, and noctilucent clouds, at a height of about 82 km.

Nacreous clouds appear rarely, mainly in high latitudes characterized by mountainous terrain. They are generally observed in the direction of the sun during sunset or sunrise and are iridescent. The characteristic synoptic con-

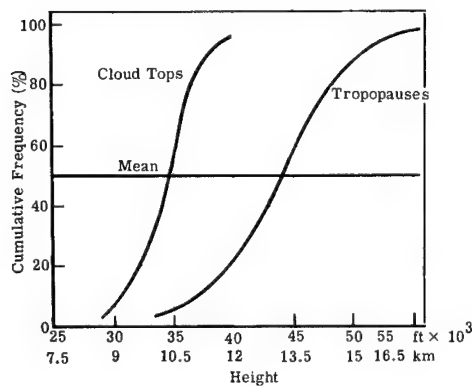


Fig. 3.84 Distribution of cloud top and tropopause heights (U.S. average).⁵⁷

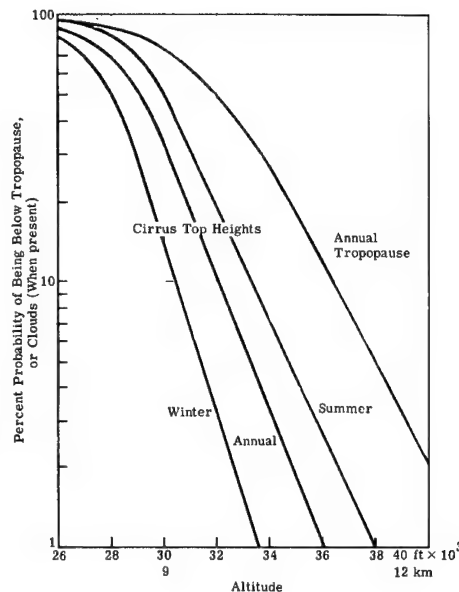


Fig. 3.85 Distribution of tropopause and cloud tops (50 to 70° N latitude, Eurasian average).⁵⁷

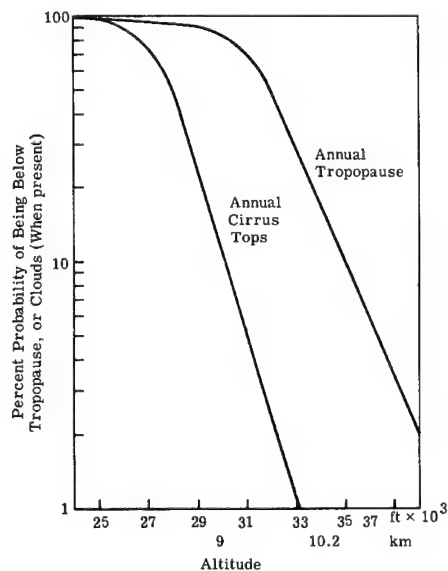


Fig. 3.86 Distribution of tropopause and cloud tops (65 to 90° N latitude, Eurasian average).⁵⁷

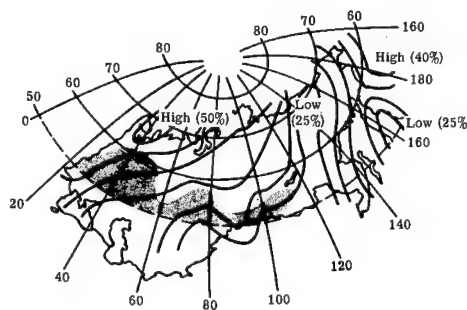


Fig. 3.87 The estimated annual temporal frequency of cirriform clouds. The shaded portion delineates the area where 20 or more thunderstorms per year are reported (overall average = 35%).⁵⁷

ditions that exist with these clouds are strong and consistent northwest winds extending to great heights with below average stratospheric temperatures. Theoretical considerations of water-droplet and ice-crystal growth in nacreous clouds suggest that the radii are less than $1.2\text{ }\mu\text{m}$, with a very narrow size distribution of about $0.1\text{ }\mu\text{m}$. The particle concentration should be essentially that of the available condensation nuclei. The liquid water content, therefore, would be between 10^{-12} to $10^{-11}\text{ g cm}^{-3}$. Such liquid water content is lower by about a factor of 10^4 than those observed in the tropospheric clouds.

Noctilucent clouds are visible against the nighttime sky when the upper levels of the atmosphere are still illuminated by sunlight. These clouds have generally been reported only in the northern hemisphere during summer (August through October) within a restricted zone of latitudes extending from about 45 to 63°N .

Sunlight scattered from noctilucent clouds exhibits a spectrum and a degree of polarization that can be attributed to the scattering of sunlight by dielectric particles with predominant radii of around $0.1\text{ }\mu\text{m}$ and not greater than 0.2 to $0.4\text{ }\mu\text{m}$. The observed brightness of the clouds suggests that the corresponding concentrations and matter content should be between 1 to 10^{-2} particles cm^{-3} and between 10^{-17} to $10^{-16}\text{ g cm}^{-3}$, respectively. Such cloud-particle concentrations are about 5 orders of magnitude less than those even for nacreous clouds.

Probability of Coverage at Various Altitudes.⁹⁹ Figures 3.88 through 3.103 are charts showing, for the northern hemisphere, altitudes above which the probabilities of less than 0.1 sky coverage are 95, 90, 80, and 60%. Charts are presented for the midseason months of January, April, July, and October. The criterion of less than 0.1 sky cover (actually less than 0.05 sky cover) can be taken as essentially no interference by clouds for air-to-air operation.

3.8 PROPERTIES OF NATURAL MATERIALS

3.8.1 Soils, Rocks, and Minerals

Soils. Soil reflectance measurements of U.S. soils were made by Condit¹⁰⁰ in the 0.32 - to $1.0\text{-}\mu\text{m}$ range. He observed that there were three main types of soil spectra as exemplified in Figs. 3.104(a), 3.104(b), and 3.104(c). The application of characteristic vector analysis to these spectra showed that, along with the average spectral reflectances of all soil samples, the spectral reflectance values at only five different wavelengths (0.44 , 0.54 , 0.64 , 0.74 , and $0.86\text{ }\mu\text{m}$) were needed to replicate closely the entire spectral reflectance curve from 0.32 to $1.0\text{ }\mu\text{m}$. His spectral reflectance curves are shown in Figs. 3.104 where the circles are predicted values and the solid lines are measured values.

Spectral reflectances extending into the thermal infrared range are shown in Fig. 3.105.

Rocks. The spectral emissivities shown in Fig. 3.106 were obtained at room temperature by a reflectance measurement where

$$\epsilon(\lambda) = 1 - \rho(\lambda) . \quad (3.60)$$

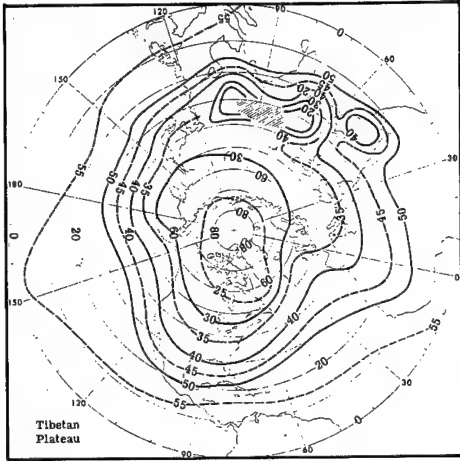


Fig. 3.88 Altitudes (thousands of feet msl) above which there is 95% probability of having less than 0.1 sky cover for the month of January.⁹⁹

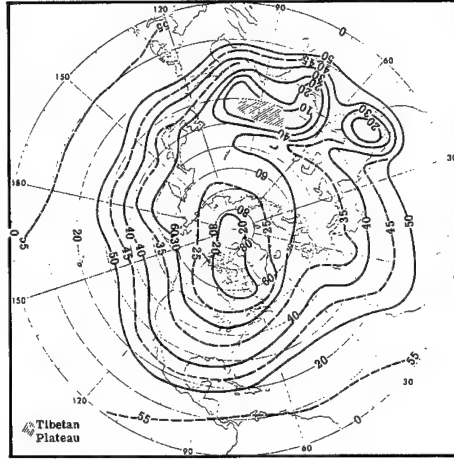


Fig. 3.89 Altitudes (thousands of feet msl) above which there is 90% probability of having less than 0.1 sky cover for the month of January.⁹⁹

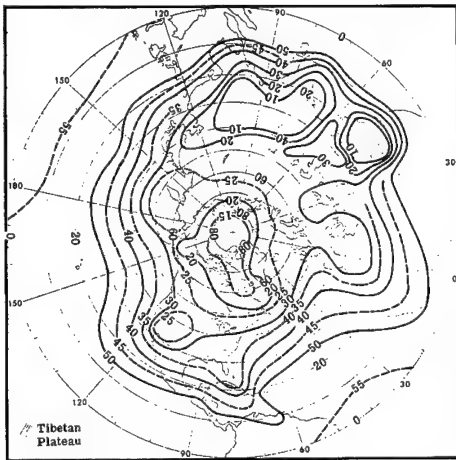


Fig. 3.90 Altitudes (thousands of feet msl) above which there is 80% probability of having less than 0.1 sky cover for the month of January.⁹⁹

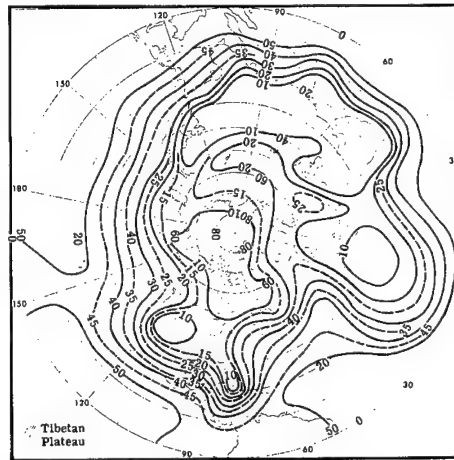


Fig. 3.91 Altitudes (thousands of feet msl) above which there is 60% probability of having less than 0.1 sky cover for the month of January.⁹⁹

The spectrometer field of view on the samples was about 0.5×12.0 mm. Coarse-grained rock, such as granite, yielded variable results depending on sample position. Figure 3.107 illustrates the degree of variation with sample position for three granite samples.

Under daylight conditions where convective heat transfer to the atmosphere is very low, some rock surfaces may sustain a large temperature gradient. This condition will alter the apparent emissivity because the effective-radiation temperature is the temperature at a depth of $1/\alpha(\lambda)$ below the surface where $\alpha(\lambda)$ is the spectral absorption coefficient of the rock. Figure 3.108 shows a

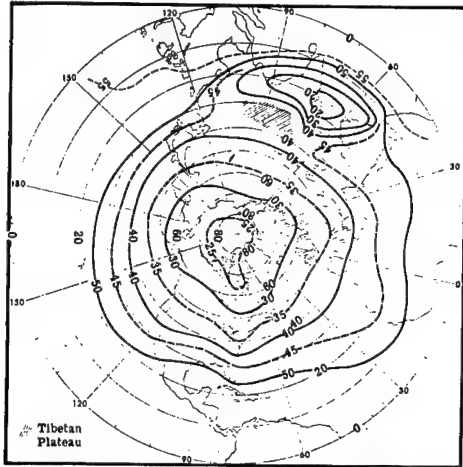


Fig. 3.92 Altitudes (thousands of feet msl) above which there is 95% probability of having less than 0.1 sky cover for the month of April.⁹⁹

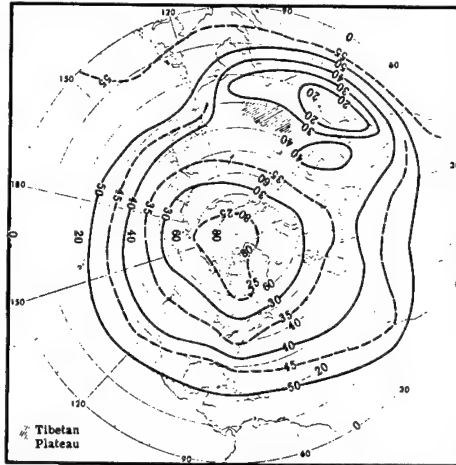


Fig. 3.93 Altitudes (thousands of feet msl) above which there is 90% probability of having less than 0.1 sky cover for the month of April.⁹⁹

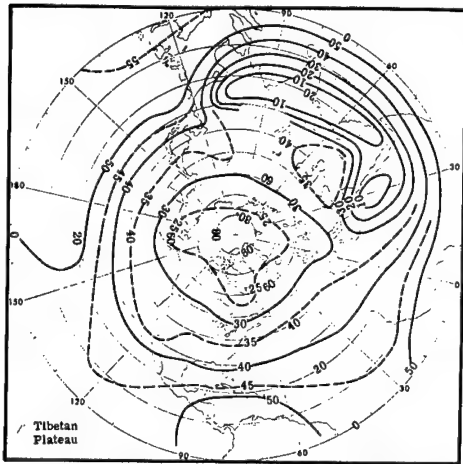


Fig. 3.94 Altitudes (thousands of feet msl) above which there is 80% probability of having less than 0.1 sky cover for the month of April.⁹⁹

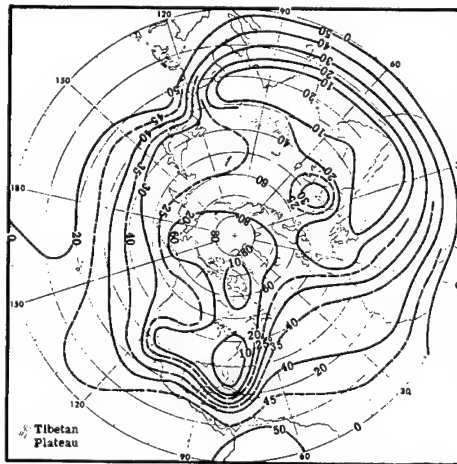


Fig. 3.95 Altitudes (thousands of feet msl) above which there is 60% probability of having less than 0.1 sky cover for the month of April.⁹⁹

comparison between spectral emissivity derived from reflectance measurements and a direct spectral emissivity measurement,

$$\epsilon(\lambda) = \frac{M_{\lambda}(\text{rock}, \lambda, T)}{M_{\lambda}(\text{BB}, \lambda, T)}, \quad (3.61)$$

with the rock sample holder held at room temperature and the rock surface exposed to about 100 K radiation from a liquid nitrogen container. Rock surface contact temperature was measured and was used as the temperature of the reference blackbody surface.

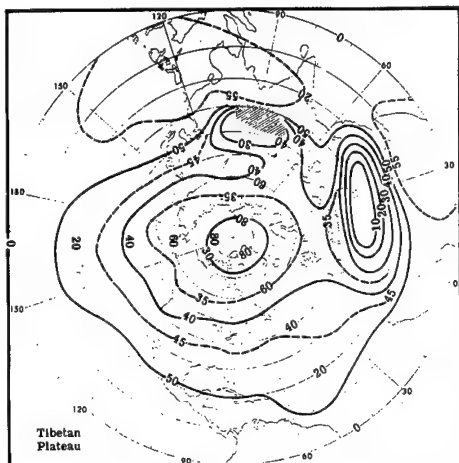


Fig. 3.96 Altitudes (thousands of feet msl) above which there is 95% probability of having less than 0.1 sky cover for the month of July.⁹⁹

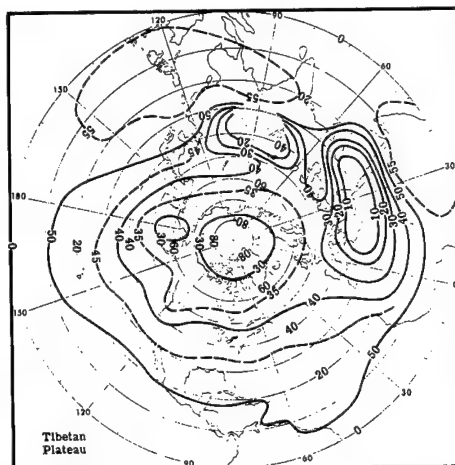


Fig. 3.97 Altitudes (thousands of feet msl) above which there is 90% probability of having less than 0.1 sky cover for the month of July.⁹⁹

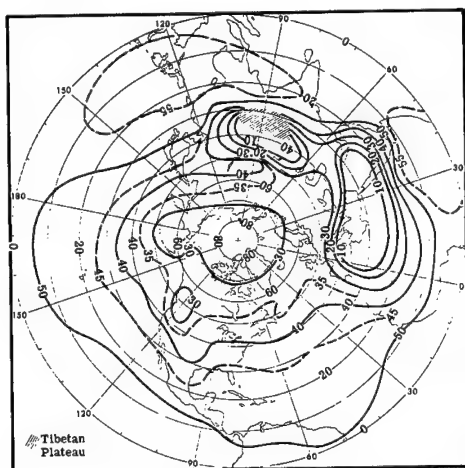


Fig. 3.98 Altitudes (thousands of feet msl) above which there is 80% probability of having less than 0.1 sky cover for the month of July.⁹⁹

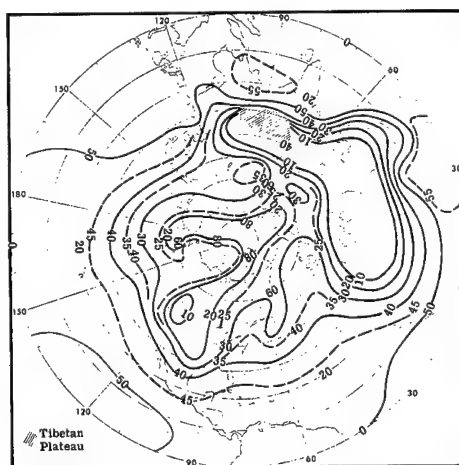


Fig. 3.99 Altitudes (thousands of feet msl) above which there is 60% probability of having less than 0.1 sky cover for the month of July.⁹⁹

Figure 3.109 shows the spectral emissivity of iron rust. Iron rust stain, hematite, occurs on rocks frequently. Spectral reflectances and emissivities of other common rock types are shown in Fig. 3.110.

3.8.2 Construction Materials

Figures 3.111, 3.112, and 3.113 show the spectral apparent temperature of some common natural and construction materials *in situ*. The contact temperature of each subject was not taken, so a spectral emissivity cannot be inferred from these data. One may observe temperature variations of several

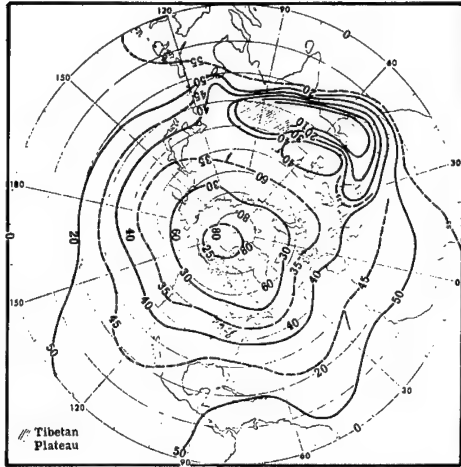


Fig. 3.100 Altitudes (thousands of feet msl) above which there is 95% probability of having less than 0.1 sky cover for the month of October.⁹⁹

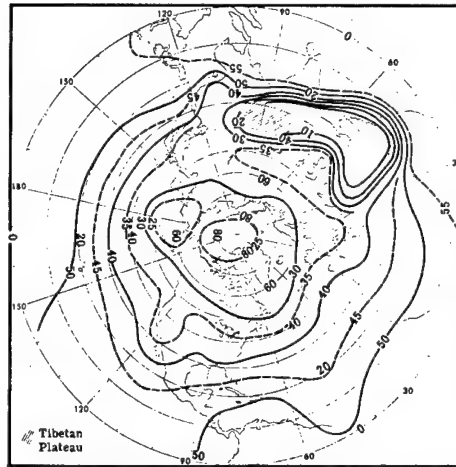


Fig. 3.101 Altitudes (thousands of feet msl) above which there is 90% probability of having less than 0.1 sky cover for the month of October.⁹⁹

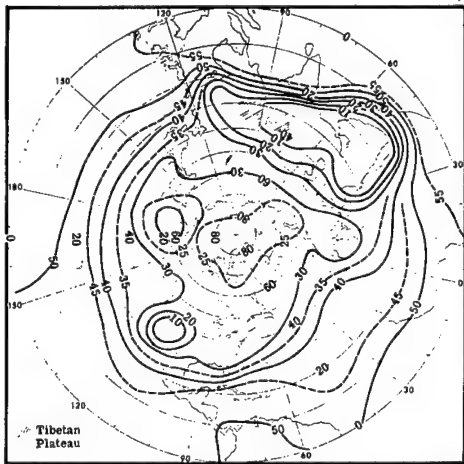


Fig. 3.102 Altitudes (thousands of feet msl) above which there is 80% probability of having less than 0.1 sky cover for the month of October.⁹⁹

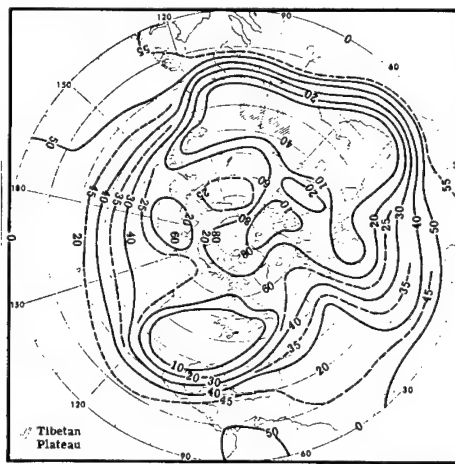
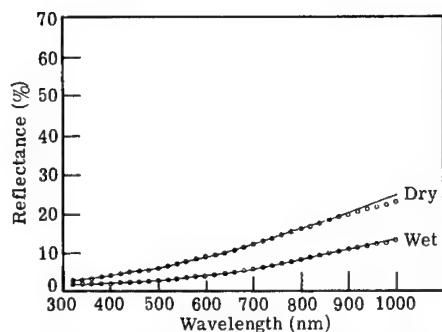


Fig. 3.103 Altitudes (thousands of feet msl) above which there is 60% probability of having less than 0.1 sky cover for the month of October.⁹⁹

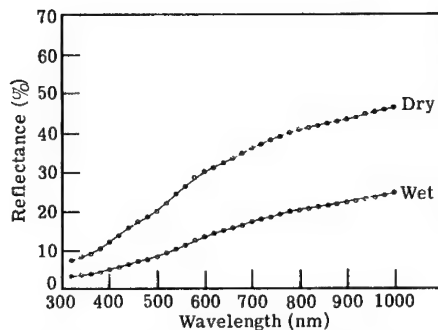
degrees Celsius on stone concrete only a few millimeters apart when the concrete is under direct solar illumination due to differential heating of the components. The same should be true of a gravel road. The curves at the bottom of each graph indicate the expected accuracy of the measurements. The precision is indicated by the replication of data in each figure.

A graybody would plot as a horizontal line, except in the 3- to 4- μm atmospheric window where scattered solar radiation may increase the surface radiance by reflection. Under overcast skies, the reflection of cloud radiation tends to remove spectral details produced by emission.

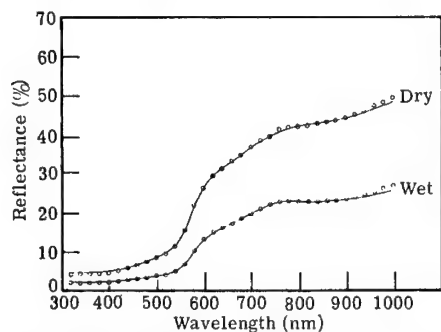
Spectral reflectance curves of common construction materials are shown in Fig. 3.114.



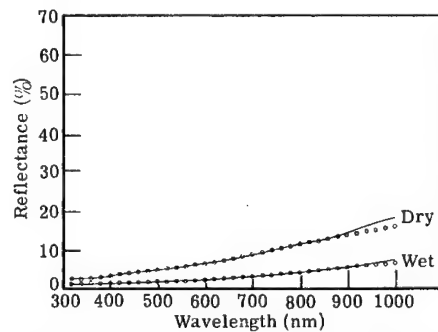
(a) Chernozem-type soil. Type-one curves. 20 miles E. of Lincoln, Nebraska.



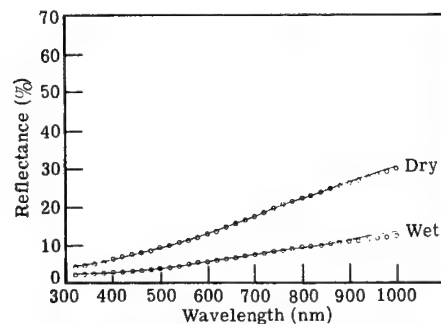
(b) Pedialier-type silt. Type-two curves. 15 miles S.E. of Hot Springs, Arkansas.



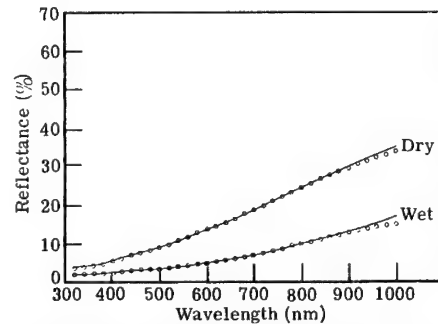
(c) Red quartz and calcite sand. Type-three curves. Monument Valley, Utah.



(d) Chernozem-type soil. Type-one curves. 4 miles N. of Neodesha, Kansas.

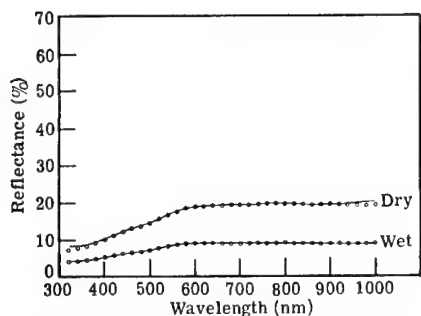


(e) Chernozem-type soil. Type-one curves. 1 mile E. of Lindsborg, Kansas.

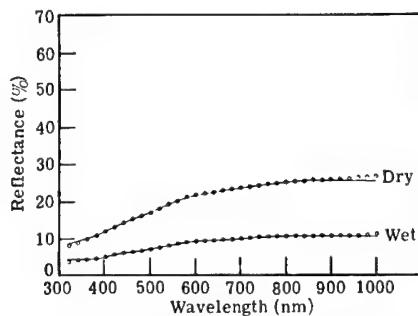


(f) Chernozem-type soil. Type-one curves. 4 miles S.E. of Avenet, Oklahoma.

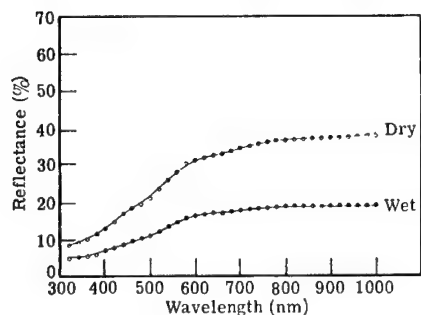
Fig. 3.104 Spectral reflectance curves. Measured values are shown by lines and predicted values by a series of circles.¹⁰⁰ (continued on following pages)



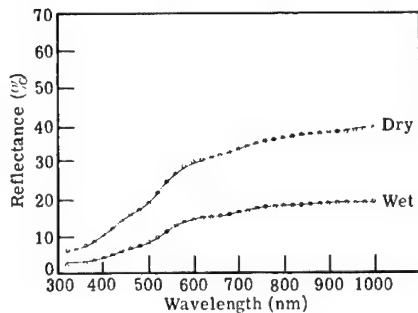
(g) Sand of quartz, rock and shell fragments. Type-two curves. Public beach, Newport, Rhode Island.



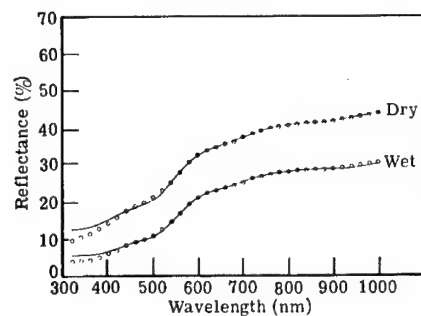
(h) Sand of quartz and rock fragments. Type-two curves. Snake River at Copper Mt. in Hell's Canyon.



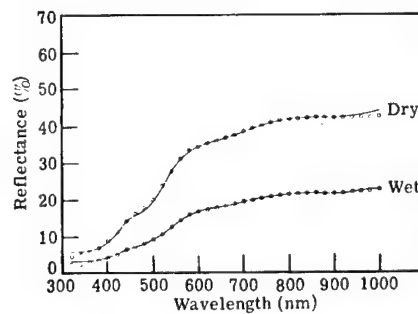
(i) Sand of quartz and rock fragments. Type-two curves. Pacific ocean beach, Santa Monica, California.



(j) Sand of quartz and rock fragments. Type-two curves. Cousins Island in Casco Bay, Maine.

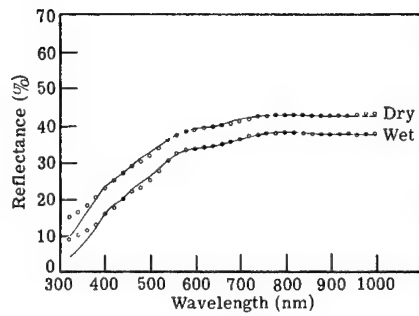


(k) Sand of quartz and carbonate. Type-two curves. Miami Beach, Florida.

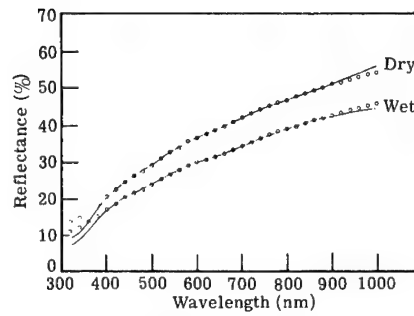


(l) Pedocal-type soil. Type-two curves. 1 mile S. of Sagamore Hills, Ohio.

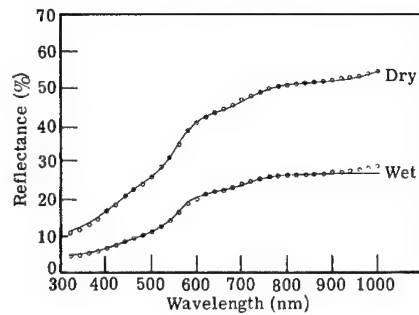
Fig. 3.104 (continued)



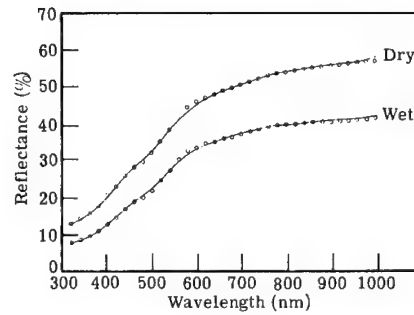
(m) Pedocal-type soil. Type-two curves. 10 miles S. of Lyman, Nebraska.



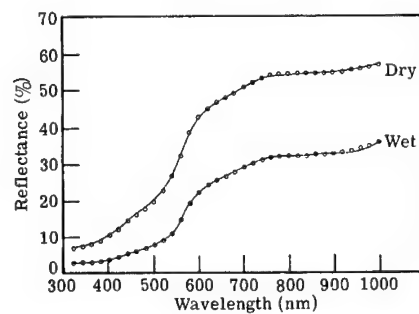
(n) Clay. Type-two curves. 3 miles E. of Paris, Missouri.



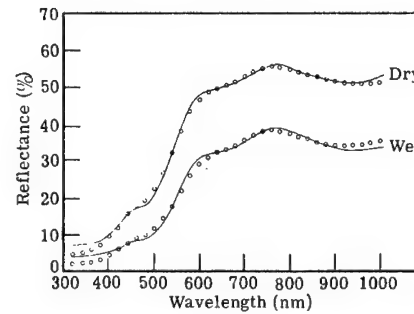
(o) Quartz sand. Type-two curves. 20 miles N. of Coos Bay, Oregon.



(p) Carbonate sand. Type-two curves. Waikiki Beach, Honolulu, Hawaii.

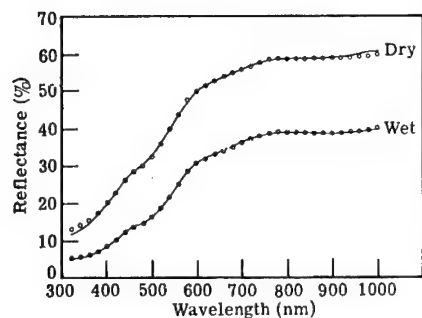


(q) Pedalfer-type Soil. Type-two curves. 3 miles E. of Mountain View, Missouri.

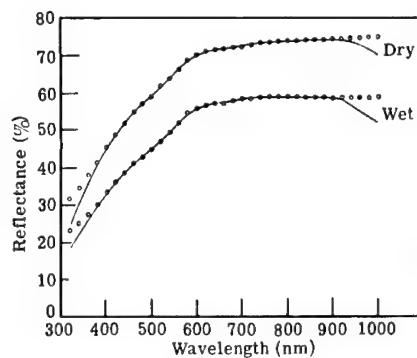


(r) Pedalfer-type soil. Type-two curves. 12 miles N. of Dalton, Georgia.

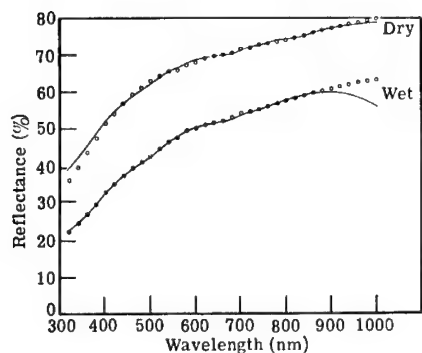
Fig. 3.104 (continued)



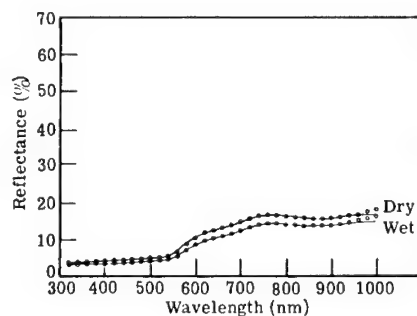
(s) Pedocal-type soil. Type-two curves. 3 miles W. of Phillipsburg, Missouri.



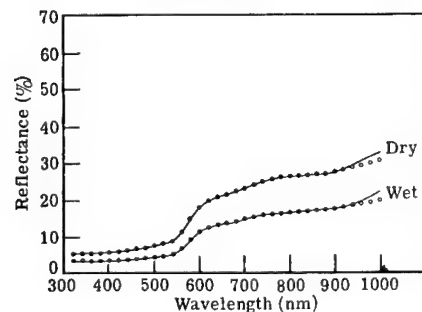
(t) Gypsum sand. Type-two curves. White sands National Monument, New Mexico.



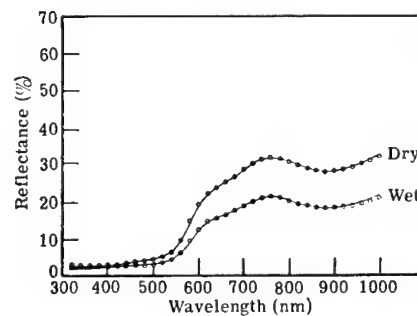
(u) Quartz sand. Type-two curves. Ft. Walton Beach, Florida.



(v) Pedalfer-type soil. Type-three curves. 5 miles S.E. of Rowe, New Mexico.

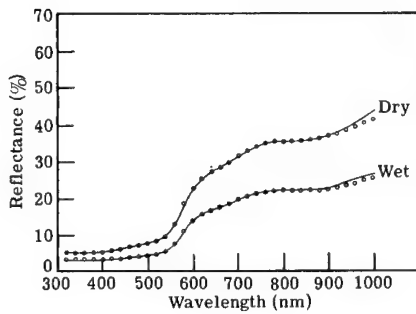


(w) Pedalfer-type soil. Type-three curves. Garden of the Gods, Colorado.

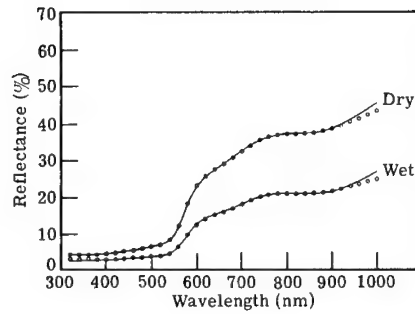


(x) Laterite-type soil. Type-three curves. 2 miles N.E. of Lexington, North Carolina.

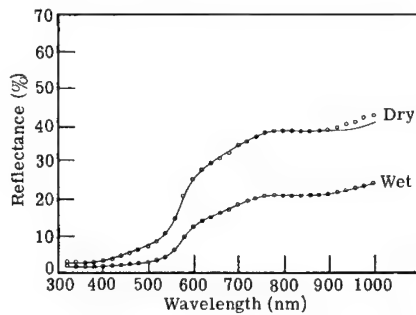
Fig. 3.104 (continued)



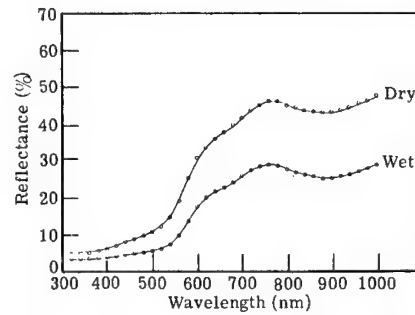
(y) Pedalfer soil. Type-three curves. Woodlawn, Colorado.



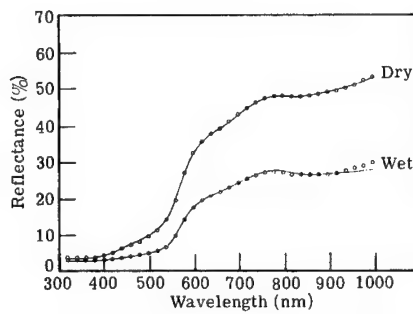
(z) Pedocal-type soil. Type-three curves. 12 miles W. of Elk City, Oklahoma.



(aa) Pedalfer-type soil. Type-three curves. 6 miles N. of Del Rio, Texas.



(bb) Pedalfer-type soil. Type-three curves. 4 miles N. of Griffin, Georgia.



(cc) Quartz sand with hematite stain. Type-three curves. Bok Tower, Florida.

Fig. 3.104 (continued)

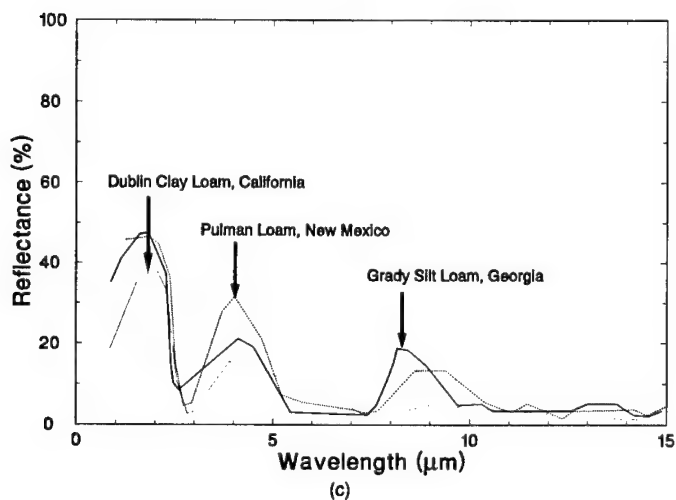
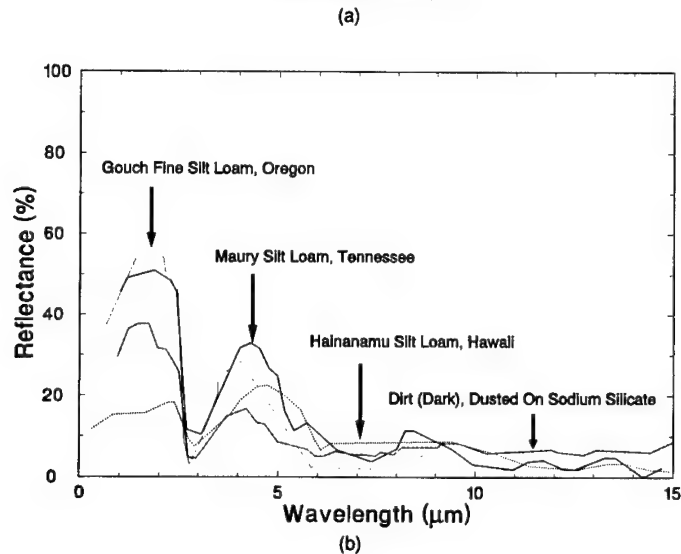
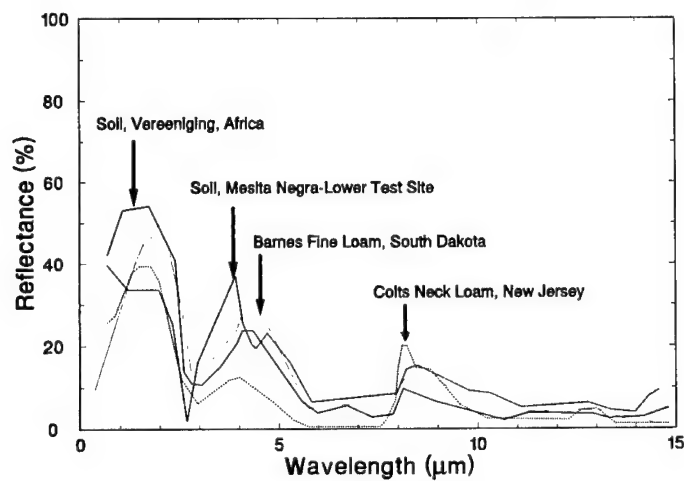
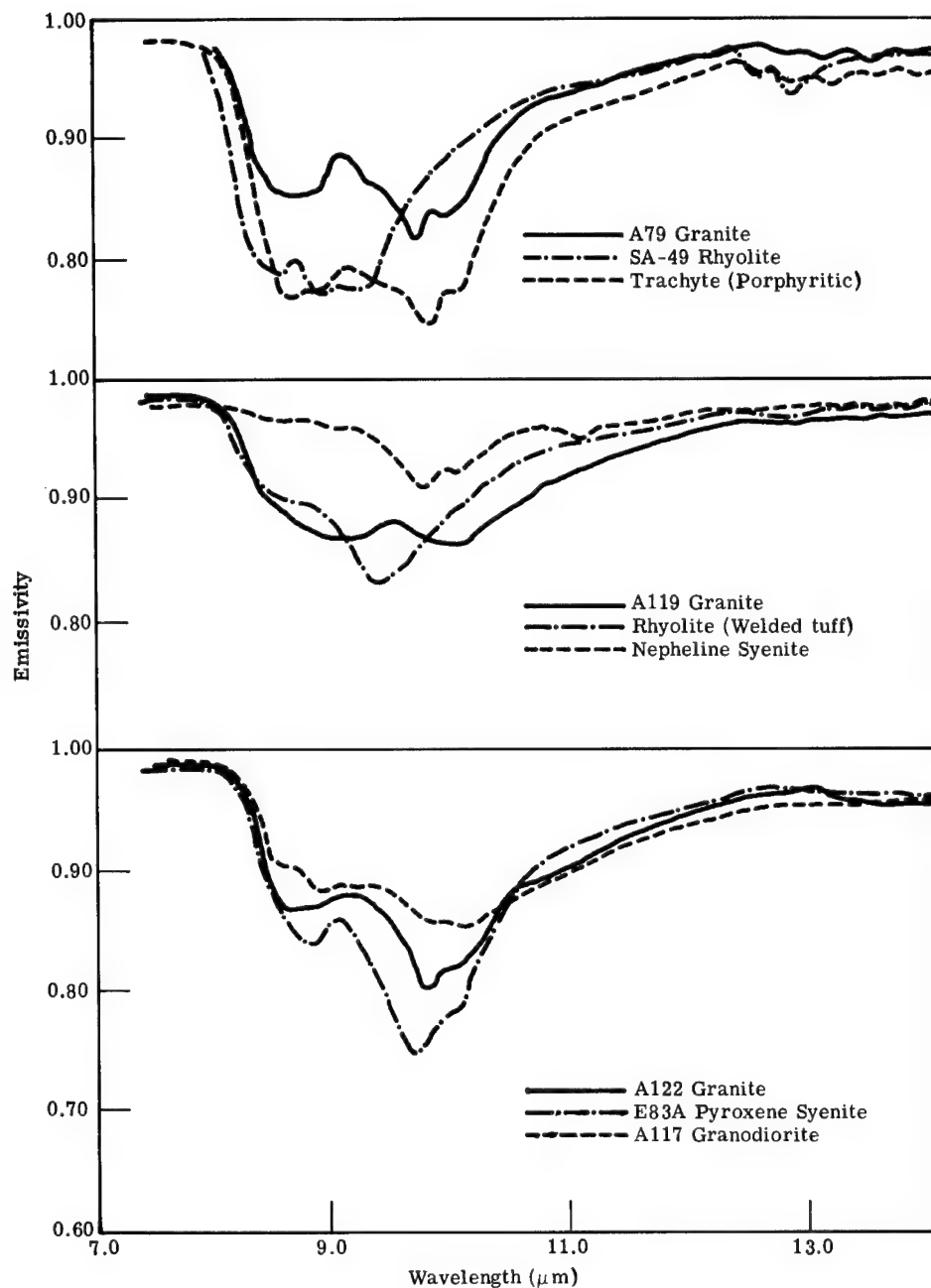
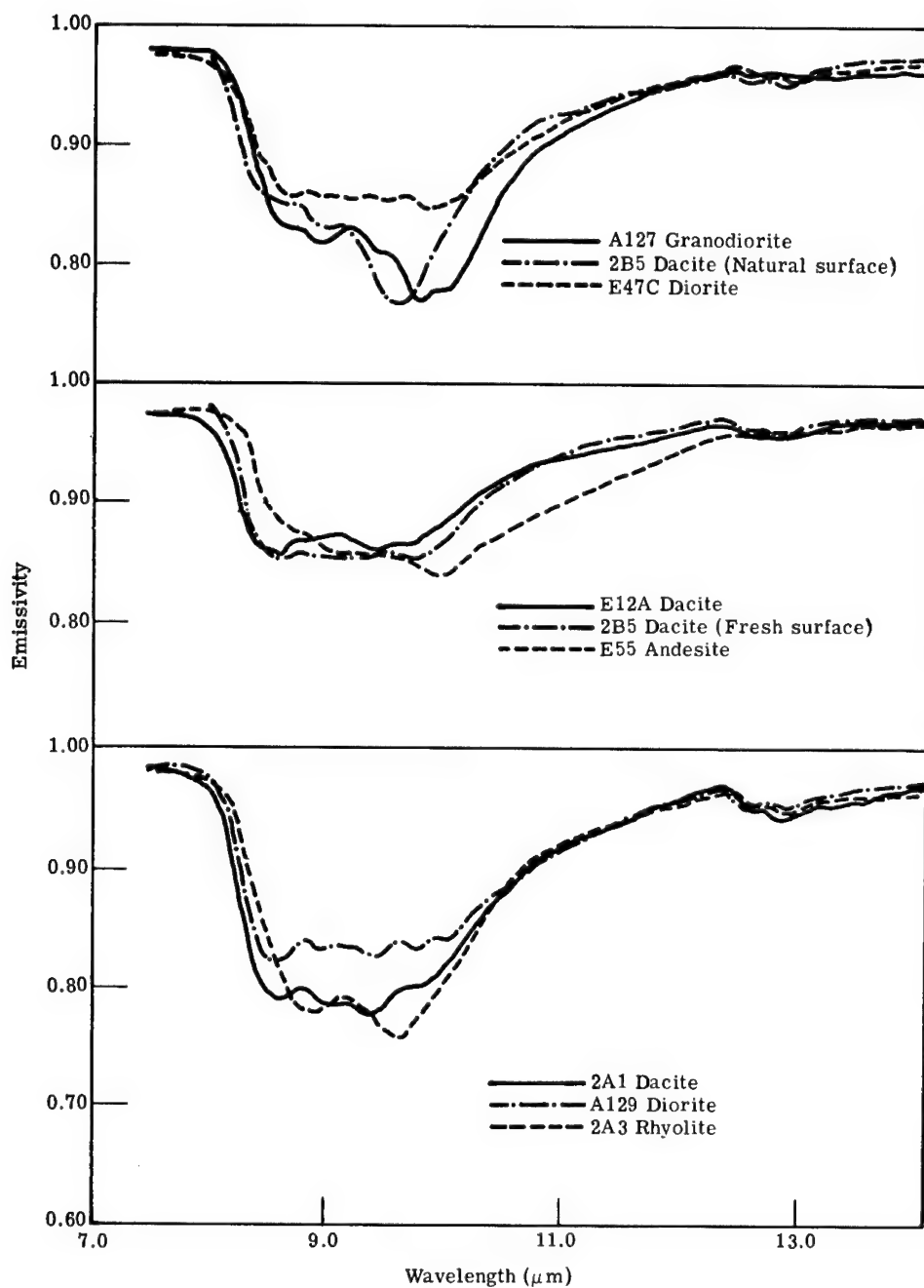


Fig. 3.105 Spectral reflectances of selected soils extending into the thermal IR range.¹⁰¹

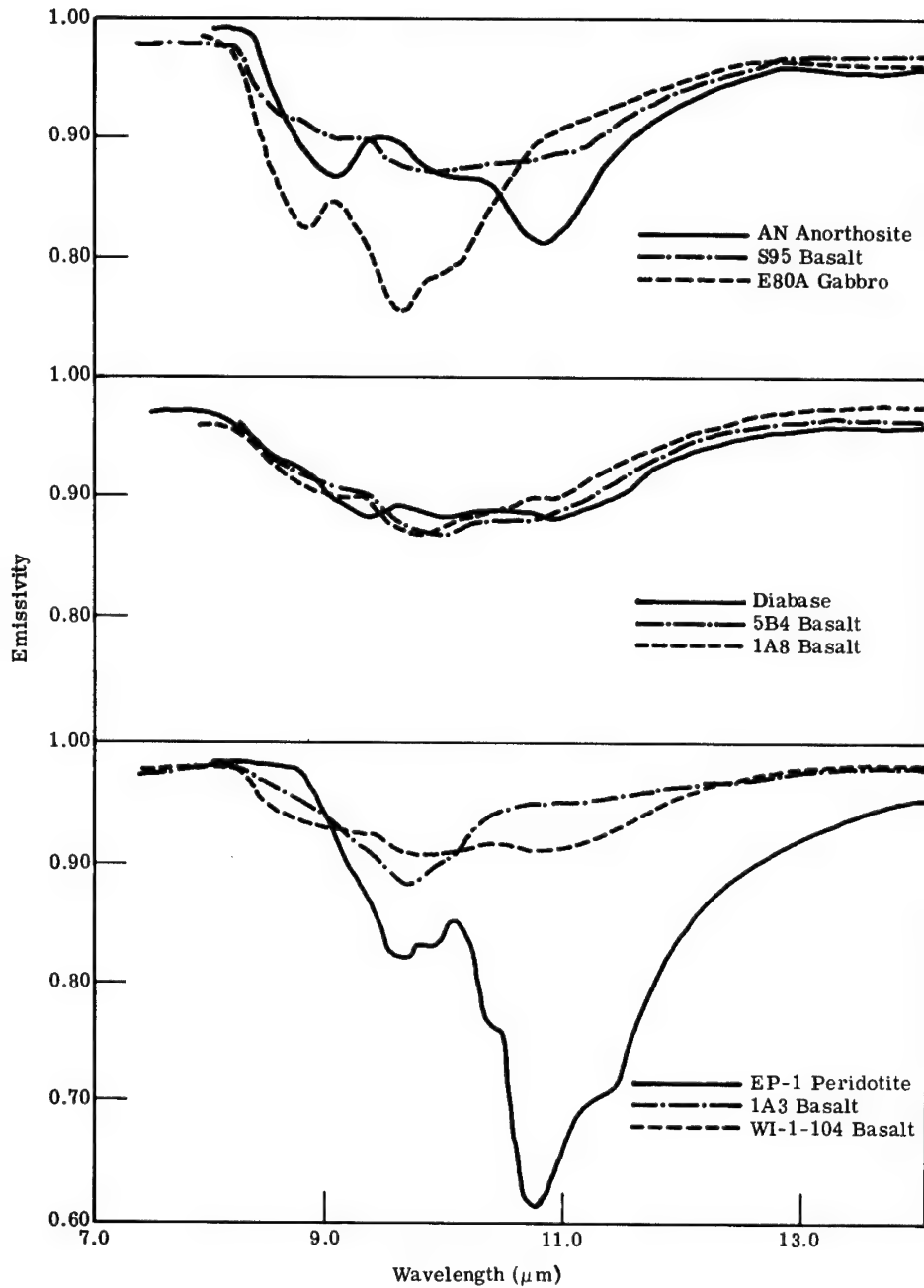


(a) A79 granite; SA-49 rhyolite; trachyte (Porphyritic); A119 granite; rhyolite (welded tuff); nepheline syenite; A122 granite; E83A pyroxene syenite; and A117 granodiorite.



(b) A127 granodiorite; 2B5 dacite (natural surface); E47C diorite; E12A dacite; 2B5 dacite (fresh surface); E55 andesite; 2A1 dacite; A129 diorite; and 2A3 rhyolite.

Fig. 3.106 (continued)



(c) An anorthosite; S95 basalt; E 80A gabbro; diabase; 5B4 basalt; 1A8 basalt; EP-1 peridotite; 1A3 basalt; and WI-1-104 basalt.

Fig. 3.106 (continued)

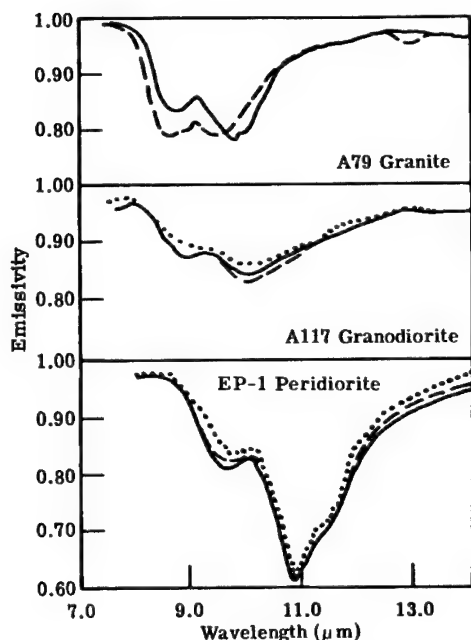


Fig. 3.107 Spectral variations resulting from measurements taken at different locations on the samples.¹⁰²

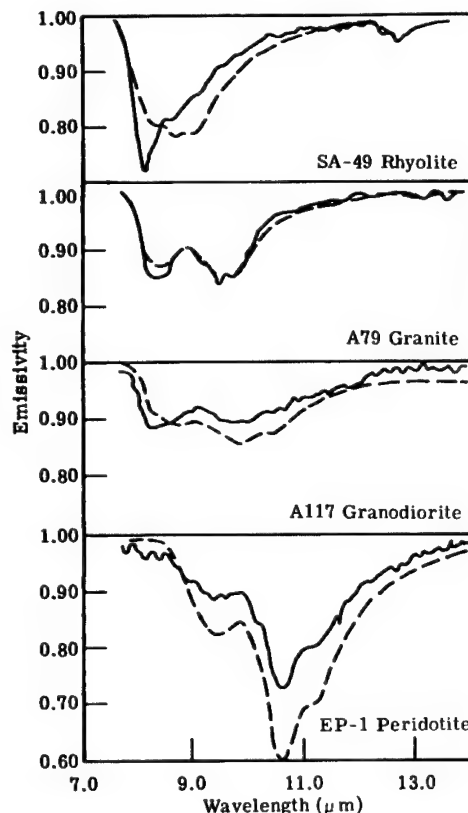


Fig. 3.108 Comparison of direct spectral emissivity measurements (solid line) with spectral emissivity curves derived from Kirchhoff's law and reflectance measurements (dashed line).¹⁰²

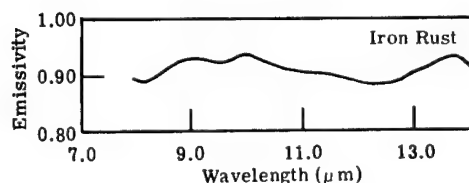
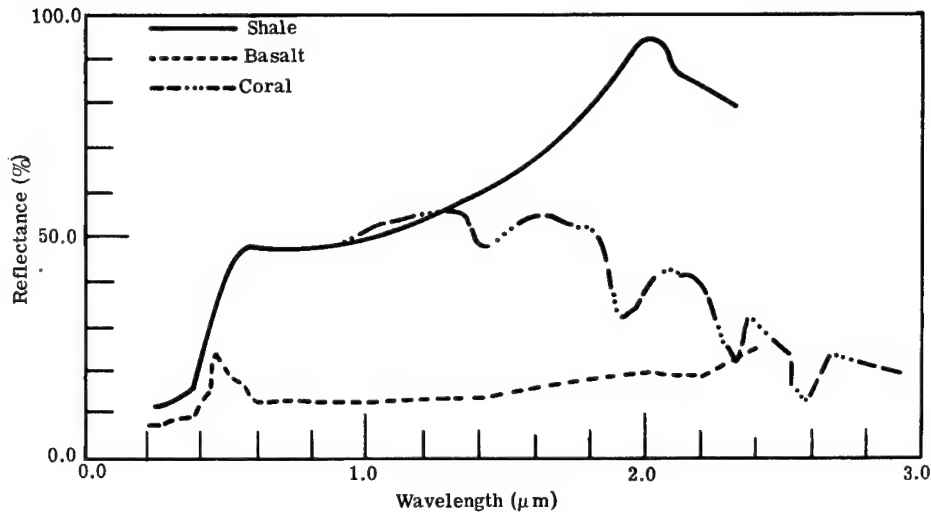
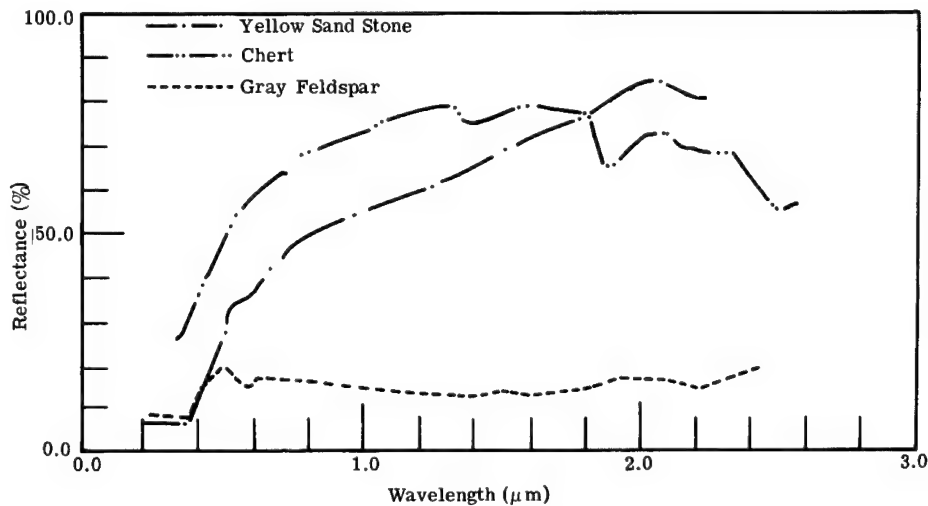


Fig. 3.109 Spectral emissivity of iron rust.

Painted Surfaces. Many exposed surfaces of buildings are covered with a paint or stain for purposes of weather protection. A popular binder for the pigments in paints is linseed oil. The reflectance spectrum of linseed oil is shown in Fig. 3.115(a) along with a variety of paints and coatings. There are absorption bands near 3.5 and 5.9 μm and a broadband near 9 μm . Paints using linseed oil generally exhibit these same bands if the substrate is reflective and the pigments are not opaque at these wavelengths. These absorption bands are not apparent in aluminum paints, as shown in Fig. 3.115(b). The paint coatings exhibit considerable spectral detail in the thermal infrared range so that graybody approximations are likely to lead to significant error. Figures 3.115(c) through 3.115(k) are other various reflectance spectra of paints and coatings.



(a) Shale; basalt; coral; and Manitou limestone, weathered surface viewing angle of 15° .



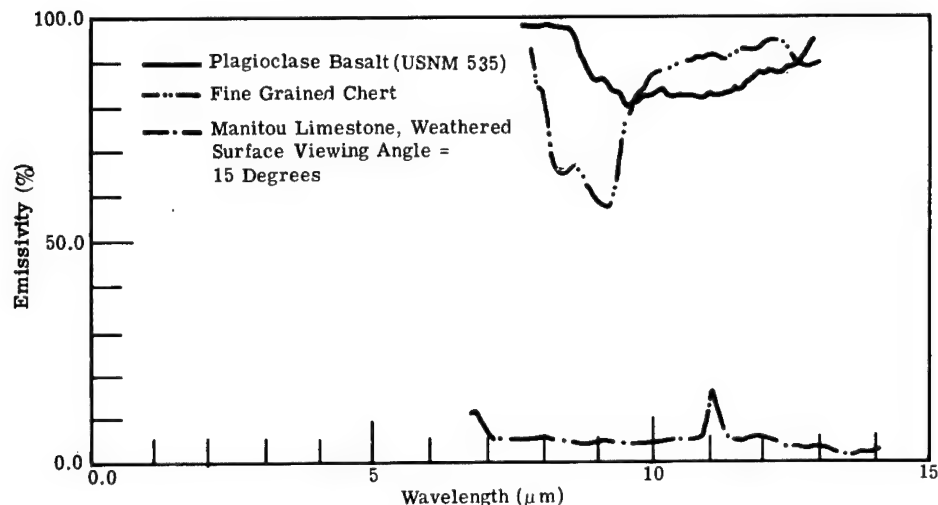
(b) Yellow sand stone; chert; and gray feldspar.

Fig. 3.110 Spectral reflectances and emissivities of common rock types.¹⁰¹ (continued on following page)

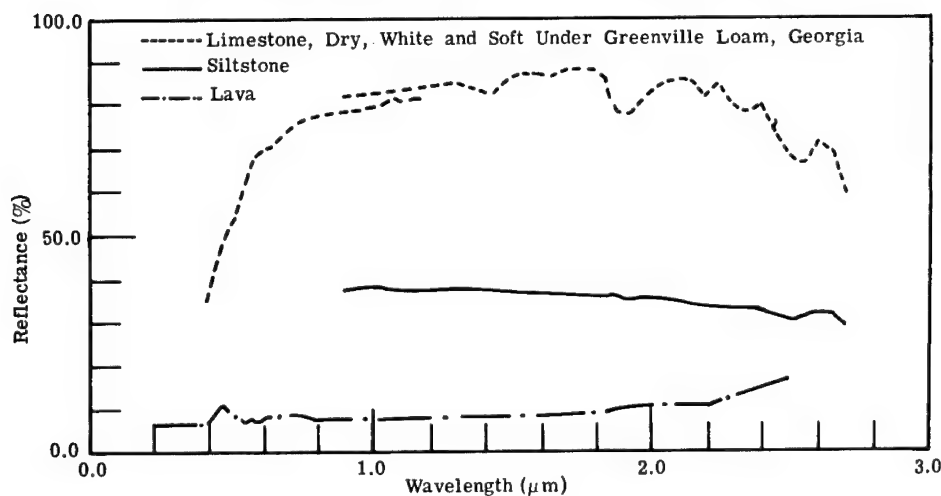
3.8.3 Water

The radiance of the sea surface is the sum of its thermal emission and reflected incident radiation. Factors that determine the character of the marine background are the following:

1. the optical properties of water
2. surface geometry and wave-slope distribution
3. surface temperature distribution
4. bottom material properties.



(c) Plagioclase basalt (USNM 535) and fine grained chert.

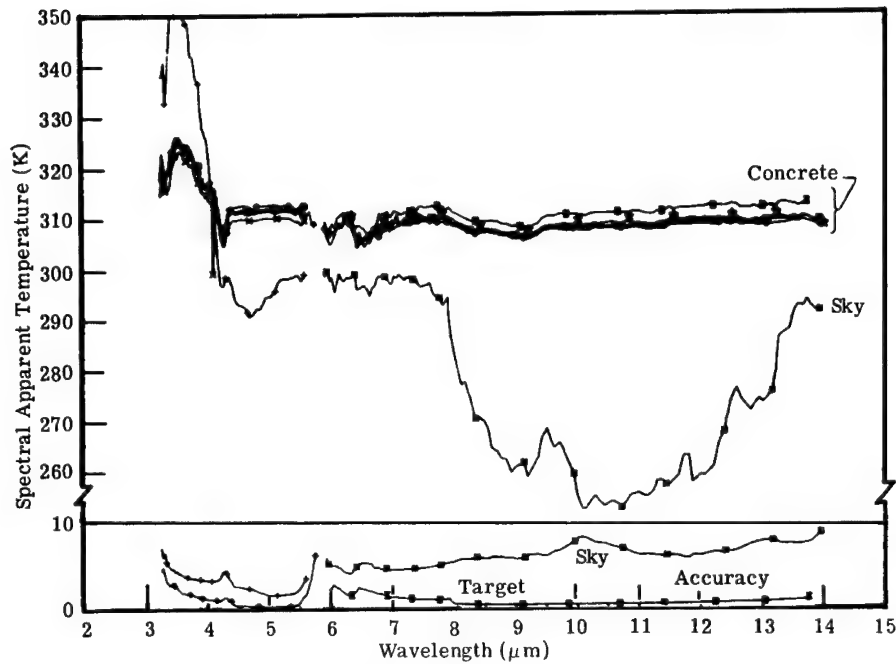


(d) Limestone, dry white and soft under Greenville loam, Georgia; siltstone; and lava.

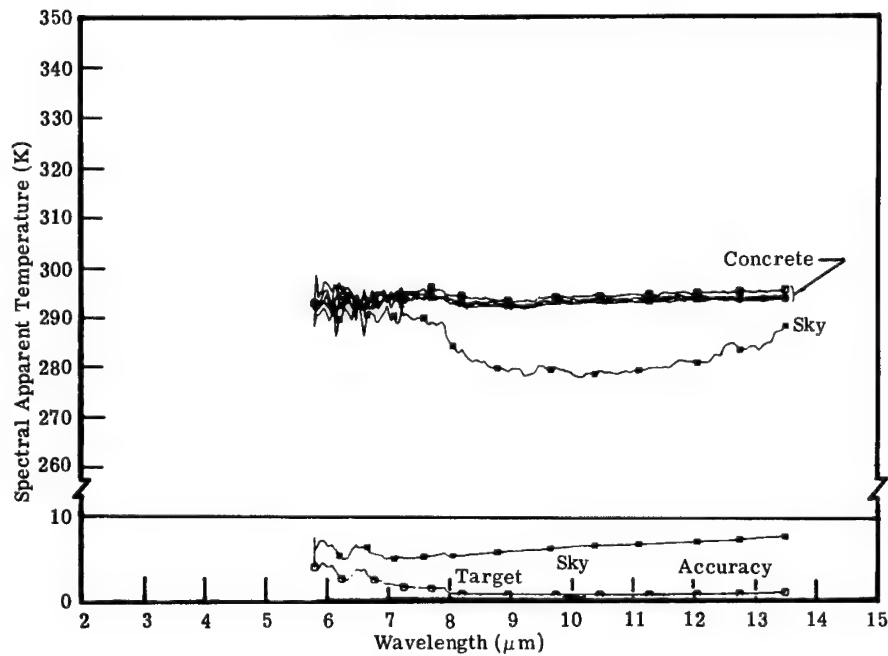
Fig. 3.110 (continued)

Atmospheric scattering, transmission, and emission in the optical path from the scene to the observing instrument contribute significantly to observed radiances.

Optical Properties of Water in the Thermal Range. Water is essentially opaque to infrared radiation longer than 3 μm . Few liquids have absorption coefficients of the same order of magnitude. Consequently, the water surface, which is 0.01 cm thick, determines the thermal radiance of the water. Subsurface scattering of sky radiation is absent in the thermal range. The optical influence in the thermal range of thin layers of surface contamination is negligible except for the suppression of capillary waves by surface tension changes causing slicks and the alteration of heat exchange by evaporation. There is

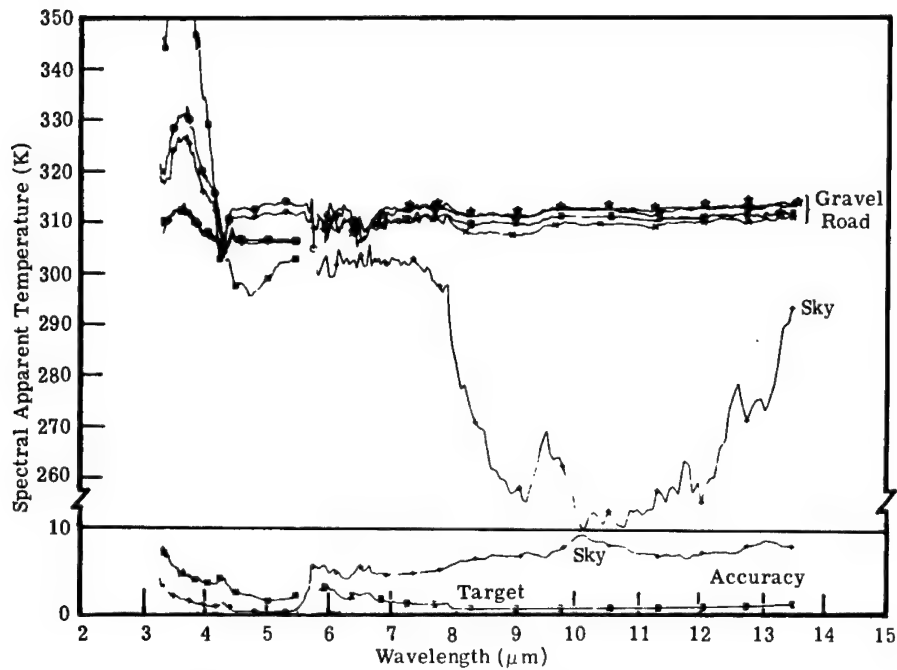


(a) 78-81°F ambient Temperature 0.0 cloud cover.

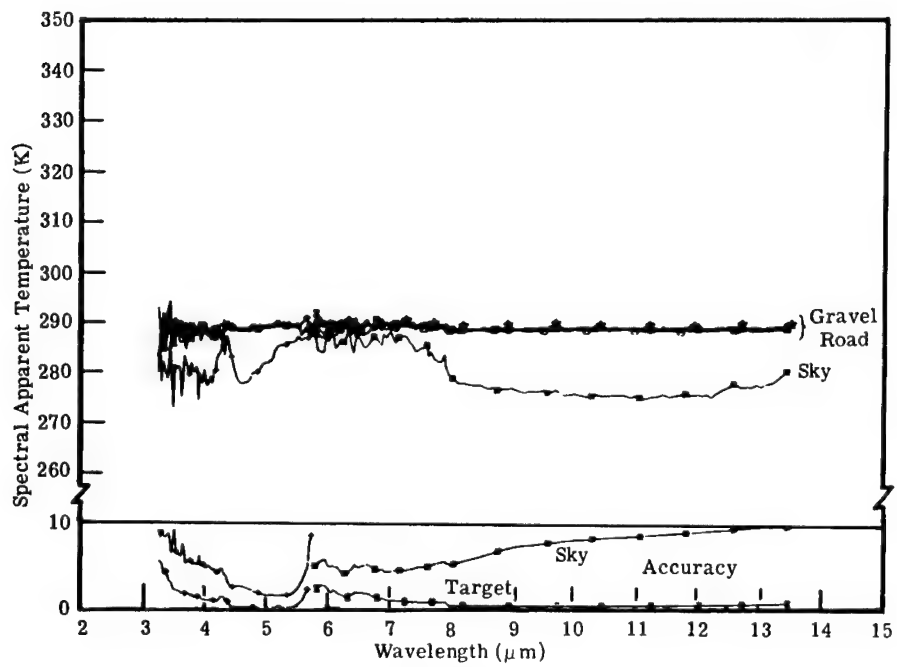


(b) 72-73°F ambient temperature 1.0 cloud cover.

Fig. 3.111 Concrete runway and sky spectral apparent temperature.¹⁰³

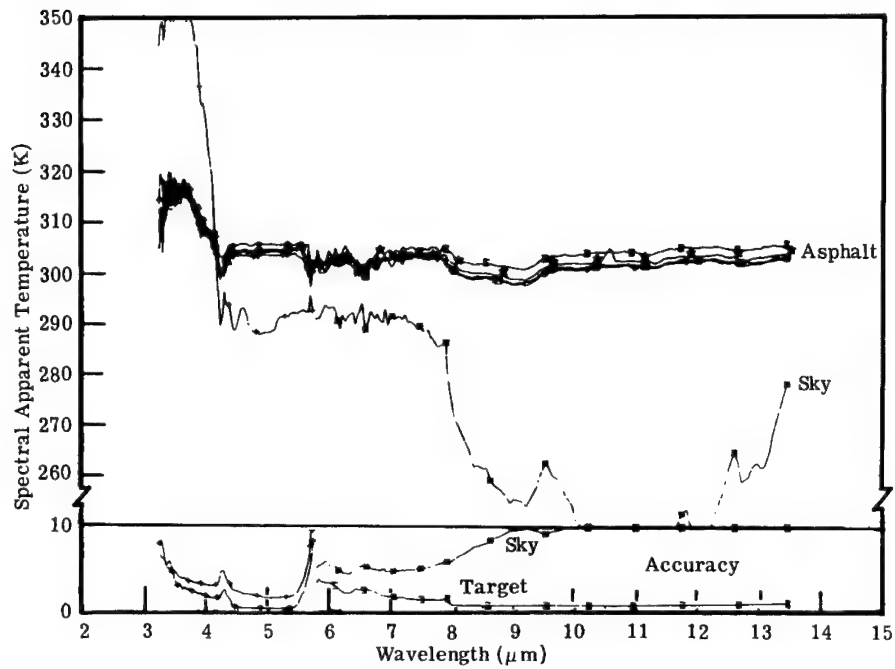


(a) 83-87°F ambient temperature 0.0 cloud cover.

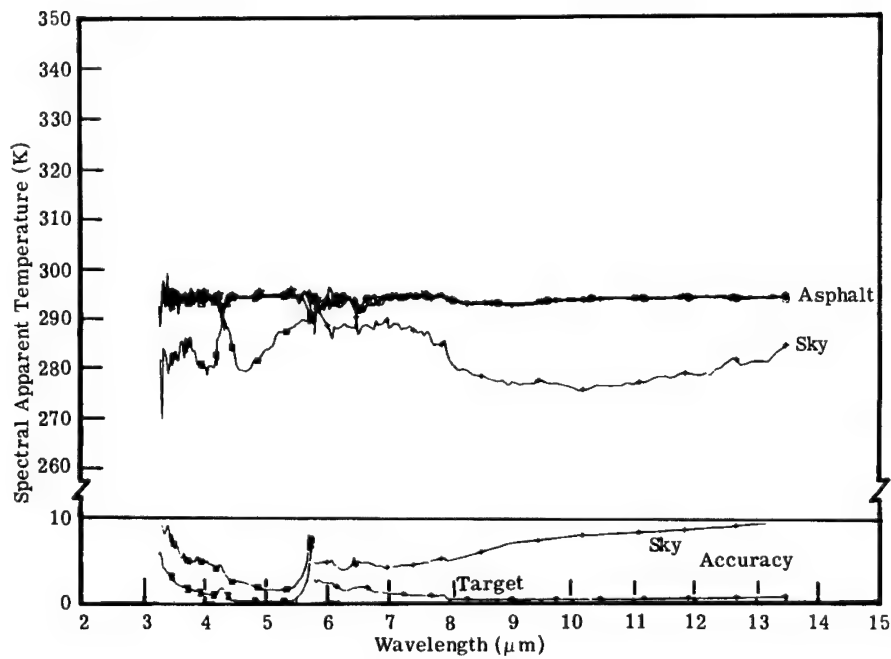


(b) 57-58°F ambient temperature 1.0 cloud cover.

Fig. 3.112 Heavily used gravel road and sky spectral apparent temperature.¹⁰³

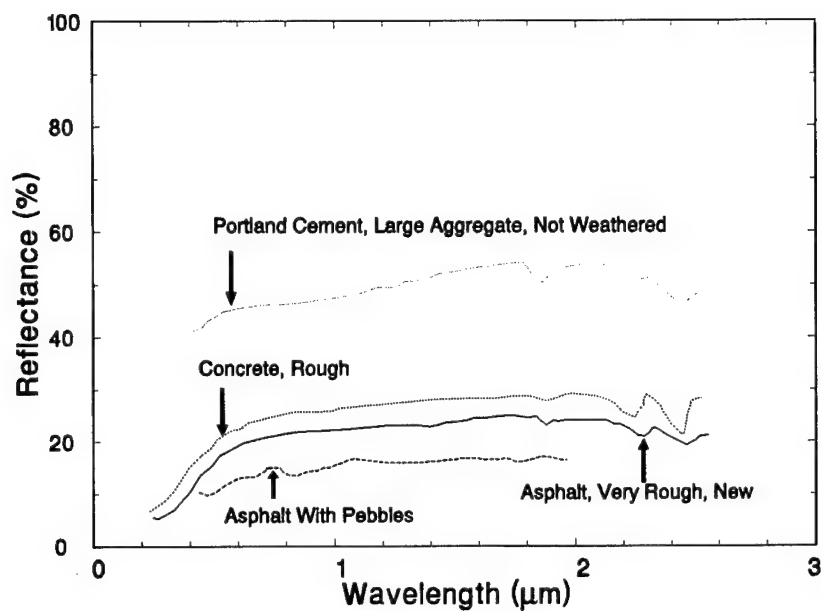


(a) 48-51°F ambient temperature 0.3 cloud cover.

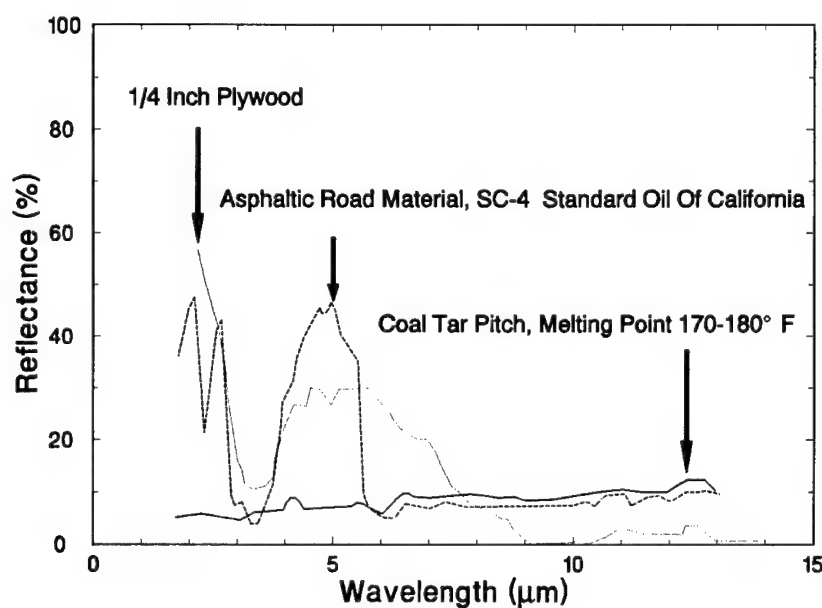


(b) 54-56°F ambient temperature 1.0 cloud cover.

Fig. 3.113 Asphalt and sky spectral apparent temperature.¹⁰³



(a)



(b)

Fig. 3.114 Spectral reflectances of various construction materials.^{104,105}

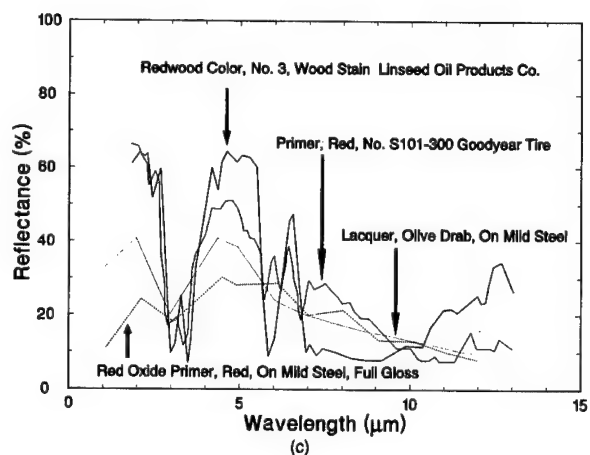
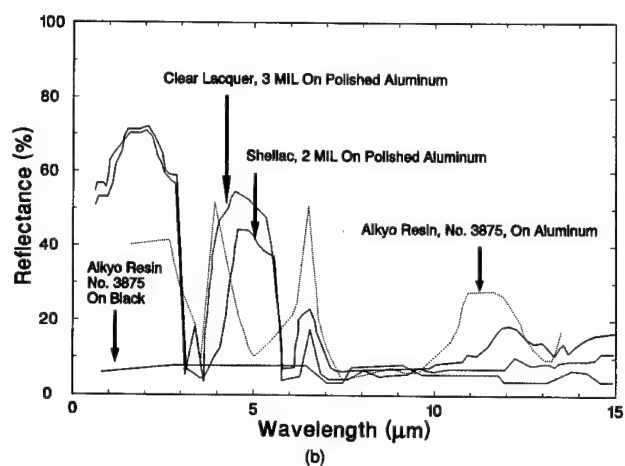
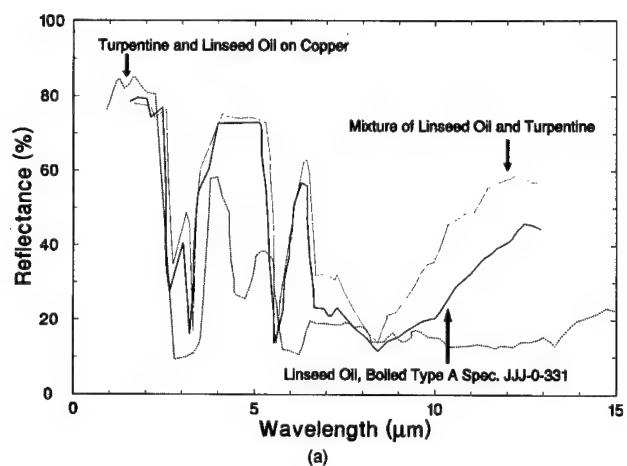


Fig. 3.115 Spectral reflectances of various paints and coatings.^{104,105} (continued on following pages)

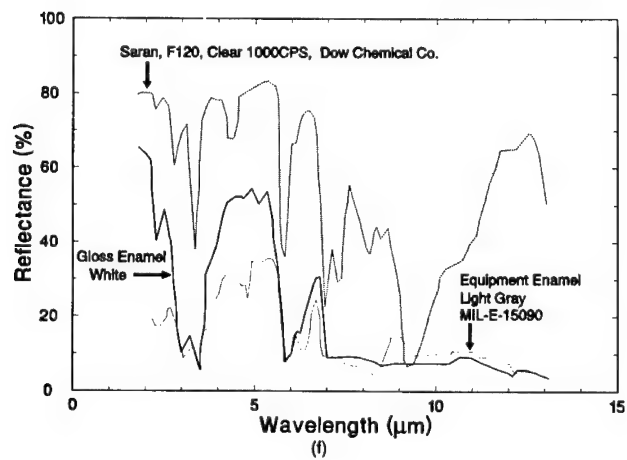
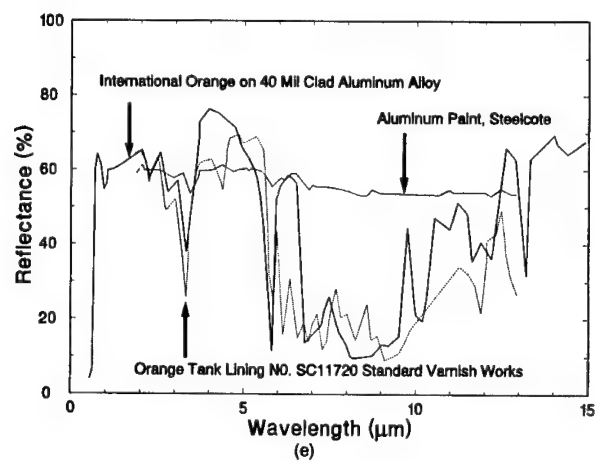
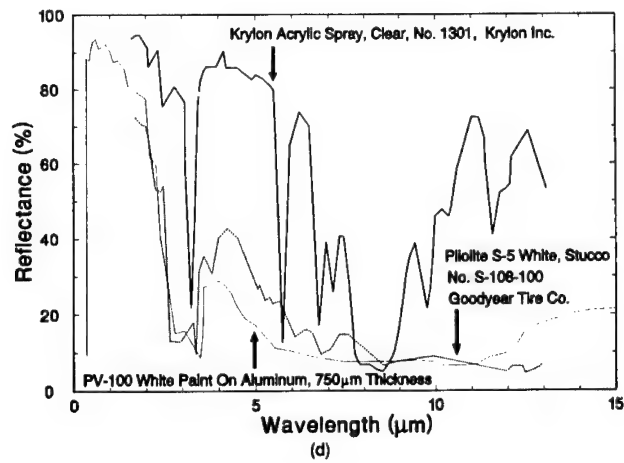


Fig. 3.115 (continued)

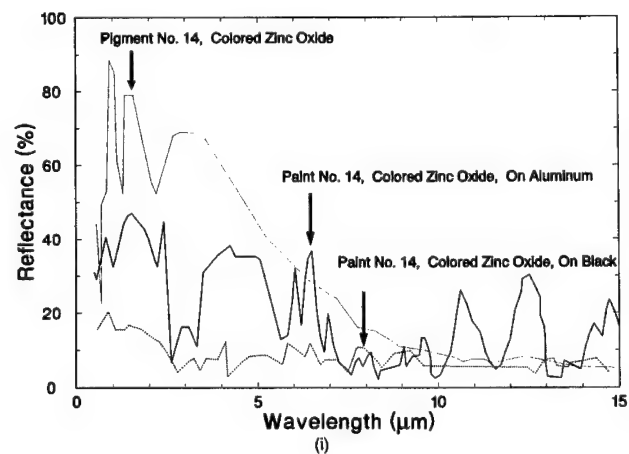
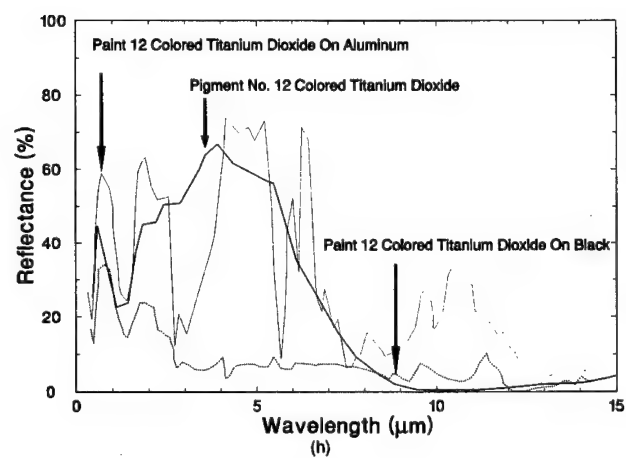
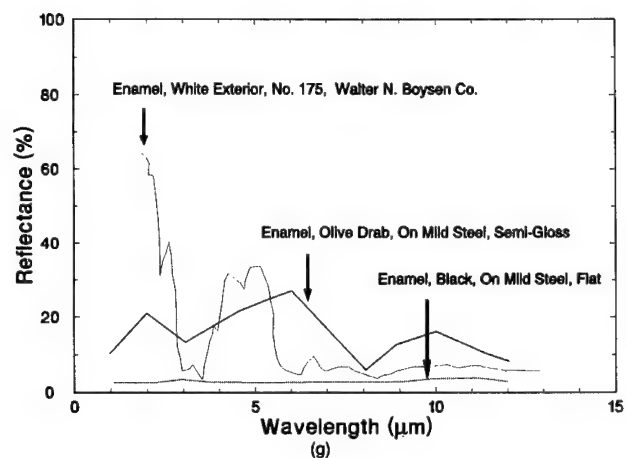


Fig. 3.115 (continued)

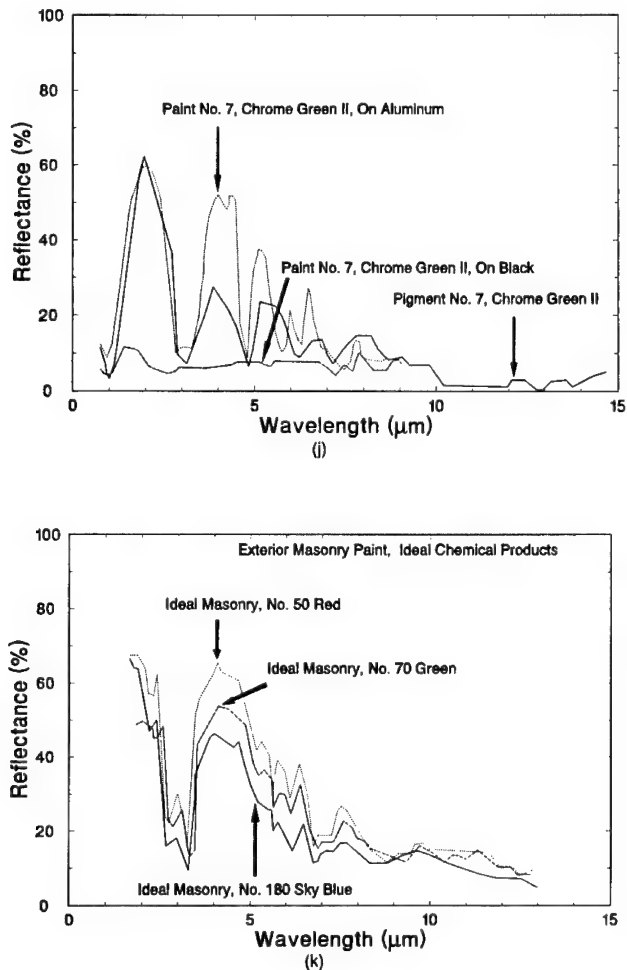


Fig. 3.115 (continued)

no significant difference in the transmittance of seawater and distilled water for these thin layers in the 2- to 15-μm region.

The infrared transmittance, reflectance, emissivity, and indices of refraction for water are shown in Figs. 3.116 through 3.119. The spectral absorption coefficient for seawater is shown in Figs. 3.120 and 3.121.

Sea Surface Geometry. The effect of wave slope on the reflectance of a sea surface roughened by a Beaufort 4 wind (11 to 16 knots, white caps) is seen in Fig. 3.122. Here, for an average rough sea, the reflectance approaches 20% near the horizon. Consequently, the emissivity remains at 80% or higher. The radiance of the sea surface along an azimuth 90° from that of the sun (in daylight, for clear and for overcast conditions) is shown in Fig. 3.123.

Information is not available on similar observations for the radiance of the sea surface at night. However, the variation of sky radiance with zenith angle

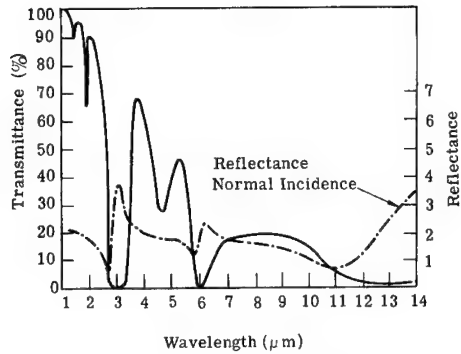


Fig. 3.116 Transmittance of 0.002 cm of seawater and reflectance of a free seawater surface.¹⁰⁶

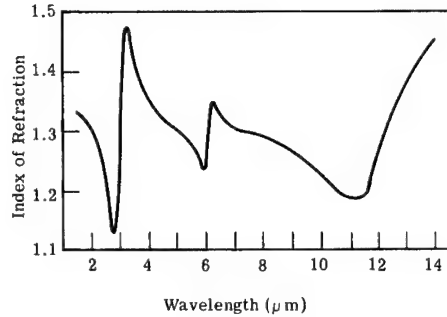


Fig. 3.117 Indices of refraction of water calculated from reflectivity data in Fig. 3.116.

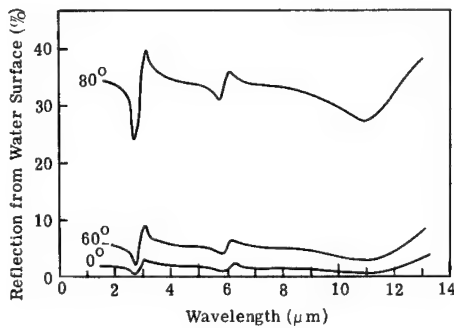


Fig. 3.118 Reflection from a water surface at 0, 60, and 80° angles of incidence calculated from data in Fig. 3.117.

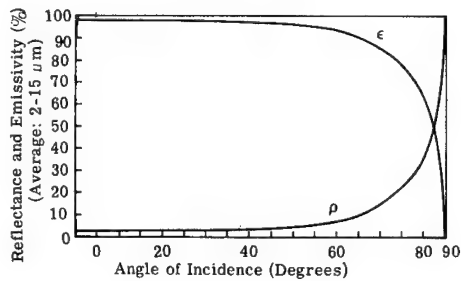


Fig. 3.119 Reflectance and emissivity of water (2 to 15 μm average) versus angle of incidence, calculated from averaged data of Fig. 3.117 (note the scale change).¹⁰⁷

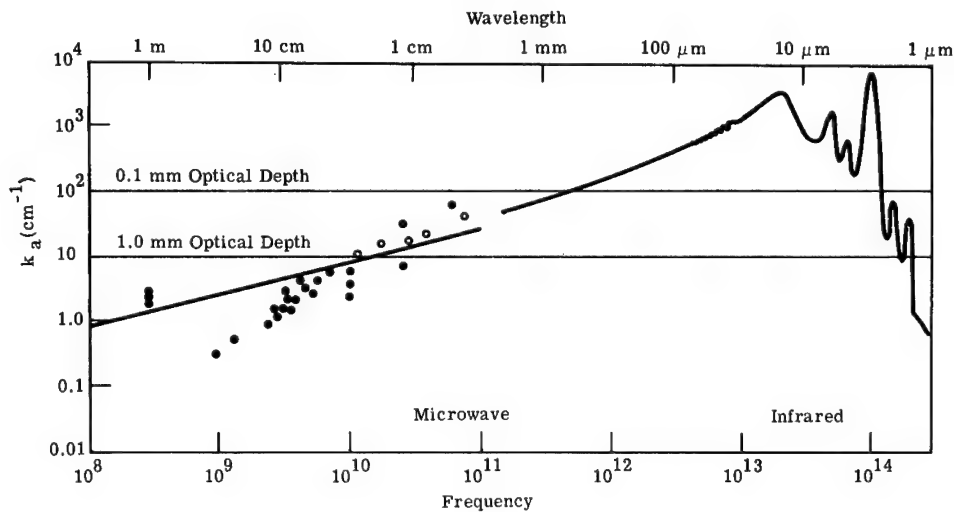


Fig. 3.120 Absorption coefficient k_a of seawater versus wavelength.¹⁰⁸

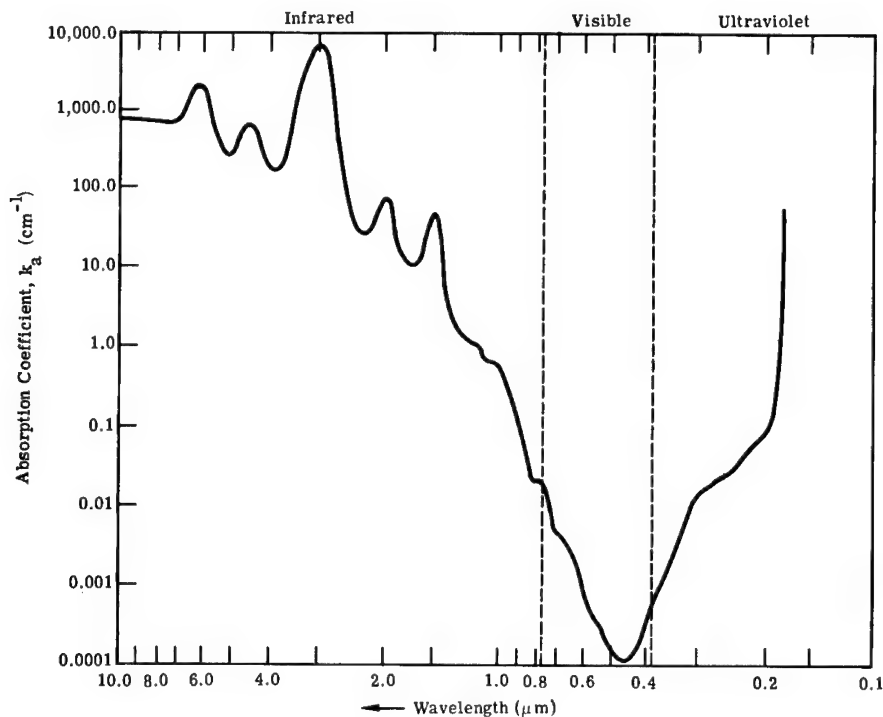


Fig. 3.121 Absorption of radiation by seawater.¹⁰⁸

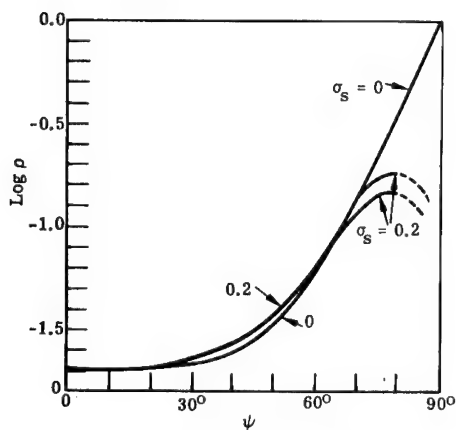


Fig. 3.122 Reflection of solar radiation from a flat surface ($\sigma_s = 0$) and a surface roughened by a Beaufort 4 wind ($\sigma_s = 0.2$). The albedo varies from 0.02 for a zenith sun ($\psi = 0^\circ$) to unity for the sun at the horizon ($\psi = 90^\circ$) on a flat sea surface. For a rough surface, shadowing and multiple reflections become important factors when the sun is low. The lower and upper branches of the curve marked $\sigma_s = 0.2$ represent two assumptions regarding the effect of multiple reflection. True values are expected to lie between the indicated limits.¹⁰⁹

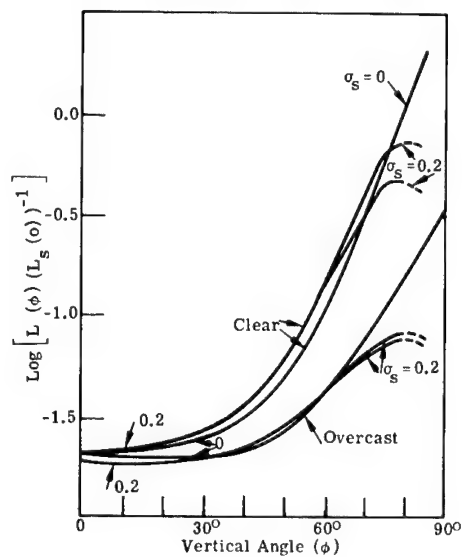


Fig. 3.123 The radiance of the sea surface $L(\phi)$ divided by the sky radiance at the zenith $L_s(0)$, as a function of the vertical angle ϕ . The curves are computed for a flat ($\sigma_s = 0$) and rough ($\sigma_s = 0.2$) surface for two sky conditions.

is similar day and night and the photographic reflectance is about equal to the average for the infrared from 2 to 15 μm (Fig. 3.119). Consequently, the curves in Fig. 3.123 are instructive because they show the general shape of that part of the radiance of the sea surface at night caused by the reflection of sky radiation. To these curves must be added the infrared radiance of the sea surface because of its thermal emission. Examples of the spectral radiance of the sea for day and after sundown are shown in Figs. 3.124, 3.125, and 3.126.

For further data on sea-surface geometry see Refs. 110, 111, and 112.

Sea Surface Temperature Distribution. The temperature of the sea surface determines the contribution of emission to its total radiance. In arctic regions, this temperature is near 0°C ; near the equator it rises to 29°C . Currents, such as the warm water of the Gulf Stream, produce anomalies of several degrees Celsius as they flow into colder areas. However, in most infrared scenes of marine interest, it is the radiance variation from point to point that determines the background against which a target is seen. Improvements in thermal mappers have shown details of this variation, which is usually caused by temperature differences over the sea surface, but under some conditions reflected sky radiance predominates.

The temperature of the upper 0.1 mm of the sea surface under evaporative conditions has been measured as 0.6°C colder than water a few centimeters below.¹¹³ The sharpest gradient¹¹⁰ is in the upper 1.0 mm. Measurements typical for the conditions noted are shown in Fig. 3.127.

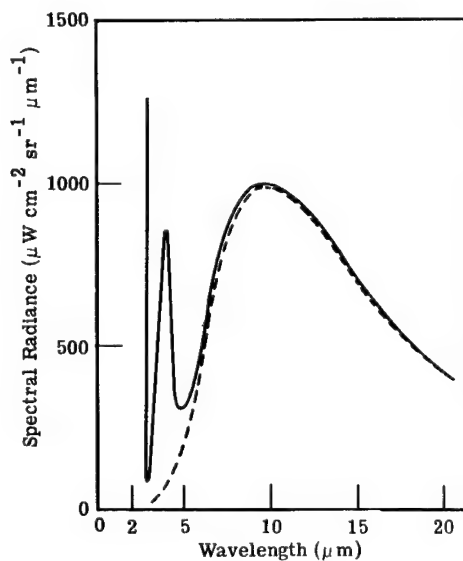


Fig. 3.124 Spectral radiance of the Banana River at Cocoa Beach, Florida.⁹²

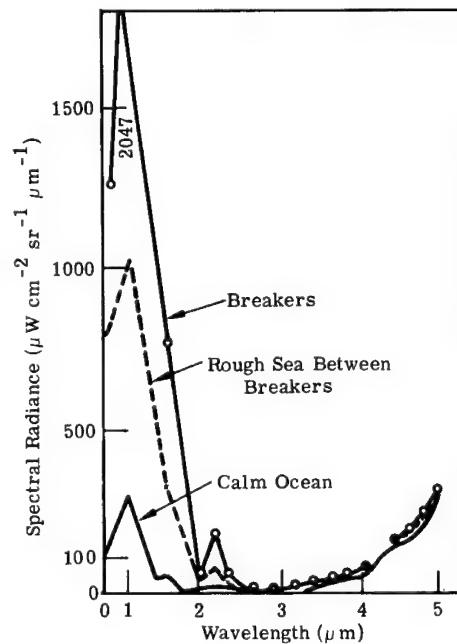


Fig. 3.125 Spectral radiance of the ocean.⁹²

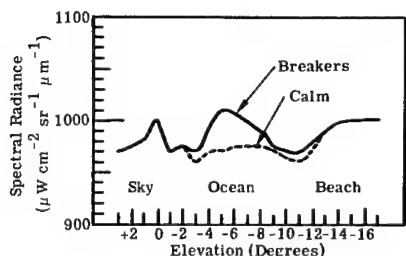


Fig. 3.126 Spectral radiance of the ocean versus the elevation angle.⁹²

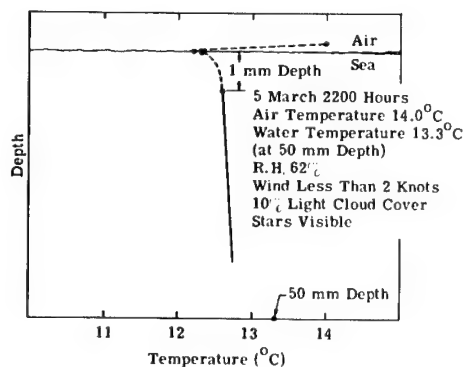


Fig. 3.127 Thermal structure of the sea boundary layer. Previous conditions: 12 h cool (12 to 15°C), no rain. The data were taken during the passage of a warm front.

The temperature of this layer with low heat capacity is determined by the rate of evaporation, radiation exchange, and the flow of heat from the air and from below. It has been found experimentally that the presence of surface contamination slightly reduces the flow of heat from below so that a slick (a region in the sea with enough surface contamination to alter surface tension) appears colder than adjacent areas outside the slick. Finally, the flow of heat from below is also influenced by the convective activity of the water layer above the thermocline.

Optical Properties of Water in the Solar Range of 0.35 to 3.0 μm. The spectral absorption coefficient for pure water falls to very low values in the 0.4- to 0.7-μm range, so radiation can penetrate deeply into the water body and scatter from suspended particulates and from the bottom. The spectral absorption coefficient $a(\lambda)$, defined by the relation

$$\tau(\lambda) = \exp[-a(\lambda)x] \quad (3.62)$$

for pure water of depth x , is given in Table 3.29. Figure 3.120 shows the spectral absorption coefficient of seawater over the infrared and microwave spectral regions.

Natural water bodies contain both solutes and particulates in suspension. The spectral extinction or attenuation coefficient $k(\lambda)$ is a measure of the combined effects of the absorption of the solution and particulates (as well as the backscattering due to the particulates) in reducing the downward-welling radiation in natural water so that

$$E_\lambda(x) = E_\lambda(0) \exp[-k(\lambda)x], \quad (3.63)$$

where $E_\lambda(x)$ is the spectral irradiance just below the upper surface of a horizontal plane and x is the depth of plane. Because of multiple scattering and particulate absorption, $k(\lambda)$ is not necessarily the simple sum of the absorption coefficients of the solution and backscattering coefficient of the particulate.

Table 3.29 Absorption Coefficients per Meter of Pure Water at Wavelengths Between 0.32 and 0.65 μm According to W. R. Sawyer and at Wavelengths Greater than 0.65 μm According to J. R. Collins (from Ref. 89)

Wave-length (μm)	Absorption Coefficient (m^{-1})	Wave-length (μm)	Absorption Coefficient (m^{-1})	Wave-length (μm)	Absorption Coefficient (m^{-1})	Wave-length (μm)	Absorption Coefficient (m^{-1})
0.32	0.58	0.52	0.019	0.85	4.12	1.60	800.0
0.34	0.38	0.54	0.024	0.90	6.55	1.70	730.0
0.36	0.28	0.56	0.030	0.95	28.80	1.80	1700.0
0.38	0.148	0.58	0.055	1.00	39.70	1.90	7300.0
0.40	0.072	0.60	0.125	1.05	17.70	2.00	8500.0
0.42	0.041	0.62	0.178	1.10	20.30	2.10	3900.0
0.44	0.023	0.65	0.210	1.20	123.20	2.20	2100.0
0.46	0.015	0.70	0.84	1.30	150.00	2.30	2400.0
0.48	0.015	0.75	2.72	1.40	1600.00	2.40	4200.0
0.50	0.016	0.80	2.40	1.50	1940.00	2.50	8500.0

Figure 3.128 shows the spectral attenuation coefficient for natural water bodies. The attenuation coefficients for fresh water fall below that for distilled water. This difference may be an artifact of the experimental methods used. The downward-welling spectral irradiance varies greatly with water composition. Figures 3.129 and 3.130 present actual measurements.

The reflectance of water bodies has a surface reflectance component given by Fresnel's equations, as well as a bulk reflectance component that depends on specific water composition. The calculated reflectance of a deep ocean, including surface reflection and the effects of a turbid atmosphere, is shown in Fig. 3.131 with $\text{mg}\cdot\text{m}^{-3}$ of chlorophyll as a parameter. The calculated bulk spectral reflectance of a deep sand bottom ocean is shown in Fig. 3.132 with and without the phytoplankton scattering.

Note that in both Figs. 3.131 and 3.132 the curves tend to cross near 0.5 μm . This crossover point is sometimes called the *hinge point*. The location of the hinge point changes somewhat with the introduction of other materials in the water. Airborne spectral reflectance data for sea surfaces are shown in Fig. 3.133. No correction was made for path radiance of the atmosphere or surface reflectance of the sky. Curves B, C, and E appear to exhibit the hinge point.

The spectral attenuation coefficients of prepared algae suspensions are presented in Table 3.30. The algae concentrations were measured as the weight per liter of filtered dry solids dried at 103°C for 90 min. *Chlorella* and *Selenastrum* are green algae. *Anabaena* and *Microcystis* are blue-green algae. The spectral reflectances of prepared columns of algae suspensions are shown in Figs. 3.134 and 3.135. These spectra were made using a specialized optical arrangement that included reflected radiation from the container walls so that these spectra will not correspond quantitatively to spectra made by other arrangements.

Yellow Substance. According to Kalle,¹¹⁹ seawater may contain a yellow soluble material that he calls *yellow substance*. This material is presumed to be related to humic acids from decaying vegetation. Water runoff from forested areas may be a source of yellow substance in lake and river water. Yellow substance is easily prepared by placing dead tree leaves in a plastic container,

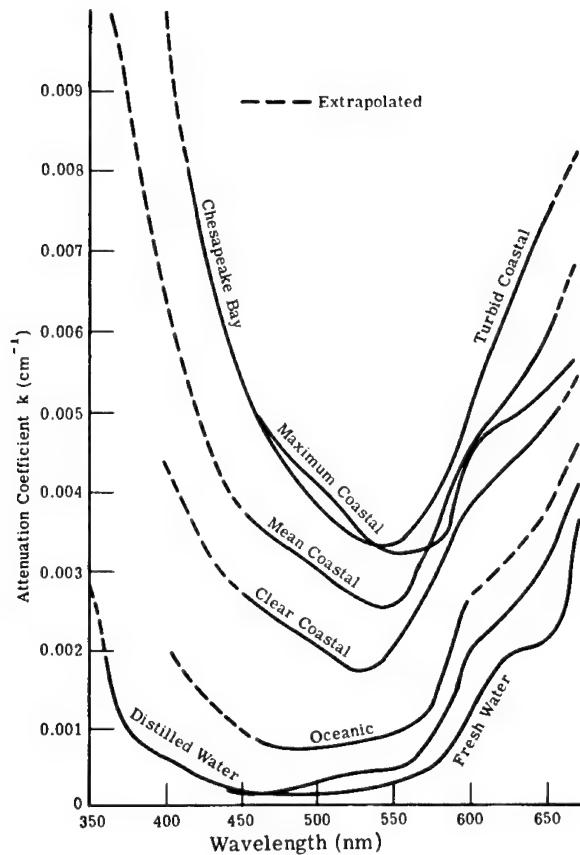


Fig. 3.128 Attenuation coefficient k versus wavelength for distilled, fresh, and seawater.¹¹⁴

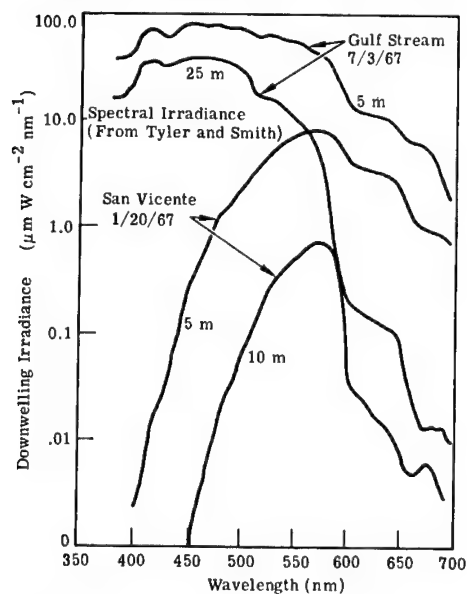


Fig. 3.129 Downward-welling spectral irradiance measured by Tyler and Smith.¹¹⁵

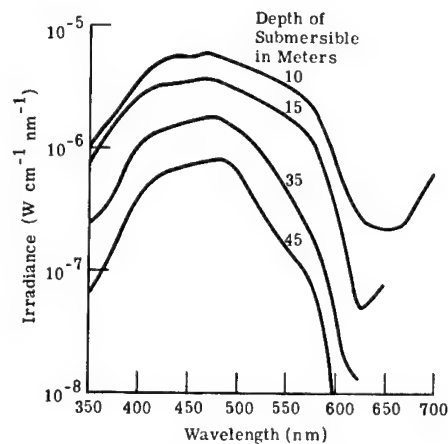


Fig. 3.130 Downward-welling spectral irradiance measured in the Ben Franklin experiment.¹¹⁵

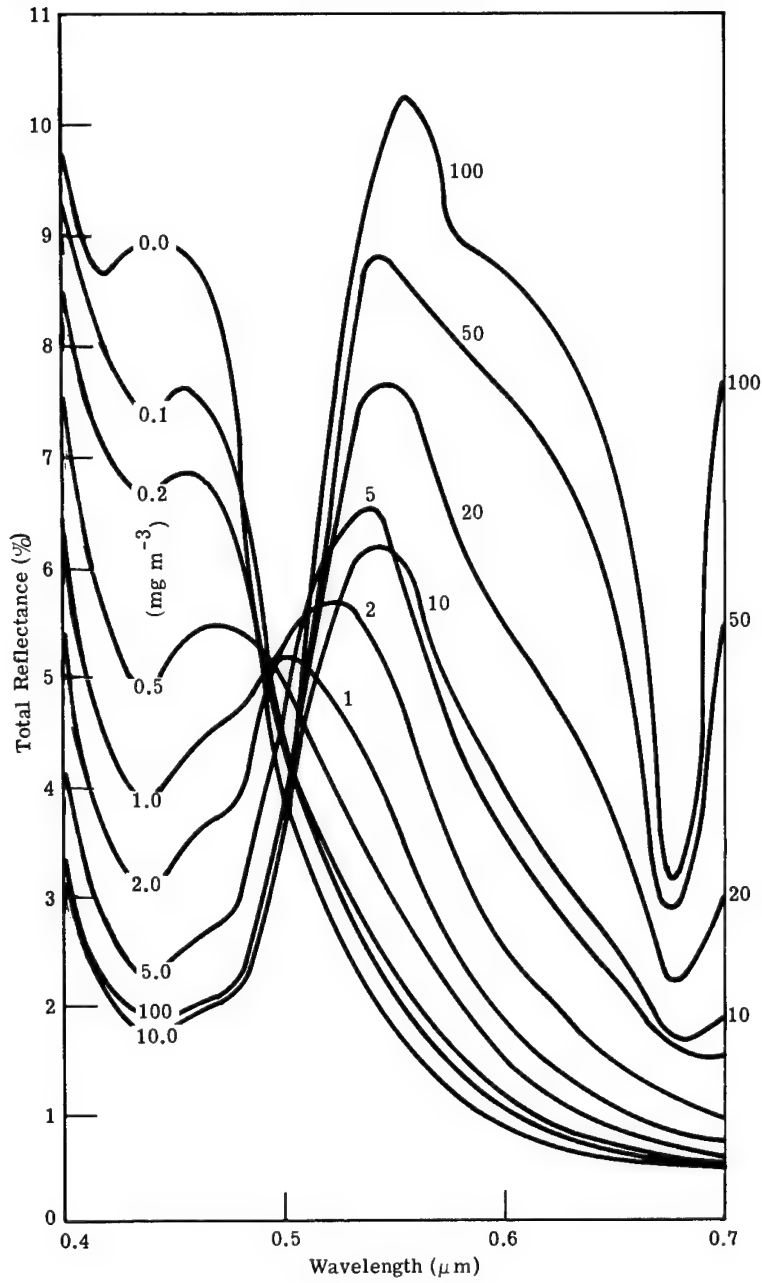


Fig. 3.131 Calculated spectral reflectance of deep ocean with varying amounts of chlorophyll. A clear sunny day, 45° solar zenith angle, includes surface reflection from smooth ocean with turbid atmosphere.¹¹⁶

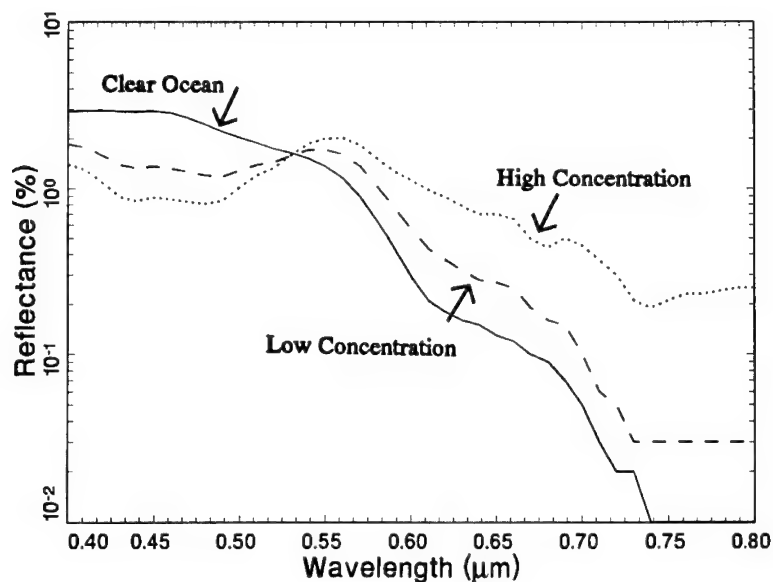


Fig. 3.132 Calculated change in bulk reflectance of ocean water with different phytoplankton concentrations illustrating the hinge point.¹¹⁷

Table 3.30 Attenuation Coefficients* at Selected Wavelengths for the Four Experimental Algae (from Ref. 118)

λ (μm)	<i>Anabaena</i>		<i>Microcystis</i>		<i>Chlorella</i>		<i>Selenastrum</i>		<i>Dist.</i> H_2O^{**}
	4 mg l^{-1}	8 mg l^{-1}	4 mg l^{-1}	8 mg l^{-1}	4 mg l^{-1}	8 mg l^{-1}	4 mg l^{-1}	8 mg l^{-1}	
375	2.09	4.24	1.66	3.24	2.48	4.80	2.24	4.39	0.017
400	2.30	4.36	1.83	3.31	2.73	5.13	2.52	4.81	0.046
425	2.45	4.80	1.97	3.84	3.04	5.86	2.80	5.46	0.050
450	2.26	4.31	1.97	3.58	2.99	5.72	2.72	5.32	0.045
475	1.76	3.17	1.67	2.96	2.79	5.32	2.53	4.73	0.051
500	1.65	2.95	1.57	2.74	2.50	4.47	2.17	3.83	0.059
525	1.43	2.56	1.19	2.20	1.61	2.59	1.46	2.39	0.075
550	1.28	2.42	1.07	1.95	1.48	2.29	1.33	2.07	0.098
575	1.59	2.85	1.17	2.11	1.56	2.49	1.40	2.24	0.117
600	2.04	3.52	1.56	2.56	1.85	2.85	1.63	2.54	0.262
625	2.40	4.12	1.77	2.78	2.09	3.22	1.92	2.96	0.316
650	2.23	3.64	1.76	2.61	2.44	4.08	2.08	3.38	0.341
675	2.55	4.08	2.16	3.26	3.34	5.71	3.06	5.27	0.408
700	2.24	3.11	2.08	2.76	2.60	3.61	2.37	3.32	0.612
725	2.57	3.28	2.73	3.32	3.07	3.60	2.86	3.46	1.183
750	4.07	4.85	4.21	4.91	4.55	5.22	4.40	5.05	2.576
775	4.08	4.79	4.12	4.77	4.28	5.01	4.15	4.85	2.195
800	3.62	4.54	3.59	4.35	3.83	4.73	3.65	4.51	1.723

*Attenuation coefficients expressed per meter, calculated from 30 inch column data.

**Distilled water plus 75 mg l^{-1} of MgSO_4 and 20 mg l^{-1} of Na_2CO_3 .

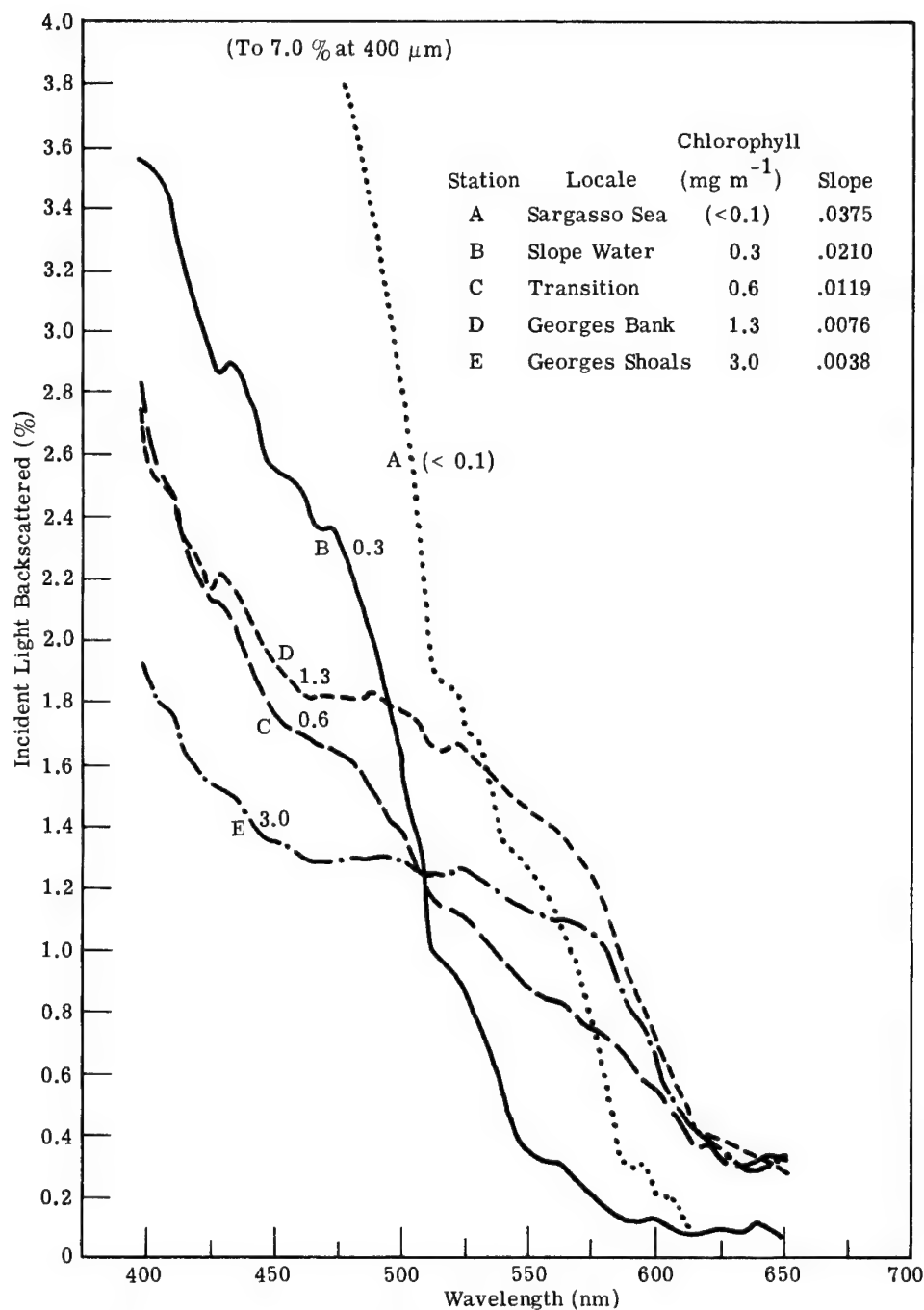


Fig. 3.133 Spectra of backscattered light, measured from the aircraft at 305 m on 27 August 1968 at the following stations and times (all EDT): Station A, 1238 hours; Station B, 1421 hours; Station C, 1428.5 hours; Station D, 1445 hours; Station E, 1315 hours. The spectrometer with polarizing filter was mounted at a 53° tilt and directed away from the sun. Concentrations of chlorophyll a were measured from shipboard: Station A, 1238 hours (27 August); Station B, 0600 hours (28 August); Station C, 0730 hours (28 August); Station D, 1230 hours (28 August).¹¹⁶

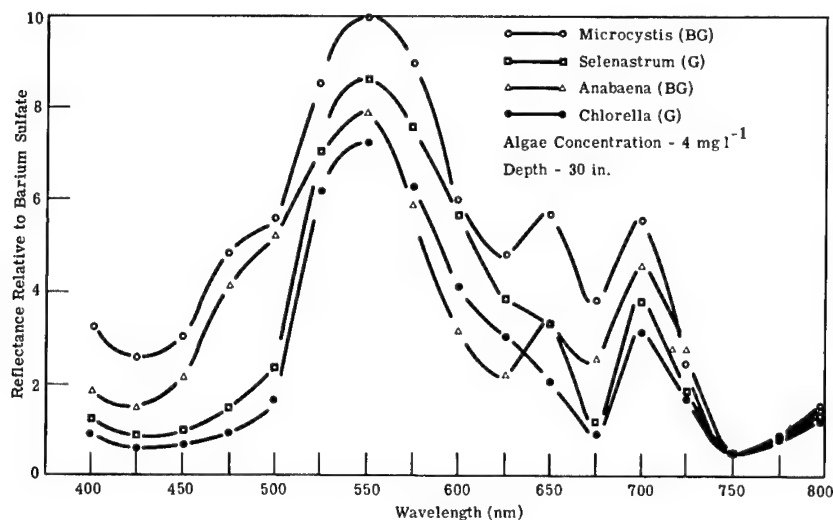


Fig. 3.134 Relative spectral reflectance curves for two green and two blue-green algae at 4 mg l^{-1} concentration.¹¹⁸

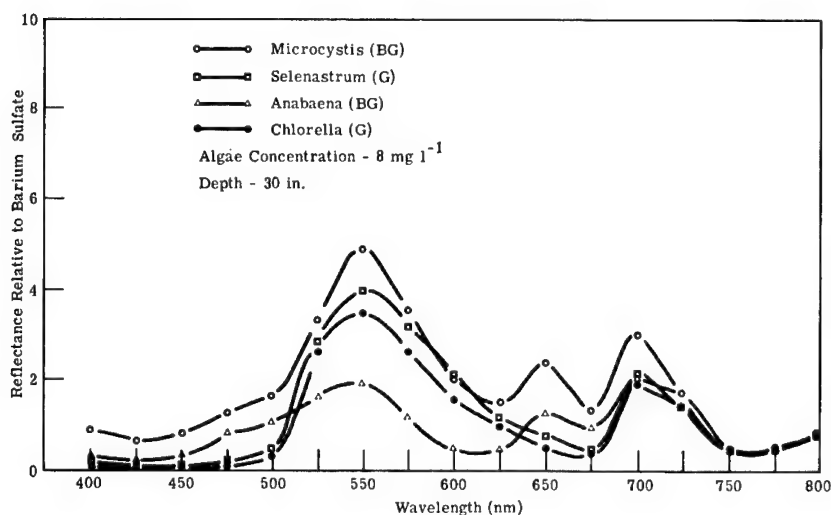


Fig. 3.135 Relative spectral reflectance curves for two green and two blue-green algae at 8 mg l^{-1} concentration.¹¹⁸

covering with water, and letting stand at room temperature for one week. The filtered liquid is yellow substance and has the appearance of tea. The spectral absorption coefficient (per meter) of yellow substance is given empirically in the visible and near-IR by

$$a(\lambda) = 25330C \times 10^{-0.004935\lambda}, \quad (3.64)$$

where C is the concentration relative to room temperature saturation and λ is the free-space wavelength in nanometers. Relative concentrations of yellow

substance in seawater range from 10^{-5} to 10^{-3} of saturation. Coastal regions contain higher concentrations than open ocean.

Oil Films. Petroleum products are commonly encountered pollutants of large water bodies. The pollution is caused by natural seepage from the earth, accidental loss from oil-processing or oil-using equipment, or dumping of oil waste. Oils are normally insoluble in water and less dense than water so that they form thin films on the surface.

Table 3.31 gives the constants of the Cauchy formula for index of refraction for some common oils in the 0.4- to 2.4- μm range:

$$n = A + \frac{B}{\lambda^2} + \frac{C}{\lambda^4} . \quad (3.65)$$

The constants were derived from experimental data utilizing direct and indirect index of refraction measurements.¹²⁰ Only two to three decimal-place accuracy can be expected from these data.

Figures 3.136, 3.137, and 3.138 show the index of refraction of oils in the 1.5- to 10.0- μm range.

Figures 3.139 and 3.140 show the spectral extinction coefficients of oils. The spectral details of the spectral extinction coefficient generally correspond to similar spectral variation in the index of refraction. Figures 3.141, 3.142, and 3.143 present the calculated spectral radiance of oil slicks on seawater under solar illumination viewed at the nonspecular angle. Figures 3.144, 3.145, and 3.146 show the measured spectral radiance of oil samples under ultraviolet lamp excitation. The magnesium oxide is not fluorescent.

Normal emittance values for a number of oils and for seawater are presented in Table 3.32. These values were obtained from the normal specular reflectances of the bulk (i.e., optically thick) oil, which, in turn, were calculated from the refractive indices [Eq. (3.65) and the Fresnel equation]. The bulk-

Table 3.31 Constants for Cauchy Relation for Index of Refraction of Oils 0.4 to 2.4 μm (from Ref. 120)

$(n = A + B/\lambda^2 + C/\lambda^4)$				
Oil	Sample No.	A	B (μm^2)	C (μm^4)
Bradford crude oil	A1654	1.417	-0.00161	0.00359
Bradford residual fuel oil	A1655	1.494	0.01394	-0.00073
Bradford medium lube	A1656	1.432	0.00284	0.00146
Bradford diesel fuel	A1657	1.410	0.00558	-0.00030
Hastings crude oil	A1658	1.433	-0.00964	0.00843
Wilmington crude oil	A1659	1.456	-0.00653	0.00725
SAE 30 lube oil	A1660	1.436	-0.00748	0.00779
Used SAE 30 lube oil	A1661	1.438	0.00425	0.00149
Menhaden fish oil	A1662	1.428	0.00205	0.00211

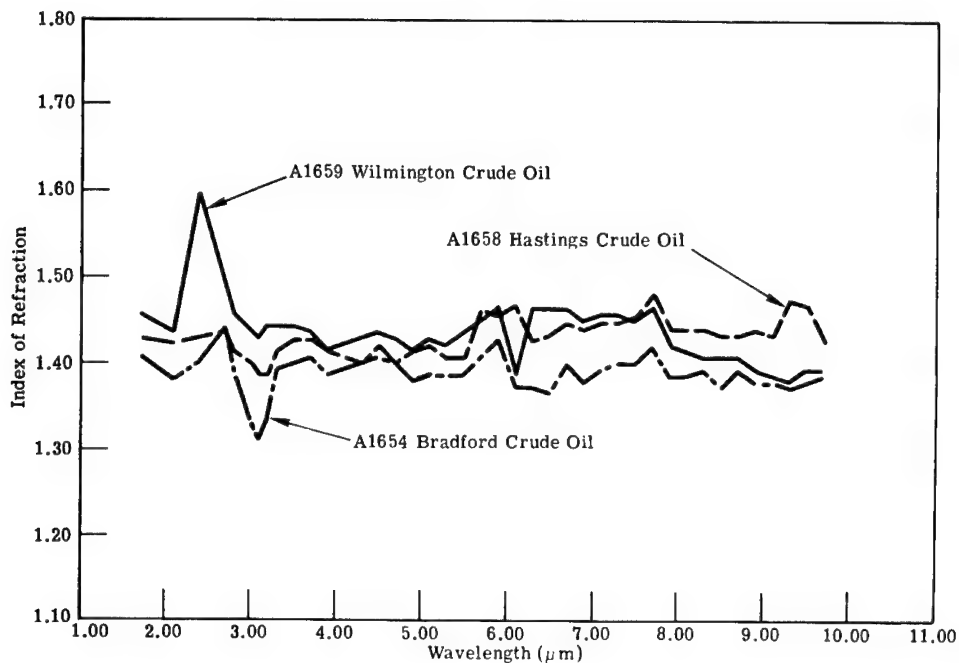


Fig. 3.136 The index of refraction of A1659 Wilmington crude oil, A1658 Hastings crude oil, and A1654 Bradford crude oil.¹²⁰

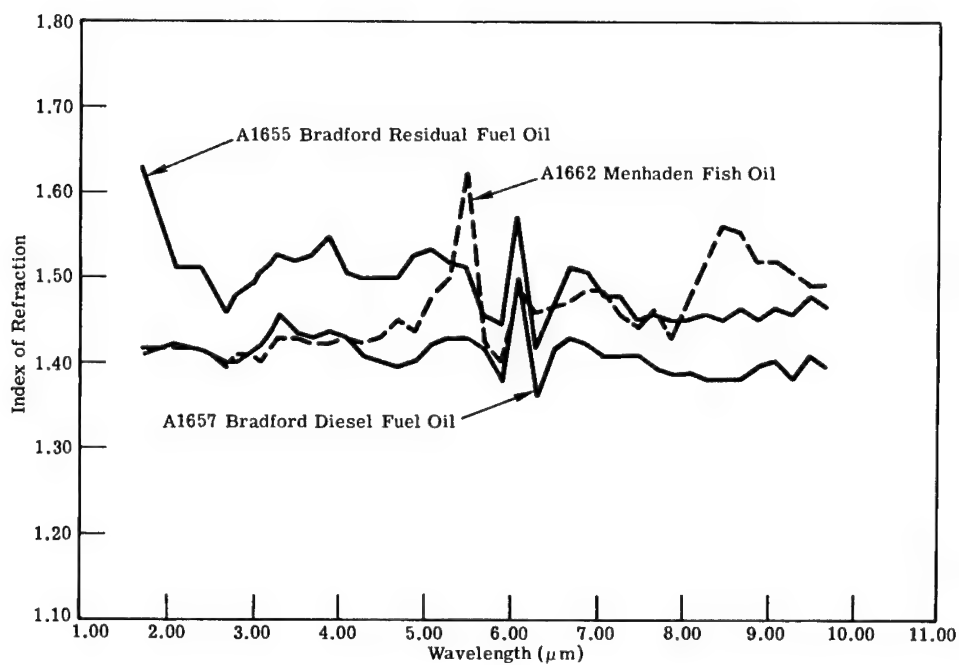


Fig. 3.137 The index of refraction of A1655 Bradford residual fuel oil, A1662 Menhaden fish oil, and A1657 Bradford diesel fuel oil.¹²⁰

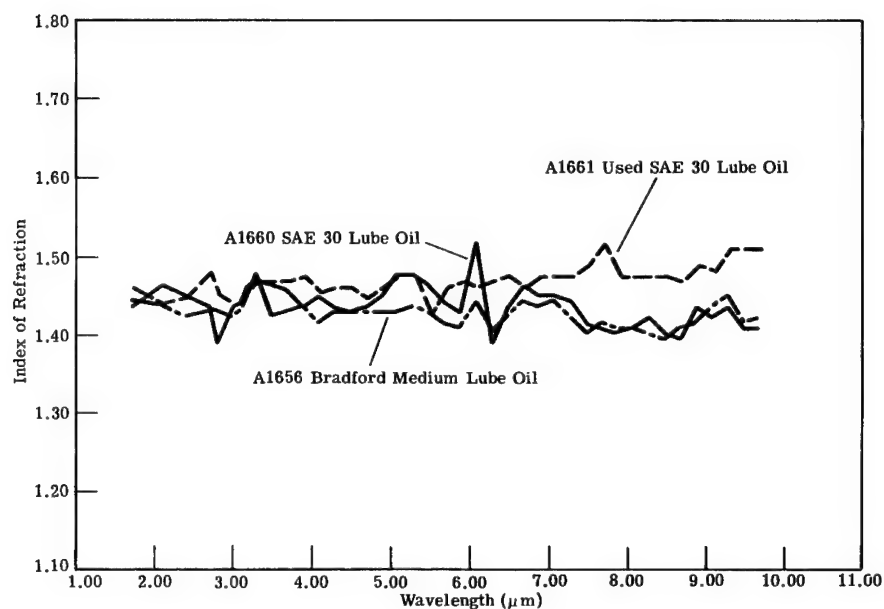


Fig. 3.138 The index of refraction of A1661 used SAE 30 lube oil, A1660 SAE 30 lube oil, and A1656 Bradford medium lube oil.¹²⁰

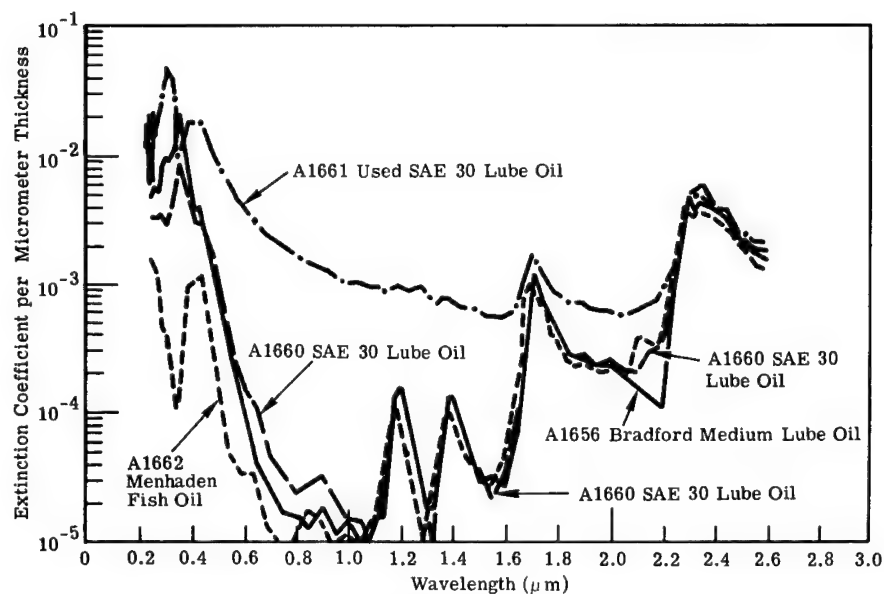


Fig. 3.139 The spectral extinction coefficients of A1661 used SAE 30 lube oil, A1660 SAE 30 lube oil, A1656 Bradford medium lube oil, and A1662 Menhaden fish oil.¹²⁰

emittance values of Table 3.32 represent the maximum emittance possible for the various oils (assuming a smooth surface). These values will tend to decrease for thin slicks and for angles away from the normal since the specular reflectance will tend to increase under these conditions.

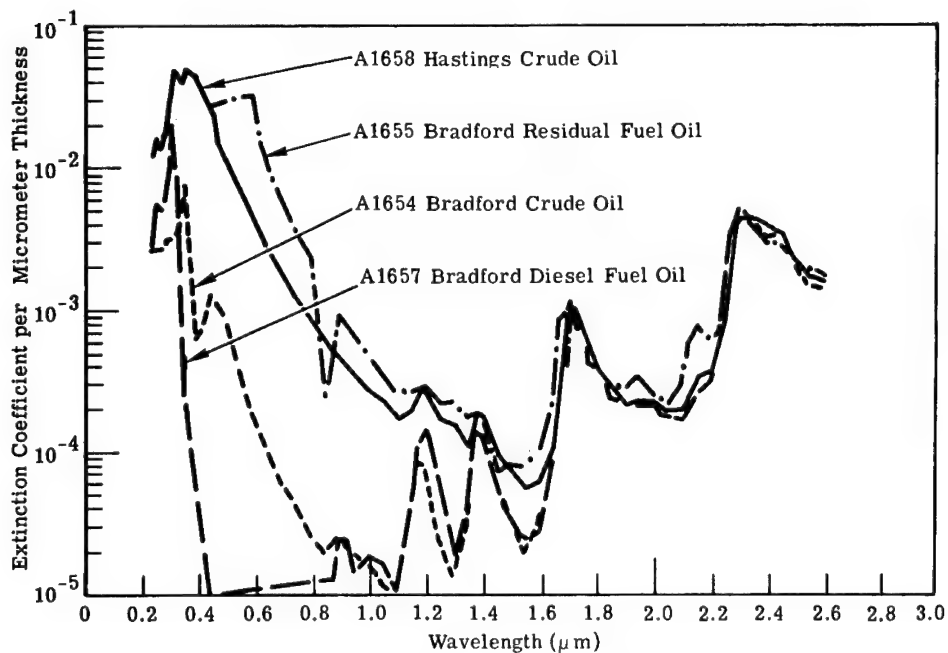


Fig. 3.140 The spectral extinction coefficients of A1658 Hastings crude oil, A1655 Bradford residual fuel oil, A1654 Bradford crude oil, and A1657 Bradford diesel fuel oil.¹²⁰

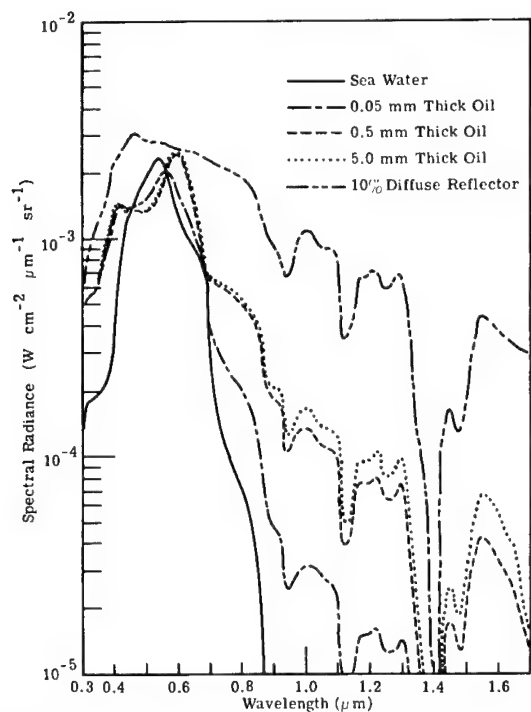


Fig. 3.141 The calculated spectral radiance of used SAE 30 lube oil on seawater under solar illumination viewed at the nonspecular angle.¹²⁰

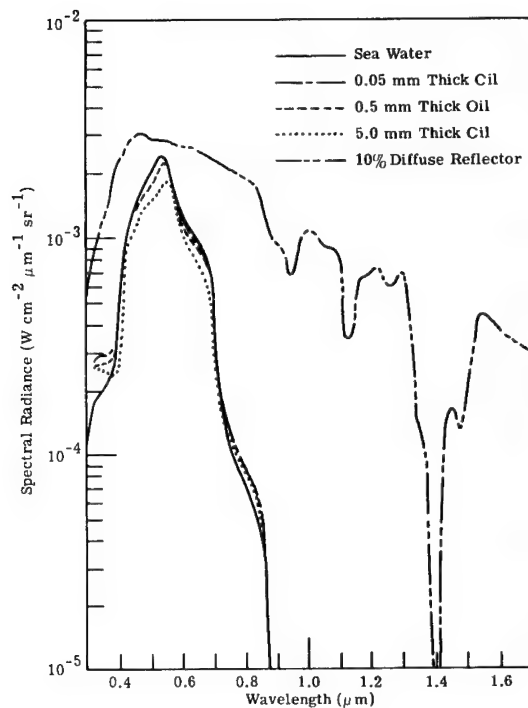


Fig. 3.142 The calculated spectral radiance of Bradford diesel oil on seawater under solar illumination viewed at the nonspecular angle.¹²⁰

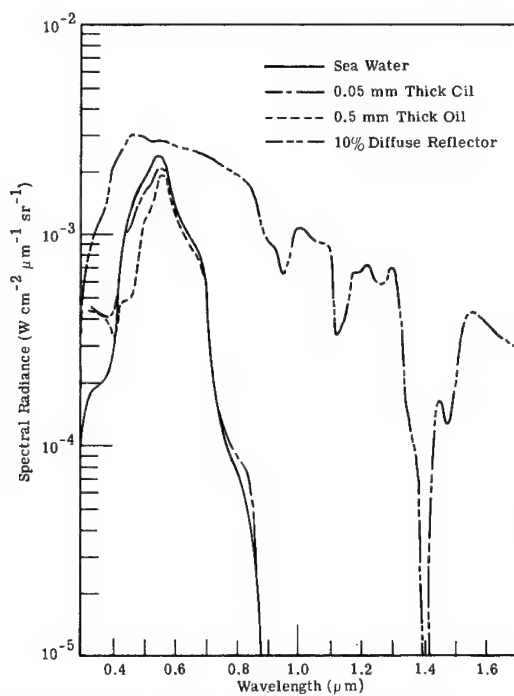


Fig. 3.143 The calculated spectral radiance of Menhaden oil on seawater under solar illumination viewed at the nonspecular angle.¹²⁰

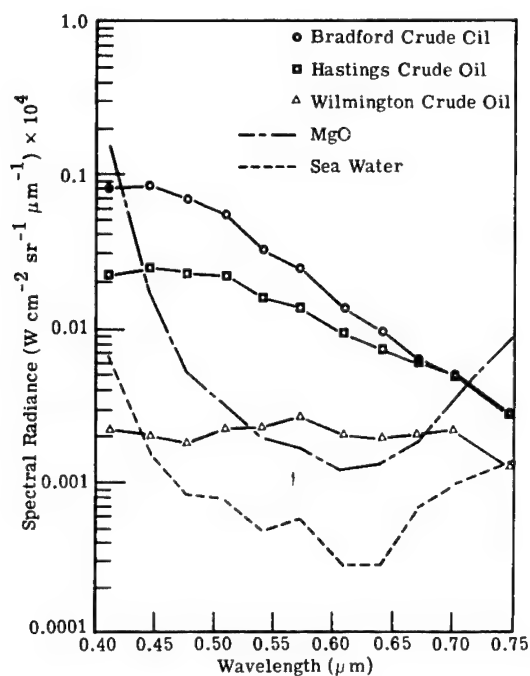


Fig. 3.144 The measured spectral radiance of Bradford crude oil, Hastings crude oil, and Wilmington crude oil under ultraviolet lamp excitation.¹²⁰

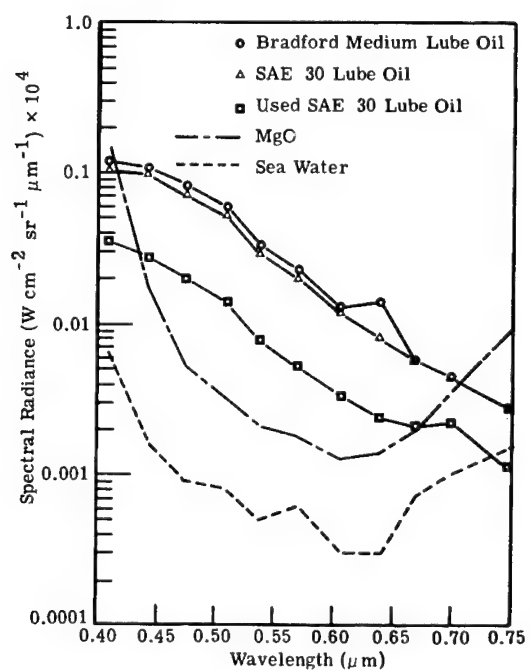


Fig. 3.145 The measured spectral radiance of Bradford medium lube oil, SAE 30 lube oil, and used SAE 30 lube oil under ultraviolet lamp excitation.¹²⁰

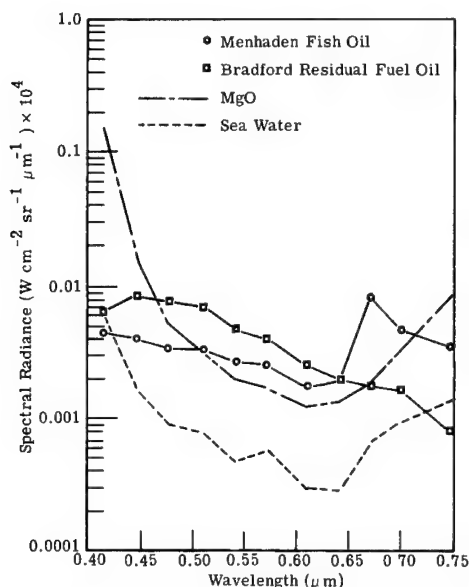


Fig. 3.146 The measured spectral radiance of Menhaden fish oil and Bradford residual fuel oil under ultraviolet lamp excitation.¹²⁰

Table 3.32 Normal Emittance of Oil and Water for Atmospheric Window Regions (from Ref. 121)

Material	3 to 4 μm	4.5 to 5.5 μm	8 to 14 μm
100-Octane Fuel	0.98	0.979	0.973
Kerosine	0.968	0.968	0.968
Diesel Oil	0.968	0.969	0.972
SAE-30 Oil	0.965	0.965	0.970
8.6° API Residual Fuel Oil	0.958	0.958	0.964
44.7° API Crude Oil	0.973	0.972	0.973
31.3° API Crude Oil	0.969	0.970	0.967
19.5° API Crude Oil	0.969	0.970	0.972
Fish Oil	0.969	0.961	0.959
Sea Water	0.972	0.980	0.985

3.8.4 Snow and Ice

The generic term given to the solid state of water is ice. However, the term *ice* is also used to specify solid forms of water that are created in a variety of natural ways on the surfaces of water bodies with different inclusions and states of compaction. The ice formed by precipitation is called snow. The radiative properties of both natural ice and snow depend on the properties of generic ice, the solid state of water.

Properties of Generic Ice. A key paper on the properties of ice is that by Warren.¹²² Warren not only summarizes the multitude of previous papers on

ice but also presents important numerical tables from which the absorption coefficient for ice may be derived for wavelengths from the microwaves to the ultraviolet. The inverse of the absorption coefficient is the effective depth of penetration of radiation into the ice and is also the effective depth at which radiation is emitted.

In the thermal infrared range, the depth of penetration is less than 0.1 mm with the real part of the index of refraction near 1.3. In the near-IR range, 1 to 5 μm , absorption band details become evident with the depth of penetration varying between 0.1 mm to 50 cm. In the visible range, the depth of penetration increases markedly to a maximum of 24 m at 460 nm. In the ultraviolet range, the depth of penetration decreases to 4.3 m at 300 nm but still exceeds that for pure water.

The reflectance and emission for naturally formed snows and ices depend on these generic properties as well as the state of division and the possible presence of free water. Reflection of radiation can be expected at every ice/air interface by surface reflectance. The penetrating radiation is spectrally selectively absorbed in the bulk ice. Bulk reflectance will be zero unless optical inhomogeneities or a reflecting substrate exist below the surface to produce scattering and reversal of direction of propagation before radiation is absorbed completely.

Properties of Snow. Snow forms as a precipitate from clouds that may often be at high altitude. The flakes take many different forms depending on the temperature and moisture content of the air through which the original precipitate falls. Hallett¹²³ describes a number of common forms of snowflakes. The principal form is a small hexagonal rod or plate, which may reach the ground in this simple form or may grow dendritically with large numbers of hexagonal rods joined together in hexagonal symmetry. These rods are usually about 0.1 mm thick even in large flakes. A layer of dendritic snowflakes contains much more air than ice.

The penetration of a beam of radiation through a snowfall decreases with decreasing wavelength until the wavelength becomes less than the dimensions of the flakes. Penetration then remains fairly constant into the visible range. The extinction rate for a snowfall of 1 mm/h (water equivalent) or about 1 cm/h of snow cover is about 3 dB/km as shown by Kulpa and Brown¹²⁴ in the spectral range from 1 mm to the visible.

Snow cover on terrain changes with time under several influences. Flakes near the surface can be broken into smaller fragments by the wind. Snow below the surface can recrystallize by melting and refreezing or by the pressure of the overlying snow. The snow becomes more dense with age, resulting in larger crystals and less air space. The ultimate limit of compacted snow is glacial ice.

In the infrared thermal range, the depth of penetration is so small that the first top crystals of snow cannot be penetrated. The snow will appear nearly black by reflection, and thermal emission will occur from this same layer and at the temperature of this layer. A reflectance and emission model for snow has been developed by Dozier and Warren.¹²⁵ Their calculations predict very small variations in emissivity due to crystal size and view angle. They calculate an emissivity of close to 0.98 for various grain sizes and view angles.

The reflectances of terrestrial snow cover by O'Brien et al.¹²⁶ are shown in Figs. 3.147 to 3.158. The absorption bands of ice at 1.5 and 2.0 μm are clearly defined. One may observe that the increased depth of penetration between these absorption bands results in an increase in bulk reflectance from crystals below the surface. The snow crystals of aging snow should be larger and more compact with fewer scattering surfaces. Thus, bulk reflectance of aging snow should be less than for new fallen snow.

Although snow crystals may be coated with free water even well below 0°C , the absorption bands of free water are so close to those for ice that the effects of free water absorption are combined with the absorption of ice and cannot be observed as a separate feature.

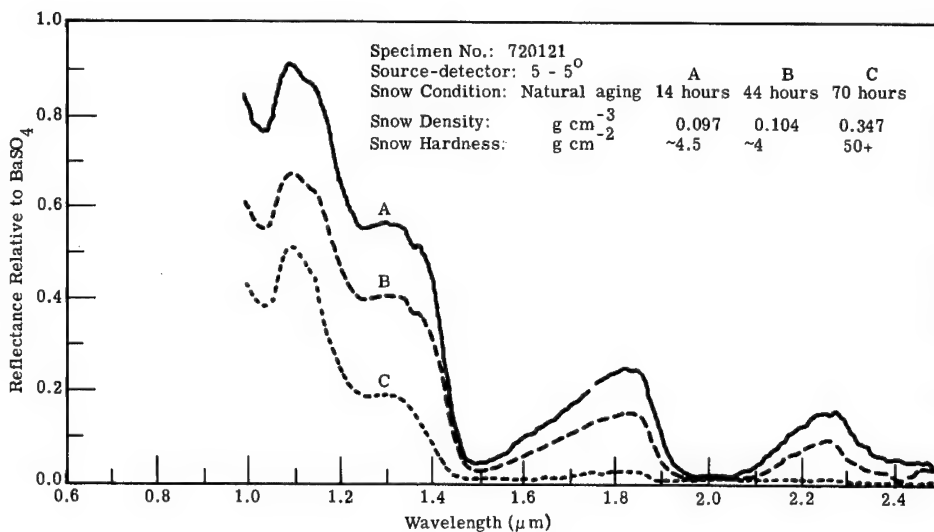


Fig. 3.147 Changes in snow reflectance with natural aging ($5-5^\circ$ source-detector).¹²⁶

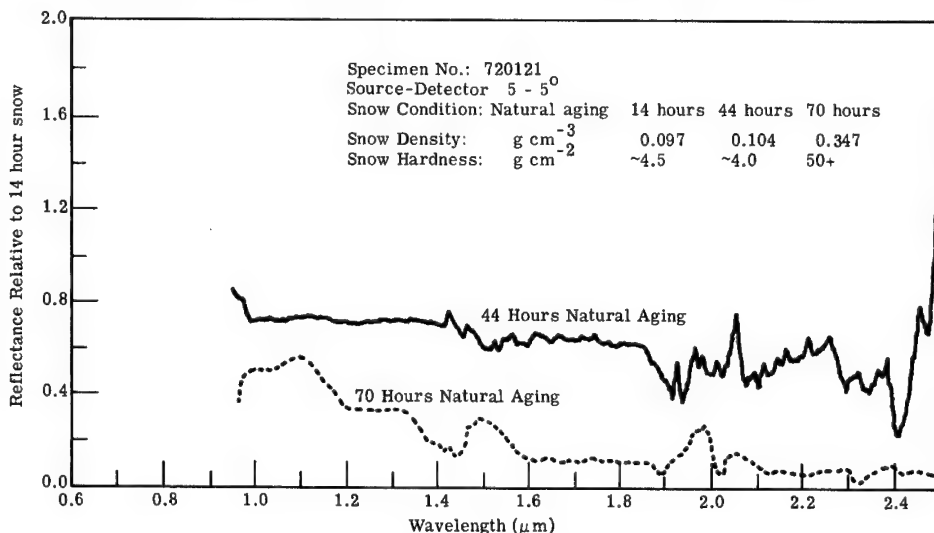


Fig. 3.148 Reflectance of aging snow relative to fresher (14-h) snow ($5-5^\circ$ source-detector).¹²⁶

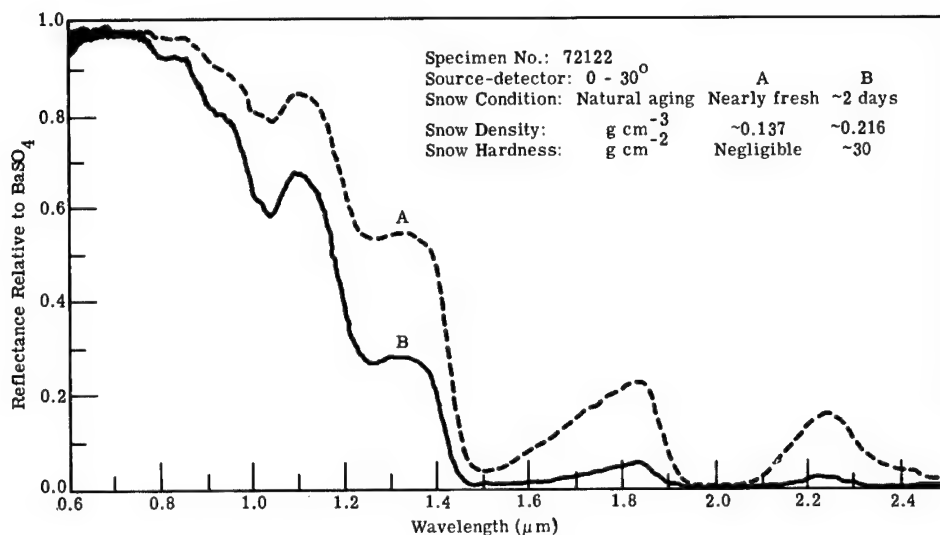


Fig. 3.149 Changes in snow reflectance with natural aging (0-30° source-detector).¹²⁶

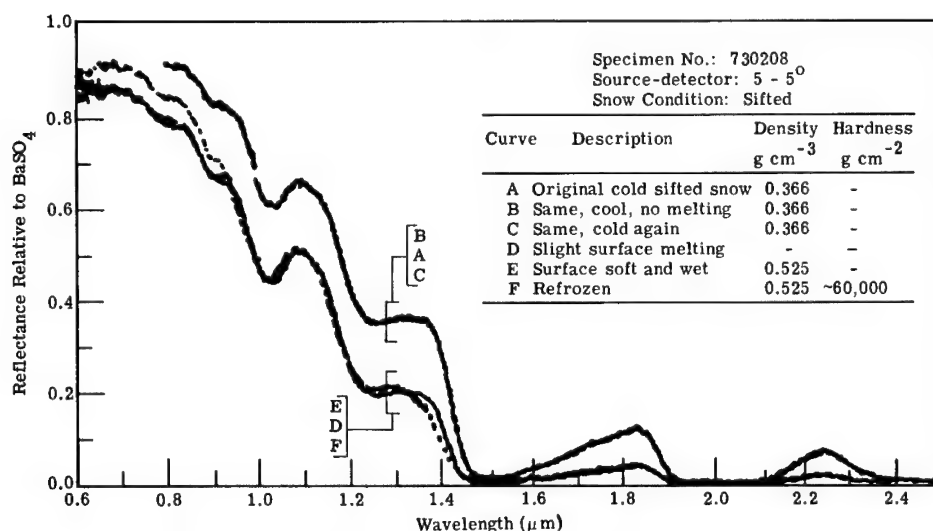


Fig. 3.150 Effects of temperature conditions on sifted snow reflectance (5-5° source-detector).¹²⁶

Properties of Natural Ice. Ice forms as a solid layer on the surface of free water. As ice forms slowly from the melt, the crystallization tends to exclude impurities and foreign matter. The spectral reflectances of some freshwater ice formations were acquired by Bolsenga.¹²⁷

New Ice or Clear Ice. New ice or clear ice formed on freshwater ponds and lakes will tend to be smooth, homogeneous generic ice with a specularly reflecting surface. An ice thickness of 0.1 mm will be opaque to thermal infrared radiation. Bulk reflectance of new ice will be near zero at all wavelengths. The

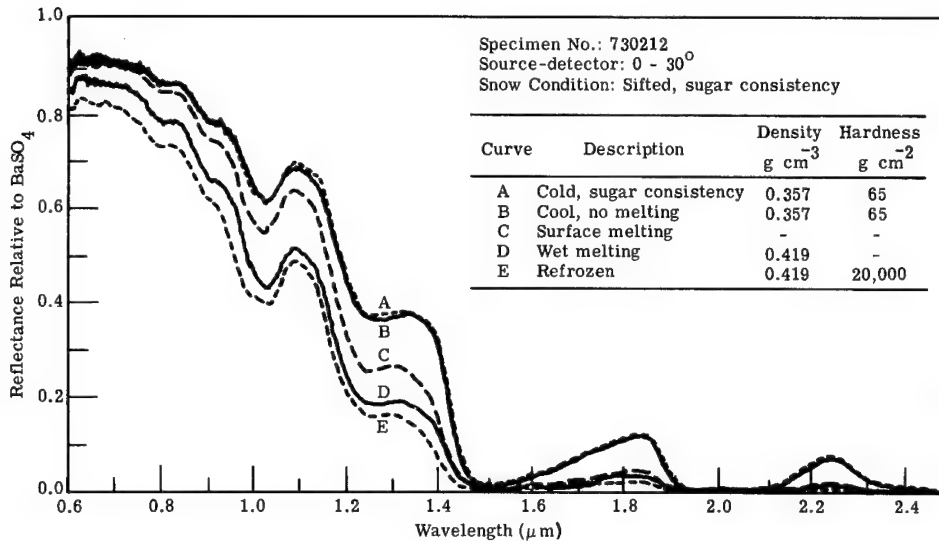


Fig. 3.151 Effects of temperature conditions on sifted snow reflectance (0-30° source-detector).¹²⁶

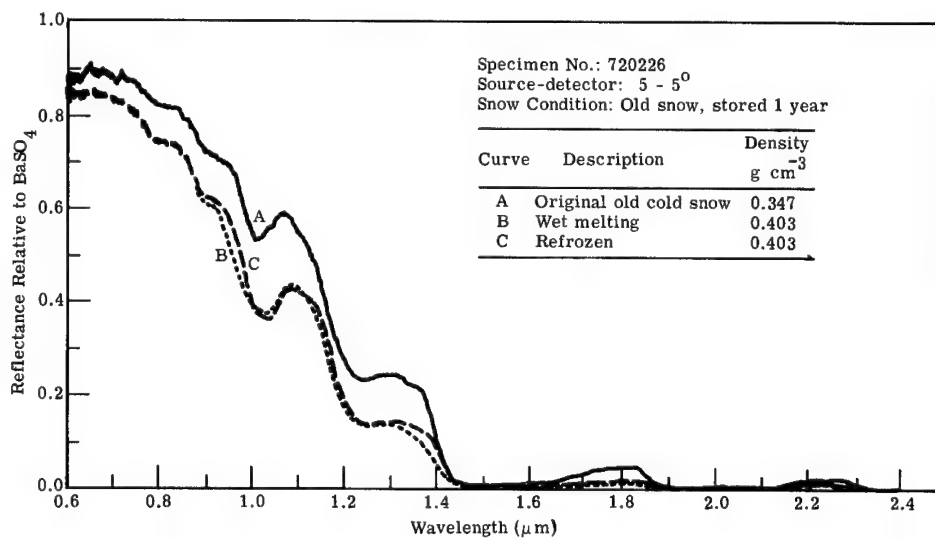


Fig. 3.152 Effects of temperature conditions on old snow reflectance (5-5° source-detector).¹²⁶

spectral reflectance of two samples are shown in Fig. 3.159. New ice does not stay new for long. A common alteration is to be coated by a top layer of snow. A number of secondary ice formations that occur in the Great Lakes are described by Bolsenga.¹²⁷ These are composites of ice, air, and water.

Some other types of ice are:

1. *Snow ice* is milky white in appearance due to the inclusion of air bubbles. It is formed after a snow cover load causes the ice layer to sink below water level. Free water enters the snow cover through ice layer fissures and refreezes in the snow as frozen slush.

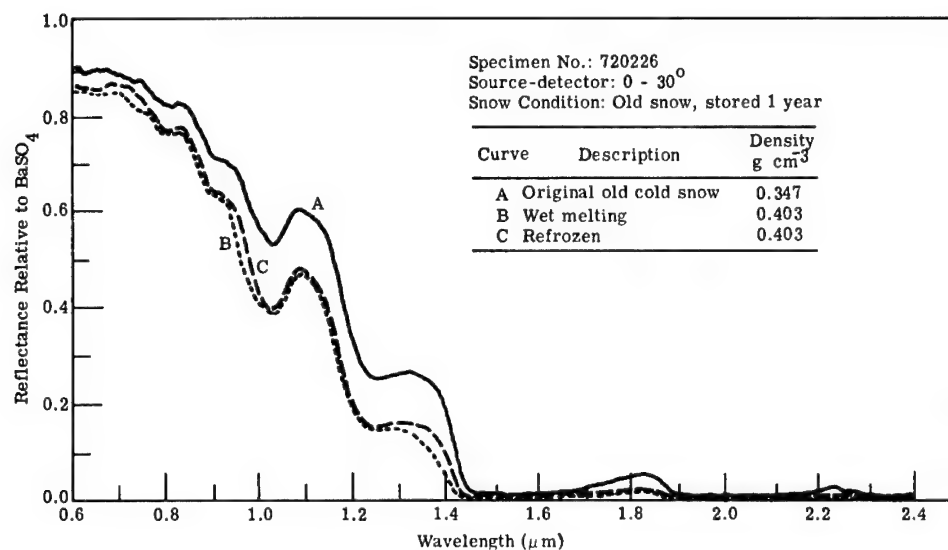


Fig. 3.153 Effects of temperature conditions on old snow reflectance (0–30° source-detector).¹²⁶

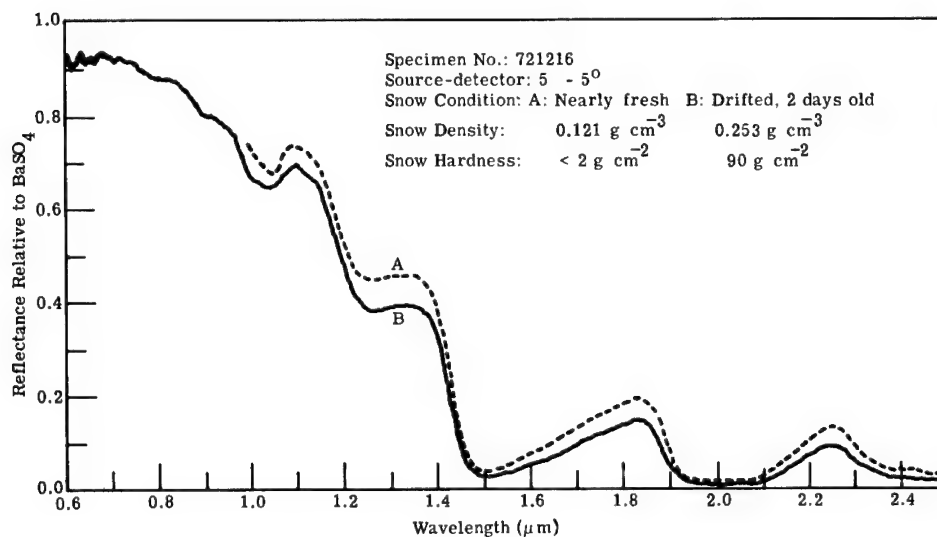


Fig. 3.154 Effect of snow drifting on snow reflectance.¹²⁶

2. *Refrozen-slush ice* has the same appearance as snow ice but is formed by rain on the snow cover. The snow is converted into slush by the rain and refreezes. The spectral reflectance of a sample is shown in Fig. 3.160.
3. *Slush curd ice* is a slush ice that has been reformed by wave action (see Fig. 3.161).
4. *Brash ice* is a refrozen mass of irregular ice fragments that have been broken and pushed together by water turbulence and wind. New ice and slush ice form the binder (see Figs. 3.162 and 3.163).

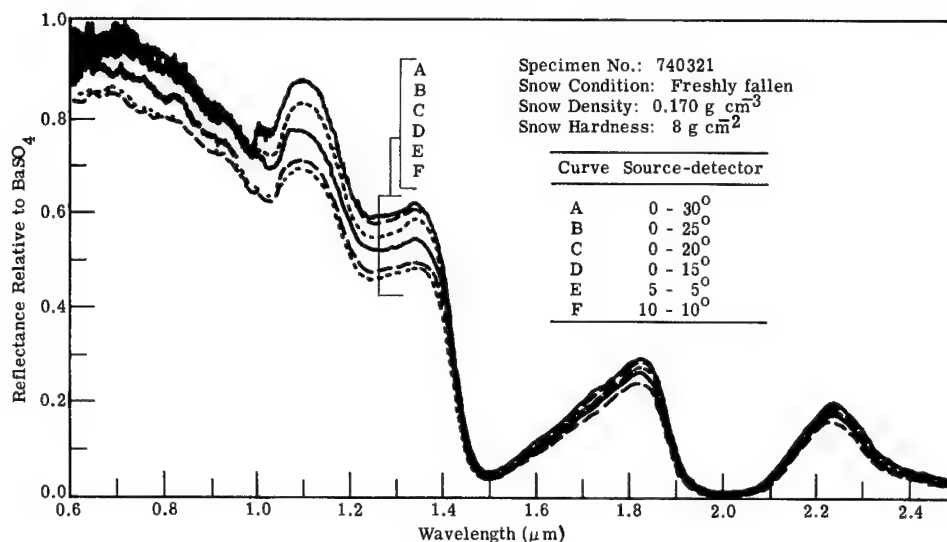


Fig. 3.155 Comparison of relative reflectance of freshly fallen snow at various source-detector angles.¹²⁶

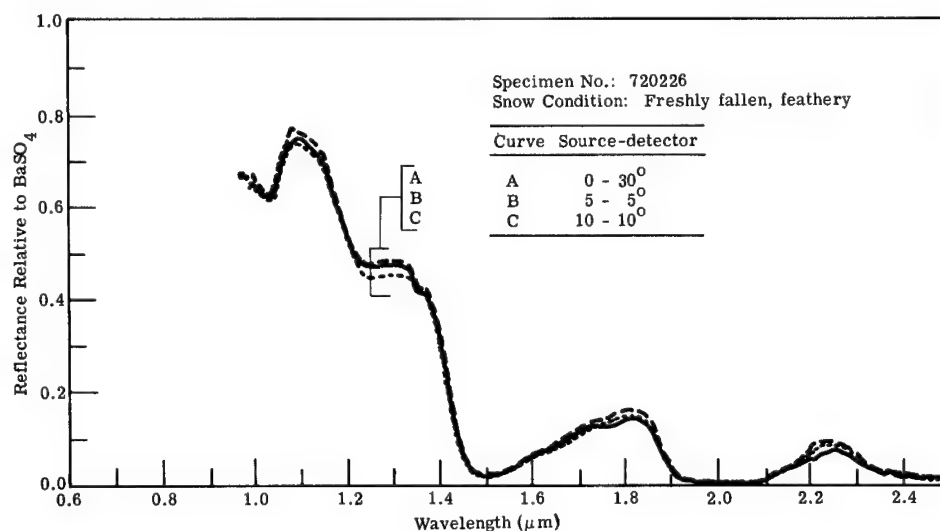


Fig. 3.156 Comparison of relative reflectance of freshly fallen, feathery snow at various source-detector angles.¹²⁶

5. *Pancake ice* is a refrozen mass of ice fragments that have been first broken and chipped by neighboring fragments by wave action creating nearly circular discs 0.5 to 2 m in diameter with raised rims. The binder is new ice and slush ice (see Fig. 3.164).

3.8.5 Biological Materials

Botanical Materials. The major spectrally significant constituents of terrestrial botanical materials are water, cellulose, and chlorophyll. For this reason, botanical materials appear very similar both by reflected solar radiation and by thermal emission.

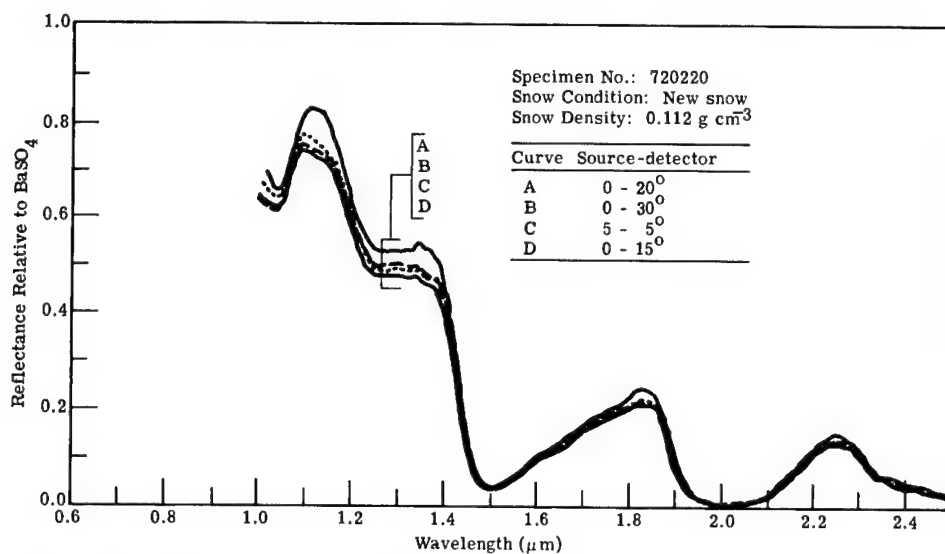


Fig. 3.157 Comparison of relative reflectance of new snow at various source-detector angles.¹²⁶

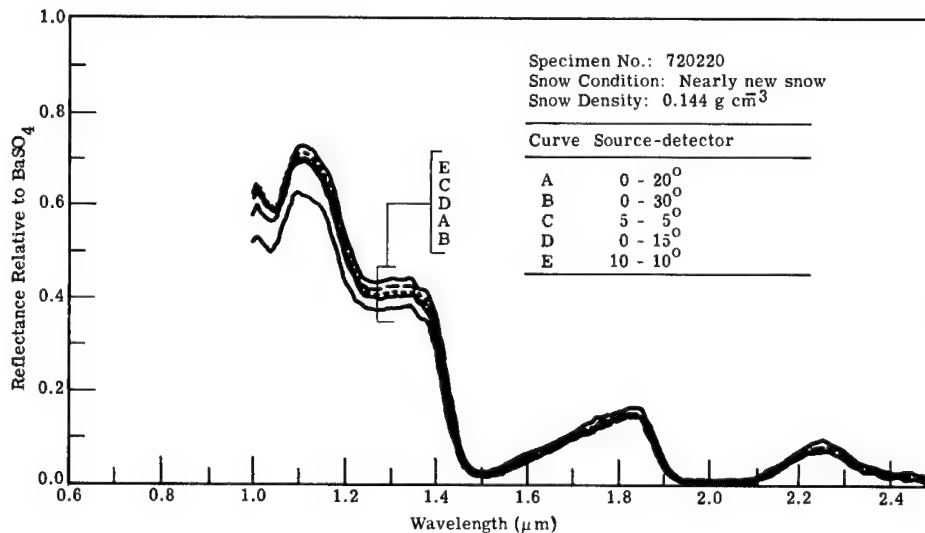


Fig. 3.158 Comparison of relative reflectance of nearly new snow at various source-detector angles.¹²⁶

According to Nobel,¹²⁸ carotenoids and phycobilins also occur commonly in botanical materials as accessory pigments. Carotenoids are found in essentially all green plants but are largely masked by the predominant spectral absorptance properties of chlorophyll. Carotenoids absorb strongly in the 0.425- to 0.490- μ m spectral band and, to a somewhat lesser extent, in the 0.49- to 0.56- μ m band; they are primarily responsible for the yellow and orange fall colors of trees. Phycobilins generally have their major absorption bands in the 0.5- to 0.65- μ m band with a minor band in the ultraviolet. One of the two

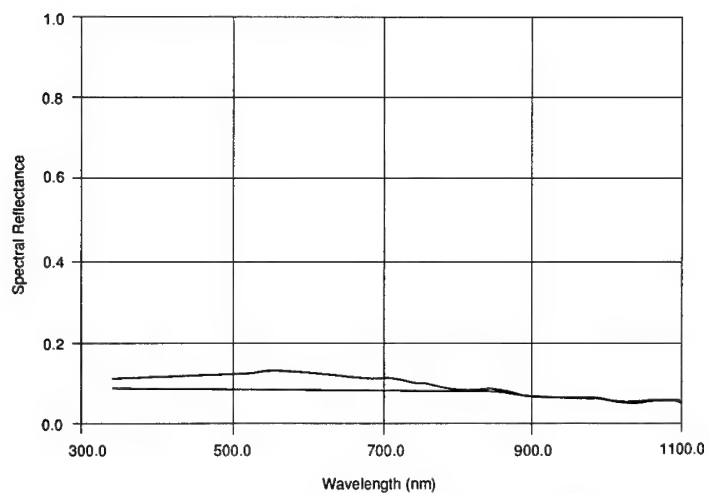


Fig. 3.159 Spectral reflectances of North Lake clear ice (upper trace) compared to Straits of Mackinac clear ice.

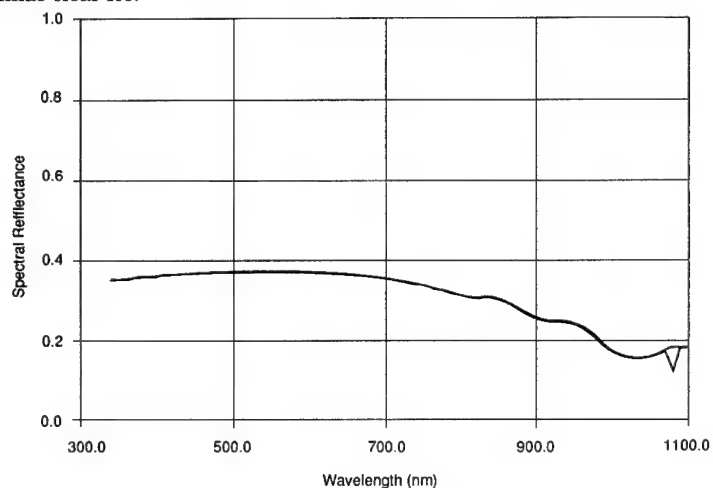


Fig. 3.160 Spectral reflectances of refrozen slush ice on North Lake (two runs).

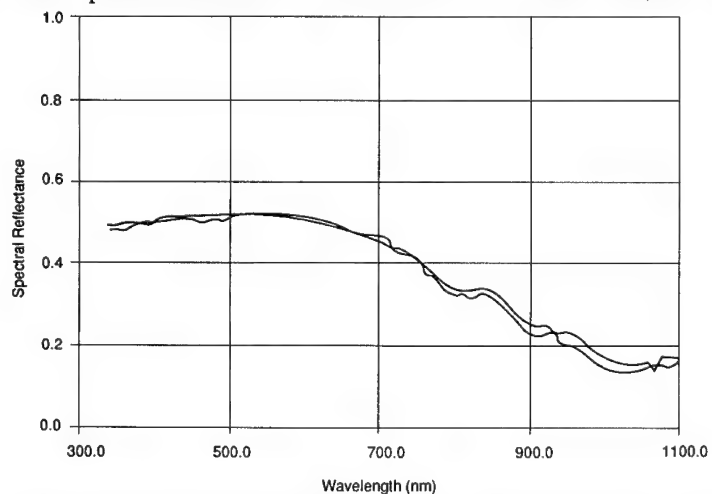


Fig. 3.161 Spectral reflectances of slush curd ice. Lower values are from a run under totally diffuse radiation, while higher values are from a run where the solar beam was slightly visible.

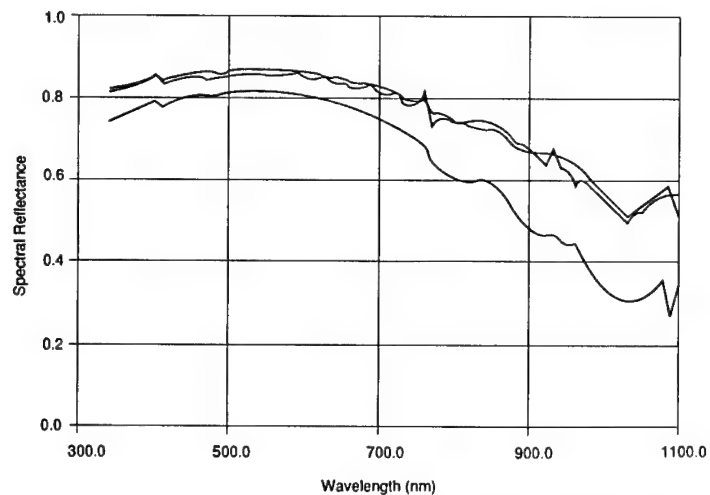


Fig. 3.162 Spectral reflectances of brash ice with upthrust blocks (upper traces) and the same ice surface with appreciable snow removed.

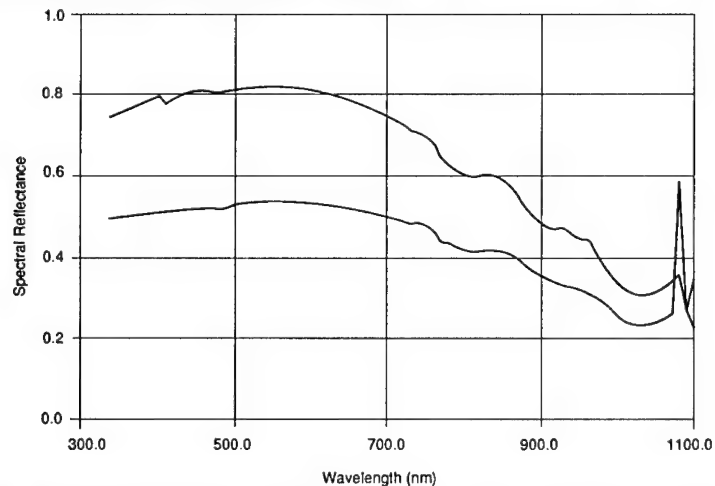


Fig. 3.163 Spectral reflectances of the two dissimilar brash ice types (upthrust—upper trace; flat—lower trace).

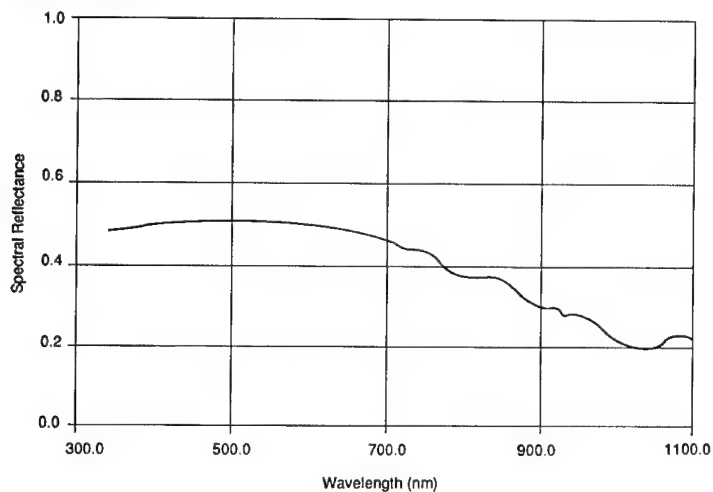


Fig. 3.164 Spectral reflectances of pancake ice at the Straits of Mackinac.

main phycobilins, phycoerythrin, has an absorption band between 0.53 and 0.57 μm , so that the visual appearance of phycoerythrin alone would be magenta. The other phycobilin, phycocyanin, has an absorption band maximum between 0.61 and 0.66 μm and should visually appear cyan.

There are several kinds of chlorophyll, all of which absorb in the UV, but more strongly in the 0.4- to 0.45- μm band and in the 0.64- to 0.69- μm band. One type of chlorophyll has an absorption maximum near 0.67 μm , while another has a maximum near 0.68 μm . The absorption of both decreases sharply at 0.70 μm , producing the characteristic sharp rise to high values of spectral reflectance of green botanical materials in the 0.72- to 1.3- μm range. The spectral absorptance falls to low values of 5 to 15% in the near infrared range for many types of green leaves. Multiple scattering becomes a major contributor to canopy reflectance. Thick leaves tend to exhibit high reflectance and low transmittance, while thin leaves exhibit low reflectance and high transmittance.

The high spectral absorption coefficient of the water within healthy tissue produces deep reflectance and transmittance minima near 1.4 and 2.0 μm . Since healthy tissue containing active chlorophyll must also contain some water to permit photosynthesis, the concurrent appearance of a chlorophyll absorption band near 0.68 μm and the water absorption bands near 1.4 and 2.0 μm is generally expected. Frequently, the change of leaf spectra resulting from plant stress is first made manifest by disruption of the photosynthetic process. The disruption is caused by the destruction of chlorophyll before water has been completely lost by the leaf. Consequently, the water absorption bands may still be present in leaf spectra after the leaf is dead.

Figure 3.165 shows the spectral reflectances of particular samples of various vegetative canopies. The reflectances include the spectral properties of the understory or soil, the percentage of cover, the effects of shadow cast by opaque stems and woody parts, the effects of leaf orientation, and sun and view angles. Changes in any of these will produce a change in canopy bidirectional reflectance so that one cannot expect these simple spectral reflectances to be entirely characteristic of the canopy type.

Table 3.33 lists the descriptions of plant leaf materials that produce the reflectance and transmittance spectra listed in Tables 3.34 and 3.35. Table 3.36 lists the descriptions of plant leaf materials that produce the spectral reflectances listed in Table 3.37 and the transmittances in Table 3.38.

The dependence of leaf spectral reflectance on seasons of the year is shown for seven tree species in Fig. 3.166. The change in the spectral reflectance from the upper surface of a single immature leaf developing on a watered yellow poplar seedling as a function of time is shown in Fig. 3.167. Changes in leaf spectra as a result of moisture stress are shown in Fig. 3.168.

In the thermal infrared range, the emissivity of leaf materials is normally large due to the cellulose and water content. Considerable complexity is added to the prediction of canopy radiance because the canopy is not passive. Large amounts of water are evaporated through the leaf stomates during the day. Leaf temperature is reduced below the temperature of a passive leaf. In addition, some heat energy is generated by the respiration of the plant.

At night, the stomates are closed in all but certain arid land species. Leaf temperatures tend to follow closely to air temperature. On clear nights the air temperature near the ground level is frequently less than the temperature

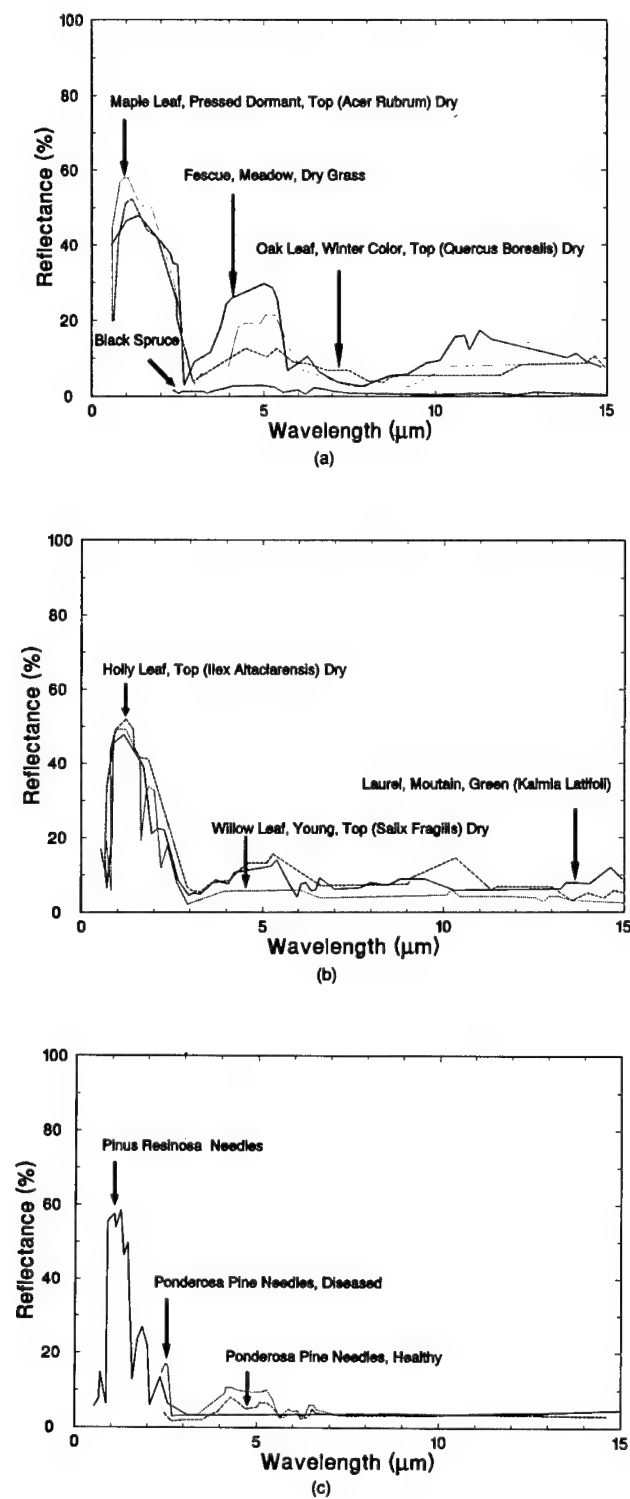


Fig. 3.165 Spectral reflectance of botanical materials.^{104,105,132}

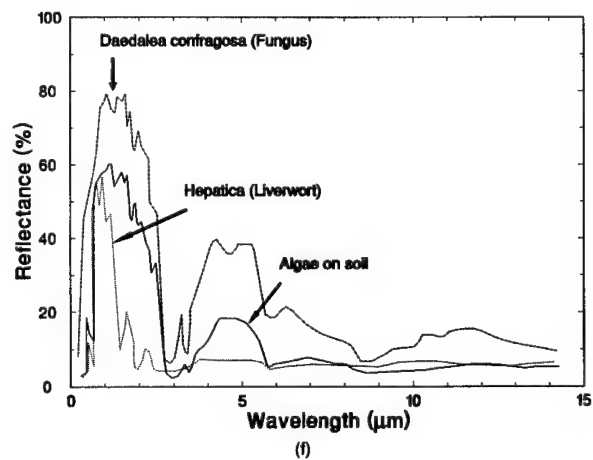
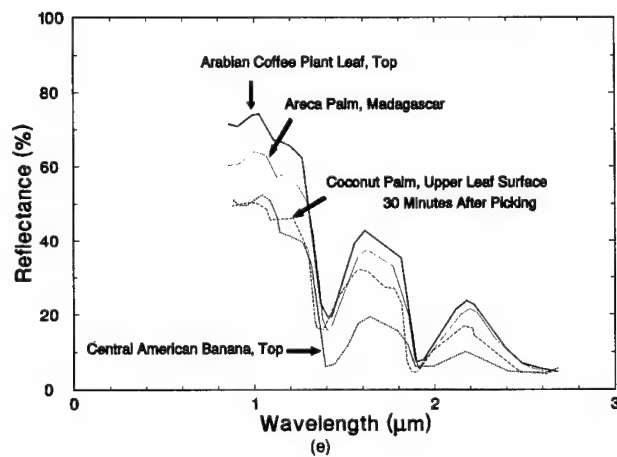
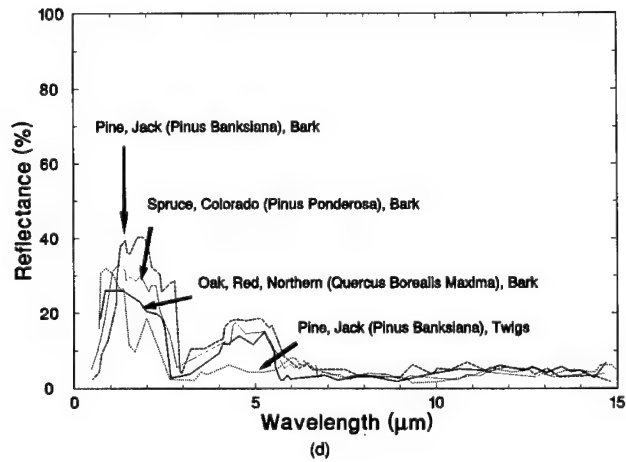


Fig. 3.165 (continued)

Table 3.33 Leaf Mesophyll Arrangement and Other Structural Characteristics of Plant Leaves Used in This Study (Common names are used in the text.) (from Ref. 129)

Common Name	Latin Name*	Mesophyll Arrangement	Additional Structural Characteristics
Corn	<i>Zea mays</i> L.	Compact	Bulliform cells on adaxial surface.
Banana	<i>Musa acuminata</i> Colla (<i>M. cavendishii</i> Lamb.)	Dorsiventral	Adaxial and abaxial hypodermal layers, palisade layer.
Begonia	<i>Begonia cucullata</i> Willd. (<i>B. sem-pertlorens</i> Link & Otto)	Succulent, central chlorenchyma	Malacophyllous-type xerophytic leaf; large thin-walled storage cells on each side of central chlorenchyma
Eucalyptus	<i>Eucalyptus camaldulensis</i> Dehnh. (<i>E. restrata</i> Schlecht.)	Isolateral	Thick adaxial cuticle; no spongy parenchyma cells.
Rose	<i>Rosa</i> var. unknown	Dorsiventral	Multiple palisade layers.
Hyacinth	<i>Eichhornia crassipes</i> (Mart.) Solms	Dorsiventral	Multiple palisade layers; large air chambers characteristic of hydrophytes.
Sedum	<i>Sedum spectabile</i> Boreau	Succulent	Well-differentiated cellular structure.
Ficus	<i>Ficus elastica</i> Roxb. ex Hornem.	Dorsiventral	Thick adaxial cuticle; multiseriate adaxial epidermis; and multiple palisade layer.
Oleander	<i>Nerium oleander</i> L.	Dorsiventral	Thick adaxial cuticle; multiseriate epidermis; multiple palisade layer abaxial grooves.
Ligustrum	<i>Ligustrum lucidum</i> Ait.	Dorsiventral	Thick adaxial cuticle; multiple palisade layer.
Crinum	<i>Crinum fimbriatum</i> Baker	Dorsiventral	Poorly differentiated and lobed palisade parenchyma cells; large central air spaces.

*Names are those used by New Crops Research Branch (Dr. Edward E. Terrell), ARS, USDA, Beltsville, Maryland 20705.

Table 3.34 Percent Diffuse Reflectance of Top (T) and Bottom (B) Leaf Surfaces of 11 Plant Genera at Seven Wavelengths (from Ref. 129)

Plant Genera	550 nm		800 nm		1000 nm		1450 nm		1650 nm		1950 nm		2200 nm	
	T	B	T	B	T	B	T	B	T	B	T	B	T	B
Ficus	8.1	19.2	54.2	54.1	52.4	53.1	7.8	17.2	27.0	34.4	3.7	7.2	10.2	20.6
Ligustrum	10.2	26.9	55.5	53.8	54.1	53.4	9.0	20.8	27.7	37.7	4.1	8.7	11.1	24.2
Rose	10.4	20.5	48.8	43.2	48.4	42.6	23.2	24.6	38.0	34.6	9.4	13.8	25.1	25.8
Banana	10.5	16.9	44.0	41.3	43.3	40.7	12.0	15.9	29.0	29.4	5.1	8.2	16.0	19.0
Oleander	10.7	18.1	54.3	53.0	54.0	52.9	13.0	20.1	32.8	37.1	5.5	9.1	16.1	23.4
Hyacinth	12.1	19.0	49.8	49.4	49.6	49.1	11.7	18.4	31.0	34.8	4.8	8.2	15.3	21.9
Eucalyptus	12.6	15.8	45.9	46.0	45.4	45.6	16.0	18.2	29.7	31.0	7.0	8.3	15.6	17.6
Begonia	12.9	20.1	45.3	39.9	43.4	38.2	6.2	9.5	21.6	21.6	3.8	4.4	8.4	11.1
Corn	15.4	15.6	42.6	43.9	42.4	43.2	17.2	19.1	31.6	32.8	7.2	8.5	19.6	21.1
Crinum	15.6	23.1	55.8	54.6	54.1	53.2	10.0	14.8	29.3	33.4	5.2	6.8	13.6	19.4
Sedum	20.1	27.1	54.2	52.2	50.9	50.0	5.2	10.1	18.4	26.1	3.2	4.2	6.2	12.8

Table 3.35 Percent Transmittance of Top (T) and Bottom (B) Leaf Surface of 11 Plant Genera at Seven Wavelengths (from Ref. 129)

Plant Genera	550 nm		800 nm		1000 nm		1450 nm		1650 nm		1950 nm		2200 nm	
	T	B	T	B	T	B	T	B	T	B	T	B	T	B
Ficus	1.2	1.5	40.1	41.5	39.8	41.2	2.8	2.8	20.6	21.2	0.5	0.5	6.6	6.9
Ligustrum	3.9	3.9	38.1	40.1	38.4	40.0	4.2	4.4	21.4	22.0	0.5	0.5	8.2	8.4
Rose	9.3	11.2	48.6	54.1	49.5	55.2	27.1	31.1	44.1	49.3	10.9	13.0	33.8	38.1
Banana	12.2	13.2	52.1	54.8	52.5	55.4	17.1	18.5	41.4	43.8	2.6	2.9	26.9	28.6
Oleander	1.6	1.8	34.1	35.8	35.0	36.8	4.4	4.7	20.9	21.8	0.5	0.5	8.4	8.8
Hyacinth	8.5	8.8	45.2	47.0	45.9	47.6	9.1	10.2	31.6	33.6	0.7	0.9	16.6	18.4
Eucalyptus	7.5	7.3	48.3	48.3	49.8	49.8	17.9	18.2	36.2	34.2	3.8	3.8	22.4	22.3
Begonia	15.5	21.0	51.7	56.6	51.4	56.3	6.4	7.6	31.6	36.9	0.5	0.5	13.9	16.4
Corn	12.9	12.6	53.1	52.6	54.3	54.0	26.2	25.8	48.1	47.7	8.3	8.2	36.5	35.9
Crinum	6.1	6.6	38.1	39.4	37.7	38.8	1.9	2.1	18.5	19.2	0.5	0.5	6.2	6.4
Sedum	10.2	10.9	42.6	44.2	40.3	42.1	0.5	0.6	14.7	15.6	0.5	0.5	3.0	3.3

several meters above the ground, so that the radiance of low-lying grass canopies may be less than the radiance of tree tops.

Reflectance measurements of plant materials in the 2.5- to 20- μm range are difficult to acquire. Elvidge¹³³ has made a series of such measurements using Fourier transform spectroscopy. He has included spectra of woody parts as well as leaves in his data. Some of his data are shown in Fig. 3.169.

3.9 STATISTICAL MEASURES OF INFRARED BACKGROUNDS

3.9.1 Probabilistic Description

A simple probabilistic model for background variation in the IR was first proposed by Carmichael.¹³⁴ An expanded and experimentally verified model was later proposed by Itakura et al.¹³⁵ The model suggests that IR backgrounds in the thermal region of 5 to 14 μm can be considered as a random set of two-dimensional pulses whose amplitudes and widths obey the Gaussian and Poisson distribution rules, respectively. In the reflective IR region of 0.2 to 5 μm , the background can be considered as a random set of two-dimensional pulses whose amplitudes and widths both obey Poisson statistics. Considering the thermal IR region, the statistics are as follows:

$$p(L_B) = \frac{1}{(2\pi\sigma_{L_B}^2)^{1/2}} \exp\left[-\frac{(L_B - E\{L_B\})^2}{2\sigma_{L_B}^2}\right], \quad (3.66)$$

$$p(r) = \frac{1}{\beta} \exp\left(-\frac{r}{\beta}\right), \quad (3.67)$$

where

L_B = radiance of a certain point on the x - y plane; a random variable
 $E\{L_B\}$ = mean value of L_B

Table 3.36 Common, Scientific, and Family Names; Leaf Mesophyll Arrangements; and Structural Characteristics of Plant Leaves Used in This Study (Common names are used in the text.) (from Ref. 130)

Common Name	Scientific Name*	Family Name	Mesophyll Arrangement**	Additional Structural Characteristics
Avocado	<i>Persea americana</i> Mill.	Lauraceae	Dorsiventral	Thick cuticle, multiple palisade layers, long and narrow palisade cells.
Bean	<i>Phaseolus vulgaris</i> L.	Leguminosae	Dorsiventral	Very porous mesophyll
Cantaloupe	<i>Cucumis melo</i> L. var. <i>cantalupensis</i> Naud.	Cucurbitaceae	Dorsiventral	Multiple palisade layers, hairs lower epidermis.
Corn	<i>Zea mays</i> L.	Gramineae	Compact	Bulliform cells, hairs upper epidermis
Cotton	<i>Gossypium hirsutum</i> L.	Malvaceae	Dorsiventral	Glandular hairs, nectaries, lysigenous glands.
Lettuce	<i>Lactuca sativa</i> L.	Compositae	Compact	Large cells, porous mesophyll.
Okra	<i>Hibiscus esculentus</i> L.	Malvaceae	Dorsiventral	Well differentiated, porous mesophyll.
Onion	<i>Allium cepa</i> L.	Amaryllidaceae	Dorsiventral	Tubular leaves.
Orange	<i>Citrus sinensis</i> (L.) Osbeck	Rutaceae	Dorsiventral	Thick cuticle with wax layers, multiple palisade layers, lysigenous cavities.
Peach	<i>Prunus persica</i> (L.) Batsch	Rosaceae	Dorsiventral	Multiple palisade layers, porous mesophyll
Pepper	<i>Capsicum annuum</i> L. and other spp.	Solanaceae	Dorsiventral	Druse crystals
Pigweed	<i>Amaranthus retroflexus</i> L.	Amaranthaceae	Compact	Druse crystals, veins surrounded by large, cubical, parenchymatous cells
Pumpkin	<i>Cucurbita pepo</i> L.	Cucurbitaceae	Dorsiventral	Multiple palisade layers, hairs upper, and lower epidermis
Sorghum	<i>Sorghum bicolor</i> L. Moench	Gramineae	Compact	Bulliform cells
Soybean	<i>Glycine max</i> (L.) Merr.	Leguminosae	Dorsiventral	Porous mesophyll
Sugarcane	<i>Saccharum officinarum</i> L.	Gramineae	Compact	Bulliform cells
Sunflower	<i>Helianthus annuus</i> L.	Compositae	Isolateral	Hairs upper and lower epidermis
Tomato	<i>Lycopersicon esculentum</i> Mill.	Solanaceae	Dorsiventral	Hairs upper and lower epidermis, glandular hairs lower surface
Watermelon	<i>Citrullus lanatus</i> (Thumb.) Mansf.	Cucurbitaceae	Dorsiventral	Multiple palisade layers, glandular hairs lower surface
Wheat	<i>Triticum aestivum</i> L.	Gramineae	Compact	Bulliform cells

*Names are those used by New Crops Research Branch (Dr. Edward E. Terrell), ARS, USDA, Beltsville, Maryland.

**Arbitrary definitions of mesophyll arrangements used herein are: dorsiventral, a usually porous (many intercellular air spaces) mesophyll with palisade parenchyma cells in its upper and spongy parenchyma cells in its lower part; compact mesophyll with intercellular air space and no differentiation into palisade and spongy parenchyma cells; isolateral, tending to have long narrow cells through a porous mesophyll.

- $\sigma_{L_B}^2$ = variance of L_B
 β = average pulse width or scale length or correlation length
 r = interval length whose points are all of the same radiance value; a random variable.

The model is spatially *stationary* in that the statistics do not change with position in the x - y plane. Additionally the model is spatially *isotropic* in that the statistics have no preferred orientation in the x - y plane. Finally, the model assumes that the radiance on an interval is independent of the radiance of another interval.

3.9.2 Correlation Function Representation

Two common two-dimensional correlation functions are the exponential and the Whittle¹³⁶:

$$\text{Exponential: } R(\Delta) = \sigma_B^2 \exp\left(-\frac{\Delta}{\beta}\right), \quad (3.68)$$

$$\text{Whittle: } R(\Delta) = \sigma_B^2 \left(\frac{\pi\Delta}{2\beta}\right) K_1\left(\frac{\pi\Delta}{2\beta}\right), \quad (3.69)$$

where $K_1(\cdot)$ is the modified Bessel function of order 1 and Δ is the interval length between two adjacent points in the x - y plane, which equals $(\Delta_x^2 + \Delta_y^2)^{1/2}$.

The parameter Δ is called the *lag variable* and it represents the distance between any two points on the background. It is not tied to any absolute origin. The parameter β is referred to as the *scale length*. It is defined as the distance where two points on the background become statistically unrelated from each other (that is, background point A does not provide any information as to the value of background point B). A common definition for scale length is

$$\beta = \frac{1}{R(0)} \int_0^{\infty} R(\tau) d\tau. \quad (3.70)$$

Figure 3.170 shows both the Whittle and the exponential correlation function (both one dimensional) plotted for $\beta = 1$ and $\sigma_B^2 = 1$.

The autocorrelation function for a stationary process is defined to be

$$R(\Delta) = E\{L_B(r)L_B(r + \Delta)\}. \quad (3.71)$$

The correlation function resulting from the probabilistic description is easily obtained after computation of the probability that two adjacent points on the x - y plane belong to the same pulse. This is given by

Table 3.37 Average Percent Reflectances of Top Leaf Surfaces of 10 Leaves for Each of 20 Crops for 41 Wavelengths (nm) Over the 500- to 2500-nm Wavelength Interval (from Ref. 130)

Crop	500	550	600	650	700	750	800	850	900	950	1000	1050	1100	1150
Avocado	8.2	8.9	6.8	7.2	26.6	47.9	50.4	50.3	50.1	49.4	49.7	49.7	49.3	47.1
Bean	15.2	18.5	12.0	10.7	37.3	55.7	56.9	56.9	56.5	55.8	56.2	56.6	56.0	53.6
Cantaloupe	11.6	12.7	10.0	9.9	28.6	46.1	47.7	47.7	47.5	46.8	47.3	47.6	47.0	44.6
Corn	12.7	16.2	12.0	9.3	24.8	45.4	46.3	46.4	46.2	45.5	45.7	46.0	45.5	43.3
Cotton	9.8	11.8	8.0	7.7	28.6	45.8	47.2	47.2	46.9	46.2	46.6	47.0	46.4	44.2
Lettuce	27.6	30.3	26.8	23.6	33.7	37.6	37.6	37.5	36.7	34.6	35.3	36.3	35.0	30.3
Okra	10.8	12.9	9.5	9.2	29.0	47.2	49.0	49.2	49.0	48.4	48.7	49.0	48.5	46.6
Onion	10.1	11.6	8.5	8.1	25.0	39.4	40.5	40.4	39.6	37.7	38.5	39.4	38.2	33.3
Orange	8.9	10.2	7.2	7.1	28.9	53.2	55.8	55.9	55.7	55.2	55.6	55.7	55.4	53.1
Peach	9.6	10.9	8.3	8.6	29.1	47.7	49.5	49.5	49.3	49.0	49.3	49.4	49.1	47.7
Pepper	12.8	16.8	11.0	9.3	32.8	50.5	51.6	51.6	51.4	50.7	51.0	51.4	40.8	48.5
Pigweed	10.9	12.4	9.3	9.0	26.6	43.9	45.7	45.5	45.4	44.8	45.1	45.1	44.6	42.8
Pumpkin	10.2	11.8	8.9	10.6	29.1	44.9	46.4	46.3	46.2	45.8	46.7	46.2	45.7	44.2
Sorghum	15.0	17.2	13.3	11.3	28.2	45.8	47.3	47.4	47.3	46.9	47.0	47.0	46.8	45.5
Soybean	10.9	13.1	8.7	7.9	28.8	45.6	46.6	46.5	46.3	45.9	46.0	46.2	45.8	44.5
Sugarcane	15.9	18.6	13.4	11.4	29.9	45.8	46.9	46.8	46.4	45.6	45.7	46.0	45.4	42.9
Sunflower	9.6	11.0	8.4	8.5	27.5	45.4	47.3	47.3	47.1	46.5	46.9	47.2	46.6	44.1
Tomato	10.0	11.1	8.6	8.6	25.9	46.6	48.4	48.6	48.5	47.8	48.3	48.6	48.0	45.4
Watermelon	11.9	14.4	10.7	9.9	30.4	45.6	46.8	47.0	47.0	46.3	46.8	47.2	46.6	44.5
Wheat	10.3	13.4	9.6	7.7	27.3	50.2	51.5	51.7	51.4	51.0	51.2	51.5	51.0	48.9
Crop	1200	1250	1300	1350	1400	1450	1500	1550	1600	1650	1700	1750	1800	1850
Avocado	46.8	47.1	45.2	41.0	26.3	19.2	23.1	29.0	32.5	34.1	33.2	31.2	30.3	23.1
Bean	53.5	53.6	50.8	44.9	25.6	18.5	24.6	33.1	38.4	40.9	40.6	37.5	35.2	24.2
Cantaloupe	44.3	44.5	41.9	36.7	20.6	14.8	19.1	25.5	29.9	32.0	31.5	28.9	27.4	19.4
Corn	43.2	43.5	41.8	38.3	23.4	16.8	21.0	27.1	31.0	32.9	32.6	30.1	28.8	23.1
Cotton	44.0	44.2	42.0	37.5	21.7	15.2	19.6	26.2	30.4	32.3	31.9	29.4	27.9	19.9
Lettuce	29.6	29.8	26.4	21.4	11.8	9.1	10.4	13.0	15.4	16.8	16.8	15.0	13.8	10.6
Okra	46.2	46.4	44.5	40.4	25.6	18.1	22.3	28.8	33.0	35.0	34.5	32.3	30.8	23.0
Onion	32.5	32.9	29.0	23.0	10.3	6.8	8.4	12.0	15.1	17.2	17.0	14.6	13.1	9.4
Orange	52.8	53.0	51.2	47.1	31.2	22.3	26.6	33.3	37.6	39.8	39.0	36.6	35.4	27.8
Peach	47.7	47.8	46.5	43.0	30.3	24.3	28.8	34.3	37.5	38.9	38.0	38.4	35.6	27.4
Pepper	48.4	48.6	46.4	41.7	25.0	17.6	22.6	30.0	34.7	36.9	36.6	33.9	32.2	23.4

Table 3.37 (continued)

Crop	1200	1250	1300	1350	1400	1450	1500	1550	1600	1650	1700	1750	1800	1850
Pigweed	42.5	42.6	40.6	36.2	21.5	15.6	19.9	26.1	30.0	31.8	31.3	29.1	27.6	19.5
Pumpkin	44.0	44.0	42.1	37.4	24.6	19.0	23.6	29.2	32.6	34.6	33.1	31.3	29.5	21.6
Sorghum	45.3	45.4	44.3	41.7	30.9	24.7	28.2	33.2	36.1	37.4	36.9	35.3	34.2	28.2
Soybean	44.5	44.4	43.1	40.1	27.7	21.8	26.1	31.9	35.2	36.6	36.3	34.5	33.3	25.5
Sugarcane	42.6	42.7	40.5	35.9	20.7	14.4	18.3	24.2	28.0	30.4	30.0	27.5	25.9	18.8
Sunflower	44.0	44.2	41.7	36.4	20.4	14.3	18.4	24.9	29.3	31.3	30.5	28.1	26.6	18.9
Tomato	45.2	45.4	42.7	37.3	20.5	14.4	18.9	25.6	30.0	32.1	31.7	28.9	27.3	19.1
Watermelon	44.4	44.5	42.2	37.5	22.0	16.6	21.2	27.4	31.2	33.0	32.4	29.9	28.7	20.5
Wheat	48.8	49.2	47.2	43.5	27.7	21.7	26.5	32.7	36.4	38.2	37.4	35.2	34.3	27.3
Crop	1900	1950	2000	2050	2100	2150	2200	2250	2300	2350	2400	2450	2500	-
Avocado	9.7	7.5	10.2	13.2	15.7	18.1	19.5	17.4	14.2	11.6	9.5	7.8	7.0	-
Bean	8.0	6.0	9.4	14.1	18.9	22.6	24.0	21.5	17.2	12.8	9.5	7.2	5.9	-
Cantaloupe	8.1	6.9	8.6	11.1	14.2	16.5	17.5	15.7	12.6	9.9	8.0	6.6	6.0	-
Corn	7.9	7.2	9.7	12.6	15.8	18.3	19.8	17.6	14.4	11.6	9.3	7.5	6.7	-
Cotton	7.6	6.0	7.9	10.8	14.1	16.7	16.8	15.8	12.5	9.8	7.5	6.0	5.3	-
Lettuce	6.2	5.6	6.4	7.4	8.4	9.2	9.4	8.8	7.7	6.6	5.8	5.2	4.9	-
Okra	9.4	7.0	9.4	12.8	16.3	19.0	20.2	18.3	14.9	11.8	9.3	7.3	6.5	-
Onion	4.9	4.4	4.9	5.6	6.6	7.6	8.0	7.4	6.3	5.4	4.8	4.6	4.5	-
Orange	11.4	8.6	12.0	15.8	19.2	22.1	23.6	21.2	17.4	14.1	11.1	9.0	7.8	-
Peach	12.5	10.5	14.4	18.3	21.6	24.3	25.7	23.1	19.3	16.0	13.2	10.7	9.5	-
Pepper	8.5	6.6	9.4	13.2	17.1	20.2	21.5	19.3	15.4	11.7	8.9	6.8	5.7	-
Pigweed	7.7	5.8	8.0	11.0	14.3	16.8	17.8	15.9	12.9	9.9	7.6	5.9	5.1	-
Pumpkin	9.0	7.1	10.6	14.0	17.2	19.5	20.9	18.2	14.9	12.1	9.6	7.6	7.0	-
Sorghum	14.1	12.0	15.6	19.1	22.1	24.5	25.8	23.7	20.4	17.4	14.7	12.4	11.3	-
Soybean	10.2	8.1	12.1	16.6	20.6	23.5	24.8	22.7	19.1	15.4	12.1	9.5	8.2	-
Sugarcane	7.6	6.2	8.2	10.5	13.1	15.5	16.4	14.5	11.8	9.5	7.8	6.5	6.0	-
Sunflower	8.0	6.5	8.1	10.4	13.2	15.4	16.2	14.4	11.6	9.3	7.6	6.5	6.0	-
Tomato	7.3	6.0	7.9	10.7	13.7	16.3	17.3	15.3	12.2	9.5	7.4	6.0	5.4	-
Watermelon	8.0	6.9	9.1	12.1	15.3	17.7	18.8	16.8	13.5	10.8	8.5	6.9	6.2	-
Wheat	9.7	9.0	12.8	16.6	20.2	22.6	24.4	21.7	18.2	15.0	12.2	9.7	8.5	-

Table 3.38 Average Percent Transmittances of Top Leaf Surfaces of 10 Leaves for Each of 20 Crops for 41 Wavelengths (nm)
Over the 500- to 2500-nm Wavelength Intervals (from Ref. 130)

Crop	500	550	600	650	700	750	800	850	900	950	1000	1050	1100	1150
Avocado	2.3	4.1	1.4	3.1	24.9	42.4	44.8	45.4	45.5	45.5	46.1	46.6	46.3	45.0
Bean	6.9	10.9	5.5	3.6	26.6	40.9	42.0	42.2	42.0	41.5	42.2	42.4	41.9	39.9
Cantaloupe	4.9	8.7	3.9	2.4	27.5	46.3	48.1	48.6	48.6	48.0	48.8	49.5	49.0	46.5
Corn	8.1	9.8	3.7	0.7	22.6	48.9	50.5	50.9	51.1	50.7	51.2	51.7	51.6	49.7
Cotton	8.1	13.1	7.0	4.2	30.6	47.8	49.1	49.4	49.3	39.0	49.4	49.9	49.6	47.8
Lettuce	38.4	44.3	39.5	34.0	49.5	55.3	55.6	55.5	54.8	52.6	53.7	54.9	53.7	48.2
Okra	5.9	14.8	5.8	4.1	27.1	44.6	46.4	46.7	46.9	46.7	47.3	47.8	47.6	46.0
Onion	11.7	18.8	10.8	6.6	35.8	54.3	55.7	55.7	55.0	52.9	54.0	55.4	54.1	48.2
Orange	0.7	1.9	0.5	0.5	17.6	36.0	38.2	38.6	38.6	38.4	38.9	39.5	39.3	37.7
Peach	3.5	6.2	2.6	2.8	27.1	45.5	47.3	47.6	47.7	47.6	47.9	48.3	48.1	47.1
Pepper	6.9	12.6	6.4	3.1	28.4	44.8	46.2	46.5	46.4	46.0	46.5	47.0	46.7	44.9
Pigweed	5.4	9.5	3.7	2.7	28.6	49.2	51.6	52.0	52.0	51.9	52.4	52.9	52.6	51.0
Pumpkin	5.6	8.8	4.3	5.6	30.0	47.1	48.9	49.4	49.6	49.5	50.1	50.6	50.4	49.1
Sorghum	5.0	9.0	4.2	2.1	24.4	46.7	49.1	49.6	49.8	49.9	50.3	50.8	50.7	49.8
Soybean	10.0	15.6	8.7	5.4	32.5	50.0	51.4	51.8	51.9	51.8	52.2	52.6	52.4	51.4
Sugarcane	7.5	12.2	6.9	4.1	26.7	45.0	46.9	47.2	47.3	46.9	47.6	48.1	47.9	46.0
Sunflower	6.3	9.1	5.7	5.1	27.8	46.4	48.4	48.8	48.8	48.4	49.1	49.7	49.2	46.8
Tomato	2.6	5.5	1.5	0.9	23.6	41.9	43.8	44.3	44.4	44.0	44.7	45.3	44.9	42.6
Watermelon	5.2	9.6	4.3	2.0	28.7	45.2	46.6	47.1	47.4	47.2	47.9	48.5	48.2	46.3
Wheat	1.9	5.8	2.1	0.7	20.3	41.8	43.4	43.9	44.1	43.9	44.6	45.2	45.1	43.4
Crop	1200	1250	1300	1350	1400	1450	1500	1550	1600	1650	1700	1750	1800	1850
Avocado	45.1	45.6	44.0	39.4	26.1	20.5	25.6	32.0	35.8	37.6	37.0	35.4	34.1	25.1
Bean	40.0	40.2	38.1	33.5	17.3	11.8	17.3	24.9	29.6	32.2	32.2	29.5	27.9	18.5
Cantaloupe	46.6	47.0	44.5	39.2	20.6	14.6	19.7	28.2	33.7	36.6	36.5	33.6	32.0	21.8
Corn	49.8	50.5	49.0	45.9	28.8	20.5	26.8	35.1	40.2	43.0	43.1	40.6	39.6	32.0
Cotton	47.9	48.3	46.6	42.7	26.7	19.6	25.4	33.2	38.0	40.4	40.3	38.1	37.0	27.1
Lettuce	47.4	48.0	43.7	35.9	14.6	6.2	11.1	19.9	26.6	30.5	31.0	27.0	24.4	15.2
Okra	46.1	46.5	45.0	41.5	26.8	19.3	24.5	32.0	36.6	39.2	39.1	37.0	35.9	27.3
Onion	47.4	48.1	43.4	35.1	12.5	4.1	8.7	17.5	24.3	28.4	28.8	24.7	22.0	13.1
Orange	37.6	38.2	36.9	33.7	20.1	13.0	17.2	23.5	27.6	30.0	29.6	27.6	26.9	20.2
Peach	47.3	47.7	46.7	43.9	31.5	26.2	31.3	37.4	40.9	42.8	42.3	40.9	40.6	31.7
Pepper	45.0	45.4	43.7	39.8	23.9	16.9	22.7	30.4	35.3	37.8	37.8	35.4	34.0	25.0

Table 3.38 (continued)

Crop	1200	1250	1300	1350	1400	1450	1500	1550	1600	1650	1700	1750	1800	1850
Figweed	51.2	51.6	49.9	45.8	29.9	23.1	29.1	37.1	41.9	44.5	44.4	42.2	41.0	30.3
Pumpkin	49.3	49.7	48.2	43.7	29.5	23.8	29.7	36.8	41.2	43.5	43.1	41.1	39.5	29.2
Sorghum	50.0	50.4	49.6	47.3	35.1	28.2	33.2	39.9	44.0	46.2	46.3	44.8	44.1	36.6
Soybean	51.6	51.9	50.8	48.0	34.9	28.7	34.3	41.3	45.3	47.4	47.5	45.8	44.8	35.5
Sugarcane	46.0	46.5	44.9	40.8	24.6	17.3	23.0	30.7	36.0	38.5	38.4	36.0	34.8	25.1
Sunflower	46.8	47.3	45.1	40.0	22.2	15.0	21.0	29.1	34.4	37.0	36.6	34.0	32.7	22.5
Tomato	42.6	43.0	40.7	35.9	18.6	12.3	17.9	25.7	30.8	33.4	33.3	30.5	29.1	19.0
Watermelon	46.5	47.0	45.0	40.7	24.1	18.3	24.3	31.8	36.5	38.8	38.6	36.2	35.3	25.3
Wheat	43.6	44.2	42.8	39.7	24.3	18.5	23.9	30.7	34.7	36.8	36.3	34.3	33.7	26.7
Crop	1900	1950	2000	2050	2100	2150	2200	2250	2300	2350	2400	2450	2500	—
Avocado	8.8	6.7	12.3	17.3	21.2	24.0	25.2	23.3	19.8	16.2	12.1	9.8	6.9	—
Bean	3.7	1.9	5.4	10.3	15.3	18.6	19.7	18.4	15.2	11.3	7.8	4.9	3.5	—
Cantaloupe	4.2	2.1	6.0	11.5	16.9	20.5	21.8	20.1	16.4	12.1	8.1	5.0	3.4	—
Corn	6.5	5.0	11.8	18.6	24.6	28.5	30.3	28.3	24.4	19.9	14.8	9.7	7.0	—
Cotton	7.4	4.5	10.2	16.8	22.6	26.2	27.7	26.1	22.5	17.9	12.9	8.8	6.6	—
Lettuce	2.1	0.5	1.7	4.5	8.8	12.2	13.5	12.2	9.0	5.6	2.9	1.4	0.8	—
Okra	8.6	5.2	10.7	16.8	22.2	25.7	27.1	25.7	22.2	18.1	13.6	9.7	7.5	—
Onion	1.2	0.5	0.6	2.5	6.0	9.0	10.2	8.8	6.0	3.1	1.2	0.5	0.5	—
Orange	5.3	2.6	6.2	10.3	14.1	16.8	18.1	16.5	13.6	10.7	7.8	5.1	3.8	—
Peach	12.6	10.4	17.3	23.4	28.1	31.2	32.5	30.6	27.2	23.6	19.1	14.7	12.2	—
Pepper	6.3	3.8	8.9	15.0	20.5	24.2	25.6	24.2	20.8	16.4	11.9	8.1	6.0	—
Figweed	9.9	6.9	13.5	20.7	26.8	30.7	32.2	30.6	26.9	22.2	17.0	12.4	9.6	—
Pumpkin	10.2	8.3	14.9	21.4	26.8	30.1	31.3	29.4	25.8	21.5	16.7	11.9	10.2	—
Sorghum	15.4	12.2	19.9	26.7	31.9	35.3	36.9	35.4	32.1	28.2	23.6	18.4	15.6	—
Soybean	14.6	11.7	19.3	26.7	32.7	36.3	37.7	36.3	33.0	28.6	23.5	18.5	15.8	—
Sugarcane	6.7	4.0	9.3	15.1	20.0	23.7	25.0	23.0	19.3	15.1	10.8	7.0	4.9	—
Sunflower	6.0	2.3	6.5	11.9	17.1	20.5	21.6	19.7	16.1	12.1	8.2	5.0	3.3	—
Tomato	3.7	1.8	5.4	10.2	15.2	18.6	19.8	18.2	14.8	10.8	7.2	4.3	3.0	—
Watermelon	6.1	4.6	10.1	16.1	21.3	24.7	26.1	24.4	20.7	16.6	12.2	8.2	6.3	—
Wheat	6.0	5.2	10.7	15.9	20.4	23.3	24.7	22.8	19.6	16.2	12.3	8.6	6.5	—

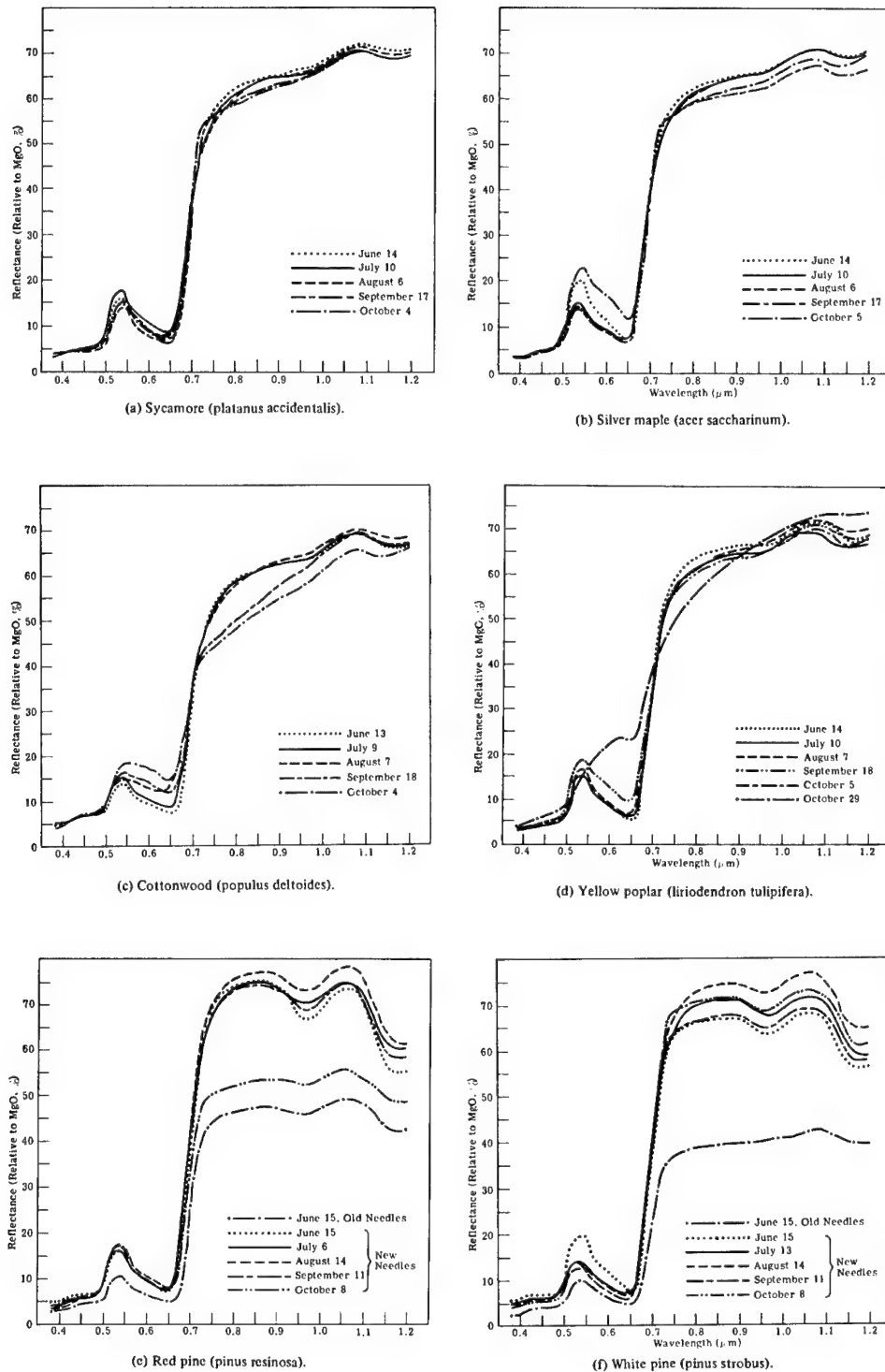


Fig. 3.166 Selected average reflectance curves for the upper surface of leaves from various trees.¹³¹

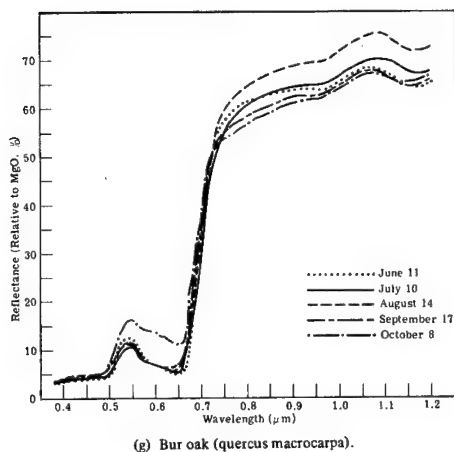


Fig. 3.166 (continued)

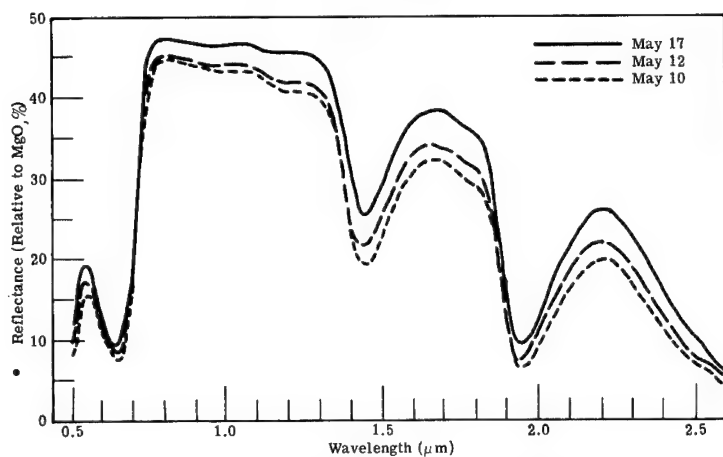


Fig. 3.167 Change in spectral reflectance from the upper surface of a single immature leaf developing on a watered yellow poplar seedling as a function of time.¹³¹

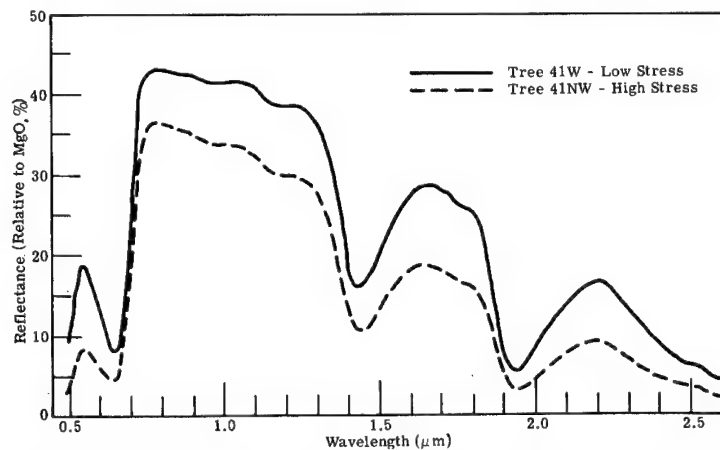
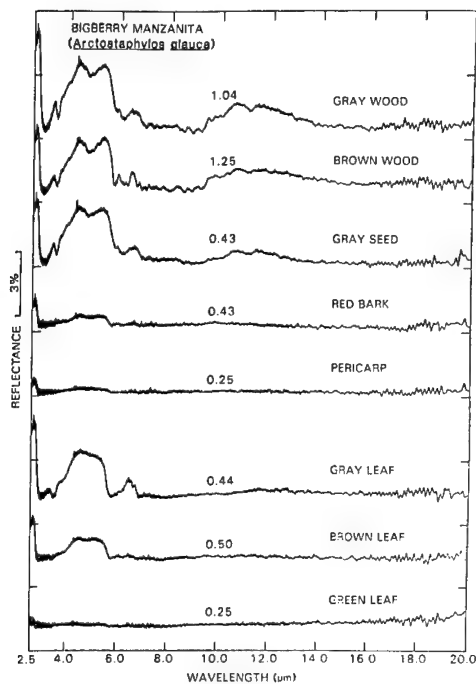
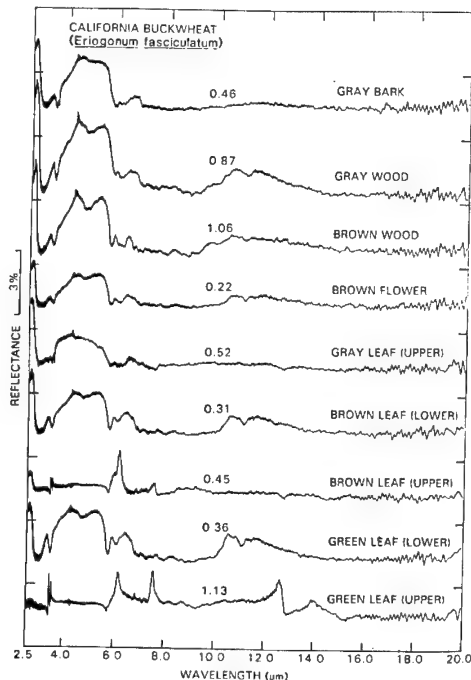


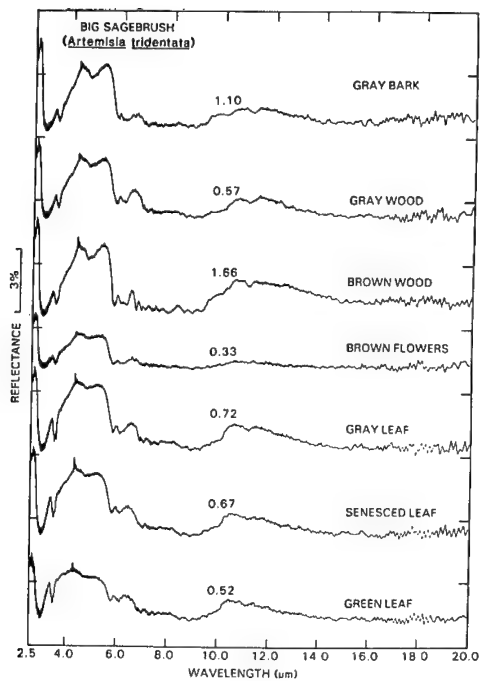
Fig. 3.168 Spectral reflectance from the upper surface of recently unfolded leaves on yellow poplar seedlings growing under low (41 W) and high (41 NW) water stress regimes.¹³¹



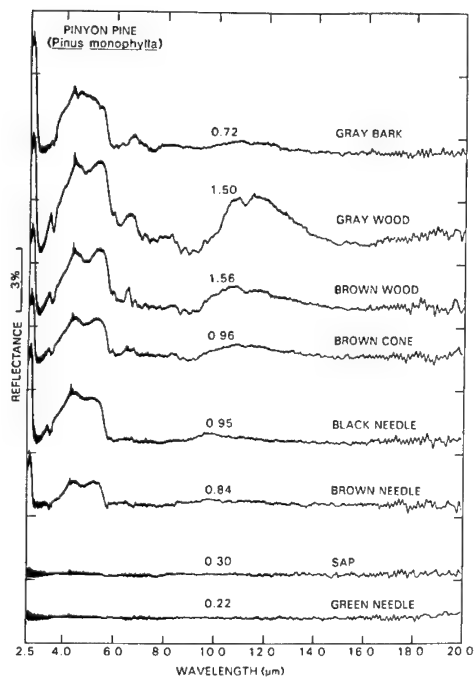
(a) Bigberry Manzanita



(b) California Buckwheat

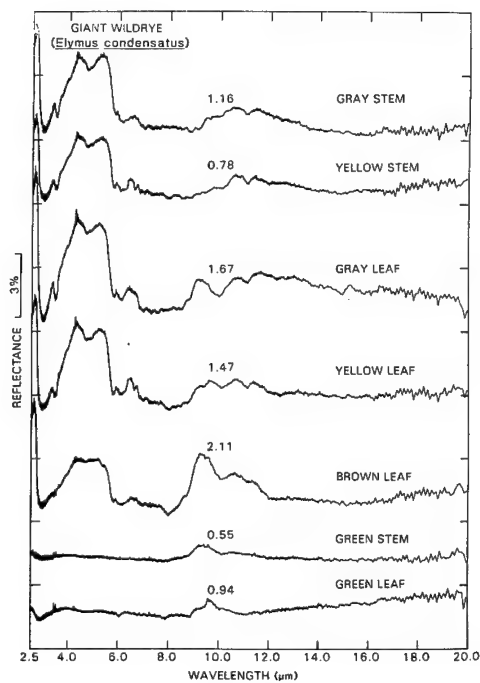


(c) Big Sagebrush

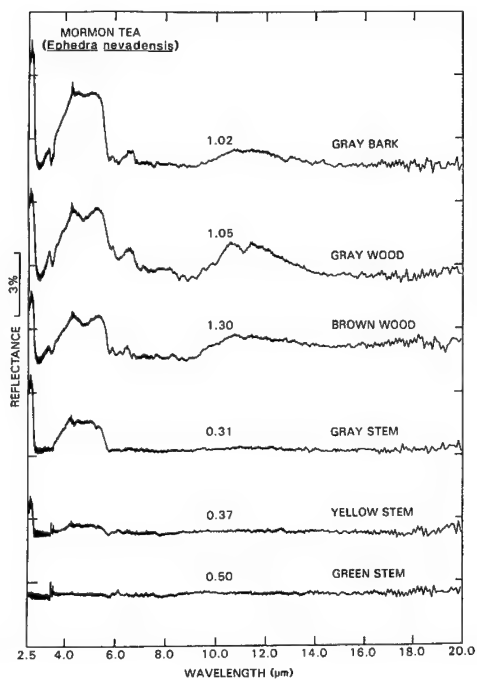


(d) Pinyon Pine

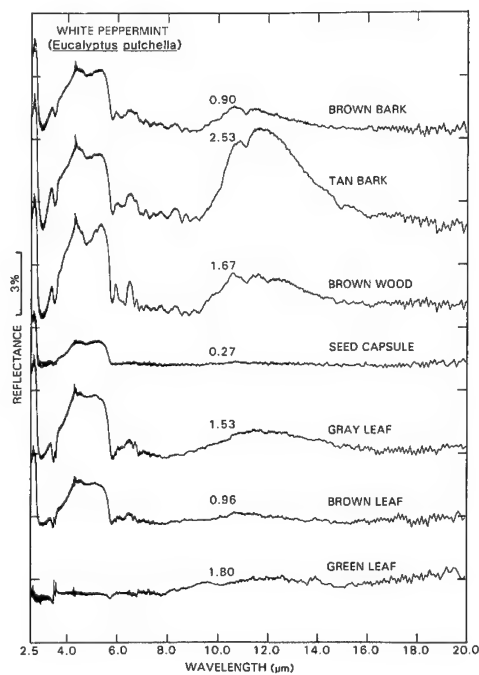
Fig. 3.169 Reflectance spectra of plant materials. The spectra have been displaced vertically to avoid overlap. The percent reflectance at 10.0 μm is provided for each spectrum.¹³³



(e) Giant Wildrye



(f) Mormon Tea



(g) White Peppermint

Fig. 3.169 (continued)

$$P(\Delta) = P\left(\begin{array}{c} \text{that two adjacent points on the } x\text{-}y \text{ plane} \\ \text{whose interval length is } \Delta \text{ belong to the same pulse} \end{array}\right) \quad (3.72)$$

$$= \int_0^{\infty} \left(1 - \frac{\Delta}{r}\right) p(r) dr = \exp\left(-\frac{\Delta}{\beta}\right). \quad (3.73)$$

Using Eq. (3.71) the autocorrelation function can be expressed as

$$\begin{aligned} R(\Delta) &= E\{L_B^2\}P(\Delta) + E\{L_B\}^2[1 - P(\Delta)] \\ &= \sigma_{L_B}^2 \exp\left(-\frac{\Delta}{\beta}\right) + E\{L_B\}^2. \end{aligned} \quad (3.74)$$

The form of the correlation function is exponential. The constant term is generally of no consequence (the mean can almost always be computed and subtracted from the random process). When the mean is removed from the process, the correlation is defined to be the covariance function.

Ben-Yosef et al.¹³⁷ have shown that using the heat balance equation for each resolvable element in an image, an exponential correlation function will arise, assuming that the heat conductivity and absorptivity are Gaussian distributed. The model predicts that the correlation length specific to a given type of terrain is larger when the heat input is low and tends to become shorter with increasing heat source strength.

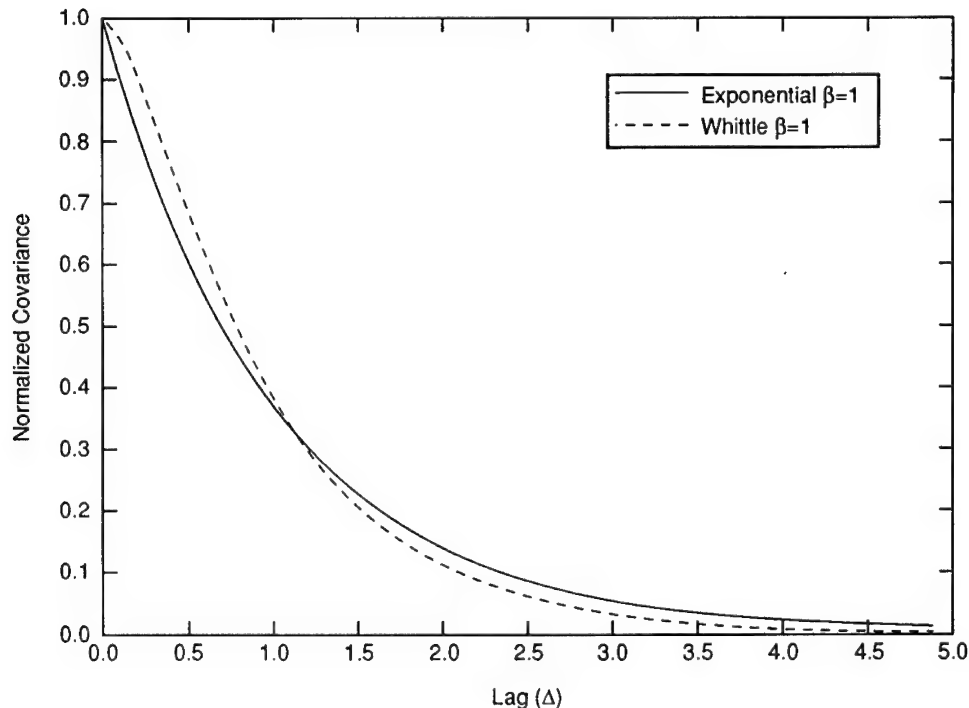


Fig. 3.170 Two common correlation functions plotted with scale length $\beta = 1$.

3.9.3 Power Spectrum Representation

The Fourier transforms of the two example correlation functions are their respective power spectra:

$$\Phi_{\text{exponential}}(\omega_x, \omega_y) = \sigma_B^2 \frac{2\pi\beta^{-1}}{\left(\omega_x^2 + \omega_y^2 + \frac{1}{\beta^2}\right)^{3/2}}, \quad (3.75)$$

$$\Phi_{\text{Whittle}}(\omega_x, \omega_y) = \sigma_B^2 \frac{\pi^3\beta^{-2}}{\left[\omega_x^2 + \omega_y^2 + \left(\frac{\pi}{2\beta}\right)^2\right]^2}. \quad (3.76)$$

The corresponding *one-dimensional* correlation functions and power spectral densities can be obtained by setting $\Delta_x = 0$ or $\Delta_y = 0$ in Eqs. (3.68) and (3.69):

$$\text{Exponential: } R(\Delta_x) = \sigma_B^2 \exp\left(-\frac{|\Delta_x|}{\beta_x}\right), \quad (3.77)$$

$$\text{Whittle: } R(\Delta_x) = \sigma_B^2 \left(\frac{\pi|\Delta_x|}{2\beta}\right) K_1\left(\frac{\pi|\Delta_x|}{2\beta}\right), \quad (3.78)$$

$$\Phi_{\text{exponential}}(\omega_x) = \sigma_B^2 \frac{2\beta_x^{-1}}{\omega_x^2 + \beta_x^{-2}}, \quad (3.79)$$

$$\Phi_{\text{Whittle}}(\omega_x) = \sigma_B^2 \frac{\pi\left(\frac{\pi}{2\beta_x}\right)^2}{\left[\omega_x^2 + \left(\frac{\pi}{2\beta_x}\right)^2\right]^{3/2}}. \quad (3.80)$$

Equations (3.79) and (3.80) are plotted for $\beta = 1$ in Fig. 3.171. Both spectra behave similarly for low frequencies but differ in the behavior at high frequencies. Specifically, the exponential falls off like ω^2 and the Whittle falls off like ω^3 . The frequency where the slope changes is called the *break frequency* and this frequency is different for the two spectra. The break frequencies are specified by the constant term in the denominators of Eqs. (3.79) and (3.80).

Futterman et al.¹³⁸ discuss the more general situation of the p 'th power law power spectrums where the exponential and Whittle are specific realizations of a more general correlation function/power spectral density pair. Specifically, the correlation function is

$$R_{p^{\text{th}} \text{ law}}(\Delta) = \sigma_{L_B}^2 \frac{2^{1-\nu}(2\pi a\Delta)^\nu K_\nu(2\pi a\Delta)}{\Gamma(\nu)}. \quad (3.81)$$

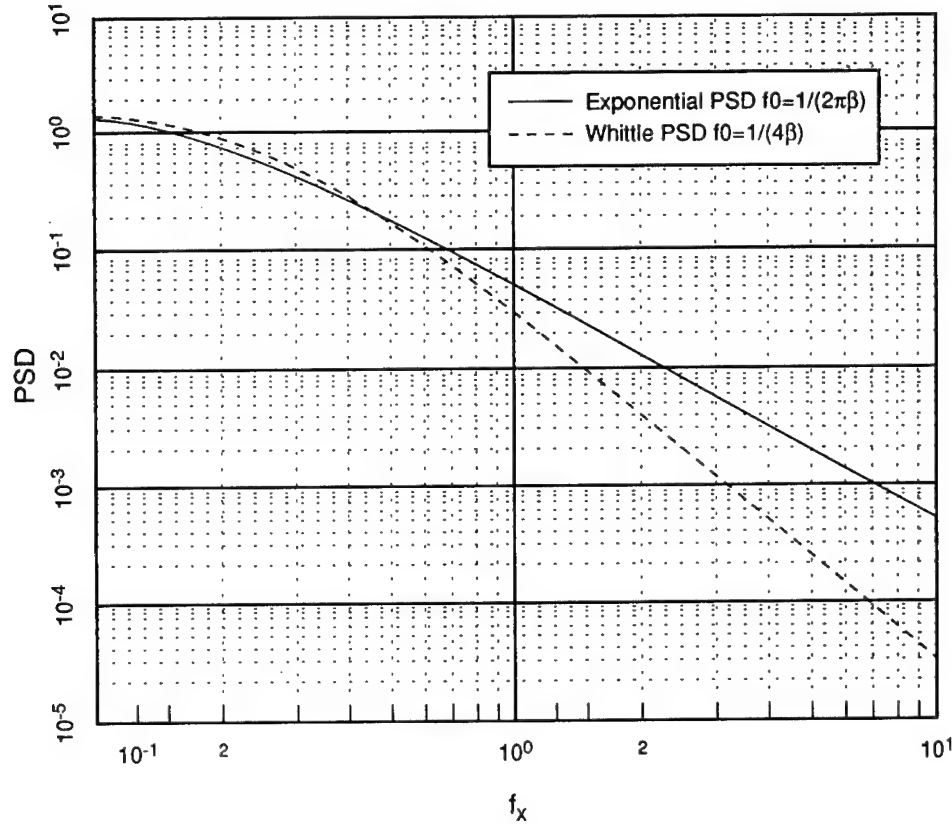


Fig. 3.171 Two common power spectral density functions plotted with scale length $\beta = 1$.

The corresponding power spectral density is

$$\Phi_{p^{\text{th law}}} \left(\frac{\omega}{2\pi} \right) = \sigma_{L_B}^2 \frac{\Gamma(\nu + 1/2)}{\Gamma(\nu)} \frac{a^{2\nu}}{\pi^{1/2}} \frac{1}{[a^2 + (\omega/2\pi)^2]^{\nu+1/2}}. \quad (3.82)$$

The parameter $p = 2\nu + 1$ describes the slope of the high-frequency rolloff of the power spectral density. The parameter a^{-1} is the break frequency. The break frequency is a function of ν and is given by

$$a^{-1}(\nu) = \frac{2\pi^{1/2}\Gamma(\nu)}{\Gamma(\nu + 1/2)} \beta. \quad (3.83)$$

The even-integer power laws (half-integer ν) have exponential-type correlation functions. Here $\Gamma(\nu)$ is the gamma function.

3.9.4 Nonisotropic Correlation Functions

It is not always possible to assume the form of the correlation function to be isotropic. A common approach to include nonisotropic behavior is to assume

separability in the x and y directions and to form a new correlation function as the product of two one-dimensional correlation functions. For example, using the exponential correlation function, we obtain the separable two-dimensional nonisotropic correlation by forming

$$R(\Delta_x, \Delta_y) = \sigma_{LB}^2 \exp\left(-\frac{|\Delta_x|}{\beta_x}\right) \exp\left(-\frac{|\Delta_y|}{\beta_y}\right). \quad (3.84)$$

3.9.5 Statistics of Various Terrain Backgrounds

Figures 3.172 through 3.176 are summary statistics of various types of terrain backgrounds covering spectral ranges in the near-, mid-, and long-wave infrared regions. The statistics include radiance and temperature histograms,

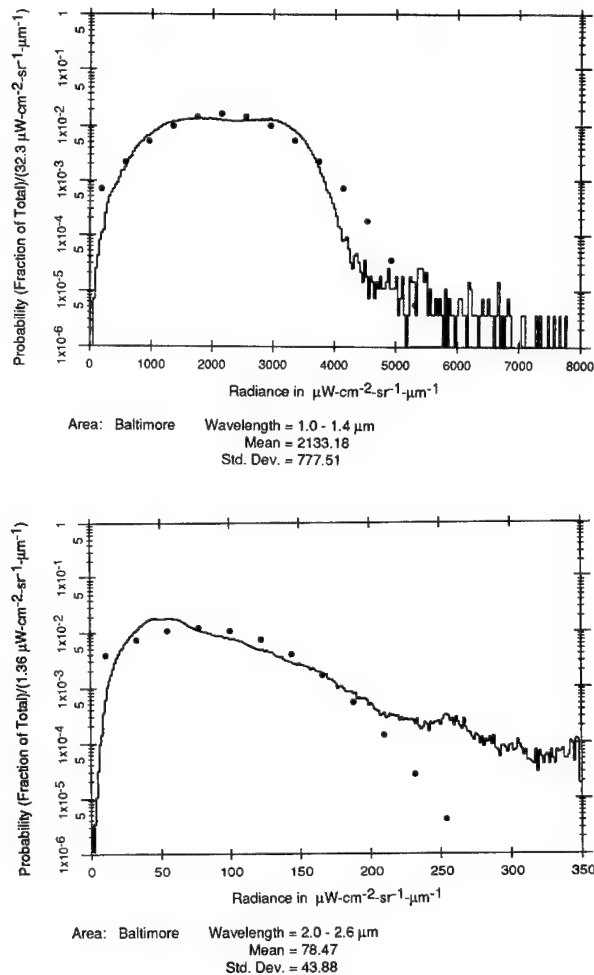
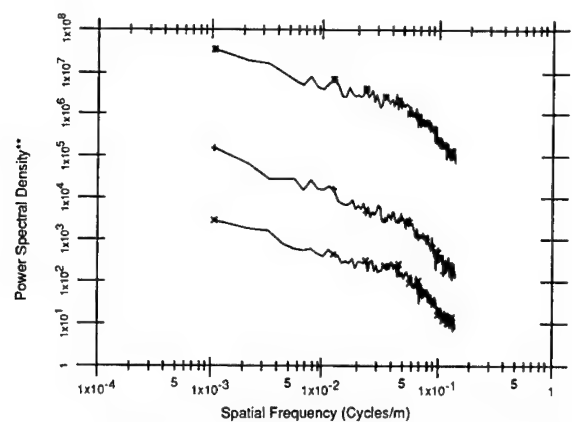
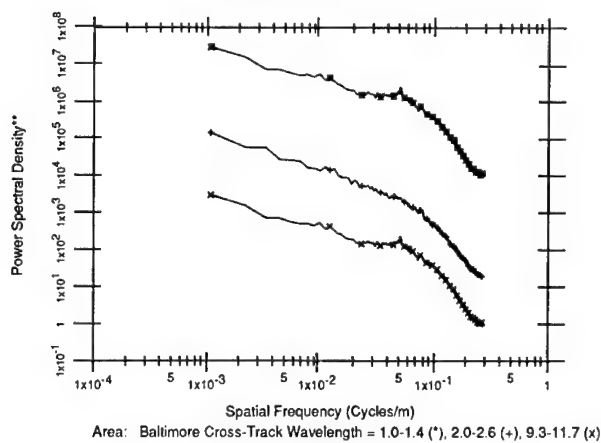
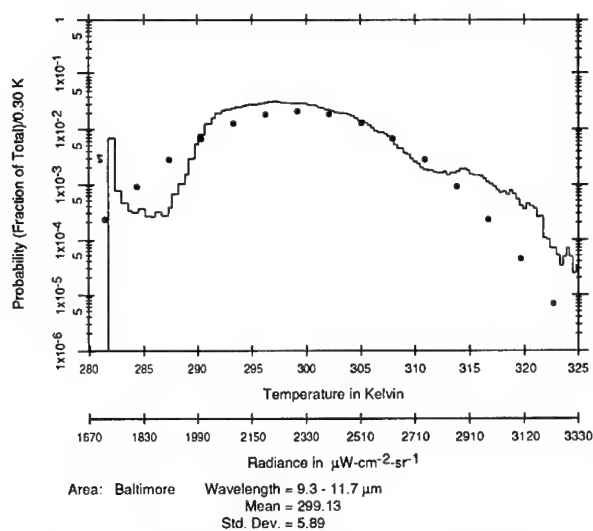


Fig. 3.172 Histogram and power spectral density plots of a residential area in Baltimore, Maryland. IFOV in-track, 5 mrad; IFOV cross-track, 2.5 mrad; altitude 2500 ft; time, 1140; clear sky, light haze at 5 kft, dry condition; depression angle, 90°. ¹³⁹ (continued on following page)



Power Spectra

** Power Spectral Density is $(\mu\text{W}\cdot\text{cm}^{-2}\cdot\text{sr}^{-1}\cdot\mu\text{m}^{-1})^2/\text{Cycle/Meter}$ for 1.0 to 1.4 μm and 2.0 to 2.6 μm Bands and $(^\circ\text{K})^2/\text{Cycle/Meter}$ for 9.3 to 11.7 μm Band



Power Spectra

** Power Spectral Density is $(\mu\text{W}\cdot\text{cm}^{-2}\cdot\text{sr}^{-1}\cdot\mu\text{m}^{-1})^2/\text{Cycle/Meter}$ for 1.0 to 1.4 μm and 2.0 to 2.6 μm Bands and $(^\circ\text{K})^2/\text{Cycle/Meter}$ for 9.3 to 11.7 μm Band

Fig. 3.172 (continued)

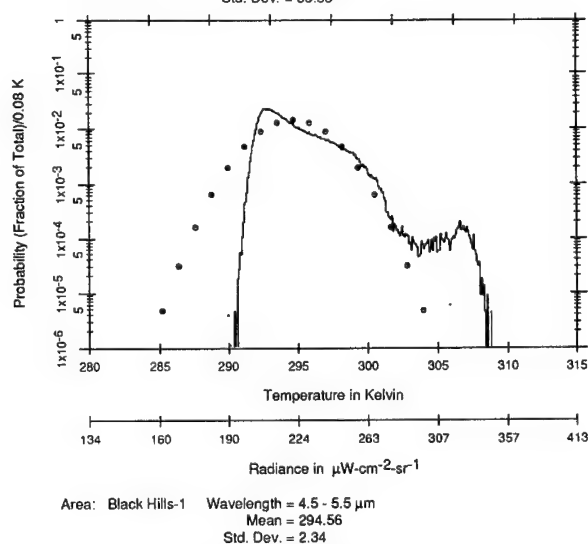
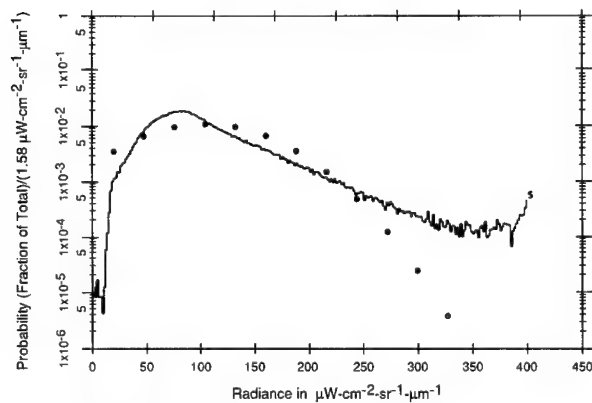
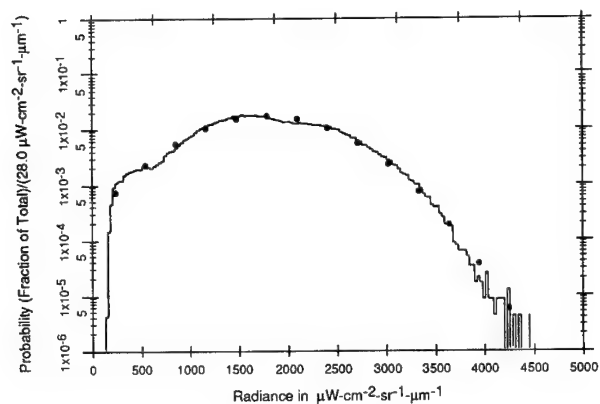
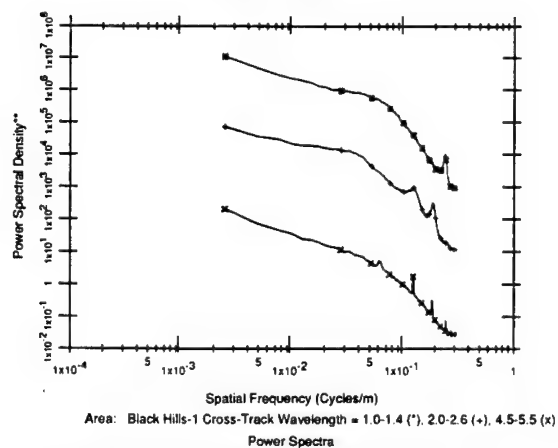
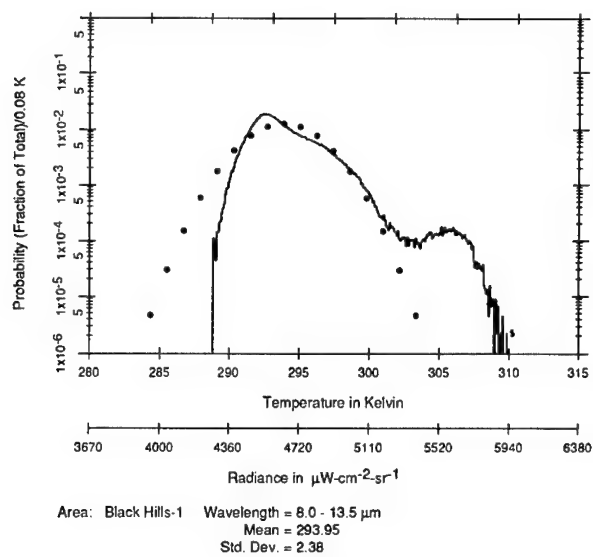
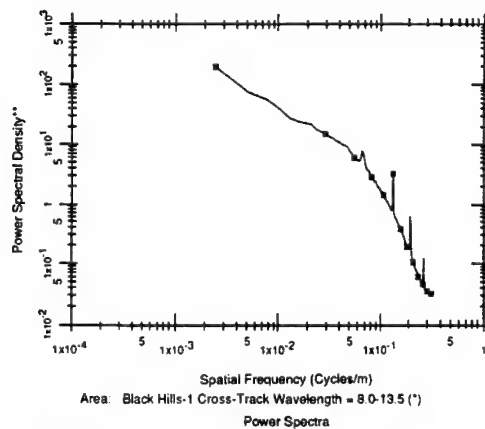


Fig. 3.173 Histogram and power spectral density plots of forested mountains (Black Hills, South Dakota). IFOV in-track, 6.6 mrad; IFOV cross-track, 3.5 mrad; altitude, 1500 ft; time, 1340; visibility > 15 miles, clear day, dry, cloud over 10%; depression angle, 90°. ¹³⁹
 (continued on following pages)



** Power Spectral Density is $(\mu\text{W}\cdot\text{cm}^{-2}\cdot\text{sr}^{-1}\cdot\mu\text{m}^{-1})^2/\text{Cycle/Meter}$ for 1.0 to 1.4 μm and 2.0 to 2.6 μm Bands and $(^\circ\text{K})^2/\text{Cycle/Meter}$ for 4.5 to 5.5 μm Band



** Power Spectral Density is $(^\circ\text{K})^2/\text{Cycle/Meter}$ for 8.0 to 13.5 μm Band

Fig. 3.173 (continued)

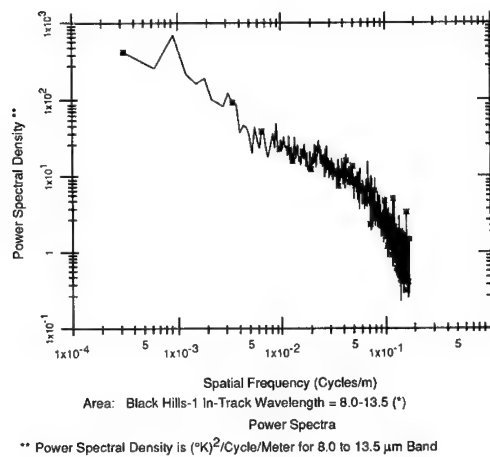
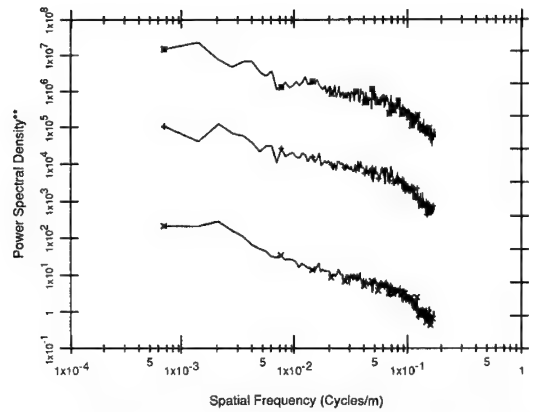


Fig. 3.173 (continued)

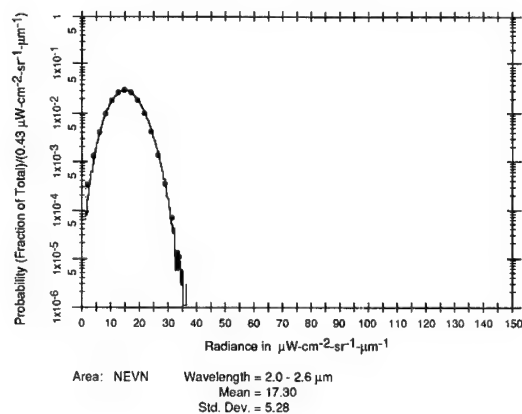


Fig. 3.174 Histogram and power spectral density plots of mountainous terrain in Nevada. IFOV in-track, 2.5 mrad; IFOV cross-track, 2.5 mrad; altitude, 1000 ft; time, 1100; visibility 15 miles, high overcast, light haze; depression angle, 35° .¹³⁹ (continued on following pages)

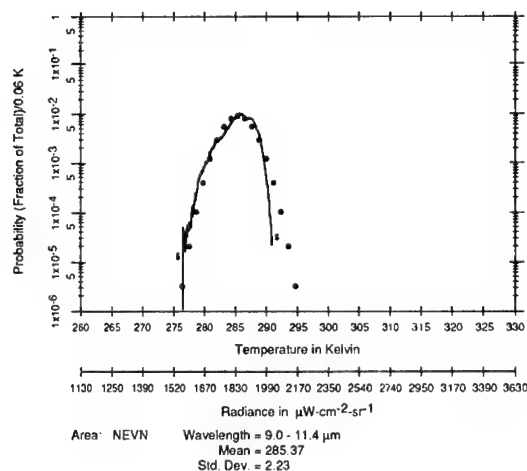
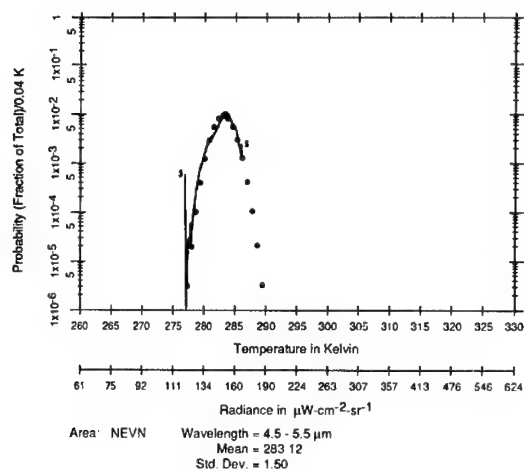
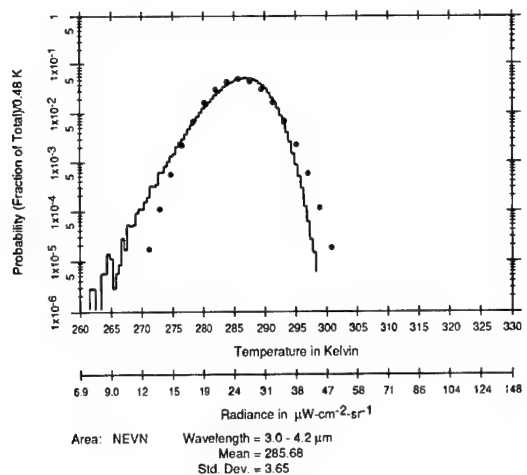
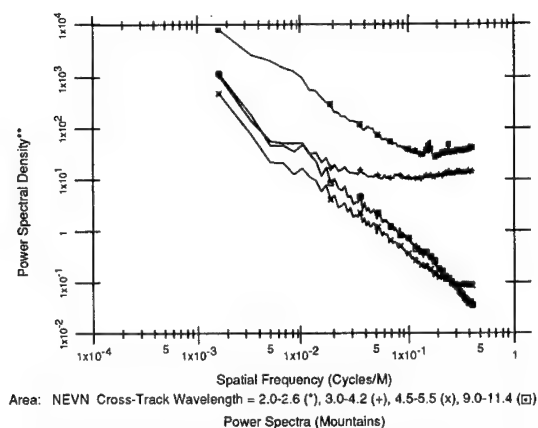
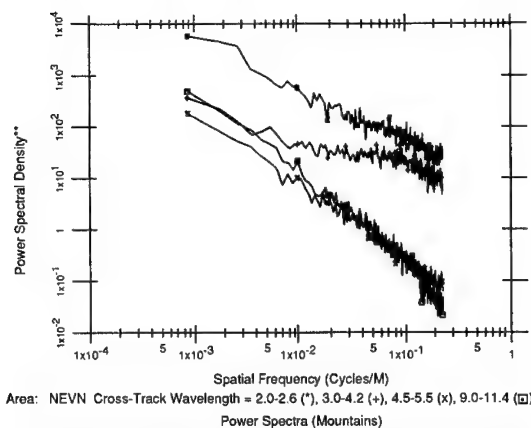


Fig. 3.174 (continued)



** Power Spectral Density is $(\mu\text{W}\cdot\text{cm}^{-2}\cdot\text{sr}^{-1}\cdot\mu\text{m}^{-1})^2/\text{Cycle/Meter}$ for the 2.0 to 2.6 μm Band, and $(^\circ\text{K})^2/\text{Cycle/Meter}$ for the 3.0 to 4.2, 4.5 to 5.5, and 9.0 to 11.4 μm Bands



** Power Spectral Density is $(\mu\text{W}\cdot\text{cm}^{-2}\cdot\text{sr}^{-1}\cdot\mu\text{m}^{-1})^2/\text{Cycle/Meter}$ for the 2.0 to 2.6 μm Band, and $(^\circ\text{K})^2/\text{Cycle/Meter}$ for the 3.0 to 4.2, 4.5 to 5.5, and 9.0 to 11.4 μm Bands

Fig. 3.174 (continued)

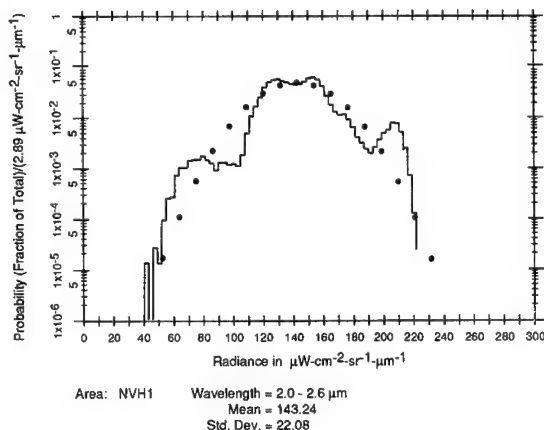
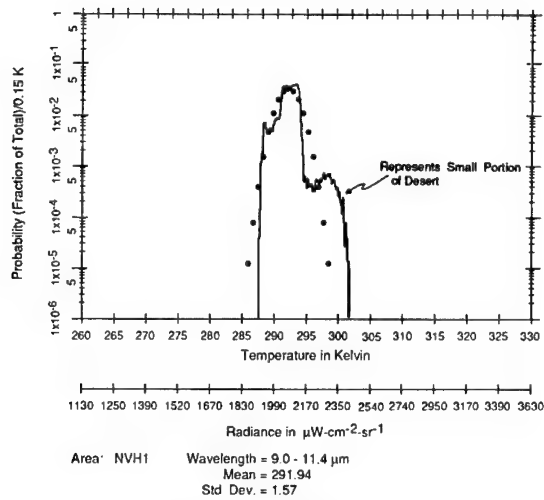
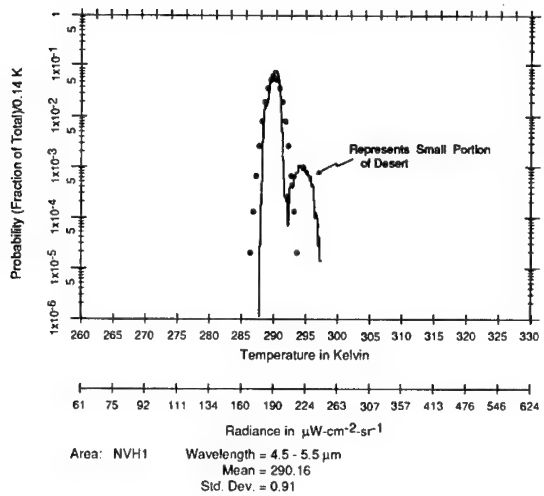
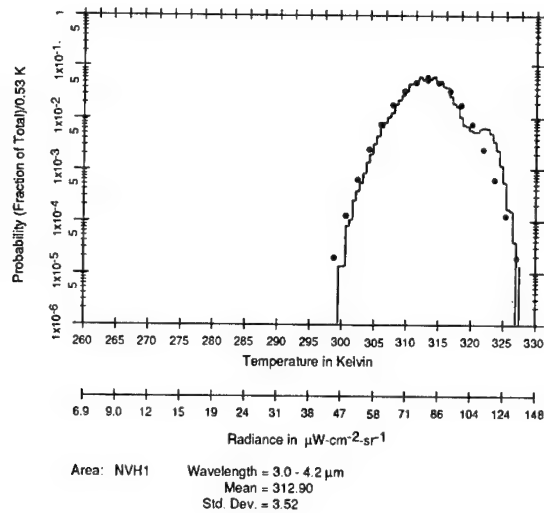


Fig. 3.175 Histogram and power spectral density plots of a dry lake bed in Nevada. IFOV in-track, 2.5 mrad; IFOV cross-track, 2.5 mrad; altitude, 1000 ft; time, 1100; visibility 15 miles, with high thin scattered clouds; depression angle, 35° .¹³⁹ (continued on following pages)


Fig. 3.175 (continued)

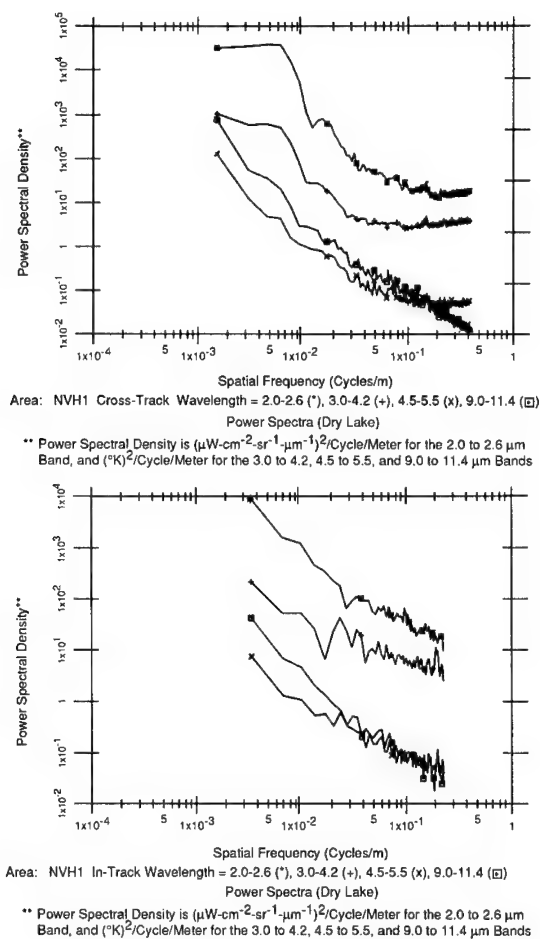


Fig. 3.175 (continued)

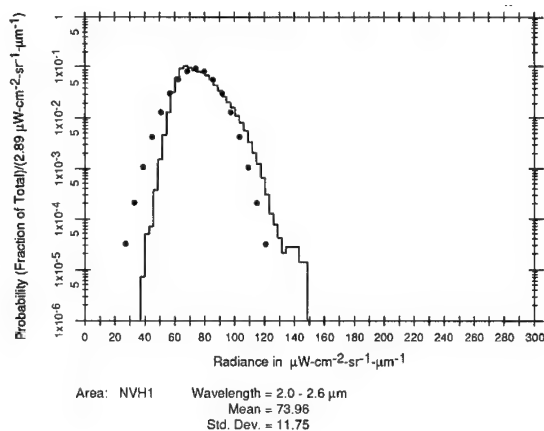


Fig. 3.176 Histogram and power spectral density plots of desert terrain in Nevada. IFOV in-track, 2.5 mrad; IFOV cross-track, 2.5 mrad; altitude, 1000 ft; time, 1100; visibility 15 miles, with high thin scattered clouds; depression angle, 35° .¹³⁹ (continued on following pages)

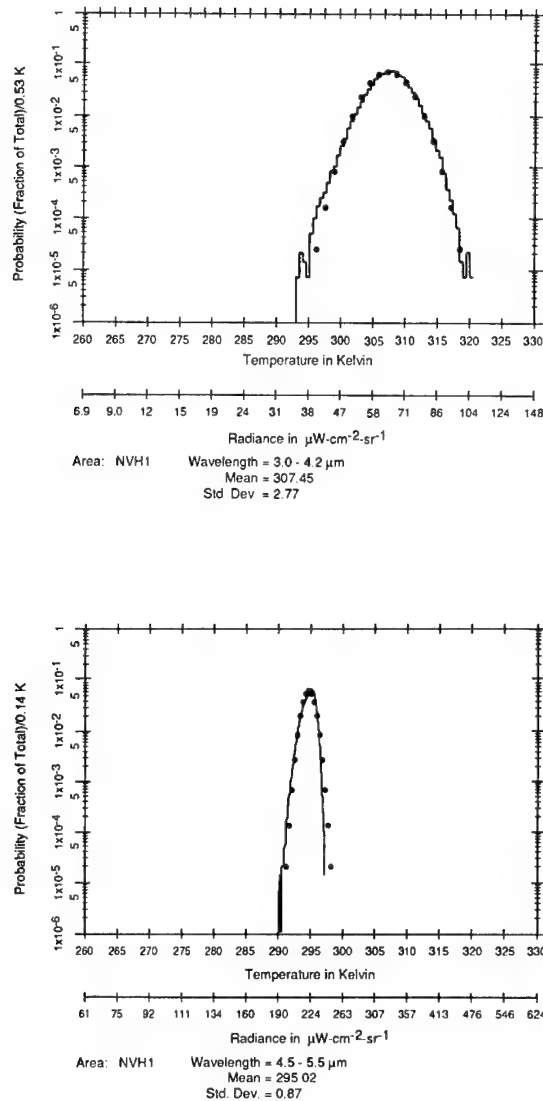


Fig. 3.176 (continued)

with means and standard deviations and power spectra. One-dimensional power spectra, both in the direction of flight and across the flight line, are called the *in-track* and *cross-track* spectra, respectively. Each histogram includes a Gaussian curve having the same mean and standard deviation as the actual curve, and indicated by circles superimposed over the actual curve. Additionally the "S" on some of the histograms indicates that saturation has occurred. The digital range of the image signals is between 0 and 255. Because of the difficulty in properly setting the amplifier gains, the digital range is sometimes exceeded.

The scanner can be set in two configurations, looking directly downward and looking at an angle of 35° below the horizon. The difference in results from each viewing geometry is essentially undiscernible in most cases.

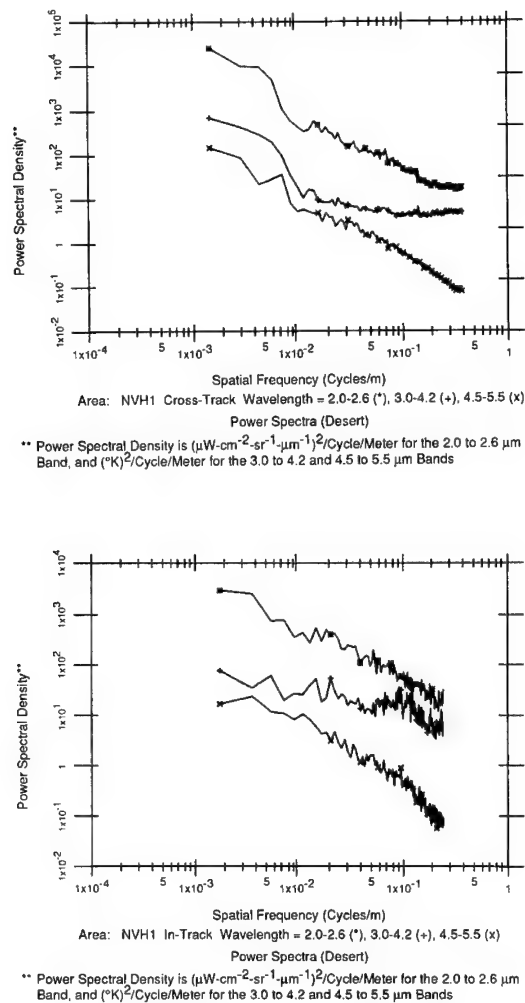


Fig. 3.176 (continued)

References

1. N. N. Vygodskaya and I. I. Gorshokova, "Calculations of canopy reflectances using the Goudriaan reflectance model and their experimental evaluation," *Remote Sensing of Environment* **27**, 321-336 (March 1989).
2. S. B. Idso and R. D. Jackson, "Thermal radiation from the atmosphere," *Journal of Geophysical Research* **74**, 5397 (1969).
3. F. Kreith, *Principals of Heat Transfer*, 3rd ed., Intext Educational Publishers (1973).
4. *Handbook of Chemistry and Physics*, CRC Press, Cleveland, OH (1976).
5. M. P. Thekakara, "Extraterrestrial solar spectrum, 3000-6100 \AA at 1 \AA intervals," *Applied Optics* **13**(3), 518-522 (March 1974).
6. D. M. Gates, "Spectral distribution of solar radiation at the earth's surface," *Science* **151**, 523 (1966).
7. *Electro-Optics Handbook*, Technical Series EOH-11, RCA, Commercial Engineering, Harrison, NJ (1974).
8. D. S. Bond and F. P. Henderson, "The conquest of darkness," AD 346 297 (1963).

9. L. M. Biberman and S. Nudelman, Eds., *Photoelectronic Imaging Devices*, Plenum Press, New York (1971).
10. A. P. Lane and W. M. Irvine, "Monochromatic phase curves and albedos for the lunar disk," *The Astronomical Journal* **78**(3) (April 1973).
11. R. U. Sexl et al., "The directional characteristics of lunar infrared radiation," *The Moon* **3**(2) (August 1971).
12. B. W. Hapke, W. D. Partlow, J. K. Wagner, and A. J. Cohen, "Reflectance measurements of lunar materials in the vacuum ultraviolet," in *Proceedings of the 9th Lunar Planetary Science Conference*, pp. 2935–2947 (1978).
13. J. W. Salisbury, G. R. Hunt, and L. M. Logan, "Infrared spectra of Apollo 16 fines," in *Proceedings of the Fourth Lunar Science Conference, Geochimica et Cosmochimica Acta* **3**(suppl. 4), 3191–3196 (19xx).
14. K. R. Lang, *Astrophysical Formulae*, Springer-Verlag, Berlin (1980).
15. A. S. Jursa, Ed., *Handbook of Geophysics and the Space Environment*, Chaps. 13 and 25, ADA 167000, Airforce Geophysics Laboratory (1985).
16. M. M. Waldrop, "COBE confronts cosmic conundrums," *Science* **247**, 411–413 (January 1990).
17. L. Larmore, "Infrared radiation from celestial bodies," U.S. Air Force Project, RAND Research Memo RM-791, RAND Corporation (March 17, 1952).
18. F. J. Low and H. L. Johnson, "Stellar photometry at 10 μm ," *Journal of Applied Physics* **139**, 1130 (1964).
19. T. J. Jones et al., "A search for the infrared counterpart of type II OH masers—I. A model for the IR background source confusion," *Mon. Nat. Roy. Ast. Soc.* **197**, 413 (1981).
20. C. W. Allen, *Astrophysical Quantities*, 3rd ed., University of London, Athlone Press (1974).
21. *Infrared Engineering Handbook*, Aerojet-General Corporation, El Monte, CA (August 25, 1961).
22. R. Leighton, *Astrophysical Journal*, No. 4 (1965).
23. R. G. Walker, "Infrared celestial backgrounds," Air Force Cambridge Research Laboratories, Bedford, MA (July 1962).
24. P. E. Barnhart and W. E. Mitchell, Jr., "Stellar background measurement program," The Ohio State University, Columbus Research Foundation, Columbus, OH (July 1964).
25. "Space background study for project DEFENDER," AD 403 780, Eastman Kodak Company, Rochester, NY (April 1963).
26. *Space Handbook No. 1*, ACF Industries Inc., ACF Electronics Division, Riverdale, MD (November 1962).
27. "Celestial background radiation," AD 602 616, Air Force Cambridge Research Laboratories, Bedford, MA (March 1964).
28. L. L. Collins and R. B. Freund, "Celestial background simulation techniques," AD 282 788, Northrop Space Laboratories, Hawthorne, CA (1961).
29. H. L. Johnson, R. I. Mitchell, B. Iriarte, and W. K. Wisniewski, "Magnitudes and colors of 1300 bright stars," *Sky and Telescope* **30**(1) (July 24, 1965).
30. C. A. Beichman, G. Neugebauer, H. J. Habing, P. E. Clegg, and I. J. Chester, *Infrared Astronomical Satellite (IRAS) Catalogs and Atlases Explanatory Supplement*, Joint IRAS Science Working Group, Jet Propulsion Laboratory, Pasadena, CA (1988).
31. R. G. Walker and R. D. Sears, "An empirical model of the distribution of infrared point sources in the galaxy," Jamieson Science and Engineering, Felton, CA (1987).
32. S. D. Price, "Infrared celestial backgrounds," Air Force Geophysics Laboratory, Hanscom AFB, MA (1985).
33. G. H. Rieke and F. J. Low, *Astrophysical Journal* **176**, L95 (1972).
34. D. W. Sciama, *Modern Cosmology*, Cambridge University Press, New York (1971).
35. R. P. Binzel, T. Gehrels, and M. S. Matthews, Eds., "The IRAS asteroid and comet survey," in *Asteroids II*, University of Arizona Press, Tucson (1989).
36. D. Morrison, *Astrophysical Journal* **194**, 203 (1974).
37. T. L. Murdock, "Contribution of asteroids to the infrared astronomical sky survey," AFCRL-TR-70154 (1973).
38. S. D. Price, "Structure of the extended emission in the infrared celestial background," *Optical Engineering* **27**(1), 75–85 (1988).

39. T. L. Murdock and S. Price, "Infrared measurements of zodiacal light," *The Astronomical Journal* **90**(2), 375–386 (Feb. 1985).
40. E. N. Frazier, "Infrared radiation of the zodiacal light," *Proceedings of the SPIE* **124**, 139–146 (1977).
41. E. N. Frazier, D. J. Boucher, and G. F. Mueller, "A self-consistent model of the zodiacal light radiance," *Proceedings of the SPIE* **819**, 2–6 (1987).
42. J. C. Good, M. G. Hauser, and T. N. Gautier, "IRAS observations of the zodiacal background," *Advanced Space Research* **6**(7), 886 (1986).
43. J. Tigg and G. Pearce, "An infrared model of the zodiacal emission," *Earth, Moon, and Planets* **43**, 101–105 (1988).
44. "Measurement of infrared radiation gradients in the sky," AD 206 453, Midwest Research Institute, Kansas City, MO (1953).
45. R. C. Jones, "Sky noise—analysis of circular scanning," Polaroid Corporation, Cambridge, MA (November 1953).
46. R. C. Jones, "Sky noise—its nature and analysis," Polaroid Corporation, Cambridge, MA (September 1953).
47. R. E. Eisele, "Infrared background investigation," AFCRC-TN59-843, Ramo-Wooldridge Division of Thompson-Ramo Wooldridge, Inc., Los Angeles, CA (June 1959).
48. R. E. Eisele, "Infrared background investigation," AD 236913, Thompson-Ramo Wooldridge, Inc., Canoga Park, CA (March 1960).
49. H. E. Bennett, J. M. Bennett, and M. R. Nagel, "The spatial distribution of infrared radiation from the clear sky including sequences of sky maps at various elevations," NAVORD Report 6577, U.S. Naval Ordnance Test Station, China Lake, CA (September 1959).
50. H. E. Bennett, J. M. Bennett, and M. R. Nagel, "Measurements of infrared and total radiance of the clear winter sky of Wright-Patterson Air Force Base, Ohio," ADI 18127, Wright Air Development Center, USAF Air Research and Development Command, Wright-Patterson AFB, OH (March 1957).
51. E. E. Bell, L. Eisner, J. Young, and R. A. Oetjen, "Spectral radiance of sky and terrain at wavelengths between 1 and 20 microns. II. sky measurements," *Journal of the Optical Society of America* **50**, 1311–1320 (December 1960).
52. A. Adel, "Observations of atmospheric scattering near the sun's limb," AD 273 599, Arizona State College, Flagstaff, AZ (January 1961).
53. E. E. Bell, I. L. Eisner, and R. A. Oetjen, "The spectral distribution of the infrared radiation from the sky," *Proc. Symp. Infrared Backgrounds*, Nonr-1224 (12), AD 121010, Engineering Research Institute, The University of Michigan, Ann Arbor, MI (March 1956).
54. G. A. Wilkins and J. A. Hoyem, "The terrestrial night horizon and sky, 4.3 micron radiance data generated by the HITAB-TRIS experiments," NAVWEPS Report 8552, U.S. Naval Ordnance Test Station, China Lake, CA (June 1964).
55. R. Sloan, J. Shaw, and D. Williams, "Infrared emission spectrum of the atmosphere," *Journal of the Optical Society of America* **45**(6), 455, 459 (June 1955).
56. J. Gordon and P. Church, "Overcast sky luminances and directional luminous reflectances of objects and backgrounds under overcast skies," *Applied Optics* **5**, 919 (June 1966).
57. "Infrared satellite backgrounds, part I: atmospheric radiative processes," AFCRL 1069(I), Aero-Space Division, The Boeing Company, Seattle, WA (September 30, 1961).
58. R. C. Jones and A. M. Nagvi, "Satellite navigation of terrestrial occultations of stars; III: interference due to brightness of the earth's atmosphere," AD 287 869, Geophysics Corporation of America, Boston, MA (October 1962).
59. A. M. Nagvi, "Satellite navigation by terrestrial occultations of stars—considerations relating to refraction and extinction," AD 287 868, Geophysics Corporation of America, Bedford, MA (October 1962).
60. G. Newkirk and J. Eddy, "Light scattering by particles in the upper atmosphere," University of Colorado, Boulder, CO (May 1963).
61. R. K. McDonald, The Boeing Company, Seattle, WA, private communication.
62. N. P. Laverty and W. M. Clark, The Boeing Company, Seattle, WA, private communication.
63. F. A. Berry et al., *Handbook of Meteorology*, McGraw-Hill, New York (1945).
64. J. W. Chamberlain, *Physics of the Aurora and Airglow*, Academic Press, New York (1961).

65. A. W. Harrison and A. V. Jones, *Journal of Atmospheric and Terrestrial Physics* **11**, 192–199 (1957).
66. A. V. Jones, "Possible methods for studying the auroral spectrum in the 2.0 to 3.5 micron region," Saskatchewan University, Saskatoon, Canada (November 1959).
67. D. M. Hunten, "Optics of the upper atmosphere," *Applied Optics* **3**(2), (February 1964).
68. "Aurorae and Airglow," National Aeronautics and Space Administration, Washington, DC (April 1964).
69. I. Sellin, "Auroral radiations in the infrared," Laboratories for Applied Sciences, University of Chicago (October 1961).
70. R. Chapman, R. Jones, A. Dalgarno, and D. Beining, "Investigation of auroral, airglow and night emissions as related to space-based defense systems," Geophysics Corporation of America, Bedford, MA (June 1962).
71. A. W. Harrison and A. V. Jones, *Journal of Atmospheric and Terrestrial Physics* **13**, 291–294 (1957).
72. A. T. Stair, Jr., J. C. Ulwick, K. D. Baker, and D. J. Baker, "Rocketborne observations of atmospheric infrared emissions in the auroral region," in *Atmospheres of Earth and Planets*, pp. 335–346, Reidel Publishing Company, Boston, MA (1975).
73. E. H. Vestine, "Terrestrial magnetism," *Journal of Geophysical Research* **49**, 77–102 (June 1944).
74. F. W. G. White and M. Geddes, "Terrestrial magnetism," *Journal of Geophysical Research* **44**, 367–377 (December 1939).
75. L. Harang, *The Aurorae*, John Wiley & Sons, New York (1951).
76. C. Störmer, *The Polar Aurora*, Clarendon Press, Oxford (1955).
77. E. L. Krinov, "Spectra reflectance properties of natural formations" (originally published in Russian) (1947); translation: National Research Council of Canada, Technical Translation TT439, Ottawa, Canada (1953).
78. F. F. Roach, *Proc. Institute of Radio Engineers* **47**, 267 (1959).
79. J. F. Noxon, A. Harrison, and A. V. Jones, "The infrared spectrum of the night airglow 1.4 μm to 4.0 μm ," *Journal of Atmospheric and Terrestrial Physics* **16**, 246–251 (1959).
80. A. Vallance Jones and H. Gush, *Nature* **172**, 496 (September 12, 1953).
81. D. M. Hunten, *Journal of Atmospheric and Terrestrial Physics* **7**, 141–151 (1955).
82. M. J. Seaton, *Journal of Atmospheric and Terrestrial Physics* **4**, 285–294 (1954).
83. J. C. Brandt and J. W. Chamberlain, "Resonance scattering by atmospheric sodium—V, theory of the day airglow," *Journal of Atmospheric and Terrestrial Physics* **13**, 90–98 (December 1958).
84. J. C. Brandt, *Astrophysical Journal* **128**, 118–123 (1958).
85. J. C. Brandt, *Astrophysical Journal* **130**, 228–240 (July 1959).
86. J. W. Chamberlain and C. Sagan, *Planetary and Space Sciences* **2**, 157–164 (1960).
87. H. P. Gush and H. L. Buijs, "The near infrared spectrum of night airglow observed from high altitude," *Canadian Journal of Physics* **42**, 1037 (1964).
88. S. Chandra, E. I. Reed, and B. E. Troy, Jr., "Equatorial airglow and the ionospheric geomagnetic anomaly," *Journal of Geophysical Research* **78**, 4630–4639 (August 1973).
89. H. U. Sverdrup, M. Johnson, and R. Fleming, *The Oceans*, Prentice Hall, New York (1972).
90. R. D. Sharma, A. J. Ratkowski, R. L. Sundberg, J. W. Duff, L. S. Bernstein, P. K. Acharya, J. H. Gruninger, D. C. Robertson, and R. J. Healy, "Description of SHARC, the strategic high-altitude radiance code," GL-TR-89-0229, Environmental Research Papers No. 1036, Geophysics Laboratory, Hanscom Air Force Base, Bedford, MA (1989).
91. S. L. Valley, Ed., *Handbook of Geophysics and Space Environments*, Air Force Cambridge Research Laboratories, Hanscom Air Force Base, Bedford, MA (1965).
92. E. E. Bell, L. Eisner, J. Young, and R. A. Oetjen, *Journal of the Optical Society of America* **52**, 201–209 (February 1962).
93. H. Rose et al., *The Handbook of Albedo and Thermal Earthshine*, 190201-1-T, Environmental Research Institute of Michigan, Ann Arbor, MI (1973).
94. Y. P. Novoseltsev, "Spectral reflectivity of clouds," translation of "Spektralnaya Otrazhatelnaya Oblakov," Trudy Glavnogo, Geofizicheskoy Observatorii Uneni A. I. Voykova, NASA TT F-328, Washington, DC, No. 152, pp. 186–191 (1964).

95. K. Y. Kondratyev, Z. F. Mironova, and A. N. Otto, "Spectral albedo of natural surfaces," *Pure and Applied Geophysics* **59**(3), 207–216 (1964).
96. K. Y. Kondratyev, "Actinometry," translation of "Aktinometriya," *Gidrometeorologicheskoye izdatel'stvo*, Leningrad, NASA TT F-9712, Washington, DC (November 1965).
97. B. G. Orr, S. E. Dwamik, and L. M. Young, "Reflectance curves of soils, rocks, vegetation and pavement," 7746-RR, U.S. Army Engineer Research and Development Laboratories, Fort Belvoir, VA (April 22, 1963).
98. D. Anding, R. Kauth, and R. Turner, "Atmospheric effects on multispectral sensing of sea surface temperature from space," 26760-6-T, Willow Run Laboratories, Institute of Science and Technology, The University of Michigan, Ann Arbor, MI (December 1970).
99. I. Soloman, "Estimates of altitudes with specified probabilities of being above all clouds," Technical Report 159, Air Weather Service (MATS), U.S. Air Force (October 1961).
100. H. R. Condit, "The spectral reflectance of American soils," *Photogrammetric* **36**(9) (September 1970).
101. V. Leeman, D. Earing, R. Vincent, and S. Ladd, "The NASA earth resources spectral information system: a data compilation," NASA CR-31650-24-T, Institute of Science and Technology, The University of Michigan, Ann Arbor, MI (May 1971).
102. R. K. Vincent, "A thermal infrared ratio imaging method for mapping compositional variations among silicate rock types," PhD thesis, The University of Michigan, Ann Arbor, MI (1973).
103. D. Faulkner, R. Horvath, J. Ulrich, and E. Work, "Spectral and polarization characteristics of selected targets and backgrounds: instrumentation and measured results (3.14.0 μm)," 3692-2T, AD 886 916 L, Willow Run Laboratories, Institute of Science and Technology, The University of Michigan, Ann Arbor, MI (1971).
104. D. Earing, "Target signature analysis center: data compilation, second supplement," 8492-5-B, AD 819 712, Willow Run Laboratories, Institute of Science and Technology, The University of Michigan, Ann Arbor, MI (July 1967).
105. D. Carmer, "Target signature analysis center: data compilation, seventh supplement," 8492-35-B, AD 856 343, Willow Run Laboratories, Institute of Science and Technology, The University of Michigan, Ann Arbor, MI (January 1969).
106. E. D. McAlister, University of California, private communication (1951–52).
107. H. O. McMahon, "Thermal radiation from partially transparent reflecting bodies," *Journal of the Optical Society of America* **40**, 376–380 (June 1950).
108. G. C. Ewing, Ed., *Oceanography from Space*, WHOI Ref. No. 65-10, Woods Hole Oceanographic Institution, Woods Hole, MA (April 1965).
109. C. Cox and W. Munk, *Bulletin of the Scripps Institution of Oceanography* **6**, 401–488 (1956).
110. E. D. McAlister, "Application of infrared-optical techniques to oceanography," *Journal of the Optical Society of America* **52**, 607 (May 1962).
111. P. M. Saunders, "Radiance of sea and sky in the thermal infrared window 800–1200 cm^{-1} ," *Journal of the Optical Society of America* **58**(5) (May 1968).
112. C. Cox and W. Munk, "Measurement of the roughness of the sea surface from photographs of the sun's glitter," *Journal of the Optical Society of America* **44**(11) (November 1954).
113. G. C. Ewing and E. D. McAlister, *Science* **131**, 1374–1376 (May 6, 1960).
114. R. D. Watson et al., "Prediction of the Fraunhofer line detectivity of luminescent materials," in *Proc. Ninth Symp. Remote Sensing of Environment*, p. 1969, Environmental Research Institute of Michigan, Ann Arbor, MI (April 1974).
115. M. R. Specht, D. Needler, and N. L. Fritz, "New color film for water photography penetration," *Photogrammetric Engineering* **39**, 359 (April 1973).
116. V. E. Derr, *Remote Sensing of the Troposphere*, Catalog No. C55.602 T75, Stock No. C32001 1, U.S. Department of Commerce, NOAA (August 1972).
117. C. T. Wezernak, "The use of remote sensing in limnological studies," in *Proc. Ninth Symp. Remote Sensing of Environment*, p. 973, Environmental Research Institute of Michigan, Ann Arbor, MI (April 1974).
118. L. C. Gramms and W. C. Boyle, "Reflectance and transmittance characteristics of several selected green and blue-green unialgae," in *Proc. Seventh Symp. Remote Sensing of Environment*, pp. 1637, 1642, 1643, Environmental Research Institute of Michigan, Ann Arbor, MI (May 1971).

119. K. Kalle, "Zurn Problem der Meereswasserfarbe," *Ann. d. Hydrogr. und Mar. Meteor. Bd.* **66**, S1-13 (1938).
120. R. Horvath, W. L. Morgan, and R. Spellicy, "Measurements program for oil slick characteristics," 2766-7-F, pp. 17, 19, 21, 23, 24, 28, 30, 32, 891, 144-146, 154-156, Institute of Science and Technology, The University of Michigan, Ann Arbor, MI (1970).
121. R. Horvath, W. L. Morgan, and S. R. Stewart, "Optical remote sensing of oil slicks: signature analysis and systems evaluation," Willow Run Laboratories, Institute of Science and Technology, The University of Michigan, Ann Arbor, MI (October 1971).
122. S. G. Warren, "Optical constants of ice from the ultraviolet to the microwaves," *Applied Optics* **23**(8) (April 15, 1984).
123. J. Hallett, "How snow crystals grow," *American Scientist* **72**, 582 (November-December 1984).
124. S. Kulpa and E. Brown, *Propagation and Target/Background Characteristics*, Vol. 1, p. 19, U.S. Army Electronics Research and Development Command, Harry Diamond Laboratory (November 1979).
125. J. Dozier and S. Warren, "Effect of viewing angle on the infrared brightness of snow," *Water Resources Research* **18**, 1424 (October 1982).
126. H. W. O'Brien et al., "Red and near infrared spectral reflectance of snow," AD A007732, U.S. Army Cold Region Research and Engineering Laboratory, Hanover, NH (1975).
127. S. J. Bolsenga, "The spectral reflectances of fresh water ice and snow from 340 to 1100 nm," PhD Thesis, The University of Michigan, Ann Arbor, MI (1981).
128. P. S. Nobel, *Introduction to Biophysical Plant Physiology*, W. H. Freeman and Company, San Francisco (1974).
129. H. W. Gausman et al., "Leaf light reflectance, transmittance, absorptance, and optical and geometrical parameters for eleven plant genera with different leaf mesophyll arrangements," *Proc. Seventh Symp. Remote Sensing of Environment*, pp. 1606-1608, Environmental Research Institute of Michigan, Ann Arbor, MI (May 1971).
130. H. W. Gausman et al., "The leaf mesophylls of twenty crops, their light spectra, and optical and geometrical parameters," U.S.D.A. Technical Bulletin 1465, U.S. Department of Agriculture, Washington, DC (1973).
131. C. E. Olson, Jr., "Seasonal change in foliar reflectance of five broadleaved forest tree species," PhD Thesis, p. 76, The University of Michigan, Ann Arbor, MI (1969).
132. "Target signatures study interim report," Vol. V in *Catalog of Spectral Reflectance Data*, 5698-22-T(V), The University of Michigan, Ann Arbor, MI (October 1964).
133. C. D. Elvidge, "Thermal infrared reflectance of dry plant materials: 2.5-20.0 μm ," *Remote Sensing of the Environment* **26**, 265-285 (1988).
134. G. W. Carmichael, "The transformation of infrared background modulation noise into equivalent detector noise," *Infrared Physics* **7**, 111-115 (1967).
135. Y. Itakura et al., "Statistical properties of the background noise for the atmospheric windows in the intermediated infrared region," *Infrared Physics* **14**, 17-29 (1974).
136. P. Whittle, "On stationary processes in the plane," *Biometrika* **41**, 434-449 (1954).
137. B. Ben-Yosef et al., "Natural terrain in the infrared: measurements and modeling," *Proc. SPIE* **819**, 66-71 (1987).
138. W. I. Futterman et al., "Estimation of scene correlation lengths," *Proc. SPIE* **1486**, 127-140 (1991).
139. A. J. LaRocca and D. J. Witte, *Handbook of the Statistics of Various Terrain and Water (Ice) Backgrounds from Selected U.S. Locations*, 139900-1-X, Environmental Research Institute of Michigan, Ann Arbor, MI (January 1980).

CHAPTER 4

Radiometry

George J. Zissis

*Environmental Research Institute of Michigan
Ann Arbor, Michigan*

CONTENTS

4.1	Introduction	317
4.2	Radiometers	318
4.2.1	Responsivity of a Radiometer	319
4.2.2	Normalization	323
4.2.3	Reference Radiation Level	325
4.2.4	Calibration of Radiometers	326
4.2.5	Infrared Radiometry	331
4.3	Spectroradiometers	334
4.3.1	Prisms	335
4.3.2	Gratings	337
4.3.3	Prism and Grating Configurations and Instruments	337
4.4	Interferometers	347
4.4.1	Two-Beam Interferometers	347
4.4.2	Multiple-Beam Interferometers	354
4.5	Other Spectroscopic Instruments and Techniques	360
	References	362

4.1 INTRODUCTION

This chapter presents radiometry in terms of calibration and measurement. Figures of merit are covered for radiometric instruments, spectrally dispersing components (specifically prisms and diffraction gratings) are reviewed, and interferometers are treated.

Radiometry is the measurement of any radiometric quantity such as irradiance E or radiance L . Broad, tutorial treatments of this subject are available in many texts and reference books; see, for example, Refs. 1 through 6.

Measurement is the process by which a quantitative comparison is made between two or more states of a physical observable such as length, temperature, or spectral radiance. The performance of any measurement system can be defined as the measure of its usefulness to make unambiguous quantitative comparison. Thus, calibration is the special measurement process by which one determines all parameters significantly affecting an instrument's performance. The goal of calibration is to make the results of measurement as independent as possible of the particular measuring system employed. If an absolute calibration has been carried out, then the measured value is referred to internationally accepted standards. In the United States, this requires the use of standards with traceability to the National Institute of Standards and Technology (NIST, formerly the National Bureau of Standards, NBS).

Radiometric measurements of E or L are often made for the remote determination of I or L of some distant source that is not accessible for close-in measurement. Calibration determines, within experimental error, the quantitative relationship between system outputs and the incident radiation that is being measured. The system entrance aperture is selected to be the reference position for incident radiation, since incident radiation would affect any other measurement system similarly placed.

Determination of the significance of all possible system outputs requires a complete determination of three performance characteristics: *Responsivity*, R , the system gain, that is, the output/input; *Detectivity*, D , the system ability to measure a signal in relation to noise; and the *level of reference radiation*. Statements about the accuracy (precision and systematic error) of the results of calibration measurements must be provided as the basis for similar estimates of the accuracy of subsequent measurement results. Calculation of the desired radiometric quantity at some point remote to the instrument by use of the values determined at the radiometer aperture requires more information. For example, the determination of the radiant intensity of a star requires, in addition to measurement of the irradiance at the observatory radiometer aperture, knowledge of the effects of the intervening atmosphere and a value of the distance to the star.

For the most part, the challenge of radiometry stems from the desire to state completely the significance of all possible instrument outputs. Radiometers measure the magnitude of radiometric quantities within some region of the wavelength, time, space, polarization, coherence domains created by the dependency of the radiation on these parameters. Broadly, a radiometer is any apparatus for quantifying some property of incident radiation.

Names of radiometric devices traditionally have been created by combinations of the prefix and suffix words (or modifications of those words), shown in Table 4.1, to correspond with the design purposes of these instruments.

Table 4.1 Instrumentation Nomenclature

Prefix	Suffix
<i>Radio-</i> pertaining to any electromagnetic radiation	<i>-meter</i> numerical output, representing quantity of input
<i>Photo-</i> visible or photographic film spectral region	<i>-graph</i> output is recorded graphically
<i>Spectro-</i> spectrally dispersive	<i>-scope</i> seen directly by eye

Additional prefixes may be used to specify the spectral region of the band, for example, infrared radiometer, ultraviolet radiometer, and microwave radiometer. Photometer is used instead of photoradiometer, but with the additional implication that the relative spectral response is the same as that of the visibility curve. Other modifying terms may be used with these names. For example, "double-pass" refers to the use of an optical component twice by causing the radiation to pass through it twice in the same direction. A double-pass prism spectrometer disperses the radiation by sending radiation through a prism first forward and reflected back through once, then reflected from another mirror so as to enter forward and back through a second time. A "double monochromator" is composed of two monochromators used in series. The output of the first forms the input to the second.

If one seeks the variation of the amount of radiation as a function of any of the spatial, spectral, temporal, or other parameters, then an instrument is used that responds to a selectable narrow range of values of the parameters, and the total range of interest is scanned. The narrow range is specified by statement of the instrumental resolution. The specifications are not independent. One cannot, for example, arbitrarily reduce the wavelength interval. The limits are determined by the signal-to-noise ratio (SNR) attainable for the specific experiment.

The development of radiometers, spectroradiometers, and interferometers, together with their standards, has historically taken separate paths, largely divided by wavelength regions. Instrument development occurred for fields identified separately as photometry, optical pyrometry, spectroscopy, interferometry, and radiometry. The procedures and equipment for calibration also evolved within these separate technical camps. In our treatment, commonality and unification is stressed within the broadest meaning of radiometry.

4.2 RADIOMETERS

Radiometers are radiation-measuring instruments having substantially equal spectral response to radiation over a relatively wide band of wavelengths. Radiometers respond to the difference between source radiation incident on the radiometer detector and a radiation reference level. All radiometers and radiometric measuring systems consist of at least three essential components (Fig. 4.1):

- *Optics* collect the radiation through the entrance aperture of area A , disperse or spectrally filter the radiation, and direct it onto a field stop of area a .
- *Detector(s)* transduce the radiation on the field stop to a signal, usually an electrical voltage or current, of magnitude V or I .
- *Electronics* process, display, and/or record the signal.

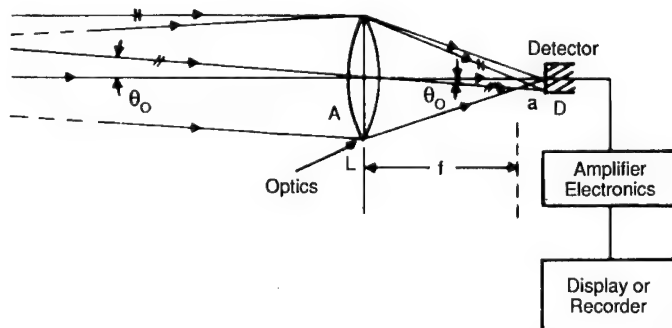
The radiometric performance is characterized by:

- *responsivity, R* : the output signal per input of incident radiation
- *detectivity, D* : the reciprocal of the noise equivalent input (incident radiation), or the responsivity divided by the noise voltage, i.e., the rms noise fluctuation of the output
- *reference radiation level*: level of incident radiation corresponding to a zero reading on the output scale of the instrument.

4.2.1 Responsivity of a Radiometer

Of the three defined characteristics, responsivity is used most often. It is always involved in transforming an output reading into the corresponding value of incident radiation, or input. Thus, a precise determination is valuable. In contrast, it is often sufficient to know the rough order of the detectivity if the measurements to be made are so far above the instrument noise level that noise considerations are not involved. Similarly, a rough measure of the reference radiation is often sufficient if a truly negligible amount of radiation is represented by an output reading of zero. These last two characteristics are easily overlooked, however, in those rather rare instances when they may be highly significant factors in the interpretation of instrument output. For this reason, they should always be checked.

The responsivity of a detector is defined as the change in output signal, ΔV , divided by the change in incident flux, $\Delta \Phi$, on the detector. For a radiometer as a complete system, it is useful to extend the meaning of responsivity to include either the change in output signal divided by the change in irradiance,



L = Collecting Optics Which Also Form a Circular Aperture Stop of Area A

D = Detector Element Which Also Forms a Circular Field Stop of Area a

Ω = Solid Angle in Steradians of Conical Field Corresponding to a Half-Angle, θ_0 ,

Measured in Radians ($\Omega = 2\pi (1 - \cos \theta_0) \approx \pi \theta_0^2 = a/f^2$)

f = Focal Length of Collecting Optics

Fig. 4.1 Simple form of basic radiometer.

ΔE , at the entrance aperture of the radiometer, or the change in output signal divided by the change in radiance, ΔL . Thus, three forms of responsivity can be stated for a radiometer:

$$\begin{aligned} R_\Phi &= \Delta V / \Delta \Phi , \\ R_E &= \Delta V / \Delta E , \\ R_L &= \Delta V / \Delta L . \end{aligned} \quad (4.1)$$

Similarly, while the detectivity of a detector is defined as $D = R/V_n$, where V_n is the rms noise fluctuation of the detector output, radiometer detectivity can be stated in three forms.

The output voltage of a simple radiometer as a function of the irradiance E at the radiometer aperture is illustrated in Fig. 4.2. (The simplest radiometer is an isolated detector element, which therefore is simultaneously the aperture stop, field stop, entrance pupil, exit pupil, entrance window, and exit window. The output signal value is indicated directly by an electrical current meter. Ordinary photographic exposure meters are of this type.) The equation for the function is

$$V = R_E(E - E_0) + V_n , \quad (4.2)$$

where R_E is as defined before and E_0 is the reference irradiance level. The value of E_0 can be determined by use of an external calibration source that uniformly irradiates the instrument. The source is adjusted until the radiometer output reads zero. The value of E at the radiometer aperture due to this adjustment is calculated to establish the value of E_0 , provided the noise voltage is negligibly small. Frequently, the values of E to be measured are quite large so that

$$E \gg E_0$$

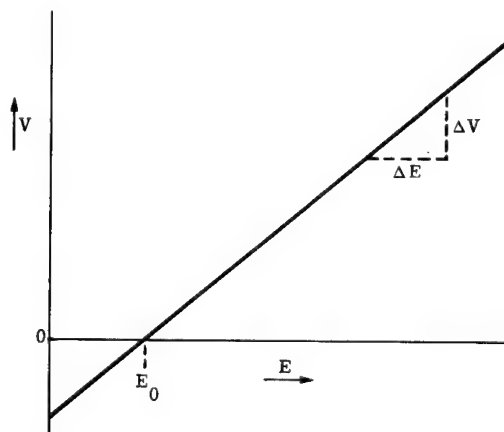


Fig. 4.2 Radiometer response to input irradiance.

and

$$V \gg V_n .$$

Then the relation may be approximated well enough by

$$V = R_E E . \quad (4.3)$$

A similar relation can be derived for R_L under similar circumstances with the use of uniform radiance sources.

Since radiance and irradiance are functions of wavelength, location, direction, polarization, coherence, and time, the radiometer responsivity must also be a function of these parameters. The spatial dependency defines the field of view (FOV); the spectral dependency defines the spectral response; and the dependency on time defines the fluctuation-frequency response or temporal-frequency bandwidth. Radiometer designers aim at making these dependencies mutually independent factors so that the responsivity is the product of several relative responsivity factors and a responsivity normalization constant, ${}^{\circ}R$. Thus,

$$R = {}^{\circ}R r_1(\lambda) r_2(t) r_3(x, y) r_4(\theta, \phi) \dots . \quad (4.4)$$

In the idealized case of a "perfect radiometer," the responsivity is zero outside the geometrical bounds established by a solid angle Ω and is constant within these bounds. Similarly,

$$r_1(\lambda) = \begin{cases} 1 & \text{for } \lambda_1 < \lambda < \lambda_2 , \\ 0 & \text{for } \lambda \text{ outside of } \lambda_2 - \lambda_1 , \end{cases} \quad (4.5)$$

and, with f for the temporal frequency,

$$r_2(f) = \begin{cases} 1 & \text{for } f_1 < f < f_2 \\ 0 & \text{for all other } f . \end{cases} \quad (4.6)$$

The radiance spectral responsivity, $R_L(\lambda)$, of an ideal radiometer is shown in Fig. 4.3. The sought-for value of L between wavelength λ_1 and λ_2 is equal to the shaded area under the curve for $L_\lambda(\lambda)$ in Fig. 4.4. The voltage output of the radiometer is equal to the area under the product curve shown in Fig. 4.5. In equation form, this is

$$V = \int R_L(\lambda) L_\lambda(\lambda) d\lambda \quad (4.7)$$

over all wavelengths. Since, for an ideal radiometer, the spectral responsivity is a constant between λ_1 and λ_2 , and is otherwise zero, then

$$V = {}^{\circ}R_L \int L_\lambda d\lambda , \quad (4.8)$$

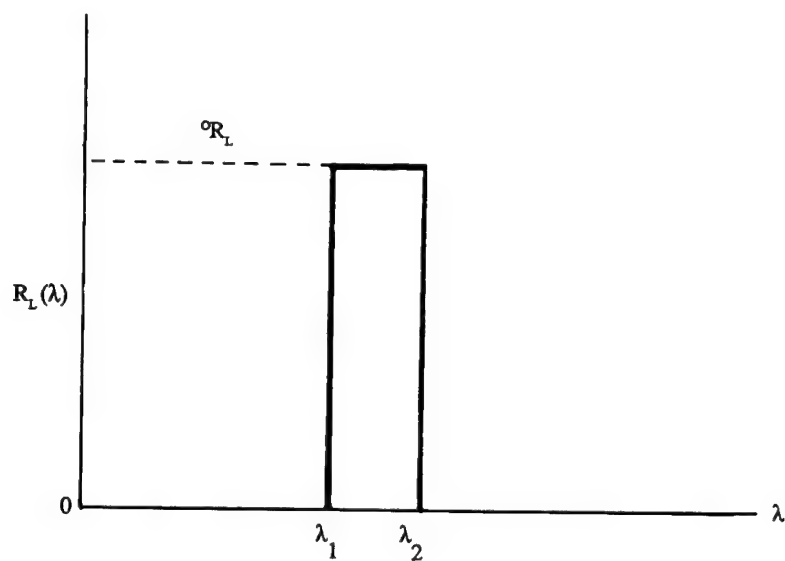


Fig. 4.3 Ideal radiometer spectral responsivity.

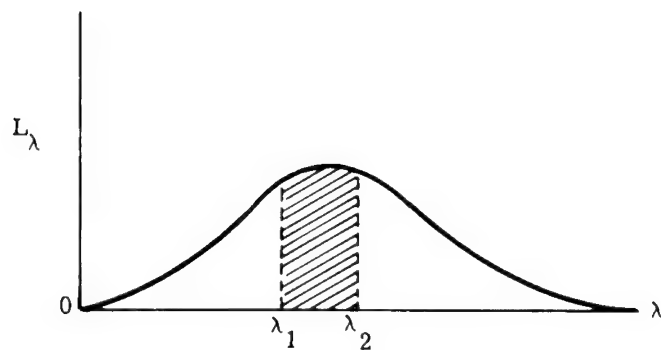


Fig. 4.4 A smoothly varying spectral radiance.

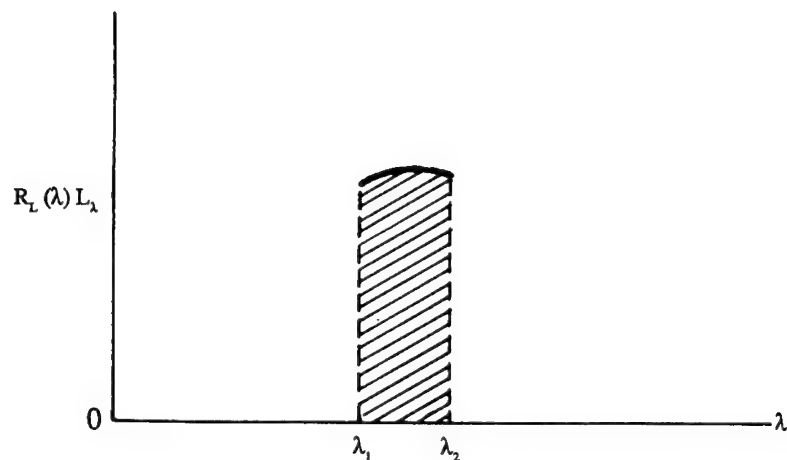


Fig. 4.5 The product of spectral radiance and spectral responsivity.

where the integration is from λ_1 to λ_2 . The relationships between the three forms of responsivity are obtainable from the relation between Φ , E , and L . Thus,

$$R_\Phi = R_E/A = R_L/[\text{Th}] , \quad (4.9)$$

where

$$\text{Th} = \int \cos\theta \, d\omega \, dA. \quad (4.10)$$

("Th" is often called the instrumental "throughput.") The $\cos\theta$ factor arises from the differential definition of radiance. In this example, if L is defined to be constant in the $\Delta\lambda$, then

$$V = {}^\circ R \, L . \quad (4.11)$$

Most radiometers are not ideal in spectral responsivity. Yet a direct relation between voltage output and the value of radiance between two wavelengths is required. With real radiometers, $R(\lambda)$ is measured as a property of the radiometer and is used in the process of normalization, discussed next.

4.2.2 Normalization

In Fig. 4.6 a radiometer spectral responsivity is shown as triangular in shape. In Fig. 4.7 the unknown spectral radiance L_λ of the source is shown as a smooth, slowly changing function of λ . The value of V , which the actual radiometer would exhibit, is equal to the area under the product curve in Fig. 4.8. The product curve is not quite triangular in shape because L_λ is not quite constant. The equivalent, ideal radiometer spectral responsivity, which has the same maximum responsivity as the actual radiometer, is shown as a dashed rectangle in Fig. 4.6. The rectangle has the same area as the triangle. That ideal radiometer would produce a product curve as shown by the dashed line in Fig. 4.8. The area under the dashed product curve is equal to the value of V , which an ideal radiometer would provide. Notice that these two product curve areas

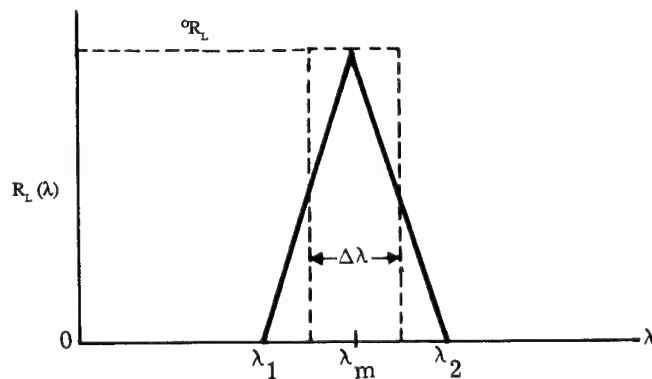


Fig. 4.6 Triangular spectral responsivity.

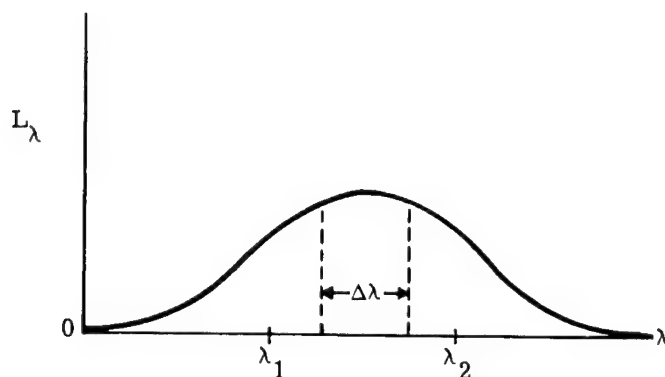


Fig. 4.7 Smoothly varying spectral radiance.

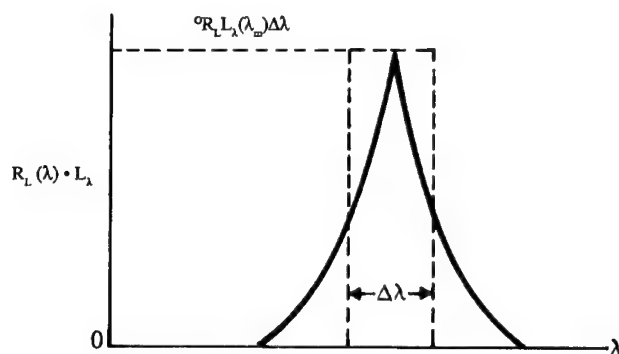


Fig. 4.8 The product of triangular spectral responsivity and spectral radiance.

are approximately equal and would be exactly equal if L_λ were truly constant.

The determination of the equivalent ideal radiometer having the same maximum or peak spectral responsivity as the real radiometer is called *normalization of the radiometer response to the peak*. Other equivalent ideal radiometers can be utilized in the normalization process. One can easily determine the peak spectral responsivity of the ideal radiometer whose spectral bandwidth is limited by the wavelengths for which the actual radiometer spectral response has fallen to one-half of its maximum value, i.e.,

$${}^{\text{IDEAL}}R_L(\Delta\lambda) = \int R_L(\lambda) d\lambda / (\Delta\lambda \text{ for half response}) . \quad (4.12)$$

The values would then be stated as that radiance within the half-value spectral responsivity points.

Normalization to specify the equivalent ideal radiometer responsivity for the other parameters, such as FOV and fluctuation frequency bandpass, follows analogous reasoning. Likewise, symmetry of the responsivity for these other parameters permits good accuracy for the linear variation of radiance with these other parameters for the same reasons.

A much more complete and detailed treatment of the general process of normalization has been given by Nicodemus.⁷ The applications to radiometry have received extensive review in the NBS series of reports edited by Nicodemus.⁸

4.2.3 Reference Radiation Level

Either absolute or relative measurements of infrared radiation levels may be made, depending on the design of the radiometer. Absolute measurements of radiation levels require a known reference level. The detector itself or a radiation chopping system can be used to provide the reference radiation level. For absolute measurements, the chopping system is usually preferred.

Radiometers that measure the difference in radiation from two neighboring spatial positions provide relative information only, because no stationary reference level exists. Radiometers used to compare any element of a large area to the average radiation associated with the entire area can supply an absolute measurement, provided the average is known absolutely. Similarly, in the time domain, the power level due to radiation at one instant may be compared to that of a previous instant or to an average associated with all past measurements.

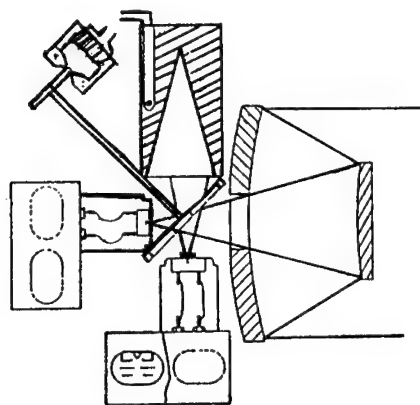
A radiometer that uses the detector as a radiation reference level is often referred to as a dc radiometer. This terminology is used for instruments that measure the change in the dc electrical properties of a thermoelectric or bolometric infrared detector. These radiometers may be subject to drift because the reference level is determined by the temperature of the detector; however, drift can often be reduced to acceptable levels by accurate and stable detector and electronics temperature control.

Chopped or ac radiometers provide an ac output from the detector for signal processing and are often convenient for absolute radiation measurements. The electrical output of such radiometers is proportional to the difference between the amount of radiation falling on the detector from the external source within the field of view and that from a blackened chopper blade or a controlled internal reference source. In the latter case, a chopper mirror may be used to direct radiation alternately from the external source and the reference "blackbody" onto the detector.

The characteristics of three different types of absolute radiometers, including the form of reference level they employ, are listed in Table 4.2. Figure 4.9 shows radiometers capable of using either a blackened chopper, so the detector alternately receives radiation from the external source image and the blackened chopper, or a mirrored chopper.⁹ The temperature and emissivity of the blackened chopper determine the reference radiation level. At wavelengths out to about 1 μm , a very stable reference level is obtained by ensuring that the chopper has a uniformly coated black surface. To about 3 μm , the blackened chopper temperature is not usually a critical factor because at ambient temperatures there is little radiation in this region from a blackbody or a graybody.

Table 4.2 Three Types of Absolute Radiometers (from Ref. 9)

Type	Signal Out; Detector Type	Measures Difference of:
dc	EMF from compensated dc thermopile	Source radiation and thermopile radiation
ac with a blackened chopper	ac from compensated thermistor bolometer bridge	Source radiation and chopper radiation
ac with a mirrored chopper	ac from compensated thermistor bolometer bridge	Source radiation and reflected blackbody radiation



Radiometer Performance Specifications
for Detector Size of: 1.5x1.5mm Active Area
Field of View 0.5x0.5 Degrees
System Bandwidth, CPS 10.0 1.0 0.1 CPS
System Time Constant 0.016 0.16 1.6 Sec.
Measured Noise (Over all System) Microvolts
Peak to Peak 6.0 2.0 0.6

Radiation Input in Watts/CM² Equal to
Peak to Peak Noise 4.6×10^{-9}
 1.5×10^{-9}
 4.6×10^{-10}

Black Body Temperature
Difference Equivalent
to Peak to Peak Noise 0.43° 0.14° 0.043° DEG. C
(Barnes 4" Radiometer Performance)

Schematic of Mirror Chopper ac Infrared Radiometer
(Barnes 4" OptiTherm Radiometer)

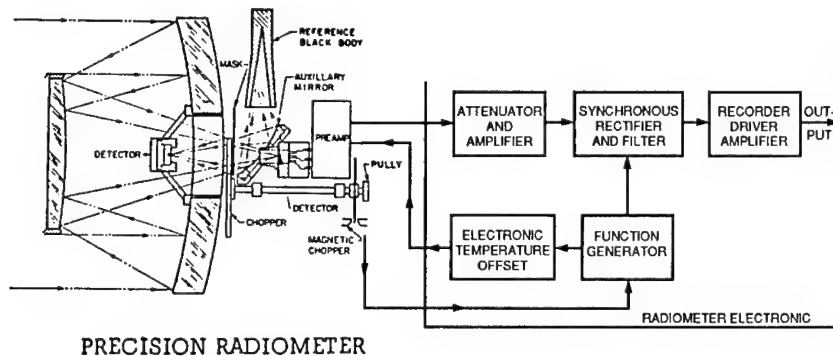


Fig. 4.9 Absolute radiometers—1950s and 1960s (Ref. 9).

At wavelengths longer than about 3 μm , however, the effects of variations in chopper temperature and emissivity become a serious consideration. Emissivity effects can be minimized by using a highly polished chopper blade, i.e., a chopper mirror. However, incident radiation reflected from the surrounding area to the detector by the polished chopper must be controlled. Suitable and realized configurations are shown in Fig. 4.9. The internal reference blackbody is often placed with a 45-deg chopper mirror so that radiation from the internal reference and external source is alternated onto the detector. This not only provides a stable source of reference radiation but also an adjustable one when temperature controls are provided for changing the reference source temperature. In addition, if the reference source is adjustable, its radiance can be matched to the source radiance and the detector can then be used as a sensitive null or quantitative error detector.

4.2.4 Calibration of Radiometers

In this discussion, the assumption has been made that a standard source of radiance, a high-emissivity graybody traceable to NIST, is used for radiometric calibration and accurate measurement of R . Such calibration sources are de-

scribed in Chapter 2 of this volume. They must possess the necessary stability for consistent quantification from time to time by one observer and from observer to observer. For practical reasons, they must be reasonably accessible and easily replicated for use by others.

However, two approaches exist for providing infrared radiation standardization. One is the standard source; the other is a standard receiver. Clearly, if the primary standard is a source, one can calibrate a receiver and use that as a secondary, transfer standard to calibrate other sources. If, instead, the primary standard is a receiver, one can specify the properties of a source to be used as a secondary standard to calibrate other receivers.

One approach to standards for infrared radiometric calibrations by attainment of a standard receiver was taken by scientists at the National Physical Laboratory (NPL) in England and, more recently, at NIST. This approach was to make a "black" detector with extremely stable response characteristics and to use it in a nulling mode—specifically, with electrical heating introduced to balance the heat due to absorption of incoming radiation. The resulting configuration, often called an *absolute radiometer* or *electrically calibrated radiometer* (ECR), has been used by NPL with Moll thermopiles as transfer or working standards. The original Guild drift radiometer¹⁰ was extended by Gillham^{11–13} to higher levels of precision. The NPL transfer standards and spectral responsivity scales as of 1989 were reviewed briefly by Freeman and Nettleton.¹⁴

The U.S. work along these lines (at the NBS from 1968 to 1971) was described by Phelan and Cook¹⁵ and by Geist and Blevin.¹⁶ Following the attainment of an electrically calibrated pyroelectric radiometer (ECPR), the status in the mid-1970s was described by Karl Kessler, then chief of the NBS Optical Physics Division, at the June 1976 meeting of the Council for Optical Measurements (CORM) as follows¹⁷:

With these devices [ECPRs], NBS now has the capability of 1% accuracy in the measurement of radiant power from 0.1 to 100 mW over the wavelength range from 250 nm to 10 micrometers. The ECPR has recently been used to run an intercomparison between itself, the C-series calorimeter used for laser measurements at NBS Boulder Laboratories, the electrically calibrated thermopile radiometer at the West German national standards lab [PTB], and the electrically calibrated solar radiometer at the World Radiation Center in Davos, Switzerland. In all cases the virtually independent measurement communities represented by these installations were found to be in very good agreement with each other. . . . ECPRs are now commercially available. . . .

Further details were given in the mid-1970s by Zalewski¹⁸ and Zalewski and Linda.¹⁹ For shorter wavelengths, a silicon photodiode standard detector for absolute calibration was realized²⁰ in 1980. Finally, in 1989, Hengstberger presented a very complete treatment of electrically calibrated thermal detectors.²¹ The resources for calibration available in the United States from NIST are summarized in the Users Guide²² under the section on Optical Radiation Measurements. NIST began implementing the International Temperature Scale of 1990 for optical radiometry on July 1, 1990. This slightly changes the quoted values and uncertainties for some of the NIST calibrations from those given in Ref. 22. Details are available from the NIST Radiometric Physics Division in Gaithersburg, Maryland.

Methods of calibration using standard sources are usefully categorized into two groups: those in which the radiometer field stop is partially illuminated

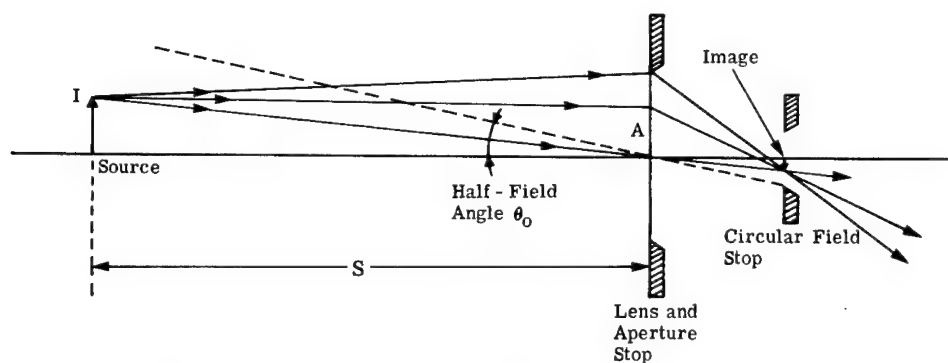


Fig. 4.10 Distant-small-source configuration. The source image is entirely within the field stop and $R_E \equiv V/E = VS^2/I$.

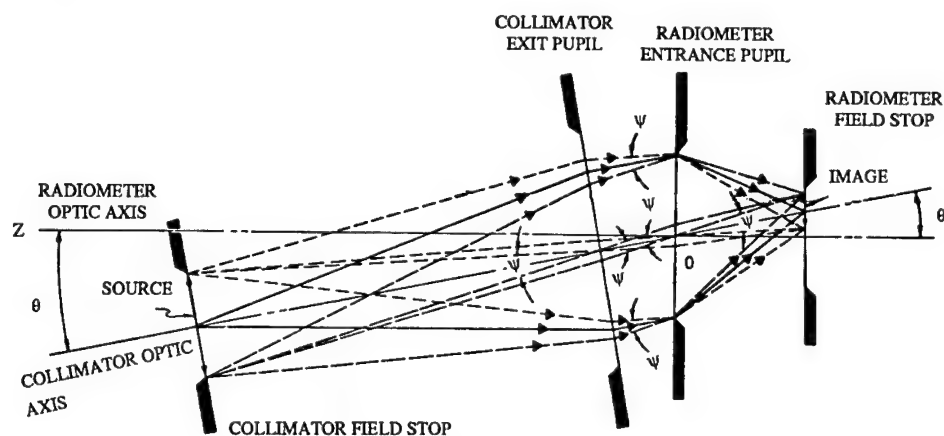


Fig. 4.11 Geometry for mapping the field with a collimator, where O is the center of the radiometer entrance pupil, θ is the angle between the optic axes, which intersect at O , and ψ is the angle between the extreme rays in the collimated beam and the angle subtended at O by the image of the source $\psi \ll \theta$ (the relative dimensions are exaggerated to emphasize the angles).

by the calibration source, and those in which the stop is totally filled with uniform calibration radiation. The first may be achieved by a *distant point (small) source*, illustrated in Fig. 4.10, or by a collimator with suitable magnification and a small source (Fig. 4.11). The latter can be realized with a so-called "extended" source, either *distant* (Fig. 4.12) or *close* (at the entrance aperture in Fig. 4.13), by a collimator (with different magnifications) or by proper placement of a small source very close to the entrance aperture (the so-called "Jones method" of calibration shown in Fig. 4.14).

Clearly, a more accurate and more easily made measurement can be realized if the radiometer is calibrated directly in the responsivity form matched to the quantity to be measured. If one wants to measure irradiance at the entrance aperture using the value of the power responsivity, then the effective aperture area must be measured with a precision at least as great as all other parts of the measurement procedure. Unexpected errors may creep in here. This is even more true for radiance measurements made with a power responsivity calibration, for now one must determine the throughput of the radiometer, a

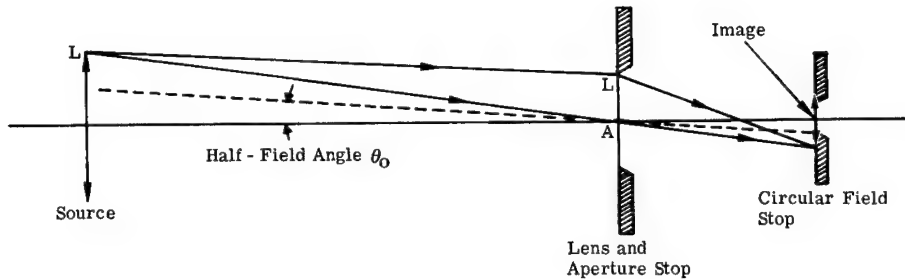


Fig. 4.12 Distant-extended-source configuration. The source image completely fills the circular field stop and $R_L \equiv V/L$.

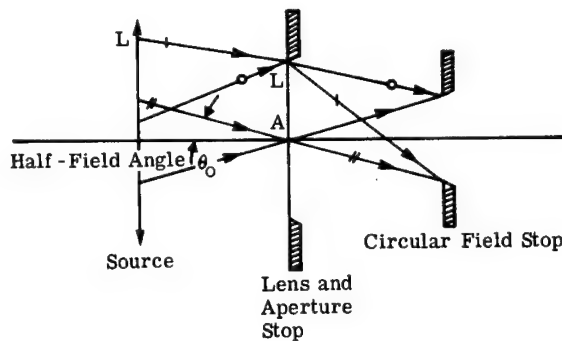


Fig. 4.13 Near-extended-source configuration. The source completely fills both the aperture and the field, but the image of the source is not at the field stop. The rays that meet at the field stop are not parallel as they leave the source, $R_L \equiv V/L$.

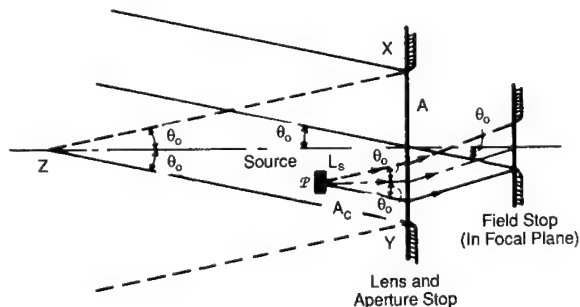


Fig. 4.14 Near-small-source (Jones method) calibration. The source with area A_c and radiance L_s is completely within the region bounded by XZ and YZ , each of which makes an angle, θ_0 , with the optical axis, where θ_0 is the half-field angle. ϕ is any arbitrary point of the source. Rays from any such point, ϕ , within a cone of half-angle θ_0 , will uniformly irradiate the circular field stop as shown.

difficult and unnecessary complication. For this reason, the following is a good general rule: Always carry out a calibration under conditions that reproduce as completely as possible the situation expected when measurements based on that calibration are made. On the other hand, for maximum versatility and as a check on consistency, it is important to conduct additional calibrations covering as wide a range of variation of as many parameters as possible. Thus,

the calibration should be in terms of E if measurements of E are to be made with the radiometer. Using the distant small (point) source method one would obtain, for an ideal radiometer,

Distant point source:

$$(\Delta V S^2)/\Delta I = \Delta V/\Delta E = R_E \quad [V/(W \text{ cm}^{-2})] , \quad (4.13)$$

where S is the distance from the source to the radiometer aperture area A . Here atmospheric attenuation has been neglected, i.e., 100% transmission is assumed, an assumption that is not always valid (see Fig. 4.15).

Similarly, with a distant extended source of radiance L ,

Distant extended source:

$$\Delta V/\Delta L = R_E([Th]/A) = R_L \quad [V/(W \text{ cm}^{-2} \text{ sr}^{-1})] \quad (4.14)$$

where Th is the throughput of the radiometer.

If this method were used to obtain R_E , then, besides accounting for the intervening atmosphere (ΔL in the above equation is at the entrance aperture), one must also determine the angular FOV of the radiometer. However, the distant extended source method gives a radiance calibration directly. When the extended source is placed at the radiometer aperture, while the source is not imaged on the field stop, the adjustment for atmospheric attenuation is minimized and R_L is obtained directly.

A near, not imaged, small calibration source of area A_c and radiance L_c can be used (see Fig. 4.14) to establish R_L by the relation

$$R_L = (\Delta V/\Delta L)(A/A_c) . \quad (4.15)$$

Radiometer linearity of response must be assessed in calibration. Since calibration must be done at different levels of radiation input, the classes listed above should be examined for specific methods. For example, in the distant-small-source configuration one may increase the source size, as long as it still fits entirely within the radiometer FOV. Or the distance may be changed to use the inverse square law as long as the source distance changes do not create unacceptable levels of interaction with the spatial responsivity variations or

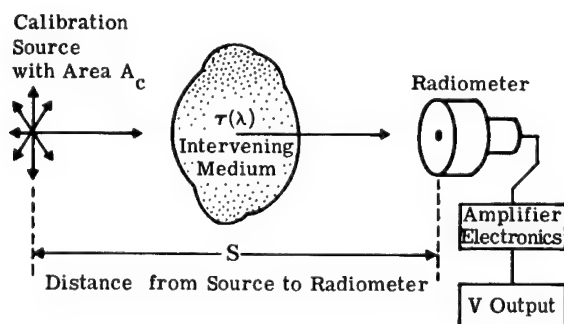


Fig. 4.15 Calibration of radiometers.

problems with proper focusing. The source temperature may be varied in any calibration configuration as long as the interactions of changes in the spectral distribution of the radiation with the radiometer spectral responsivity are manageable. Special attenuators have been made and used, especially with collimators. Again, the neutrality of such devices must be carefully assessed. Any changes in spectral distribution or polarization of the radiation must be determined and taken into account.

Calibration is summarized and compared to measurement in Table 4.3. The following equations are used in conjunction with Table 4.3:

$${}^{\circ}R_E = \frac{V_c}{A_c S^{-2} \int_0^{\infty} r_E(\lambda) \tau(\lambda) \epsilon_c(\lambda) L_{\lambda}^{BB}(\lambda, T_c) d\lambda}, \quad (4.16)$$

$${}^{\circ}I = \frac{V}{{}^{\circ}R_E S^{-2} \int_{\text{All}\lambda} r_E(\lambda) \tau(\lambda) i_{\lambda}(\lambda) d\lambda} \quad (4.17)$$

and

$$I_{\lambda}(\lambda) = {}^{\circ}I i_{\lambda}(\lambda),$$

$${}^{\circ}R_L = \frac{V_c}{\int_{\text{All}\lambda} r_L(\lambda) \tau(\lambda) \epsilon_c(\lambda) L_{\lambda}^{BB}(\lambda, T_c) d\lambda}, \quad (4.18)$$

$${}^{\circ}L = \frac{V}{{}^{\circ}R_L \int_{\text{All}\lambda} r_L(\lambda) \tau(\lambda) l_{\lambda}(\lambda) d\lambda}. \quad (4.19)$$

4.2.5 Infrared Radiometry

Classical. The development of infrared radiometry is revealed in a series of papers by Barr²³⁻²⁵ beginning with the discovery of the infrared spectral region by Sir Fredrick William Herschel in the spring of 1800. His "relative infrared radiometry" was done with thermometers with blackened bulbs, and was followed in 1830 by Macedonio Melloni who modified Nobili's thermopile (itself derived from Seebeck's thermocouple) into a radiation-measuring electric thermometer. By 1880 Samuel Pierpont Langley had obtained measurements of temperature differences as small as 1×10^{-5} °C. He also measured infrared solar spectra to 2.8 μm . Charles Vernon Boys made refinements using a thermocouple and galvanometer to detect temperature differences of 5×10^{-7} °C in connection with measurements of radiation from the moon and stars. In an April 1916 meeting of the American Physical Society, Samuel O. Hoffman presented a paper,²⁶ published in 1919, in which he reported on thermopile galvanometer systems used with 35.6-mm-diam mirrors to "detect" men at

Table 4.3 Calibration-Measurement Taxonomy

Calibration		Measurement	
Distant small (point) source	<i>Given</i> $\tau(\lambda)$, intervening medium transmittance S , source distance $r_E(\lambda)$, relative spectral irradiance responsivity $\epsilon_c(\lambda)$, source spectral emissivity A_c , source area, which is < projected field of view T_c , temperature of calibration source c .	<i>Case 1: Given</i> $\tau(\lambda)$ S $r_E(\lambda)$ and ${}^\circ R_E$	<i>Case 2: Given</i> $\tau(\lambda)$ S $r_E(\lambda)$ and ${}^\circ R_E$ $i_\lambda(\lambda, T)$, source relative spectral radiant intensity
	<i>Obtain</i> V_c , radiometer output	<i>Obtain</i> V , output	<i>Obtain</i> V , output
	<i>Calculate</i> ${}^\circ R_E$, irradiance responsivity normalization constant from use of Eq. (4.16)	<i>Can Calculate</i> I' , apparent radiant intensity from: $I' = ES^2$ where E is irradiance at radiometer aperture, $E = V/{}^\circ R_E$	<i>Can Calculate</i> ${}^\circ I$, spectral radiant intensity normalization constant from Eq. (4.17) and thus $I_\lambda(\lambda) = {}^\circ I i_\lambda(\lambda)$
Distant extended source	<i>Given</i> $\tau(\lambda)$, intervening medium transmittance S , source distance $r_L(\lambda)$, relative spectral radiance responsivity $\epsilon_c(\lambda)$, calibration source spectral emissivity A_c , calibration source area > projected IFOV T_c , calibration source temperature	<i>Case 1: Given</i> $\tau(\lambda)$ S $r_L(\lambda)$ and ${}^\circ R_L$	<i>Case 2: Given</i> $\tau(\lambda)$ S $r_L(\lambda)$ and ${}^\circ R_L$ 4) $l_\lambda(\lambda)$, source relative spectral radiance
	<i>Obtain</i> V_c , radiometer output	<i>Obtain</i> V , output	<i>Obtain</i> V , output
	<i>Calculate</i> ${}^\circ R_L$, radiance responsivity normalization constant from use of Eq. (4.18)	<i>Can Calculate</i> L' , apparent radiance at radiometer aperture from $L' = V/{}^\circ R_L$	<i>Can Calculate</i> ${}^\circ L$, spectral radiance normalization constant from Eq. (4.19) and thus source spectral radiance $L_\lambda(\lambda) = {}^\circ L l_\lambda(\lambda)$

120 m and 100-cm-diam mirrors to pick up and follow a Curtis JN4H aircraft from 4000 ft to over a one-mile range.

Radiometry continued to develop, especially as new infrared detectors, in particular photodetectors, emerged. In the late 1930s, E. Kutzcher and others at Electro-Acoustic Kommanditgesellschaft (ELAC) in Kiel, Germany, made lead sulfide and, later, lead telluride photoconductive cells. With appropriate

Table 4.4 Airborne Radiation Thermometer Performance (from Ref. 28)

	Initial Design	Actual Performance
Thermistor detector		
Area	1 mm × 1 mm	2 mm × 2 mm
Time constant	8 ms	2.5 ms
NEP	1.25×10^{-9}	8×10^{-9}
Optics		
Diameter	2 in. (50 mm)	3 in.
Focal length	2 in.	2 in.
Field of view	20 mr × 20 mr	40 mr × 40 mr
Chopping rate	20 Hz	20 Hz
Reference bandwidth	30 Hz	100 Hz
NEFD	2.8×10^{-10} W/ cm ²	6.6×10^{-10} W/cm ²
NET	0.02 °C	0.01 °C

cooling, the response to 500 K blackbody radiation, at a SNR equal to one, was reported²⁷ as 1×10^{-11} W/cm². Still, thermal detectors, especially thermistor bolometers (thermistors) with their broad, uniform spectral coverage without cooling, were used extensively in radiometers. A classical design was available in the 1950s from Barnes Engineering Company (BEC), which incorporated the major features needed for absolute radiometry.⁹ One variation, shown earlier in Fig. 4.9, was called the "precision radiometer." Wormser developed yet another radiometer design at BEC in 1959 (Ref. 28, p. 381). Later this was built by BEC as an airborne radiation thermometer for the U.S. Navy Hydrographic Office. Table 4.4 shows the results as summarized by Wormser (Ref. 28, p. 392).

Contemporary. The past 25 years have seen the development of many sophisticated and complex radiometric instruments. These include imaging (spatially scanning) radiometers, precision and ultrastable radiometers, and imaging spectroradiometers. Examples are the early Barnes thermograph (an object-plane scanning system using their standard radiometric designs to create quantitative spatial distributions of radiance in selected infrared bands)⁹ and the AGA (now AGEMA) Thermovision[™] systems.²⁹ Other systems from the 1970s include several thermal imagers by Inframetrics, the Hughes A/C Probe[™] series, thermal imaging systems from FLIR Systems, and many more described in Ref. 29, including airborne and space-based scanning radiometers deployed on NASA's LANDSATs and the NOAA satellites.

Radiometric laboratory, field, and industrial instruments and facilities continue to be developed by many companies throughout the world. The products include:

- Specially designed "laser power meters" and calorimeters. For example, EG&G Gamma Scientific supplies radiometers to measure pulses from 1 ns to 1 ms; Laser Precision Corporation has a family of laser and thermal radiometers including the electrically calibrated pyroelectric radiometer developed with the NBS in 1981; and Scientech Inc. offers products covering power ranges from 1 mW to 5 kW cw.
- Dual-band radiometers. The techniques for this type of radiometer are reviewed in depth by DeWitt and Nutter³⁰ and summarized by Barron.³¹ In the United Kingdom, GEC Avionics offers a dual-waveband

thermal imaging system as a full function imaging radiometer. An airborne IR imaging radiometer designed for field use is well documented in a 1989 paper by McGlynn.³²

- Complete radiometric sensor calibration systems. For example, consider the Boeing Infrared Sensor (BIRS) Calibration Facility,³³ the Low Background Infrared Calibration Facility (LBIR) at NIST,³⁴ and similar facilities, although photometric, using the large-aperture sources of NASA and CNES as major components.³⁵

Precision instruments and techniques have also advanced, as seen, for example, in the products of Optronics Laboratories, especially as derived from NBS UV work, and of Electro Optical Industries, such as the precision null radiometer, model 467A. Among the more noteworthy advances in precision radiometry are two space-borne systems: one is the Earth Radiation Budget Experiment (ERBE) involving three separate satellites as described by Tira, Mahan, and Lee³⁶ and many others³⁷; the other is the radiometric package on NASA's Cosmic Background Explorer (COBE).³⁸ Others are being planned.³⁷

4.3 SPECTRORADIOMETERS

Spectroradiometers are radiometers designed specifically to allow determination of the wavelength distribution of radiation. This category of measurement systems usually consists of those in which separation of the radiation into its spectral components, or dispersion, is accomplished by the use of an optical element possessing a known functional dependence on wavelength, specifically prisms and diffraction gratings. Interferometers can also provide spectral dispersion as is discussed later.

The essential components of any prism or grating spectroradiometer are the same as those of any radiometer with the addition of the following:

1. an entrance slit, which usually acts as the field stop of the collecting optics
2. a collimator, with lenses or mirrors, with the entrance slit at its focus
3. a dispersing element, prism, or grating
4. a focusing element, which produces an image of the entrance slit from the parallel beam at each wavelength so that these images are dispersed linearly to form the familiar spectrum
5. one or more exit slits to select the radiation in any desired region of the spectrum and allow it to pass to the detector.

A spectroradiometer can be said to be a radiometer with a monochromator located between the collecting optics and the detector. Figure 4.16 shows a schematic for any simple prism or grating spectroradiometer. Radiometers that rapidly sequence through a set of narrow filters can also be called spectroradiometers. The same result can be obtained by means of a continuously varying filter (CVF). Either can be realized by the rotation of a filter wheel. If the speed of rotation is sufficiently high, the dwell time for any one filter can approach the response time of the unfiltered radiometer. In any case, the response time should be determined under dynamic rather than static conditions.

An example is the infrared spectral radiometer covering the spectral range of 3 to 23 μm installed on the 1.6-m telescope at the DARPA Maui Optical Station (AMOS), Mt. Haleakala, Maui, Hawaii.³⁹ CVFs are used to cover the

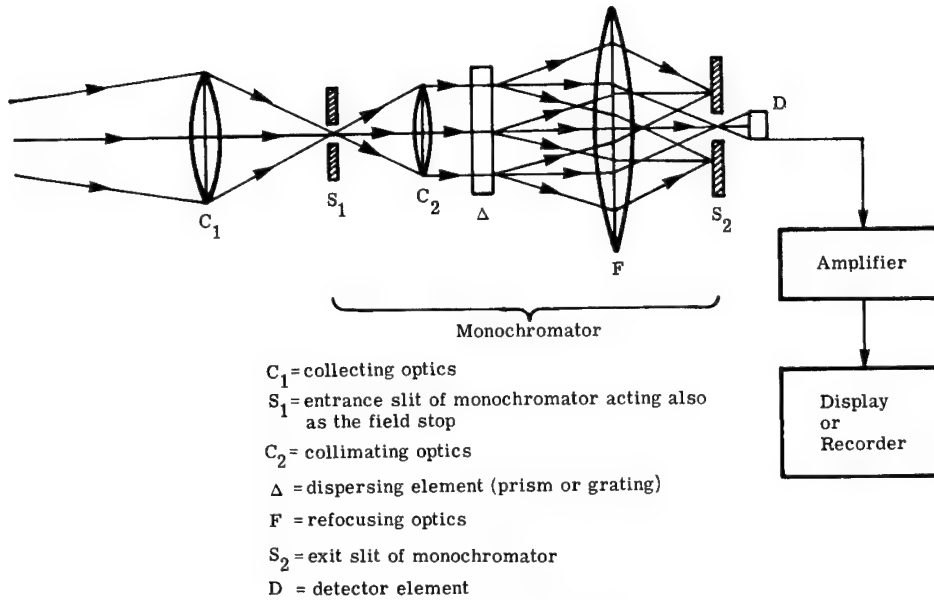


Fig. 4.16 Basic spectroradiometer.

3- to 5- μm and 8- to 14- μm regions, while fixed filters are used for other wavelengths.

4.3.1 Prisms

The wavelength dependence of the index of refraction is used in prism⁴⁰⁻⁴² spectrometers. Such an optical element disperses parallel rays or collimated radiation into different angles from the prism according to wavelength. Distortion of the image of the entrance slit is minimized by the use of plane wave illumination. Even with plane wave illumination, the image of the slit is curved because not all of the rays from the entrance slit can traverse the prism in its principal plane. A prism is shown in Fig. 4.17 in the position of minimum angular deviation of the incoming rays. At minimum angular deviation, maximum power can pass through the prism. For a prism adjusted to the position of minimum deviation,

$$r_1 = r_2 = A_p/2 \quad (4.20)$$

and

$$i_1 = i_2 = (D_p + A_p)/2, \quad (4.21)$$

where

D_p = angle of minimum deviation for the prism

A_p = angle of the prism

r_1, r_2 = internal angles of refraction

i_1, i_2 = angles of entry and exit.

The angle of minimum deviation D_p varies with wavelength. The angular dispersion is defined as $dD_p/d\lambda$, while the linear dispersion is $dx/d\lambda = F dD_p/d\lambda$,

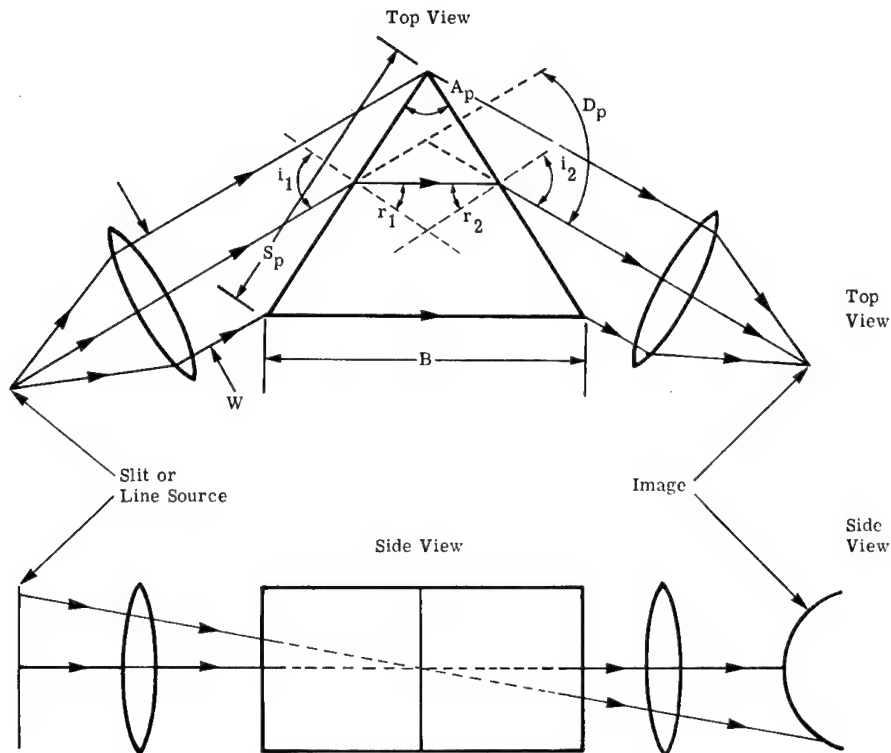


Fig. 4.17 Elementary prism spectrometer schematic, where W is the width of the entrance beam, S_p is the length of the prism face, and B is the prism base length.

where F is the focal length of the camera or imaging lens and x is the distance across the image plane. It can be shown (see Ref. 40, for example) that

$$dD_p/d\lambda = (B/W)(dn/d\lambda) , \quad (4.22)$$

where

- B = base length of the prism
- W = width of the illumination beam
- n = index of refraction
- $dx/d\lambda = F(B/W)(dn/d\lambda)$.

The resolving power RP of an instrument may be defined as the smallest resolvable wavelength difference, according to the Rayleigh criterion, divided into the average wavelength in that spectral region. The limiting resolution is set by diffraction due to the finite beam width, or effective aperture of the prism, which is rectangular. Thus,

$$RP_p = B(dn/d\lambda) . \quad (4.23)$$

If the entire prism face is not illuminated, then only the illuminated base length must be used for B .

4.3.2 Gratings

A grating is an N -slit system used in Fraunhofer diffraction with interference arising from division of the incident, plane wave front. Thus it is a multiple-beam interferometer:

$$p\lambda = d(\sin\theta + \sin\phi) , \quad (4.24)$$

where

- p = order number (= 0, 1, 2, ...) of the principal maxima
- d = the grating constant or spacing (the distance between adjacent slits)
- ϕ = angle of incidence
- θ = angle of diffraction
- w = width of any one slit.

The most common case is $\phi = 0$, so that

$$p\lambda = d \sin\theta , \quad (4.25)$$

and the irradiance distribution is

$$E = E_0 \{ \sin[(\pi w \sin\theta)/\lambda] / [(\pi w \sin\theta)/\lambda] \}^2 \\ \times \{ \sin[(N\pi d \sin\theta)/\lambda] / \sin[(\pi d \sin\theta)/\lambda] \}^2 , \quad (4.26)$$

where N is the number of slits or grooves. This equation is more often written as:

$$E = E_0 [(\sin\beta)/\beta]^2 [(\sin N\gamma)/\sin\gamma]^2 , \quad (4.27)$$

which can be considered to be

$$E = (\text{constant}) \times (\text{single-slit diffraction function}) \\ \times (N\text{-slit interference function}). \quad (4.28)$$

These considerations are for unblazed gratings. For a diffraction grating, the angular dispersion is given (for angle ϕ constant) by

$$dD_g/d\lambda \quad \text{or} \quad d\theta/d\lambda = p/(d \cos\theta) . \quad (4.29)$$

The resolving power is given by

$$RP_g = pN . \quad (4.30)$$

4.3.3 Prism and Grating Configurations and Instruments

Classical. Several basic prism and grating configurations and spectrometer designs continue to be useful. One of the oldest spectrometer configurations⁴⁰ is shown in Fig. 4.18. Reflective interactions and prism combinations are used in Figs. 4.19, 4.20, and 4.21. Dispersion without deviation is realized in Figs.

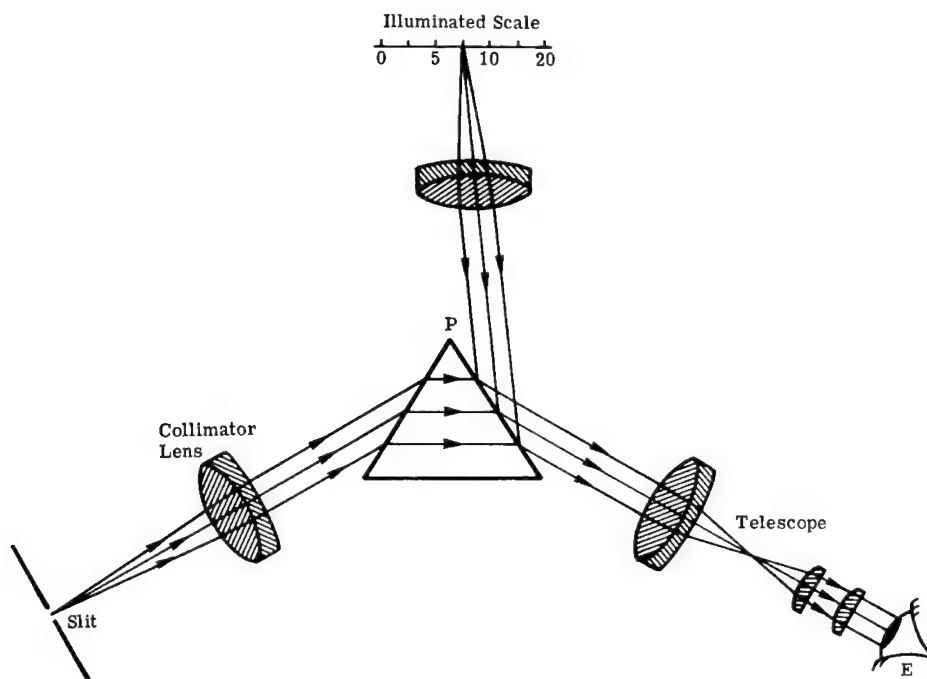


Fig. 4.18 Bunsen-Kirchhoff spectrometer. An illuminated scale is reflected from the prism face into the telescope.

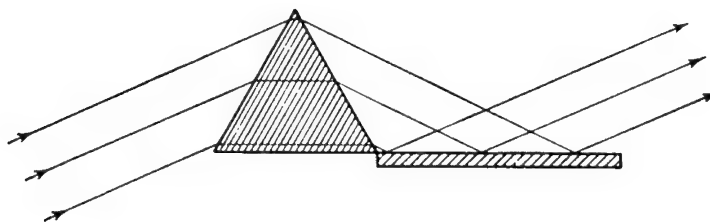


Fig. 4.19 Wadsworth constant-deviation, prism-mirror arrangement. The beam enters the prism at minimum deviation and emerges displaced but not deviated from its original direction.

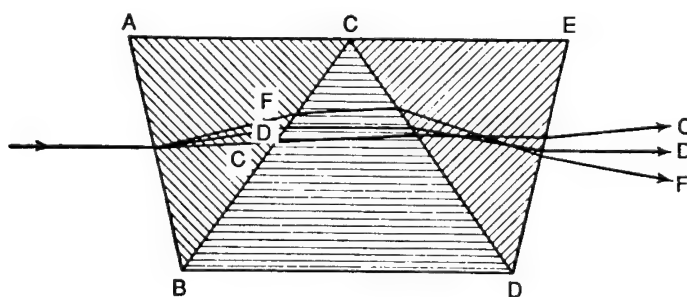


Fig. 4.20 Amici prism. The central ray *D* enters and leaves parallel to the base. The *C* and *F* rays are deviated and dispersed.

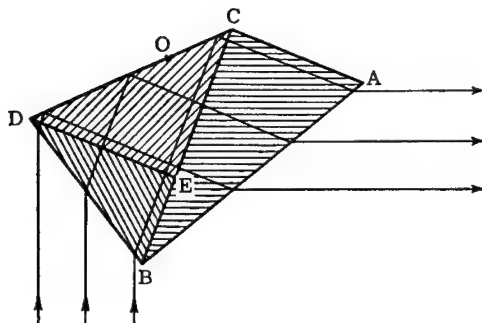


Fig. 4.21 Pellin-Broca prism. The prism is equivalent to two 30-deg prisms, ABC and BED , and one 45-deg prism, DEC , but is made in one place. The beam shown, entering at minimum deviation, emerges at 90-deg deviation to its entrance direction.

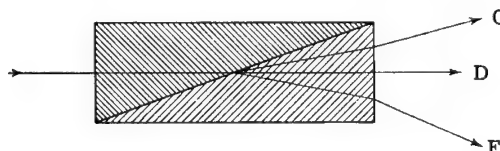


Fig. 4.22 Zenger prism. The central ray D is undeviated. The C and F rays are deviated and dispersed.

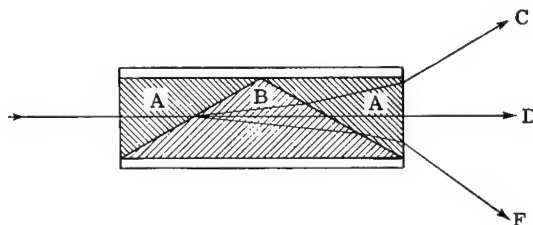


Fig. 4.23 Wernicke prism. This arrangement is essentially two Zenger prisms, back to back.

4.22 and 4.23, while half-prisms are used in Fig. 4.24 in an arrangement that uses smaller prisms but still attains the same beamwidth B . A few classical prism instrumental configurations are shown in Figs. 4.25, 4.26, and 4.27. Single-pass and double-pass prism configurations are illustrated^{43,44} in Figs. 4.28 and 4.29.

A well-known example of a single-beam double-pass prism infrared spectrometer was the Perkin-Elmer model 112 instrument shown in Fig. 4.30. Infrared radiation from a source is focused by mirrors M_1 and M_2 on entrance slit S_1 of the monochromator. The radiation beam from S_1 , path 1, is collimated by the off-axis paraboloid M_3 , and a parallel beam traverses the prism for a first refraction. The beam is reflected by the Littrow mirror, M_4 , through the prism for a second refraction, and focused by the paraboloid, path 2, at the corner mirror, M_6 . The radiation returns along path 3, traverses the prism again, and is returned along path 4 for reflection by mirror M_7 to exit slit S_2 . By this double dispersion, the radiation is spread out along the plane of S_2 . The radiation of the frequency interval that passes through S_2 is focused by

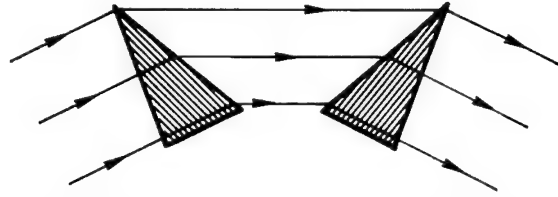


Fig. 4.24 Young-Thollon half-prisms. The passage of a beam at minimum deviation is shown.

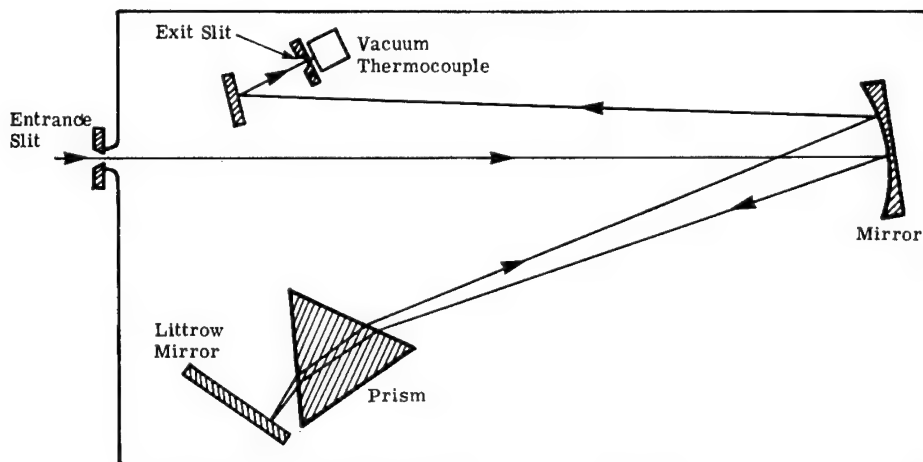


Fig. 4.25 Infrared spectrograph of the Littrow-type mount with a rock salt prism.

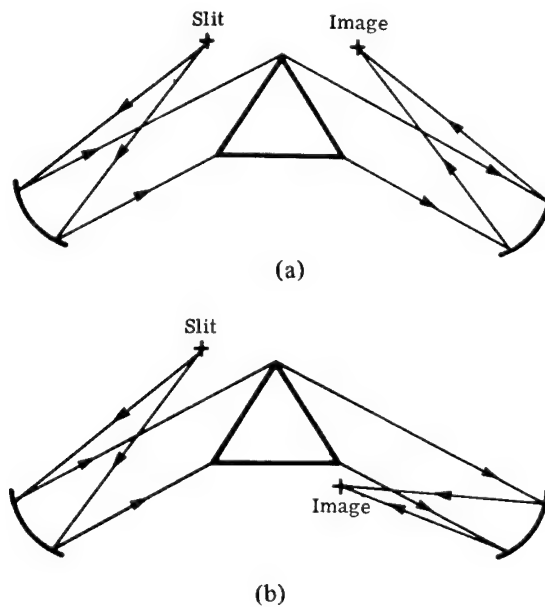


Fig. 4.26 Mirror spectrometer with two choices of the location of the image. Arrangement (b) leads to smaller aberrations than arrangement (a) and is used in the Czerny-Turner mount.

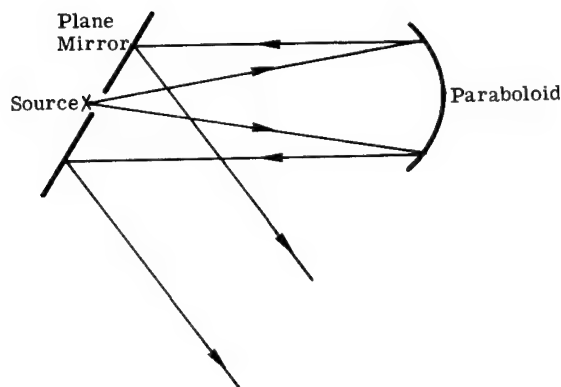


Fig. 4.27 Pfund mirror. The use of a plane mirror to avoid astigmatism in the use of a paraboloidal mirror.

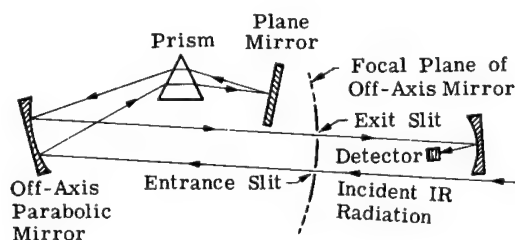


Fig. 4.28 Single-pass monochromator.

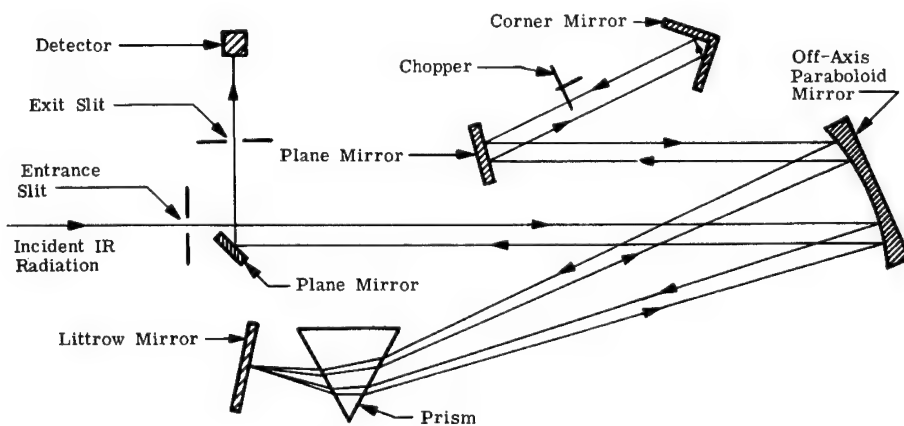


Fig. 4.29 Perkin-Elmer model 99 double-pass monochromator.

mirrors M_8 and M_9 on the thermocouple TC . The beam is chopped by CH , near M_6 , to produce an ac voltage (at the thermocouple) that is proportional to the radiant power or intensity of the beam. This voltage is amplified and recorded by an electronic potentiometer. Motor-driven rotation of Littrow mirror M_4 causes the infrared spectrum to pass across exit slit S_2 , permitting measurement of the radiant intensity of successive frequencies.

Gratings can be used either in transmission or reflection.⁴⁵ Another interesting variation comes from their use in plane or concave reflection form. The

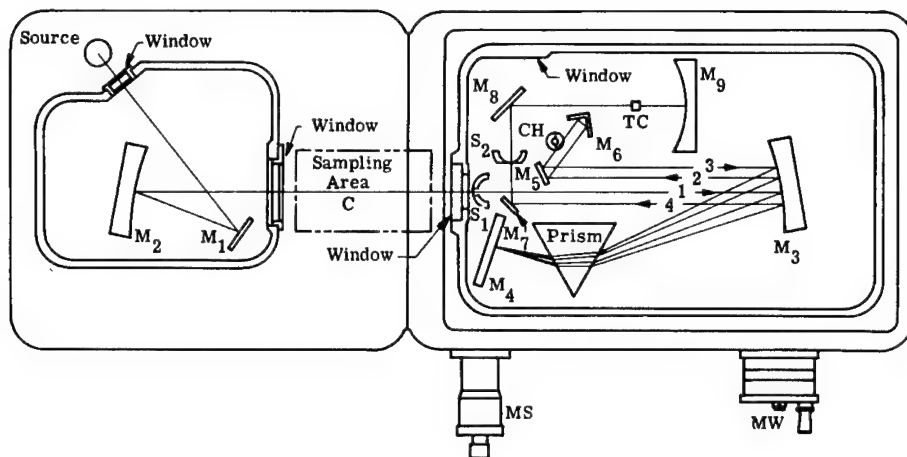


Fig. 4.30 Perkin-Elmer model 112 single-beam double-pass infrared spectrometer.

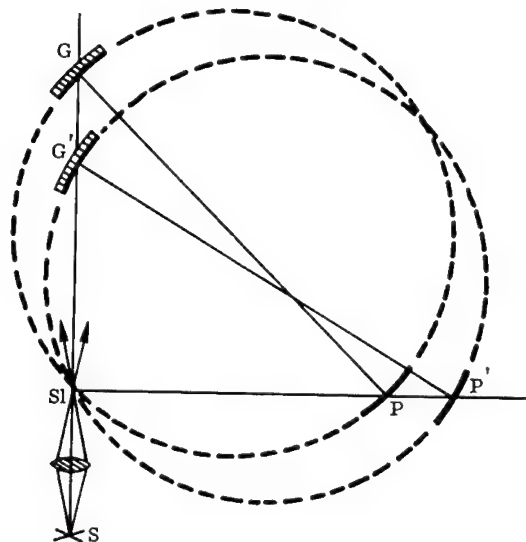


Fig. 4.31 Rowland mounting of the concave grating. The grating plate-holder bar, which slides on the two perpendicular ways, is shown in two positions, GP and $G'P'$. The slit Sl and source S remain fixed.

last was treated most completely by Rowland, who achieved a useful combination of focusing and grating action. He showed that the radius of curvature of the grating surface is the diameter of a circle (called the Rowland circle). Any source placed on the circle will be imaged on the circle, with dispersion, if the rulings are made so that d is constant on the secant to the grating-blank (spherical) surface. The astigmatism acts so that a point source on a Rowland circle is imaged as a vertical line perpendicular to the plane of the circle. Rowland invented and constructed the first concave-grating mounting,⁴⁰ illustrated in Fig. 4.31.

If dispersion is sufficiently large, one may find overlapping of the lines from one order with members of the spectra belonging to a neighboring order. Errors and imperfections in the ruling of gratings can produce spurious images, which

are called "ghosts." Also, the grooves in a grating can be shaped so as to send more radiation along a preferred direction corresponding to an order other than the zero order. Such gratings are said to be *blazed* in that order. These issues and many more involved in the production of gratings by ruling engines have been thoroughly discussed by Harrison.⁴⁶

Six more grating configurations⁴⁰ that are considered to be "classics" are:

1. *Paschen-Runge*: In this arrangement, one or more fixed slits are placed to give an angle of incidence suitable for the uses of the instrument. The spectra are focused along the Rowland circle PP' , and photographic plates, or other detectors, are placed along a large portion of this circle (Fig. 4.32).
2. *Eagle*: This is similar to the Littrow prism spectrograph. The slit and plate holder are mounted close together on one end of a rigid bar with the concave grating mounted on the other end (Fig. 4.33).
3. *Wadsworth*: The Rowland circle is not used in this mounting in which the grating receives parallel light (Fig. 4.34).
4. *Ebert-Fastie*: The Ebert-Fastie configuration features a single, spherical, collimating mirror and a grating placed symmetrically between the two slits. The major advantage of the Ebert system is the fact that it is self-correcting for spherical aberration. With the use of curved slits, astigmatism is almost completely overcome (Fig. 4.35).
5. *Littrow*: The Littrow system has slits on the same side of the grating to minimize astigmatism. An advantage of the Littrow mount, therefore, is that straight slits can be used. In fact, such slits may be used even for a spherical collimating mirror if the aperture is not too large. Its greatest disadvantage is that it does not correct for spherical aberration, which is not too serious a defect for long-focal-length/small-aperture instruments. If an off-axis parabola is used to collimate the light, aberrations are greatly reduced (Fig. 4.25).
6. *Pfund*: This is an on-axis, Pfund-type grating instrument.⁴⁴ Incident infrared radiation, focused by a collimating lens on the entrance slit and modulated by a chopper, passes through the central aperture of

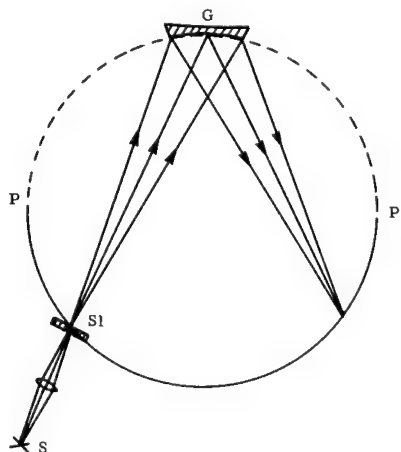


Fig. 4.32 Paschen-Runge mounting of the concave grating, where Sl is the slit, G is the grating, and S is the light source.

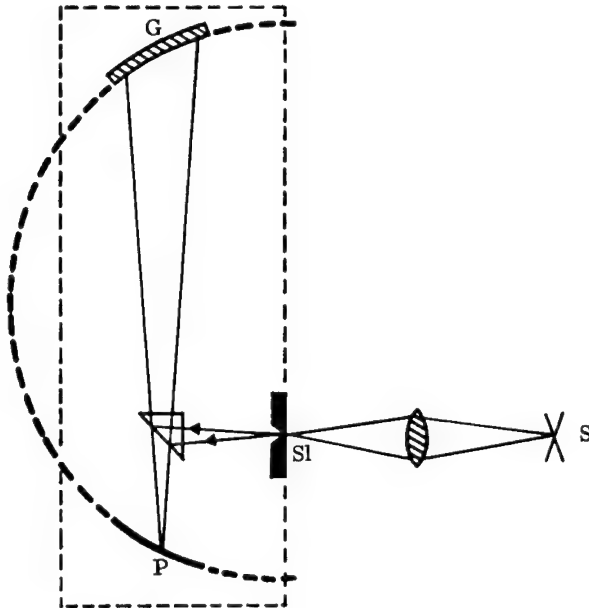


Fig. 4.33 Eagle mounting on the concave grating, where Sl is the slit, G is the grating, S is the light source, and P is the plate holder.

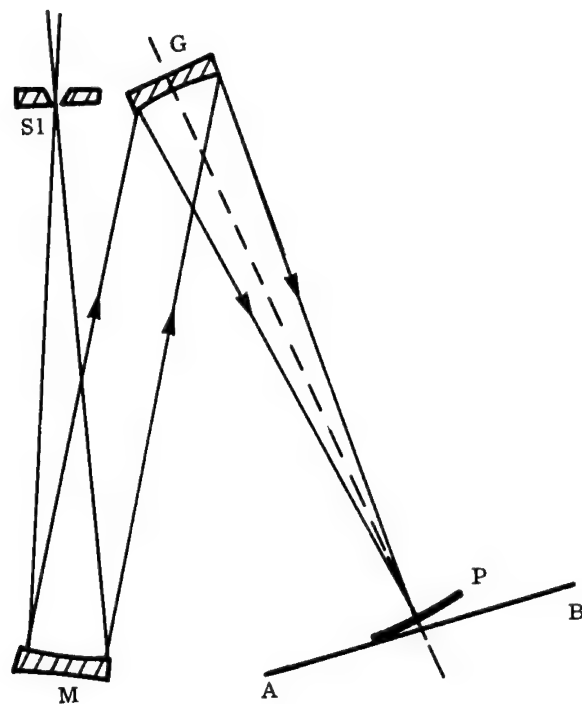


Fig. 4.34 Wadsworth mounting of the concave grating, where Sl is the entrance slit, G is the concave grating, M is the concave mirror, P is the plate holder, and AB is the rail for the plate holder. To minimize aberrations, one must locate the slit close beside the grating.

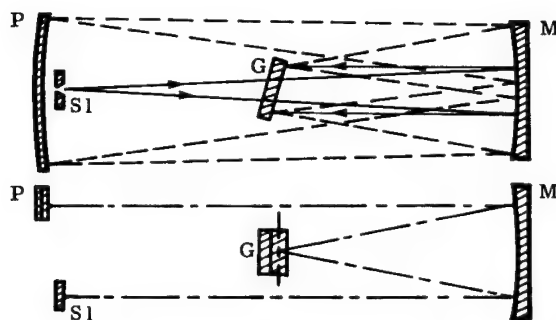


Fig. 4.35 Ebert mounting of the plane grating designed by Fastie, where *S1* is the entrance slit, *G* is the grating, *M* is the concave mirror, and *P* is the photographic plate. The horizontal section is at the top and the vertical section is at the bottom.

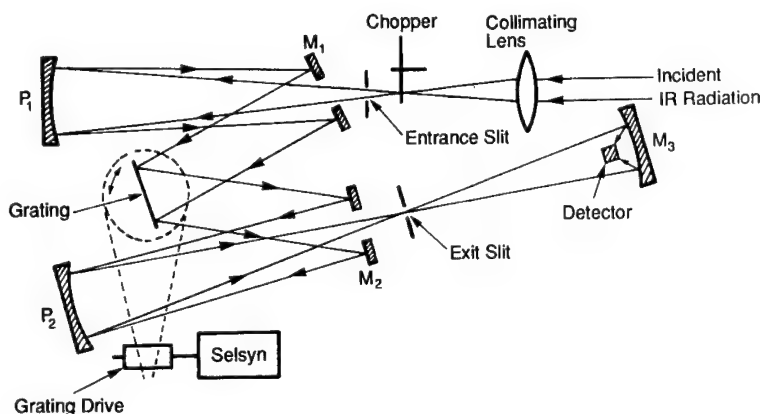


Fig. 4.36 On-axis Pfund grating spectrograph.

plane mirror M_1 . Reflected by the paraboloidal mirror P_1 , it emerges as a parallel beam of radiation, which is reflected by mirror M_1 to the grating. The grating is accurately located on a turntable, which may be rotated to scan the spectrum. From the grating, the diffracted beam, reflected by mirror M_2 , is focused by a second paraboloid, P_2 , through the central aperture of mirror M_2 to the exit slit. The emerging beam is then focused by the ellipsoidal mirror, M_3 , on the detector (Fig. 4.36).

An off-axis, double-pass grating instrument⁴⁵ is illustrated in Fig. 4.37. Combinations of prisms and gratings are not uncommon. An illustrative and complex prism-grating, double-monochromator spectrometer⁴⁴ designed by Unicam Instruments is shown in Fig. 4.38. The prism monochromator had four interchangeable prisms, and the grating monochromator had two interchangeable gratings. The two monochromators, ganged by cams that are linear in wave number, were driven by a common shaft. The instrument could be used either as a prism-grating double monochromator, or as a prism spectrometer by blanking the grating monochromator. Gratings, prisms, and cams could be automatically interchanged by means of pushbuttons. Magnetically operated slits, programmed by a taped potentiometer, provided a constant energy background. A star-wheel, time-sharing beam attenuator was used in the double-beam photometer.

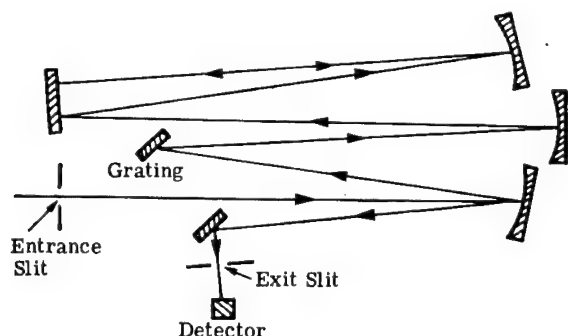


Fig. 4.37 Off-axis, double-pass grating spectrograph.

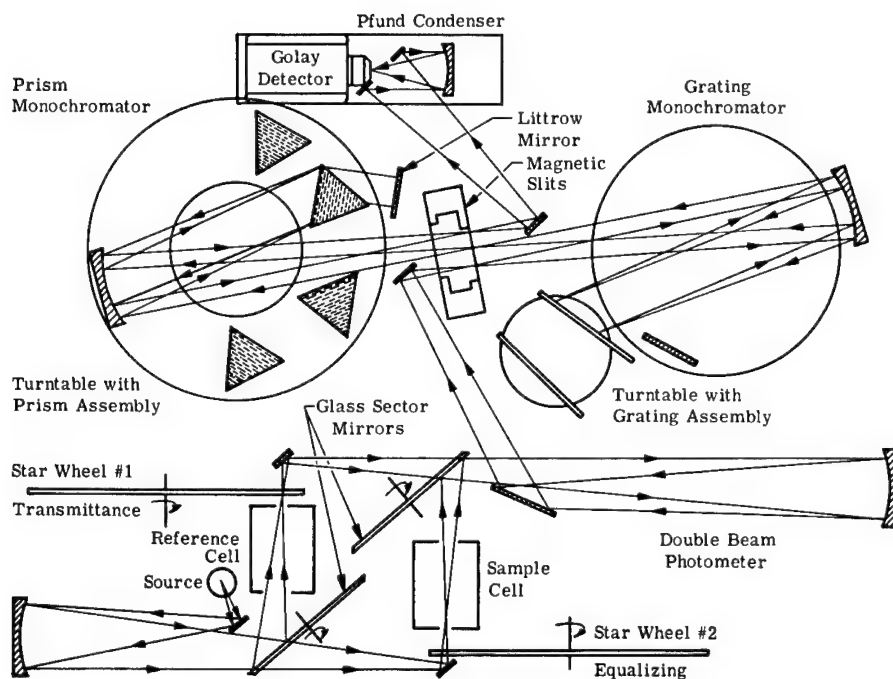


Fig. 4.38 Unicam prism-grating, double-monochromator spectrometer.

Contemporary. In recent years more attention has been paid to total system design and integration for specific purposes and applications, such as for analytical atomic and molecular spectroscopy in analytical chemistry. Thus the conventional dispersive elements are often used in the classical configurations with variations. Innovations have come especially in designs tailored for complete computer control, introduction of one- and two-dimensional detector arrays as well as new detector types (especially for signal matching), the use of holographic optical elements either alone or combined with holographic gratings, and special data-processing software packages, displays, and data storage systems. This is the case also for interferometric systems as discussed later.

Some examples found by a brief look through manufacturers' literature and journals such as *Spectroscopy*, *Physics Today*, *Laser Focus*, *Photonics Spectra*,

and *Lasers and Optronics*⁴⁷ are presented in Table 4.5. Most of these systems are designed for analytical spectroscopy with techniques described in many texts such as Ref. 48.

4.4 INTERFEROMETERS

While many uses exist for interferometers, such as those involving spatial distributions of radiation for optical element testing and flow-field visualization, this discussion will stress obtaining spectral data by use of interferometers. Classically, interference may be considered as it arises in instruments with division of the wave front itself (as in gratings) and with division of the amplitude associated with the wave front. Amplitude-dividing interferometers are particularly useful instruments. The other classification is in terms of the number of interfering beams.

4.4.1 Two-Beam Interferometers

Michelson Interferometer. The Michelson interferometer, shown in Fig. 4.39, consists of two plane mirrors, M_1 and M_2 , one of which is adjustable, and two plane-parallel plates, G_1 and G_2 . Radiation from an extended source is incident at 45 deg on G_1 (partially silvered on the rear surface) and is divided into reflected (path A) and transmitted beams (path B) of equal strength. The radiation reflected from mirror M_1 passes through plate G_1 a third time before it reaches the eye or the detector. The radiation reflected from mirror M_2 passes back through G_2 a second time, is reflected from the surface of plate G_1 , and then on to the detector. The two beams have a phase difference governed by the difference in the two paths.

Compensating plate G_2 compensates for the phase change caused by passage of radiation through the plate in path A. Its use is not essential for producing fringes in monochromatic light but is indispensable when white light is used. The radiation from every point on the extended source interferes with itself according to the distance between mirrors, or according to the difference in length of arms A and B. Constructive interference will occur when

$$2x \cos \theta = p\lambda \quad , \quad (4.31)$$

where

x = path difference

θ = angle to a source element imaged by M_1 or M_2

λ = wavelength

p = the order number, an integer = 0, 1, 2,

The adjustment of M_1 perpendicular to M_2 gives circular fringes, while a slight deviation from this condition leads to straight-line fringes. The shape or profile of the fringes is given by

$$E = E_0[1 + \cos(4\pi x/\lambda)] \quad (4.32)$$

or

$$E = E_0[\cos^2(2\pi x/\lambda)] \quad , \quad (4.33)$$

Table 4.5 Examples of Prism/Grating Spectroradiometers

Manufacturer	Comments
ARC (Acton Research Corporation), Acton, MA	Czerny-Turner or Rowland systems with triple indexable VacUV/IR gratings
ARIES (Acton Research Instrument & Equipment Services Inc.) and QEI (Quantum Electronics Instruments Inc.), Concord, MA	Czerny-Turner variation with double or triple selectable gratings for 165-nm to 40- μ m regions
Beckman Instruments Inc., Fullerton, CA	DU Series 60 and 70 modular construction, computer-controlled spectrophotometers for analytical applications
Cary/Varian Instrument Group, San Fernando, CA	Cary 1, 3, 4, and 5 spectrophotometers for UV-visible-IR; double-beam, dual-chopper/grating Littrow systems; attachments (e.g., reflectance) and applications software
CI Systems Ltd., New York and Israel	CVF spectroradiometers for 0.4- to 20- μ m scanning
CVI Laser Corporation, Albuquerque, NM	Digikrom monochromators, 1/8-, 1/4-, and 1/2-m Czerny-Turner grating systems for 186-nm to 20- μ m regions
Infrared Systems, Inc., Orlando, FL	CVF spectroradiometer
Instruments SA, Inc. and J-Y Optical Systems, Edison, NJ	Monochromators, spectrometers for UV-visible-IR, holographic gratings in Czerny-Turner or concave aberration-corrected holographic gratings and Rowland mounts; single and double pass; imaging spectrographs
LECO Corporation, St. Joseph, MI	Inductively coupled plasma (ICP) spectrometer system with Paschen-Runge mount concave grating followed by an echelle and a linear detector array
Leeman Labs, Inc., Lowell, MA	ICP system with a fixed echelle grating followed by a prism with crossed order dispersion and scanned photomultipliers or detector arrays
McPherson, Division of SI Corporation, Acton, MA	Double- or triple-monochromator spectroradiometers using gratings and/or prisms in Seya-Namioka, Czerny-Turner (C-T), crossed C-T, or Rowland configurations
Minirad Systems, Inc., Fairfield, CT	CVF and discrete filters in spectroradiometers for field measurements, 0.2 to 30 μ m
Optometrics Corporation, Ayer, MA	Monochromators, prism or grating, Ebert-Fastie systems for UV-visible-NIR.
Optronic Laboratories, Inc., a subsidiary of Kollmorgen Corporation, Orlando, FL	Spectroradiometers for UV-visible-IR for precision measurements; filter wheels, gratings, and prisms in single- and double-monochromator configurations
Oriel Corporation, Stratford, CT	Scanning monochromators, rotation filter wheels, and detector array instruments
Perkin-Elmer Corporation, Norwalk, CT	Complete sets of UV-visible-IR spectroscopic systems using gratings and prisms, or FT-IR, with software and hardware for computer control, and accessories for microscopy, reflectance measurement, etc.
Shimadzu Scientific Instruments, Inc., Columbia, MD	UV-visible-NIR spectroscopic systems using holographic gratings in Czerny-Turner mounts in single- and double-beam configurations, computer controlled, with accessories for analyses
SPEX Industries, Inc., Edison, NJ	UV through IR grating 1/2- and 1/4-m spectrometers, with CCD or PDA multichannel detectors
Thermo Jarrell Ash Corporation, a subsidiary of Thermo Instrument Systems, Inc., Franklin, MA	Monochromators and spectroscopic systems for analyses, UV-visible-IR with gratings in 1942 in Wadsworth, then in 1953, Ebert, and now Paschen-Runge and crossed Czerny-Turner mounts; complete systems

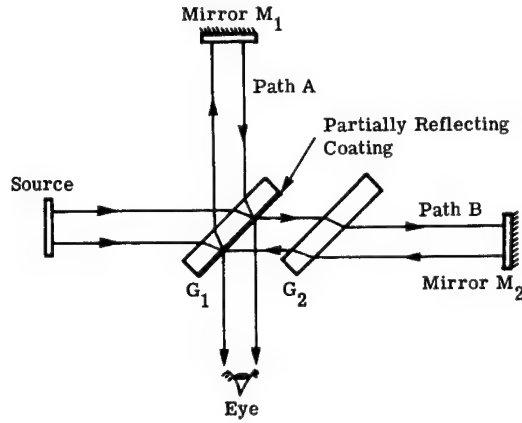


Fig. 4.39 Michelson interferometer.

where E is the irradiance at the detector. Since E_0 is the maximum value of E ,

$$2\pi x/\lambda = p\pi, \quad (4.34)$$

while at the minimum, i.e., when $E = 0$,

$$2\pi x/\lambda = (p + 1/2)\pi. \quad (4.35)$$

Michelson used the "visibility" of fringes to determine small wavelength differences, e.g., the sodium doublet separation. He defined this quantity as follows:

$$\text{visibility} = (E_{\max} - E_{\min}) / (E_{\max} + E_{\min}). \quad (4.36)$$

If mirror M_1 is moved at a constant speed, i.e., dx/dt is kept constant, in a sawtooth pattern repeated over the distance interval of

$$-C/4 < x < C/4 \quad (4.37)$$

in a time interval of δ , then

$$x(t) = (Ct)/(2\delta) \quad (4.38)$$

and

$$E = E_0 \{1 + \cos[(2\pi Ct)/(\lambda\delta)]\}. \quad (4.39)$$

Thus modulation frequency f depends on the wavelength of the radiation so that

$$f = C/(\lambda\delta) \quad (4.40)$$

and

$$E = E_0(1 + \cos 2\pi f t). \quad (4.41)$$

This result illustrates the basis of scanning Michelson interferometry for spectroscopic instrumentation.

A pioneer in practical implementation of this concept was M. Block. An early configuration of the Block Engineering interferometer is shown in Fig. 4.40. Incoming infrared radiation is received by the interferometer, and a fringe pattern is produced. When one of the mirrors in the interferometer is moved back and forth at a slow, constant velocity, the motion is manifested as an alternate brightening and darkening of the central fringe.

An infrared detector placed at the central fringe converts these cyclic changes into an ac signal. If the mirror velocity is kept constant at a predetermined value, the frequency of the ac signal from the detector is directly related to the wavelength of incident radiation, assuming that the incident radiation is at one given wavelength (monochromatic). If another wavelength twice as long as the first (half the frequency) should be substituted as the incident radiation source, the ac output signal from the detector would be at one-half the frequency of the first. The amplitudes of the two signals would remain the same if the maximum brightness of the two sources were the same. If incident radiation containing many wavelengths were introduced into the system, the output of the detector would consist of a superposition of all the ac signals that correspond to all wavelengths in the source.

The output of the Block interferometer system was tape recorded and played back through an audio wave analyzer to recover the infrared spectrum. The scan drive must be linear and constant and the effects of source-intensity variations must be negligible. Either of these can cause apparent spectral peaks in the output.

Such an interferometer-spectrometer has greater throughput than a conventional spectrometer because the interferometer has a large entrance aperture determined by the mirror size. This enables the instrument to accept more radiant flux from the source than prism or grating instruments in which the entrance aperture is limited by narrow slits.

High-sensitivity gain is a result of the fact that the instrument examines each wavelength throughout the entire time period of each scan, i.e., the *multiplex* advantage. In a conventional instrument, each wavelength is examined for only a very short part of the scan time ($1/n$ 'th the scan time if n is the

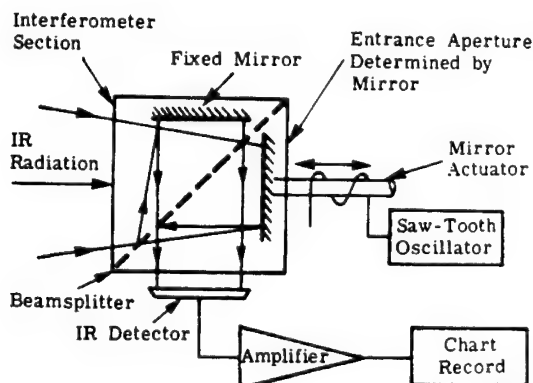


Fig. 4.40 Block Associates interferometer spectrometer.

number of resolution elements); the interferometer achieves a gain that is \sqrt{n} for the same scan time. For typical instruments, this can be a factor of 50. Furthermore, this gain is realized even when one examines point sources where the throughput gain is not large.

The general field of Fourier transform spectroscopy (FTS), especially for the infrared spectral region, was reviewed in 1965 by Loewenstein⁴⁹ and in 1976 by Bates.⁵⁰ Discussions of Fellgett's (the multiplex) advantage and the throughput gain are referenced in his treatment of slow-scanning (including step-scanned) and fast-scanning Michelson interferometers. The work by Janine and Pierre Connes was reported in a now classic paper which treats the step-scanned interferometer, an instrument they used so successfully, primarily in planetary spectroscopy.⁵¹ In 1976, a far-infrared (50 to 100 μm) Michelson-type Fourier transform spectrometer⁵² was constructed to have a theoretical resolution of 0.007 cm^{-1} . The instrument was used with an absorption (White) cell to achieve separations of 0.05 cm^{-1} in the 200-cm^{-1} region using about 1000 sampling points, and 0.04 cm^{-1} in the 100-cm^{-1} region. The optical layout of the instrument is shown in Fig. 4.41.

By the end of the 1970s, work at MIT on a precision scanning Michelson interferometer had achieved accuracy of several parts in 10^9 at $10\text{ }\mu\text{m}$ and several parts in 10^{11} in the visible.⁵³

With the employment of the fast Fourier transformation (FFT) the field of commercial FTS developed swiftly. A brief look at manufacturers' literature finds the following examples:

- Bio-Rad Laboratories, Digilab Division, Cambridge, MA, offers modular FT-IR systems such as their FTS 7 with 1- or 2-cm^{-1} resolution over ranges such as 4400 to 400 or 225 cm^{-1} and with DTGS or LN2 cooled MCT or PbSe detectors.
- Bomem, Inc., Quebec, Canada, has several instruments designed for teaching as well as research.
- Bruker Instruments, Inc., Billerica, MA, and Karlsruhe, Germany, has a series of FT-UV as well as FT-IR systems, operating at wave-

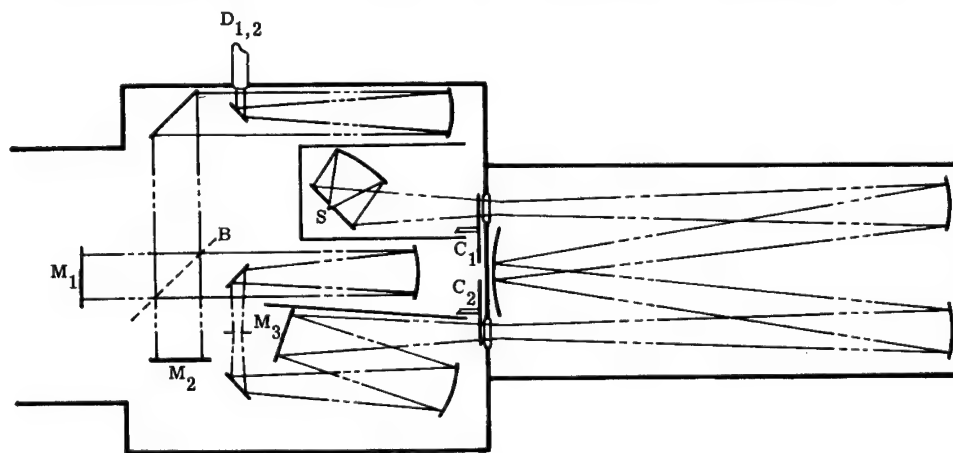


Fig. 4.41 Optical layout of the instrument, where M_1 and M_2 are the Michelson mirrors, M_3 may be replaced by a diffraction grating, C_1 and C_2 are choppers, S is the source, $D_{1,2}$ represents light pipes to the detectors, and B is the beam splitter.

lengths as short as 250 nm. With a family of detectors the IFS series can cover ranges from 4800 to 450 cm^{-1} or 40,000 to 10 cm^{-1} with resolution from 0.002 to 0.008 cm^{-1} . Resolving power can be 10^6 . Scans can be stepped or rapid (up to 50 Hz).

- MIDAC Corporation, Costa Mesa, CA, offers its low-cost Collegian FTIR with 5- cm^{-1} resolution covering 5000 to 400 cm^{-1} for academic instructional purposes.
- Nicolet Instrument Corporation, Madison, WI, has a very complete FT-IR product line from their System 800 to the low-cost model 250 FT-IR. Configurations for Raman spectroscopy, IR microscopy, gas analysis, etc., are available.

These and many other FTS systems continue to be presented and discussed at many conferences dedicated to this particular technology (see, for example, Ref. 54).

Twyman-Green Interferometer. In the Twyman-Green interferometer, a Michelson interferometer is illuminated with parallel monochromatic radiation, produced by a point source at the principal focus of a well-corrected lens.⁵⁵ As shown in Fig. 4.42, radiation comes from a pinhole P at the principal focus of lens L_1 . A second lens, L_2 , focuses the emerging radiation onto the detector. By the use of collimated radiation, the fringes at infinity can be seen at finite distance (such as on one of the surfaces of a prism) because of the greatly increased depth of focus. In addition, the radiation is made to traverse the optical part under test (a prism in Fig. 4.42), and the result of the test is explicit.

Modifications of the Twyman-Green interferometer have been described by Françon,⁵⁶ for example, the Martin-Watt-Weinstein interferometer, and by Steel,⁵⁷ for example, the Williams interferometer, shown in Fig. 4.43.

WYKO Corporation of Tucson, Arizona, offers an infrared interferometer system for testing at 10.6 μm with a Twyman-Green unequal path using a

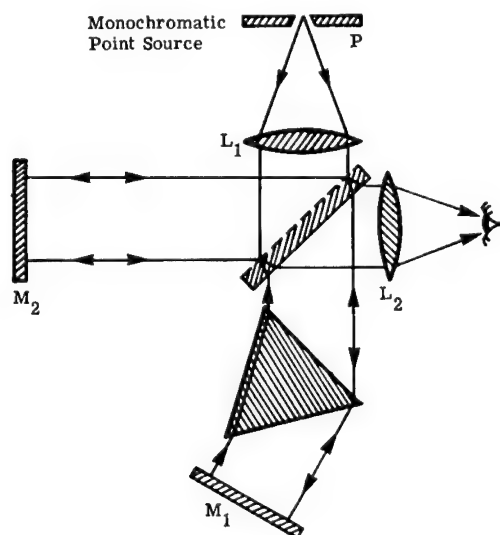


Fig. 4.42 Twyman-Green interferometer.

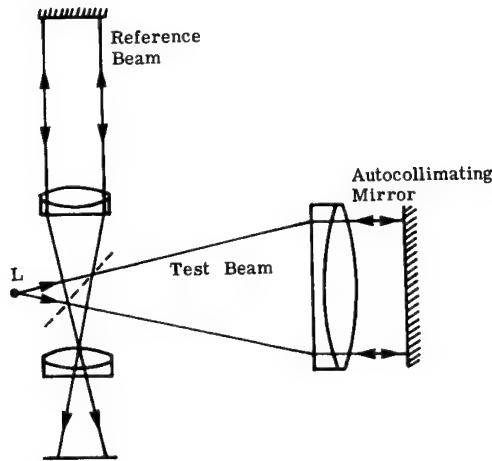


Fig. 4.43 Williams interferometer.

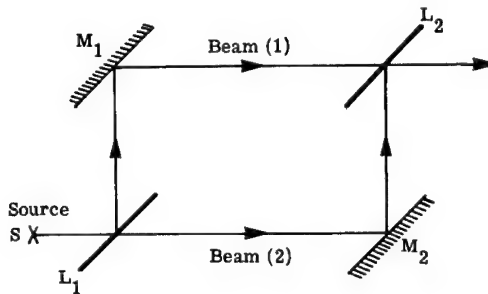


Fig. 4.44 Mach-Zehnder interferometer.

CO₂ laser and a pyroelectric vidicon. A Fizeau-type two-beam system is used in the visible region with a HeNe laser. Zygo Corporation, Middlefield, Connecticut, also offers a Fizeau interferometer system using HeNe and CCD vidicons. A large number of options in computer hardware and software are available from these and other companies.

Mach-Zehnder Interferometer. Another two-beam amplitude-division interferometer is the Mach-Zehnder interferometer,⁵⁶ shown in Fig. 4.44. It has two beamsplitters, or semitransparent reflectors, L_1 and L_2 , and two mirrors, M_1 and M_2 . Derived from this configuration is the Jamin interferometer (Fig. 4.45), which uses two plane-parallel plates, L_1 and L_2 , with reflective coatings, A_1 and A_2 . Other interesting variations of the Mach-Zehnder interferometer are described by Steel.⁵⁷ These include the use of diffraction gratings as the beamsplitters and the use of arms of different cross sections as realized by Johnson and Scholes.

Sagnac or Cyclic Interferometer. The Sagnac or cyclic interferometer⁵⁷ can be realized by either an even or odd number of reflections in each beam. Two forms are shown in Fig. 4.46. This concept has been used in the ring laser gyro (RLG) for application to problems of battlefield navigation.⁵⁸ Sagnac fiber optic interferometers are interesting extensions of RLGs.^{59,60}

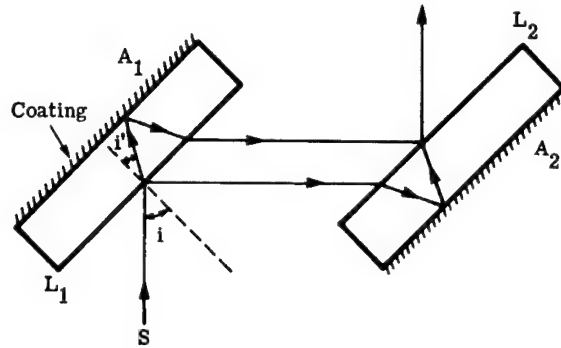


Fig. 4.45 Jamin interferometer.

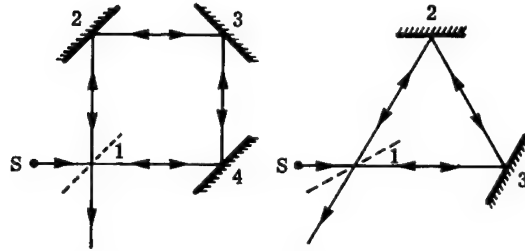


Fig. 4.46 Sagnac or cyclic interferometer.

4.4.2 Multiple-Beam Interferometers

Fabry-Perot Interferometer. Two optical flats, coated to obtain high values of reflectance, are separated by a precision spacer (or etalon) in what is called a Fabry-Perot (F-P) interferometer. The materials and thickness of the flats can be disregarded for this discussion. From Fig. 4.47, we can obtain the equation for the shape of the resulting fringes. We add the amplitudes of the transmitted waves for the Airy function:

$$A = \sum_{m=1}^{\infty} \tau \rho^m \exp[j(\omega t - m2\pi p)] , \quad (4.42)$$

where

t = time

τ = the transmittance of the coatings

p = the order number, 0, 1, 2, ...

ρ = the reflectivity of the coatings

m = the summation running index 0, 1, 2, ...

$\omega = 2\pi\nu = 2\pi c/\lambda$.

The time dependence and τ can be removed from the summation, so that the equation may be rewritten as

$$A = \tau \exp(j\omega t) / [1 - \rho \exp(-j2\pi p)] \quad (4.43)$$

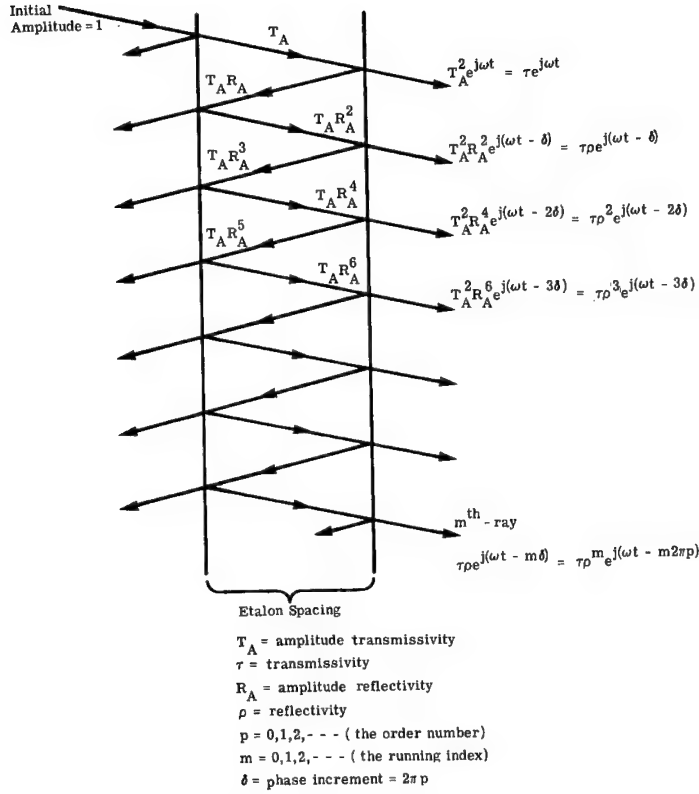


Fig. 4.47 Fabry-Perot interferometer schematic.

using the binomial expansion. The resulting irradiance is

$$E = A^*A = \tau^2 \{ [1 - \rho \exp(-j2\pi p)] [1 - \rho \exp(j2\pi p)] \}^{-1} \quad (4.44)$$

$$= \tau^2 / [1 + \rho^2 - 2\rho \cos(2\pi p)] .$$

Since $\cos(2\pi p) = 1 - 2 \sin^2(\pi p)$, this may be written as

$$E = [\tau^2 / (1 - \rho^2)] / [1 + 4\rho \sin^2(\pi p) / (1 - \rho^2)] . \quad (4.45)$$

The maximum irradiance value is $E_{\max} = \tau^2 / (1 - \rho^2)$ at all integer values of p , while the minimum is $E_{\min} = \tau^2 / (1 + \rho^2)$ for all values of $p = \text{integer} + 1/2$. Thus,

$$E = E_{\max} \{ 1 + [4\rho \sin^2(\pi p) / (1 - \rho^2)] \}^{-1} . \quad (4.46)$$

The resolving power, RP_{PF} , can be obtained by requiring that the superposition of the irradiance curves of two just-resolved, equal-intensity lines yield an envelope with a value of 0.8 for the ratio of saddle to maximum intensity.⁶¹ (For gratings, the Rayleigh criterion gives 0.8106 for this ratio.) We have

$$RP_{PF} = \lambda / \Delta\lambda \approx p [3\sqrt{\rho} / (1 - \rho)] . \quad (4.47)$$

From comparison to the equation for the grating resolving power, this interferometer may be considered to have a resolving power of

$$RP_{PF} = pN_{\text{effective}} . \quad (4.48)$$

If a lens of focal length F is used to produce an image of the circular fringes obtained from a F-P interferometer, then

$$p\lambda = 2d \cos\theta = 2d(1 - D^2/8F^2) , \quad (4.49)$$

where D is the diameter of the bright fringe of order p , and d is the spacing of the plates.

The angular dispersion is

$$d\theta/d\lambda = [\lambda \tan\theta]^{-1} . \quad (4.50)$$

The spectral range is that difference between two wavelengths which is sufficient for the order numbers to differ by one. Thus

$$\begin{aligned} p_1\lambda_1 &= p_2\lambda_2 = (p_1 + 1)\lambda_2 , \\ p_1(\lambda_1 - \lambda_2) &= \lambda_2 \quad \text{or} \quad \Delta\lambda = \lambda/p = \lambda^2/2d . \end{aligned} \quad (4.51)$$

Often the spectral range is shown as $\langle\Delta\lambda\rangle$. In wave number the spectral range is just $1/2d$ where d , the plate spacing, is in centimeters. It can be used to predict overlapping of orders.

At the center of the pattern (Fig. 4.48), we can assign an order number of P , which is an integer plus a fraction smaller than one. The first bright fringe or ring has order number p_0 so that

$$\begin{array}{ccccccc} \text{center} & \text{1st ring} & \text{2nd ring} & \dots & (k+1) \text{ ring} & \dots \\ P & > p_0 & > p_1 & > \dots & > p_k & > \dots \end{array} .$$

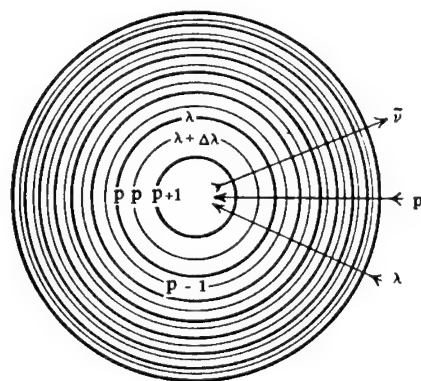


Fig. 4.48 Interference system of two close lines.

At the center, since $\theta = 0$ (or $D = 0$),

$$P\lambda = (p_0 + \varepsilon)\lambda = 2d = (p_k + k + \varepsilon)\lambda \quad (4.52)$$

or

$$\varepsilon = P - p_k - k = 2d/\lambda - p_k - k . \quad (4.53)$$

If we subtract p_k from p_i , we get

$$p_i - p_k = (d/\lambda F^2)(D_k^2 - D_i^2) = (p_0 - i) - (p_0 - k) = k - i . \quad (4.54)$$

Thus, the difference between the squares of the ring's diameters is

$$\Delta D^2 = (D_k^2 - D_i^2)/(k - i) = 4F^2(\lambda/d) \quad (4.55)$$

and

$$\varepsilon = (D_k^2/\Delta D^2) - k . \quad (4.56)$$

For the first ring, $\varepsilon = D_0^2/\Delta D^2$ and thus

$$D_k^2 = D_0^2 + k \Delta D^2 . \quad (4.57)$$

Now both D_0^2 and ΔD^2 are treated as constants to be determined such that the sum of the squares of the deviations is minimized. Then these values are used to calculate ε :

$$\varepsilon = \text{mean } D_0^2 / \text{mean } \Delta D^2 . \quad (4.58)$$

The method of least squares is applied as follows. One measures the n -innermost rings obtaining values for D_0 through D_{n-1} . Then

$$\text{mean } \Delta D^2 = \{6/[n(n^2-1)]\} \times \sum_i (n+1-2i)(D_{n-1}^2 - D_{i-1}^2) , \quad (4.59)$$

where the summation is from $i = 1$ through $i \geq n/2$, and

$$\text{mean } D_0^2 = \text{mean } D_k^2 - \text{mean } (k\Delta D^2) , \quad (4.60)$$

where mean k is the average of $0, 1, 2, \dots, n-1$.

The process of absolute wavelength measurement starts with determination of d from use of a standard wavelength λ_s in $(p_s + \varepsilon_s)\lambda_s = 2d$. To find p_x , one starts with approximate values of the unknown wavelength λ_x and the now known value of d . If the values of λ_x are very poor, one must start with *small* values of d :

$$(p_x + \varepsilon_x)\lambda_x = 2d . \quad (4.61)$$

This also helps avoid the confusion of overlapping orders, a problem that can be reduced in impact by various nomographic methods. One method, rigorously presented in Ref. 62, can be approximated by differentiation of

$$P = p_0 + \epsilon = 2d/\lambda \quad (4.62)$$

to obtain

$$dP = d\epsilon = (2d)d\nu \quad \text{where } \nu = 1/\lambda, \text{ wave number} \quad (4.63)$$

A plot of d against $d\epsilon$ for the available values of $d\nu$ will provide a useful nomograph.

A Fabry-Perot interferometer with a value of $d = 1.0197$ m has been successfully assembled and used.⁶³ As reported by Meissner and Kaufman, for the 422.6-nm resonance line of calcium, this spacer thickness corresponds to $p = 4.82 \times 10^6$. With plates whose coatings had a reflectivity of about 81%, this interferometer yields a resolving power of 68.5 million; for $\rho = 95\%$, $RP = 10^7$.

When working with such high resolving power values, investigators have often turned to the spherical Fabry-Perot interferometer, a more efficient configuration for high-resolution work, especially with weak sources. One design, shown in Fig. 4.49, consisted of two spherical mirrors whose separation is equal to the radius of curvature r , so that the paraxial foci coincide and the instrument is an afocal system. One half of the surface of the mirrors is semireflecting and the other half is fully reflecting. Any incident ray gives rise to an infinite number of outgoing rays, which are coincident, and not only parallel, as with the plane Fabry-Perot instrument. Neglecting aberrations, their path difference is $4r$, a constant. This requires that both mirrors be stopped down with circular diaphragms of diameter D . It can be shown that D increases with r , and that the light-gathering power is proportional to r (and thus to the theoretical resolving power RP , instead of being inversely proportional to RP). For practical values of r (a few centimeters), D always remains quite small (a few millimeters).⁶⁴

The use of two Fabry-Perot interferometers in series was introduced to solve the problem of overlapping orders encountered in studies of complex spectra.⁶⁵ The resulting "compound interferometer" has a resolving power greater than that of either interferometer alone. This concept, whose history was traced and

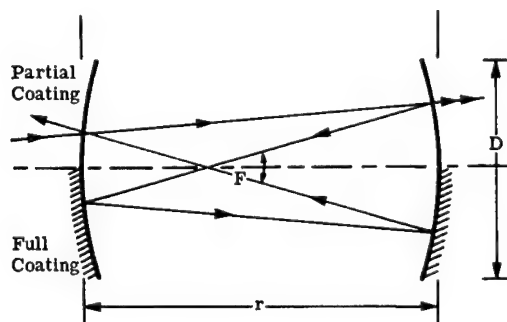


Fig. 4.49 Spherical Fabry-Perot interferometer.

reported by Mack et al.,⁶⁶ was extended by Mack and his coworkers into the PEPSIOS spectrometer.⁶⁶⁻⁶⁸ The pilot model PEPSIOS spectrometer used three etalons and pressure scanning (e.g., variation of the ambient pressure). A resolving power exceeding 4×10^5 was achieved by this pilot model. Comparison of the single Fabry-Perot, the PEPSIOS, and the SISAM (SISAM used two identically blazed reflection gratings to replace the two totally reflecting mirrors of a conventional Michelson interferometer) instruments was made by Meaburn⁶⁹ for use in studies of visible nebular lines. Döbele and Massig compared the use of a single Fabry-Perot spectrometer to the use of a grating spectrometer to measure spectral line shifts much smaller than the line width.⁷⁰ They concluded that the Fabry-Perot instrument was superior, experimentally showing a lower limit to the measurable shift of 1/1000 of the line width. A single-etalon Fabry-Perot interferometer with blocking filters was combined with an SEC vidicon for use in observational astronomy.⁷¹ The configuration, dubbed the SPIFI (spectroscopic photoelectric imaging Fabry-Perot interferometer), is shown in Fig. 4.50. The interferometer was step-scanned by means of piezoelectric elements used to change the spacing of the plates.

Burleigh Instruments of Fishers, New York, offers fixed, variable space, and PZT-tuned Fabry-Perot etalons with a wide variety of components and attachments. A broad range of systems using these etalons is available.

Michelson Echelon. This instrument consists of a stack of optically flat plates "wrung" together so as to produce a stair-step structure of steps that is S wide and h deep (Fig. 4.51). In transmission, as realized by Michelson, for near-normal angles of incidence and small diffraction angles,

$$p\lambda = (n - 1)h + S\theta_d, \quad (4.64)$$

where

- p = order number
- n = index of refraction
- θ_d = angle of deviation.

In reflection, as produced by Williams,⁵⁷

$$p\lambda = (2h + S\theta_d), \quad (4.65)$$

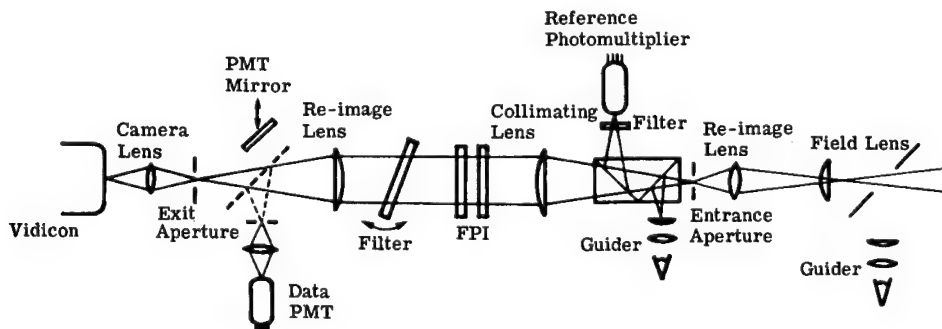


Fig. 4.50 Layout of the optical system of the SPIFI indicating the positions of all components.

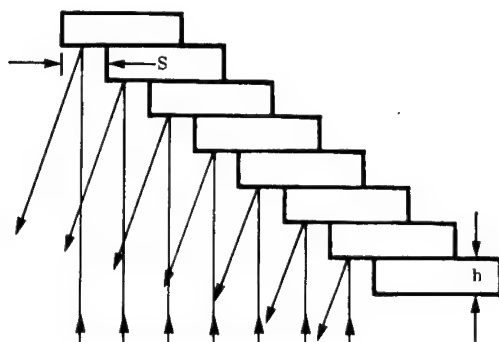


Fig. 4.51 Reflection Michelson echelon.

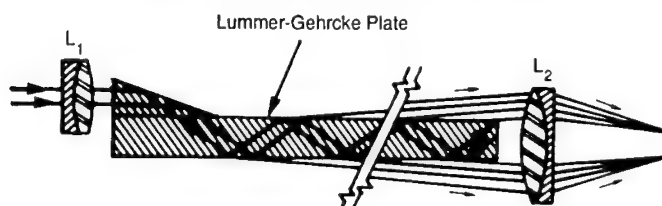


Fig. 4.52 Lummer-Gehrcke plate interferometer.

and the dispersion is

$$d\theta_d/d\lambda = p/S = 2h/\lambda S, \quad (4.66)$$

with a spectral range of

$$\langle \Delta \nu \rangle = 1/(2h) \quad (4.67)$$

and

$$RP_{ME} = \lambda/\Delta\lambda = pN = 2hN/\lambda, \quad (4.68)$$

where N is the number of steps (often from 25 to 40).

The Lummer-Gehrcke Plate. The Lummer-Gehrcke plate,⁵⁷ shown in Fig. 4.52, utilizes the interference between successive reflections in a thin flat plate. Radiation can be introduced to the plate by a total reflection prism from lens L_1 . It then undergoes multiple internal reflections very near the critical angle of total reflection. The beams emerging at a grazing angle are brought to interference by a second lens, L_2 . A high reflectance and resolving power are thus obtained with unsilvered surfaces.

4.5 OTHER SPECTROSCOPIC INSTRUMENTS AND TECHNIQUES

Many other spectroscopic instrumentation and techniques are to be found in the literature. Some few may be of interest. The use of coding masks was first demonstrated by Golay.⁷² He showed that infrared spectra produced by use of

Table 4.6 Imaging Spectrometer Design Specifications

Wavelength range	2 to 5 μm and 8 to 14 μm	
Spectral resolving power	~ 60	
Spectral channels	63	
Field of view	8.88 deg \times 9.45 deg	
Spatial resolution	0.005 rad	
Spatial resolution elements	1023 (31 \times 33)	
Detectors	PbSe (2 to 5 μm)	pyroelectric
Scanning drive speed	720 rpm	20 rpm
Spatial frame time	25 ms	1 s
Spatial/spectral frame time	2.6 s	95 s

a dispersing system (e.g., grating or prism spectrometer) could be treated by use of modulating patterns or masks placed at the entrance and/or exit apertures. The resulting modulated beam would allow obtaining spectra at a far greater rate or with increased SNRs. Others have followed this direction to achieve multiplexing by use of binary optical encoding masks. As reported by Swift et al.,⁷³ the development of Hadamard transform spectrometers was achieved in the late 1960s. The combination of two-dimensional spatial encoding with one-dimensional spectral encoding has been realized by Swift and his coworkers in their Hadamard transform imaging spectrometer. The design specifications are shown in Table 4.6.

The advent of laser technology has made possible another set of techniques. For example, it became feasible to carry out tunable laser spectroscopy⁷⁴ or, more broadly, "laser spectroscopy." The review by Letokhov⁷⁵ pointed out that laser spectroscopy brought a new level of sensitivity and resolution, spectrally, spatially, and temporally. Spectral analyses on very small volumes, of the order of the wavelength cubed, also came within reach. Spectral resolving powers of up to 10^{11} have been attained.

Pine reported⁷⁶ work with a cw difference-frequency spectrometer that operated in the 2.2- to 4.2- μm region by mixing radiation from an argon-ion laser with that from a tunable dye laser in the nonlinear optical crystal, LiNbO_3 . His drift compensation and scan-calibration techniques allowed high-resolution spectra of methane to be produced with a precision and reproducibility of $5 \times 10^{-4} \text{ cm}^{-1}$.

Work at NBS applied saturated absorption in neutral molecules to the wavelength stabilization of gas lasers, leading to systems exceeding the stability and reproducibility of the ^{86}Kr standard by several orders of magnitude.⁷⁷

Infrared heterodyne spectroscopy can be accomplished by mixing infrared radiation from the source being measured and radiation from a much stronger local oscillator (laser). The signal is detected at the difference frequency. When the local oscillator power is sufficiently large, its shot noise dominates all other detector noise, and the minimum detectable power at this difference frequency can be considered to be of the order of $h\nu \Delta\nu$ for an assumed detector quantum efficiency of one. Abbes and colleagues⁷⁸ analyzed the effect of factors degrading performance from this ideal and concluded that a practical astronomical heterodyne spectrometer would differ only by about a factor of 30. This technique provides a powerful radiometric tool, especially for astronomical observations such as line profile determinations in stellar sources.

Laboratory spectroscopy supporting such astronomical studies has brought into being some very clever high-resolution spectroscopic systems. An example is the Berkeley tunable far-IR laser spectrometer, used for measurements of the spectra of carbon clusters in the 350- to 10-cm^{-1} region.⁷⁹

References

1. R. W. Boyd, *Radiometry and the Detection of Optical Radiation*, John Wiley & Sons, New York (1983).
2. F. Grum and R. J. Becherer, Eds., *Optical Radiation Measurements*, Vols. 1–5, Academic Press, New York (1979–1984).
3. Fred E. Nicodemus, *Radiometry*, Vol. 4, Chap. 8, *Applied Optics & Optical Engineering*, Academic Press, New York (1967).
4. William L. Wolfe, *Radiometry*, Vol. 7, Chap. 5, *Applied Optics & Optical Engineering*, Academic Press, New York (1980).
5. C. L. Wyatt, *Radiometric System Design*, Macmillan, New York (1987).
6. C. L. Wyatt, *Radiometric Calibration: Theory and Methods*, Academic Press, New York (1978).
7. F. E. Nicodemus, "Normalization in radiometry," *Applied Optics* **12**(12), 2960 (1973).
8. F. E. Nicodemus, coeditor, *Self-Study Manual on Optical Radiation Measurements*, NBS Technical Notes 910-1-910-8, U.S. Government Printing Office (1976–1986).
9. J. R. Yoder, Notes of the IEEE April 1966 Foothill Lecture and Techniques, Spring Issue, Barnes Engineering Company, Stamford, CT (1956).
10. J. Guild, "Investigations in absolute radiometry," *Proceedings of the Royal Society of London A* **161**, 1 (1937).
11. E. J. Gillham, "The measure of optical radiation," *Research Applied in Industry* **12**, 404–411 (1959).
12. E. J. Gillham, "Radiometric standards and measurements," *Notes, Applied Science*, National Physics Laboratory, London, England, Vol. 23 (1961).
13. E. J. Gillham, "Recent investigations in absolute radiometry," *Proceedings of the Royal Society of London A* **269**, 240–276 (1962).
14. G. H. C. Freeman and D. H. Nettleton, "Infrared spectral responsivity scales at NPL and the calibration of detectors," *Proceedings of the SPIE* **1191**, 400 (1989).
15. R. J. Phelan, Jr., and A. R. Cook, "Electrically calibrated pyroelectric optical radiation detector," *Applied Optics* **12**, 2494 (1973).
16. J. Geist and W. R. Blevin, "Chopper stabilized null radiometer based upon an electrically calibrated pyroelectric detector," *Applied Optics* **12**, 2532 (1973).
17. E. S. Steeb, Minutes of the CORM-NBS Spring Meeting, General Electric Company, Nela Park, Cleveland, OH (June 1976).
18. E. F. Zalewski, "A modern approach to accurate radiometry," 12e Informal Conference on Photochemistry, National Bureau of Standards, Washington, DC, Paper A1 (June 1976).
19. E. F. Zalewski and M. A. Linda, "Improving the accuracy of radiant power measurements based on photodetector instrumentation," in *Proceedings of the Spring 1976 Symposium*, Bureau of Radiological Health, Rockville, MD (1976).
20. J. Geist, E. F. Zalewski, and A. R. Schaefer, "Spectral response self-calibration and interpolation of silicon photodiodes," *Applied Optics* **19**, 3795 (1980).
21. F. Hengstberger, Ed., *Absolute Radiometry*, especially Chap. 1 by F. Hengstberger, Academic Press, New York (1989).
22. J. D. Simmons, Ed., *NIST Calibration Services Users Guide*, NIST Special Publication 250 (Revised Jan. 1989).
23. E. Scott Barr, "Historical survey of the early development of the infrared spectral region," *American Journal of Physics* **29**, 42 (Jan. 1960).
24. E. Scott Barr, "The infrared pioneers—I. Sir William Herschel," in *Infrared Physics*, Vol. 1, p. 1, Pergamon Press, Elmsford, NY (1961).
25. E. Scott Barr, "The infrared pioneers—II. Macedonio Melloni," in *Infrared Physics*, Vol. 2, p. 67, Pergamon Press, Elmsford, NY (1962).

26. Samuel O. Hoffman, *Physics Review* **XIV**(2), 163–166 (1919).
27. T. F. Johns, "German photoconducting cells for the detection of infra-red radiation," Final Report No. 2, Item No. 9, British Intelligence Objectives Subcommittee (1945).
28. M. Holter, S. Nudelman, G. Suits, W. Wolfe, and G. Zissis, *Fundamentals of Infrared Technology*, 2nd printing, Macmillan, New York (1963).
29. C. T. Due, "Optical-mechanical, active/passive imaging systems," Vol. II, ERIM Report 153200-2-T(II), Environmental Research Institute of Michigan, Ann Arbor, MI (May 1982).
30. D. P. DeWitt and Gene D. Nutter, Eds., *Theory and Practice of Radiation Thermometry*, John Wiley & Sons, New York (1988).
31. W. R. Barron, "Advances in dual-wavelength radiometry," *Sensors*, 15 (Jan. 1990).
32. J. B. McGlynn, "IR imaging radiometer," *Proceedings of the SPIE* **1167** (Aug. 1989).
33. Gene Ihlenfeldt, *Boeing Infrared Sensor (BIRS) Calibration Facility*, pamphlet, Boeing, Seattle, WA (1988).
34. Stephen C. Ebner, LBIR, NIST, Gaithersburg, MD, private communication (May 1990).
35. B. Guenther, J. McLean, M. Leroy, and P. Henry, "Comparison of CNES spherical and NASA hemispherical large aperture integrating sources," *Remote Sensing in the Environment* **31**, 85 (1990).
36. N. E. Tira, J. R. Mahan, and R. B. Lee III, "Dynamic electrothermal model for the Earth Radiation Budget Experiment nonscanning radiometer with applications to solar observations and evaluation of thermal noise," *Optical Engineering* **24**(4), 351 (1990).
37. *Long-Term Monitoring of the Earth's Radiation Budget*, *Proceedings of the SPIE* **1299** (April 1990).
38. "Search and discovery," *Physics Today*, p. 17 (Mar. 1990) and p. 19 (July 1990).
39. G. W. Ashley, "Spectral radiometer for the AMOS 1.6 m telescope," *Proceedings of the SPIE* **430**, 93 (1983).
40. R. A. Sawyer, *Experimental Spectroscopy*, 3rd ed., especially Chap. 4, pp. 75–79, 87, 137, 152, 155, 158, 291, Dover, New York (1963).
41. F. A. Jenkins and H. E. White, *Fundamentals of Optics*, 4th ed., McGraw-Hill, New York (1976).
42. E. Hecht, *Optics*, 2nd ed., Addison-Wesley, Reading, MA (1988).
43. A. Walsh, "Multiple monochromators. 11. application of a double monochromator to infrared spectroscopy," *Journal of the Optical Society of America* **42**, 95 (1952).
44. H. L. Hackforth, *Infrared Radiation*, pp. 209, 211, 214, McGraw-Hill, New York (1960).
45. A. H. Nielsen, "Recent advances in IR spectroscopy," Technical Memo 53-2, Office of Ordnance Research, Durham, NC (Dec. 1953).
46. G. R. Harrison, "The diffraction grating—an opinionated appraisal," *Applied Optics* **12**(9), 2039 (1973).
47. See, for example, *Spectroscopy*, especially issues of May and June, Aster Publishing Corporation, Eugene, OR; *Physics Today Annual Buyers Guide*, 7th ed., American Institute of Physics, New York (Aug. 1990); *Laser Focus World* and LFW's *The Buyers' Guide*, 25th ed., PennWell Publishing Company, Westford, MA (1990); *Photonics Spectra* and *The Photonics Director*, 4 Vols., 36th ed., Laurin Publishing Company, Pittsfield, MA (1990); and *Lasers & Optronics* and L&O's *1990 Buyer's Guide*, Gordon Publications, Morris Plains, NJ (1990).
48. J. W. Robinson, *Atomic Spectroscopy*, Marcel Dekker, New York (1990).
49. E. V. Loewenstein, "The history and current status of Fourier spectroscopy," *Applied Optics* **5**(5), 845 (1966).
50. J. B. Bates, "Fourier transform infrared spectroscopy," *Science* **191**, 31 (Jan. 1976).
51. Janice Connes and Pierre Connes, "Near-infrared planetary spectra by Fourier spectroscopy. 1. instruments and results," *Journal of the Optical Society of America* **56**, 896 (July 1966).
52. J. Kachmarsky, C. Belorgeot, A. Pluchino, and K. D. Moller, "Far-infrared high resolution Fourier transform spectrometer: applications to H₂O, NH₃, NO₂ lines," *Applied Optics* **15**, 708 (Mar. 1976).
53. J. P. Monchalin et al., "Accurate laser wavelength measurement with a precision two-beam Michelson interferometer," *Applied Optics* **20**, 736 (Mar. 1981).
54. *High-Resolution Fourier Transform Spectroscopy*, Optical Society of America 1989 Technical Digest Series, postconference edition (Feb. 1989).
55. J. Strong, *Concepts of Classical Optics*, App. B, p. 382, Freeman Press, San Francisco (1958).

56. M. Françon, *Optical Interferometry*, pp. 98, 99, 202, Academic Press, New York (1966).
57. W. H. Steel, *Interferometry*, pp. 88, 94, 166, 176–177, 201, Cambridge University Press, New York (1967).
58. Defense Electronics, "Battlefield navigation," p. 96 (Oct. 1985).
59. V. Vali and R. W. Shorthill, *Applied Optics* **15**, 1099 (1976).
60. W. K. Burns, "Fiberoptic gyroscopes," *Laser Focus/Electro-Optics*, p. 83 (Feb. 1984).
61. K. W. Meissner, "Interference spectroscopy, part I," *Journal of the Optical Society of America* **31**, 405–413 (1941).
62. G. V. Deverall, K. W. Meissner, and G. J. Zissis, "Selection of optical spacers in Perot-Fabry interferometer," *Journal of the Optical Society of America* **43**, 673 (Aug. 1953).
63. K. W. Meissner and V. Kaufman, "Calcium atomic beam source and interference beyond two-meter retardation," *Journal of the Optical Society of America* **49**, 942 (Oct. 1959).
64. P. Jacquinot, "New developments in interference spectroscopy," in *Reports on Progress in Physics*, Vol. 23, pp. 267–312, American Institute of Physics, New York, and The Institute of Physics and the Physical Society, London, (1960).
65. K. W. Meissner, "Interference spectroscopy, part II," *Journal of the Optical Society of America* **32**, 185 (Apr. 1942).
66. J. E. Mack, D. P. McNutt, F. L. Roesler, and R. Chabbal, "The PEPSIOS purely interferometric high-resolution scanning spectrometer, 1. the pilot model," *Applied Optics* **2**, 873 (Sep. 1963).
67. D. P. McNutt, "PEPSIOS purely interferometric high-resolution scanning spectrometer, II. theory of space ratios," *Journal of the Optical Society of America* **55**, 288 (Mar. 1965).
68. J. O. Stoner, Jr., "PEPSIOS purely interferometric high-resolution scanning spectrometer. III. calculation of interferometer characteristics by a method of optical transients," *Journal of the Optical Society of America* **56**, 370 (Mar. 1966).
69. J. Meaburn, "Nebular Fabry-Perot, PEPSIOS, and SISAM monochromators," *Applied Optics* **12**, 279 (Feb. 1973).
70. H. F. Döbele and J. H. Massig, "Application of a Fabry-Perot spectrometer to the measurement of spectral line shifts much smaller than line width," *Applied Optics* **15**, 79 (Jan. 1976).
71. W. H. Smith, J. Born, W. D. Cochran, and J. Gelfand, "Spectroscopic photoelectric imaging Fabry-Perot interferometer: its development and preliminary observational results," *Applied Optics* **15**, 717 (Mar. 1976).
72. M. J. E. Golay, "Multi-slit spectrometry," *Journal of the Optical Society of America* **39**, 437 (1949).
73. R. D. Swift, R. B. Wattson, J. Decker, Jr., R. Paganetti, and M. Harriet, "Hadamard transform imager and imaging spectrometer," *Applied Optics* **15**, 159 (June 1976).
74. M. R. Querry, "Tunable laser spectroscopy," in *Methods of Experimental Physics*, Vol. 13, Spectroscopy, Part B, D. Williams, Ed., Academic Press, New York (1976).
75. V. S. Letokhov, "Nonlinear high resolution laser spectroscopy," *Science* **190**, 344 (Oct. 1975).
76. A. S. Pine, "Doppler-limited molecular spectroscopy by difference-frequency mixing," *Journal of the Optical Society of America* **64**, 1683 (1974).
77. H. P. Layer, R. D. Deslattes, and W. G. Schweitzer, Jr., "Laser wavelength comparison by high resolution interferometry," *Applied Optics* **15**, 734 (Mar. 1976).
78. M. M. Abbas, M. J. Mumma, T. Kostiuk, and D. Buhl, "Sensitivity limits of an infrared heterodyne spectrometer for astrophysical applications," *Applied Optics* **15**, 427 (Feb. 1976).
79. C. A. Schmuttenmaer et al., "Tunable far-IR spectroscopy of jet-cooled carbon clusters: the ν_2 bending vibration of C_3 ," *Science* **249**, 897 (Aug. 1990).

Index

- Absolute wavelength measurement, 357
- Absorptance, 23, 64, 148
solar absorptance of spacecraft materials, 113
- Absorption, 23, 145, 147, 174
of H_2O , 113
- Absorption, atmospheric, 111
- Absorption bands
of water vapor, 194–195
- Absorption coefficient, 144–146
- Absorptivity, 21, 23
- Aerosols, 199
- Air mass vs solar zenith angle, 154
- Air temperature, 198
- Aircraft, 110–118, 123
- Airglow, 201, 204–210. *See also* Night airglow
- Airy function, 354
- Albedo
earth, 213–218
lunar, 158
- Algae, 259
attenuation coefficients, 262
spectral reflectance, 264
- Alkali halides, spectra, 34
- Anisotropic radiators, 28–29
- Apertures, 64
- Apparent temperature, 139
- Areance, 7
- Artificial sources, 49–135
- Asteroids, 190
- Atmosphere, 151–153
spectral radiance, 217–218
- Atmospheric attenuation, effects on aircraft, 123
- Atmospheric effects, 127
- Atmospheric emission, 195
- Atmospheric particulates, 141
- Atomic spectra, 32–34
Bohr model, 32–33
hydrogen spectra, 33–34
quantum number, 32–33
Sommerfeld model, 32
- Aurora, 200–208
auroral spectra, 201–203
emission, 200
frequency distribution, 204–205
photon emission, 208
photon radiance, 201
spectral radiance, 201, 203
- Auroral zones, 201–202
- Backgrounds. *See also* Infrared backgrounds
from extragalactic sources, 181, 190
galactic, 181, 190–191
sky, 194
terrain, 299–309
- Backscattering, 191, 263
- Band radiance, 6
- BASIC programs, 8, 38–47
- Bidirectional reflectance distribution function (BRDF), 26
- Biological materials. *See* Botanical materials
- Blackbodies, 3, 32, 52–59, 64–65, 79, 139, 146, 180. *See also* Sources
cylindrical, 52–58
goldpoint, 58–59
spectral radiance, 196
variable-temperature, 58–59
- Blackbody (Planckian) functions, 8–21, 38–47
BASIC programs, calculations and formulas, 38–47
contrast, 10–11
conversions
to other geometries, 10
to photons, 9
spectral scale conversions, 9–10
maxima, 11–12
Planck equations, 8, 24–25
power, 12
radiance, 8–9
radiant exitance, 8–9, 12
radiation constants, 9
relative contrast, 10
Stephan-Boltzmann law, 12
total integrals, 12
universal curves and equations, 10–21
Wien displacement law, 11, 15
- Blackbody cavity theory, 52–57
conical cavity, 52
cylindrical cavity, 52, 55–56
DeVos method, 53–57
Gouffé method, 52
spherical cavity, 53, 56
- Blackbody simulators, 57

- Bohr model, 32
 Bolometer region, 175
 Bolometers, 333
 Botanical materials, 277–295. *See also* Algae; Chlorophyll; Leaves; Vegetation
 Brightness temperature, 30–31, 139

 Calibration, 59, 317, 326–331. *See also* Radiometers, calibration of
 absolute, 317
 of spectral irradiance, 62
 of spectral radiance, 61
 of UV sources, 62–63
 Calorimeters, 333
 Candela, 57
 Carbon arc lamps, 77–84
 Carbon dioxide, 35, 111, 195
 Carotenoids, 278, 281
 Celestial background, 160–194
 cosmic microwave background, 165
 in the range 2.0–100.0 μm , 175–176
 in the visible range, 165–167
 Celestial coordinates, 160–165
 circle of celestial latitude, 163
 circle of galactic latitude, 164
 ecliptic, 161
 ecliptic coordinate system, 164
 equatorial coordinate system, 164
 galactic center, 163
 galactic coordinate system, 164–165
 galactic equator, 163
 horizon, 163
 hour circle, 163
 meridian, 163
 north and south celestial poles, 161
 north galactic pole, 163
 north point, 163
 vernal equinox, 161
 vertical circle, 163
 zenith and nadir, 161
 Chinese restaurant system, 7
 Chlorophyll, 261, 263, 278, 281
 Cities, radiance of, 219–220
 Cloud meteorology, 218–230
 cirrus clouds, 218
 noctilucent clouds, 230
 stratospheric clouds, 229–230
 water content, 230
 Clouds
 background radiation, 194–197
 emission, 197
 reflectance, 216
 scattering, 196–197
 sky cover, 230–234
 spectral radiance, 197
 temperature, 197
 Coatings, 64
 Color temperature, 32, 79, 139, 174, 176
 Computer programs, 13, 38–47
 Concentrated arc lamps, 93, 99–100
 Condensation, 150
 Construction materials, 233–234, 247–250
 Contrast, 11
 photon, 18, 20–21
 radiant, 19–20
 relative, 11
 Correlation function, 287, 296–297
 autocorrelation function, 296
 covariance function, 296
 exponential, 287
 lag variable, 287
 scale length, 287
 Whittle, 287
 Cosmic Background Explorer (COBE), 165, 334
 Council for Optical Measurements (CORM), 327
 Cylindrical blackbody, 52–58
 Czerny-Turner mount, 340

 Detectivity of a radiometer, 317, 319–320
 Detector optics, 177
 DeVos method, 53–57
 Dielectric surfaces, 144, 146
 Diffraction, 336–337
 angular dispersion, 337
 Fraunhofer, 337
 gratings, 337
 resolving power, 337
 Distribution temperature, 31, 139
 Doppler line, 37
 Dust, interstellar (IR cirrus), 176, 179–180, 190–194. *See also* Zodiacal radiance
 particle distribution, 193
 particle temperature relation, 192–192
 power spectral densities of, 191
 spectral radiance of, 191–193
 stratospheric particulates, 200
 Earth, 140, 210–230
 albedo, 213–218
 emission, 214
 luminance, 216
 spectral reflectance, 215
 satellite viewing, 210–211
 Earth Radiation Budget Experiment (ERBE), 334
 Earth surface, emission spectra, 213–226
 Ecliptic coordinate system, 177
 Emissance, 21, 23
 Emission, 23, 145–146
 of exhaust plume, 113
 of industrial smokestack, 113
 Emissivity, 23, 27, 145
 blackbody, 52–57
 of common materials, 112
 for a cylindrical blackbody, 56
 directional, 23
 for a spherical blackbody, 56
 hemispherical, 23
 of exhaust gases, 111–115

- hemispherical, 23
- of spacecraft materials, 113
- spectral, 23
- for a spherical blackbody, 56
- total, 23
- weighted, 23
- Emittance, 21. *See also* Radiant exitance
- Enclosed arc and discharge sources (low pressure), 90–93
- Enclosed arc and discharge sources (high pressure), 82–90
- Energy density, 10
- Engine radiation, 113
- Entrance aperture, 317
- Etalons, 354, 359
- Etendue. *See* Throughput
- Evaporation, 150, 246, 257–258
- Exhaust plumes. *See* Gases, exhaust
- Exitance, 5–6, 8, 21, 139, 145–148
- stellar, 174, 180
- Exoatmospheric illuminance, 174
- Exposure, 8
- Extended galactic background, 190–191
- Extragalactic infrared sources, 181, 190
- Fabry-Perot interferometers, 354–359
 - Airy function, 354
 - compound interferometer, 358
 - etalon, 354, 359
 - interference, 356
 - PEPSIOS spectrometer, 359
 - SISAM spectrometer, 359
 - spherical Fabry-Perot interferometer, 358
 - SPIFI interferometer, 359
- Field trials, 129
- Flares, 124–125
- Fluence, 8
- Fluence exposure, 5
- Fluometry, 6
- Flux, 5, 8
- stellar, 180
- Flux density, 5, 29
- Foot-candle, 8
- Fraunhofer diffraction, 337
- Fresnel's law, 143–144
- Full width at half-maximum (FWHM), 37
- Galactic background. *See* Background, galactic
- Galactic infrared point sources, 179–190
 - blackbody spectral exitance, 180
 - number of, 179–180
 - spectral energy distribution of, 179
 - spectral index, 180
 - spectral irradiance, 179–190
- Galaxies, 190–191
- Gases, 32, 34–35
 - exhaust, 110–118, 123
 - hot, 117, 119
 - spectral lines, 35
- Gegenschein, 191
- Glow modulator tubes, 100, 103–105
- Goldpoint blackbody, 59
- Gouffé method, 52, 113
- Gratings, 337–348
 - angular dispersion, 337
 - blazed, 343
 - concave, 342
 - configurations, 337–346
 - diffraction, 337
 - multiple-beam interferometer, 337
 - resolving power, 337
 - slits (grooves), 337
 - unblazed, 337
- Graybodies, 70
 - temperature, 30
- Guns, muzzle flash, 117–121
- Heat exchange, 146–151
- Heat flux, 148–149
- Heat transfer, 148, 150–151, 231
- Helicopters, 124
- Helmholtz reciprocity theorem, 26
- Henry Draper classification, 168
- Hinge point, 259, 262
- Histograms, of terrain backgrounds, 299–309
- Hubble constant, 181
- Hydrogen, 33–34
- Hydrogen and deuterium arc lamps, 103, 107
- Ice, properties of, 271–280
 - brash ice, 276
 - bulk reflectance, 271
 - depth of penetration, 271
 - index of refraction, 271
 - new (clear) ice, 274
 - pancake ice, 277
 - refrozen-slush ice, 276
 - slush curd ice, 276
 - snow ice, 275
 - spectral reflectance, 279–280
- Illuminance, 140
- Incandescent sources, 65, 70–77
- Incidance, 5–6, 8
- Index of refraction, 143–144
- Infrared Astronomical Satellite (IRAS), 177–179, 191–192
- Infrared backgrounds, statistical measures, 285
 - correlation function representation, 287, 296–297
 - nonisotropic correlation functions, 298–299
 - power spectra representation, 297–309
 - probabilistic model, 285–287
 - terrain background statistics, 299–308
- Infrared cirrus, 179
- Infrared image simulation, 130–133

- mathematical model, 130
 - radiance calculation, 131
 - temperature computation, 131
 - thermal model, 130
- Infrared point sources, 179–190
- Infrared radiance map, 130
- Infrared radiometric standards, 60–62
- Infrared radiometry, 331–334
- Infrared simulation and modeling, 128–133
 - of threat signatures, 128
- Instantaneous field of view (IFOV), 140
- Intensity, 5, 8, 113, 140
- Interference, 347
- Interferometers, 347–360
 - Fabry-Perot interferometers, 354–359
 - Mach-Zehnder interferometers, 353–354
 - Michelson interferometers, 347–352
 - multiple-beam, 337, 354–360
 - Sagnac interferometer, 353–354
 - two-beam, 347–353
- Interstellar extinction, 166–167, 181
- Irradiance, 139–140, 151, 174–175, 179–181
- Isotropic disks, 29
- Isotropic radiators, 10, 28

- Jansky, 177

- Kirchhoff's law, 26

- Lambertian radiator. *See* Isotropic radiator
- Lamps, 60–103. *See also* Sources
 - airway beacon lamps, 60
 - argon mini-arc lamps, 62–63
 - bulbs, shapes and sizes, 85
 - calibration of, 63
 - carbon arc lamps, 77–83
 - color temperature standard lamps, 60
 - compact-source arcs, 87–90
 - concentrated arc lamps, 93, 99–100
 - tungsten-arc (photomicrographic) lamps, 93, 99–100, 103
 - zirconium-arc lamps, 93, 102
 - construction of, 88–89
 - deuterium arc lamps, 62–63, 103, 107
 - enclosed arc and discharge sources (high pressure), 82–90
 - capillary mercury-arc lamps, 87
 - compact-source arcs, 87–90
 - Lucalox™ lamps, 85–86
 - mercury-arc lamps, 84–87
 - multivapor-arc lamps, 84
 - short-arc lamp, 89, 91
 - Uviarc™, 84
 - enclosed arc and discharge sources (low pressure), 90–93
 - black-light fluorescent lamps, 91, 93
 - electrodeless discharge lamps, 92–93
 - germicidal lamp, 90–91
 - hollow-cathode lamps, 91, 94–99
 - Pluecker spectrum tubes, 93, 102
 - spectral lamps, 93, 100–101
 - Sterilamp™, 91
 - far-UV sources, 62–63
 - glow modulator tubes, 100, 103–105
 - hydrogen arc lamps, 103, 107
 - incandescent sources, 65, 70–77
 - gas mantle, 73–74
 - globalar, 70, 72, 74
 - Nernst glower, 65, 70–71, 74
 - quartz envelope lamps, 76–77
 - tungsten-filament lamps, 73–77
 - luminous flux standards, 60
 - luminous intensity standards, 60
 - quartz-halogen lamps, 61
 - ribbon filament lamps, 60
 - for scientific purposes, 76
 - solar distribution match, 89
 - spectral transmission of, 63
 - tungsten lamps, 63
- Laser power meters, 333
- Laser sources, 63–64, 66–69
- Laser spectroscopy, 361
- Leaves, 281–284, 286, 288–295
- Light, primary standard, 57–58
 - candela, 57
 - radiator, 57
- Limb brightening, 222
- Limb darkening, 222
- Littrow-type mount, 340–341, 343
- Lorentz line, 37
- LOWTRAN, 153, 159
- Lumen, 7
- Luminance, 6–8
- Lux, 8

- Mach-Zehnder interferometers, 353–354
 - Jamin interferometer, 353–354
- Magnitude, 140
 - photographic, 169
- Magnitudes. *See* Stellar magnitudes
- Materials, emissivity of, 112
- Materials, natural properties, 230–285. *See also* Algae; Biological materials; Construction materials; Ice; Oil; Painted surfaces; Rocks and minerals; Seawater; Snow; Soil and sand; Water
- Materials, thermal properties, 150
- Measurement, 317
- Meteoroid radiation, 210
 - visual magnitude, 210
- Michelson interferometers, 347–352
 - constructive interference, 347
 - Fourier-transform spectroscopy, 351
 - fringe shape, 347
 - fringe visibility, 349
 - interferometer-spectrometer, 350
 - scanning Michelson interferometry, 350
 - step-scanned interferometer, 351
- Mirrors
 - Pfund mirror, 341
- Mixed (Voigt) line, 37

- Molecular rotations, 32, 34
- Molecular spectra of gases, 34–35
 - diatomic molecules, 34–35
 - triatomic molecules, 35
- Molecular vibrations, 32, 34
- Monochromators, 318, 334, 339, 345
 - double-pass, 341–342, 346
 - single-pass, 341
- Moon, 157–159, 163–164
 - illuminance, 157
 - lunar reflectance spectra, 164–165
 - spectral irradiance, 158, 162–163
 - surface emission spectra, 146
 - thermal emission, 159
- Mountains
 - elevation scans, 214
- Multispeed chopper, 64
- Muzzle flash, 117–121
 - intermediate flash, 119
 - secondary flash, 119–120
- Napalm, 125
- National Institute of Standards and Technology (NIST), 58–64, 107, 317
- Natural linewidth, 37
- Natural sources, 137–314
- Nebulae, 176
- Nicodemus system, 7
 - areance, 7
 - pointance, 7
- Night airglow, 204–210
 - frequency distribution, 207
 - photon emission, 208
 - radiance, 207
 - SHARC model, 208–210
 - spectrum, 207, 209
- Night horizon, spectral radiance, 197
- Nitrogen, molecular, 201
- Noise fluctuation, 320
- Nonblackbodies, 59
- Nonisotropic correlation functions, 298–299
- Oils, 265–270, 272
 - emittance, 265, 272
 - extinction coefficients, 265, 267–268
 - index of refraction, 265–267
 - spectral radiance, 265, 268–270
- Optical components, for IRAS, 177
- Optical pyrometry, 318
- Oxygen, 200, 208
- Ozone, 195, 206
- Painted surfaces
 - absorption, 244
 - spectral reflectance, 251–254
- Partial reflectivity, 54
- Particulates, atmospheric, 199–201
 - concentration of, 200
 - light scattering, 200
 - sizes of, 200
 - stratospheric aerosols, 199
- Path radiance, 5
- Phot, 8
- Photographic magnitude, 169, 172–173
- Photometer, 318
- Photometric standards, 60–62
- Photometric terms, 7–8
 - exposure, 8
 - flux, 8
 - illuminance, 8
 - lumen, 7
 - luminance, 8
 - luminous efficacy, 7
 - luminous energy, 8
 - luminous exitance, 8
 - luminous fluence, 8
 - luminous intensity, 8
- Photometry, 57, 318
- Photon (quantum) flux quantities, 6
- Photon exitance, 15, 17–18
- Photons, 12
 - conversion to, 9
- Phycobilins, 278, 281
- Pixel, 140
- Planck formulas, 8, 15, 139, 145
- Planck integration, 22, 24–25
- Planck's radiation law, 59, 174
- Plane mixtures model, 140–141
- Plane stacking reflectance model, 141–142
- Planets, visual magnitudes and color
 - temperatures, 176
- Pointance, 7
- Polarization, 143
- Power, 12, 54–55
 - conservation of, 27
- Power spectra, 297–309
 - break frequency, 297
 - exponential, 297
 - power spectral density, 298–309
 - Whittle, 297
- Predictive models, 108
- Pressure, partial, 147
- Prisms, 335–348
 - Amici prism, 338
 - configurations, 337–346
 - effective aperture, 336
 - half-prisms, 339
 - Pellin-Broca prism, 338
 - resolving power, 336
 - rock salt prism, 340
 - Wadsworth constant-deviation prism-mirror, 338
 - Wernicke prism, 338
 - Young-Thollon half-prisms, 340
 - Zenger prism, 338
- Probabilistic model, 285–287

- Quantity, 5, 8
- Quantum number, 32–33
- Radiance, 5–6, 8, 10, 28–29, 139, 145
 - band radiance, 6
 - blackbody, 53–55
 - path radiance, 5
 - spectral radiance, 6
 - steriscent, 5
 - units in astronomy, 167
 - visible radiance (luminance), 6
- Radiance temperature, 30–31
- Radiant energy, 3
- Radiant exitance, 10, 12, 13–17, 28–29
- Radiant intensity, 6, 113
- Radiation, baseline standard, 58–59
 - goldpoint blackbody, 58–59
- Radiation constants, 9
- Radiation geometry, 27–30
 - anisotropic radiators, 28–29
 - configuration factors, 29
 - angle factors, 29
 - geometric configuration factor, 29
 - interaction factors, 29
 - isotropic disks, 29
 - isotropic radiators, 28
 - radiative transfer equation, 27–28
- Radiation processes, 32–37
- Radiation reference level, 317, 319–320
- Radiation temperature, 30
- Radiation theory, 3–48
- Radiation thermometer, 333
- Radiative transfer, 27–28
 - throughput, 28
- Radiative transfer modeling, 140–151
 - plane mixtures model, 140–141
 - plane stacking reflectance model, 141–142
 - thermal modeling, 145–151
 - vegetative canopy models, 145
 - wet-dry plane stacking model, 144
- Radiators, properties of, 21–27. *See also*
 - Blackbodies
 - absorptance, 23
 - absorption, 23
 - absorptivity, 21, 23
 - emission, 23
 - emissivity, 21, 23, 27
 - emittance, 23
 - Kirchhoff's law, 26
 - nomenclature, 21–22
 - reflectance, 26
 - reflection, 26
 - reflectivity, 21, 26–27
 - transmission, 26–27
 - transmissivity, 21
- Radiometers, 318–334
 - absolute radiometers, 325–327
 - calorimeters, 333
 - components
 - detectors, 318–319
 - electronics, 319
 - optics, 319
 - dual-band, 333–334
 - ideal radiometers, 321–324, 330
 - imaging, 333
 - laser power meters, 333
 - normalization, 323–324
 - performance characterization
 - detectivity, 320
 - radiation reference level, 318
 - responsivity, 319–324
 - scanning, 140–141, 333
 - spectral radiance, 322–324
 - spectral responsivity, 318–324
- Radiometers, calibration of, 326–332
 - absolute radiometer, 325, 327
 - calibration systems, 334
 - collimator, 328
 - distant extended source, 328–332
 - distant point source, 328–332
 - electrically calibrated radiometer, 327
 - graybody, 326
 - history of, 327–328
 - Jones method, 328–329
 - near extended source, 329
 - near small source, 329
 - power responsivity, 328
 - reference radiation level, 325–326
 - ac radiometer, 325–326
 - blackened chopper, 325
 - chopper blade, 325
 - chopper mirror, 325–326
 - chopping system, 325
 - dc radiometer, 325
 - silicon photodiode standard detector, 327
 - standard receiver, 327
 - standard source, 327
- Radiometric curves, 13–21
- Radiometric measurements, 317
 - of a distant source, 317
- Radiometric symbols, nomenclature, and units, 3–8, 21, 23, 51, 167, 318–322
- Radiometric temperature, 30–32
 - color temperature, 32
 - for colored bodies, 30
 - distribution temperature, 31
 - for graybodies, 30
 - radiance (brightness) temperature, 30–31
 - radiation temperature, 30
 - ratio temperature, 31
- Radiometric terms, 5
 - exitance, 5
 - fluence exposure, 5
 - flux, 5
 - flux density, 5
 - incidence, 5
 - intensity, 5
 - quantity, 5
 - radiosity, 5
 - sterance, 5
 - steriscent, 5–6
- Radiometric transfer, 29
- Radiometric units, in astronomy, 167
- Radiometry, 315–364

- infrared radiometry, 331–334
- nomenclature, 318
- Radiometry, parameters
 - field of view, 321
 - frequency response, 321
 - incident flux, 319
 - irradiance, 319
 - noise fluctuation, 320
 - output signal, 319
 - peak spectral responsivity, 324
 - radiance, 320
 - radiance spectral responsivity, 321
 - reference irradiance level, 320
 - responsivity normalization constant, 321
 - spatial dependency, 321
 - spectral dependency, 321
 - spectral response, 321
 - spectral responsivity, 321–322
 - temporal frequency bandwidth, 321
 - throughput, 323
- Radiosity, 5
- Ratio temperature, 31
- Rayleigh, 167
- Rayleigh criterion, 336
- Reference radiation level, 317, 319, 325–326
- Reflectance, 26, 139, 142–146
 - BRDF, 26
 - bulk, 142–144
 - surface, 142–144
- Reflection, 26
- Reflectivity, 21, 26–27
 - bihemispherical, 26
 - diffuse, 26
 - hemispherical, 27
 - partial, 54
- Relative contrast, 11
- Relative humidity, 147
- Resolution, 318
- Responsivity normalization constant, 321
- Responsivity of a radiometer, 317, 319
- Reststrahlen bands, 144
- Rocks and minerals
 - spectral emissivity, 230–233, 246
 - spectral radiance, 218
 - spectral reflectance, 235–239, 241–246
- Roland mounting, 342
- S_{10} unit, 167
- Sagnac interferometer, 353–354
- Satellites
 - earth observations, 210–213
 - path length, 212
- Scanning radiometers, 140–141, 333
- Scattering, 143
 - from atmospheric particulates, 200
 - by clouds, 230
 - of solar radiation, 194–196
 - solar scattering angle, 213
 - of vegetation, 281
- Sea surface, 254–258
 - geometry of, 254
 - photographic reflectance, 256
 - radiance, 256
 - reflectance, 254, 257
 - spectral radiance, 257–258
 - temperature distribution, 257–258
- Seawater, 254–265
 - absorption coefficient, 256, 258
 - bulk reflectance, 262
 - spectral irradiance, 260
 - spectral reflectance, 261
- Shot noise, 361
- Signal-to-noise ratio, 318
- Simulation, 128–133
 - environmental conditions, 130
 - target/background geometry, 130
 - temperature prediction, 130
- SIRIM, 130–133
- Sky, 194–210
 - clear sky, 194–198
 - overcast sky, 199
 - particulate statistics, 199–200
 - sky cover, 230–234
 - spectral apparent temperature, 247–249
 - spectral radiance, 196–198, 220
 - thermal radiation, 199
- Skylight, 147
- Snell's law, 26
- Snow, properties of, 271–278
 - depth of penetration, 272–273
 - extinction rate, 271
 - free-water absorption, 273
 - reflectance, 273–278
 - reflectance and emission model, 272
- Soil and sand
 - spectral radiance, 218–219, 221
 - spectral reflectance, 230, 235–240
- Solar circle, 190
- Solar flux, 192
- Solar radiation, 151–162, 194–199
 - exoatmospheric, 151
 - scattering, 194–199
 - terrestrial, 151–152
- Solar scattering, 195–196
 - scattering angle 213
- Solar spectral irradiance, 152–162
- Solids, spectra, 36
- Sommerfeld model, 32
- Sources, artificial, 49–135. *See also* Lamps
 - activated phosphor sources, 108
 - calibration of, 59
 - carbon arc, 77–84
 - concentrated arc lamps, 93, 99–100
 - enclosed arc and discharge sources (low pressure), 90–93
 - enclosed arc and discharge sources (high pressure), 82–90
 - far-UV sources, 62–63
 - field (man-made) targets, 108–127
 - glow modulator tubes, 100, 103–105
 - hydrogen and deuterium arcs, 103, 107

- incandescent sources, 65–77
- laboratory sources, commercial, 64–108
- laboratory sources, standard, 52–64
- laser, 63–69
- light-emitting diodes, 108
- symbols, nomenclature and units, 51
- Sources, natural, 137–314. *See also* Aurora; Earth; Ice; Moon; Night airglow; Snow; Stars; Sun
 - extragalactic infrared sources, 181–190
 - galactic infrared point sources, 179–181
 - idealized sources, 139
 - ideal diffuse source, 139
 - ideal specular (mirror) surface, 139
 - isotropic point source, 139
 - Lambertian sources, 139
 - spectral energy distribution of, 179–180
- Spacecraft materials, emissivity of, 113
- Spectra
 - atomic, 32–34
 - molecular (gases), 34–36
 - solids, 36
- Spectral emissivity, 145
- Spectral exitance, 145–146
- Spectral index, 180
- Spectral line shapes, 36–37
 - Doppler line, 37
 - Lorentz line, 37
 - natural linewidth, 37
 - mixed (Voigt) line, 37
- Spectral line shifts, 359
- Spectral luminous efficiency, 174
- Spectral photon contrast, 20–21
- Spectral photon exitance, 17–18
- Spectral radiance, 6
- Spectral radiant contrast, 19–20
- Spectral radiant exitance, 8
 - vs dimensionless frequency, 16
 - vs wave number, 14–16
 - vs wavelength, 14–15
- Spectral reflectance, of materials in the near-UV/VIS, 114
- Spectral weighting function, 6
- Spectrometers, 146, 263, 338–362. *See also* Gratings; Interferometers; Prisms
 - Bunsen-Kirchhoff, 338
 - coding masks, 360
 - cw difference-frequency spectrometer, 361
 - Eagle, 343–344
 - Ebert-Fastie, 343, 345
 - examples of, 348
 - Hadamard transform spectrometer, 361
 - heterodyne spectrometer, 361
 - high altitude, 201–202, 207
 - imaging, 361
 - Littrow, 340–341, 343
 - mirror, 340–341
 - Paschen-Runge, 343
 - Pfund, 341, 343, 345
 - single-beam double-pass, 339, 342
 - tunable far-IR laser spectrometer, 362
 - unicam prism-grating, double-monochromator, 346
 - Wadsworth, 343–344
- Spectroradiometers, 333–348
 - AMOS, 334
 - components, 334–335
 - diagram of, 335
 - examples of, 348
 - gratings, 337–347
 - imaging, 333
 - prisms, 335–347
- Spreadsheets, 19, 22, 24–25
- Standards, 57–64
 - baseline standard of radiation, 58–59
 - goldpoint blackbody, 58–59
 - variable-temperature radiator, 58–59
 - color temperature standard lamps, 60
 - far-UV radiometric sources, 62–63
 - at high-temperatures, 80
 - infrared radiometric standards, 60–62
 - spectral irradiance lamps, 61
 - spectral radiance ribbon filament lamps, 61
 - laser sources, 63–64, 66–69
 - photometric standards, 60–62
 - airway beacon lamps, 60
 - luminous flux standards, 60
 - luminous intensity standards, 60
 - primary standard of light, 57–58
 - candela, 57
 - working standards of radiation, 59
- Standards, radiometric, 317, 326–332
- Stars, 140, 165–194
 - concentration of, 169, 172–173
 - number of, 167–171
 - spectral classification of, 167–170
 - spectral irradiance of, 174–175
- Stellar magnitudes, 165–176
 - absolute magnitude, 166
 - apparent magnitude, 166
 - infrared magnitude, 175
 - interstellar extinction, 166–167
 - photographic magnitude, 169, 171
 - visual magnitude, 166, 174–176
 - zero magnitude spectral flux density, 166
- Stellar radiation, spectral distribution, 173
- Stellar spectral classes, 167–173
- Stephan-Boltzmann law, 12
- Sterance, 5–6, 8
- Steriscent, 5–6
- Stratospheric aerosols, 199
- Subscripts, 6
 - band radiance, 6
 - photon (quantum) flux quantities, 6
 - spectral radiance, 6
 - visible radiance, 6
- Sun, 151–162
 - declination angle, 213–214
 - elevation angle, 213
 - spectral distribution curves, 154
 - spectral irradiance, 155–162
 - zenith angle, 154

- Sunlight, 147, 191
- Suprasil™, 107
- Surface exitance, 148
- Surface radiance, 217–226
- Surface temperature, 146–151
- Talbot, 8
- Target radiation, 108–127
 - aircraft, 110–118, 123
 - vehicles, 108–111
- Target-background contrast, 127
- Temperature, 145. *See also* Heat exchange
 - apparent, 139
 - blackbody, 57
 - brightness, 30–31
 - color, 32, 79, 139, 176
 - colored body, 30
 - contrast, 13
 - distribution, 31
 - graybody, 30
 - predicting, 130
 - radiance, 30–31
 - radiometric, 30–32
 - steady-state, 148
 - surface, 146–151
- Terrain background statistics, 299–308
- Thermal emission, 145–146, 175
- Thermal imagers, 333
- Thermal images
 - of aircraft, 124
 - of naval vessels, 126–127
 - of surface vehicle, 122
- Thermal inertia, 150
- Thermal modeling, 145–151
- Thermal properties of materials, 150
- Threat surrogate, 129
- Total internal reflection, 144
- Transmission, 26–27
- Tropopause, 218, 229
- Tungsten-filament lamps, 73–76
- Turbojet engine, diagram of, 116
- Twyman-Green interferometer, 352–353
 - Martin-Watt-Weinstein interferometer, 352
- Williams interferometer, 352–353
- U.S. Standard Atmosphere, 153–154
- Vegetation, 145, 281–284, 286–295
 - spectral radiance, 218–219
 - vegetative canopy model, 145
- Vehicles, 108–111
- Visible radiance, 6
- Volcanic magma, 151
- Voxel, 132
- Water, 35, 150, 245
 - condensed, 200
- Water, optical properties of, 246, 254–265. *See also* Seawater; Water vapor
 - in the solar range, 258–265
 - hinge point, 259, 262
 - reflectance, 259
 - spectral absorption coefficient, 258–259
 - spectral attenuation coefficient, 258–260
 - spectral irradiance, 260
 - in the thermal range, 246
 - absorption, 256
 - absorption coefficient, 246, 255
 - emissivity, 255
 - heat exchange, 246
 - indices of refraction, 255
 - reflectance, 255
 - reflection, 255
 - subsurface scattering, 246
 - transmittance, 255
- Water vapor, 111, 113
 - absorption bands, 194–195
- Wave number, 9
- Weapons sensor, simulation of, 128
- Wet-dry plane stacking model, 144
- Wien displacement law, 11, 15, 53
- Yellow substance, 259, 264–265
- Zenith sky spectra, 197–198, 203
- Zodiacal radiance, 191–194